

Loughborough University  
Institutional Repository

---

*Optical analysis of  
multi-stream GDI sprays  
under various engine  
operating conditions*

This item was submitted to Loughborough University's Institutional Repository by the/an author.

**Additional Information:**

- A Doctoral Thesis. Submitted in partial fulfillment of the requirements for the award of Doctor of Philosophy of Loughborough University.

**Metadata Record:** <https://dspace.lboro.ac.uk/2134/8503>

**Publisher:** © Mehdi Mojtabi

Please cite the published version.

This item was submitted to Loughborough's Institutional Repository (<https://dspace.lboro.ac.uk/>) by the author and is made available under the following Creative Commons Licence conditions.



**CC creative commons**  
COMMONS DEED

**Attribution-NonCommercial-NoDerivs 2.5**

**You are free:**

- to copy, distribute, display, and perform the work

**Under the following conditions:**

**BY:** **Attribution.** You must attribute the work in the manner specified by the author or licensor.

**Noncommercial.** You may not use this work for commercial purposes.

**No Derivative Works.** You may not alter, transform, or build upon this work.

- For any reuse or distribution, you must make clear to others the license terms of this work.
- Any of these conditions can be waived if you get permission from the copyright holder.

**Your fair use and other rights are in no way affected by the above.**

This is a human-readable summary of the [Legal Code \(the full license\)](#).

[Disclaimer](#) 

For the full text of this licence, please go to:  
<http://creativecommons.org/licenses/by-nc-nd/2.5/>

# **Optical Analysis of Multi-Stream GDI Sprays under Various Engine Operating Conditions**

**by**

**Mehdi Mojtabi**

Submitted in partial fulfilment of the requirements for the award of  
Doctor of Philosophy of Loughborough University



April 2011

© Mehdi Mojtabi 2011

### **Abstract**

The design and optimisation of a modern gasoline direct injection (GDI) engine requires a thorough understanding of the fuel sprays characteristics and atomisation process. Therefore this thesis presents a detailed optical analysis of atomisation, penetration and interaction of multi-stream GDI sprays under engine relevant pressures and temperatures. The characteristics of the fuel spray in a

GDI engine have a great influence on the fuel-air mixing and combustion processes as fuel injectors must provide adequate atomisation for vaporisation of the fuel to take place before combustion is initiated, whilst also avoiding spray impingement on the cylinder walls or piston crown.

In this study multi-stream injectors, to be used within GDI engines, are quantified using Laser Doppler Anemometry (LDA) on an atmospheric bench. This process allowed for highly detailed spray analysis of droplet velocities and diameter at precise locations, using a three dimensional traverse, within the injector spray. The aim of the study was to analyse plume interaction between separate plumes of multi-stream injectors. Three multi-stream injectors were subjected to testing; two six-hole injectors and one three-hole injector. The injectors differed by having different distances between the plumes. The effect of fuel type on the liquid break-up and atomisation was investigated using Phase Doppler Anemometry (PDA) and Mie imaging.

Mie imaging was also performed to capture images of fuel from a multi-stream injector as it was sprayed into a pressure chamber which was used to recreate the conditions found in an engine likely to cause flash boiling. In total, five variables were investigated: fuel pressure, ambient pressure, ambient temperature, fuel composition and injector geometry.

Once processed, the recorded images allowed measurement of spray tip penetration and cone angle. Qualitative data on the change in shape of the spray was also available.

The results showed that flash boiling has potential to reduce droplet diameters and improve fuel vaporisation, however, the associated change in spray shape must be taken into account to avoid problems with spray impingement.

Keywords: Gasoline Direct Injection, multi-stream injector, atomisation, penetration, cone angle, Mie imaging, Phase Doppler Anemometry, flash boiling.

## Publications

Y. P. Razi, **M. Mojtabi**, K. Maliwan, M.C. Charrier and A. Mojtabi, “*A dynamical model for studying the stability of thermo-solutal convection under the effect of vertical vibration*”, International Conference on Multibody Systems, Nonlinear Dynamics, and Control, Sept 24-28, 2005, Long Beach CA, USA

**Proceedings of the ASME** International Design Engineering Technical Conferences and Computers and Information in Engineering Conference, Vol 6, Pts A-C, Pages: 53-62, Published: 2005

G.Wigley, **M.Mojtabi**, M.Williams, G.Pitcher and H.Nuglisch, “*The Effect of Fuel Properties on Liquid Breakup and Atomisation in GDI Sprays*”, ICLASS 2006, 10<sup>th</sup> International Congress on Liquid Atomization and Spray Systems, Aug 27-Sept 1, 2006, Kyoto, Japan

P.Stansfield, **M.Mojtabi**, Dr. G.Wigley and G.Pitcher, “*GDI spray propagation under a variety of ambient and engine conditions*”, LTT 2007, Haus der Technik, 8<sup>th</sup>.International Congress-Engine Combustion Processes, March 15-16, 2007, Munich, Germany

**M. Mojtabi**, N. Chadwick, G. Wigley and J. Helie, “*The Effect of Flash Boiling on Breakup and Atomisation in GDI Sprays*”, ILASS 2008, 22<sup>nd</sup> European Conference on Liquid Atomization and Spray Systems, Sept 8-10, 2008, Como Lake, Italy

A. Schmid, B. Schneider, K. Boulouchos, **M. Mojtabi** and G. Wigley, “*Experimental investigation on the spray behaviour for a hollow cone piezo injector with a multiple injection strategy*”, ILASS 2010, 23<sup>rd</sup> European Conference on Liquid Atomization and Spray Systems, Sept 2010, Brno Czech Republic

R. Rothondi, J. Hélie, C. Léger, **M. Mojtabi** and G. Wigley, “*Multi-hole gasoline direct injection spray plumes*”, ILASS 2010, 23<sup>rd</sup> European Conference on Liquid Atomization and Spray Systems, Sept 2010, Brno Czech Republic

**M. Mojtabi**, G. Wigley, J. Jedelsky and J. Hélie, “*A Comparison between One and Two Component Velocity and Size Measurements in a Dense Spray*”, ILASS 2010, 23<sup>rd</sup> European Conference on Liquid Atomization and Spray Systems, Sept 2010, Brno Czech Republic

### **Acknowledgments**

First I would like to give very warm thanks to Dr. Graham Wigley for all his support and guidance during the five years I spent under his supervision at Loughborough University. Many thanks for enduring my French accent as well as my little lack of punctuality, and for giving me the opportunity to attend meetings and conferences all over Europe. It gave me a more than welcome rest from the lovely daily English weather and food.

I would also like to thanks Dr Jerome Helie from Continental Automotive for his scientific support, for hosting me many times in Toulouse and for giving me access to very useful data.

Next comes a list of people without which my experimental work would not have been possible. First Graham Pitcher for his tool box, his magical window cleaner and more particularly for his legendary good mood. Then all the departmental technical staff with a special thanks to Graham Smith, Adrian Broster, Steve Taylor and Steve Horner.

Also, many thanks to all the PhD students from my office for their friendly support, in particular, Dr. Paul Greenwood, Dr. Paul Osei-Owusu, Dr Pratap Rama, Dr Phil Stansfield and soon to be doctor Samuel Cruz-Manzo, and to all the members of the volleyball team and especially coach Phil Cobb for giving me the opportunity to let off steam after work.

Finally, and most importantly, my biggest thanks go to my parents and my brother for their limitless support and their regular visits at Loughborough bringing along with them some of south of France culinary warmth.

---

**Contents**

**Abstract..... i**

**Publications..... ii**

**Acknowledgments.....iii**

**Contents.....iii**

**List of Figures.....vii**

**List of Tables .....xiv**

**Nomenclature .....xv**

**1. Introduction ..... 1**

    1.1 Study Definition ..... 1

    1.2 Aims ..... 2

    1.3 Motivation and Relevance ..... 3

    1.4 Bio-Fuels..... 6

    1.5 GDI Engines..... 8

**2. Injection Process and Spray Characteristics .....13**

    2.1 Fuel Break-up and Atomisation .....13

    2.2 Spray Characteristics .....28

    2.3 Fuel Effects .....31

    2.4 Fuel Comparison.....37

    2.5 Gasoline Direct Injection .....39

        2.5.1 Stratified Mode .....41

        2.5.2 Homogenous Mode .....46

        2.5.3 Downsizing a Gasoline Engine Using Turbocharging with Direct Injection.....56

        2.5.4 Controlled Auto-Ignition .....57

        2.5.5 High Pressure Stratified Start .....58

        2.5.6 Homogenous Split Injection .....60

        2.5.7 GDI Injectors .....63

        2.5.8 Injector Parameters and External Conditions.....72

<b>3. Flash Boiling.....</b>	<b>85</b>
3.1 Flash Boiling Effect on Fuel Sprays.....	85
3.2 GDI Applications .....	91
<b>4. Experimental Techniques and Facilities.....</b>	<b>102</b>
4.1 Experimental Techniques.....	102
4.1.1 Shadowgraphy and Mie Scattering Imaging.....	102
4.1.2 Laser Doppler Anemometry.....	105
4.1.3 Phase Doppler Anemometry.....	106
4.2 Experimental Facilities .....	108
4.2.1 Atmospheric Bench .....	110
4.2.2 Pressure Chamber .....	116
<b>5. Preliminary Study: Spray Targeting Tool .....</b>	<b>135</b>
5.1 Introduction .....	135
5.2 Previous Spray Impact Tool .....	136
5.3 Hypothesis .....	137
5.4 IMPACT Tool.....	137
5.5 Computation Algorithm Description .....	143
5.6 Spray morphology integration.....	145
5.7 An Example of IMPACT Utilisation .....	150
<b>6. Results: Atmospheric Bench.....</b>	<b>154</b>
6.1 Pressure Swirl Injector .....	159
6.1.1 Influence of Injection Pulse Width.....	159
6.1.2 Influence of Fuel Properties.....	161
6.1.3 Summary.....	173
6.2 Multi-Hole Injector .....	174
6.2.1 Plume Interactions.....	174
6.2.2 Radial Traverse Scan .....	181
6.2.3 Circumferential Traverse Scan .....	194



<b>7. Results: Pressure Chamber</b> .....	<b>207</b>
7.1 Over-Atmospheric .....	207
7.1.1 Intensity Contour Analysis .....	210
7.1.2 Injector Analysis .....	212
7.1.3 Backpressure Analysis .....	221
7.1.4 Temperature Analysis.....	225
7.1.5 Fuel Pressure Analysis .....	232
7.1.6 Data Manipulation and Analysis.....	237
7.1.7 Summary .....	248
7.2 Sub-Atmospheric.....	253
7.2.1 Experimental Configuration .....	257
7.2.2 Qualitative Analysis .....	259
7.2.3 Quantitative Analysis .....	263
7.2.4 Summary .....	273
<b>8. Conclusions and Recommendations for Future Work .....</b>	<b>275</b>
8.1 Summary.....	275
8.1.1 IMPACT Tool.....	276
8.1.2 Plume to Plume Interactions.....	277
8.1.3 Flash Boiling.....	280
8.2 Recommendations for future work.....	283
8.2.1 Rigs.....	283
8.2.2 Imaging .....	283
8.2.3 PDA.....	284
8.2.4 Injectors.....	286
8.2.5 Fuels .....	286
<b>Bibliography .....</b>	<b>287</b>
<b>Appendices.....</b>	<b>312</b>
Appendix A D2 law of droplet evaporation.....	312
Appendix B Penetration of a single droplet in air .....	314

Appendix C	Hiroyasu model .....	318
Appendix D	Geometrical characteristics and functioning of Continental Automotive second generation multi-stream injectors.....	319
Appendix E	IMPACT tool algorithm .....	321
Appendix F	IMPACT results accuracy.....	325
Appendix G	Spray Predictions as a Function of Temperature.....	326
Appendix H	Technical drawing of the HPHT cell.....	330
Appendix I	Technical drawings of the injector housing .....	331

## List of Figures

Figure 1.1: Progress towards international CO <sub>2</sub> emissions targets <sup>[4]</sup>	4
Figure 1.2: Variation in crude oil prices from 1986-2010 <sup>[7]</sup>	6
Figure 1.3: In-cylinder air flow structures	9
Figure 1.4: Three common spray guiding techniques	11
Figure 2.1: Spray Parameter Interactions	14
Figure 2.2: Disintegration of sheet <sup>[18]</sup>	15
Figure 2.3: Ohnesorge chart for break-up regimes	17
Figure 2.4: Distribution of instantaneous vorticity fields in an axis plane <sup>[28]</sup>	22
Figure 2.5: Diagram of collision regimes: (a) Bouncing; (b) Coalescence; (c) Reflexive separation; (d) Stretching separation	27
Figure 2.6: Spray angle and penetration illustration for a multi-hole injector	29
Figure 2.7: Variation of viscosity with temperature for air and various fuel vapours <sup>[17]</sup>	31
Figure 2.8: Variation of fuel vapour density with temperature <sup>[17]</sup>	33
Figure 2.9: Surface tension-temperature relationship for hydrocarbon fuels of varying relative densities <sup>[17]</sup>	34
Figure 2.10: Comparison of acetone and cyclohexanone spray distributions <sup>[45]</sup>	35
Figure 2.11: Flow field maps for different fuels for a pressure swirl injector <sup>[51]</sup>	38
Figure 2.12: Operating modes of GDI engine <sup>[55]</sup>	40
Figure 2.13: Spray guided	42
Figure 2.14: Wall guided	43
Figure 2.15: Air guided	43
Figure 2.16: Model of GDI Application Parameter on Engine Performance and Emissions <sup>[60]</sup>	50
Figure 2.17: HC emission production for stratified start and homogenous start <sup>[66]</sup>	59
Figure 2.18: Duration of injection required for safe starting with different injector strategies with E100 fuel <sup>[69]</sup>	61
Figure 2.19: Injector driver dynamics <sup>[2]</sup>	65
Figure 2.20: The six different types of injectors used in GDI engine design <sup>[2]</sup>	66
Figure 2.21: Schematic of a solenoid actuated injector <sup>[15]</sup>	69
Figure 2.22: Schematic of a piezoelectrically actuated injector <sup>[2]</sup>	70
Figure 2.23: Piezoelectrically actuated injector	70
Figure 2.24: Image of multi-hole injector tip	71
Figure 2.25: CCD shadowgraph image of a symmetrical multi-hole injector spray	71
Figure 2.26: Multi-stream nozzle hole length and diameter	72
Figure 2.27: Effect of $l_0/d_0$ and jet velocity on break-up length for low ambient pressures (Hiroyasu et al. <sup>[72]</sup> )	73
Figure 2.28: Effect of $l_0/d_0$ and jet velocity on break-up length for high ambient pressures (Hiroyasu et al. <sup>[72]</sup> )	73
Figure 2.29: Influence of ambient pressure on break-up length (Hiroyasu et al. <sup>[72]</sup> )	74
Figure 2.30: Influence of Reynolds number and nozzle $l_0/d_0$ ratio on spray angle	77

Figure 2.31: Relationship between $D_{32}$ spray surface area and number of drops <sup>[2]</sup>	81
Figure 3.1: Break-up caused by bubble disruption <sup>[98]</sup>	90
Figure 3.2: Illustration of two-phase region	91
Figure 3.3: Flash boiling process <sup>[102]</sup>	91
Figure 3.4 – Side-view and view from beneath of a multi-hole injector during flash boiling <sup>[87]</sup>	92
Figure 3.5: Spray at room temperature.	93
Figure 3.6: Spray at 153°C.	93
Figure 3.7: Effects of flash boiling <sup>[87]</sup>	94
Figure 3.8: Comparison of measured smoke and modelled piston impingement <sup>[104]</sup>	95
Figure 3.9: Jet types dependence on nozzle (a) bubbly flow, (b) slug flow and (c) annular flow patterns <sup>[106]</sup>	97
Figure 3.10: Effect on operation of a multi-hole injector for four levels of ambient backpressure. Six-hole nozzle, 50° nozzle angle, indolene fuel, temperature 90°C, injection pressure 11MPa, fuel injected 10mg per injection <sup>[2]</sup>	100
Figure 4.1: Schematic of back lit imaging system (shadowgraphy)	103
Figure 4.2: Schematic of Mie imaging system	104
Figure 4.3: Schematic of LDA system	105
Figure 4.4: Schematic of PDA data acquisition	107
Figure 4.5: Atmospheric spray bench <sup>[82]</sup>	108
Figure 4.6: Pressure chamber	109
Figure 4.7: Single cylinder optical research engine <sup>[82]</sup>	109
Figure 4.8: Atmospheric spray rig injector mounts, traverse, extractor and imaging arrangement	110
Figure 4.9: Example of injector orientation for 6 hole symmetrical multi-stream injector	111
Figure 4.10: Schematic of optical layout of the LDA=PDA system <sup>[112]</sup>	113
Figure 4.11: Geometry of the beam expander – bragg cell unit <sup>[112]</sup>	115
Figure 4.12: Sectional view and photograph of HPHT cell	117
Figure 4.13: CCD and colour scaled images of a pressures swirl injector from existing design of HPHT cell <sup>[114]</sup>	118
Figure 4.14: Table design	119
Figure 4.15: Insulation of HPHT cell	119
Figure 4.16: Photograph of initial HPHT cell experimental set-up	120
Figure 4.17: Schematic of HPHT cell equipment	121
Figure 4.18: Modified HPHT cell experimental set-up	123
Figure 4.19: Close up view of the modified HPHT Cell	123
Figure 4.20: HPHT cell equipment schematic	124
Figure 4.21: HPHT equipment layout	125
Figure 4.22: Close-up of HPHT cell	126
Figure 4.23: Injector orientation schematic	126
Figure 4.24: HPHT cell modifications	127
Figure 4.25: Injector mounting modification	128

Figure 4.26: PicoScope screenshot _____	128
Figure 4.27: Addition of insulating foam _____	129
Figure 4.28: Cone angle at 20mm downstream for a 60°C multi-hole injector _____	132
Figure 4.29: Spray tip penetration for a 60°C multi-hole injector – 2ms ASOS _____	134
Figure 5.1: IMPACT tool presentation _____	138
Figure 5.2: Point analysis mode graphic user interface _____	139
Figure 5.3: Point analysis mode graphic window for a piezo injector _____	140
Figure 5.4: Point analysis mode graphic window for a pressure swirl injector _____	141
Figure 5.5: Point analysis mode graphic window for a multi streams injector _____	141
Figure 5.6: The three versions of IMPACT _____	142
Figure 5.7: Spray morphology definition _____	146
Figure 5.8: Jet contour definition for morphology integration _____	147
Figure 5.9: Multi-stream injector morphology in IMPACT 2 _____	147
Figure 5.10: Impact position calculation for one time step _____	148
Figure 5.11: Impact position calculation for the whole injection period _____	148
Figure 5.12: Impact ratio calculation _____	149
Figure 5.13: Engine top-view with the orientation of the 6 holes multi-stream injector _____	150
Figure 5.14: Orientation of the 6 holes multi-stream injector _____	151
Figure 5.15: IMPACT result window _____	152
Figure 5.16: IMPACT graphic window (second version of the program including the spray morphology) _____	153
Figure 6.1: Pressure swirl injector nozzle cross-section _____	154
Figure 6.2: Fuel Injector Dynamics _____	155
Figure 6.3: Swirl and Multi-hole Injectors at different chamber pressures <sup>[120]</sup> _____	157
Figure 6.4: Potential variations within multi-hole injectors <sup>[120]</sup> _____	158
Figure 6.5: Comparison of the spray penetration for different injector pulse width _____	160
Figure 6.6: Comparison of the spray angle for different injector pulse width _____	160
Figure 6.7: Mean Image for Gasoline at 2.12 ms _____	162
Figure 6.8: Axial (upper) and Radial (lower) Penetration Profiles _____	163
Figure 6.9: PDA sample number distributions in sector 69 _____	165
Figure 6.10: Axial Velocity Profiles 40 mm below the nozzle _____	166
Figure 6.11: Flow field map at Z = 40 mm and Time 2.74 ms for all fuels _____	168
Figure 6.12: Flow field map at Z = 40 mm and Time 2.98 ms for all fuels _____	168
Figure 6.13: Velocity and drop-size profiles at Z = 40 mm and time 2.98 ms _____	170
Figure 6.14: Drop-size Profiles 40 mm below the nozzle _____	172
Figure 6.15: Air Entrainment due to spray front vortex _____	174
Figure 6.16 – Plume interaction from multi-hole injector's spray <sup>[124]</sup> _____	175
Figure 6.17: Measurement location <sup>[125]</sup> _____	175
Figure 6.18: Definition of Diverging Angle between Two Holes _____	176

Figure 6.19: Axial Mean and RMS Velocities of a Spray Jet <sup>[127]</sup>	177
Figure 6.20: Six-hole 60 degree, six-hole 90 degree and 3 Hole 90 degree cone angle (from left to right)	178
Figure 6.21: PDA traverse scans. (Left radial scan, right circumferential scan)	178
Figure 6.22 Vector plot produced from the radial scan. Arrows represent average droplet velocity, Circles represent average droplet diameters.	179
Figure 6.23: Mean Axial Velocity for centre, inside and outside of plume - 60°C	182
Figure 6.24 Mean Axial Velocity for centre, inside and outside of plume – 60°C	183
Figure 6.25 Mean Axial Velocity for centre, inside and outside of plume – 60°C	184
Figure 6.26 Mean Axial Velocities for 6-hole 90°C, top left z=20mm, ±4mm, top right z=40, ±5mm, bottom left z=60, ±5mm, bottom right z=60mm, ±10mm	185
Figure 6.27 Mean Axial Velocities for 3-hole 90°C, top left z=20mm, ±2mm, top right z=40mm, ±2.5mm, bottom left z=60mm, ±5mm, bottom right z=60mm, ±10mm	186
Figure 6.28: D10 and D32 at +2, +1, 0, -1, -2mm from	188
Figure 6.29: Droplet size against axial position for 6-hole 60°C injector at z=20mm	188
Figure 6.30: Droplet size against axial position for 6-hole 90°C injector at z=20mm	189
Figure 6.31: Droplet size against axial position for 3-hole 90°C injector at z=20mm	189
Figure 6.32: Sample number at z=20mm for the three injectors	190
Figure 6.33: Droplet size against axial position for 6-hole 60°C injector at z=40mm	191
Figure 6.34: Droplet size against axial position for 6-hole 90°C injector at z=40mm	191
Figure 6.35: Droplet size against axial position for 3-hole 90°C injector at z=40mm	191
Figure 6.36: Droplet size against axial position for 6-hole 60°C injector at z=60mm	192
Figure 6.37: Droplet size against axial position for 6-hole 90°C injector at z=60mm	192
Figure 6.38: Droplet size against axial position for 3-hole 90°C injector at z=60mm	192
Figure 6.39: Three images from the circumferential scan - plume behind measurement volume (left) - plume in the centre of measurement volume (middle) - plume in front of measurement volume (right)	195
Figure 6.40: Circumferential scan across three plumes - 60°C and 90°C injector - 20mm below injector nozzle – 2.5ms ASOS - axial velocity (left) - radial velocity (right)	196
Figure 6.41: Circumferential scan across three plumes - 60°C and 90°C injectors - 20mm below injector nozzle – 2.5ms ASOS - D <sub>10</sub> droplet diameter	197
Figure 6.42: 360 degree circumferential scan - 60°C and 90°C injector - 20mm below injector nozzle – 2.5ms ASOS - axial velocity (left) - radial velocity (right) (zero on graph equivalent to plume 243 on Figure 6.40)	198
Figure 6.43: Circumferential scan across three plumes - 60°C and 90°C injector - 40mm below injector nozzle – 2.5ms ASOS - axial velocity (left) - radial velocity (right)	198
Figure 6.44: Circumferential scan across three plumes - 60°C and 90°C injectors - 40mm below injector nozzle – 2.5ms ASOS - D <sub>10</sub> droplet diameter	199
Figure 6.45: 360 degree circumferential scan - 60°C and 90°C injector - 40mm below injector nozzle – 2.5ms ASOS - axial velocity (left) - radial velocity (right) - (zero on graph equivalent to plume 243 on Figure 6.43)	199

<i>Figure 6.46: Axial and Radial mean velocity against time at the centre point of the plume for the 6-hole 90°C injector and 3-hole 90°C injector at z=20mm</i>	201
<i>Figure 6.47: Axial mean velocity against time for the 6-hole 90°C injector and 3-hole 90°C injector at z=20mm below the nozzle - ±5° rotation</i>	201
<i>Figure 6.48: Radial mean velocity against time for the 6-hole 90°C injector and 3-hole 90°C injector at z=20mm below the nozzle - ±5° rotation</i>	202
<i>Figure 6.49: Axial mean velocity against time for the 6-hole 90°C injector and 3-hole 100°C injector at z=20mm below the nozzle - ±10° rotation</i>	202
<i>Figure 6.50: Radial mean velocity against time for the 6-hole 90°C injector and 3-hole 100°C injector at z=20mm below the nozzle - ±10° rotation</i>	203
<i>Figure 6.51: Droplet diameter against time at the plume centre for the 6-hole 90°C injector and 3-hole 90 degree injector at z=20mm below the nozzle</i>	204
<i>Figure 6.52: Droplet diameter against time for the 6-hole 90°C injector and 3-hole 90°C injector at z=20mm below the nozzle - ±5° rotation</i>	204
<i>Figure 6.53: Droplet diameter against time for the 6-hole 90°C injector and 3-hole 90°C injector at z=20mm below the nozzle - ±10° rotation</i>	205
<i>Figure 7.1: Injector 1: 6-hole 90° cone angle with a flat nozzle tip</i>	207
<i>Figure 7.2: Injector 2: 6-hole 90° cone angle with a concave nozzle tip</i>	207
<i>Figure 7.3: Injector 3: 6-hole 60° cone angle with a concave nozzle tip</i>	208
<i>Figure 7.4: Injector geometrical characteristics</i>	208
<i>Figure 7.5: Injector plume geometry<sup>[101]</sup> for injectors 1 and 2</i>	209
<i>Figure 7.6: An intensity contour comparison of axial penetration at 20°C 1bar backpressure with Injector 1</i>	211
<i>Figure 7.7: An intensity contour comparison of axial penetration at 20°C 2bar backpressure with Injector 1</i>	212
<i>Figure 7.8: Axial penetration at 20°C 1bar backpressure</i>	213
<i>Figure 7.9: Axial penetration at 20°C 2bar backpressure</i>	213
<i>Figure 7.10: Radial penetration at 20°C 1bar backpressure</i>	214
<i>Figure 7.11: Radial penetration at 20°C 2bar backpressure</i>	214
<i>Figure 7.12: Cone angle at 20°C 1bar backpressure</i>	217
<i>Figure 7.13: Cone angle at 20°C 2bar backpressure</i>	218
<i>Figure 7.14: Axial penetration at 20°C with Injector 1</i>	221
<i>Figure 7.15: Radial penetration at 20°C with Injector 1</i>	222
<i>Figure 7.16: Cone angle at 20°C with Injector 1</i>	222
<i>Figure 7.17: Axial penetration at 1bar backpressure with Injector 3</i>	225
<i>Figure 7.18: Axial penetration at 2bar backpressure with Injector 3</i>	226
<i>Figure 7.19: Radial penetration at 1bar backpressure with Injector 3</i>	226
<i>Figure 7.20: Radial penetration at 2bar backpressure with Injector 3</i>	227
<i>Figure 7.21: Cone angle at 1bar backpressure with Injector 3</i>	227
<i>Figure 7.22: Cone angle at 2bar backpressure with Injector 3</i>	228

---

Figure 7.23: A plot showing the change in charge density with varying cell backpressure and temperature	229
Figure 7.24: 120bar and 190bar at 20°C and 1bar backpressure with Injector 3	233
Figure 7.25: 120bar and 190bar at 20°C and 2bar backpressure with Injector 3	233
Figure 7.26: 40°C and 1bar backpressure with Injector 3	234
Figure 7.27: 40°C and 2bar backpressure with Injector 3	234
Figure 7.28: 60°C and 1bar backpressure with Injector 3	235
Figure 7.29: 60°C and 2bar backpressure with Injector 3	235
Figure 7.30: Highlighting the increase in spray surface ripples due to increased fuel pressure	236
Figure 7.31: Axial penetration at 20°C and 1bar backpressure	238
Figure 7.32: Axial penetration at 20°C and 2bar backpressure	238
Figure 7.33: Best fit coefficients for axial penetration as a function of backpressure	239
Figure 7.34: Predicted and actual results for axial penetration at 20°C as a function of backpressure for injector3	240
Figure 7.35: Radial penetration at 20°C and 1bar backpressure	240
Figure 7.36: Radial penetration at 20°C and 2bar backpressure	241
Figure 7.37: Best fit coefficients for radial penetration as a function of backpressure	241
Figure 7.38: Predicted and actual results for radial penetration at 20°C as a function of backpressure for injector3	242
Figure 7.39: Derivation of the additional axial penetration moving from 120bar to 190bar injection pressure	244
Figure 7.40: Derivation of the additional radial penetration moving from 120bar to 190bar injection pressure	244
Figure 7.41: Predicted axial penetration and the directly interpolated axial penetration at the part load engine condition	246
Figure 7.42: Predicted axial penetration for each injector at the engine part load condition	247
Figure 7.43: Predicted radial penetration for each injector at the engine part load condition	247
Figure 7.44: N-Heptane and Iso-Octane saturation vapour pressure vs temperature <sup>[129]</sup>	254
Figure 7.45: Effect of backpressure and fuel temperature on flashing in GDI multi-hole spray <sup>[87]</sup>	255
Figure 7.46: Schematic review of the physics involved in the flash boiling of a liquid issuing from nozzle <sup>[107]</sup>	257
Figure 7.47: Pressure-swirl atomiser: mechanisms of spray/air interactions when increasing the ambient pressure <sup>[137]</sup>	262
Figure 7.48: Image processing technique	263
Figure 7.49: Spray angle comparison for ambient pressure variation. 60° cone angle injector, 120bar Fuel, 2ms ASOS	264
Figure 7.50: Penetration comparison for ambient pressure variation. 60° cone angle injector, 120bar Fuel, 2ms ASOS	264
Figure 7.51: Spray angle comparison for fuel temperature variation. 60° cone angle injector, 120bar Fuel, 2ms ASOS	266
Figure 7.52: Penetration comparison for fuel temperature variation. 60° cone angle injector, 120bar Fuel, 2ms ASOS	266

---



<i>Figure 7.53: Spray angle comparison for fuel pressure variation. 60° cone angle injector, 2ms ASOS, 20mm downstream</i>	268
<i>Figure 7.54: Penetration comparison for fuel pressure variation. 60° cone angle injector, 2ms ASOS</i>	268
<i>Figure 7.55: In Reid vapour pressure profile for gasoline-ethanol fuel blends<sup>[138]</sup></i>	269
<i>Figure 7.56: Spray angle comparison for fuel type variation. 60° cone angle injector, 120bar injection pressure, 2.0ms ASOS, 20mm downstream</i>	270
<i>Figure 7.57: Penetration comparison for fuel type variation. 60° cone angle injector, 120bar injection pressure, 2.0ms ASOS</i>	270

## List of Tables

Table 1.1: EU Emissions Standards for Passenger Cars (g/km) <sup>[3]</sup>	4
Table 1.2: Comparison of gasoline and ethanol prices	6
Table 2.1: Jet break-up regimes (images from Lin and Reitz) <sup>[19]</sup>	18
Table 2.2: Round Liquid Jet break-up regimes (Farago and Chigier) <sup>[23]</sup>	20
Table 2.3: Fuel blends of different volatility characteristics <sup>[46]</sup>	37
Table 2.4: Properties of test fuels available <sup>[51]</sup>	37
Table 2.5: Stratified operation mechanisms <sup>[2]</sup>	42
Table 2.6: Challenges of GDI engine development <sup>[2]</sup>	55
Table 2.7: Fuel injector requirements <sup>[2]</sup>	64
Table 2.8: Classification of GDI injectors <sup>[2]</sup>	68
Table 2.9: Droplet diameter terminology <sup>[81]</sup>	80
Table 3.1: Effects of different parameters on flash boiling level	94
Table 4.1: Specification of PDA operational parameteres <sup>[112]</sup>	115
Table 5.1: Injector stream angle definition	151
Table 6.1: Fuel Properties	161
Table 6.2: Fuel Spray Half Cone Angles	162
Table 6.3: Location of plume centre for radial scans at 20mm below injector nozzle	180
Table 6.4: Location of plume centre for radial scans at 40mm below injector nozzle	180
Table 6.5: Location of plume centre for radial scans at 60mm below injector nozzle	180
Table 6.6: Distance moved during circumferential scan	194
Table 7.1: Spray density near the injector axis for injectors 1 and 2	215
Table 7.2: Spray propagation at 20°C and 1bar backpressure for injector 3	219
Table 7.3: Color scaled images - injector 1 at 1.7ms ASOS - 2 and 4bar backpressure	224
Table 7.4: A series of images showing plume tip deformation with injector 3	231
Table 7.5: Spray pattern evolution with reduction in cell pressure. 60° cone angle injector, 120bar Fuel @ 60°C, 2ms ASOS	259
Table 7.6: Spray pattern evolution. Injector comparison-120bar FP-60°C-2ms ASOS	271
Table 7.7: Results summary	273
Table 8.1: Summary of available data	275

## Nomenclature

### Acronyms

ACEA	Association de Constructeurs d'Automobiles Europeens
AFR	Air-Fuel Ratio
ASOI	After Start Of Injection
ASOS	After Start Of Signal
ATDC	After Top Dead centre
AVT	Active Valve Train
BDC	Bottom Dead Centre
BSFC	Brake Specific Fuel Consumption
CCD	Charge Coupled Device
CFD	Computational Fluid Dynamics
CMOS	Complementary Metal Oxide Semiconductor
CO	Carbon Monoxide
CO <sub>2</sub>	Carbon Dioxide
DISI	Direct Injection Spark Ignition
DMC	Discrete Multi Component
EGR	Exhaust Gas Recirculation
EIVC	Early Inlet Valve Closing
EUDC	Extra Urban Driving Cycle
FFT	Fast Fourier Transform
FOV	Field of View
GDI	Gasoline Direct Injection
HC	Hydrocarbons
HOTFIRE	Homogeneous and Throttle-less for Fuel Efficiency and Reduced Emissions
HPHT	High Pressure High Temperature
HSI	Homogenous Split Injection
IC	Internal Combustion
JAMA	Japanese Automobile Manufacturers Association
LDV	Laser Doppler Velocimetry
LDA	Laser Doppler Anemometry
LIF	Laser Induced Fluorescence
LIVO	Late Inlet Valve Opening

MAF	Mass Air Flow	
MAP	Manifold Absolute Pressure	
Nd:YAG	Neodymium-doped Yttrium Aluminium Garnet	
NO <sub>x</sub>	Nitrogen Oxides	
PDA	Phase Doppler Anemometry	
PFI	Port Fuel Injection	
PIV	Particle Image Velocimetry	
RMS	Root Mean Square	
SD	Standard Deviation	
SMD	Sauter Mean Diameter	
SCORE	Single Cylinder Optical Research Engine	
SCR	Selective Catalytic Reduction	
SOS	Start Of Signal	
TVD	Total Variation Diminishing (TVD)	
UDC	Urban Driving Cycle	
UV	Ultra-Violet	
VVT	Variable Valve Timing	

## Notation

$d_o$	Initial diameter	m
$D$	Density	$\text{kg/m}^3$
$Ja$	Jakob number	
$l_o$ or $\ell_o$	Orifice or nozzle length	m
$M$	Molar mass	$\text{kg/mol}$
$m$	Mass	kg
$n$	Refractive index	
$Oh$	Ohnesorge number	
$P_A$	Ambient pressure	Pa
$p$	Pressure	Pa
$R$	Gas of specific species	
$\tilde{R}$	Universal gas constant	$\text{J/K-mol}$
$Re$	Reynold number	
$S$	Penetration	m
$T$	Temperature	K or °C
$t$	Time at which the spray is captured	Ms

---

## Nomenclature

---

$t_b$	Break up time	S
$U_L$	Liquid axial velocity	m/s
$V$	Volume	$m^3$
We	Weber number	
$\theta$	Angle	degrees
$\mu_A$	Dynamic viscosity of air	kg/(m.s)
$\mu_L$	Dynamic viscosity of liquid	kg/(m.s)
$\eta$	Kinematic Viscosity	$m^2/s$
$\rho_A$	Air density	$kg/m^3$
$\rho_L$	Liquid density	$kg/m^3$
$\sigma$	Surface tension	N/m

### **1. Introduction**

Increasing environmental concern and dwindling sources of energy are forcing automotive companies to develop new methods of propulsion for the future. Electric and energy cell vehicles are currently being researched, however, the combustion engine will remain the primary choice for the next 20 years. As automotive companies strive to reduce fuel consumption and hence CO<sub>2</sub> emission whilst maintaining performance, the characteristics and structure of the fuel spray are very important to the air/fuel mixture preparation, affecting the efficiency of combustion and the levels of emissions. This, coupled with new technologies allowing different types of combustion to occur within one engine such as the Gasoline Direct Injection (GDI) the design of injectors and their spray characteristics continue to receive significant attention.

To date, most investigations of fuel sprays involve cold bench tests or motored optical engines. For safety and convenience reasons these tests are often run with non volatile fluids. Such experiments neglect the effects of the fuel volatility and temperature on the spray structure. Therefore, there is a limited source of data in realistic operating conditions to analyse how the properties of a fuel can affect the efficiency of the atomisation process.

#### **1.1 Study Definition**

The definition of this study is to investigate *“The effect of fuel properties and injector parameters on atomisation performance.”*

The properties of fuel vary greatly due to their complex multi-component structure. The range of components changes the properties of the fuel and so it is difficult to define the exact values for the properties of fuel. With new alternative fuels such as gasoline-ethanol blends and the world-wide variation of fuel properties it is likely that the fuel properties will have a significant effect on the atomisation and combustion performance. However, of all the properties of a liquid only three density, viscosity and surface tension have an influence on the atomisation process [1].

The spray atomisation performance is important as it affects engine performance and combustion efficiency. In today's increasingly competitive and environmentally aware culture both engine performance and combustion efficiency which affects the level of emissions are vitally important design considerations.

### **1.2 Aims**

The first purpose of this study is to investigate the effect different fuels have on the atomisation performance. Relationships between the properties of the fuel and their direct effect on the atomisation process will be analysed.

The second aim is to study the influence of different injector geometry parameters in the case of multi-hole injectors and to analyse the interactions between the plumes of multi-hole injectors to establish the phenomenon that occur when the plumes are located closely together. The purpose is to gain relevant information on each injector's spray characteristics including axial and radial penetration and spray angle, at conditions comparable to those seen in a GDI engine by using a pressure chamber. A quantitative and qualitative analysis of the spray properties will be used to indicate potential reasons for the differences in emissions seen from engine testing and to explain the cause of such characteristics. The results will also provide details on the general affects of pressure and temperature on fuel sprays with different injector designs which will further the on-going research in this area in the pursuit of optimal engine design for emissions, fuel efficiency and performance.

Alongside the purposes aforementioned a more general aim is to acquire a thorough understanding of fuel spray characteristics, measurement techniques, and GDI engine operation through a thorough literature review.

The two optical techniques to be used in this study are Mie imaging and Phase Doppler Anemometry in order to obtain spray morphology and spray dynamics. These techniques provide basic physical understanding of spray processes and much needed spray propagation and interaction information for the engine designer.

### ***1.3 Motivation and Relevance***

Alongside the primary motivation for this project, there is on-going research into spray development and the effect it has on the combustion process. Future emissions regulations and public concern over climate change are putting pressure on automotive manufacturers to reduce CO<sub>2</sub> output i.e. fuel consumption from vehicles. At the same time, consumers are demanding improved safety from their vehicles and this has resulted in a trend of increased vehicle mass as vehicle models are updated with new safety structures. In order for new models to provide the same performance as the previous models, increased power must be available at the wheels to counteract the additional mass. Manufacturers therefore need to develop technologies which simultaneously reduce emissions, increase fuel efficiency and increase performance.

Much recent work in the field of spark ignition (SI) engines has focused on the use of gasoline direct injection engines which have the potential to combine the specific power output of port-injection gasoline engines with the part load efficiency of diesel engines [2].

Of primary concern to the engine manufacturers is to meet the legislation set by the European Union for 'tailpipe out' emissions. The past, present and future emissions standards are set out in Table 1.1, and what is obvious from the table is a continuing trend for reducing emissions.

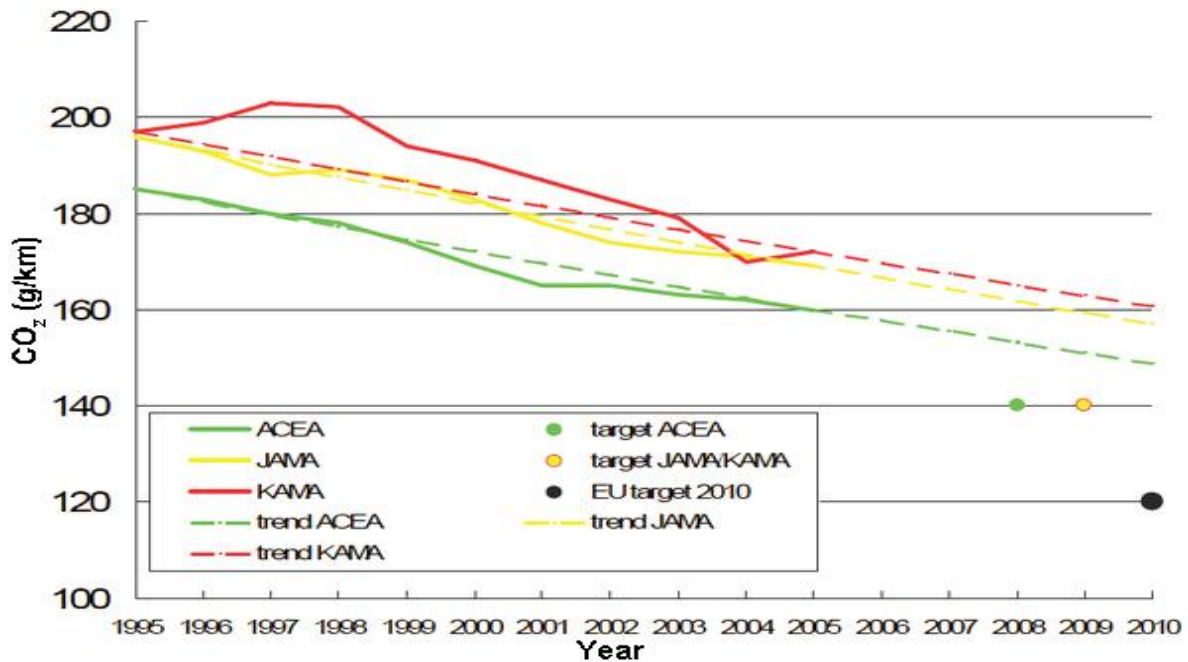
An important point to note is that there is no regulated limit on allowable CO<sub>2</sub> emissions. Instead of a limit enforced by the European Union there is a voluntary agreement between the European Automobile Manufacturers Association (ACEA) and the European Commission. Signed in 1998, the agreement was set to achieve an average of 140g/km of CO<sub>2</sub> by 2008 for new passenger vehicles sold in Europe. This target represented a reduction of 25% from the 1995 level of 186g/km. The European Commission also had agreements with the Japan Automobile Manufacturers Association (JAMA) and Korea Automobile Manufacturers Association (KAMA), however, the target date for these two was 2009.

The ultimate EU target is for a reduction to 120g/km fleet-averaged CO<sub>2</sub> for all new passenger cars by 2010. However, by 2005 the average CO<sub>2</sub> output had only been reduced to 160g/km and the European Commission announced in late 2006 that it was working on a proposal for legally binding measures. Progress towards these targets up to 2005, and predicted trends, are shown in Figure 1.1:



**Table 1.1: EU Emissions Standards for Passenger Cars (g/km)<sup>[3]</sup>**

Tier	Date	CO	HC	HC+NOx	NOx	PM
<b>Diesel</b>						
Euro 1†	1992.07	2.72 (3.16)	-	0.97 (1.13)	-	0.14 (0.18)
Euro 2, IDI	1996.01	1	-	0.7	-	0.08
Euro 2, DI	1996.01 <sup>a</sup>	1	-	0.9	-	0.1
Euro 3	2000.01	0.64	-	0.56	0.5	0.05
Euro 4	2005.01	0.5	-	0.3	0.25	0.025
Euro 5‡	2009.09 <sup>b</sup>	0.5	-	0.23	0.18	0.005
Euro 6‡	2014.09	0.5	-	0.17	0.08	0.005
<b>Gasoline</b>						
Euro 1†	1992.07	2.72 (3.16)	-	0.97 (1.13)	-	-
Euro 2	1996.01	2.2	-	0.5	-	-
Euro 3	2000.01	2.3	0.2	-	0.15	-
Euro 4	2005.01	1	0.1	-	0.08	-
Euro 5‡	2009.09 <sup>b</sup>	1	0.10 <sup>c</sup>	-	0.06	0.005 <sup>d</sup>
Euro 6‡	2014.09	1	0.10 <sup>c</sup>	-	0.06	0.005 <sup>d</sup>
* At the Euro 1..4 stages, passenger vehicles > 2,500 kg were type approved as Category N <sub>1</sub> vehicles						
† Values in brackets are conformity of production (COP) limits						
‡ Proposed						
a - until 1999.09.30 (after that date DI engines must meet the IDI limits)						
b - 2010.09 for vehicles > 2,500 kg						
c - and NMHC = 0.068 g/km						
d - applicable only to vehicles using DI engines						



**Figure 1.1: Progress towards international CO<sub>2</sub> emissions targets<sup>[4]</sup>**

In the USA legislators have agreed that 'combined car/light truck average fuel consumption should reach 35mpg in 2020, this being an increase of about 40% over 2007 average fuel consumption'.

One likely reason for the failure of manufacturers to meet these targets is the conflict between fuel efficiency and passenger safety, which increases vehicle mass. There is a great emphasis on safety in vehicle reviews in popular magazines such as Autocar, which always quotes a vehicle's Euro NCAP safety score. This leads to consumers purchasing vehicles based on safety rather than emissions, which, from a marketing point of view, means it is beneficial for a manufacturer to concentrate research efforts on safety and not only emissions. In addition to that, in some markets (American, Chinese...) even if the environmental concerns are growing, there remains a trend of customers wanting larger cars.

The emissions standards set were created to reduce the effect of vehicle emissions on the environment. The most significant environmental effect is due to the excessive production of carbon dioxide. Carbon dioxide is a primary combustion product and as such can only be reduced by a reduction in carbon combustion. The carbon dioxide produced acts to increase the concentration of greenhouse gases, allowing the earth to absorb more thermal radiation emitted from the earth's surface and thus increase the earth's surface temperature (global warming) [5]. Other combustion products and their effect on the environment include; nitric oxides and hydrocarbons that combine with sunlight to form Ozone which is the major component of ground level smog, carbon monoxide which has the effect of reducing the oxygen levels in the blood stream, particulates which can act as a transporters for other substances to get into the body, and sulphur oxides which react with water in the atmosphere to form sulphuric acid, the main contributor to acid rain [6].

Several technologies have been suggested and developed which have the potential to reduce CO<sub>2</sub> output from passenger vehicles. These include:

- Lean and lean boost Gasoline Direct Injection (GDI)
- Advanced cylinder and valve control
- Homogeneous Charge Compression Ignition
- Fuel cells
- Hybrid Electric Vehicles
- Downsized, turbocharged engines
- Bio-fuels such as E85 (blend of 85% ethanol and 15% gasoline)

## 1.4 Bio-Fuels

Current UK gasoline contains up to 5% ethanol by volume. There are several benefits to this:

- If the fuels and fertilisers used in ethanol production are produced using no CO<sub>2</sub> then production and combustion of this fuel results in no net CO<sub>2</sub> emissions. This is because the carbon released as CO<sub>2</sub> from burning the fuel is absorbed by the plants used to produce more ethanol.
- Increased use of domestically produced ethanol reduces reliance on imported oil, which often comes from politically unstable countries in the Middle East.
- Crude oil prices have risen rapidly in recent years, as shown in Figure 1.2. A comparison of recent gasoline and ethanol costs is shown in Table 1.2. This shows that currently it is cheaper to run a vehicle on ethanol than gasoline.



**Figure 1.2: Variation in crude oil prices from 1986-2010<sup>[7]</sup>**

**Table 1.2: Comparison of gasoline and ethanol prices**

US Average Gasoline Cost February 2010	US Average Ethanol Cost February 2010
\$1.96 / gallon <sup>[7]</sup>	\$1.6 / gallon <sup>[8]</sup>

There are, however, some disadvantages to using ethanol as fuel:

- Ethanol has a lower energy density than gasoline (24.0 MJ/l as opposed to 34.6 MJ/l), so an increased volume of fuel is required for the same power output, thereby reducing fuel economy.
- Increased demand for crops used to produce ethanol has increased worldwide food prices.
- Vast areas of land are required to grow crops needed for ethanol production. For example, if the US was to use corn to produce ethanol to replace all the gasoline currently used to fuel passenger vehicles, 1.1 billion acres of land would be required for sustainable production. The entire land area of the US is 1.94 billion acres [9].

In Brazil, Sweden and the United States a blend called E85, containing up to 85% ethanol with the remainder gasoline, is widely used. The increased proportion of ethanol increases the associated benefits relative to using only 5% ethanol. However, the use of this high proportion of ethanol requires engine modifications due to the different properties of ethanol when compared to regular gasoline. These modifications are:

- Elimination of bare magnesium, aluminium and rubber parts in the fuel system, as these corrode when exposed to high concentrations of ethanol.
- Use of fuel pumps capable of operating with electrically conductive fuel (ethanol) instead of non-conductive fuel (gasoline).
- Use of fuel pumps which are able to withstand the acidity and low lubricity of ethanol.
- Fuel injection systems with a wider range of injection duration, as approximately a 40% increase in volume of fuel injected is required relative to gasoline due to ethanol's lower energy density of 24.0 MJ/l as opposed to 34.6 MJ/l for gasoline.
- Stainless steel fuel line and tank [10].

The potential benefits of using E85 have led manufacturers to develop vehicles designed to run on this fuel, such as the Ford Focus Flex-fuel and Saab Biopower [11].

A literature review carried out by Orbital Engine Company [12] investigated the effects of gasoline-ethanol mixtures on engines. It was found that when ethanol was added to gasoline, the vapour pressure, and hence volatility, of the mixture was greater than that of either gasoline or ethanol alone. The reason for this is that strong hydrogen bonds exist between ethanol molecules, leading to pure ethanol having a relatively high boiling point for its

molecular mass. However, these bonds are not present in gasoline and when the two are mixed the gasoline molecules obstruct the bonds between the ethanol molecules, reducing the strength of the intermolecular forces and increasing the volatility of the mixture. Thus, gasoline-ethanol mixtures have a higher volatility than gasoline and as a result have different atomisation and vaporisation properties. This means that the resulting fuel sprays are different and must be investigated and understood when optimising an engine design to run on gasoline-ethanol blends.

### **1.5 GDI Engines**

The characterisation of a fuel spray is the process of describing it in both a qualitative and quantitative manner. The various parameters used to quantify a spray will be described in more detail in Chapter 2.

The main factors affecting combustion are in-cylinder airflow, the fuel injection process, and their mixing i.e. the mixture preparation. Therefore, an understanding of both is required if the primary design targets are to be optimised.

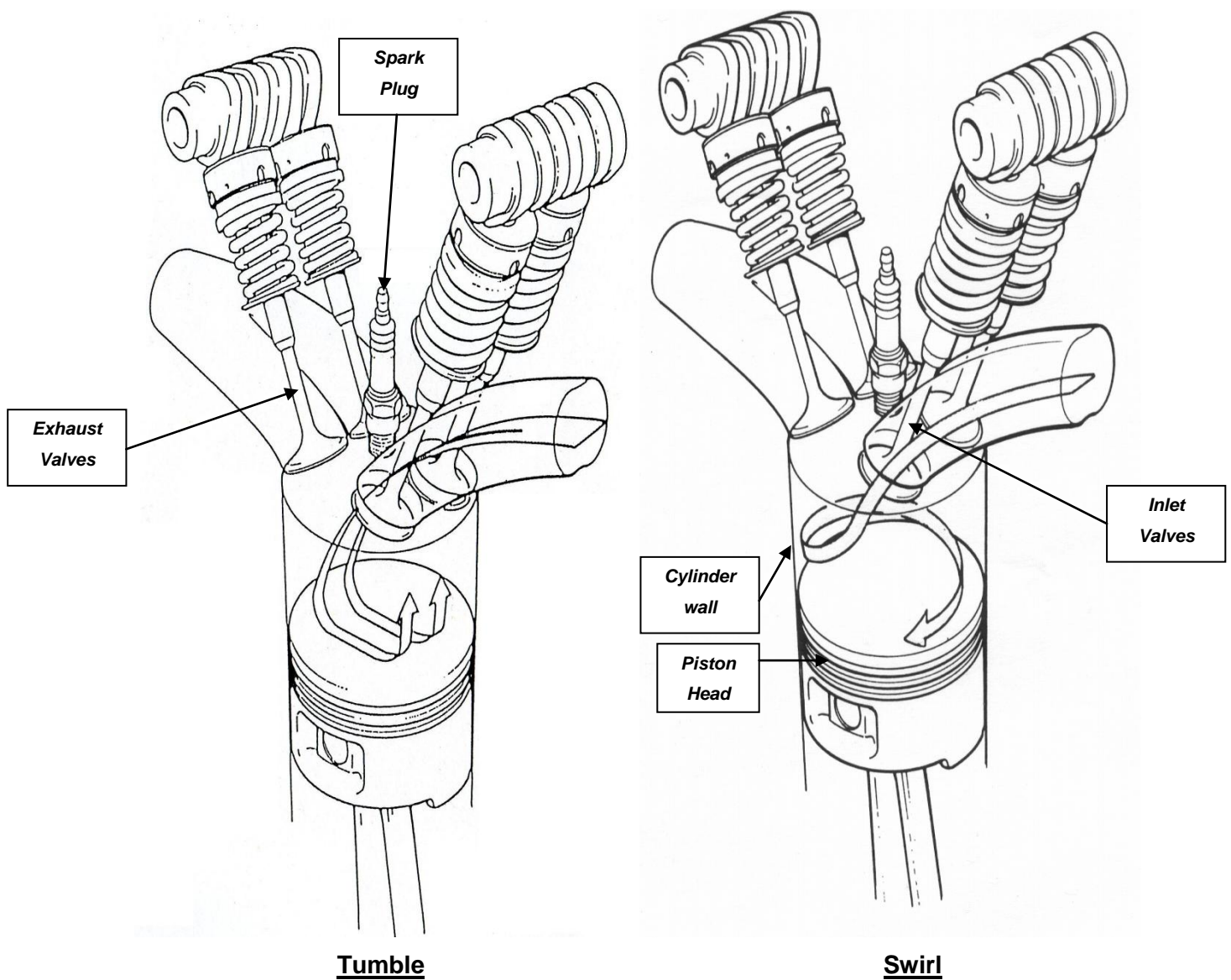
Gas motion within the cylinder is one of the major factors affecting the fuel-air mixing, and the combustion process. In addition to this, it also has a significant effect on heat transfer. The two main features of air motion are bulk gas motion and turbulence, both of which are affected by the intake process and piston movement within the cylinder. During the first part of the intake flow, the interaction with cylinder wall and moving piston create large scale rotating flows either side of the intake valve(s). Either during the latter part of the intake stroke or during the compression stroke due to the rising piston movement, these large eddies become unstable and break down into three dimensional turbulent motion [13].

Automotive manufacturers have used and developed various methods for controlling the airflow within the combustion chamber.

One method is the design of the intake port itself. There are five common intake port designs [14]:

- Directed straight port – Flow is through a straight and parallel passage, which when entering the cylinder moves tangentially towards the wall and is then directed sideways and downwards in a spiral motion.

- Deflector wall port – Flow is through a slightly curved passage so that initial cylinder motion is circular and downwards.
- Masked valve port – Flow is usually through a straight parallel port, and once at the valve, the valve mask forces the flow to enter the cylinder with a downward swirling motion.
- Helical port – Swirl is generated within the port about the valve axis prior to the cylinder and enters the cylinder with established swirl. The port guides the flow downwards which is emphasised by the downward moving piston.
- Tumble port – Flow is directed downwards through a straight parallel port, and on to the opposite cylinder wall to generate tumble.



**Figure 1.3: In-cylinder air flow structures**

Another method to control the in-cylinder airflow is the piston bowl design. Small gaps between the piston crown at top dead center (TDC) and the cylinder head can be used to create squish zones that create radially inward and transverse gas motion. The piston crown or bowl can also be used to promote further tumble bulk air motion within the cylinder. This was often used in first generation direct injection gasoline engines. In conjunction with a pressure-swirl injector, the fuel is injected towards the piston bowl and carried up towards the spark plug by the tumble air motion for ignition [13] [14].

The other main process affecting the combustion event is the fuel spray injection process. In a GDI engine, unlike a conventional gasoline port injection engine, fuel is injected directly into the cylinder. In a similar manner to diesel compression ignition engines, combustion is largely controlled by the fuel-air mixing process. The mixing process itself is determined by the time of injection, the piston bowl and combustion chamber design, and the injector spray characteristics. The degree of mixing can be controlled by the timing of injection relative to the piston and crankshaft position. To obtain a stratified charge, injection takes place late in the compression stroke. Conversely, if injection is completed during the intake stroke, a large amount of time is given for the fuel and air mixture to mix and it creates a largely homogeneous charge. By varying the point of injection in the compression or expansion stroke, the length of time available for mixing can be controlled.

The position and direction of the injector within the combustion chamber can be used to guide the spray and optimise mixing. Three common spray guiding techniques used are (see Figure 1.4); wall guided where the fuel is injected at the piston bowl which then directs the fuel up to the spark plug, air guided where the fuel is injected downwards but carried up towards the spark plug by tumble motion generated within the cylinder (enhanced by the piston bowl shape), and spray guided where the fuel is injected towards the spark plug itself [15]. Spray guided combustion systems are the focus of most research at this time [16] for their emissions and fuel efficiency benefits. In a spray guided system, the injector and timing can be configured such that a piston crown impact is avoided. This prevents a fuel film forming on the piston crown (this can occur with the other guiding techniques) that would burn rich and increase hydrocarbon and particulate emissions. The wasted fuel will also increase carbon dioxide emissions and fuel consumption.

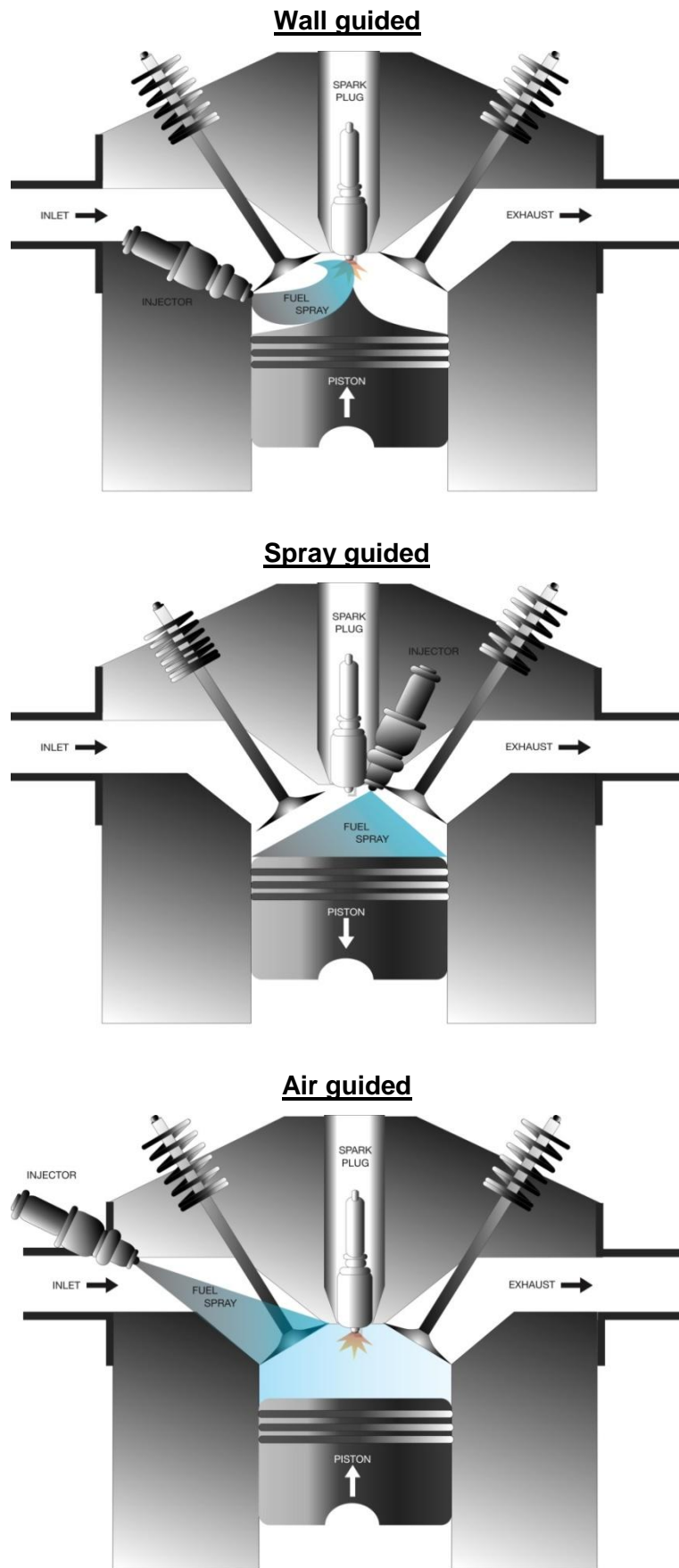


Figure 1.4: Three common spray guiding techniques



The injector spray characteristics also have a large influence on the fuel-air mixing within the cylinder. The process of atomisation and then vaporisation of the spray also directly affects the following stage of fuel-air mixing and finally combustion. Therefore if the engine design and combustion strategy is to be optimised for emissions, fuel consumption and performance, this aspect must be understood.

This study focuses on the use of different mono and multi-component fuels and GDI fuel sprays, however, knowledge of fuel properties and spray characteristics are important for any engine design and are hence applicable to almost all of the technologies previously mentioned.

Next chapter gives first a general presentation of the injection process and the spray characteristics before detailing the different gasoline direct injection operating modes and injectors.

### **2. Injection Process and Spray Characteristics**

#### ***2.1 Fuel Break-up and Atomisation***

The initial stage of this research involved a survey of the basic theory of atomisation and spray characteristics. This was to gain a basic knowledge of the processes and concepts involved to assist in the analysis of the literature review. A summary of this research, predominantly taken from '*Atomisation and Sprays*' by Arthur Lefebvre [17], follows.

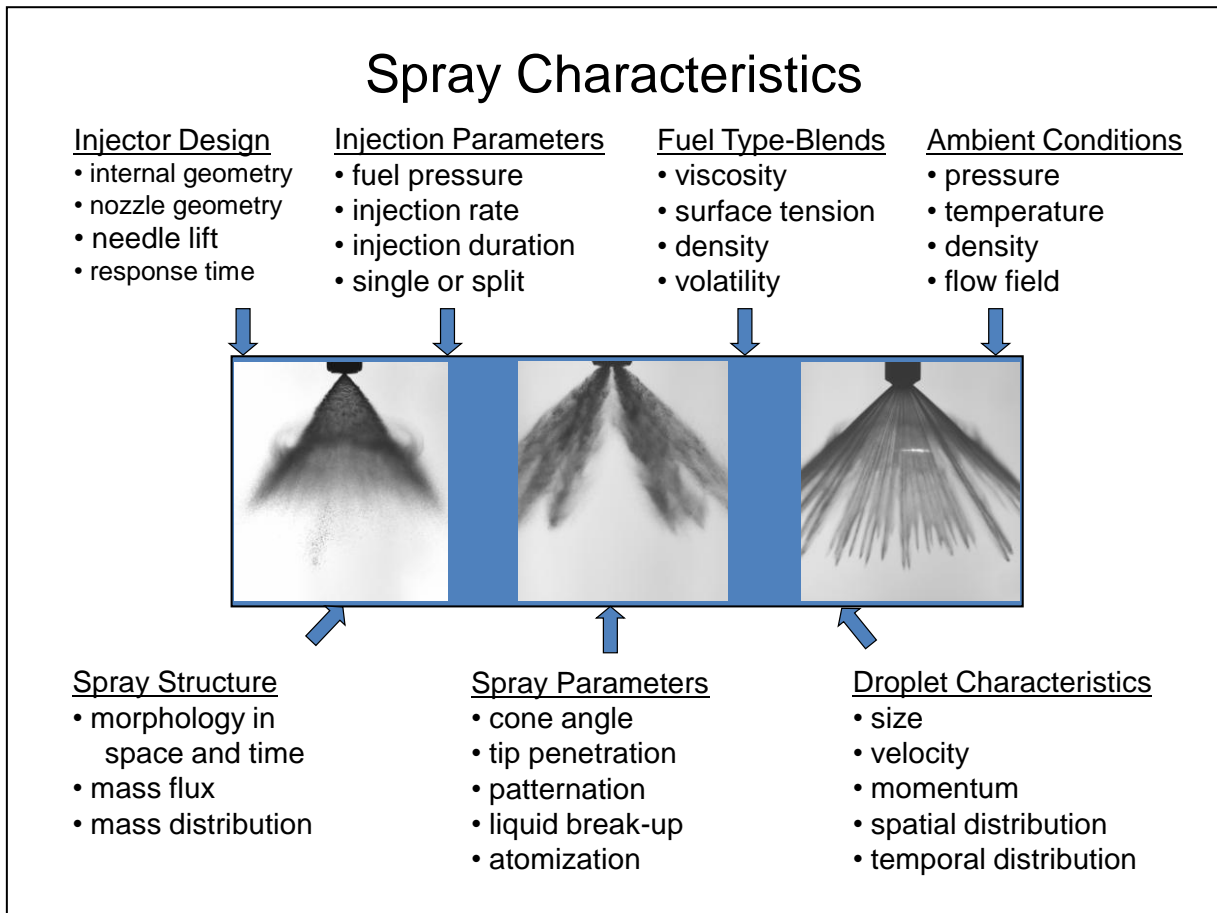
In stratified mode, the combustion starts straight after the injection of the fuel late in the compression stroke. Hence the air-fuel mixing has a direct influence on the quality of the combustion. Thus an increase in GDI engine performance requires not only an in-depth study of the combustion process but also a good comprehension of the air-fuel mixing formation.

The phenomena involved in the injection, atomisation and evaporation of the fuel have to be investigated in order to evaluate their respective impact on the quality of the combustion.

In order to analyse the detail behind fuel atomisation it is important to understand the way in which an injector creates an atomised fuel charge. In general a fuel rail at higher pressure will create a better atomised fuel through an orifice. Fuel Parameters such as density, surface tension and viscosity have an effect on how a fuel is atomised along with injector geometry parameters which can generate turbulence, cavitation and flow separation within the nozzle. However, in this section only the physical parameters that cause a fuel to be converted from liquid to a vaporised state are discussed

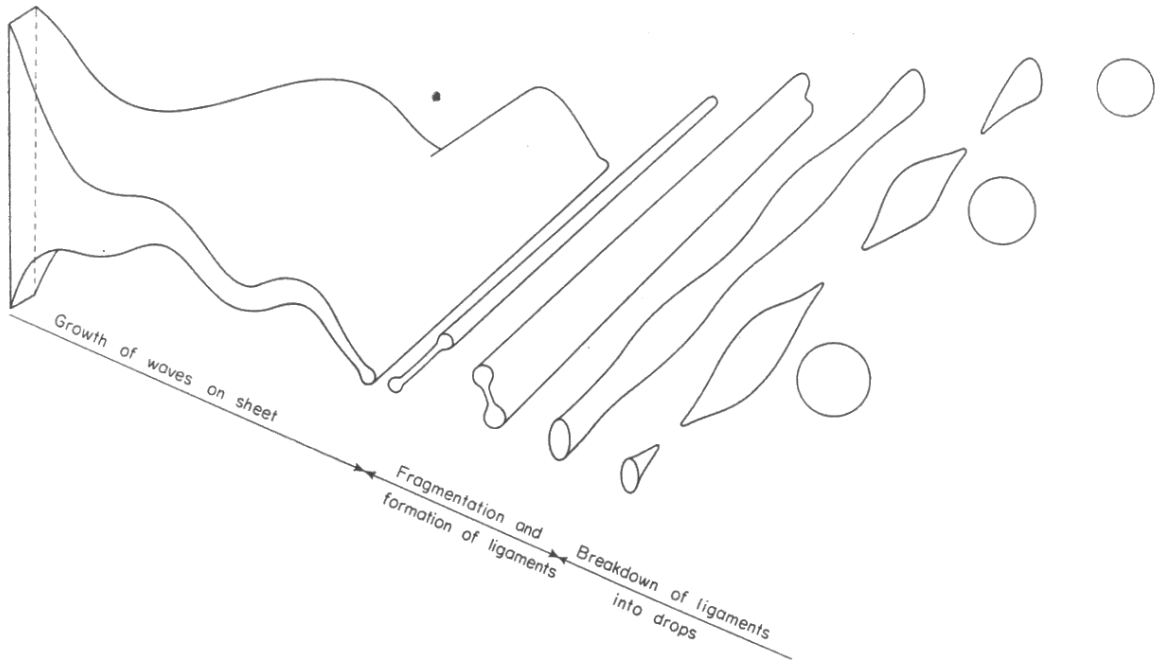
Atomisation is the process whereby a volume of liquid is disintegrated into a multiplicity of small drops. This is affected by the internal geometry of the atomiser, the properties of the gaseous medium into which the liquid is discharged and the physical properties of the liquid itself.

There are several processes involved in all methods of atomisation. The development of the jet, the small disturbances that cause ligaments which then break down into drops, and the hydraulic flow in the atomiser or nozzle that govern the turbulent flow downstream are all important in determining the shape and penetration of the spray, as well as other more detailed characteristics such as drop-size, velocity, density and distribution.



**Figure 2.1: Spray Parameter Interactions**

In many types of spray nozzle liquid is ejected from the orifice in the form of a thin liquid sheet or jet. The manner in which this sheet disintegrates into drops depends upon the operating conditions (velocity, shear gradients,...). However, the principal cause of instability is due to the interaction of the sheet with the surrounding atmosphere whereby rapidly growing waves are imposed on the sheet. Disintegration occurs when the wave amplitude reaches a critical value and fragments of sheet are torn off. The fragments rapidly contract into unstable ligaments under the action of surface tension and drops are produced as the latter subsequently break down as illustrated in Figure 2.2 [18].



**Figure 2.2:** Disintegration of sheet<sup>[18]</sup>

Ohnesorge found that by classifying data from photographic records, jet disintegration could be described according to relative importance of gravitational, inertial, surface tension and viscous forces. Three initial stages of break-up were found and characterised using Reynolds number and a dimensionless Ohnesorge Number:

$$Oh = \frac{\mu}{\sqrt{\rho\sigma l}} = \frac{\sqrt{We}}{Re} \quad (2.1)$$

Where  $We$  is the dimensionless Weber Number and  $Re$  is the dimensionless Reynolds Number:

$$We = \frac{\rho v^2 l}{\sigma} \quad (2.2)$$

$$Re = \frac{\rho v l}{\mu} \quad (2.3)$$

Where  $\rho$  ( $kg/m^3$ ) is the density of the fluid,  $v$  ( $m/s$ ) the velocity,  $l$  ( $m$ ) a characteristic length (droplet diameter),  $\sigma$  ( $N/m$ ) the surface tension and  $\mu$  ( $Pa \cdot s$ ) the dynamics viscosity.

## Chapter 2 – Injection Process and Spray Characteristics

---

Atomisation is greatly improved by using higher fuel rail pressures. The greater pressure differential between the fuel rail and the engine cylinder causes massive aerodynamic shear forces which tear the spray jets apart. This effect is related to the Weber number which is the ratio of inertial forces to surface tension forces.

At high Weber numbers aerodynamic forces dominate surface tension forces and tend to distort and disintegrate the drops. This causes drop break-up, leading to a reduction in length  $l$  and a corresponding reduction in Weber number. This break-up and Weber number reduction continues until the Weber number becomes stable at a smaller value. Lin and Reitz [19], [20] give the following description:

The initial condition for break-up is reached when aerodynamic drag is equal to surface tension force.

$We = 8/C_D$  gives the critical Weber number for break-up, where  $C_D$  is the drag coefficient. From this, the maximum stable drop-size ( $m$ ) is:

$$D_{max} = \frac{8\sigma}{C_D \rho_A U_R^2} \quad (2.4)$$

and critical relative velocity ( $m/s$ ) at which a drop will disrupt is:

$$U_{Rcrit} = \left( \frac{8\sigma}{C_D \rho_A D} \right)^{0.5} \quad (2.5)$$

Thus drop break-up will continue to occur until  $We < 8/C_D$ .

As the operating conditions are changed, liquid jets undergo different break-up regimes. These regimes are due to the action of dominant forces on the jet leading to jet break-up and it is important that these forces are identified in order to explain the jet break-up mechanism in each regime. Four main regimes have been identified [21] corresponding to different combinations of liquid inertia, surface tension and aerodynamic forces acting on the jet. The regimes are described in Table 2.1 and a classification is given in Figure 2.3.

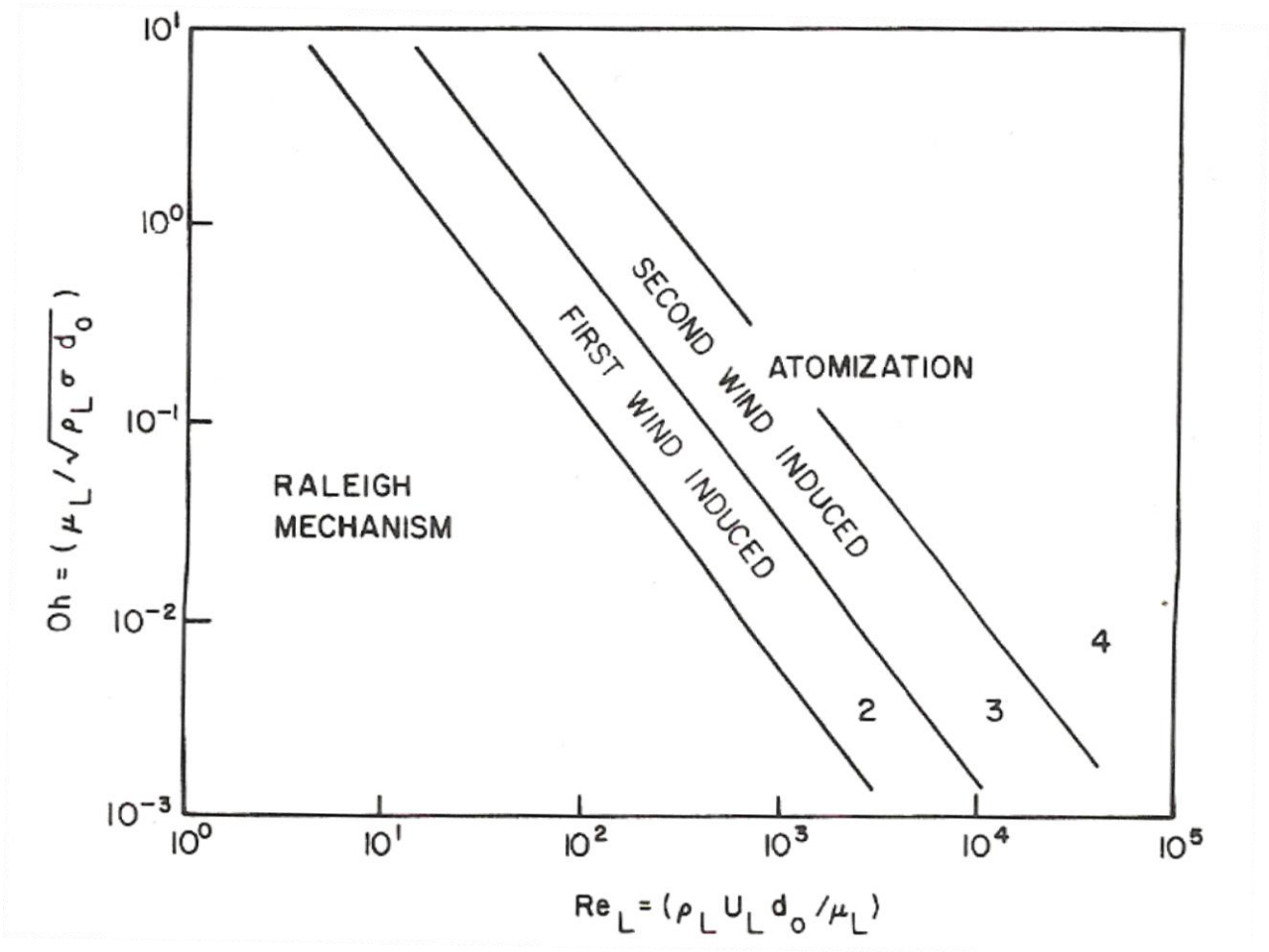





Figure 2.3: Ohnesorge chart for break-up regimes

## Chapter 2 – Injection Process and Spray Characteristics

**Table 2.1: Jet break-up regimes (images from Lin and Reitz)<sup>[19]</sup>**

<p><b>Rayleigh jet break-up:</b> At low Reynolds Numbers, jet break-up is initiated by radial, symmetric waves formed by interaction between disturbances in the liquid and surface tension forces of the jet. This is an idealistic break-up regime where drop formation is not influenced greatly by ambient air. Large drops of fairly uniform size and larger than the jet diameter are produced. The Rayleigh jet break-up or Rayleigh mechanism was defined by Rayleigh and showed that for low injection velocities the aerodynamic affect was much less significant than the affect of surface tension. The affect of surface tension on the viscous jets was further examined by Webber [22] and showed that disintegration was caused by the growth of axisymmetric oscillations that occurred at the jet surface due to viscous forces. This was an extension of Rayleigh’s mechanism. Drop diameters were found to be larger than the jet diameter, and predicted by Rayleigh to be almost twice the jet diameter.</p> <p style="text-align: center;"><b>Rayleigh jet break-up</b> occurs when <math>We_{Liq} &gt; 8</math> and <math>We_{Gas} &lt; 0.4</math></p>	
<p><b>First wind-induced break-up:</b> In this regime the affect of aerodynamic drag is beginning to create a static pressure distribution across the jet which acts to increase disintegration. The affect of drag also acts to accentuate the oscillations seen in the first regime to further increase break-up. It sees a reduction in drop-size, with diameters approximately equal to the jet diameter. Jet break-up is induced by the relative velocity of the jet and ambient air. A static pressure distribution is produced across the jet increasing the rate of break-up from the wave oscillations. Drops are produced closer to the nozzle than in Rayleigh break-up but still a relative distance away.</p> <p style="text-align: center;"><b>First wind-induced break-up</b> occurs when <math>0.4 &lt; We_{Gas} &lt; 13</math></p>	
<p><b>Second wind-induced break-up:</b> This regime sees a further increase in relative motion between jet and ambient gas which causes a corresponding unstable growth of shorter wavelength surface oscillations. The wave growth is further opposed by surface tension, but with a reducing effect. Disintegration occurs closer to the nozzle exit and the drops are now of much smaller diameter than the jet diameter.</p> <p style="text-align: center;"><b>Second wind-induced break-up</b> occurs when <math>13 &lt; We_{Gas} &lt; 40.3</math></p>	

## Chapter 2 – Injection Process and Spray Characteristics

---

**Atomisation:** Complete disintegration of the jet. Atomisation is caused at high Reynolds number (high relative velocity between jet and ambient air) The jet is broken up completely at, or in close location to, the nozzle exit in a chaotic and irregular manner. The average drop-size is now much lower than the jet diameter.

**Atomisation** occurs when  $40.3 < We_{Gas}$



The critical Weber numbers in Table 2.1 do not take into consideration any nozzle internal effects and these are known to be very important, particularly in high-speed jets. To take these effects into account, empirical formulae for the occurrence of atomisation were developed. Lin and Reitz [19] defined a dimensionless factor  $K$  based on the internal flow to predict atomisation to occur when:

$$\frac{\rho_2}{\rho_1} = K \times \text{function}(T^{-2}) \quad (2.6)$$

Where

$$K = \frac{\left(0.53 \left[3 + \left(\frac{l}{2a}\right)\right]^{0.5} - 1.15\right)}{744} \quad (2.7)$$

Where  $\rho_1$  is air density,  $\rho_2$  liquid density,  $K$  the nozzle's internal flow effect constant,  $T$  temperature,  $a$  the nozzle diameter and  $l$  is the nozzle length.

The value of  $K$  takes into account the turbulence, cavitation and flow separation inside the nozzle which cause initial flow disturbances and have a great effect on the atomisation process. This predicts that atomisation is favoured at high gas densities and with nozzles with small length to diameter ratios and sharp-inlet geometries.

A better method for categorizing the flow fields for a round liquid jet was introduced by Farago and Chigier [23] and considers the jet relationship based on jet Reynolds number and the gas Weber number. They used the limits in Table 2.2: Round Liquid Jet break-up regimes (Farago and Chigier) to show the break-up regimes they defined.



---

## Chapter 2 – Injection Process and Spray Characteristics

---

**Table 2.2: Round Liquid Jet break-up regimes (Farago and Chigier)<sup>[23]</sup>**

<u>Break-up Type</u>	<u>Limits</u>
Axisymmetric Rayleigh	$We_{Gas} < 15$
Nonaxisymmetric Rayleigh	$15 < We_{Gas} < 25$
Membrane break-up	$25 < We_{Gas} < 70$
Fiber-type break-up	$70 < We_{Gas}$
Superpulsating	$Re/We_{Gas}^{0.5} < 100$

When determining the various break-up mechanisms, several methods have been used to characterise the jet. Another of these is presented by Czerwonatis and Eggers [24], where these researchers considered three distinct regions: droplet break-up (Rayleigh break-up), wave break-up (first and second wind induced), and ligament break-up (second wind induced and atomisation). In order to characterise the various break-up regimes, these researchers identified seven primary parameters influencing the flow:  $u_{liq}$  (velocity in the axial (jet) direction),  $d$  (jet diameter),  $\sigma$  (surface tension),  $\mu_{liq}$  and  $\mu_{gas}$  (laminar viscosity) and  $\rho_{liq}$  and  $\rho_{gas}$  (density).

Mayer and Branam [25] investigated the jet behavior for a single injector element to determine the influence of the injection conditions on a round liquid jet. Their study focused on the atomisation of a liquid forming a classical spray. To adjust the relative velocity between the liquid jet and the gaseous ambient, a wind tunnel-like coaxial flow configuration was used. This made it possible to distinguish between effects of aerodynamic forces, chamber pressure and jet velocity, which determine the liquid Reynolds number and thereby the internal jet turbulence. Shadowgraphy and another image processing approach developed by the authors were used to determine the jet surface characteristics: wavelength and amplitude. The absolute injection velocity of the jet seemed to affect the structures the most with an increasing velocity causing the wavelengths to be smaller. An increase in chamber pressure seemed to have little influence on the jet with no relative velocity between the gas and liquid jet, but increased the amplitude and drop formation frequency at other testing conditions with relative motion. The study of the direction of the relative velocity demonstrated that injector performance cannot simply be described by scalar geometrical and operational injection parameters (e.g.,  $We$ ,  $Re$  or  $Oh$ ), but has to include the injection ‘vector’ or direction of the atomizing fluids in relation to each other and in relation to the ambient conditions (combustion chamber, etc.), thereby underlining the importance of injector-injector and injector-chamber interaction.

## Chapter 2 – Injection Process and Spray Characteristics

---

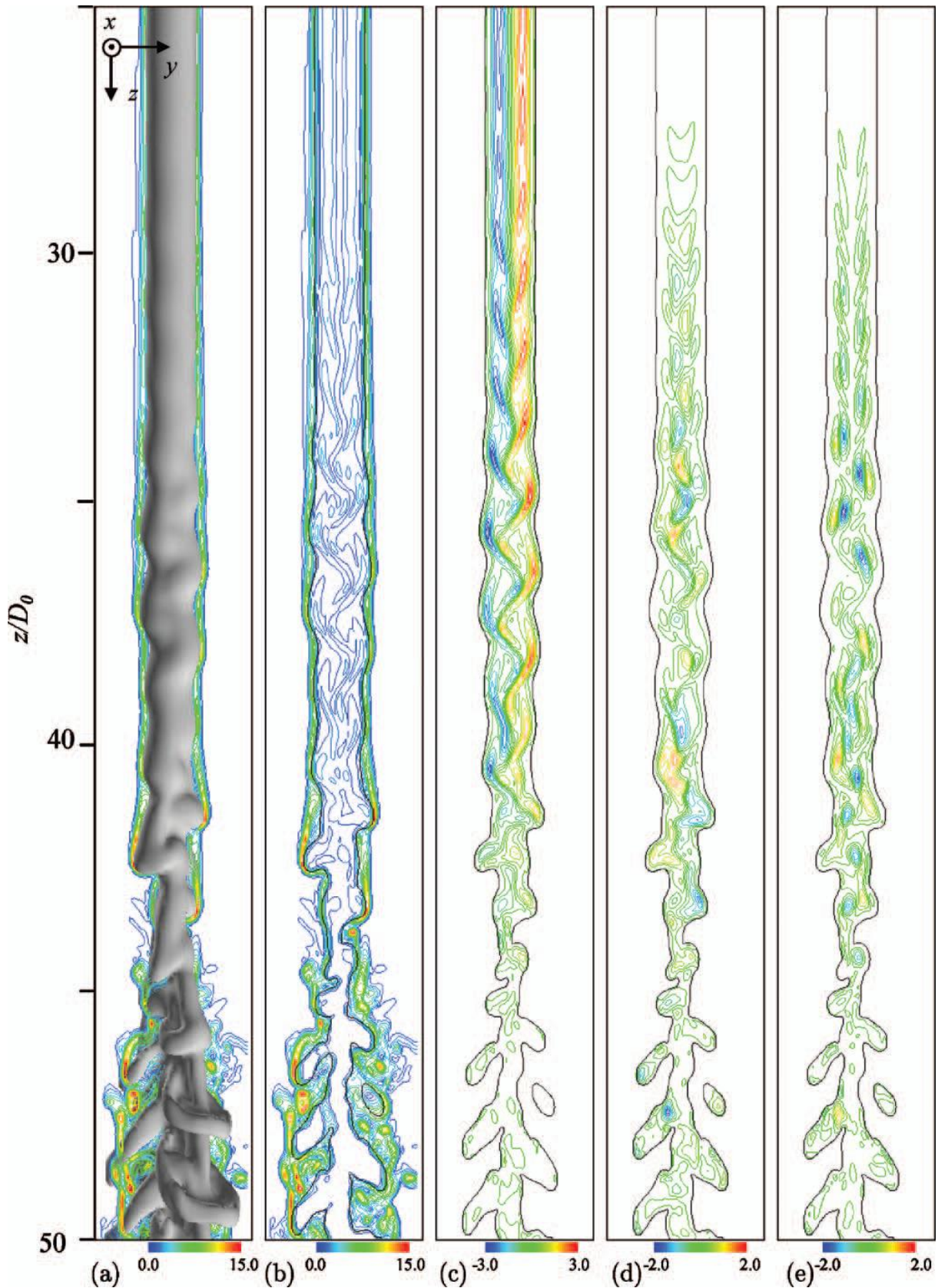
Wigley et al. [16] studied the fuel break-up and atomisation in the near nozzle region of a pressure swirl GDI injector using Mie imaging and phase Doppler anemometry to provide both morphological or macro-scale data as well as the micro-structure characteristics of the spray. They proposed a physical model of the processes of the liquid break-up and atomisation for a GDI pressure swirl injector based on the disruption of the wavy liquid cone into filaments and then droplets.

Cousin et al. [26] also studied pressure swirl injectors. They performed an experimental and theoretical investigation on the formation and primary break-up of conical liquid sheets. They used an experimental technique based on the electrical conductivity of liquids to predict accurately the orifice sheet thickness and measure the break-up length.

Kurachi et al. [27] used two methods based on laser Doppler signals to measure diesel spray break-up length. With the first method, spray tip penetration and spray break-up length are simply obtained by measuring the delay time of Doppler signals from injection start to spray tip arrival at each measuring point, as the measuring point is traversed along the center axis of the spray from the nozzle hole towards downstream. With the second one, spray break-up length is estimated by measuring the standard deviation of the delay time of Doppler signals, which indicates dispersion of the time from injection start to Doppler signal rising.

Various numerical studies on the break-up process were performed. Among them, Pan and Suga [28] studied the break-up process of laminar liquid jets into a gas. They used a Navier-Stokes solver coupled to a tension surface model to capture the dynamic of the primary break-up process (see *Figure 2.4*) and simulate the break-up length. Their results suggest that the conventional classification of the jet break-up regimes by the Weber numbers is not always successful particularly in cases of low Weber numbers whereas the classification by the Ohnesorge chart is reasonable.

In his work, Ghannam [29] developed a computational analysis that predicts the break-up distance and velocity of fluidic jets, which is one of the important factors that helps in prediction of the spray pattern and droplet strike location, thus reducing the number of required injector prototypes and saving time and cost. He also conducted a parametric study to analyze the effect the jet break-up on the spray trajectory.



**Figure 2.4: Distribution of instantaneous vorticity fields in an axis plane<sup>[28]</sup>**

- (a)  $\frac{D_0}{U_0} \sqrt{w_x^2 + w_y^2 + w_z^2}$  in the gas phase, (b)  $\frac{D_0}{U_0} \sqrt{w_x^2 + w_y^2 + w_z^2}$  in the whole field  
 (c)  $\frac{D_0}{U_0} \omega_x$ , (d)  $\frac{D_0}{U_0} \omega_y$  and (e)  $\frac{D_0}{U_0} \omega_z$  in the liquid phase

## Chapter 2 – Injection Process and Spray Characteristics

---

Most models of droplet formation and dispersion from a liquid jet are based upon a Lagrangian approach of numerical particles representing some physical droplets with identical size, velocity and temperature. The gas phase is simultaneously simulated using an Eulerian calculation. This type of model is not well adapted to the atomisation regime for high velocity liquid jet, as in recent GDI engines. These models describe the initial break-up of the jet with the aforementioned empirical laws. Moreover, the atomisation region is very dense, with significant exchanges between the two phases, which cannot be approached easily with a Lagrangian point of view.

The model, based on an Eulerian approach, proposed by Vallet and Borghi [30] allows calculating, on the one hand, the dispersion of the liquid phase and, on the other hand, the size of the fragments produced, which need not be necessarily droplets. The approach is a generalised classical approach of turbulence modeling of non constant density flows. The basic postulate is that in the limit of large Reynolds numbers and Weber numbers, the viscosity as well as the surface tension does not influence the large scales of the flow. However, they do influence the smallest scales of the flow, i.e. the size of the liquid fragments.

A spray contains a large range of drop-sizes which is the drop-size distribution; this distribution is dependent on the nozzle type and orientation. Factors such as properties of the fuel, injector nozzle capacity, spraying pressure and spray angle all affect the drop-size distribution. The ability to specify drop-size distribution can be used in calculations of heat or mass transfer between the dispersed liquid and the surrounding gas. The difficulty of specifying a drop-size distribution has led to the use of many mean or median drop-size diameters. A commonly used mean drop-size value is the Sauter Mean Diameter (SMD). This diameter is a ratio of the total volume to surface area of the spray. It is commonly used when combustion systems are being analysed where the heat and mass transfer to the spray is important.

$$SMD = D_{32} = \frac{d_v^3}{d_v^2} \quad (2.8)$$

$$d_v = \sqrt{\frac{A_p}{\pi}} \quad (2.9)$$

$$d_s = \left( \frac{6V_p}{\pi} \right)^{\frac{1}{3}} \quad (2.10)$$

Where  $d_v$  is the volume diameter,  $d_s$  the surface diameter,  $A_p$  the particle surface area and  $V_p$  the particle volume.

Viscosity is one of the major factors affecting the atomisation process since it not only affects the drop-size distribution within the spray, but also the nozzle flow rate and spray pattern. The role of viscosity is to inhibit the growth of instabilities and hence delay the disintegration process. This is due to large viscosities needing a greater amount of energy to be used to overcome viscous forces, meaning less energy available for atomisation. In a pressure swirl injector, a very high viscosity fuel can cause the spray cone to collapse into a straight stream of large ligaments and drops.

One way of characterising a spray is in terms of its increase in surface area due to atomisation. Before atomisation the surface area is simply that of the column of fuel from the nozzle. Following atomisation it becomes that of all the drops within the spray. This increase in surface area provides direct information on the level of atomisation, and is useful where surface phenomena such as evaporation and absorption are of issue.

Surface tension is important to atomisation because it is the force that resists the formation of a new surface area. Therefore the minimum energy required for atomisation is equal to the surface tension multiplied by the increase in liquid surface area.

In the study performed by VanDerWege and Hochgreb [31] on the effects of fuel volatility on the spray from a pressure-swirl injector, the authors distinguished three spray regimes depending on the fuel volatility, fuel temperature, and ambient conditions;

1. Slow evaporation, where the conditions did not exceed the boiling point of the fuel mixture.
2. Non-disruptive evaporation, that leads to the migration of more volatile components towards the spray axis.
3. Disruptive evaporation or flash boiling, where the initial spray behaviour is affected by the vaporisation of the lighter components of the fuel, which leads to a narrowing of the spray as the smaller droplets are drawn to the low pressure zone created in the centre of the spray cone.

## Chapter 2 – Injection Process and Spray Characteristics

---

They also found that the vapour core penetrated more quickly than the bulk drops in the periphery. The penetration of the main portion of the spray is faster for higher fuel temperatures, lower ambient density, earlier injection timings and higher volatility components of the fuel. The converse of these conditions reduced the penetration speed, but also increased the spray cone width. The intake flows were also shown to affect the spray pattern, and this was emphasised at early injection timings where the intake flows are high. A higher degree of flash boiling was also witnessed due to the reduced ambient gas pressure and increased ambient gas temperature.

A study into the effects of fuel spray momentum by Strauss and Zeng [32] showed that sprays with smaller droplets are more sensitive to bulk air movements and flow scavenging patterns, whereas sprays with larger drops are less sensitive. It was also seen that if the spray momentum was not large enough then unburned hydrocarbon emissions would increase greatly due to increased mixture short-circuiting despite the improved fuel vaporisation.

Combustion of a liquid fuel in an oxidising atmosphere occurs in the gaseous phase, therefore gasoline must be vaporised before it can combust [33]. Vaporisation is the process by which molecules in a liquid state spontaneously become gaseous. For molecules to vaporise they must be located on the boundary between the liquid and the surrounding gas and this is the reason for the requirement of the atomisation process to give a large surface area. The increased surface area allows all the fuel to vaporise before the spark plug ignites the mixture. If the surface area is not great enough then some fuel will not vaporise before the mixture is ignited. The resulting mixture will be lean, and in leaner mixtures with an air/fuel ratio lower than 1.3, reliable flame initiation and propagation will not occur, leading to partial burns and misfires [34].

The factors controlling the drop evaporation constant are discussed by Fang et al. [35]. They found that the droplet morphology at a specific temperature was controlled by the physical properties of the liquid itself, such as the molecular weight, density, diffusion coefficient in air, and heat of vaporisation. Two processes are included in drop evaporation: diffusion of liquid molecules into the air (diffusion part) and flow of the liquid molecules from inside the drop to the free outer shell liquid layer within the liquid-vapor interface (evaporation part). The diffusion part remained steady during drying and was not sensitive to the variation of temperature. The evaporation part, however, was an active factor and determined the differences in drop evaporation behaviors.

## Chapter 2 – Injection Process and Spray Characteristics

---

Sprays produced by GDI injectors consist of droplets containing a wide range of sizes (from  $D_{10} \sim 5\mu\text{m}$  and  $D_{32} \sim 20\mu\text{m}$  up to  $100\mu\text{m}$  for the sparse large drops) and velocities. The details of the combustion process are intimately affected by the spatial and temporal distributions of liquid and vaporised fuel within the combustion chamber, which in turn, depend on the details of the initial atomisation process.

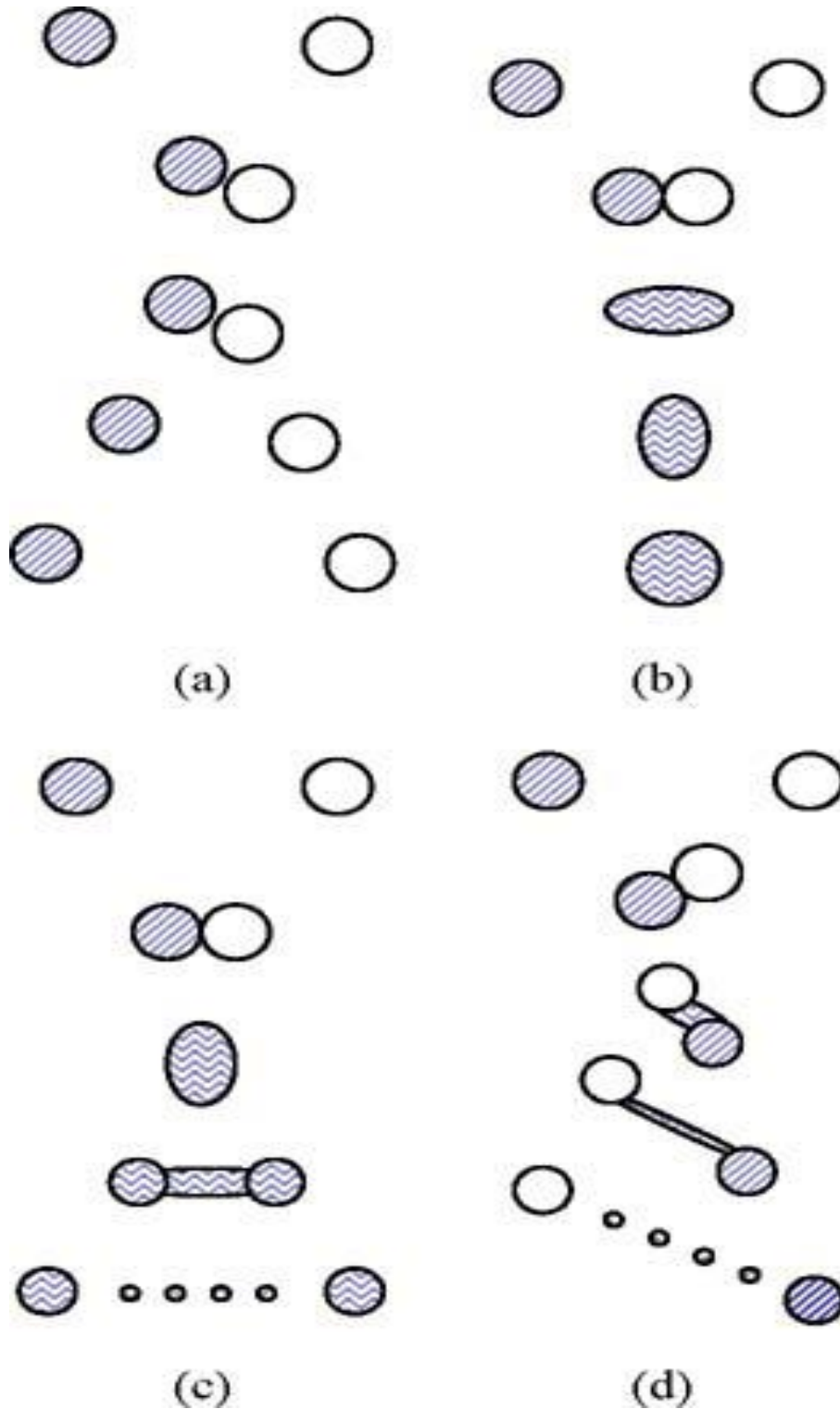
Based on the experimental observations, sprays are generally divided into three regions [36]: dilute spray region, dense spray region and churning flow region. In the churning flow region, a liquid jet emerging from the nozzle deforms and breaks into small droplets. In the dense spray region, droplets are very closely spaced so that there is a strong direct droplet-to-droplet interaction. The number density of the droplets in this region is very high so it is sometimes difficult to perform an accurate measurement of the droplet distribution. In the dilute spray region, on the other hand, droplets are spaced far enough from one another so that direct interaction between them is usually negligible. In this region, well-known empirical correlations for isolated drops can be used to calculate the exchange rate of mass, momentum and energy between an individual drop and the surrounding gas [36].

An experimental study was carried out by Ashgriz and Givi [37] in which the collision dynamics of two n-hexane fuel droplets were studied. The experiments were performed on the collision of two burning droplets, as well as two non-burning droplets, to assess the influence of the high temperature combustion environment on the dynamics of the collision. The results indicated that as the Weber number is increased, the collision type moves toward higher energy collision, and for the same Weber number, different types of collisions, depending on the local value of the collision impact parameter, may occur. In the range of Weber number studied (2 to 14), the results show that for the non-burning droplets, the collision type can be bouncing (the contact of the surfaces are prevented by the intervening air film resulting in bouncing of the droplets after the collision), grazing (the droplets just touch one another slightly without coalescence), temporary coalescence-satellite generating (the droplets coalesce temporarily with a subsequent separation accompanied by satellite drops) or permanent coalescence (the droplets coalesce and remain united permanently), depending on the local value of the impact parameter. For the burning droplets in the same initial Weber number range, only the temporary coalescence and permanent coalescence are observed.

## Chapter 2 – Injection Process and Spray Characteristics

---

A diagram of collision regimes presented by Ko et al. [38] in their numerical study on bouncing and separation collision between two droplets considering the collision-induced break-up can be seen in Figure 2.5.



**Figure 2.5: Diagram of collision regimes: (a) Bouncing; (b) Coalescence; (c) Reflexive separation; (d) Stretching separation**

---



### **2.2 Spray Characteristics**

Spray characteristics commonly used in the literature and their definition are presented and discussed in this section.

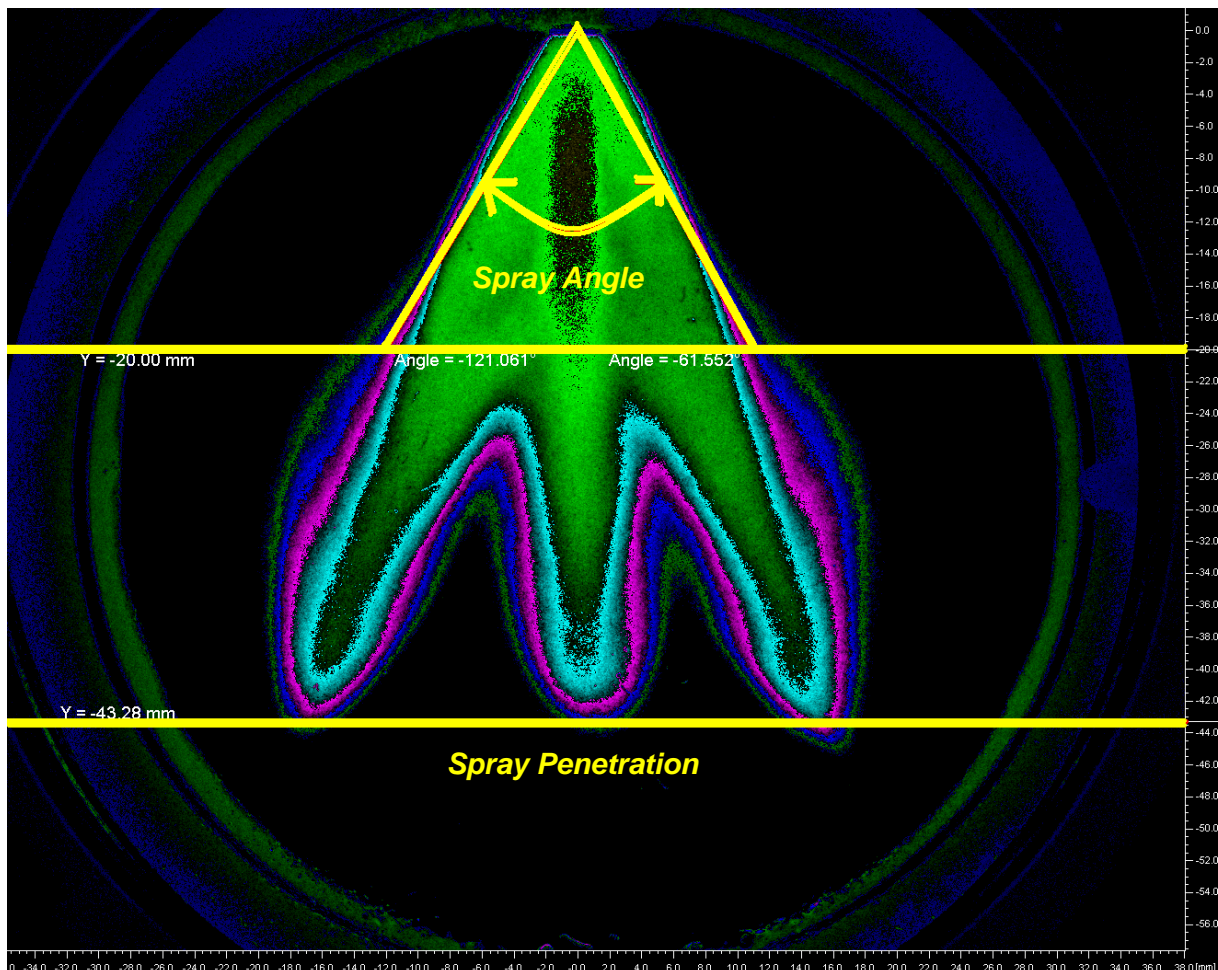
Dispersion can be defined as the ratio of the volume of a spray to the volume of a liquid in it. The main advantage of a good dispersion is that the liquid mixes rapidly with surrounding gas resulting in higher evaporation rates. GDI injectors are mainly governed by other characteristics such as cone angle, mean drop-size, drop-size distribution and properties of the fuel and surrounding medium.

The mean drop-size is the average diameter of droplets in a fuel spray. Depending on its size, a droplet may impact or fail to impact on a solid surface or may follow a different path to a droplet of a different size. The distribution of droplet sizes represents the location of different sizes of droplets within a spray.

Spray Angle is difficult to measure due to the curved boundaries of the GDI sprays so there are various methods of measurement. It is often given as the angle formed between two straight lines drawn from the discharge orifice to cut the spray contours at some specified distance from the atomiser face (see Figure 2.6). The existing definition for the measurement of spray angle as well as the correlation for the prediction of the spray angle in plain-orifice atomisers are summarised and reviewed by No [39]. The existing definition of spray angle in plain-orifice pressure atomisers can be classified into four groups; distance based on orifice diameter, distance based on spray tip penetration, definition based on surface wave, and definition based on atomisation. The existing definition of spray angle in plain-orifice effervescent atomisers can be divided into two groups: definitions based on outer boundary and axial distance. Therefore it is strongly required to specify the definition and measurement method when the data for spray angle is reported. In this study, the spray angle is defined at a distance from the nozzle tip based on spray tip penetration.

## Chapter 2 – Injection Process and Spray Characteristics

Penetration can be defined as the maximum distance a spray reaches when injected into stagnant air (see Figure 2.6). It is governed by the kinetic energy of the initial liquid jet and the aerodynamic resistance of the surrounding gas. The prediction of diesel spray penetration has been the subject of many studies and intensive investigations, both on diesel and GDI sprays, are still in process. No [40] summarised the correlations developed before 1990 and introduced the correlations reported recently in the literature. The existing zero-dimensional models for the prediction of diesel fuel spray penetration can be classified as theoretical and empirical correlations. The models considered in No's paper were selected as based on the evaluation results of previous reviews and the recently published works in the literature. Eight theoretical and two empirical correlations were included and evaluated in his review. According to the review of existing models, the dominating factors for the prediction of spray tip penetration are the spray angle, discharge coefficient, pressure drop across nozzle, ambient density and orifice diameter and time after the start of injection.



**Figure 2.6: Spray angle and penetration illustration for a multi-hole injector**

## Chapter 2 – Injection Process and Spray Characteristics

---

In all cases the penetration of a spray is better than that of a single drop due to the phenomena of entrainment. This is because the first few drops of a spray transfer their energy to the surrounding gas, which then begins to move with the spray which creates less resistance for the following drops and thus overall a greater penetration.

It is known that one of the main parameters that govern the spray penetration development is spray momentum flux. In Desantes et al. [41], a model capable of predicting the development of the spray penetration using as an input the temporal variation of the spray momentum flux is presented. The model is based on the division of the momentum flux signal in momentum packets sequentially injected and the tracking of them inside and at the tip of the spray. These packets follow a theoretical equation which relates the penetration with the ambient density, momentum and time. In order to validate the method, measurements of momentum flux (impingement force) and macroscopic spray visualisation in high density conditions have been performed on several mono-orifice nozzles. High agreement has been obtained between spray penetration prediction from momentum flux measurements and real spray penetration from macroscopic visualisation.

Patternation can be defined as the symmetry of the fuel spray pattern which is important for the even distribution of fuel to achieve low emissions and good combustion efficiency. Radial liquid distribution is the measure of patternation both radially and circumferentially to determine the distribution of liquid within a spray.

### 2.3 Fuel Effects

Commercial fuels are generally a mixture of many different compounds, the properties of which can differ greatly depending on the climate and the market in which it is sold. “Market to market variations in octane and cetane lead to un-optimised calibrations and product availability limitations.” [42]. For instance in colder climates, additional additives are added to aid combustion due to the colder environment. These additives will change the volatility of the fuel which preliminary reading has indicated will affect the spray characteristics of a fuel spray [31]. Fuel viscosity, density and surface tension are three of the most important physical properties of fuel with respect to spray atomisation and resulting spray characteristics [43].

The viscosity of a fuel will have an effect on the atomisation quality and spray angle. It will also affect the pumping power requirements and will vary with temperature [17]. It is a complex subject, the viscosity of a homogeneous liquid depends on the properties of the liquid only in the range of laminar flow; in the range of turbulent flow it depends on the motion of the liquid [1].

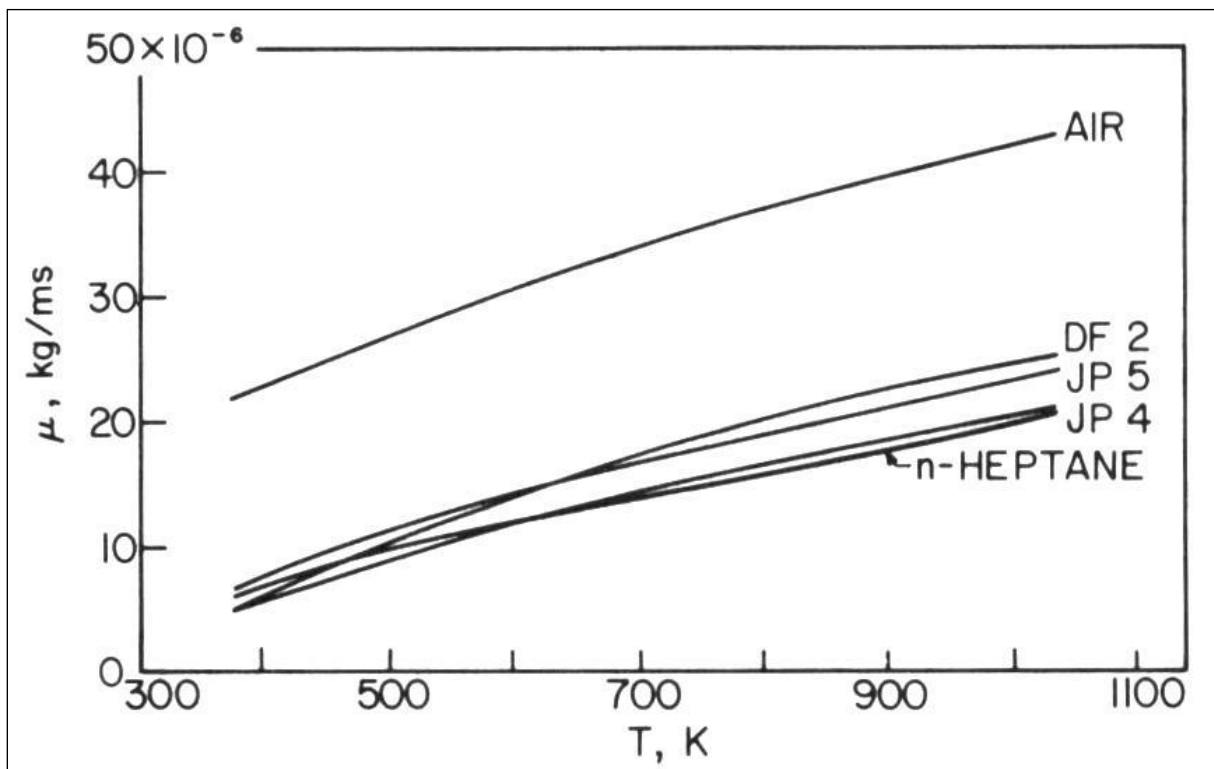


Figure 2.7: Variation of viscosity with temperature for air and various fuel vapours<sup>[17]</sup>

## Chapter 2 – Injection Process and Spray Characteristics

---

The variations of viscosity with temperature for various fuels (N-Heptane, American army Diesel Fuel DF2 and Jet Propellant fuels JP4 and JP5) are shown in Figure 2.7. It can be seen clearly that different fuels have different viscosities and that the viscosity increases fairly linearly with an increase in temperature. The difference in viscosity is therefore likely to have an effect on the fuel spray characteristics due to its influence on the atomisation process.

The density of a homogenous liquid is defined as the ratio of the mass  $m$  to the volume  $V_m$  of the liquid under certain conditions (temperature, pressure) and can be seen in equation (2.11):

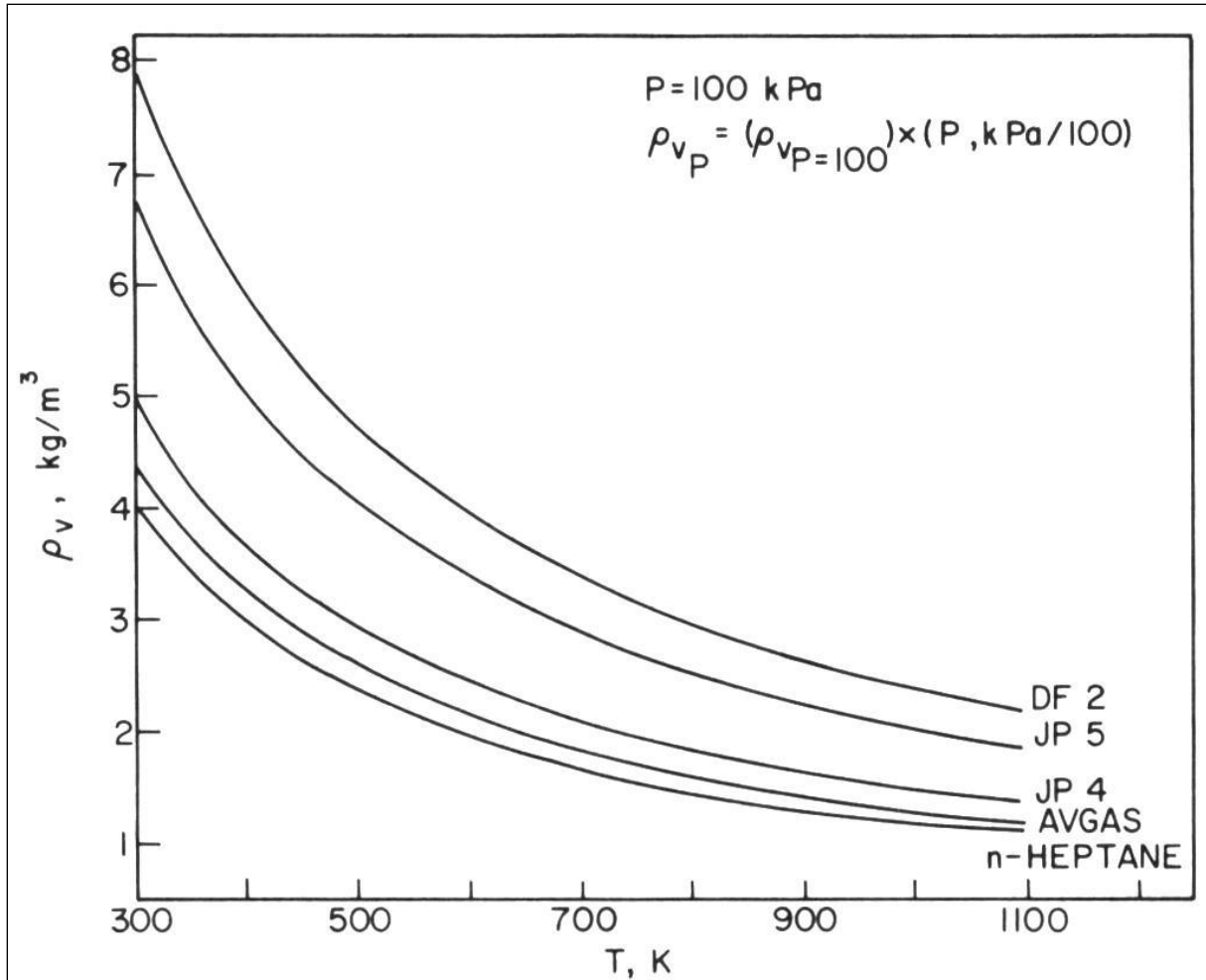
$$\rho = \frac{m}{V_m} \quad (2.11)$$

The density  $\rho$  is a unique characteristic of every liquid; however this is difficult to define for hydrocarbon fuels due to the multi-component nature of their structure.

As temperature increases by  $\Delta T = T_2 - T_1$  the density will decrease from  $\rho_1$  to  $\rho_2$  and can be calculated using equation (2.12):

$$\rho_2 = \frac{\rho_1}{1 + \alpha \Delta T} \quad (2.12)$$

Where  $\alpha$  is the coefficient of volumetric expansion the value of which is specific for every liquid. This decrease in density will vary depending on the properties of the fuel. An indication to the variations between fuel vapour densities for different fuels (N-Heptane, American army Diesel Fuel DF2, Jet Propellant fuels JP4 and JP5, and aviation gasoline AVGAS) is given in Figure 2.8. As expected, it shows density to decrease with an exponential decay when temperature increases.



**Figure 2.8: Variation of fuel vapour density with temperature**<sup>[17]</sup>

Surface tension can be defined as the property of a liquid that resists the expansion of the liquids surface area. Surface tension forces must be overcome by aerodynamic, centrifugal or pressure forces to achieve atomisation [17]. In the case of mixtures the problem of surface tension depends on the type of mixture and the concentrations of its components. Figure 2.9 shows the variation of surface tension for different fuels (Gasoline relative density = 0.745 and Ethanol relative density = 0.789) with relation to temperature.

A temperature increase as the surface area tension decreases is shown in Figure 2.9, therefore the break-up of droplets will be faster at higher temperatures due to the reduced surface tension. Liquid streams injected into a gaseous environment tend to be unstable under a wide range of conditions. An important parameter is the Weber number, at higher Weber numbers, the aerodynamic force dominates, leading to distortion and disintegration. [44]

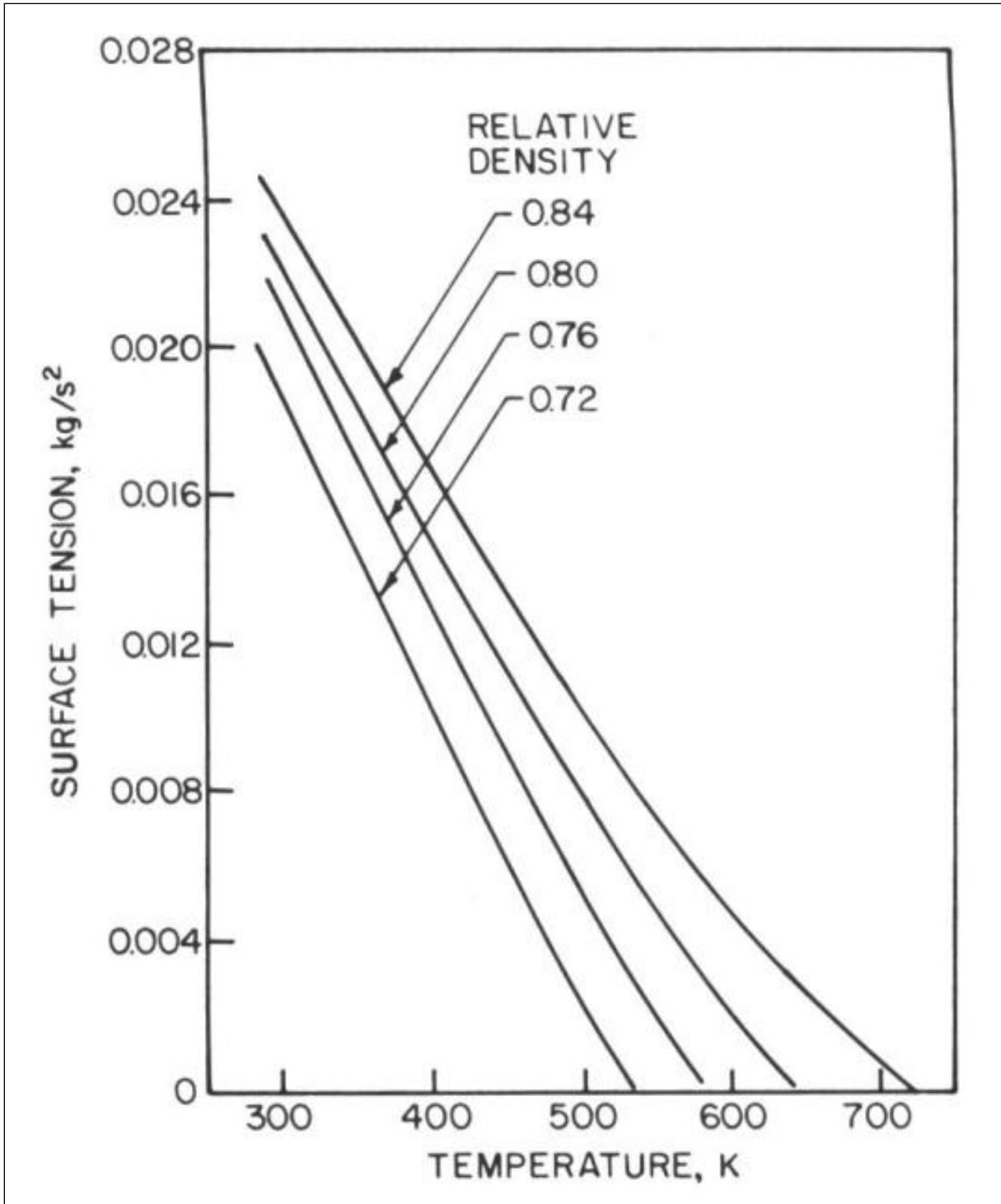
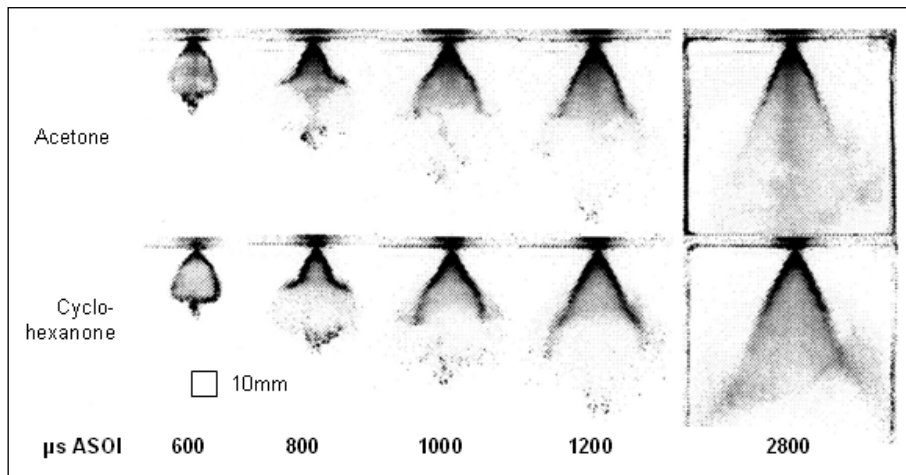


Figure 2.9: Surface tension-temperature relationship for hydrocarbon fuels of varying relative densities<sup>[17]</sup>

## Chapter 2 – Injection Process and Spray Characteristics

VanDerWege and Hochgreb [45] and [31] show that for a direct injection spark ignition engine (DISI), high pressure swirl injector, the spray structure changes not only with ambient gas density, but also with fuel temperature and fuel volatility. As ambient pressure decreases and temperature increases the volatile ends of multi-component fuels evaporate quickly, disrupting the spray and producing a vapour core along the axis of the spray. Beyond a certain point, the evaporation is rapid enough to expand the initial cone angle of the spray while causing a decrease in the overall spray width and a reduction in the mean droplet diameter. They used mono-constituent fuels to simulate volatility aspects of commercial gasoline using dopants of different boiling points in order to identify any differences in behaviour of light and heavy fuel components within a spray. The differences between acetone and cyclohexanone can be seen in Figure 3.1.1.



**Figure 2.10: Comparison of acetone and cyclohexanone spray distributions** [45]

Tong et al. [46] show that for a GDI engine, fuel volatility affects spray development and fuel-air mixing and as a result the in-cylinder fuel distribution. High volatility components vaporise more quickly, resulting in smaller droplets, which have less penetration, whereas low volatility components vaporise more slowly resulting in larger drops which have greater penetration which are more likely to impinge on cylinder walls which leads to increased wall wetting. An increase in wall wetting is not good as it increases the level of emissions in the combustion process. Tong et al supports the findings of VanDerWege and Hochgreb with the high evaporation rates of volatile fuels resulting in reduced penetration due to the lack of momentum due to faster rates of vaporisation.



## Chapter 2 – Injection Process and Spray Characteristics

---

This is supported further by the research of Change and Farrell [43] who discuss the effects of fuel viscosity. Using a high injection pressure diesel spray it was determined that low viscosity fuel sprays gave a greater near nozzle spray angle than high viscosity fuel sprays did in the initial part of the injection. This would suggest that low viscosity and high volatile fuels induce greater evaporation rates but reduced penetration as the increase in cone angle means that a greater proportion of the velocity is in a radial direction, coupled with the high evaporation rates means that there is less momentum within the spray to achieve higher penetration levels.

The low viscosity fuels had larger projected area per unit mass than high viscosity fuel sprays did, indicating more dispersion of the spray. This supports the findings of Chen and Lefebvre [47] about the liquid viscosity having an inverse effect on the spray angles. Sprays of low viscosity liquid had larger spray angles than those of high viscosity liquid sprays.

Schick [48] found that an increase in the viscosity and surface tension increases the amount of energy required to atomise the spray. Therefore an increase in any of these properties will typically increase the drop-size. This is supported by Change and Farrell [43] whose investigation showed the Sauter mean diameter to have increased with an increase of kinematic viscosity and surface tension.

Tong et al [46] stated that the spray development, fuel-air mixing and the resulting in-cylinder fuel distribution were affected by fuel component volatility. They concluded that the in cylinder fuel distribution of individual fuel components in a fuel blend depends on both the volatility of that component and the volatility of other components.

Canaan et al [49] investigated the influence of fuel volatility on the liquid-phase fuel penetration in a Heavy-Duty Direct Injection Diesel Engine. It was concluded that the maximum liquid penetration is strongly influenced by fuel volatility and that there is a strong correlation (approximately linear) between measured maximum liquid length and fuel mid-boiling point.

---

## Chapter 2 – Injection Process and Spray Characteristics

---

### 2.4 Fuel Comparison

Most investigations involving fuels use fuel blends with different volatility characteristics such as the investigation by VanDerWege et al [50]. This may be of interest to determine the extent fuel volatility has on the atomisation performance. An example of a range used by Tong et al [46] can be seen in Table 2.3: Fuel blends of different volatility characteristic (Ethanol boiling point = 78°C).

**Table 2.3: Fuel blends of different volatility characteristics**<sup>[46]</sup>

Volatility	High Volatility	Baseline	Low Volatility
Fuel	2,3 dimethyl butane	iso-octane	n-nonane
Boiling Point (°C)	57.95	99.25	150.85

During design and development the performance of gasoline fuel injectors is often tested with standard single component fuels rather than gasoline. For spray studies this is more than often the case, this is in order to improve safety, or to utilise laser induced fluorescence (LIF). Furthermore, within the research community, idealised fuels are used where the chemistry is simplified and well documented as the analysis and understanding of the behaviour is then made simpler. However, the use of single component fuels can have a pronounced effect on the spray in comparable engine conditions [51].

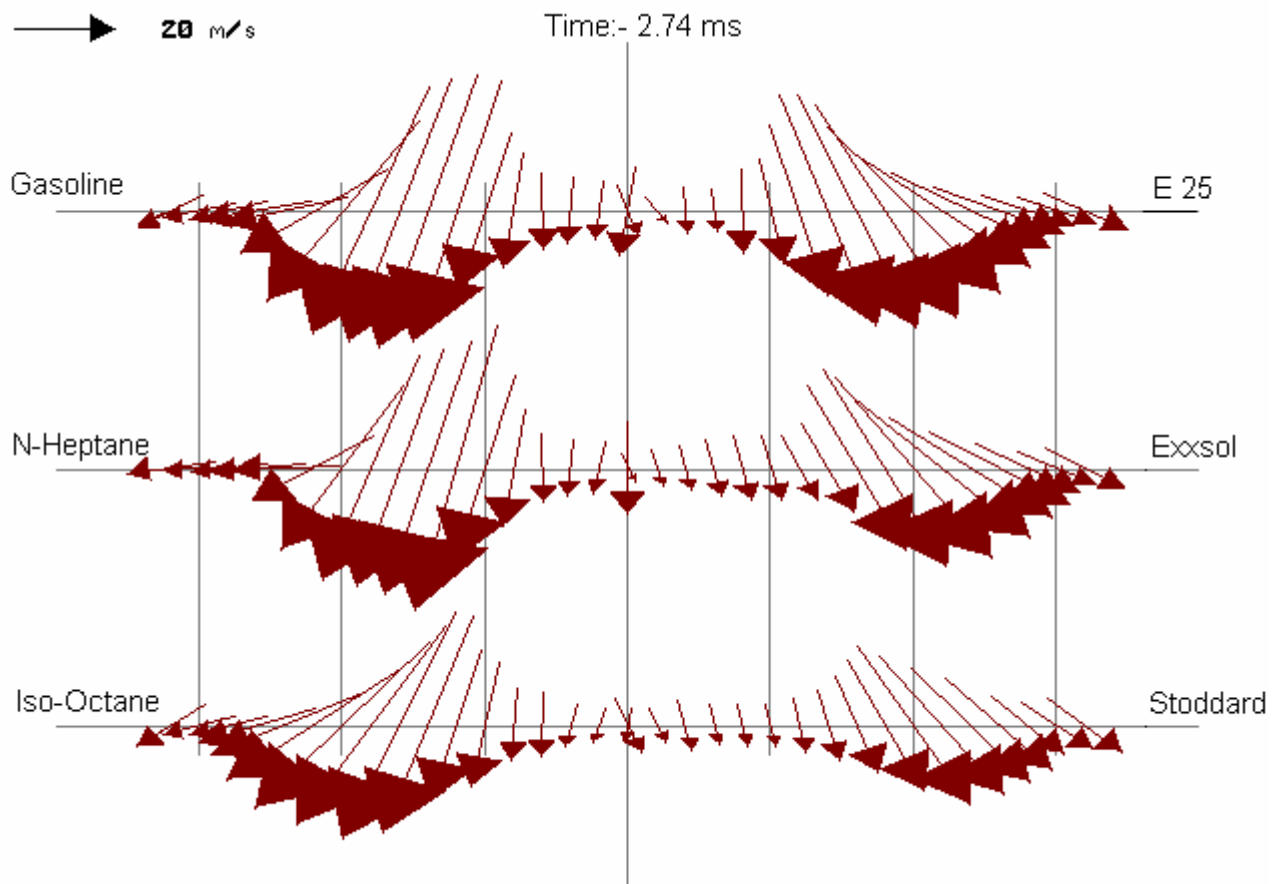
An investigation into the effect of fuel properties on liquid break-up and atomisation in GDI sprays by Wigley et al. [51] showed that different fuels generate different spray characteristics and behaviour. The fuels tested and their properties can be seen in Table 2.4. Obvious variations between properties for the different fuels can clearly be seen.

**Table 2.4: Properties of test fuels available**<sup>[51]</sup>

Fuel	Fuel Density (kg/m <sup>3</sup> )	Kinematic Viscosity (mm <sup>2</sup> /s)	Surface Tension (10 <sup>-3</sup> kg/s <sup>2</sup> )
Gasoline	745	0.74	21.0
N-heptane	682	0.60	20.14
Iso-Octane	690	0.72	18.77
E25	755	0.94	22.0
Exxsol	772	1.30	24.7
Stoddard	780	1.28	26.0

## Chapter 2 – Injection Process and Spray Characteristics

The results from this investigation are shown in Figure 2.11. Although the flow fields for each fuel show a general trend the difference between the magnitudes and direction of the velocities are quite substantial. No fuel is seen to penetrate and the spray to develop faster than gasoline.



**Figure 2.11: Flow field maps for different fuels for a pressure swirl injector<sup>[51]</sup>**

As illustrated in Figure 2.11, N-heptane can be used to model gasoline as regards to spray morphology and droplet dynamics. The same is true for iso-octane to model E25. However, for scientific purposes it would be difficult to relate data from Exxsol and Stoddard to describe a gasoline spray even though these are common ‘calibration’ fluids in automotive industry.

---

## Chapter 2 – Injection Process and Spray Characteristics

---

### ***2.5 Gasoline Direct Injection***

Gasoline Direct Injection (GDI) differs from traditional port injection systems in that the fuel is injected directly into the cylinder rather than into the intake ports prior to the intake valves. Injecting the fuel in this manner allows much more flexibility over the conditions and mixture within the cylinder, and thus allows the designer to control the output emissions to a much higher degree.

All automotive manufacturers nowadays are either developing or have developed a GDI combustion system within the market place. There are many variations in injection strategies used (although the basic principles of all systems are the same).

In a PFI engine, fuel is injected into the inlet manifold manifold and on to the back of the hot inlet valve for fuel evaporation and mixing with the air. When the valve opens the aerodynamic shear forces caused by the rapid flow of air into the cylinder further break-up and atomise the fuel. These methods of atomisation have little reliance on the characteristics of the spray itself, provided that the spray is directed correctly onto the inlet valve. A PFI engine, using the concept of external mixture formation, has advantages in that there is a relatively long duration available for mixture generation outside the cylinder and that the fluid-dynamics conditions are simpler and easier to control. Injecting the fuel into the intake manifold either continuously or sequentially allows for long trajectories of fuel droplets; an advantage for fuel atomisation and vaporisation. Good fluid-dynamic conditions result mainly from air wave propagation within the intake ducts and are characterised by well defined velocity and direction. However, during the mixture formation, the direct contact of fuel with walls and other surfaces cannot be completely avoided. In the intake manifold fuel contact can be caused by air waves or partial spray impacts with surfaces. In the combustion chamber droplet impacts on surfaces caused by the intake flow conditions lead to localised incomplete combustion. Despite the advantages of a PFI engine, major disadvantages in terms of fuel consumption and emissions are created which makes a PFI engine unlikely to reach future legislations [52].

## Chapter 2 – Injection Process and Spray Characteristics

In comparison to direct-injection compression-ignition diesel engines, gasoline spark-ignition engines (using PFI) generally have lower brake specific fuel consumption (BSFC) for a similar sized engine. GDI implements direct injection within a gasoline engine to try to achieve low BSFC without the drawbacks of a diesel engine (i.e. high levels of noise, higher particulate, nitrous oxides (NO<sub>x</sub>) emissions and limited speed range) while keeping the specific power output of a gasoline engine. A GDI engine can offer a potential further advantage over the diesel engines due to the fact that ignition is initiated by a spark source which eliminates many of the stringent quality requirements for the fuel in a diesel engine [53], [54].

In GDI engines fuel is injected directly into the cylinder. The spray characteristics directly influence the vaporisation process and hence are of paramount importance to combustion efficiency and engine-out emissions. By controlling the time at which the injector injects fuel into the cylinder, there is a possibility for these engines to run in both a stratified mode for improved fuel economy at low load and a homogeneous mode for maximum power output at high load. These operating modes are shown in Figure 2.12 which will be discussed further.

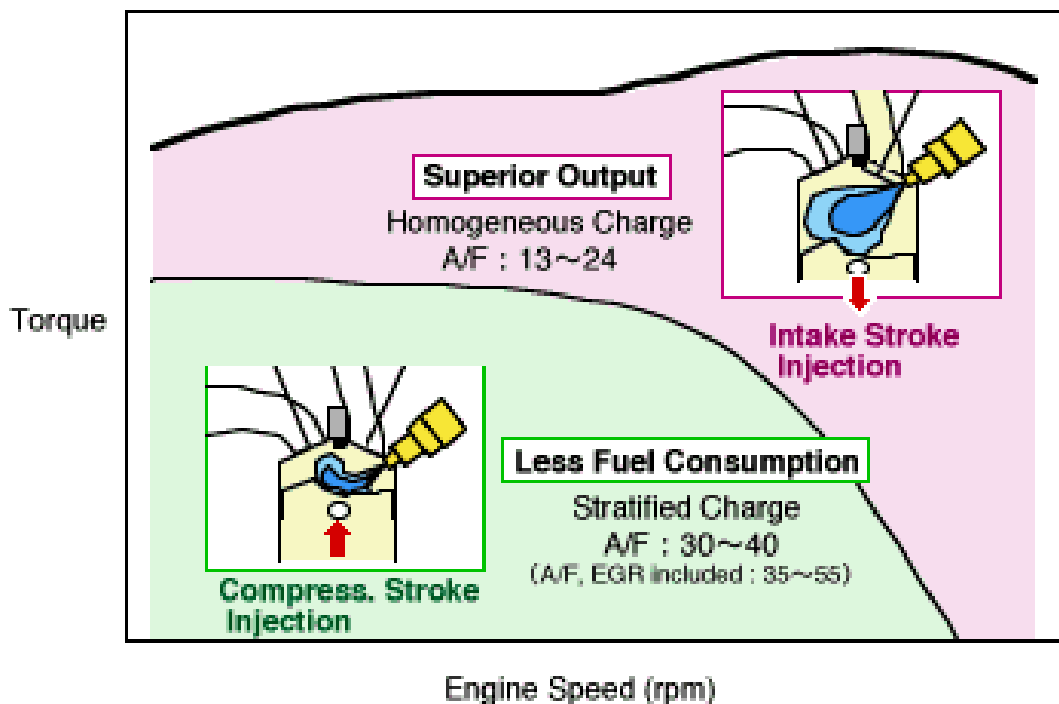


Figure 2.12: Operating modes of GDI engine<sup>[55]</sup>

## Chapter 2 – Injection Process and Spray Characteristics

---

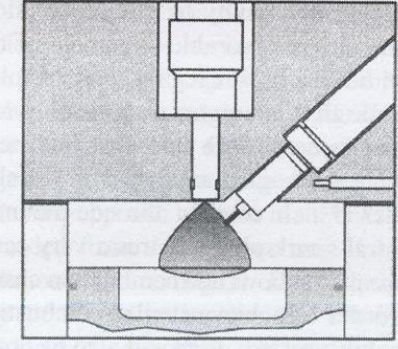
### 2.5.1 Stratified Mode

The first mode to achieve high economy which is utilised at lower engine speeds and loads is stratified operation. This mode creates a stratified charge mixture by injecting late in the compression cycle so there is not enough time for the fuel and air to mix before ignition. The concept is to create a rich or close to stoichiometric mixture near the injector but with an overall air-fuel mixture that is very lean, i.e. in much the same way as in diesel engines. Injecting at this late point in the engine cycle also means that injection occurs at higher in-cylinder pressures which provides improved atomisation and reduced spray penetration. When this is combined with bulk air motion (tumble and swirl) already present, it acts to concentrate the spray around the spark plug. Within a port injection system utilising homogenous charge operation, the air-fuel ratio (AFR) is limited by flame stability. Utilising GDI in this manner allows much lower air-fuel ratios to be used due to the fuel concentration around the spark plug being maintained (this creates a stoichiometric charge at the spark plug whilst keeping the overall AFR very lean, possibly as much as 45:1 [56]), and this also helps to reduce the cycle-to-cycle variation inherent when operating very lean with homogeneous operation. Operating in this manner allows the load to be controlled by injection quantity, while eliminating the throttling losses associated with controlling the load by air flow rate. This mode of operation shares many similarities with diesel combustion operation.

There are three methods currently used for directing the fuel spray towards the spark plug for stratified operation. These are outlined in Table 2.5. Although there are three basic separate mechanisms designed for achieving fuel stratification, the stratification in a working engine is generally achieved by a combination of these. The three different ways in which spray can be guided within a combustion chamber to achieve a stratified charge are: spray-guided, wall-guided and air-guided. Spray-guided uses the concept that the fuel spray is directed towards the spark plug from close proximity, with stratification created by the fuel spray penetration and mixing. Wall-guided uses piston crown design, often a bowl shape design within the crown, to direct the spray toward the spark plug. Air-guided enables a stratified charge via the interaction between the spray and charge motion. Both wall-guided and air-guided designs are generally designed with a relatively large distance between spark and injector. Due to the close arrangement of injector and spark plug, the spray-guided combustion system allows a spatially limited stratification, which allows a non-restricted operation down to idling loads with overall air/fuel ratios up to approximately 115 [52]. The appropriate air/fuel ratio at different engine loads (injected fuel quantities) must be realised by the penetration depth of the injected spray and is therefore mainly determined by the spray characteristics.

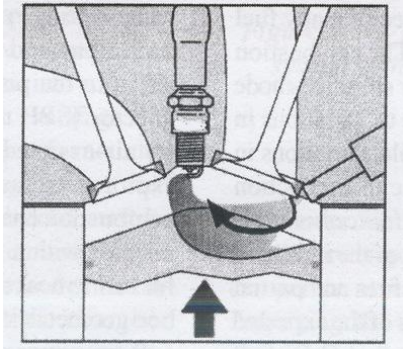
## Chapter 2 – Injection Process and Spray Characteristics

**Table 2.5: Stratified operation mechanisms<sup>[2]</sup>**

<p><b>Spray guided</b></p> <p>Stratification is controlled by the relative positioning of the injector and spark plug. Fuel is sprayed directly into the area near the spark plug with very little interaction with the air charge or cylinder geometry. Atomisation quality is critical to the success of this system due to the limited time available for vaporisation.</p> <div style="text-align: center;">  </div> <p style="text-align: center;"><b>Figure 2.13: Spray guided</b></p>	<p><b>Advantages:</b></p> <ul style="list-style-type: none"> <li>Easiest to apply to existing PFI engine design.</li> <li>Highest stratification capability.</li> <li>Achieved without a strong dependence on charge motion or piston crown design.</li> </ul> <p><b>Disadvantages:</b></p> <ul style="list-style-type: none"> <li>Problems with spark plug fouling and soot generation due to presence of relatively large fuel droplets near spark gap.</li> <li>Very sensitive to fuel spray characteristics, for example variations in spray symmetry, skew and cone angle due to production tolerances or injector deposits can cause excessive COV of IMEP.</li> <li>Requirements for close positioning of injector and spark plug can result in reduction of inlet valve area.</li> </ul>
<p><b>Wall guided</b></p> <p>Fuel spray is injected towards a specially shaped piston crown and this directs the fuel towards the spark plug via charge motion and the momentum of the spray-induced air flow field. Only a minority fraction of droplets actually impinge on the piston crown and form a fuel film. The majority follow the wall contour whilst entrained within a highly transient air flow field generated by the</p>	<p><b>Advantages:</b></p> <ul style="list-style-type: none"> <li>Increased distance between spark plug and injector relative to spray-guided systems gives increased time for mixing leading to lower HC and particulate emissions.</li> <li>Reduced sensitivity to spray characteristics and therefore more robust to spray quality degradation due to injector deposits and production tolerances.</li> </ul> <p><b>Disadvantages:</b></p>

## Chapter 2 – Injection Process and Spray Characteristics

injection event. The specific design of the combustion bowl is very important and must be carefully matched to the fuel spray. The majority of systems use in-cylinder air swirl as the primary air motion to transport the fuel.



**Figure 2.14: Wall guided**

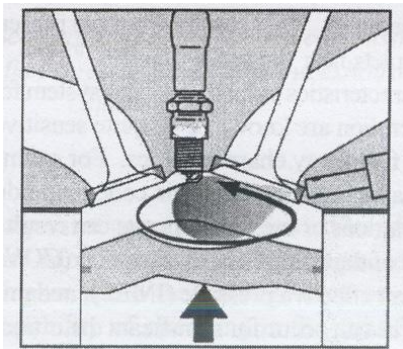
Possibility of increased spray impingement on combustion chamber surfaces.

Shaping the piston crown for part-load stratified operation is detrimental to air utilisation at high loads when a homogeneous mixture is required.

There is a trade-off between emissions and performance which must be optimised by the injector inclination angle.

### **Air guided**

Charge stratification is controlled by the interaction of the fuel spray with the bulk in-cylinder air motion. The piston bowl shape must be optimised in order to create the necessary in-cylinder flow field.



**Figure 2.15: Air guided**

### **Advantages:**

Widest spacing between spark plug and injector allowing best air-fuel mixing.

Reduction in wall wetting gives reduced oil dilution and HC emissions.

### **Disadvantages:**

Flow-field fluctuations can cause combustion instabilities.

At low engine speeds the overall strength of charge motion is reduced, leading to greater combustion instabilities.

Careful calibration is required to match charge motion and spray characteristics over the whole engine speed range.

Piston bowl design for flow-field generation is detrimental to air utilisation at high loads.



## Chapter 2 – Injection Process and Spray Characteristics

---

The stratified combustion mode has the disadvantage of increasing NO<sub>x</sub> and HC emissions due to increased local combustion temperatures, despite reduced peak cycle thermodynamic temperatures [2], and the presence of unburned fuel. The issue with this mode of operation lies with the fact that the conventional three way catalyst operates around a stoichiometric air-fuel ratio. Therefore when the engine is operating using a stratified mixture (the overall AFR is lean), the three way catalyst cannot function properly, and due to the increased oxygen quantity, will mean an increase in nitrous oxide emissions. Due to the engine running lean, unburned hydrocarbons and carbon monoxide emissions are minimal. To control the nitrous oxides formed during this period, GDI engines utilise exhaust gas recirculation (EGR) and either a NO<sub>x</sub> trap or Selective Catalytic Reduction (SCR) catalyst.

Introducing recirculated exhaust gas into the fresh charge acts to dilute the charge, reducing the combustion flame adiabatic temperature. The exhaust gas also acts to increase the specific heat capacity of the mixture, further lowering the peak combustion temperatures. Since NO<sub>x</sub> chemistry is heavily temperature dependent and rises exponentially with temperature, the reduction in combustion temperature as a consequence of introducing EGR reduces the nitrous oxides formed during GDI stratified operation. Cooling the EGR mixture can also amplify this affect on flame temperature and hence reduce NO<sub>x</sub> emissions further.

Using EGR can have a significant effect in reducing nitrous oxide emission but it is not sufficient to reduce emissions below current legislation and therefore further reductions are required, most of which included post-engine reductions in the tail pipe itself. One method of achieving this is to use a 'NO<sub>x</sub> Absorber' or 'NO<sub>x</sub> Trap'. The absorber features a zeolite base material that traps the nitrous oxides NO and NO<sub>2</sub>. The absorber can be purged by introducing hydrocarbons into the exhaust. The stored nitrous oxides are unstable in the presence of hydrocarbon and will join to form water (H<sub>2</sub>O) and Nitrogen (N<sub>2</sub>). This can be easily achieved during the second mode of operation when using a homogeneous charge mixture.

Another method to reduce nitrous oxide is to use an SCR catalyst. An SCR catalyst uses a reducing agent to reduce NO<sub>x</sub> into water and Nitrogen. The most commonly used reductants are ammonia or urea. The largest issues with this form of emissions control is the supply of reductant and the narrow temperature window in which the catalyst will operate. A supply of reductant is required at all times for the catalyst to function and for this to be possible the re-fuelling infra-structure must be available. The temperature of the exhaust can be controlled to ensure the exhaust temperature remains within the operational window of the catalyst, but anywhere outside of this window and the performance of the catalyst drops of rapidly.

## Chapter 2 – Injection Process and Spray Characteristics

---

Due to issues mentioned with respect to SCR emissions control, many manufacturers are using NO<sub>x</sub> absorber based catalysts. Unlike diesel engines (which tend to almost entirely operate with a stratified lean mixture), direct injection gasoline engines tend to have periods where they operate with a stoichiometric/slightly rich mixture for performance benefits. This provides the reducing agent in the form of hydrocarbons in which to purge the catalyst.

In some examples, multiple injections during the compression stroke have been used to increase exhaust gas temperatures much more rapidly during the engine's warm-up phase. This has been used with dramatic effects (reports of reducing hydrocarbons by almost 50%) on reducing unburned hydrocarbons during this phase.

Within GDI engines, stratified combustion systems are capable of realising optimised thermodynamic efficiency by avoiding any wall film generation without excessive air charge motion. The spark plug position in these combustion systems nowadays represents a compromise of cylinder head construction, water cooling jacket requirements, and the combustion system demands themselves. However, different atomiser concepts used in gasoline engines with direct injection lead to different combustion systems and thus, need different spark plug locations. For this reason a prototype combustion system with totally centered injector position and a low voltage spark ignition system was set up by Raimann et al. [57]. The idea was to reveal regions with perfect ignition conditions for the three different spray types with nominally an equal spray cone angle layout. In this engine the general spray propagation properties, generated by the different injectors, were investigated by high-speed (HS) imaging of Mie scattered light. These tests were performed using regular super gasoline (RON 98). The use of model fuels, a nearly regular fuel free of aromatic hydrocarbons, traced by an exciplex makes fluorescent signals from liquid and vaporised fuel phases distinguishable. Statistical evaluation of Laser Induced Exciplex Fluorescence (LIEF) measurements allowed the identification of locations with and without high liquid and vapor concentration probabilities. Locations with a maximum vapor and a minimum liquid occurrence probability were chosen as potentially optimal spark positions. The chosen positions were tested for the different injectors in the transparent engines within 250 ignited cycles. Misfire rates and indicated mean pressure data were compared with the signals from high-speed color pictures taken from the combustion cycles. Finally, the correlation of the statistical evaluation of the combustion process with the gained results from the mixture formation investigations by LIEF was discussed [57].

## Chapter 2 – Injection Process and Spray Characteristics

---

### 2.5.2 Homogenous Mode

The second mode of operation is used at higher engine speeds and loads for improved performance. It also removes the flame instability issues associated with stratified combustion. This mode sees fuel injected during the intake stroke. This gives rise to improved mixing due to the larger time allowed for mixing to occur and is intended to provide a homogeneous mixture within the cylinder. In addition to this, the injected fuel has a cooling effect on the cylinder charge due to the vaporising fuel. This acts to improve volumetric efficiency due to higher charge density and improved knock resistance. The improvements in knock resistance allow a higher compression ratio to be used for improved efficiency, or if the engine is supercharged, higher boost ratios for further performance increases.

A third mode can be created by a combination of the first two modes, utilising a largely stratified mixture with the majority of the injection late in the compression stroke, but also injecting a small quantity of fuel during the intake stroke. The initial injection causes the intake charge to cool in the same manner as used during the second homogeneous mode. This reduces the probability of knock and allows the ignition timing to be further advanced, improving performance and efficiency. This mode is used during high load low engine speed conditions for improved torque output, and to bridge the gap between the two main modes for smoothness of operation.

The most fuel-efficient mode of operating a gasoline engine is to burn fuel in excess air without the use of a throttle to modulate the engine load. With homogeneous charge spark-ignition burning a lean air-fuel mixture reduces the flame propagation speed until ignition limits are reached, therefore the engine can only be operated unthrottled over a restricted range of loads and speeds. The lean throttle-less operating region of the engine can be significantly extended using stratified charge combustion systems. In addition to pumping work reduction, operating lean increases the thermodynamic efficiency of the engine through increasing the ratio of specific heats and stratified charge combustion reduces heat transfer to the cylinder walls [58].

## Chapter 2 – Injection Process and Spray Characteristics

---

The direct injection spark ignition, DISI, engine under homogeneous charge mode offers improved full-load performance and full-load fuel economy when compared with the present generation of port injected gasoline engines. Moreover, the DISI engine also offers the possibility of significant fuel savings under low and part-load conditions through the adoption of a stratified charge injection strategy. Stratified-charge operation in DISI combustion systems is achieved through the injection of fuel late during the compression stroke, therefore, the time available for air-fuel mixing and fuel vaporisation is restricted. This can lead to a high probability of finding liquid fuel, locally rich and extreme air-fuel regions in the overall air-fuel vapour mixture within the cylinder at the time of ignition.

Many of the first generation wall-guided and air-guided GDI engines produced disappointing improvements in fuel economy and emissions due to the difficulty in optimising the complex nature of their combustion systems and the lack of appropriate lean exhaust gas after-treatment. The most serious threat to the full acceptance of the DISI engine lies in the nature of the stratified charge combustion process itself, locally undiluted mixtures give rise to high flame temperatures,  $\text{NO}_x$  production and the emission of high levels of sub-micron particulate matter. The development of the de- $\text{NO}_x$  catalyst,  $\text{NO}_x$  sensing and control technology has enabled the benefits of lean operation via a stratified charge combustion system to be partially realised, though compromises in fuel economy potential due to emissions compatibility still remain [58].

The introduction of fully variable valve trains (FVVT) has allowed new strategies in engine control to be realised, two of the most significant being those of throttle-less combustion control and controlled auto-ignition. However, when combined with gasoline direct injection, whole new areas of engine control can be explored using conventional spark ignition, and offering some of the gains of fuel economy from lean burn operation to be obtained with homogeneous charge combustion. The FVVT systems remove the need for a throttle, as the inlet charge can be controlled by the valve events, and so minimise the throttling losses associated with a conventional throttle plate. This offers the chance to run the engine in direct injection, homogeneous mode, while still gaining the benefits of no throttle in the inlet system. The main advantage of homogeneous direct injection strategies is the avoidance of using a  $\text{NO}_x$  trap and, with it, the associated extra materials costs. Additionally, there is a fuel consumption penalty with lean burn, to regenerate the  $\text{NO}_x$  trap, which diminishes the theoretical benefits [59].

## Chapter 2 – Injection Process and Spray Characteristics

---

Two principal valve strategies can be employed to control the quantity of fresh charge being introduced to the cylinder, early inlet valve closing, EIVC, and late inlet valve opening, LIVO. These processes will have a direct effect on both the in-cylinder pressure, and the flow structure developed during the inlet valve opening phase. The work presented by Pitcher et al. [59] investigates the morphology and penetration of the spray, with early injection, 40 degrees after top dead center (ATDC), to gauge the effects of the in-cylinder conditions on the spray development. Four different valve timing strategies were used, standard, early inlet valve closing, EIVC, late inlet valve opening, LIVO and late inlet valve opening with early exhaust valve closing. The latter combustion mode is for controlled auto-ignition, CAI.

Homogeneous direct injection strategies have the potential to reduce fuel consumption and emissions, without the requirement for a de-NO<sub>x</sub> trap. Combined with a fully variable valve system, the fuel consumption is improved by having the ability to run without a throttle. The work presented by Wigley et al. [58] is a preliminary study of the spray morphology with injection into different in-cylinder conditions due to three different valve strategies and engine speeds representative of all part load engine conditions. An initial analysis of the spray morphology has shown that the spray dynamics during injection are sensitive to flow structure at engine speeds over 1000 rpm for the standard and EIVC valve lift profiles. However, the in-cylinder pressure is seen to have the most important effect on both the early and late spray propagation. This is especially true for the LIVO valve timing profiles where the low in-cylinder pressure generates flash evaporation of the fuel and plays a significant role in determining spray shape and penetration even during the injection period. The paper [58] describes these mixing processes for each case and also discusses how the internal flow structure plays a controlling factor for spray distribution after injection for a range of engine speeds up to 4000 rpm.

## Chapter 2 – Injection Process and Spray Characteristics

---

In order to create the two main combustion modes in a direct injection gasoline engine, homogenous and stratified, it is important that an optimum relationship between spray characteristics and engine speed is achieved. The possible contribution of different components on the mixture formation is as follows [52]:

### **Fuel Contribution on Mixture Formation:**

- Injection rate modulation and injection quantity
- Injector location and nozzle shape
- Start of injection
- Duration of injection

### **Air Contribution on Mixture Formation:**

- Intake duct position and shape
- Control of the distribution by variable valve timing
- Air pressure history at the intake port (supercharging, turbocharging, etc.)

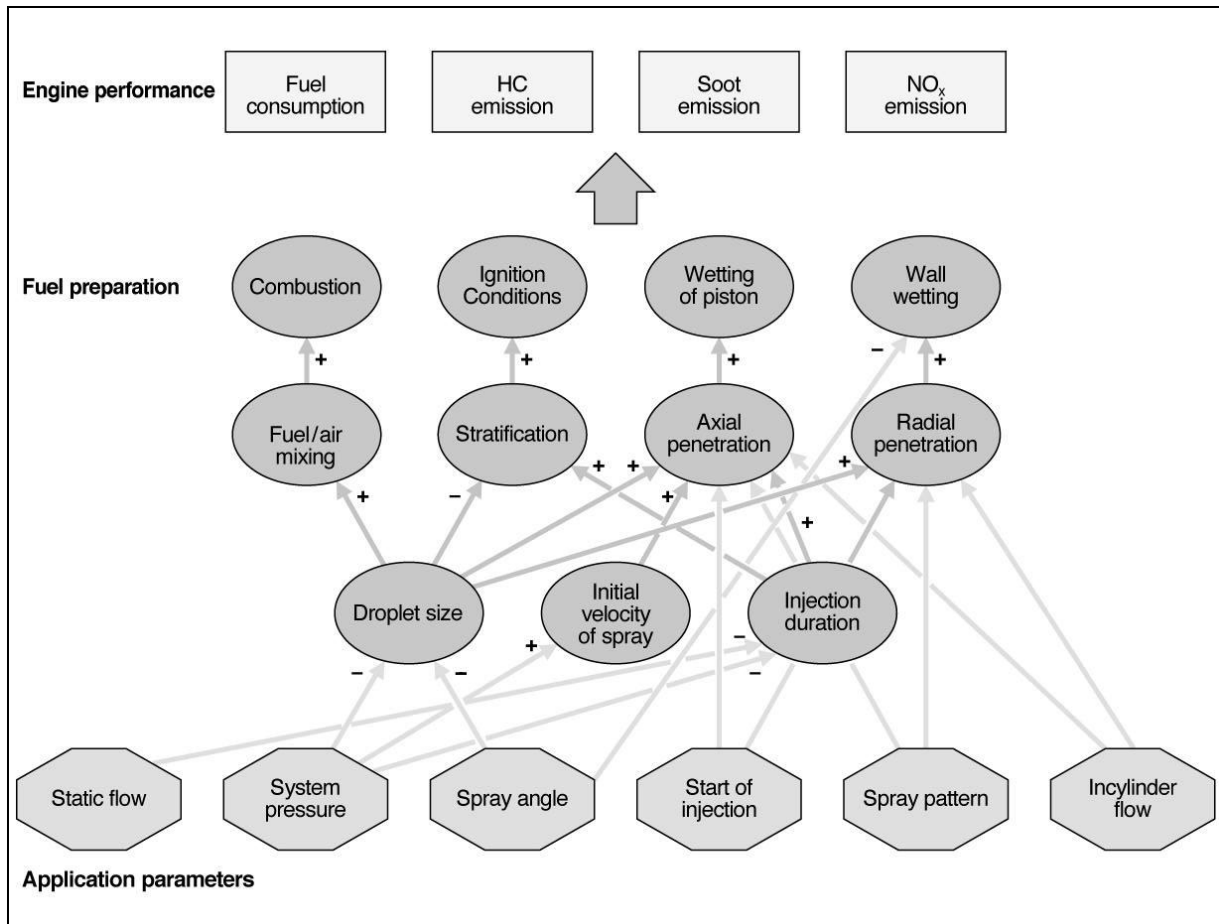
### **Combustion Chamber Design Contribution on Mixture Formation:**

- Piston surface and head geometry
- Spark plug location

### **Spark Plug Mixture Support:**

- Ignition timing
- Ignition duration

To achieve an optimum fuelling and combustion design, each of the factors should be adapted to changing conditions with respect to load, speed, thermodynamic state of fuel and air, surrounding conditions (i.e. wall temperature), transient conditions. However, some of the factors cannot be adapted during engine operation, for example spark plug location, therefore an optimisation for a variation of conditions is required. The following diagram shows an alternative system analysis of mixture formation mechanisms.



**Figure 2.16: Model of GDI Application Parameter on Engine Performance and Emissions<sup>[60]</sup>**

It can be seen from Figure 2.16 that compensations and compromises needed to be made between certain parameters. Effects of one parameter on another are indicated by plus and minus signs to highlight counteracting mechanism (A higher injection system pressure for example leads to a lower droplet size, higher initial velocity and shorter injection duration). The injector parameters; spray angle, start of injection, and spray pattern are of particular interest for research in this study.

A GDI engine has the potential to avoid disadvantages found with PFI engines and generates the potential for numerous advantages:

- **Avoidance of air throttling:** Within a GDI engine system the engine load is controlled by the injection of the fuel therefore there is no need for throttling, hence reducing engine pumping losses at part load. The inlet air mass is adjustable via an electronically controlled throttle valve linked to an air/fuel ratio sensor.

## Chapter 2 – Injection Process and Spray Characteristics

---

- **Increase of compression ratio:** The compression ratio for a GDI engine can be set higher than that of a PFI. A higher compression ratio cannot be used for PFI engines as the extra pressure causes auto-ignition, with a GDI engine injecting the fuel directly into the cylinder gives a charge cooling effect, reducing the temperature and chance of detonation (or “knocking”).
- **Increase in the absolute heating value of the mixture:** The maximum heating value of an air fuel mixture for a fixed volume is produced when homogenous and slightly under the stoichiometric value. This appears to be a benefit for PFI external mixture formation. However, in a direct injection engine, scavenging occurring with pure air allows for optimum design of intake ducts, creating lower pressure losses. With no throttling the air mass captured during scavenging can be increased. Increasing the fuel mass proportionally with a higher air mass (maintaining a stoichiometric mixture) keeps the relative heating value constant while the absolute heating value is increased. An increase in the absolute heating value of the mixture results in a higher Brake Mean Effective Pressure (BMEP) [52].
- **Possibility of mixture formation control until start of ignition:** By adjusting the correlation of injection quantity, injection rate and ignition timing; control of the mixture formation can be achieved. In the stratified mode of combustion two zones are created in the combustion chamber: a combustible air/fuel mixture cloud at the spark plug embedded in an insulating layer of air and residual gas. This achieves a higher thermodynamic efficiency by reducing heat losses to the chamber walls.
- **Combustion control by mixture formation:** Theoretically a mixture formation that is controlled in the optimum way can reduce the emissions that occur in a GDI engine. The control of the air fuel mixture has a great effect on the reduction of emissions from wall-wetting and localised rich mixtures. The air pressure within the cylinder during the compression process works against the injected fuel flow. When fuel is injected later in the process a higher opposing pressure acts of the mixture formation, affecting the spray development. Different combustion chamber designs also allow the control of mixture formation.



## Chapter 2 – Injection Process and Spray Characteristics

---

GDI has difficulties that need to be overcome. In terms of emissions, nitrous oxides (NO<sub>x</sub>) levels are higher than PFI at both part and full load meaning that three-way catalysts need to be replaced. High hydrocarbon (HC) and increased particulate levels are also found due to wetting of the walls, possibly in a combustion chamber that is not of optimum design. When the spray is in close contact with the spark plug the liquid fuel can cause carbon fouling, affecting the performance of the spark plug. However, it is important that sufficient fuel is within close proximity to the spark plug at ignition especially in stratified conditions. It is also important that the fuel is sufficiently atomised and guided correctly with the combustion chamber.

Levels of liquid fuel impingement on in-cylinder surfaces in direct injection spark ignition engines have typically been higher than those in port-fuel injection engines due to in-cylinder injection and higher injection pressures. The result is typically an increase in the levels of unburned hydrocarbons and smoke emissions which reduce the potential fuel economy benefits associated with direct injection engines. Although different injection strategies can be used to reduce these effects to some extent, full optimisation of the injection system and combustion process is only possible through improved understanding of spray development that can be obtained from optical engine investigations under realistic operating conditions. To this extent, Serras-Pereira et al. [61] studied the spray formation from a centrally mounted multi-hole injector in a single-cylinder optical direct injection spark-ignition engine under part-load conditions (0.5 bar intake plenum pressure) at 1500 RPM. A high-speed camera and laser illumination were used to obtain Mie-scattering images of the spray development on different in-cylinder planes for a series of consecutive engine cycles. The engine temperature was varied to reflect cold-start (20°C) and fully warm (90 °C) engine conditions. A multi-component fuel (commercial gasoline) and a single-component fuel (iso-octane) were both tested and compared to investigate the effects of fuel properties on spray formation and wall impingement. An experimental arrangement was also developed to detect in-cylinder liquid fuel impingement using heat flux sensors installed on the cylinder liner. Two different injection strategies were tested; a typical single-injection strategy in the intake stroke to promote homogeneous mixture formation, as well as a triple-injection strategy around the same timing to assess the viability of using multiple-injection strategies to reduce wall impingement and improve mixture preparation. A sweep of different locations around the cylinder bore revealed the locations of highest fuel impingement levels which did not correspond directly to the nominal spray plume trajectories as a result of spray-flow interactions. These results were analysed in conjunction with the observed effects from the parallel imaging investigation [61].

## Chapter 2 – Injection Process and Spray Characteristics

---

In a GDI engine, the formation of the air-fuel mixture, which is governed by the fuel spray geometry, the air motion, and the interaction among the spray, air motion, and wall, directly influences the engine performance. The fuel injected into the cylinder generates air motion and evaporates to form the air-fuel mixture. The mixture is forced near a spark plug by the spray penetration, air motion, and/or wall reflection. In Kawajiri et al. [62], the authors investigated the spray wall impingement and the interaction between the spray, air motion, and wall using an experiment and a numerical simulation. A high-pressure swirl injector simulation model was developed and applied to calculate the spray characteristics and spray wall impingement. The simulation results of the spray shapes under atmospheric and pressurised ambient pressure agreed with the experimental results. Experimental tests of a normal and oblique spray-wall impingement by using a high-pressure swirl injector were then carried out to clarify the spray shapes after the impingement. The developed spray simulation model successfully calculated the spray-wall impingement and evaluated the fuel wall adhesion and the details of the spray shapes. The influence of the spray geometry on the mixture formation and fuel wall impingement was investigated. A full-cone spray and various hollow-cone sprays were tested. The interaction between the spray and air motion was investigated using an experiment and a numerical simulation involving fuel spray in a constant-volume swirl vessel. It was found that the main part of the hollow-cone spray was influenced strongly by the air motion, although the influence of the air motion on the central part was weak. Finally, DI engine combustion calculations were described using a developed spray and combustion model. A hybrid combustion model combining a flame area evolution model and a turbulent mixing model was developed to calculate the stratified combustion of the DI engine [62].

When a high load is required a homogenous air-fuel mixture is optimum to achieve the best possible combustion throughout the chamber. To achieve a homogenous mix within a GDI engine the fuel is injected during the intake stroke. However the major advantage of a GDI engine over a PFI engine is the ability to run a lean mixture at low engine loads. As the fuel is sprayed directly into the combustion chamber during the compression stroke the spray can be controlled and directed towards the spark plug, therefore achieving a stoichiometric mixture for combustion at the spark plug is achievable with a lower overall air/fuel ratio. An overall AFR in the region of 40-50:1, compared to stoichiometric (ideal value for complete combustion) value of 14:1, can be achieved at low loads for a GDI engine. This injection strategy is known as stratified, assuming that through injection timing a homogenous-lean mixture is not created [2].

## Chapter 2 – Injection Process and Spray Characteristics

---

To summarise, the advantages of using a direct injection system are:

- Due to being able to produce very precise fuel injection quantities, only the required fuel is supplied and therefore a reduction in emissions and fuel economy is achieved. This also helps to achieve higher power and torque outputs.
- Using stratified operation allows a very overall lean mixture to be used, almost eliminating unburned hydrocarbons and carbon monoxide emissions.
- Unlike diesel engines, gasoline direct injection engines have periods where they operate under homogenous charge conditions. This allows the NO<sub>x</sub> absorbers to be regenerated easily.
- Due to the engine load being controlled by injected fuel quantity the throttle, usually employed by gasoline engines, can be removed therefore greatly reducing pumping losses.
- The evaporative cooling affect associated with injecting fuel into the intake charge can be used reduce the risk of knock. Therefore a higher compression ratio (or increased boost pressure in supercharged applications) can be used for improved performance and efficiency.
- Engine and catalyst light-up time can be reduced using multiple injections during the compression stroke to greatly reduce unburned hydrocarbon emissions during engine warm-up periods.
- Using either, a pressure-swirl injector with dished piston crown geometry to direct the spray up towards the spark plug, or a multi-hole injector positioned with the periphery of the spray in close proximity to the spark plug, a very rich combustible mixture close to the point of ignition can be designed.
- Maintaining the air-fuel mixture near the spark plug and away from the cylinder walls prevents wall wetting and excessive heat transfer, reducing hydrocarbon emissions and improving efficiency.

## Chapter 2 – Injection Process and Spray Characteristics

---

The theoretical benefits of GDI engines merit priority status for further development, however there are many challenges which need addressing before the GDI engine replaces the Port Fuel Injection (PFI) engine as the standard engine for production vehicles.

These challenges are shown in Table 2.6.

**Table 2.6: Challenges of GDI engine development<sup>[2]</sup>**

Challenge	Reason	Mechanism
Emissions	High local NO <sub>x</sub> production at part load, stratified charge operation	Locally rich mixture burns at high temperature
	High unburned HC	Fuel spray impingement on cylinder walls and piston crown
	High particulate emissions	Locally rich mixture burns incompletely, creating soot
Control system	Highly complex system required	Seamless load changes need accurate cycle-to-cycle fuel metering
	Increased system development time	Increased number of calibration variables which must be optimised
Fuel economy	Parasitic losses	Increased fuel system pressure requires pump with high power consumption
		Increased electrical load required by injectors and drivers
	Periodically rich AFR	Fast catalyst light-off and catalyst regeneration
Durability	Fouling of injectors and spark plugs	Locally rich mixture burns incompletely, creating soot deposits
	Fuel system component wear	Combination of increased system pressure and low lubricity of fuel
	Cylinder bore wear	Dilution of engine oil with fuel due to cylinder wall impingement of fuel

---

## Chapter 2 – Injection Process and Spray Characteristics

---

### 2.5.3 Downsizing a Gasoline Engine Using Turbocharging with Direct Injection

Nowadays, downsizing (reduction of the engine size by reducing the cylinder size or by removing one or more cylinders) appears as a major way of improving fuel consumption of spark ignited engines while maintaining the advantage of the low emission capability of three ways catalytic system. The downsizing approach with turbocharging to restore the power is now more and more oriented towards fuel economy, thanks to dedicated solutions. The use of gasoline direct injection system coupled with adapted turbochargers provides several ways of enhancing the engine resistance to knock especially at high load and low engine speed where existing PFI turbocharged engines are still limited [63].

The purpose of Lecointe and Monnier [63] was to highlight the combustion behaviour of the new generation of turbocharged direct injection engines and to demonstrate the potential of such a solution on a specific application. First, the authors explained the global system approach (injection, turbocharger, fluid motion, valve timing ...) used to reach the necessary goals: high low end torque and specific power capabilities and low specific fuel consumption over the whole engine map. Then, they presented all the results at part load and full load obtained on the Renault basis 1.8l IDE concept modified by the French Petrol Institute (IFP) for a turbocharged application. This engine allowed advantage to be taken of its high knocking limit to replace a 3.0 liter naturally aspirated engine and thus to obtain a fuel consumption benefit of more than 15% with at least the same acceleration performance.

With the 1.4 litre 125 kW TSI (Turbo Stratified Injection) engine with direct injection and dual charging, Volkswagen was the first volume manufacturer to introduce with great success a downsizing strategy which reduces CO<sub>2</sub> emissions while also increasing driving fun. The new 1.4 l TSI with 88 kW and a single-stage turbocharger starts off the next step in the implementation in the field of cost-effective high volume production engines. The special technical features of the engine include the further development of the combustion process, simplification of the injector engineering, meticulously optimised turbocharger in conjunction with optimised charge exchange and a newly developed design for water-cooling charge air. Due to the moderate downsizing of the new 1.4l 88 kW engine, about a 30 % reduction in displacement compared to the naturally aspirated engine with the same torque, the new engine can be configured with an economical, one-stage turbocharger, fulfilling all the requirements for the introduction of TSI technology in Volkswagen's volume segment. The combination of the new TSI technology with the new Volkswagen 7-speed dual clutch gearbox with dry clutches makes possible an improvement of 22 % in fuel consumption

## Chapter 2 – Injection Process and Spray Characteristics

---

compared to the predecessor Golf, completely attaining the target of 139g CO<sub>2</sub>/km in the European driving cycle (compared to 178g CO<sub>2</sub>/km for the previous golf) [64].

### 2.5.4 Controlled Auto-Ignition

Controlled Auto Ignition (CAI) or Homogenous Charge Compression Ignition (HCCI) is characterised by the spontaneous ignition and burning of fuel and air charge within the cylinder in a short space of time. This self-ignition of fuel depends mainly on the charge temperature with the process being controlled by chemical reactions rather than turbulent flame preparation in direct injection spark-ignition (DISI) gasoline engines or by fuel spray and air mixing in direct injection diesel engines. In comparison with lean-burn charge stratification technology within a GDI engine, CAI gives the following advantages [65]:

- Complex combustion chamber geometry and intake design not required as the ignition process is controlled by the charge temperature.
- No need for lean NO<sub>x</sub> catalytic converters to meet emissions regulations.

The challenges that CAI faces, however, are as follows:

- Combustion infrequently occurs before Top Dead Centre (TDC) as it ignites once the charge has reached the auto-ignition temperature.
- The combustion process is much faster in auto-ignition compared to a standard spark-ignition engine. This creates a large pressure rise, creating a noisy engine or damage in the extremes.
- CAI operation range limited by knocking at high loads and misfires at low loads.
- Unburned HC and CO are higher than in spark-ignition combustion due to incomplete combustion.
- In order to cover complete engine operation range, smooth switching between CAI and SI combustion is required.

The charge temperature can be controlled by intake air heating or faster thermal management, variable compression ratio and introducing or trapping hot burned gases in the cylinder. High centane-number fuels (diesel, dimethyl ether and n-heptane) can enhance CAI combustion because of their lower auto ignition temperature, with potential for dual-fuel mixing to be utilised to reduce the large pressure rise.

There is a great potential for CAI to be used as an option for GDI engines. With injection timing and split injections viable for mixture control, there is a need for experimental research into spray development while varying both of these parameters [65].

---

## Chapter 2 – Injection Process and Spray Characteristics

---

### 2.5.5 High Pressure Stratified Start

Generally for start-up within a GDI engine system, a homogenous mixture formation is used. Low pressure primary fuel pumps are usually the only pump utilised which produces a start-up pressure of around 0.5MPa, however, since the working pressure required in GDI combustion processes is in the range of 4 to 15MPa, this results in poor mixture preparation at start-up. Typical average droplet diameter at start-up are approximately 100µm (compared to 10 to 40µm for injection pressures between 4 to 15MPa); at this size the droplets have a resistance against atomisation and are relatively high momentum. The high momentum causes the droplets to travel further into the combustion chamber and being a likely cause of start-up emissions due to wall-wetting. Using a low pressure system start up, a large proportion of the injected fuel is wasted and produces HC and particulate emissions.

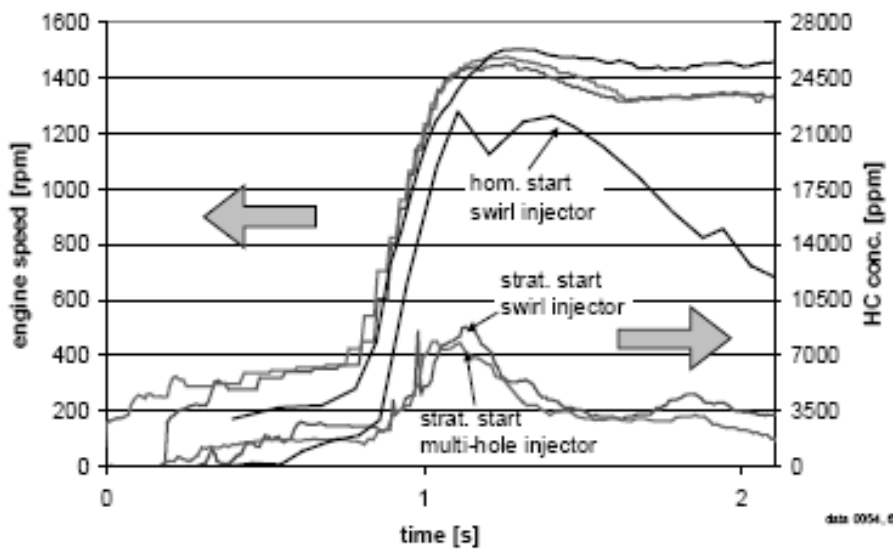
At cold start, the poor mixture preparation for homogenous means that an enrichment factor of two to three times more than stoichiometric at 20°C (and higher at lower temperature) is used. Bosch systems have produced extensive research into stratified start processes [66]. Stratified Start requires a high pressure build up; this is because injection takes place late in the compression phase in contrast to injection in the intake phase permitted for low pressure homogenous start. For a successful injection in the compression phase, sufficient pressure is required. Previous research found a minimum pressure required in compression to be 2 MPa for the first start up injection. In the Dahlander and Lindgren investigation [66] the fuel system components were optimised and produced such that a value of pressure of 2.2 MPa was created for the first stroke of the pump. This means that high pressure stratified start was possible for use within a direct injection gasoline engine.

With the stratified start being produced at higher pressure the average droplet diameter produced will be lower than the equivalent low pressure homogenous start (approximately 40µm). The fuel charge will have higher temperature and due to compression pressure allowing for greater vaporisation. To allow for the rich localised air fuel mixture at the spark plug for stratified start, injector and combustion chamber design must be optimised. An optimum design can allow for greater efficiency and reliability of start-up and allow for the enrichment factor to be reduced in relation to low pressure homogenous start.

## Chapter 2 – Injection Process and Spray Characteristics

To allow a detailed comparison between stratified start and homogenous start, a wall-guided standard combustion process with both swirl and multi-hole injectors was performed by Dahlander and Lindgren [66]. The HC emissions produced in the exhaust for both start strategies is shown in

Figure 2.17. It was possible to reduce the amount of fuel used in start up by half and therefore the HC emissions in the exhaust are shown to be greatly reduced. This process is not only advantageous for start-up but the reduction of fuel film on the combustion chamber due to wall wetting allows for less HC emissions during engine warm-up further into the combustion process.



**Figure 2.17: HC emission production for stratified start and homogenous start<sup>[66]</sup>**

Spray angle and penetration length data were taken under cold start conditions for a Direct Injection Spark Ignition engine to investigate the effect of transient conditions on spray development. Previous investigations ([67], [68]) demonstrated that during cold start, spray development depends primarily on fuel pressure, followed by Manifold Absolute Pressure (MAP). Injection frequency had little effect on spray development. The spray for a single hole, pressure-swirl fuel injector was characterised using high speed imaging [67] and phase Doppler anemometry [68]. The fuel spray was characterised by three different regimes. Regime 1 comprised fuel pressures from 6 to 13 bar, MAPs from 0.7 to 1 bar, and was characterised by a large pre-spray along with large drop-sizes. The spray angle (45°) and penetration lengths (30 to 70mm) were comparatively small. Regime 2 comprised fuel pressures from 30 to 39 bar and MAPs from 0.51 to 0.54 bar. A large pre-spray and large drop-sizes were still present but reduced compared to Regime 1. The spray angle (50°) and penetration lengths (40 to 85mm) were typically larger than in Regime 1. Regime 3 comprised fuel pressures from 65 to 102 bar and MAPs from 0.36 to 0.46 bar. The fuel spray



## Chapter 2 – Injection Process and Spray Characteristics

---

had a fully developed hollow cone structure with recirculation vortices at the edges of the spray, which constricted the spray angle due to the effect of the pressure (higher on the outside edge of the spray). The spray angle was similar to Regime 2, while the penetration length increased. The pre-spray and drop-size were reduced compared to Regime 2. In all regimes, decreasing MAP enlarged the spray angle, while injection frequency was not a significant factor.

### 2.5.6 Homogenous Split Injection

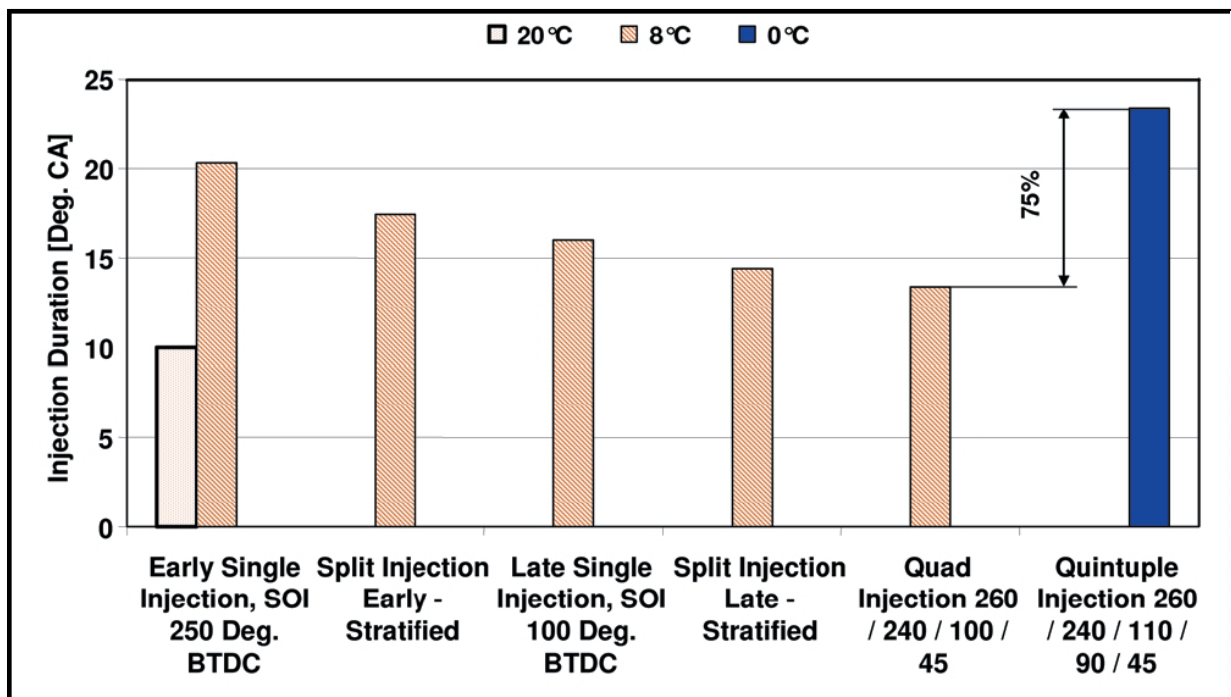
The current process for catalyst heating, called 'lean warm up', is not sufficient to meet future emission legislations. The amount of emissions created by internal combustion engines at start-up and cold start produces a significant proportion of total emissions during the time to working temperature of the catalyst.

A Homogenous Split Injection (HSI) strategy combines low emissions with powerful heating capacity. It uses separate injections to produce optimum mixture formation. The first injection takes place during the intake stroke creating a homogenous lean base mixture. The second injection is timed within the compression stroke, allowing the benefits of good mixture formation mentioned in the stratified start process. The distribution of fuel mass between the two injection pulse and the timing of the injections need to be calculated; such that combustion reliability and engine speed stability is achieved. The ignition timing within a homogenous split injection process is after TDC within the combustion stroke. The lateness of the ignition is the reason that the catalyst heating can be utilised. The ignition at this late engine angle means that part of the combustion energy is not converted to mechanical energy but converted to heat energy, heating the catalytic converter. There are numerous potential positives in emission reduction using homogenous split injection. The stable combustion with slightly lean air fuel mixture results in a low concentration of unburned hydrocarbons; as produced in stratified start. This heating strategy can reduce noxious emissions by up to 50% compared to 'lean warm up' when running on the FTP75 cycle, US equivalent to the Urban Driving Cycle (UDC) + Extra Urban Driving Cycle (EUDC). With the catalyst reaching working temperature earlier for homogenous split injection then HC, CO and NO<sub>x</sub> emissions will be reduced. A slight reduction of fuel consumption was also found during the FTP cycle due to the shortened heating phase of the catalytic converter [69].

## Chapter 2 – Injection Process and Spray Characteristics

When studying the reduction of emissions for gasoline engines it is important to investigate the cold-start process. Hydrocarbon emissions during cold start and subsequent engine warm-up constitute the majority of the HC emitted. Reducing HC emissions during this operating period is necessary to meet future HC emissions regulations.

Research has been introduced into the investigation of split or multiple injections for a GDI engine during cold start [69]. It has been found that with split or multiple injections the duration of injection required for safe starting at low temperatures is significantly reduced.



**Figure 2.18: Duration of injection required for safe starting with different injector strategies with E100 fuel<sup>[69]</sup>**

The injection duration required for safe starting at cold-start using different injection strategies is shown in Figure 2.18. E100 fuel was used as it was less likely to reduce imaging quality, the trend can be closely linked to which would be observed using gasoline.

Further research into how the separate injection mixtures interact is required. This could reduce the emissions at cold start, thereby improving the overall fuel economy of the engine.

## Chapter 2 – Injection Process and Spray Characteristics

---

Lee et al. [70] investigated the effects of split injection, with a relatively short time interval between the two sprays, on the spray development process, and the air entrainment into the spray, by using laser induced fluorescence and particle image velocimetry (LIF-PIV) techniques. The velocities of the spray and the ambient air were measured. The cumulative mass of the ambient air entrained into the spray was calculated by using the entrainment velocity normal to the spray boundary. The vortex structure of the pressure swirl injector spray, formed around the leading edge of the spray, showed a true rotating flow motion at low ambient pressures of 0.1 MPa, whereas at 0.4 MPa, it was not a true rotating flow, due to the phenomenon of the small droplets (i.e. smaller than 10 $\mu$ m) separating from the leading edge of the spray and falling behind, due to air drag. The development processes of the 2<sup>nd</sup> spray were considerably different from that of the 1<sup>st</sup> spray since the 2<sup>nd</sup> spray was injected into the flow fields formed by the 1<sup>st</sup> spray. Therefore, the status of the flow field immediately before the 2<sup>nd</sup> spray injection, including the ambient air motion formed by the 1<sup>st</sup> spray, should be considered in the development process of the 2<sup>nd</sup> spray. Consequently, the development processes of the 2<sup>nd</sup> spray cannot be predicted without prior analysis of the effect of the 1<sup>st</sup> spray. Furthermore, the authors observed that the averaged mass flow rate increases with the time interval between injection events. This increase in mass flow rate is the result of eliminating the effects of the injection duration from the total mass of the ambient air entrained into the fuel spray. Nevertheless, the mass flow rate increases slightly because the air entrainment continues late into the injection period. Consequently, it is shown that the split injection, which has the same total injection duration as the single injection, favorably increases the air entrainment into the fuel spray over the single injection spray [70].

For all the different types of injection mode mentioned within this section, the atomisation quality of the injection is of particular importance. In the current study measurement techniques have been used which can quantify the fineness of an injector spray, which is of great importance for the development stage of GDI injection modes.

## Chapter 2 – Injection Process and Spray Characteristics

---

### 2.5.7 GDI Injectors

The design of the fuel injector has significant impact on the air-fuel mixture preparation and therefore performance of GDI engines. Compared to traditional port injection engines, the available space and time for the atomisation process is significantly reduced for GDI engines. This requires the injector to deliver sprays with sufficiently small droplet size (smaller than  $40\mu\text{m}$ ) and large flow rates (larger than  $10\text{g/s}$ ) for high-load conditions. Consequently, high-pressure direct-injection fuel systems and swirl injectors dominate GDI engine applications worldwide because they can achieve both requirements simultaneously. However, this technology also has many inherent drawbacks, such as high system cost, complicated system configuration, excessive wall wetting, and lack of spray tailoring flexibility [71].

In order to obtain stable combustion the air-fuel charge resulting from mixing and vaporisation must be controlled both spatially and temporally. Preparing and locating the desired mixture over the full range of engine operating conditions is difficult as the mixing process is influenced by many time-dependent variables. This places great demands on the fuel injection system and in particular the injectors. Successful GDI engine design requires optimisation of the fuel system components and subsequent matching of this system to the in-cylinder flow field and combustion chamber geometry.

GDI combustion systems require a "well atomised" spray under all operating conditions, with the definition of "well atomised" being one in which the  $D_{32}$  is less than  $20\mu\text{m}$  [2].

The injectors must be able to provide for at least two distinct operating modes, stratified and homogeneous, or the engine would have a limited operating range of either low-load and low-speed or high-load and high-speed. Stratified operation requires injection during the compression stroke, with ambient backpressures up to  $0.9\text{MPa}$ . This requires the injectors to work with an elevated fuel rail pressure relative to PFI injectors to ensure an adequate pressure differential across the injector tip to produce sufficient fuel atomisation.

Many of the requirements of GDI injectors are the same as for PFI injectors, possibly with more stringent tolerances, however, there are also additional requirements. These are outlined in Table 2.7, based on information from Zhao et al. [2].

## Chapter 2 – Injection Process and Spray Characteristics

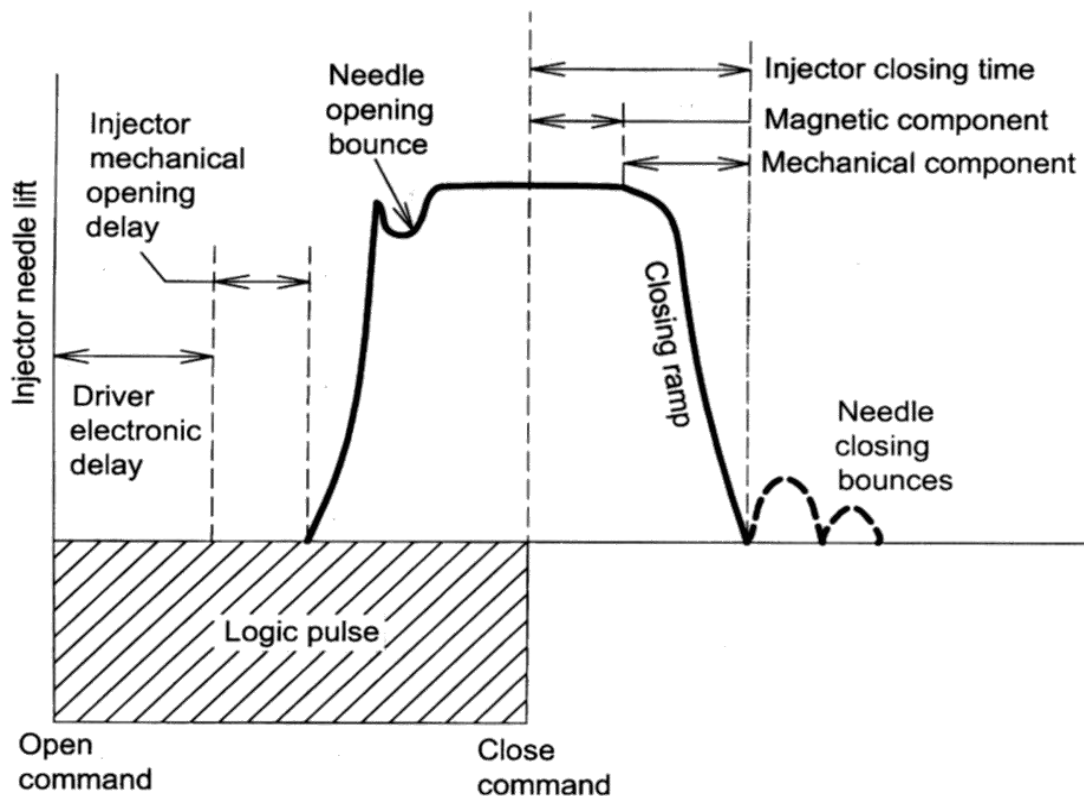
---

**Table 2.7: Fuel injector requirements<sup>[2]</sup>**

<b>General Requirements for GDI and PFI Injectors</b>	<b>Specific Requirements for GDI Injectors</b>
Accurate fuel metering (generally $\pm 2\%$ over the flow range)	Significantly enhanced atomisation level; application dependent but always under $20\mu\text{m} D_{32}$
Desirable fuel mass distribution for the application	Ability to deliver desired spray distribution under varying ambient backpressures
Minimal spray skew for both sac and main sprays	Expanded dynamic range
Good spray axisymmetry over the operating range	Combustion sealing capability (injector tip essentially part of combustion chamber)
Zero drippage and fuel leakage, particularly for cold operation	Avoidance of needle bounce which causes secondary injections
Small sac volume	Reduced bandwidth tolerance for static flow and flow linearity specifications
Good low-end linearity between dynamic flow and fuel pulse width	Greater emphasis on spray penetration control
Small pulse-to-pulse variation in fuel quantity and spray characteristics	Greater emphasis on control of sac volume spray
Minimal variation in the above parameters from unit to unit	Enhanced resistance to deposit formation
	Reduced flow variability under larger thermal gradients
	Ability to operate at higher injector body and tip temperatures
	Leakage resistance at elevated fuel and ambient pressures
	Greater emphasis on packaging requirements
	Flexibility to produce off-axis sprays at various angles to meet specific combustion system requirements
	Ability to conduct multiple injections within one engine cycle

## Chapter 2 – Injection Process and Spray Characteristics

Injection of gasoline directly into the combustion chamber is accomplished by an electronically actuated injector connected to a high-pressure common-rail fuel system. The fuel metering is achieved by precise control of the duration of a square-wave voltage pulse signal designated by the Fuel Pulse Width (FPW). The required FPW is calculated by the Engine Control Module (ECM) from calibration maps based on the output of sensors for engine speed, driver load demand and emissions after-treatment systems. This pulse is sent to the injector driver which is used to activate the injector solenoid. The square-wave voltage pulse and resulting needle lift dynamics are shown in Figure 2.19. It can be seen that there is a delay between the open command from the logic pulse and the physical opening of the injector which comprises of two components. The driver electronic delay is sometimes incorporated to charge a capacitor on systems which deliver over 36 volts to the injector and is used to enhance the injection-to-injection repeatability for a wide range of injection dwell periods and also minimise injector response times.



**Figure 2.19: Injector driver dynamics**<sup>[2]</sup>

The mechanical opening delay is caused by the time taken for the magnetic field in the solenoid to become powerful enough to overcome the fuel line pressure and to move the injector needle and the hydraulic time response. Added together these delays are called the "dead-time", below which no fuel is injected. As the needle begins to move, the lift increases very rapidly, reaching full lift in the region of tens of microseconds [2]. During this period the

## Chapter 2 – Injection Process and Spray Characteristics

fuel flow rate is non-linear and for accurate fuel metering the time taken for the needle to reach maximum lift and the injector to reach full flow capacity should be minimised.

Once the close command is sent by the logic pulse, there is another delay. The magnetic component is due to the time taken for the magnetic field of the solenoid to decay to the level where the needle spring starts to close, and the mechanical component is due to the time taken for the needle to actually spring back to the close position. The needle closing bounces will cause additional sprays of fuel to be injected and should be eliminated if possible.

Many different types of injectors have been researched to find sufficient atomisation and control to be used within a GDI engine. The main types of injectors are mentioned in Figure 2.20 below:

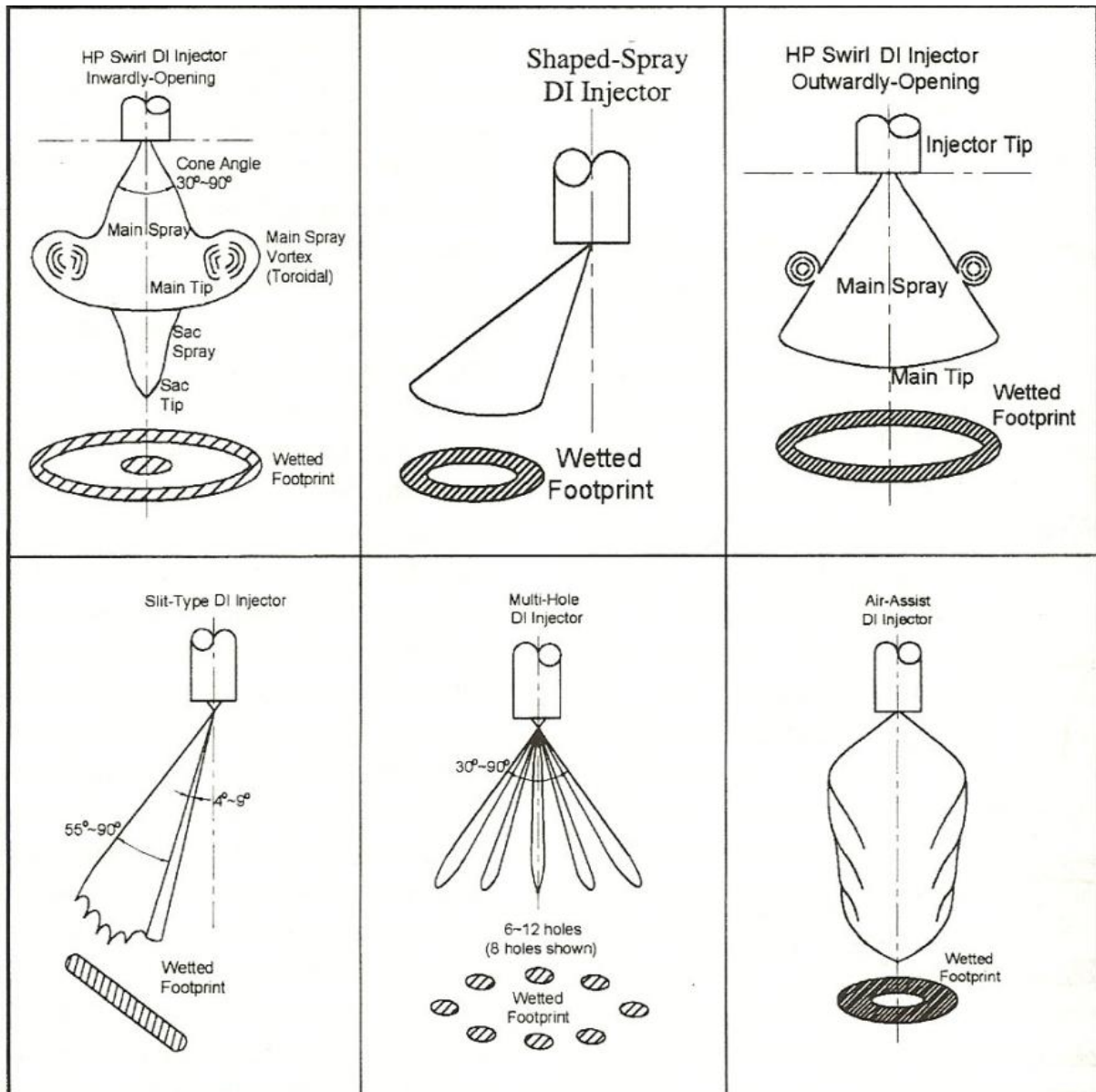


Figure 2.20: The six different types of injectors used in GDI engine design <sup>[2]</sup>

## Chapter 2 – Injection Process and Spray Characteristics

---

### **Inwardly-Opening, Single-Fluid, High-Pressure, Swirl Injector:**

- Hollow-cone spray
- Solid-cone spray
- Symmetric spray - spray is symmetrically distributed across the spray axis. The spray axis can be either aligned with the injector axis or offset from the injector axis
- Asymmetric (shaped) spray - mass distribution across the spray axis is not symmetric. The spray axis may or may not be on the injector axis

### **Outwardly-Opening, Single-Fluid, High-Pressure, Swirl Injector:**

- In general, it produces a hollow-cone spray without a sac spray. It is difficult to produce an offset spray from this type of injector.

### **Slit-Type Nozzle:**

- The geometry of the nozzle is in the form of a slit, which delivers a fuel spray in a fan shape

### **Hole-Type Nozzle:**

- Single-hole
- Multi-hole pattern – spray structure varies with the number and arrangement of the holes.

### **Pulse-Pressurised, Air-Assisted Injector:**

- This type of injector uses a significantly reduced fuel pressure, but requires two separate solenoids and a source of compressed air for improved spray atomisation and dispersion.



## Chapter 2 – Injection Process and Spray Characteristics

---

There are several classifications of GDI injector, each of which generates different spray geometry. These can be further classified according to atomisation method, actuation mechanism, fluid state, pintle opening direction and nozzle configuration. These are summarised in Table 2.8.

**Table 2.8: Classification of GDI injectors<sup>[2]</sup>**

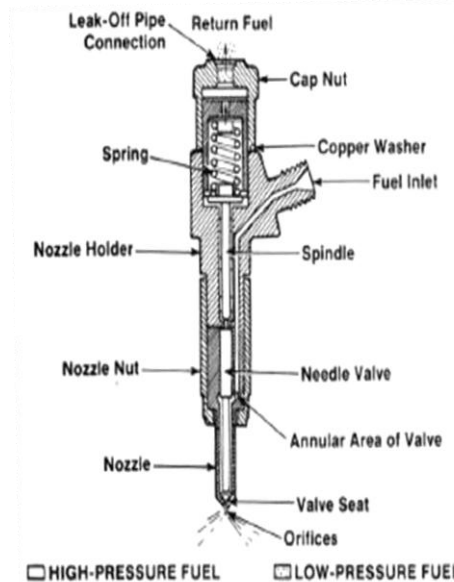
Actuation Mechanism	Single solenoid Double solenoid Piezoelectric Hydraulic Cam	Most common
Fluid State	Single fluid Two-phase (air assist)	Most common
Primary Atomisation Method	Sheet (swirl plate) Pressure (slit type) Pressure (hole type) Turbulence (compound plate) Pneumatic (air assist) Cavitation Impingement	Most common for first generation GDI injectors (swirl)  Most common for second generation GDI injectors (Multi-hole)
Nozzle Configuration	Swirl Slit Multi-hole Cavity	Most common for first generation GDI injectors  Most common for second generation GDI injectors
Pintle Opening Direction	Inwardly opening Outwardly opening	Most common
Spray Configuration	Hollow cone Solid cone Fan Offset Multi-plume Shaped	Most common for first generation GDI injectors (swirl)  Most common for second generation GDI injectors (Multi-hole)

Several combinations of these characteristics have been developed for use in GDI engines, however this study focuses on the use of the solenoid actuated, single fluid, inwardly opening, multi-hole nozzle injector. Next section will discuss the solenoid actuated injector design configuration.

## Chapter 2 – Injection Process and Spray Characteristics

### 2.5.7.1 Solenoid Actuated Injector

Electromechanical solenoids consist of an electromagnetically inductive coil wound around a moveable armature. When a current flows through the coil the armature is moved and this movement is used to open the injector nozzle. Most of the injectors tested in this study are solenoid actuated.



**Figure 2.21: Schematic of a solenoid actuated injector**<sup>[15]</sup>

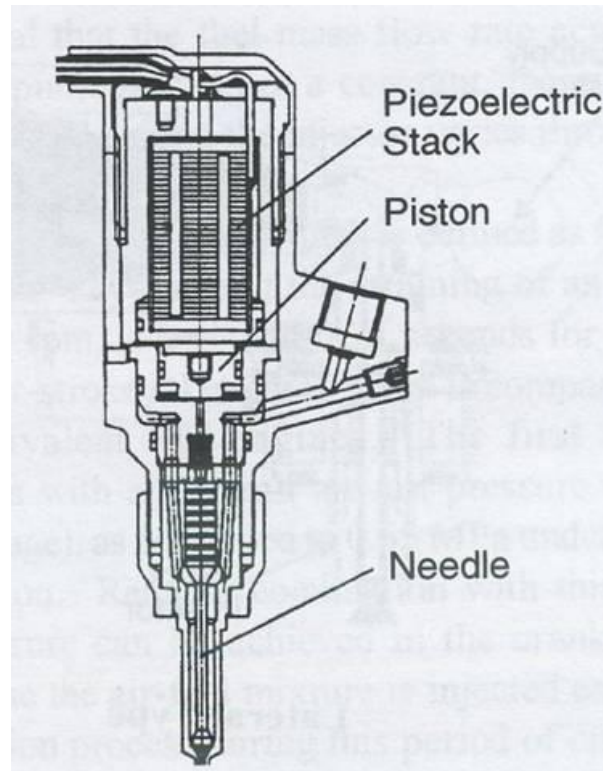
### 2.5.7.2 Piezoelectrically Actuated Injector

Piezoelectric actuation utilises the rapid change in the dimensions of quartz crystal lattices when a voltage is applied. If these crystals are arranged in series then they create a piezo stack and the total dimensional change is the sum of the changes of the individual crystals. The dimensional change (up to 40 microns) can be used to move the needle of a GDI injector. This movement occurs at least with an order of magnitude faster than a solenoid operated injector (around 80 $\mu$ s compared to 250 $\mu$ s for a solenoid actuated injector). The rapid opening time results in less time being spent in the period of low needle lift and creates a large pressure difference at the nozzle exit. This improves atomisation during injector opening. The injector dead-time is reduced and this has the effect of lowering the minimum operating pulse width to shorter values. This means that several injection events can occur during each engine cycle, giving additional control over in-cylinder mixture preparation. The variation in actuator dynamics from cycle to cycle is also improved with the piezo stack. A piezo stack is no more complex than a solenoid and has the benefit of reduced power consumption, however the level of manufacturing precision of each individual component is

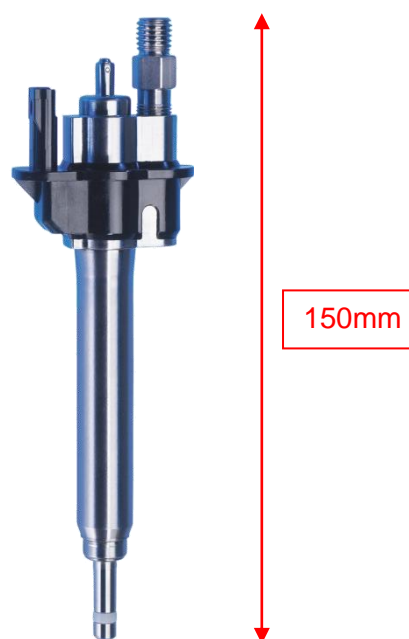
## Chapter 2 – Injection Process and Spray Characteristics

---

higher for the piezo stack, leading to much increased production costs. A schematic diagram and a picture of a piezoelectrically actuated injector are shown in Figure 2.22 and Figure 2.23.



**Figure 2.22: Schematic of a piezoelectrically actuated injector<sup>[2]</sup>**

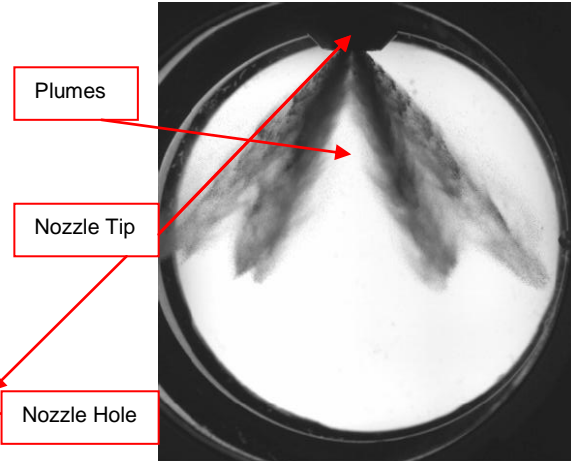


**Figure 2.23: Piezoelectrically actuated injector**

## Chapter 2 – Injection Process and Spray Characteristics

### 2.5.7.3 Multi-Hole Injector

Many manufacturers have developed multi-hole nozzles for use in GDI applications. These injectors are similar to diesel injectors in that they have several holes for fuel delivery, although the conical pattern is much narrower than the ones found in diesel applications, approximately  $30\text{-}90^\circ$  as opposed to  $130\text{-}170^\circ$  [2]. Multi-hole injectors are defined by the number of holes, angle or angles of the spray pattern, the offset of the centroid of the pattern from the injector axis and the spray pattern itself. In principle, an infinite number of spray patterns may be generated by the manufacturer by altering the hole distribution, orientation and sizes (length/diameter ratios). Thus, it is possible for many combustion applications to be served by one base injector by changing the nozzle tip, thereby reducing development costs. The main advantage of the multi-hole injector is that nearly any spatial distribution of fuel mass can be obtained by varying the hole geometries, giving great flexibility in placing the fuel exactly where it is needed. Unfortunately, knowledge of exactly where this fuel should be targeted is not likely to be known during engine development, so some trial and error will take place in developing the optimised nozzle tip. The further development of CFD programmes will, however, enable quicker optimisation as in-cylinder flow fields can be more accurately predicted. An additional advantage of this style of injector is that the spray can be offset from the injector axis with little or no penalty in atomisation quality, since the pressure differential between the fuel rail and the in-cylinder conditions is responsible for the atomisation, as opposed to the swirl strength in a swirl injector. This results in the disadvantage that even higher fuel pressures than in a swirl injector are required to provide the required atomisation, with the added cost and durability penalties that this brings.



**Figure 2.24: Image of multi-hole injector tip**

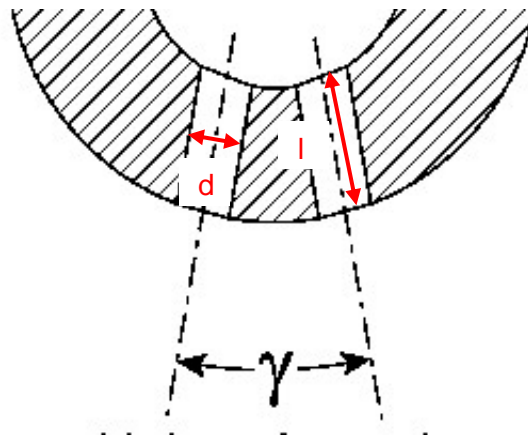
**Figure 2.25: CCD shadowgraph image of a symmetrical multi-hole injector spray**

## Chapter 2 – Injection Process and Spray Characteristics

### 2.5.8 Injector Parameters and External Conditions

#### 2.5.8.1 Injector Geometry

Plain-orifice atomisers, as in multi-hole injectors, produce a narrow compact spray in which only the liquid on the periphery of the spray is subjected to aerodynamic shear effects. The distribution of the spray is mainly dictated by the magnitude and directional components of velocity of the spray at the orifice exit. Thus a feature of this type of nozzle (and the same can be said for airblast atomisers) is a lack of sensitivity of spray geometry characteristics to the physical properties of both the liquid and the ambient gas. This is not the case for pressure-swirl atomisers where the initial cone angle formed at the nozzle exit is extremely dependent on nozzle design features, operating conditions and liquid properties. This is why cone angle is such an important feature of pressure-swirl spray analysis.



**Figure 2.26: Multi-stream nozzle hole length and diameter**

The effect of nozzle, orifice length and diameter (see Figure 2.26) on jet velocity has been studied by many workers, some with contradictory evidence. One piece of work performed by Hiroyasu et al. [72] showed that jet break-up length increased with increasing jet velocity up to a maximum break-up length with jet velocities approximately 60m/s. Above this the break-up length was seen to decline with any further increase in jet velocity. This trend was also noticed at high ambient gas pressures but showed a reduction in break-up length and reduction in influence of nozzle orifice length-to-diameter ratio,  $l_o/d_o$  (see Figure 2.27 and Figure 2.28).

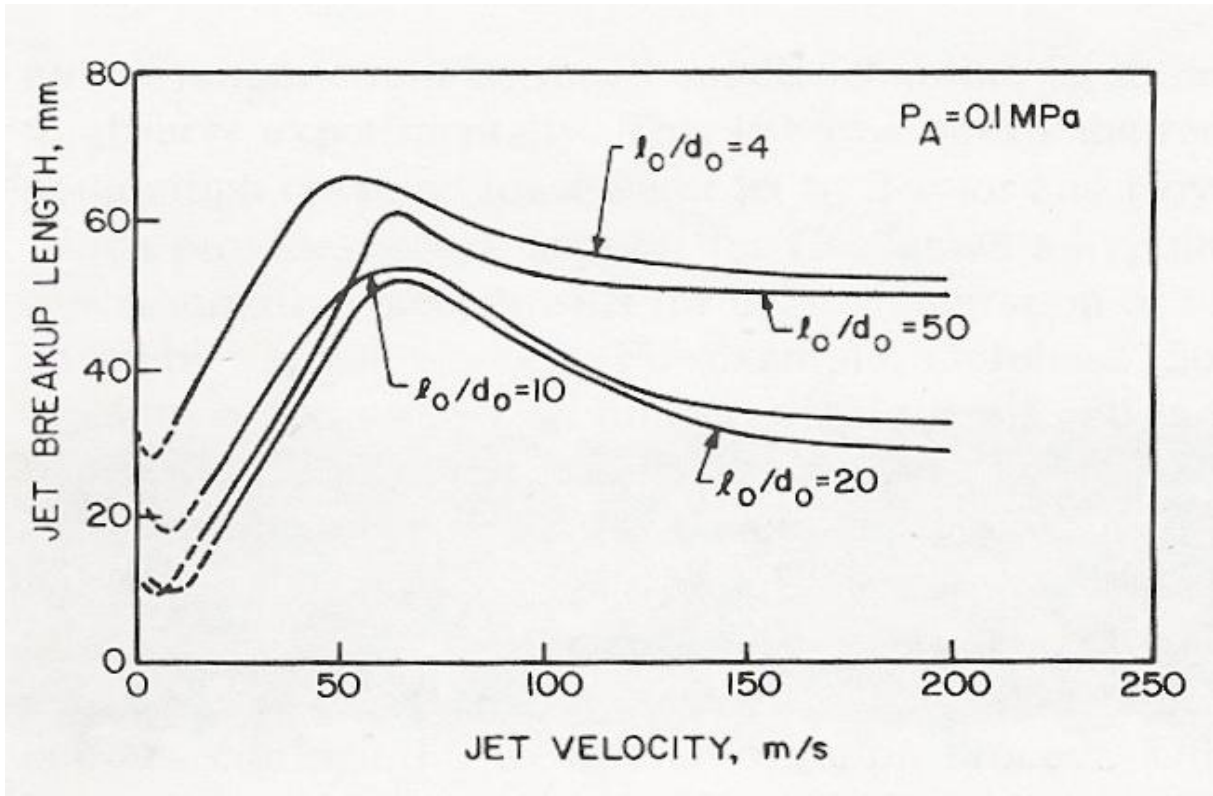


Figure 2.27: Effect of  $l_0/d_0$  and jet velocity on break-up length for low ambient pressures (Hiroyasu et al. [72])

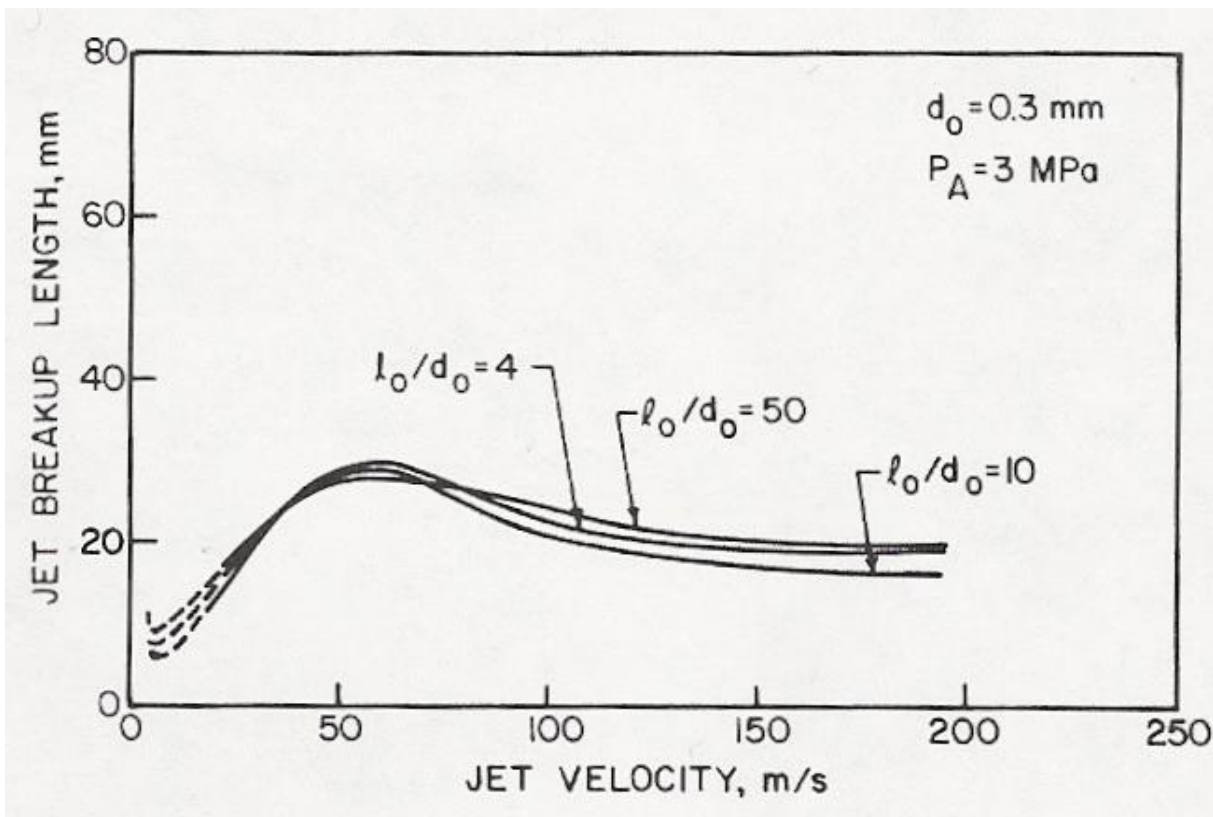


Figure 2.28: Effect of  $l_0/d_0$  and jet velocity on break-up length for high ambient pressures (Hiroyasu et al. [72])

### 2.5.8.2 Ambient Gas Conditions

The influence of ambient gas pressure on jet break-up length at varying jet velocity has been studied by Hiroyasu et al. [72]. It was shown that increasing the ambient pressure from 0.1-3MPa has a large effect on jet break-up length, whereas 3-4MPa shows little effect on break-up length. The influence of ambient gas pressure also shows a similar trend to that seen with the affect of  $l_0/d_0$  on break-up length, a maximum break-up length is achieved at approximately 60m/s and there after a reduction in break-up length is seen.

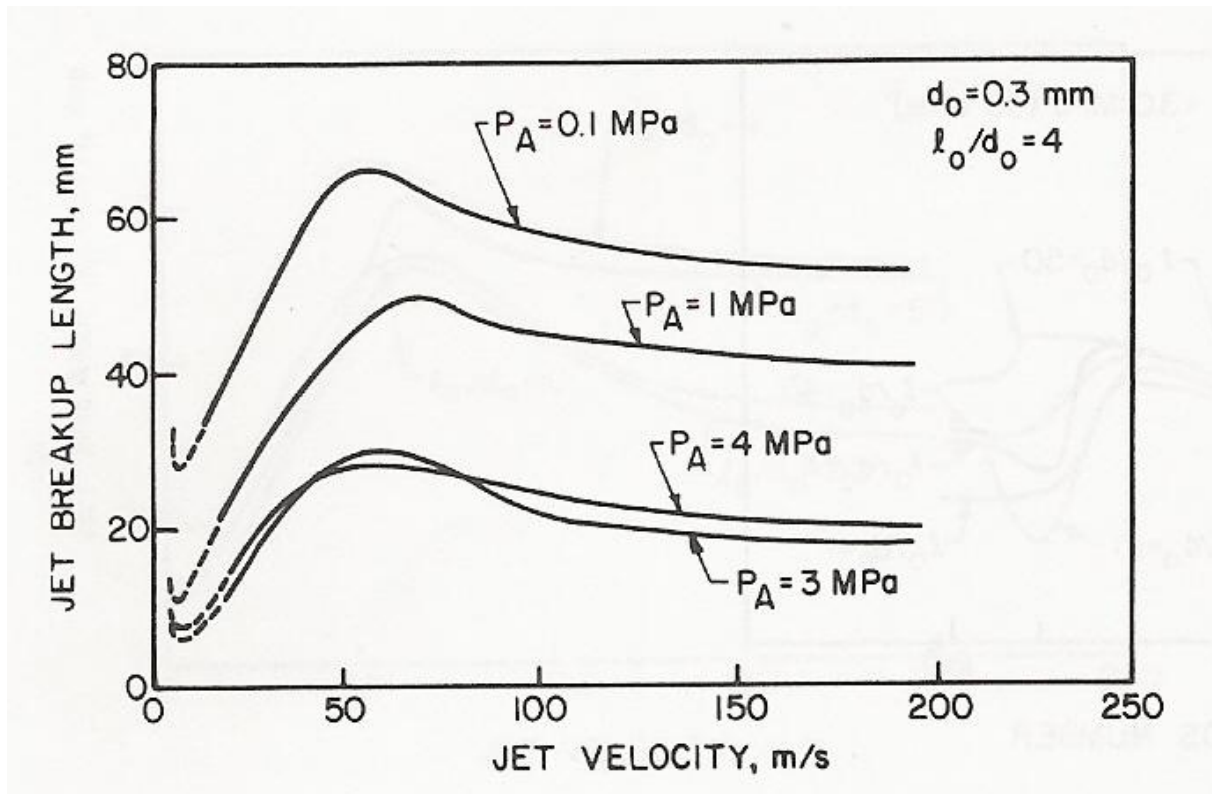


Figure 2.29: Influence of ambient pressure on break-up length (Hiroyasu et al. [72])

### 2.5.8.3 External Spray Characteristics

The dispersion of a spray can be expressed quantitatively if at a given moment the volume of liquid within the spray is known. The degree of dispersion can be defined as the ratio of the volume of the spray to the volume of the liquid contained within it. Good dispersion shows that the liquid mixes rapidly with the surrounding gas, and the subsequent rates of evaporation are high. In general, it has been seen that the factors that increase the spray cone angle also tend to increase the degree of spray dispersion.

Spray penetration is of significant importance in diesel and gasoline direct injection engines. In case of over-penetration, the fuel will impinge on the cylinder wall. If the cylinder wall is

## Chapter 2 – Injection Process and Spray Characteristics

---

cold or there is inadequate in-cylinder flow (as is the case in most quiescent combustion chambers) the fuel will deposit and cool. This can lead to an increase in soot and unburned hydrocarbon emissions and also reduce fuel economy due to the fuel wastage. If penetration is low, the cylinder air utilisation will be low and reduce the degree of fuel-air mixing, therefore limiting combustion efficiency. Therefore knowledge of the affects on spray penetration and the ability to predict spray penetration is necessary for efficient combustion chamber design.

The penetration of a spray can be defined as the maximum distance it reaches when injected into stagnant air. It is controlled by the kinetic energy of the initial jet and the aerodynamic drag as a consequence of its contact with the ambient gas. Initial jet velocity is usually high, but as the jet proceeds to disintegrate and the surface area of the spray increases, the kinetic energy is dissipated to the surrounding gas due to frictional losses.

A spray will penetrate further than a single drop due to the leading drops in a spray imparting their momentum into the ambient gas, which then results in entrainment. Therefore the following drops will experience less resistance than the first and will penetrate further.

Many analytical studies have been performed in diesel engines with plain-orifice atomisers to create equations relating spray penetration in plain-orifice atomisers. Hiroyasu and Arai [73] managed to build upon work performed by others to create two equations for penetration.

For injection times shorter than the jet break-up time,  $t_b$ , the penetration  $S$  (in m) is:

$$S = 0.39 \left( \frac{2\Delta P_L}{\rho_{fuel}} \right)^{0.5} t \quad (2.13)$$

And for  $t > t_b$ :

$$S = 2.95 \left( \frac{\Delta P_L}{\rho_{air}} \right)^{0.25} (d_0 t)^{0.5} \quad (2.14)$$

Where the jet break-up time is equal to:

$$t_b = 28.65 \rho_{fuel} d_0 (\rho_{air} \Delta P_L)^{-0.5} \quad (2.15)$$

where  $\Delta P_L = P_{inj} - P_{amb}$  (in Pa) is the difference between the injection pressure and the ambient pressure and  $d_0$  (in m) is the nozzle hole diameter.

---



## Chapter 2 – Injection Process and Spray Characteristics

---

Aerodynamic drag also causes the spray to spread out. The drops on the periphery of the spray are subjected to shear forces as a consequence of aerodynamic drag. The shear forces cause the outer drops to slow down, and since the drops and liquid within the centre of the spray are unimpeded, the outer drops are pushed outwards further, thus widening the cone angle, and in the case of plain-orifice atomisers increases the spray head size. Thus an increase in ambient gas pressure increases the kinetic energy losses due to aerodynamic drag and causes an increase in cone angle and reduction in penetration.

The angle of a spray is usually defined as the angle formed by two straight lines drawn from the discharge orifice to the outer periphery of the spray at a distance  $60d_o$  downstream of the nozzle.

Much work has been performed on quantifying spray angle. Abramovich [74] created a very simple equation based only on the density of the liquid and air. This has been elaborated by many other workers, namely Reitz and Bracco [75], where Bracco et al. [76] then went on to simplify their previous work, resulting in equation (2.16):

$$\tan \theta = \frac{2\pi}{\sqrt{3A}} \left( \frac{\rho_A}{\rho_L} \right)^{0.5} \quad (2.16)$$

Hiroyasu and Arai [73] have also applied dimensional analysis to their work that was acquired at high pressures with which they derived the following equation (in radians):

$$\theta = 0.025 \left( \frac{\rho_A \Delta P_L d_0^2}{\mu_A^2} \right)^{0.25} \quad (2.17)$$

## Chapter 2 – Injection Process and Spray Characteristics

The effect of Reynolds number and nozzle orifice length-to-diameter ratio has also been investigated by Arai et al. [77], who produced Figure 2.30. Arai states that the shapes of the curves from Figure 2.30 are a consequence of a complex relation between jet turbulence, jet break-up length, and orifice discharge coefficient, all of which act to change the Reynolds number and nozzle  $l_o/d_o$  ratio.

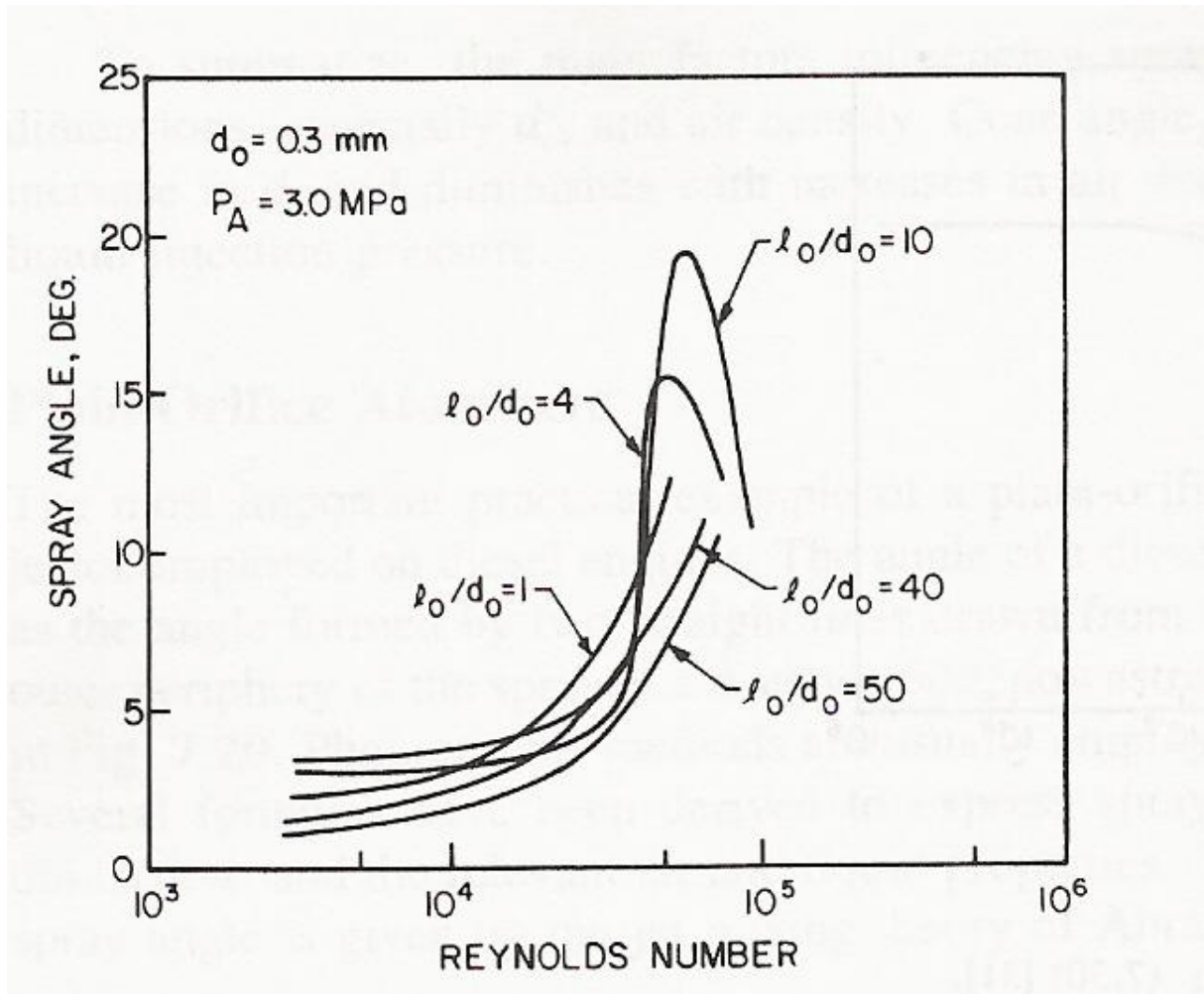


Figure 2.30: Influence of Reynolds number and nozzle  $l_o/d_o$  ratio on spray angle (Arai et al. [77])

## Chapter 2 – Injection Process and Spray Characteristics

---

Hung et al. [78] present an imaging-based diagnostic technique to quantify the pulse-to-pulse variability of macroscopic fuel spray characteristics for Direct-Injection Spark-Ignition (DISI) engine applications. The analysis approach is based on the construction of a spray ensemble image, reflecting the regions of probability of liquid presence for a set of images. Overlaying of an individual spray boundary on the probability-based ensemble image can further enhance the two-dimensional visualisation of the pulse-to-pulse spray variations. Spray structures at three experimental conditions were examined: room ambient, and early and late injection conditions inside an optical engine. While the spray structure was observed to be considerably different for the three conditions, the magnitudes of variation of global spray shape and spray tip penetration distance were found to be of similar order [78].

An experimental study has been performed by de Francqueville et al. [79] in which the air entrainment characteristics within the periphery of gasoline direct injection sprays have been measured by particle image velocimetry (PIV). Two single fluid injector technologies, namely a pressure-swirl atomiser (PSA) and a piezoelectric atomiser (PEA) have been compared. Measurements have been performed, first of all, in a high-pressure constant volume chamber and, subsequently, in an optically-accessible, motored, single-cylinder GDI engine. The in-cylinder aerodynamics were characterised by PIV with and without fuel injection. The aim was to compute the coefficient of air entrainment into the spray, which was used as a basis for comparing air entrainment efficiency and the propensity of injector sprays to influence air/fuel mixing. The air entrainment characteristics have been studied for both injectors with variations in start of injection (SOI) timing, injection pressure and for three piston geometries. Subsequently, a proper orthogonal decomposition (POD) has been used to study the impact of the spray on the in-cylinder flow field.

Chatterjee [80] provides an introduction to the Proper Orthogonal Decomposition which is a powerful and elegant method of data analysis aimed at obtaining low-dimensional approximate descriptions of high-dimensional processes. The POD was developed by several people (among the first was Kosambi), and is also known as *Principal Component Analysis*, the *Karhunen–Loève Decomposition*, and the *single value decomposition*. The POD has been used to obtain approximate, low-dimensional descriptions of turbulent fluid flows, structural vibrations and has been used for damage detection, to name a few applications in dynamic systems. It has also been extensively used in image processing, signal analysis and data compression. Data analysis using the POD is often conducted to extract ‘mode shapes’ or basis functions, from experimental data or detailed simulations of high-dimensional systems, for subsequent use in Galerkin projections that yield low-dimensional dynamical models [80].

---

## Chapter 2 – Injection Process and Spray Characteristics

---

De Francqueville et al. [79] results show that the calculated air entrainment coefficient which gives an indication of the efficiency to generate air/fuel mixing is similar for both injector technologies. However, the injection velocity and the rate of air/fuel mixing is increased in the case of the PEA. More importantly, the macroscopic spray structure generated by the PEA is maintained even under high density, gas-phase, conditions. As a result, the spray interacts more efficiently with the air available in the combustion chamber. Air entrainment induced by the spray significantly alters the natural engine flow that was present prior to injection. Injection with PEA enhances the energy of the mean in-cylinder aerodynamic motion by a factor of three. POD calculations were used to decompose the aerodynamic flow field according to kinetic energy criteria: 75% of the in-cylinder flow energy corresponds to the macroscopic scale motion, 15% is attributed to cyclic fluctuations and 10% to turbulence phenomena (down to the turbulence integral scale) [79].

### 2.5.8.4 Microscopic Characteristics

There are several mean and characteristic diameters used for evaluating spray droplet size,  $D_{ab}$ , each suited to a particular application.

For diameters of the form  $D_{ab}$ , the calculation is as follows:

$$D_{ab} = \left[ \frac{\sum N_i D_i^a}{\sum N_i D_i^b} \right]^{\frac{1}{a-b}} \quad (2.18)$$

Where  $D_i$  is the actual droplet diameter ( $N_i$  is a multiplicative coefficient).

The droplet diameter terminologies and their applications are summarised in Table 2.9.

## Chapter 2 – Injection Process and Spray Characteristics

---

**Table 2.9: Droplet diameter terminology<sup>[B1]</sup>**

Term	Description
$D_{V50}$	Also known as Volume Median Diameter (VMD). The VMD is the value where 50% of the total volume of liquid sprayed is made up of drops with diameters larger than the median value and 50% smaller than the median value. Used to express drop-size in terms of the volume of liquid sprayed.
$D_{V10}$	The value where 10% of the total volume of liquid sprayed is made up of drops with diameters smaller than or equal to this value. Used to evaluate a nozzle's drift potential, which is the likelihood of droplets to drift off-target.
$D_{V90}$	The value where 90% of the total volume of liquid sprayed is made up of drops with diameters smaller than or equal to this value. Used in applications where complete evaporation of the spray is required. This is at least as important as SMD for emission correlation because a high proportion of relatively large drops will increase HC emissions [10].
$D_{min}$	The minimum drop-size by volume in the sample. Also used to evaluate a nozzle's drift potential.
$D_{max}$	The maximum drop-size by volume in the sample. Also used in applications where complete evaporation of the spray is required.
$D_{32}$	Also known as Sauter Mean Diameter (SMD). The $D_{32}$ is a measure of the degree of atomisation of the spray. It is the diameter of a drop having the same volume to surface area ratio as the total volume of all the drops to the total surface area of all the drops. Used to evaluate the efficiency and mass transfer rates in chemical reactions. Reduced $D_{32}$ results in the fuel evaporating more readily and improves ignitability, reducing HC emissions.
$D_{10}$	Arithmetic mean diameter. Used to calculate evaporation rates.
$D_{20}$	Surface mean diameter. Used in surface-controlling applications such as absorption.
$D_{30}$	Volume mean diameter. Used in volume-controlling applications such as hydrology.
$D_{21}$	Surface mean diameter. Used in surface-controlling applications such as absorption.
$D_{31}$	Mean evaporative diameter. Used for evaporation and molecular diffusion studies.
$D_{43}$	Herdan or De Brouckere diameter. Used in combustion studies.

## Chapter 2 – Injection Process and Spray Characteristics

In order for fuel to undergo stable combustion it must first be vaporised. The vaporisation rate is related to the surface area and to the volume ratio of the fuel and it follows that an increase in surface area for a given fuel volume leads to an increased vaporisation rate. The process of atomisation is used to generate the required surface area for all the fuel to vaporise in the time available between injection and combustion. An average GDI engine running at light load uses approximately 10mg of gasoline per cylinder per cycle. This amount of fuel can have an infinite number of possible surface areas depending on the level of atomisation. In the limiting case, an unatomised spherical drop of fuel of diameter 3mm has a surface area of 28mm<sup>2</sup>. If that same amount of fuel was injected using a PFI injector, giving a  $D_{32}$  of 100 $\mu$ m, then there will be approximately 26,000 drops with a total surface area 30 times that of a single drop. It has been established by Zhao et al. [2] that, for a late-injection, a GDI engine will operate only marginally if fuel is introduced with a  $D_{32}$  of 35 $\mu$ m or greater. This value gives 600,000 drops with a surface area of 85 times that of the single drop. The time available for vaporisation is only 8ms and this surface area is still not adequate for all of the fuel to vaporise. Efficient GDI combustion will occur at a  $D_{32}$  of 15 $\mu$ m, at which point 10mg of gasoline is atomised into 8 million drops with a combined surface area 200 times that of a single drop. In order for a  $D_{32}$  of 10 $\mu$ m to be achieved the same 10mg of fuel must be atomised into 26 million drops and this requires fuel rail pressures in the order of 200bar. This reliance on good atomisation to provide the necessary surface area for vaporisation in a short time period has led to much research being undertaken to understand and improve the process. A graph showing the variation in spray surface area and number of droplets with  $D_{32}$  is shown in Figure 2.31. The maximum allowable  $D_{32}$  for stable combustion in both GDI and PFI engines is indicated.

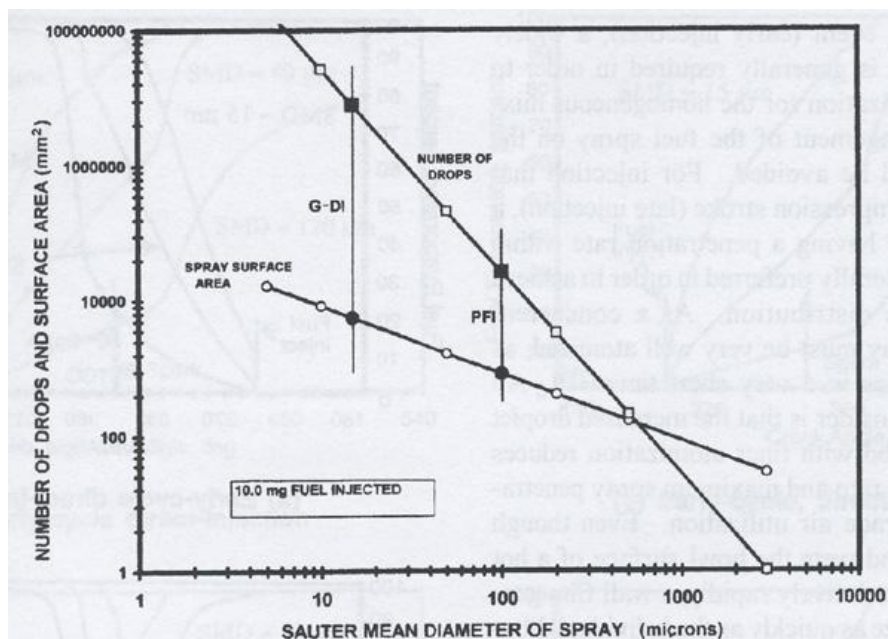


Figure 2.31: Relationship between  $D_{32}$ , spray surface area and number of drops [2]

## Chapter 2 – Injection Process and Spray Characteristics

---

The symmetry of a spray pattern created by an atomiser is an important spray feature for most applications. In an internal combustion engine a symmetrical spray pattern is desirable to achieve maximum of in-cylinder air utilisation and hence combustion efficiency unless the combustion chamber shape has been designed to perform with a specifically asymmetrical spray pattern.

VanDerWege and Hochgreb [3] state that most investigations of fuel sprays from high-pressure swirl injectors involve cold bench tests or motored optical engines, such experiments neglect the effects of fuel volatility and temperature on the spray structure. This finding highlights the potential for an investigation into the behaviour of fuel under different conditions and the influence of fuel properties on atomisation performance as there are currently limited resources to assist in the design process.

Research into injector design includes investigating how the spray develops at different back pressures and temperature. There has been extensive research into different injector types in recent years, especially using swirl or multi-hole injectors. To evaluate how effective the injector is a general criterion is often used. This includes atomisation quality, robustness against fouling, ability to achieve inclined or offset spray and robustness through manufacture.

Stansfield et al. [82] analysed the structure and penetration of the fuel spray produced by a multi-stream gasoline fuel injector in three experimental facilities using a Mie imaging technique. The facilities available were an atmospheric spray bench, a high pressure-temperature cell and an optical engine. The cell was operated at pressures and temperatures from 1 to 10 bar and 20° to 80°C respectively while the engine was motored at 2000 rpm under throttled and un-throttled conditions to represent the in-cylinder environments necessary to achieve 2.7 bar IMEP<sub>(720°)</sub> under firing conditions. The fuel spray structure and propagation have been quantified using the iso-intensity contour image processing technique to identify the spray boundaries in an attempt to quantify the variations due to the experimental environments. The analysis revealed that, although high shear inlet air flows lead to a redirection of some of the fuel streams, and, while un-throttled conditions lead to the development of sub-atmospheric pressures, the axial propagation of the whole spray in the engine may be predicted with the use of spray penetration data obtained from atmospheric spray bench and high pressure-temperature cell data. The relationship between backpressure and axial spray penetration gives the capability of estimating the likelihood of spray-piston crown impact [82].

## Chapter 2 – Injection Process and Spray Characteristics

---

The fuel break-up and atomisation processes in the near nozzle region of a second generation high pressure-swirl direct injection gasoline fuel injector have been characterised by Stansfield et al. [83]. The Phase Doppler technique has been used to measure the axial and radial droplet velocities and the resultant flow angles of the fuel droplets. Mean estimates, based on time bin averaging the data over 20 microsecond time bins, have shown that, during the transient formation of the hollow fuel cone there is a distinct high frequency fluctuation in the mean flow angle. Images of the spray cone have confirmed the fluctuations found by the PDA analysis and suggest that the phenomenon is due to waves in the spray cone which can be attributed to the instabilities behind the break-up of the conical liquid sheet.

A phenomenological engine model has been developed by Siewert [84] to study direct injection of liquid fuels in diesel and gasoline engines. Sub-models were obtained from the literature wherever possible and include those for initial drop-size, droplet vaporisation, and spray penetration. The progress of the injected spray, including both liquid and vapour, was visualised relative to the combustion chamber bowl boundaries and gave valuable insight on where the spray tip intersected the piston bowl surface, and whether it was in a liquid or gaseous state. The one-dimensional spray penetration used in the model is oblivious to surfaces (thus no spray-wall interactions), air motion, turbulence and mixing with air, but is properly influenced by gas temperature and density. An ignition delay sub model, based on the sum of droplet vaporisation time and reaction time, has been calibrated to experiments run at Sandia National Laboratories, and provides good results over a wide range of applications, including those for very late injection timings as used in low soot combustion (LSC), and those of very early injection where pre-mixed compression ignition (PCI or HCCI) combustion is desired [84].

A multi-component fuel vaporisation model has been developed by Tonini et al. [85] and implemented into an in-house multi-phase computational fluid dynamics flow solver simulating the flow, spray, and air–fuel mixing processes taking place in GDI engines.

Multi-component fuel properties were modeled assuming a specified composition of pure hydrocarbons. High-pressure and temperature effects, as well as gas solubility and compressibility, were considered. Remote droplet vaporisation was initially investigated in order to quantify and validate the most appropriate vaporisation model for conditions relevant to those realised with GDI engines. Phenomena related to the fuel injection system and pressure-swirl atomiser flow as well as the subsequent spray development were considered using an one-dimensional fuel injection equipment model predicting the wave dynamics inside the injection system, an Eulerian volume of fluid-based two-phase flow model



## Chapter 2 – Injection Process and Spray Characteristics

---

simulating the liquid film formation process inside the injection hole of the swirl atomizer and a Lagrangian spray model simulating the subsequent spray development, respectively. The computational results were validated against experimental data obtained in an optical engine and include laser Doppler velocimetry measurements of the charge air motion in the absence of spray injection and charge coupled device images of the fuel spray injected during the induction stroke. The results confirmed that fuel composition affects the overall fuel spray vaporisation rate, but not significantly relative to other flow and heat transfer processes taking place during the engine operation.

In their book, before addressing the various industrial spraying processes Nasr et al. [86] provided background coverage of the basics of droplet behaviour, spray structure, measurement techniques, modelling methods and described atomisation techniques as well as spray processes such as vaporisation and wall impaction. They also provided information on applications of sprays in industry, on the atomiser designs and performances with emphasis on their operating conditions for each application. This involves, first, a description of the application itself, the role of the spray in the process and thus the requirements that the process enforces on the ideal spray properties. Then a comparative description is given of the atomisers currently used in the process, their normal operating conditions and spray properties, and the experimental techniques used in diagnosing the spray performance as part of the process. A discussion is then given of problems and possible future developments for the process and the implications for future needs for atomisers and operating conditions.

### 3. Flash Boiling

#### 3.1 *Flash Boiling Effect on Fuel Sprays*

A fuel at high temperature which is injected into a low pressure environment has its boiling point lowered. As the fuel expansion from the injector occurs in such a short time scale, the heat cannot be conducted by surface evaporation but causes rapid and explosive bubble growth inside the droplets. The phenomenon is known as flash boiling. It is known that this occurs within multi-hole injectors and that droplet size is affected. There is potential for flash boiling to reduce drop-sizes, increase spray cone angles, and produce more favourable fuel mixtures for a GDI engine than before.

Flash boiling dramatically changes the fuel distribution and improves atomisation. The difference in temperature between the fuel exiting the injector nozzle and the boiling point at the pressure condition the fuel is injected drive the flash boiling phenomenon. To understand, and control, flash boiling could produce a more combustible fuel mixture for a GDI engine [87].

VanDerWege mentioned in his work [88] regions of flash boiling which results in the formation of vapour bubbles. If there is an internal flash region, in which the bubbles are formed inside the injector orifice it can lead to the injection of a two phase flow changing the characteristics of atomisation and the spray structure. The pressure will also change the boiling point or bubble point of a fuel, increased pressure will increase the chances of bubbles forming due to flash boiling. He also mentioned the effect of superheat on vapour distribution. The superheat is the difference between the liquid temperature and the prevalent ambient temperature or can be described as the difference between the ambient pressure and the fluid vapour pressure and defined by:

$$\Pi = \frac{P_{vapour} - P_{ambient}}{P_{ambient}} \quad (3.1)$$

Despite being a relatively new field, some research has already been carried out specifically on the effects of flash boiling of sprays. The flash boiling phenomenon occurs when fuel is injected into a combustion chamber where the ambient pressure is lower than the saturation pressure of the fuel. The fuel is defined as superheated. Such a system is in a state of thermodynamic non-equilibrium and thus unstable. The system regains equilibrium by undergoing flash boiling [89].

A research paper by Sher et al. [90] summarised current knowledge on the flash boiling mechanism. It was found that there are three stages to flash boiling:



There are two different forms of bubble nucleation:

- Homogeneous, in which nucleation sites form within the liquid itself with a homogeneous distribution.
- Heterogeneous, in which the nucleation sites are the container walls and impurities within the fluid.

Once the bubble nucleation sites have developed, small pressure fluctuations in the fluid can cause the sites to either collapse or grow. The stages of bubble growth were explained by Plesset et al. [91]:

1. Whilst the bubble is still relatively small, the rate of growth is low and restricted by surface tension of the bubble.
2. If the degree of superheat is great enough, the rate reaches a maximum as the bubble size increases.
3. Liquid surrounding the bubble is cooled due to the transfer of heat energy required for evaporation. The vapour pressure decreases and bubble growth rate is controlled by inertia and thermal diffusion.
4. Bubble growth rate further decreases and inertial effects become less important. Growth rate is controlled by thermal diffusion. The bubble interior pressure and temperature approach ambient values and when this happens the growth stops.

The two-phase flow consisting of both fluid and vapour is in equilibrium and the flash boiling process is complete.

Micro-boiling is commonly used in thermal inkjet atomisers (TIJ) and micro-electromechanical (MEM) devices. The TIJ and MEM devices performance is closely related to the dynamics of the bubble used to operate them; therefore, it is important to determine the conditions of input energy and power leading to specific bubble dynamics. The objective of Escobar-Vargas et al. [92] was the characterisation, in a confined space, of the bubble dynamics on a range of input conditions of energy and power and what is the effect of the input conditions on the bubble extractable mechanical efficiency. Mechanical efficiency is defined by the ratio of the integral of the mechanical work (work done by the bubble expansion due to the

elevated internal pressure relative to atmospheric pressure minus the increase in bubble surface energy) to the total energy input to the micro-heater. Bubbles are generated with energies of 7–17  $\mu\text{J}$  under high heating rates and short pulses in de-ionised water. Resulting nucleation temperature measurements are consistent with homogeneous nucleation. The bubble lifecycle shows strong dependence on the input heater energy and input heating rate. This work presents new results in bubble growth where growth–shrink–growth derived from specific energy conditions. The bubble growth–shrink–growth may be due to sub-cooled fluid, local variation in the pressure field, and by the surface tension driven change in curvature of the bubble. Mechanical bubble efficiencies result in small values suggesting most of the energy applied to the heater is distributed in other processes which may include increasing the internal energy of the heater film and the fluid [92].

Accurate modeling of bubble growth is needed to design fuel injectors that take full advantage of the potential of flash boiling sprays to reduce drop-sizes and to promote fuel vaporisation in direct injection spark ignition (DISI) engines. A new simplified bubble growth model has been developed by Chang and Lee [93] to substantially reduce the computational cost of capturing the bubble size and growth rate distributions at the fuel injector exit. These distributions have important effects on the formation and break-up of droplets. The simplified bubble growth model makes a parcel approach for simulating the bubble growth in a flash boiling fuel injector affordable. A parcel approach makes it possible to capture the distributions of large numbers of bubbles forming under different conditions within the fuel injector. The simplified bubble growth model was validated with experimental data of bubble growth in superheated water. The model showed excellent agreement with experimental data at more than 100 times less computational cost than coupling the bubble growth equation with the conservation of energy equation numerically. The model was applied to the simulation of a flash boiling spray from a swirl atomiser, and the simulated flashing spray resulted in smaller droplets and faster vaporisation than a non-flashing spray at ambient conditions of 0.445 MPa and 430°K [93].

When phase-change between vapor and liquid is present, a new key parameter is needed to define the system: the Jakob number,  $Ja$ , characterises the ratio of sensible to latent heat associated with the phase change. A Jakob number approaching zero means that the latent heat needed for phase change is diverging, so that a vapor bubble initiated with a certain size, remains that size. As the Jakob number is increased from zero, phase change occurs more readily so that a vapor bubble will grow or shrink rapidly depending on the local thermal environment. As a bubble grows in size, it rises rapidly, driving microscale convection and generating pseudo-turbulence, leading to an overall destabilisation of the flow [94].

The Jakob number is defined as:

$$Ja = \frac{\rho_{liq} C_{liq} (T_{\infty} - T_{sat}(P_{\infty}))}{\rho_{vap} h_{fg}} \quad (3.2)$$

where:  $C_p$  is the specific heat (J/kg.K)

$h_{fg}$  is the latent heat of evaporation (J/kg)

$sat$  corresponds to the saturation condition

$\infty$  corresponds to the far field condition

The heat transfer mechanism in Rayleigh-Bénard convection in a liquid with a mean temperature close to its boiling point has been studied by Oresta et al. [94] through numerical simulations with point-like vapour bubbles, which are allowed to grow or shrink through evaporation and condensation and which act back on the flow both thermally and mechanically. It was shown that the effect of the bubbles was strongly dependent on the ratio of the sensible heat to the latent heat as embodied in the Jakob number  $Ja$ . For very small  $Ja$  the bubbles stabilise the flow by absorbing heat in the warmer regions and releasing it in the colder regions. With an increase in  $Ja$ , the added buoyancy due to the bubble growth destabilises the flow with respect to single-phase convection and considerably increases the Nusselt number [94].

Spherically symmetric bubble expansion in uniformly superheated infinite pools of liquid have been simulated numerically by Robinson and Judd [95]. Bubble growth curves have been generated for a range of Jakob numbers,  $3 \leq Ja \leq 3167$ , by altering the initial metastable state of the system facilitated by changes in the initial superheat and system pressure. The detailed physics of vapour bubble growth is studied through delineation of the parameters governing the changes in the growth dynamics from surface tension, to inertia dominated, to diffusion controlled, and the domains between them [95].

The dynamics of boiling succeeding spontaneous nucleation on a small film heater immersed in ethyl alcohol are investigated by Okuyama et al. [96] for heating rates ranging from  $10^7$  K/s to approximately  $10^9$  K/s, under which spontaneous nucleation is dominant for the inception of boiling. Immediately after the concurrent generation of a large number of fine bubbles, a vapour film that covers the entire surface is formed by coalescence and rapidly expands to a single bubble. As the heating rate is increased, the coalesced bubble flattens and only a thin vapour film grows before cavitation collapse. Similar behavior was also observed with water. Based on the observed results, a theoretical model of the dynamic bubble growth due to the

self-evaporation of the superheated liquid layer, which develops before boiling incipience, is presented. The calculated results are compared with the observed results [96].

VanDerWege [88] identified two regimes of flash boiling. Internal flashing occurs when bubbles are formed inside an injector orifice leading to the ejection of a two-phase flow consisting of both liquid and vapour. The spray expands rapidly when exiting the injector. External flashing occurs when the liquid jet is intact as it exits the injector orifice and is then shattered by rapid bubble growth as it moves downstream of the orifice.

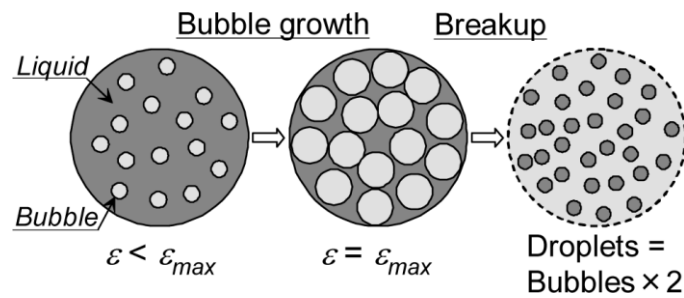
Work carried out by Gebhard [97] investigated the effects of length to diameter ratio of the injector nozzle and found that for  $l/d < 3$ , there is no internal flash boiling inside the nozzle. The driving force for this phenomenon is the temperature difference between the fuel as it exits the injector nozzle and the fuel's boiling point at the pressure condition the fuel expands into. This can be quantified as the "degree of superheat" and research has shown that atomisation of a liquid jet is greatly enhanced when the degree of superheat is great enough to cause flash boiling. Previous work [91] has suggested that flash boiling will affect the spray structure noticeably when the degree of superheat is 20°C or more, however, the exact degree of superheat needed to cause flash boiling is reliant on the surface quality of the injector orifice and the Weber number of the liquid jet. The degree of superheat can also be defined as the difference between ambient pressure and the fluid vapour pressure.

Once the bubble nucleation sites have developed, pressure fluctuations in the fluid can cause the sites to either collapse or grow. The stages of bubble growth were explained by Plesset et al. [91]:

1. Whilst the bubble is still relatively small, the rate of growth is low and restricted by surface tension of the bubble.
2. If the degree of superheat is great enough, the growth rate reaches a maximum as the bubble size increases.
3. Liquid surrounding the bubble is cooled due to the transfer of heat energy required for evaporation. The vapour pressure decreases and bubble growth rate is controlled by inertia and thermal diffusion.
4. Bubble growth rate further decreases and inertial effects become less important. Growth rate is controlled by thermal diffusion. The bubble interior pressure and temperature approach ambient values and when this happens the growth stops.

Kawano et al. [98] proposed a bubble growth analysis based on the following assumptions:

- The temperature and pressure inside bubbles are uniform and temperature must be identical to the temperature of liquid fuel.
- Bubbles grow spherically.
- The phase change from liquid to vapor occurs continuously due to the growth process of cavitation bubbles inside the nozzle orifice and fuel droplets.
- Marangoni convection in the liquid increases coalescence frequency among the growing bubbles [99].



**Figure 3.1: Break-up caused by bubble disruption<sup>[98]</sup>**

The growth of bubbles inside a droplet is limited. This limit is determined by the diameter of the droplet, surface tension, liquid viscosity, the number density of bubble nuclei, and growth rate. The limit of bubble growth rate inside a droplet is described by the void fraction,  $\varepsilon$ , defined as the volume ratio between the vapor and liquid phases:

$$\varepsilon = \frac{V_{bubble}}{V_{bubble} + V_{liquid}}$$

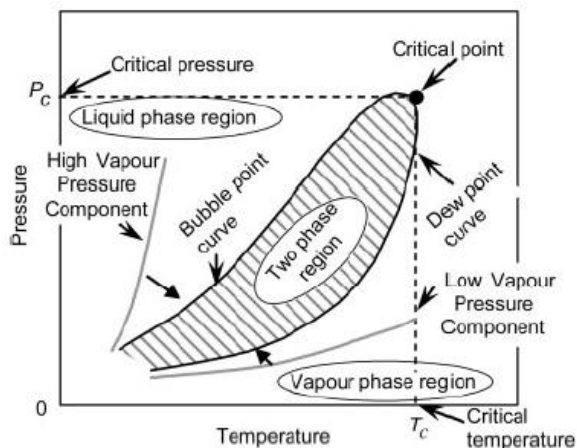
where  $V_{bubble}$  is the volume of bubbles and  $V_{liquid}$  is the volume of liquid. Suma and Koizumi observed that break-up of a fuel jet occurs at  $\varepsilon$  ranging from 0.51 to 0.53 [100]. Then, it is assumed that the droplet breaks up into small droplets twice as many as the number of bubbles, as illustrated in Figure 3.1. As a consequence, both the number and diameter of droplets after break up caused by bubble disruption can be calculated. The momentum of the parent droplet is uniformly distributed among the child droplets. Once the flash boiling process is completed a two-phase flow consisting of both fluid and vapour in equilibrium is obtained.

### 3.2 GDI Applications

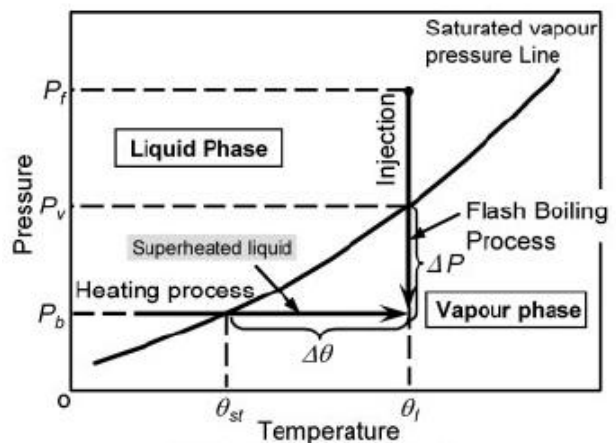
For a direct injection gasoline engine flash boiling of the injected fuel can occur under part load operation, particularly when operation late inlet valve opening strategies, [101]:

1. Fuel in injector is at high temperature ( $<100^{\circ}\text{C}$ ) due to conductive heat transfer from the cylinder head.
2. The downward movement of the piston with the inlet valves closed creates a partial vacuum (down to around 0.1bar).
3. The boiling temperature of the fuel at the in-cylinder pressure is below the temperature of the fuel inside the injector.
4. Superheated liquid fuel is injected into the cylinder.
5. Latent heat cannot be conducted by surface evaporation.
6. Rapid and explosive bubble growth occurs inside the droplets and vapourises the fuel.

Work carried out by Senda et al. [102] involved mixing n-tridecane, which represents diesel fuel, with a relatively low boiling point additive. When mixing the fuels the vapour-liquid equilibrium in the two-phase region, where both liquid and vapour of both fuel components are present, was taken into account. By controlling the proportion of additive the authors could control the physical processes in the spray such as fuel evaporation and vapour-air mixing. In the two-phase region, illustrated in Figure 3.2, the vapour of the lower boiling point fuel dominates, with the vapour of the higher boiling point fuel coexisting.



**Figure 3.2: Illustration of two-phase region**



**Figure 3.3: Flash boiling process** [102]

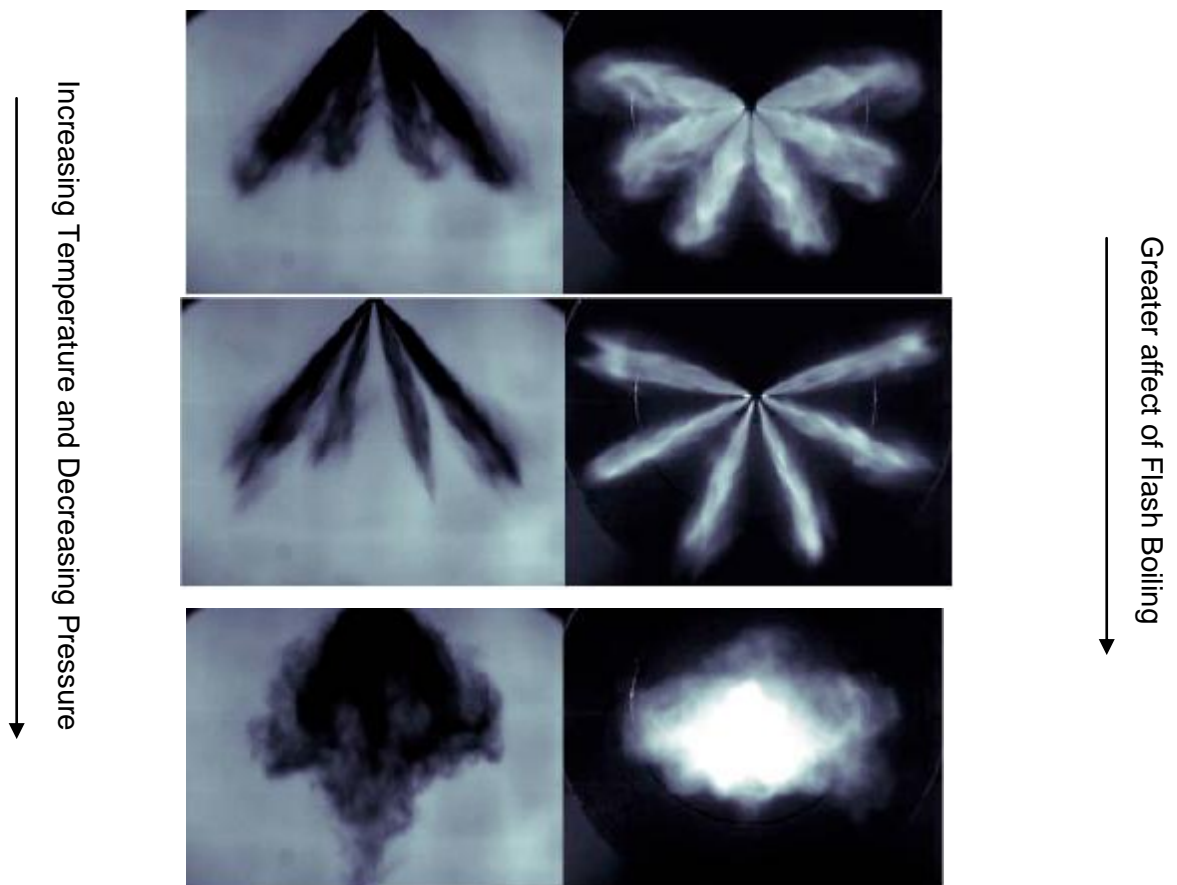


The vapour of the higher boiling point fuel would not be present under the same conditions if it was the only component present in the system as this region lies below the fuel's saturated vapour pressure line, shown in Figure 3.3. This shows that blending a low boiling component fuel with a high boiling component fuel leads to an increase in fuel evaporation and hence multi-component fuels, such as gasoline, are more susceptible to flash boiling than single component fuels.

Benefits of flash boiling are:

- Reduced drop-sizes (smaller  $D_{32}$  for larger surface area and improved vaporisation)
- Increased cone angles (for better air utilisation)
- Reduced drop velocities (for reduced risk of piston crown impact)

The combination of these three benefits results in reduced spray-impingement and gives lower engine-out HC emissions [87].

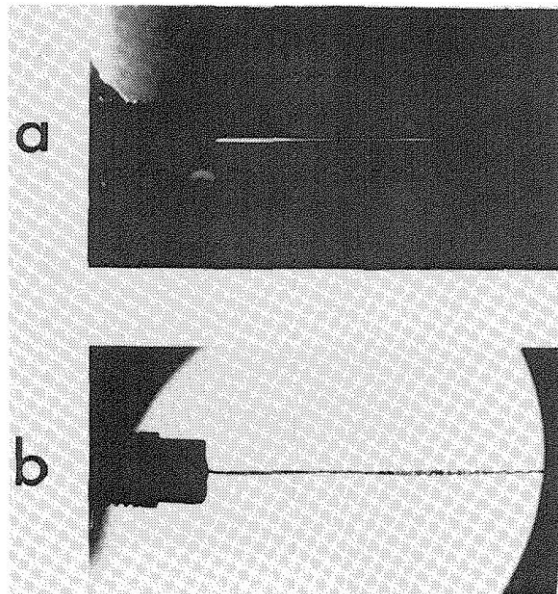


**Figure 3.4 – Side-view and view from beneath of a multi-hole injector during flash boiling<sup>[87]</sup>**

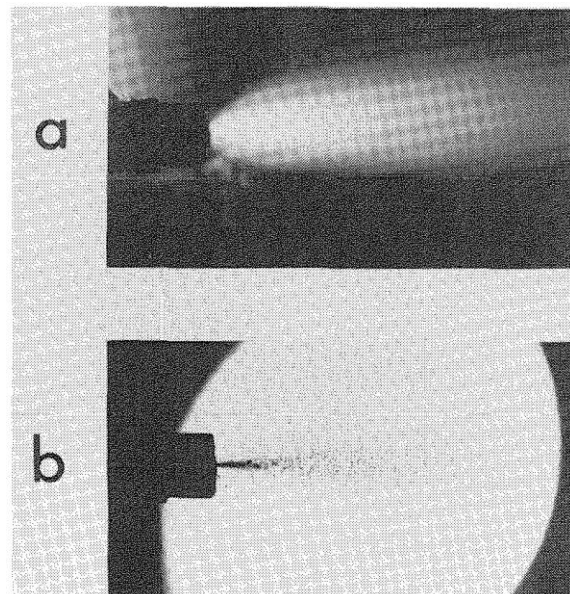
A fundamental study, where heated water was injected from a single-hole orifice into heated air, was performed by Reitz [103] to specifically investigate the mechanisms of flash boiling. Test conditions were:

- Liquid pressure 0.7 MPa
- Ambient air pressure
- Liquid and air temperatures within 5°C of each other, tested between 27°C and 153°C
- Orifice diameter 0.34mm and orifice length 1.37mm

Both a backlit photography technique and regular photography were used to capture images of the spray under various temperature conditions. It was found that the flashing jets had an intact inner core, surrounded by a fine spray. The spray droplets were expelled from the unbroken liquid jet starting at the nozzle exit by rapid vapour bubble growth within the jet. The core spray remained intact for some distance downstream of the nozzle and eventually broke up into large drops. The length of the core and the eventual drop-size both decreased as temperature was increased. Thus it was concluded that operation close to the boiling point of water gave improved atomisation.



**Figure 3.5: Spray at room temperature.**  
**a) regular photographic image, exposure time 4000ns,**  
**b) backlit image, exposure time 20ns**



**Figure 3.6: Spray at 153°C.**  
**a) regular photographic image, exposure time 4000ns,**  
**b) backlit image, exposure time 20ns**

Two practical difficulties were discovered. Firstly, as the water temperature was increased to boiling point, bubbles of vapour forming within the nozzle caused the phenomenon of vapour-lock, greatly reducing mass flow rate from the nozzle. However, this is unlikely to cause a problem in GDI fuel injectors as the internal pressures are high enough to prevent the formation of bubbles. Secondly, the backlit spray images did not clearly show the fine spray surrounding the core and the regular photographic images did not show the core, therefore both techniques were needed to show the effects of flash boiling. This can be seen in Figure 3.5 and Figure 3.6. It is possible that overlaying several backlit images could clarify the vapour drop cloud, eliminating the need for regular photography.

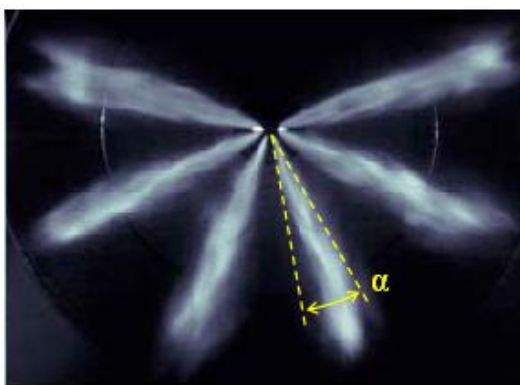
A study by Bouilly [104] investigated the occurrence of flash boiling in order to understand the phenomenon and how it could be modelled for use in computer software. Bubble nucleation in the fuel was found to have two origins:

1. Cavitation inside the injector nozzle due to local low pressure in the internal flow.
2. Flash boiling due to superheated fuel.

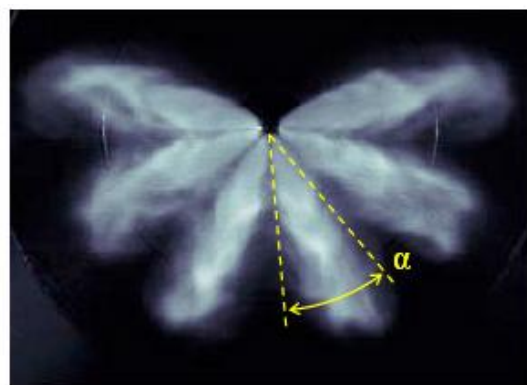
Flash boiling was controlled by the parameters in Table 3.1:

**Table 3.1: Effects of different parameters on flash boiling level**

Increase in:	Flash boiling level tendency
Fuel temperature	↑
Cylinder pressure	↓
Fuel specific heat	↓
Fuel enthalpy of vaporisation	↓
Temperature of fuel normal boiling point	↓



**Normal spray pattern**

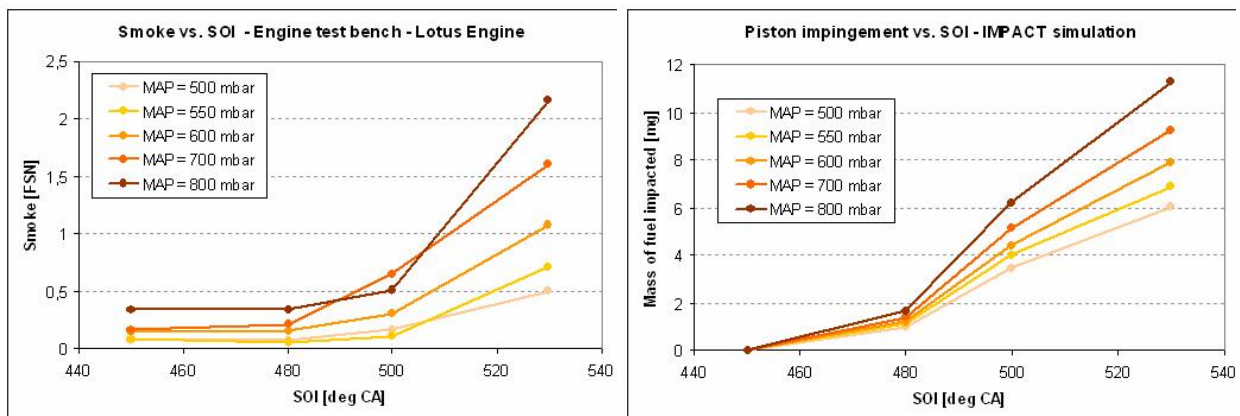


**Spray pattern with flash boiling**

**Figure 3.7: Effects of flash boiling<sup>[87]</sup>**

Increased flash boiling caused an increase in atomisation and spray plume angle, as seen in Figure 3.7. This had the effect of increasing the spray interaction with in-cylinder aerodynamics. The flash boiling phenomenon was modelled for four single-component fuels with various carbon contents and the models used to predict levels of fuel impingement on the piston under different levels of manifold absolute pressure. These results were then compared to smoke and HC emissions from a Lotus 3 cylinder low CO<sub>2</sub> engine, which are highly dependent on fuel impingement. Example results are shown in Figure 3.8.

It was found that increased piston impingement increased both HC and smoke emissions, however, the specific effects of flash boiling were unclear. The small variation in smoke and HC emissions at low manifold absolute pressure (MAP) is possibly caused by increased flash boiling resulting in spray being deflected away from the piston by air motion, but further investigation is needed to confirm this.



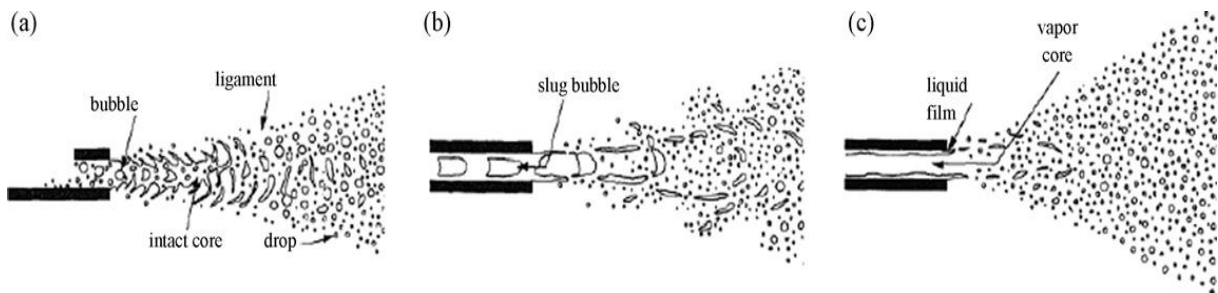
**Figure 3.8: Comparison of measured smoke and modelled piston impingement<sup>[104]</sup>**

From this it is clear that targeted use of flash boiling has the potential to reduce engine-out HC emissions and thus mitigate one of the major disadvantages of GDI over PFI engines. This research will therefore investigate flash boiling in order to increase understanding of the conditions under which it occurs, the mechanisms involved and how it can best be used to improve GDI spray atomisation. An important point to note is that the high-temperature, low-pressure conditions which cause flash-boiling are present during hot idle, for example when a vehicle is stuck in traffic. This means flash-boiling is likely a common occurrence in many vehicles under normal driving conditions and must be understood when designing and optimising an engine.

The major concern on the management of superheated liquids, in industrial environments, is the large potential hazards involved in cases of any accidental release. There is a possibility that a violent phase change could take place inside the fluid released generating a flashing jet. This violent phase change might produce catastrophic consequences, such as explosions, fires or toxic exposure, in the installations and in the surroundings. The knowledge and understanding of the mechanisms involved in those releases become an important issue in the prevention of these consequences and the minimisation of their impact. Polanco et al. work [105] presents a comprehensive review of information about flashing processes. The review begins with a description of the single phase jet followed by a description of the two-phase flashing jet. The concepts and implications of the thermodynamic and mechanical effects on the behaviour of the jets are considered at the beginning of the review. The second part of the review is devoted to the classification of the different study approaches used to understand flashing processes in the past, highlighting various critical parameters on the behaviour and the hazard consequences of flashing jets. The review also contains an extensive compilation of experimental, theoretical and numerical data relating to these phenomena, which includes information on the distinct characteristics of the jet, since type of jet, velocity distribution, expansion angle and mass phase change all require individual estimation.

Park and Lee [106] found that the internal flow pattern inside the nozzle governs the behaviour outside the nozzle. For longer nozzles or larger degrees of superheat the spray droplets are smaller and more uniform in size because of active bubble formation inside the nozzle. The flow regime changes as a response to the steady increase in superheat. The flow changes from bubbly flow to slug flow and then to annular flow. As a result, the spray droplets become smaller and more uniform, providing the basis for a classification into the three different regimes of flashing, namely a, b and c, respectively, in Figure 3.9. In all these experiments, the aspect ratio ( $l/d$ ) of the nozzle was about 7 and the fluid used was water. Initially, at low superheat a large intact core region is observed, and the droplets are formed at the sides of the nozzle. If the superheat is increased at the same ambient pressure, the nucleation and the growth of the bubbles become more active, so that when the bubbles collide with each other they coalesce inside the nozzle to form large slugs of liquid. When these slugs are discharged from the nozzle they break into ligaments and then disintegrate into small drops, but, exceptionally, with some of the larger ones remaining intact. In the annular flow regime, a liquid film forms on the nozzle wall and the vapour flows at a much higher velocity along the core region. In this regime, as the fluid is discharged from the nozzle, the liquid films disintegrate into fine droplets. The effect of the length of the nozzle on

droplet formation is similar to that of superheat, which means that longer nozzles encourage the formation of smaller droplets outside the nozzle.



**Figure 3.9: Jet types dependence on nozzle (a) bubbly flow, (b) slug flow and (c) annular flow patterns<sup>[106]</sup>**

A flash evaporation model was developed by Bianchi et al. [107] to capture the effects of bubble nucleation and growth inside multi-hole injector nozzles to investigate the flash evaporation in fuel injector sprays in Gasoline Direct Injection (GDI). The 1D flash evaporation model is a key tool for providing the 3D Eulerian-Eulerian or Lagrangian spray simulation model with the right droplet size in order to properly predict the effect of degree of superheating on mixture formation. Super heating conditions are likely to be found under partial load conditions in GDI applications or they might be deliberately induced to enhance fuel atomisation and vaporisation. A quasi-1D nozzle flow model has been developed to help quantifying the effects of main physical and geometrical parameters in promoting fuel flash evaporation. This model is based on a weakly compressible homogenous two-phase mixture assumption. A non-equilibrium model is used to predict the vapour formation rate along the nozzle. A fully explicit method based on a two-step Lax-Wendroff method is used together with a total variation diminishing (TVD) scheme. An atomisation model has been proposed to correlate the void fraction at nozzle exit to the most probable radius of the droplet generated from flashing atomisation. An accurate two phase speed of sound was adopted allowing to predict the choked flow conditions once saturation has been reached. Metastable states were not considered in this first approach. A preliminary validation has been carried out based on an experimental nozzle flow configuration at two different values of superheating degree. A preliminary assessment of the model capability in capturing the effect of fuel conditions on droplet most probable diameter was presented [107].

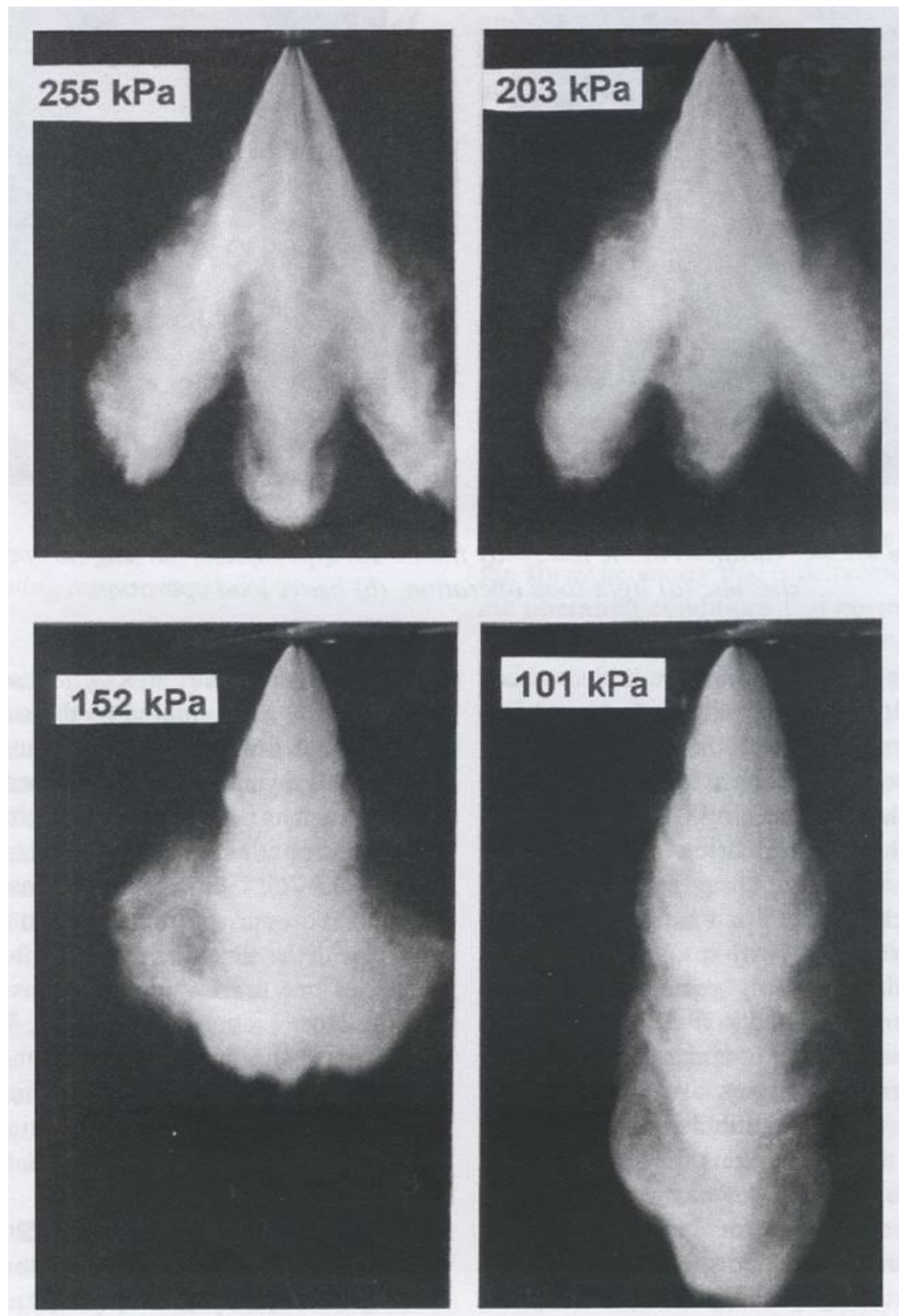
Flash boiling conditions, where the fuel is superheated with respect to cylinder pressure, are often found in gasoline direct injection engines. This phenomenon affects the flow rate of the fuel and can cause choking of the nozzle. In their work, Gopalakrishnan and Schmidt [108] present multi-dimensional simulations of flashing internal injector flow. The modeled fluid quality (mass fraction of vapor) tends towards the equilibrium quality based on the Homogenous Relaxation Model. The relaxation time is dependent on the local pressure, the vapor pressure, and the void fraction. Simulations of the internal flow are presented and, where possible, validated with experimental data. Both two- and three- dimensional computational results show geometrically-induced phase change, similar to cavitation, near the nozzle entrance. Near the nozzle exit plane the phase change occurs at all radial locations and can be quite sensitive to temperature. Three-dimensional simulations run in an asymmetric injector tip at higher injection pressure showed reduced sensitivity to temperature [108].

A vaporisation model for multi-component fuel sprays was described by Ra and Reitz [109]. The discrete multi-component (DMC) fuel approach was used to model the properties and composition of gasoline and diesel model fuels. Unsteady vaporisation of single and multi-component fuel droplets and sprays was considered for both normal and flash-boiling evaporation conditions. An unsteady internal heat flux model and a model for the determination of the droplet surface temperature were formulated. An approximate solution to the quasi-steady energy equation was used to derive an explicit expression for the heat flux from the surrounding gas to the droplet-gas interface, with inter-diffusion of fuel vapor and the surrounding gas taken into account. The density change of the drop as a function of temperature was also considered. In order to treat phase change under trans-critical conditions, a characteristic length was defined to determine the amount of vaporised fuel as a function of time. The present vaporisation models were implemented into a multi-dimensional CFD code and applied to calculate evaporation processes of single and multi-component fuel droplets and sprays for various ambient temperatures and droplet temperatures. Differences between representing model fuels using the single and multi-component fuel description were discussed [109].

Many projects investigating the behaviour of multi-hole injectors under different temperature and pressure conditions have been conducted by various universities, research institutions and commercial companies. The combined effects of operating temperature and ambient back pressure on the spray development of multi-hole injectors were summarised by Zhao et al. [2]. Multi-hole spray development and wetted footprint were found to change markedly between the two extremes of operation of high-load, early-injection and low-load, late-injection, although the changes were less pronounced than for a swirl injector. The fuel spray collapsed from clearly defined spray plumes to a single plume as the ambient pressure was reduced, which is the opposite trend to swirl injectors. This trend was found during operation with injector bodies and fuel at 75°C or more. Some spray collapse was also observed as backpressures were increased over 0.45MPa. This transition region was much more robust than for swirl injectors, where the spray often oscillates between fully formed and collapsed from cycle to cycle. Experiments were carried out on a 50° spray angle, six-hole injector at four levels of ambient back pressure using indolene as fuel and a fuel rail pressure of 11MPa. Spray development images from the indolene experiments are shown in Figure 3.10. Indolene is a chemical manufactured to have the same physical properties as gasoline. During bench tests at room ambient conditions, the spray was a collection of narrow, individual spray plumes with one plume for each hole and one wetted spot for each plume. As the injector body and hence fuel temperature were increased to normal engine operating temperatures of 75 to 90°C the plumes became wider with less well defined boundaries. As ambient pressure was decreased from typical late-injection values of 0.45MPa the plumes began to broaden and combine, eventually becoming a single plume at approximately 0.15MPa back pressure. At this point the spray appeared very similar to that from a swirl injector, complete with outer toroidal vortex. The total cross-sectional area of the spray was decreased, as was the area of the wetted footprint. Further back-pressure reduction to 0.1MPa gave a fully collapsed, highly penetrating spray very similar to a pressure swirl injector spray under the same conditions. Some increase in penetration rate was due to reduced droplet drag at lower back pressure, with the remainder due to the decreased drag of one narrow spray plume as opposed to multiple plumes. The atomisation of the spray was also found to change, but once again the multi-hole injector was affected to a lesser degree than the swirl injector. For the 50° angle, six-hole injector tested, there was a moderate increase in  $D_{32}$  as backpressure was increased. This was due to increased droplet coalescence at higher ambient densities. An improvement in the level of atomisation with increased fuel temperature was identified and was significant at all but the highest ambient backpressures. For injection into 0.1MPa backpressure, the  $D_{32}$  was halved by increasing the fuel temperature from 20 to 90°C, whereas at 0.6MPa the improvement was only 1.9µm. The enhancement in  $D_{V90}$  was also found to be very significant with heating. At elevated



operating temperature and low ambient backpressure, acetone-doped iso-octane was found to undergo flash boiling. The transition to flash boiling conditions occurred at 70°C, however, as the ambient backpressure was increased this transition became less pronounced. Experiments conducted using indolene as the fuel produced similar results.



**Figure 3.10: Effect on operation of a multi-hole injector for four levels of ambient backpressure. Six-hole nozzle, 50° nozzle angle, indolene fuel, temperature 90°C, injection pressure 11MPa, fuel injected 10mg per injection<sup>[2]</sup>**

The observed solid-cone structure associated with flash boiling is explained by rapid evaporation of the volatile species followed by transportation of the smaller droplets to the centre of the jet. For common-grade gasoline which is a multi-component blend, low-boiling point components would be present that could alter the spray characteristics and result in flash boiling.

Next chapter will first detail the experimental techniques and then gives a description of the facilities used and developed in the scope of this study.

### **4. Experimental Techniques and Facilities**

#### ***4.1 Experimental Techniques***

This section will document the various optical measurement techniques used to measure and analyse fuel sprays. Imaging techniques are classified by their output providing data over the entire measurement space but at one single point in time. A brief introduction of the techniques and facilities most commonly seen in the literature is presented and a detailed description of those used in this work is presented later.

##### **4.1.1 Shadowgraphy and Mie Scattering Imaging**

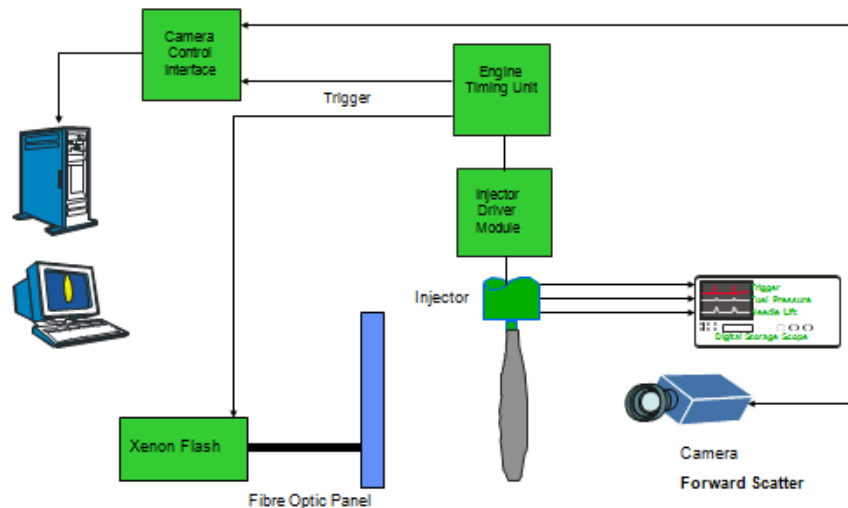
In both shadow and Mie imaging an image is taken of the spray at a specific point in its development phase using a high speed CCD camera. The CCD camera has a fast frame transfer rate (up to 16Hz), which enables it to store an image, and then be ready to capture another image very quickly. Due to the small timeframes involved in fuel injection this is still not fast enough. The time taken to take an image, and the speed with which it is required to be transferred to a PC, is sufficiently long that high resolution images cannot be taken at very high speeds using current CCD technology. Therefore a compromise is made between the number images taken per second and the pixel resolution of the images. This issue has been addressed by the manufacturer 'LaVision' who have created an ultra high speed camera, based on CMOS (Complementary Metal Oxide Semiconductor) technology, that can maintain a large degree of resolution and still have a very large frame rate (1000\*1000 pixels at 10kHz).

A study was performed by Eisenberg [110] using an ultra high speed camera from LaVision into investigating shot-to-shot variation. It was found that using the ultra high speed camera that many high resolution images could be taken on a single spray, and when this data was compared to further results one could easily see the distinction between spray development phenomena occurring in one cycle from those occurring due to cycle-to-cycle variation.

The work reported here is addressed by imaging a specific instant in the spray development and then taking a series of images at that point in time for many individual sprays at identical conditions.

## Chapter 4 - Experimental Techniques and Facilities

In shadow imaging the spray is illuminated by a flash unit (usually Xenon) which consists of a panel with two dimensional array of optical fibres of uniform spatial arrangement to create a uniform field of light behind the spray. The flash unit is timed along with the injection and camera timing, so that the spray illumination and camera imaging are synchronised at the required image time after the start of injection. A schematic of the back lit imaging system used in the present work is presented in Figure 4.1.



**Figure 4.1: Schematic of back lit imaging system (shadowgraphy)**

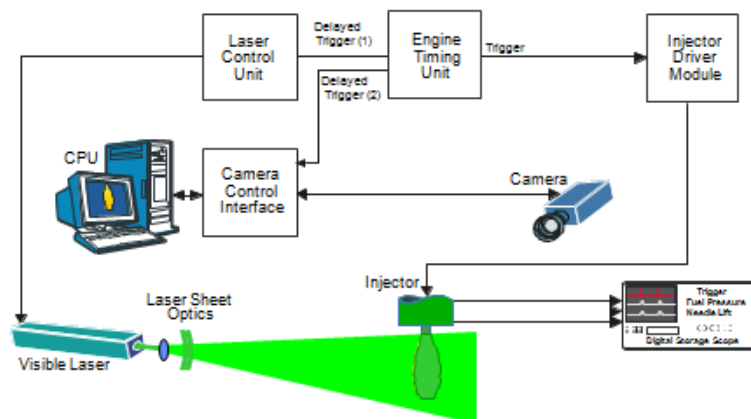
The image recorded by the camera is a grey-scale shadow of the spray with a white background and spray density related to the shade of grey. For clarity, and to assist post-processing techniques, the image is often inverted and a colour coded scale that varies with density is applied (this is more easily identified by the human eye). There are many different density based scales that can be applied to the raw spray image to assist in post processing and often a combination of several different scales are required to identify the various characteristics of a fuel spray. For example, a coloured scale is often used to assist in defining the penetration and cone angle of the spray, whereas a Sobel filter is often used to assist finding the boundary profile of a particular spray.

It was found by Wigley et al. [111] that the cone edge for a pressure swirl atomiser can be found by a single shot due to the inherent stability and repeatability of the spray in that area, but the spray penetration should be derived from a mean image of many shots due to the transient effects at the front of the spray giving rise to large shot-to-shot variation. The spray boundary is defined as a specific light intensity transmitted through the spray as percentage of the peak light intensity. This is usually taken as 50% since it has been found to be a good

## Chapter 4 - Experimental Techniques and Facilities

representation of the boundary between spray body and finely atomised drops in the periphery. Using the methods outlined above, shadow imaging can provide a very good idea of the overall boundary features of the spray, and of the development of a spray using multiple images at incremental time periods. This method can be used to fully characterise all aspects of a sprays' development. However, due to the limitations of the camera in relation to the time it takes to capture an image, the collection of images for the development of a spray can be complicated. Images are usually taken at different times in the injection process of different individual sprays and then compiled at the end to gain an average concept of spray development. It is not possible to follow accurately the development of a single spray shot. The determination of liquid and vapour mass requires additional imaging techniques.

Mie scattering imaging uses a visible laser as a light source instead of a xenon flash. It allows visualisation of the light scattered by droplets and can be used in conjunction with Laser Induced Fluorescence (LIF) to distinguish between fuel liquid and fuel vapour in the LIF images by the addition of tracers to the fuel. Mie scattering and shadow imaging techniques provide useful qualitative and even some quantitative descriptions of spray and mixture formation processes, they do not provide complete information about the internal dynamics of the spray. Mie-scatter images can be particularly deceiving as the small particles present in GDI sprays have diameters approaching the wavelength of the light used to observe them and therefore, scatter light disproportionately to their diameter or mass. Determination of the location and concentration of liquid and vapour mass requires the use of additional diagnostics such as the laser induced fluorescence techniques [78]. A schematic of a Mie imaging system is presented in Figure 4.2.



**Figure 4.2: Schematic of Mie imaging system**

## Chapter 4 - Experimental Techniques and Facilities

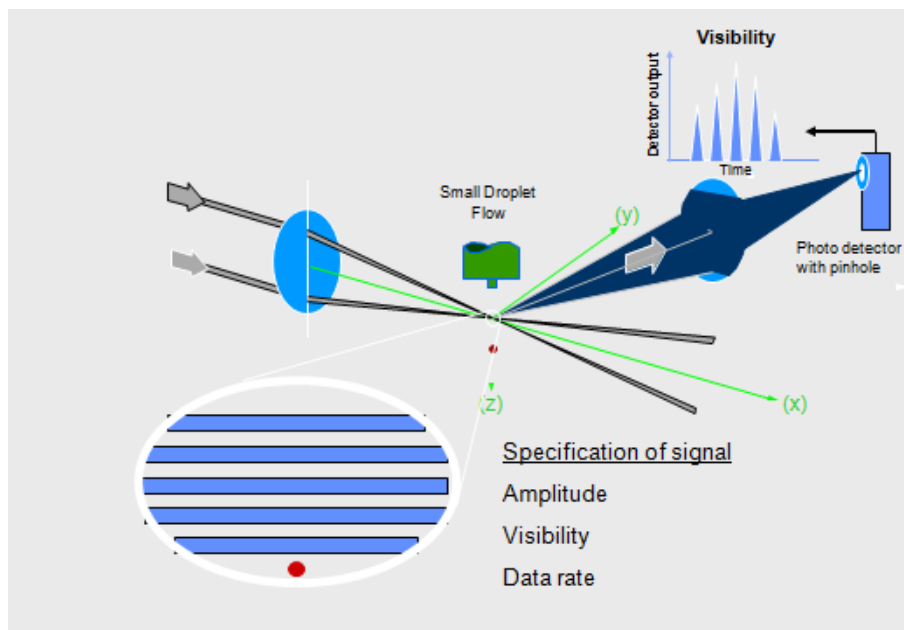
Single point imaging techniques differ from planar imaging techniques in that the measurement volume is a single point in space while the data provide the time history at that point.

### 4.1.2 Laser Doppler Anemometry

Laser Doppler Anemometry (LDA) is a measurement technique that utilises the interference pattern created when two very highly polarised and coherent laser beams cross each other. The interference pattern consists of a series of fringes, with spacing specific to the intersection angle and laser wavelength. As a particle passes through the fringe spacing, the light is scattered and Doppler shifted and it is this signal that is received by the signal detector. The velocity with which the particle is passing through is proportional to the oscillation frequency of the sinusoidal signal and the fringe spacing of the interference pattern. This is the main property of the flow that can be analysed by LDA techniques.

A schematic of a LDA system is presented in Figure 4.3. This schematic presents a static fringe pattern. In general a frequency shift is introduced by using a Bragg cell, which effectively makes the fringes move. The recorded frequency will be the addition of the frequency due to the droplet movement plus or minus the frequency shift.

Due to the fringe spacing being created in the vertical direction, any particle passing through in the horizontal direction will generate a signal frequency equal to the frequency shift. The particles passing through the fringe pattern will generate a signal relative to the vertical velocity component. Therefore this technique is said to be directionally sensitive.



**Figure 4.3: Schematic of LDA system**

## Chapter 4 - Experimental Techniques and Facilities

---

### 4.1.3 Phase Doppler Anemometry

Phase Doppler Anemometry (PDA) effectively uses the same principles and experimental set-up as the LDA analysis technique, but instead of one detector it uses two detectors, one above another. On the scattering plane, XY in Figure 4.4, defined by the axis of a transmitter and a receiver, as the particle passes through the fringe pattern, the top detector, A, receives a signal first, followed by the lower detector, B. The difference between the signal peaks on the upper and lower detectors is a time difference or phase lag, and the phase lag is directly proportional to the droplet diameter. Using this information, a correlation between particle size and velocity can be formed and used to show the variation of size/velocity over the entire fluid flow.

Using a two component transmitter with different wavelength and a third detector allows the trajectory of a particle to be found by comparing the frequency signals received by the two detectors. This can provide a two dimensional velocity field and hence trajectory.

The cross-sectional area of the measurement volume can be used with the time taken for a certain number of particles to pass through the measurement volume to find the particle concentrations and flux densities. A schematic of PDA data acquisition is presented in Figure 4.4, in which a droplet crosses a fringe pattern. For LDA applications the droplet size would normally be chosen to be about half the fringe spacing. One fringe spacing is one blue and one white line. When the droplet falls through the fringe pattern, it generates a signal with a visibility of 100% when the droplet is in a dark i.e. a blue fringe, where there no light scattered. The droplet moves down through the fringe spacing and generates the signals. The phase lag between the signal from detector A and the signal from detector B can then be measured.

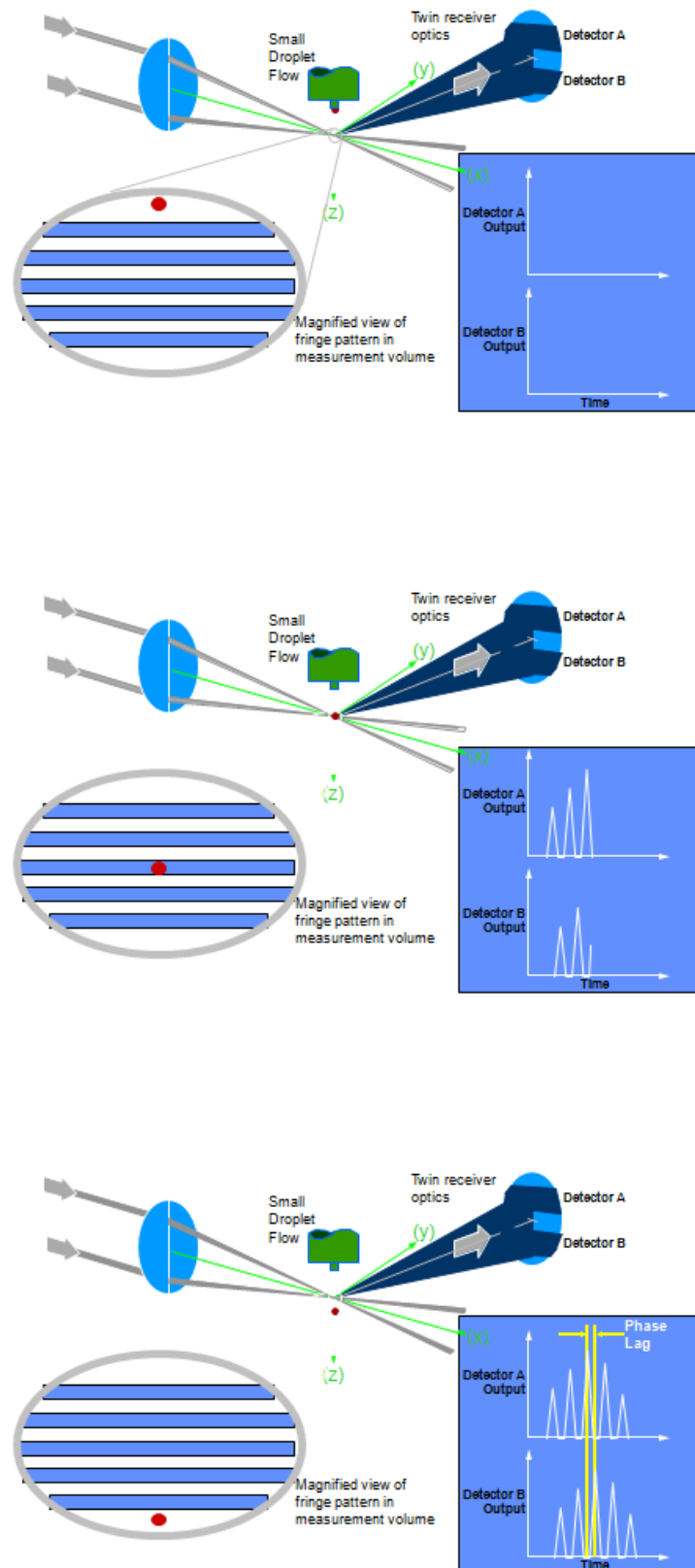


Figure 4.4: Schematic of PDA data acquisition

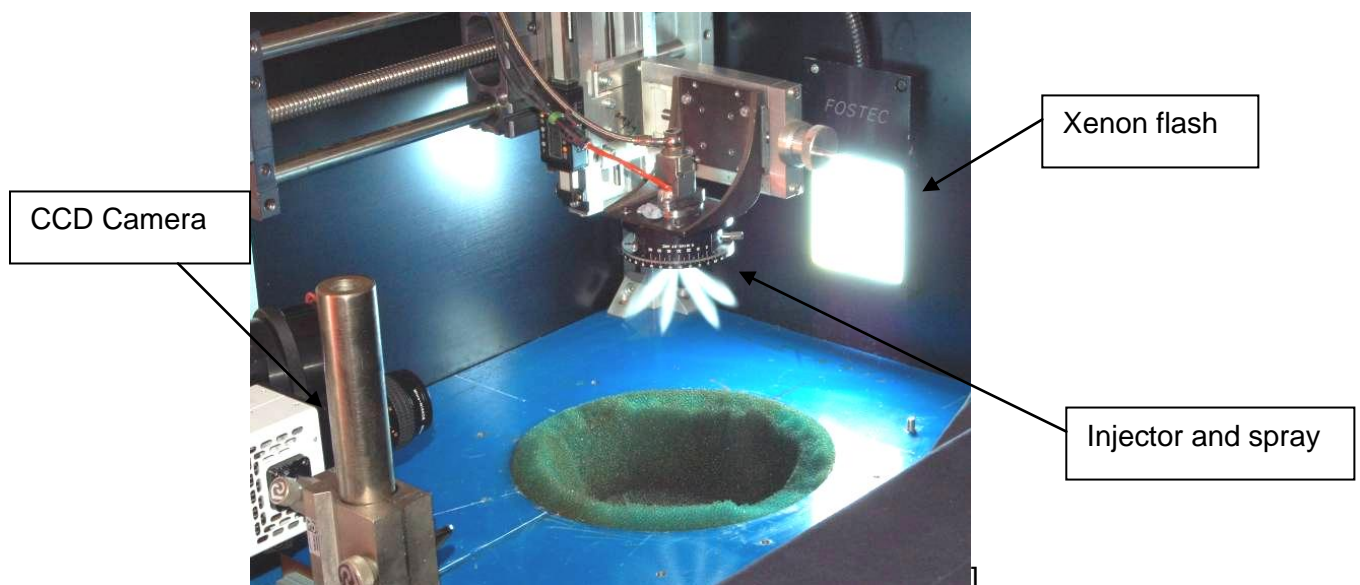


### 4.2 Experimental Facilities

There are three main experimental methods used to examine fuel sprays and each have their respective advantages and disadvantages.

#### Atmospheric Spray rigs:

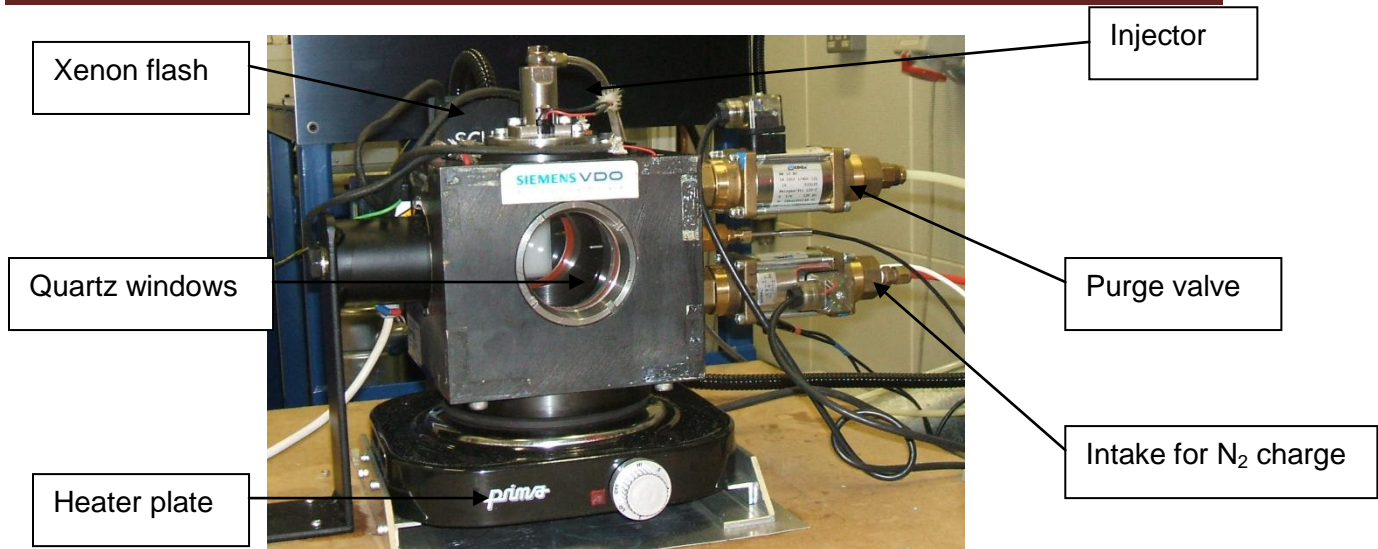
- Easy to set up.
- Optical access to the spray is simple.
- Only atmospheric conditions can be simulated which are not very representative in terms of in-cylinder charge pressure, temperature and movement.
- The lack of effect of the moving boundaries and changeable conditions the spray experiences within the engine (the moving piston and valves and the changes in pressure, temperature and airflow as a consequence) reduce the variables affecting the spray and enable simpler analysis.



**Figure 4.5: Atmospheric spray bench** <sup>[B2]</sup>

#### Pressure Chamber:

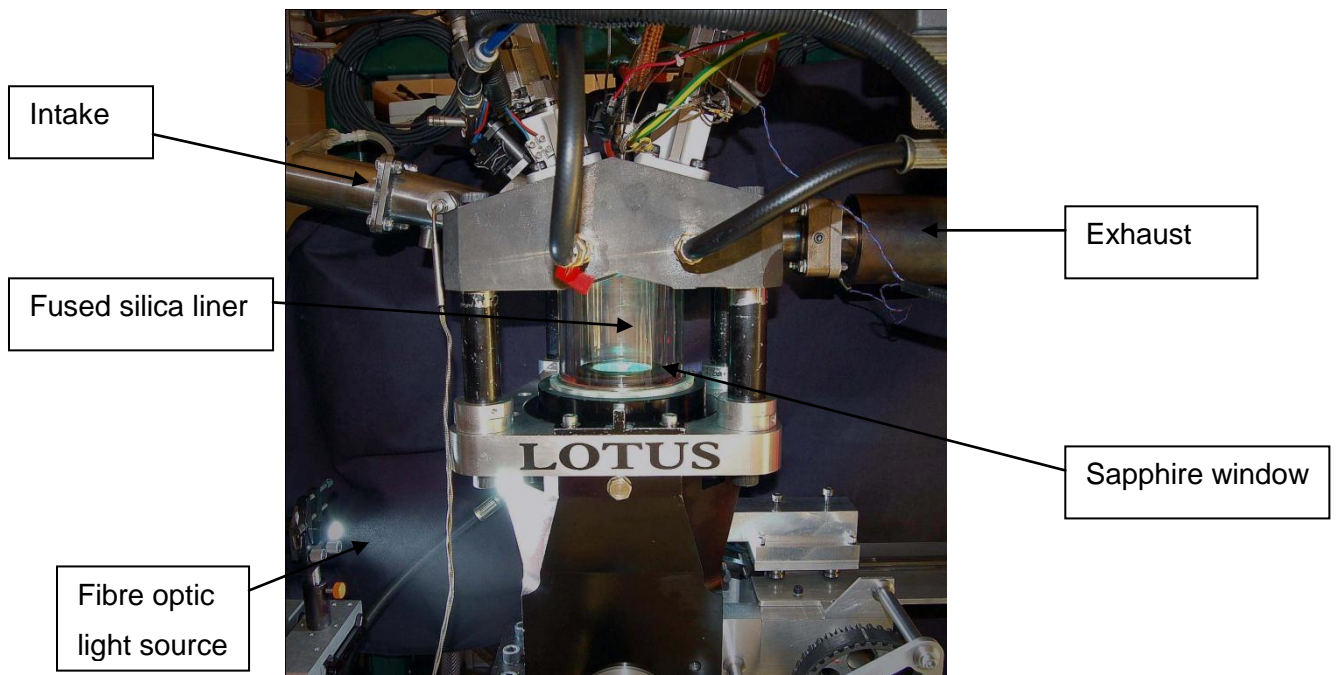
- Optical access reduced.
- Adequate illumination of the spray can be difficult.
- Pressure and temperature representative of engine operating conditions
- Engine cylinder airflow simulation not possible.



**Figure 4.6: Pressure chamber**

### Optical Engines:

- Optical access much more reduced unless a fully optical engine is used.
- A fired engine rises in temperature exceptionally quickly meaning that to prevent the glass cylinder liner cracking it can only be fired for a very short period of time. If significant periods of firing are required, often a metal cylinder liner is used to cope with the temperatures reached. This reduces even more optical access.
- Representative engine operating conditions.
- More variables affecting the spray making the analysis much more complex.



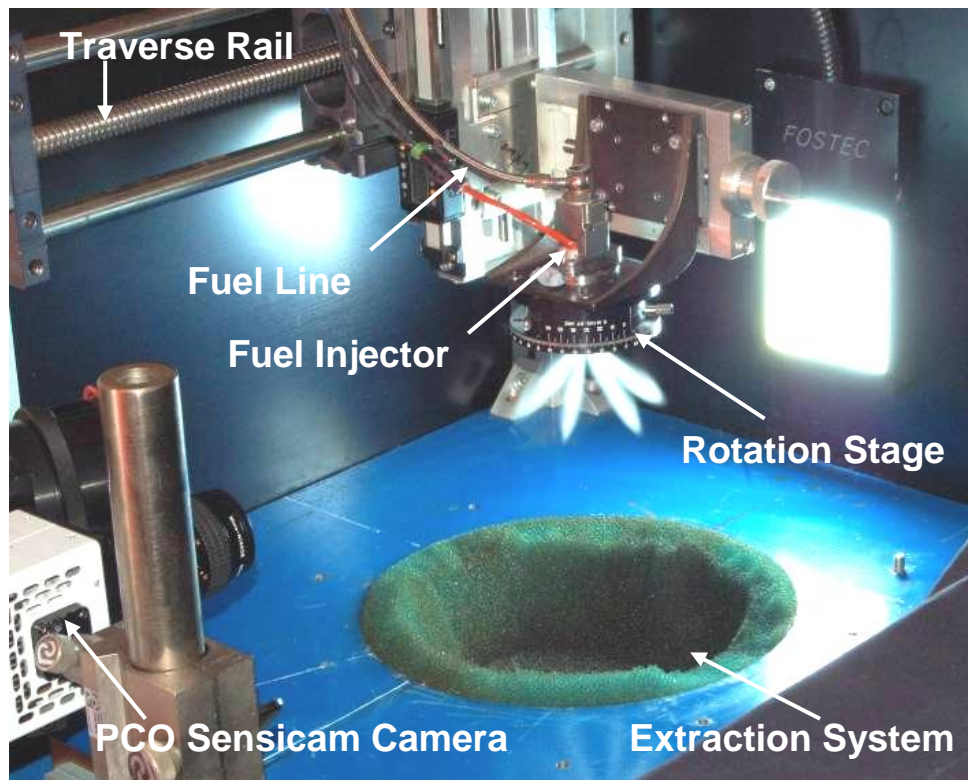
**Figure 4.7: Single cylinder optical research engine** <sup>[82]</sup>

## Chapter 4 - Experimental Techniques and Facilities

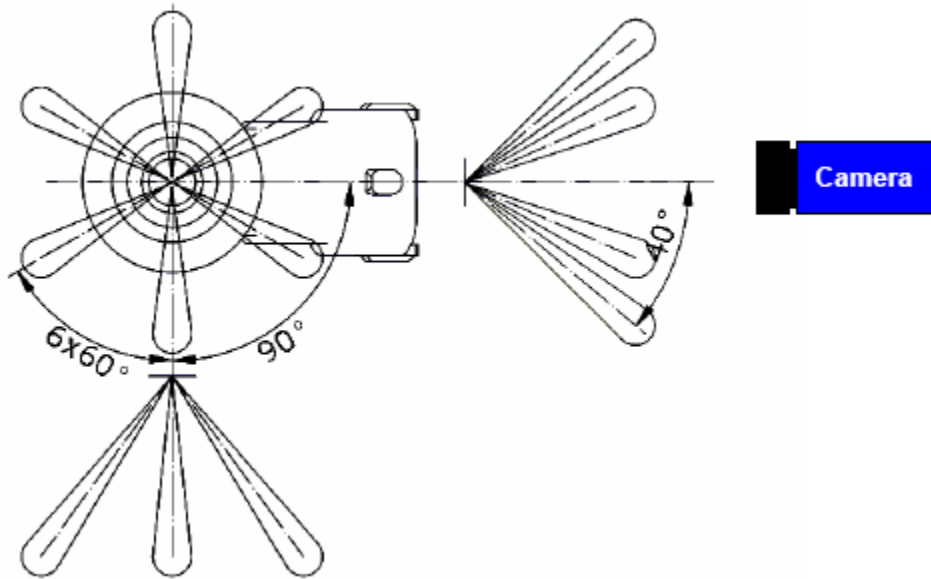
### 4.2.1 Atmospheric Bench

This rig has been developed primarily for the measurement of fuel sprays from automotive gasoline injectors, including both PFI and GDI. A two dimensional laser PDA system is capable of measuring simultaneously the droplet diameter and axial and radial velocities. In addition to this, the rig features an imaging system which is used to capture the macroscopic properties of the spray. Spray metrics of tip penetration, tip velocity and cone angle are measured from mean images of the spray (see Data Analysis at the end of section 4.2.2 Pressure Chamber for more details)

The fuel injector is rigidly held in a rotation stage which permits 360 degrees of freedom. The rotation stage is in turn mounted on a precision 3 dimension orthogonal traverse system such that the injector sprays vertically downwards into an extractor system, see Figure 4.8 and Figure 4.9.



**Figure 4.8: Atmospheric spray rig injector mounts, traverse, extractor and imaging arrangement**



**Figure 4.9: Example of injector orientation for 6 hole symmetrical multi-stream injector**

The air flow into the extractor ( $\sim 1\text{-}2\text{m/s}$ ) is sufficient to remove the entire fuel spray without introducing significant bulk air motion around the fuel spray periphery. One of the traverse systems is electronically driven through a stepper motor by the data acquisition software. This automated degree of freedom is used to move the injector relative to the PDA measurement volume radially through the fuel spray. The other dimensions of the traverse system are manually set by the operator, where injector position is measured using digital verniers.

Fuel is stored in a 5 litre aluminium fuel tank which houses a submerged low pressure fuel pump. The low pressure pump is used to feed a high pressure 3 piston triplex pump. A back pressure regulator is used to control and vary the fuel pressure to the injector. Low and high pressure relief flows are returned to the fuel tank.

The injector is driven by a pulse generator and Siemens injector driver unit. A 1 ms capacitive charging delay exists between the injector driver unit input pulse signal and the output injector driving signal. This delay is a design feature of the driver to prevent voltage drop off during the injection event and increase the speed of response.

### **Shadowgraphy System:**

The atmospheric spray rig imaging system utilises a Xenon flash unit, Fostec fibre optic panel and PCO Sencicam Fast Shutter CCD camera, with a Nikon 55mm macro lens with aperture f5.6, to produce backlight fuel spray images. Digital images of pixel resolution 1280 x 1024 pixels are handled using PCO Picture Viewer software. The triggers for the camera and flash are provided by the injector pulse generator unit. All trigger pulses are monitored using an oscilloscope to confirm camera/flash timing delays (6.5 $\mu$ s delay for the flash with 0.5 $\mu$ s camera exposure time).

### **PDA/LDA System:**

The Phase Doppler Anemometry system uses an Argon ion type Coherent INNOVA-90-4 LASER to produce two beams, blue (wavelength  $\lambda = 488$  nm) and green ( $\lambda = 514$  nm) which are used to determine the radial and the axial velocity components respectively while the latter is responsible for the drop-size measurements.

The main beam is focused to produce a circular cross sectional area with a Gaussian light intensity profile. The two colour wavelength beams are separated from the main beam using beam dispersing prisms. Each beam is steered into a Bragg cell which splits the beam with a 50/50 intensity. The Bragg cell also produces a +40MHz frequency shift on one of the split beams. The green beam prior to the Bragg cell is passed through a half-waveplate to change the polarisation by 90°.

The heart of this optical system is a Bragg cell that uses a tellurium dioxide crystal with an anisotropic acousto-optical interaction. It can provide 50=50 beam splitting of the input beam symmetrically about the optical axis and a 40MHz frequency shift between the output beam pair with low power built-in driver electronics. The main advantages of this Bragg cell are: thermal blooming with high incident laser power densities has been minimised, the output beams have a true circular cross-section and the effective Bragg angle has been increased dramatically. However, the Bragg condition is strongly polarisation and wavelength dependent while the frequency shifted beam has the polarisation direction rotated through 90 degrees.

## Chapter 4 - Experimental Techniques and Facilities

The advantages outlined above by Wigley et al. [112] have allowed the construction of a simple high power LDA/PDA transmitter system by integrating the Bragg cell with a two lens laser beam expander that offers variable beam separation and high beam expansion ratios. The excellent beam aligning properties of a symmetrical optical design are maintained so beam alignment devices are not necessary. A schematic of the LDA/PDA transmitter system, in one component form for simplicity, is shown in Figure 4.10.

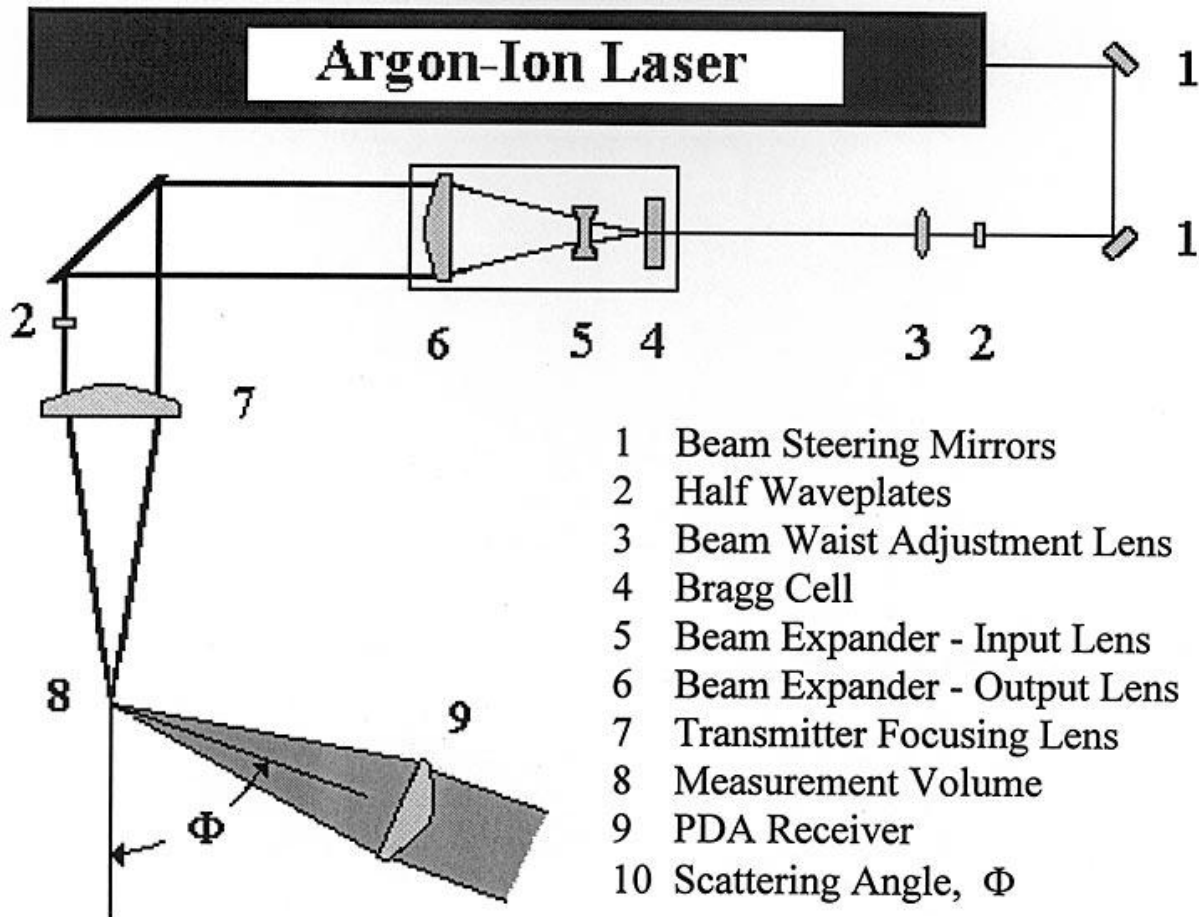


Figure 4.10: Schematic of optical layout of the LDA=PDA system<sup>[112]</sup>

For multi-component velocity measurements and high laser powers a water-cooled Argon-ion laser is essential. Mirrors (1) steer the laser beam through a half-waveplate (2) to align the polarisation plane of the beam with the Bragg cell. The lens (3) images the laser cavity's beam waist into the Bragg cell (4) to ensure plane parallel wave fronts and a beam waist at the measurement volume. The focal length of this beam waist adjusting lens is determined by the laser beam output diameter and the required measurement volume diameter.

Two beams of equal intensity exit the Bragg cell, symmetrically about the optical axis, with an angular separation of 1.88 degrees for the 514.5 nm wavelength. The first order diffracted

## Chapter 4 - Experimental Techniques and Facilities

---

beam is frequency shifted by 40MHz and has a polarisation direction orthogonal to the zero order beam. The laser beam expander, lenses (5) and (6), expand and collimate these diverging beams to produce a beam separation of up to 50mm with an expanded beam diameter of 4.4 mm. Beam separation and beam expansion are directly linked so that a constant number of fringes in the measurement volume is maintained when the beam separation is changed. Changing the focal length of lens (3) allows the measurement volume diameter to be changed independently of beam separation. The beam separation control is a simple translation of the Bragg cell, along the optical axis, followed by a small refocus of lenses (3) and (5) to achieve collimation of the beams. A second half-waveplate (2) is then required to match the shifted and input beam polarisation directions. The light intensity in each beam is now matched by adjustment to the Bragg cell drive power. A mirror at 45 degrees folds the two pairs of orthogonal beams to a three element front lens (7) and focuses the two collimated and parallel beams to form the diffraction limited measurement volume (8). The receiver optical system (9) was the larger aperture 'classic' Dantec 57X10 located at a scattering angle (10) of  $\Phi$  degrees. The signal processing was performed by the Dantec enhanced 58N50 PDA covariance processor linked to a PC by the 58G130 interface.

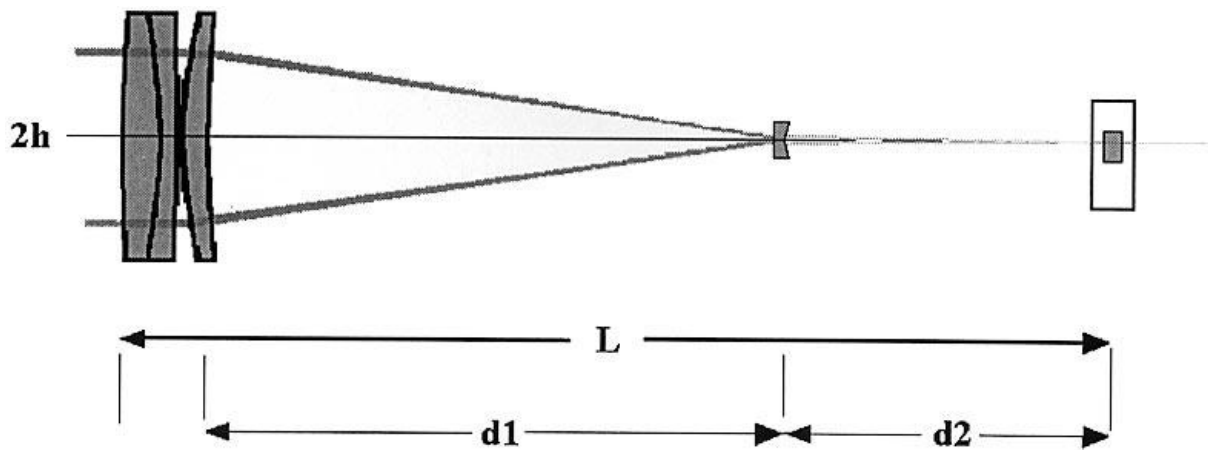
For two colour operation, 488 nm (blue) and 514 nm (green) wavelengths, the mirrors (1) are replaced by Pellin Broca dispersing prisms to separate the two wavelengths and the components (3) to (6) are duplicated, arranged side by side, with the second Bragg cell and half waveplate rotated through 90 degrees. The orthogonal blue beam pair are combined, on the optical axis of the green beam pair, with a mirror periscope positioned immediately after the beam expander lenses (6), [113]. This is not seen as an unnecessary complication due to the high degree of flexibility offered. The variable beam expanders can be set to: (a) equalise the beam separation for each wavelength; (b) equalise the diameters of the two measurement volumes or; (c) create unequal measurement volume diameters with one inside the other.

The specification for the beam diameters at the front lens and the measurement volume dimensions are given in Table 4.1. The focal length of the beam waist adjusting lens was 570 mm. These have been calculated using Gaussian beam theory but substituting equivalent simple thin lenses for the complex optical geometry of the beam expander. This is shown in more detail in Figure 4.11 which specifies the geometry and dimensions of the integrated beam expander Bragg cell unit. One important operating feature to note is that the distance,  $d_1$ , between the lenses (5) and (6) is small, a maximum adjustment of 1.15mm covers the beam separation range from 30 to 50 mm. [112].

## Chapter 4 - Experimental Techniques and Facilities

**Table 4.1: Specification of PDA operational parameters<sup>[112]</sup>**

Transmitter			Receiver	
Velocity component	Axial (u)	Radial (v)	Scattering angle	70 degrees (Brewster)
Laser Wavelength	514 nm	488 nm	Lens focal length	310 mm
Beam Power	200 mW	100 mW	Lens diameter	78 mm
Beam diameter	5 mm	5 mm	Detection aperture	0.5 mm
Beam separation	50 mm	50 mm	Refractive index	1.47
Polarisation plane	Parallel	Parallel	Phase factor	6.6 deg/mm
Lens focal length	300 mm	300 mm	<b>Signal processor</b>	
Measurement volume			Frequency bandwidth	45 MHz
Diameter	39 mm	37 mm	Amplifier gain	Low
Length	110 mm	110 mm	Max size range	<100 mm
Fringe spacing	3.1 mm	2.9 mm	Velocity range	-30 to 120 m/s



**Figure 4.11: Geometry of the beam expander – bragg cell unit<sup>[112]</sup>**

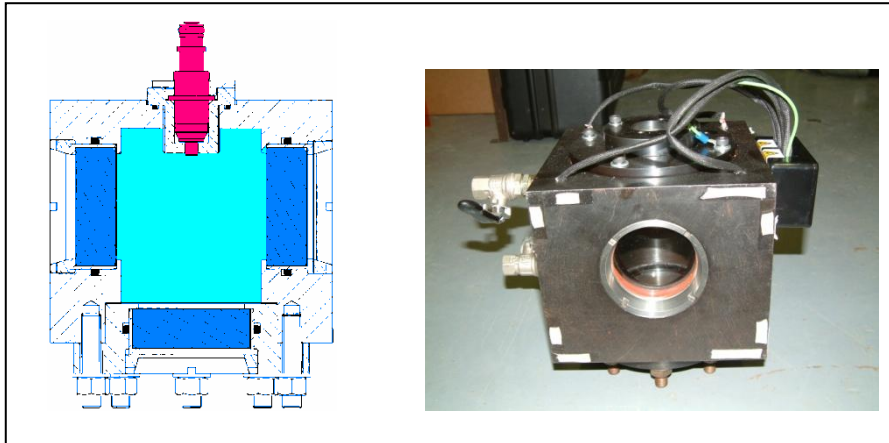


### 4.2.2 Pressure Chamber

In 2005, a final year project by Wilkie [114], investigated the effects of temperature and pressure on a GDI Fuel Spray. Essentially the same experimental set up was used for this investigation but with the aim to improve the heating and scavenging processes, the electronic control and data logging of internal pressure and temperature, and the imaging timing electronics. The purpose of the study was to test a range of fuels and injectors in order to observe the effects of fuel properties and injector geometry on atomisation performance.

Wilkie's project used an optical chamber as this created a controlled environment where both temperature and pressure can be controlled accurately over a wide range of values, and varied independently. Optical chambers, or High Pressure High Temperature (HPHT) cells, have some major drawbacks, the biggest being the necessity to scavenge it. It has been shown that unless this is done, image quality deteriorates after a maximum of 10 injections depending on the spray angle of the injector and the operating temperature. This leads to a very time-intensive method of collecting data.

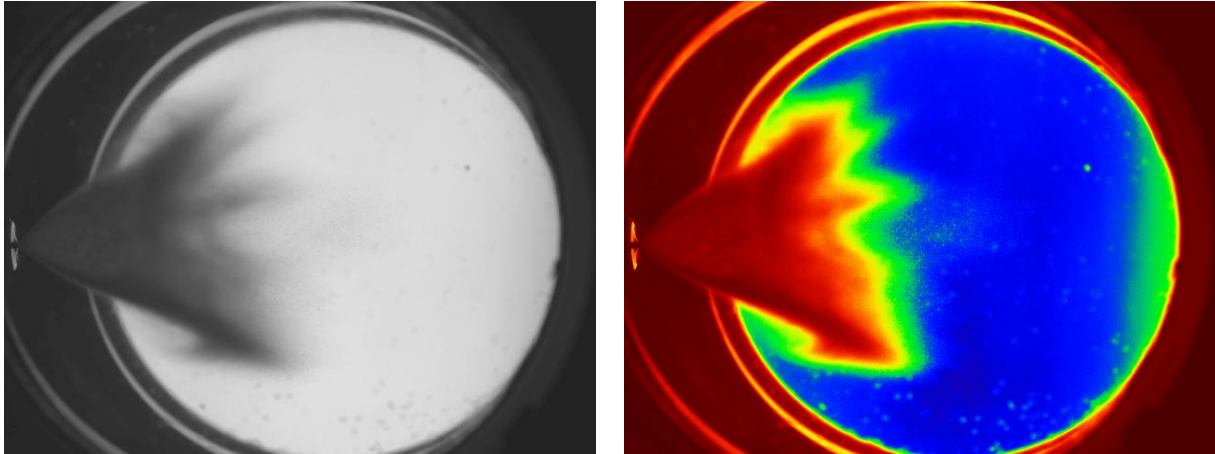
The HPHT cell used was constructed by Lotus Engineering, some 15 years ago, for a research project to investigate spray formation under stratified engine relevant conditions. The HPHT cell itself is a 180mm cube made from steel with an internal bored cylindrical volume of 725cm<sup>3</sup>. Two of the vertical faces of the cube hold 25mm thick quartz windows of 75mm diameter to allow illumination and imaging of the spray. One face is blank and is used to secure the HTHP cell to the supporting surface. The other face has three tapings of which two are used for inlet and purging of the nitrogen gas and one is used for the pressure transducer and the temperature probe. Both the pressure transducer and the temperature probe are used within the control logic to ensure the desired conditions are achieved within the cell before spray imaging commences. The top face is used to mount the injector within the cell so that the spray is orientated from top to bottom as would be found in a conventional engine (see Figure 4.12).



**Figure 4.12: Sectional view and photograph of HPHT cell**

Nitrogen is used in the cell instead of air to prevent oxidation and hence ignition of the fuel. At room temperatures Nitrogen exists as a diatomic molecule ( $N_2$ ), and the trivalent bond between the Nitrogen atoms is exceptionally strong, resulting in large amounts of energy being required to convert Nitrogen into other compounds. For this reason, Nitrogen is classed as inert and serves to ensure the fuel will not combust in this application.

Wilkie [114] highlighted a problem with the original design of the injector housing with regards to the positioning of the injector in the optical chamber when considering the capturing of an image. As seen in Figure 4.13 the initial portion of the spray was difficult to see as the tip of the injector does not penetrate far enough into the optical chamber. This results in a proportion of the spray not being within the lit background when the picture is taken. As the injector was not properly in view, the camera had to be angled to capture the entirety of the spray. This meant that there are different backgrounds present along the distribution of the spray resulting in an incomplete analysis. From this it was concluded that a design allowing the injector to sit further into the chamber would be beneficial, producing clearer images allowing better analysis of the spray structure and the activity along the entire spray boundary.



**Figure 4.13: CCD and colour scaled images of a pressure swirl injector from existing design of HPHT cell <sup>[114]</sup>**

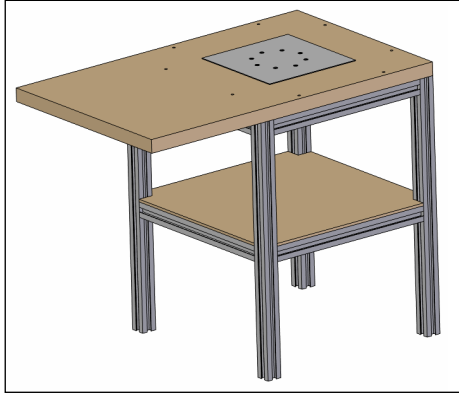
For this investigation multi-stream injectors from Continental AG. were used which required a new design for the injector housing due to the different geometries of the injectors. The positioning of the injector further into the chamber has therefore been taken into consideration.

### ***Construction of rig***

Up until 2005 testing with the HPHT Cell had made use of an existing atmospheric flow rig. Although a fairly easy rig to adapt to incorporate the HPHT cell, it meant that the atmospheric flow rig was out of use whilst the HPHT cell was in situ. It was therefore suggested that a rig for the HPHT cell would be beneficial for long-term future testing to enable testing of both the HPHT cell and the atmospheric rig to be carried out side by side.

A simple table frame was made from extruded aluminium with pieces of medium density fibreboard (MDF) for top and shelf. Holes were drilled in the table top for the location of the HPHT cell to ensure differences between capturing of images were minimised. A three dimensional model can be seen in. Figure 4.14.

As the HPHT cell would reach temperatures of 100°C it was felt that it would be sensible to create a heat shield between the HPHT cell and the MDF tabletop, this consists of a square sheet of aluminium with holes drilled in the same orientation of those on the table top for the location of the HPHT cell.

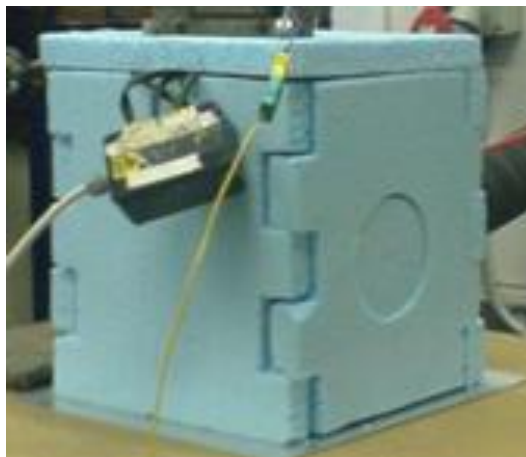


**Figure 4.14: Table design**

The camera stand was placed on a 'rail' design enabling movement to cater for different focal lengths and types of images.

### ***Insulation***

Initial attempts to heat the HPHT cell, using 250Watt cartridge heaters, highlighted the need for insulation from severe heat loss to the surroundings. Insulation of the HPHT cell also lowers the potential hazard of burns by minimising the exposed faces. As access to clean the HPHT cell is required, it was necessary to incorporate easy access into the design of the insulation. For this reason a simple box like structure was considered, using a 'jigsaw' approach to the design to minimise the effort in repeated construction. The material used was insulation foam which was readily available and considered to be capable of the task required. Two circular viewing windows were cut to allow the majority of the insulation to stay in place throughout the imaging procedure enabling the HPHT cell to be held at a more stable temperature.

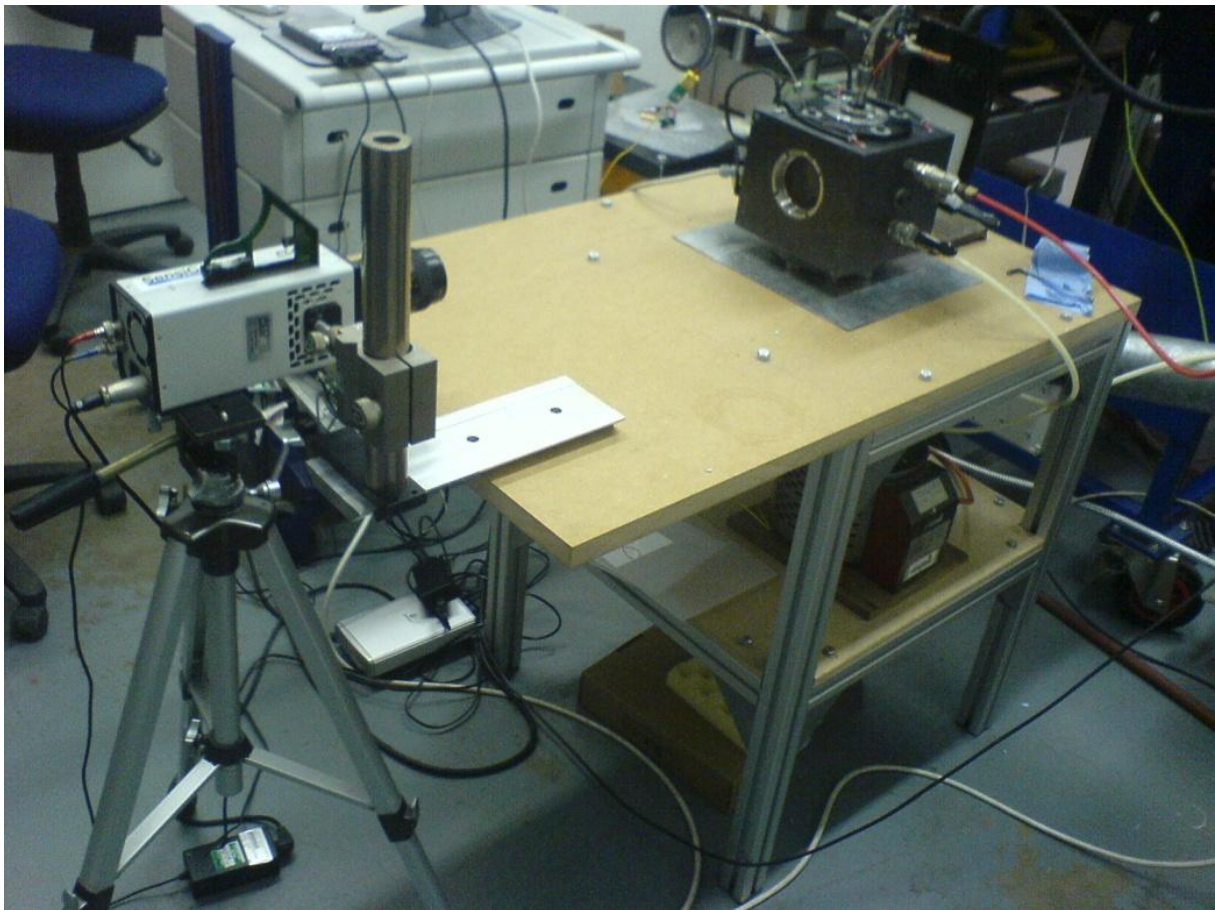


**Figure 4.15: Insulation of HPHT cell**

### *Preliminary testing*

A test over the full range of pressures to be tested was carried out. This immediately highlighted an air leak from the HPHT cell, which resulted in the purchase of a new O-ring to provide a better seal between the base of the injector housing assembly and the body of the HPHT cell itself. Once the HPHT cell was able to maintain levels of pressure over a prolonged period of time, it was considered a sealed compartment.

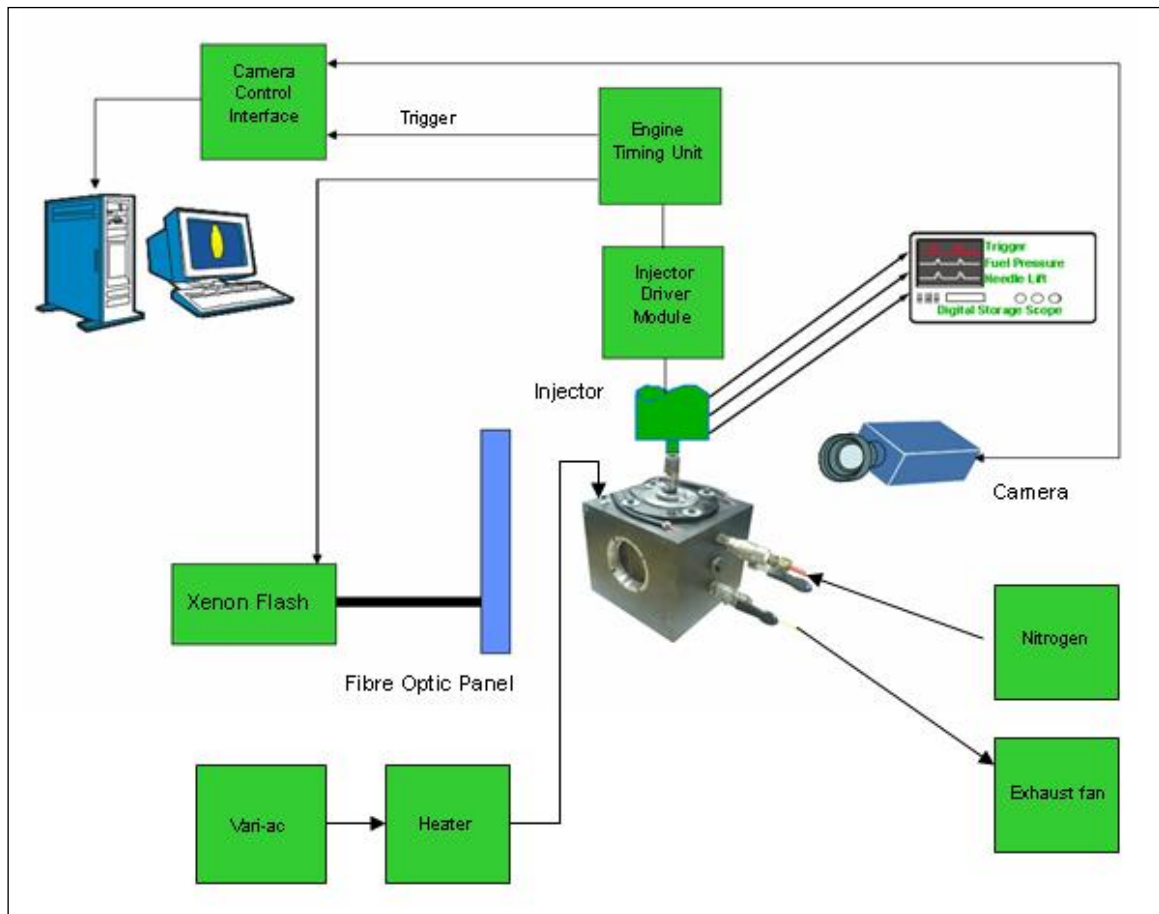
The test run also showed that there was variation in position of the camera over a period of time. To try and keep the camera from moving, a tripod was used in addition to the mount on the table to improve stability which seemed to work fairly effectively. To err on the side of caution, background images were taken for every change in temperature or pressure to insure that the analysis of images at a later date would be as accurate as possible.



**Figure 4.16: Photograph of initial HPHT cell experimental set-up**

## Chapter 4 - Experimental Techniques and Facilities

A schematic of the equipment used is seen in Figure 4.17 and a detailed list of the equipment used follows.



**Figure 4.17: Schematic of HPHT cell equipment**

- CCD camera with 55mm Nikon Lens
- Xenon flash unit in backlit spray imaging arrangement
- Continental AG multi-stream injector
- Continental AG injector driver and power supply
- Extraction rig
- Delayed pulse generator (timing unit)
- PC running “Camware” software and “PCO Viewer”
- Vari-ac, cartridge heaters and Thermocouple
- Nitrogen cylinder and regulator

## Chapter 4 - Experimental Techniques and Facilities

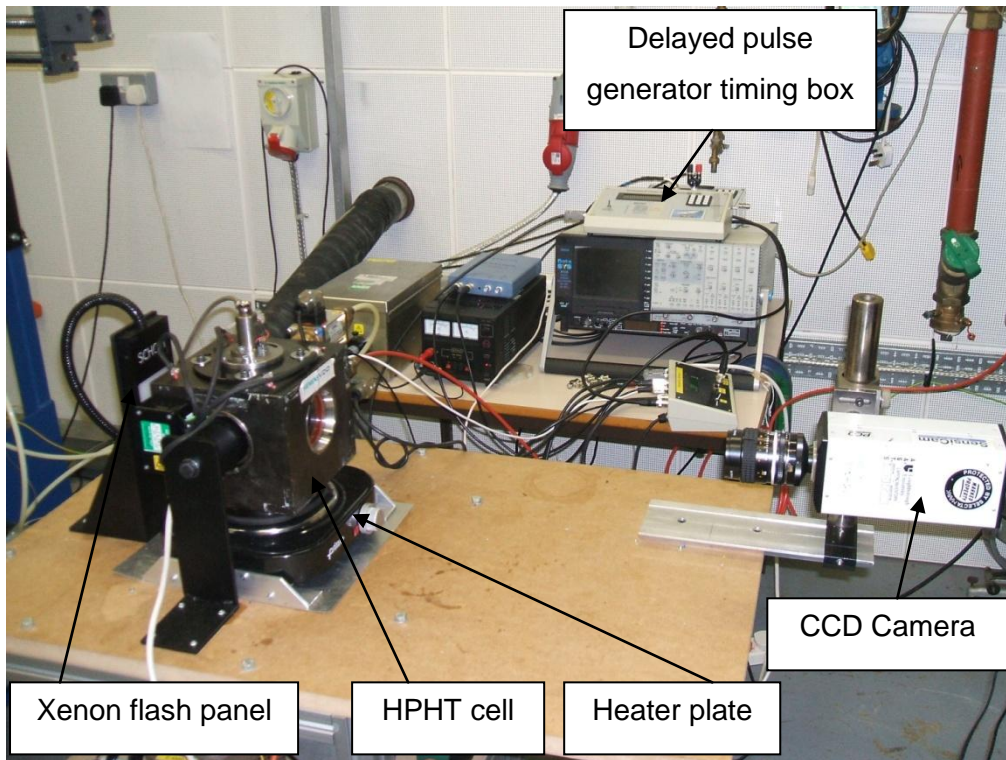
---

After a first measurement campaign, aimed at studying the injector atomisation performance difference when using gasoline and iso-octane, a number of improvements were made to the HPHT cell and the manner in which it is operated. It was identified that the process of taking images and controlling the inlet and purge valves with one person was difficult. To rectify this it was decided to make the HPHT cell operation more automated by using electronically controlled inlet and purge valves. To control the valves, a new control box was designed to be used in conjunction with the original departmental delayed pulse generator timing box. The two boxes would be used to control all the elements of the experimental set up. Another improvement to the test equipment was the addition of in-cell pressure and temperature measurements. A temperature probe was inserted into a drilling in the HPHT cell to take in-cell temperature measurements. A pressure transducer was mounted nearby to obtain in-cell pressure measurements. In previous tests the Nitrogen bottle manometer was used to provide cell pressure data and a thermocouple fixed to the body of the cell used as an approximation for the in-cell charge temperature. The new pressure and temperature readings were viewed on the PC in real time, using a PicoScope acquisition box and software, and provided a good indication of the actual in-cell conditions.

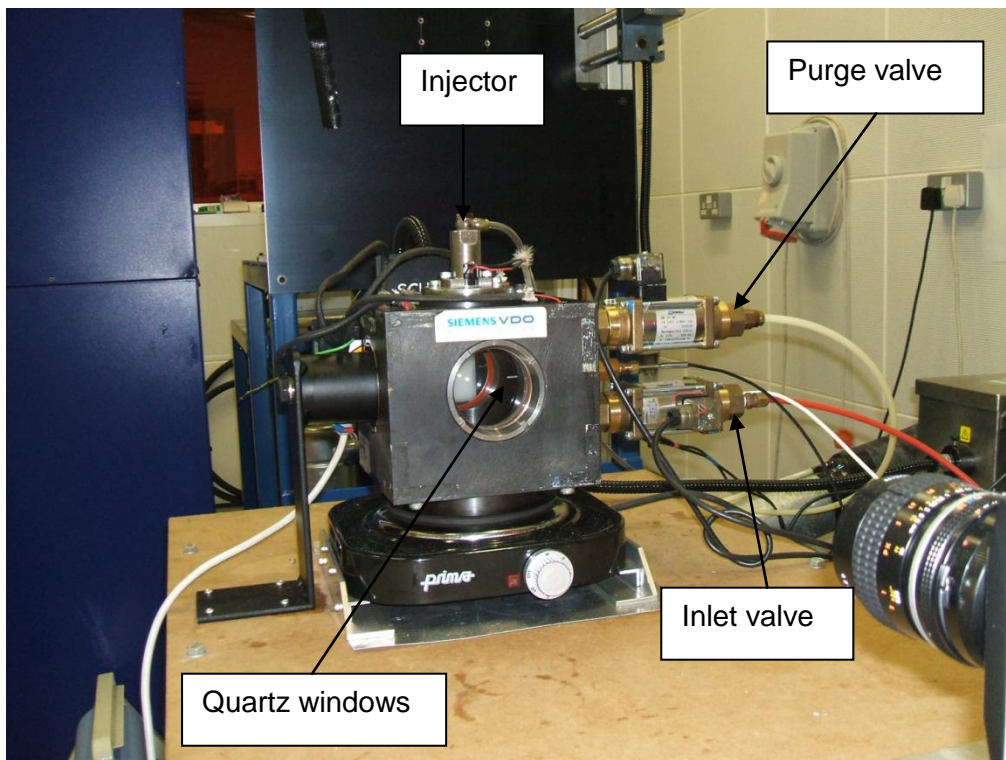
A new 3kW heater plate (electric cooking plate) was also installed which massively reduced the time taken to heat the cell. Using the previous heating elements (four cartridge heaters placed in each corner of the cell with a maximum rating of 110W each), heating the cell to 100°C took over 7 hours, but using the new heater plate this temperature can be reached within minutes. During operation at higher temperatures the cell is enclosed in insulation foam to reduce heat loss to the surroundings and help maintain a more stable in-cell temperature.

The injection frequency was set to 1Hz. When fuel is injected into the cell, the spray disturbs the air within the cell, therefore a 1Hz injection frequency would ensure sufficient time was given to allow the charge to become almost quiescent. An injection frequency of 1Hz also ensured that previous injections did not interfere with the injections following.

The spray was illuminated by a EG&G MVS 7020 Xenon flash unit (8 $\mu$ s flash duration) which was connected to a Fostec fibre optic flash panel which was 3x3inches in size and was placed behind the cell to illuminate the spray from behind. Photographs showing the modified HPHT cell experimental set-up are presented in Figure 4.18 and Figure 4.19.



**Figure 4.18: Modified HPHT cell experimental set-up**

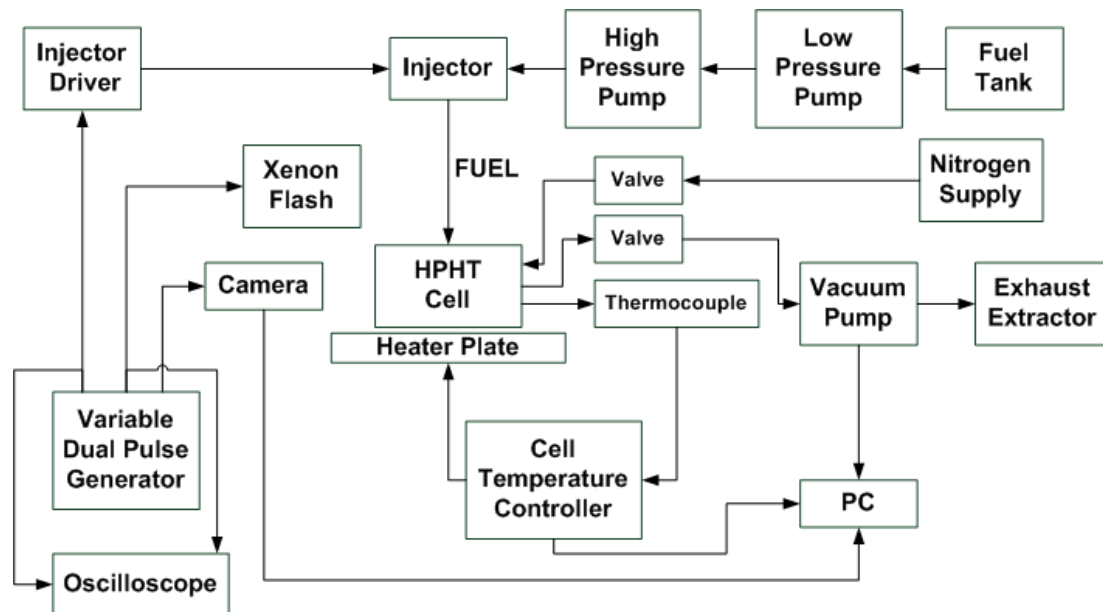


**Figure 4.19: Close up view of the modified HPHT Cell**



## Chapter 4 - Experimental Techniques and Facilities

The experimental work required control of temperature and pressure in the HPHT cell and accurate timing of the injector signal, flash panel and CCD camera. The equipment needed for this is illustrated in Figure 4.20



**Figure 4.20: HPHT cell equipment schematic**

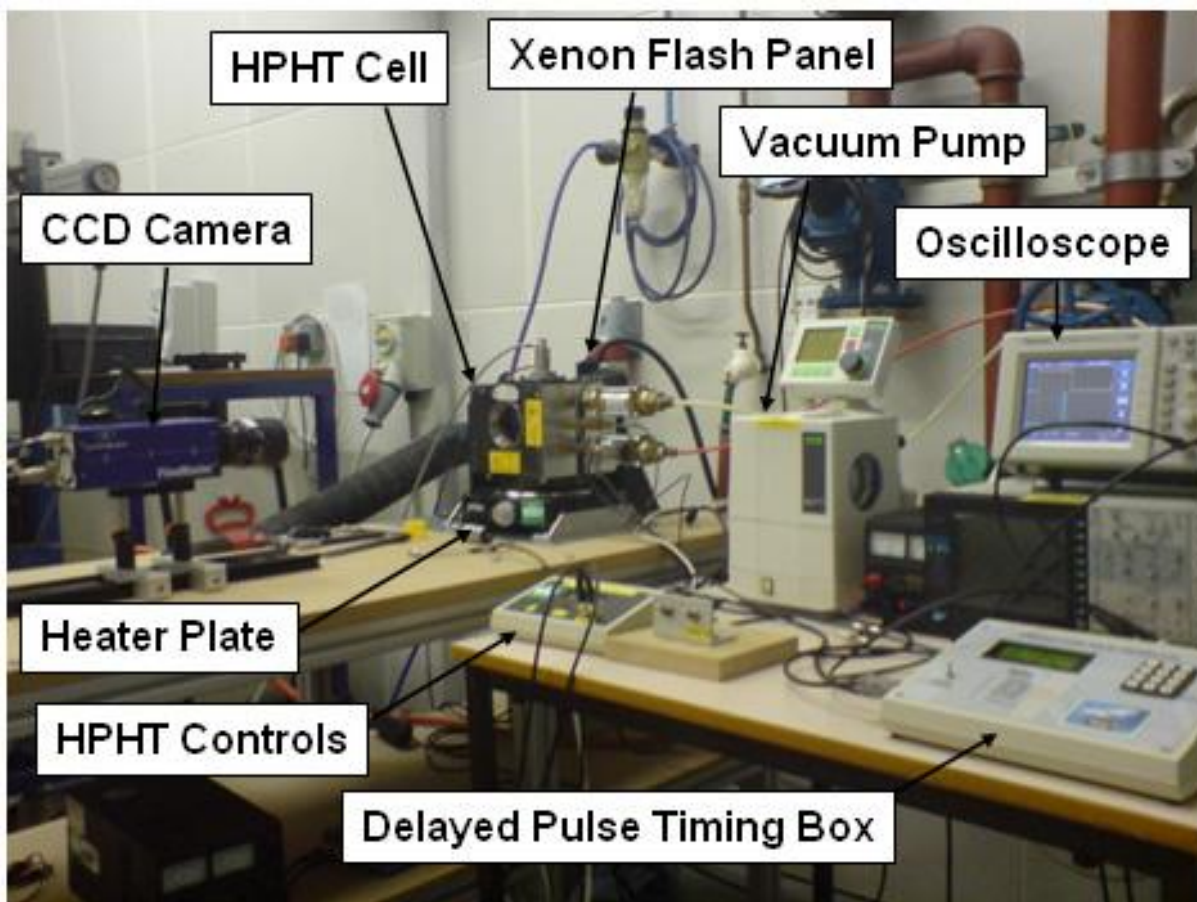
In a final version of the HPHT cell setup a Buschi vacuum pump was used to generate sub-atmospheric pressure to the required level inside the cell. This was controlled using the integral digital display on the top of the pump. The heater plate controlling the temperature of the cell and given the relative mass of the cell itself, the fuel in the injector was assumed to be at the same temperature as the cell due to conduction being the main heat transfer phenomenon. The thermocouple (PT100) measures the temperature of the gas in the cell and displays this information on the HPHT control interface, which is also used to set the required temperature by sending a signal to the heater plate. Fuel is sprayed into the cell through the Continental AG injector at a pressure controlled by the adjustable pressure fuel pump (Siemens) described earlier in the atmospheric bench setup. There are two fuel pumps, one is a low pressure pump mounted inside the fuel tank which supplies fuel at 3.5bar to an external high pressure pump which can operate at up to 200bar. The delayed pulse timing box is used to control the pulse width of the injection signal and the timing of the xenon flash panel and CCD camera relative to the start of the injection signal. This allows images to be captured at different stages of fuel spray development. The collected images are displayed on a PC running CamWare software, which saves the images for post-processing.

## Chapter 4 - Experimental Techniques and Facilities

---

A photograph of the final version of the setup is shown in Figure 4.21, with a detailed view of the HPHT cell in Figure 4.22.

The fuel injector is positioned at the top of the cell, firing directly downwards. A schematic of the injector orientation is shown in Figure 4.23. It can be seen that although the injector has six holes, only three spray streams are seen because of superposition of the streams on top of one another. Also, the measured cone angle is not the actual cone angle, as the two outer streams seen do not lie in the focal plane. This is not a problem as measuring these angles still demonstrates the trends related to fuel and injector geometry effects.



*Figure 4.21: HPHT equipment layout*

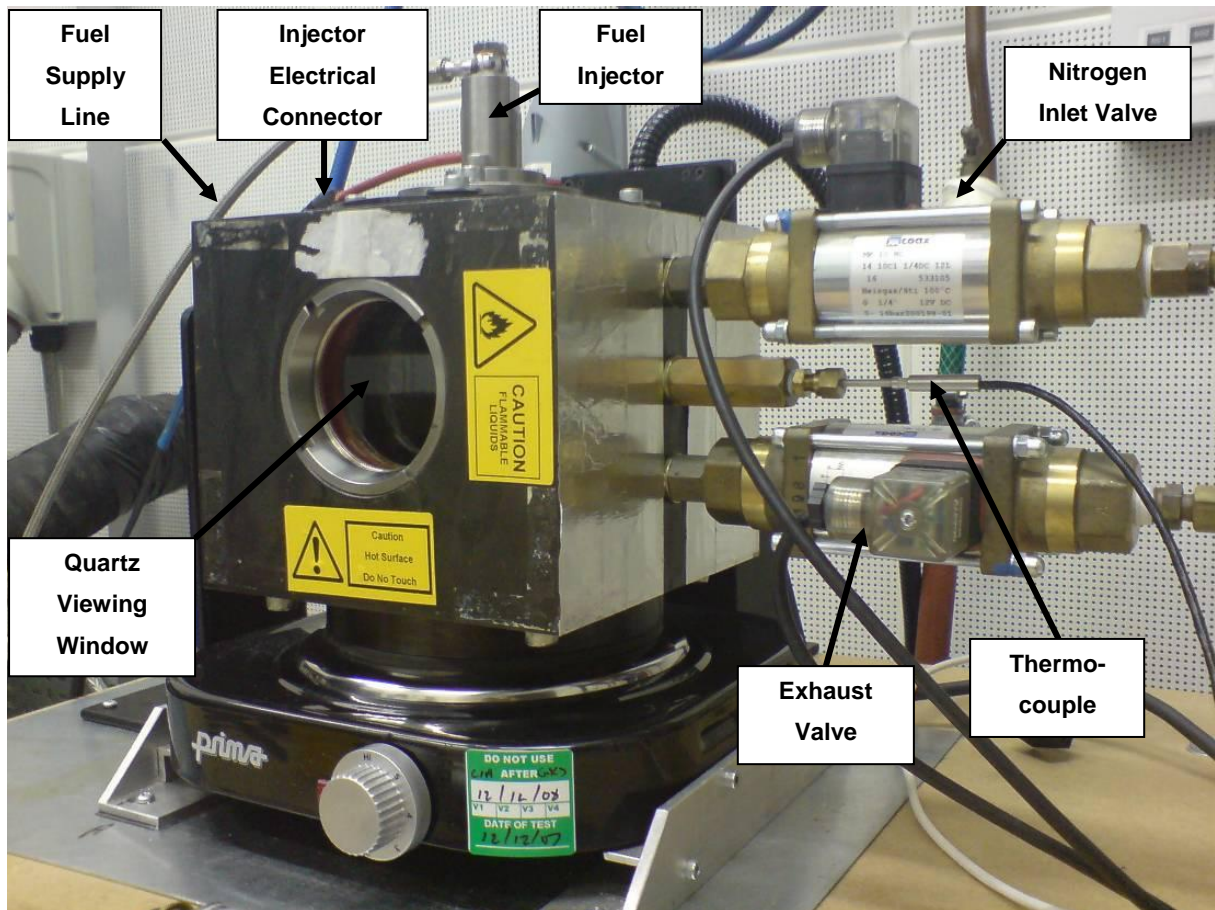


Figure 4.22: Close-up of HPHT cell

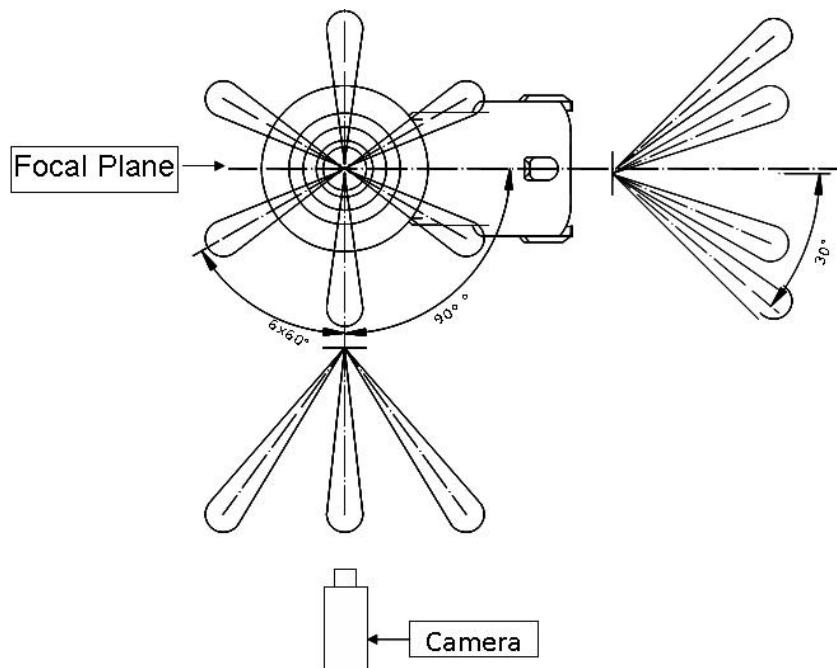


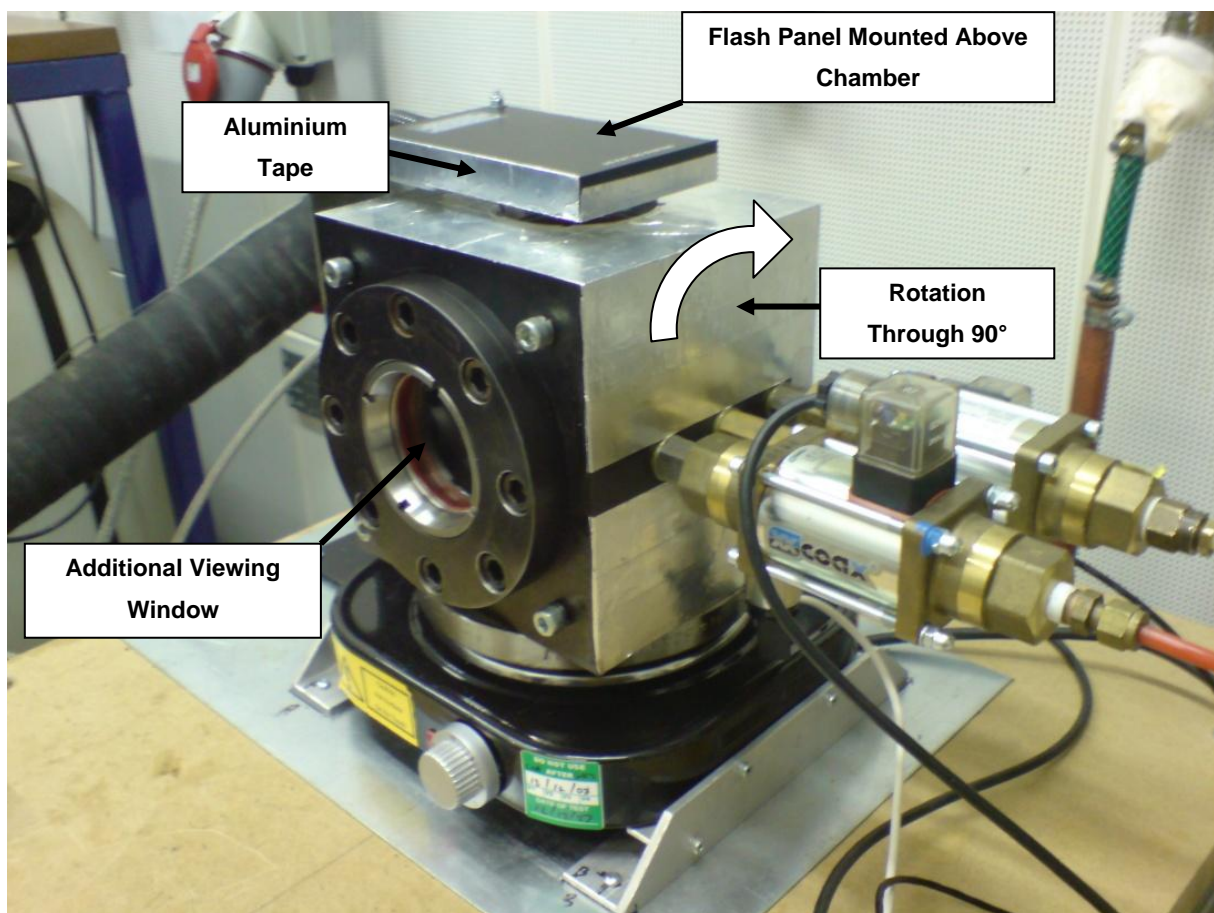
Figure 4.23: Injector orientation schematic

## Chapter 4 - Experimental Techniques and Facilities

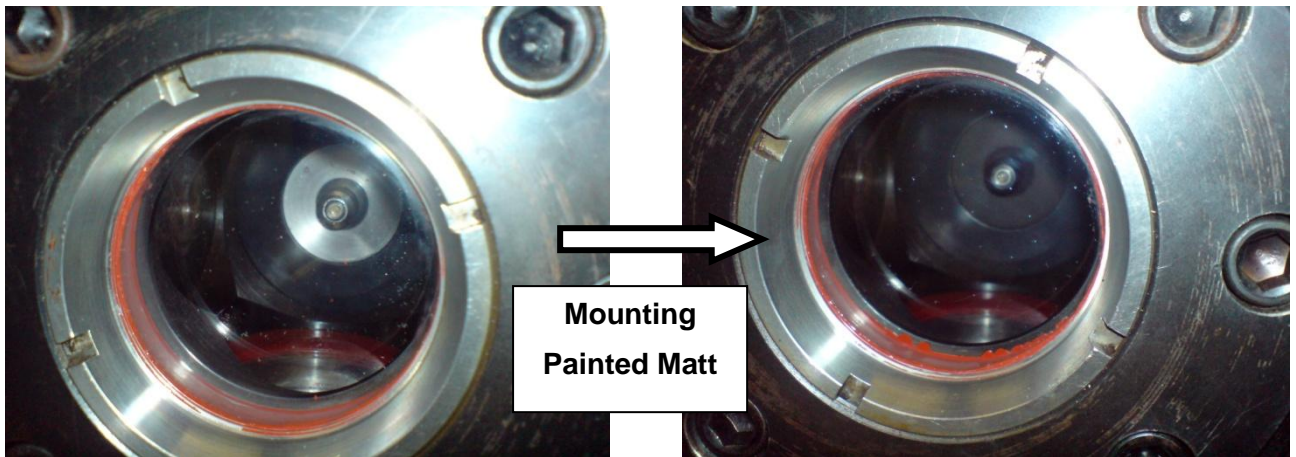
During the measurement campaign performed at sub-atmospheric pressures, it was decided that capturing images of the side of the spray was inadequate for fully characterising the effects of flash boiling. It could be seen that the individual spray fingers collapsed inwards but these images did not show the radial spray distribution. Therefore, the following modifications were made so that images could be taken from underneath the injector.

- HPHT cell rotated through  $90^\circ$  so that the injector was opposite the camera.
- Addition of an extra viewing window to allow camera access to the spray.
- Repositioning of the xenon flash panel above the cell to allow illumination of the spray.
- Aluminium tape added to outside of HPHT cell to improve light reflection into chamber.
- Injector mounting painted matt black with special high-temperature exhaust paint to reduce glare from reflected light.

These modifications are shown in Figure 4.24 and Figure 4.25.

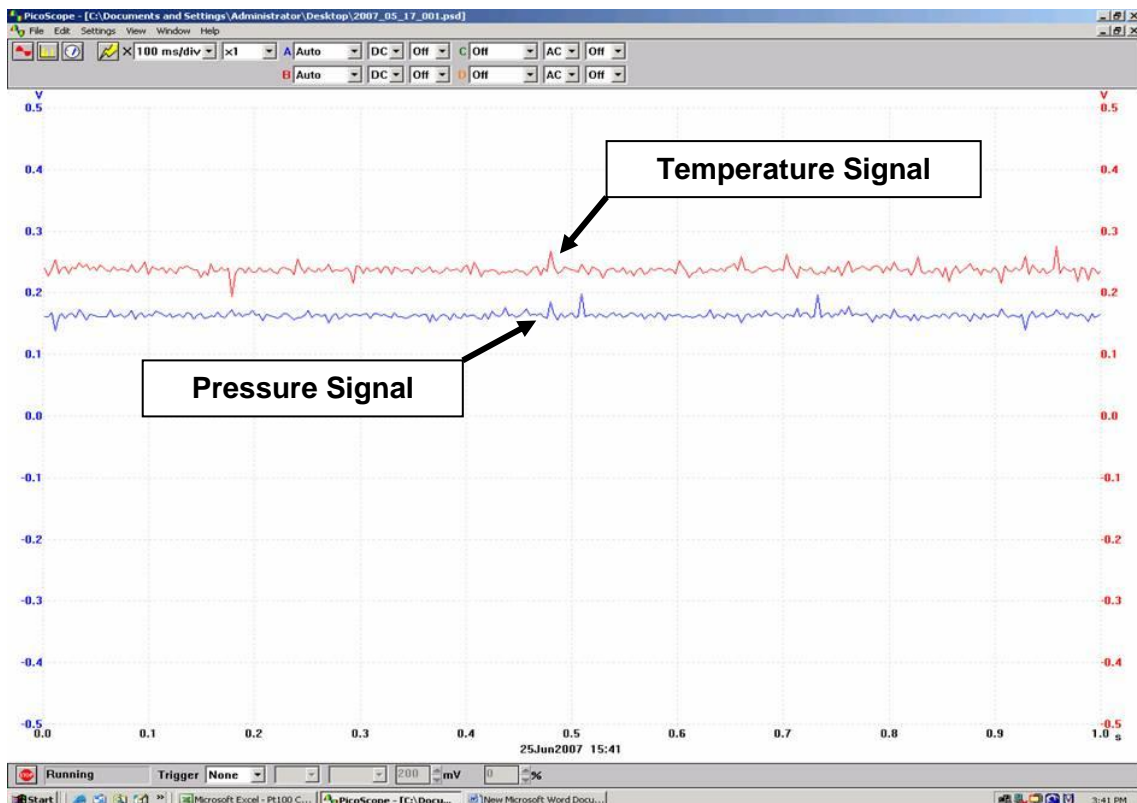


**Figure 4.24: HPHT cell modifications**



**Figure 4.25: Injector mounting modification**

Once these modifications had been made it was necessary to check the cell for any leaks, particularly around the new viewing window and the valves as these had all been modified. This was done by pressurising the cell with nitrogen, then checking for a drop in pressure with the PicoScope, a screenshot of which is shown in Figure 4.26. PicoScope is software on the PC which allows measurement of cell temperature and pressure through a connection with the temperature probe and the pressure transducer. This check was carried out whenever modifications were made to any part of the cell which could affect its sealing capability.

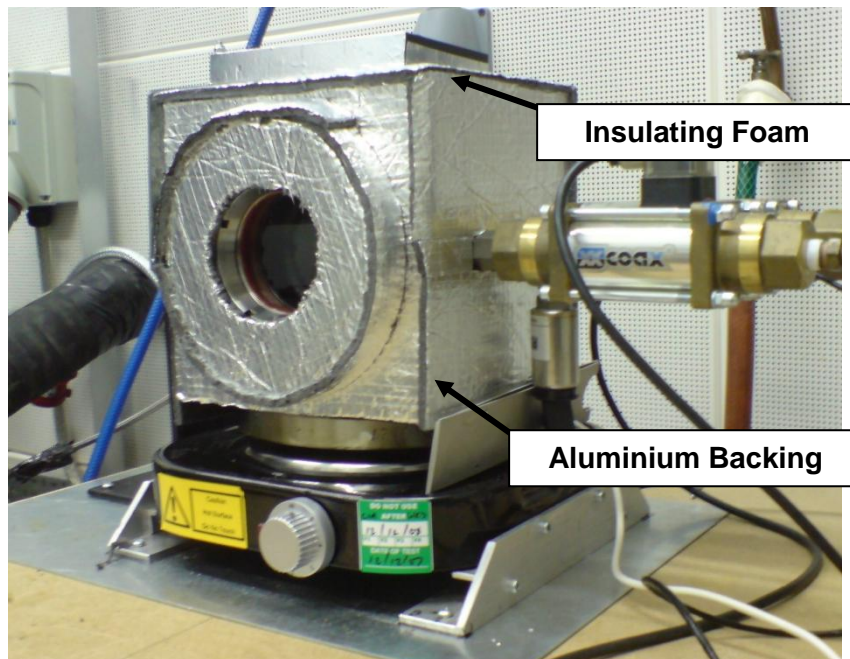


**Figure 4.26: PicoScope screenshot**

## Chapter 4 - Experimental Techniques and Facilities

---

Heating the HPHT cell to 80°C or above was problematic as a high percentage of heat was lost through the cell walls. This was inefficient as a lot of time was spent waiting for the cell to warm up instead of actually carrying out tests. To solve this problem, insulating foam with an aluminium backing was purchased from Foam Techniques Ltd. and attached to the outside of the cell. This is shown in Figure 4.27. The insulating foam significantly reduced the heat loss from the cell and resulted in less time being spent waiting for the cell to achieve the desired temperature.



**Figure 4.27: Addition of insulating foam**

**Experimental procedure** was as follows:

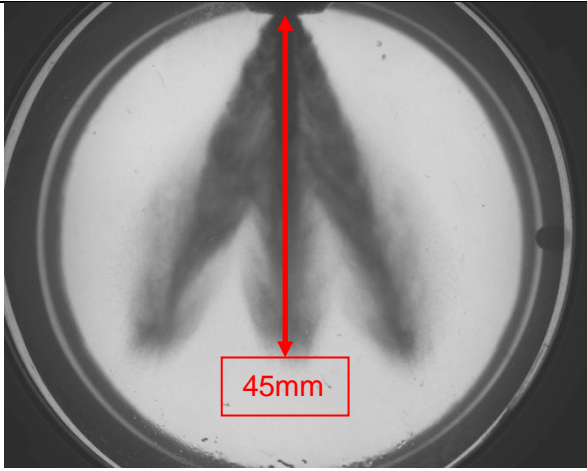
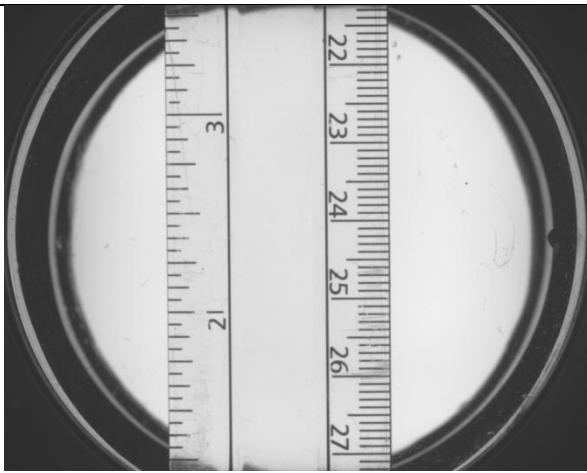
- Set HPHT temperature set point using the control interface.
- Once the temperature has been reached, switch on both the low and high pressure fuel pumps and check the pressures. Adjust these if necessary.
- Set the required flash and camera timing on the delayed pulse timing box. Also set it to give 10 injection pulses.
- Set up the CamWare software to capture 15 images. This will only capture images each time the flash panel flashes and will capture 10 spray images and 5 blank images which can be used as background images if needed.
- Set the required ambient pressure on the vacuum pump.
- Once the required ambient pressure is achieved, switch on the flash panel and injector driver, the images will be displayed on the CamWare software as they are collected.
- After 15 flashes, switch off the flash panel and injector driver.
- Stop the vacuum pump and allow the cell pressure to return to atmospheric.
- Save the images onto the computer's hard-drive.
- Open the exhaust valve and purge the cell with nitrogen.
- Repeat for the next pressure set point.

## Chapter 4 - Experimental Techniques and Facilities

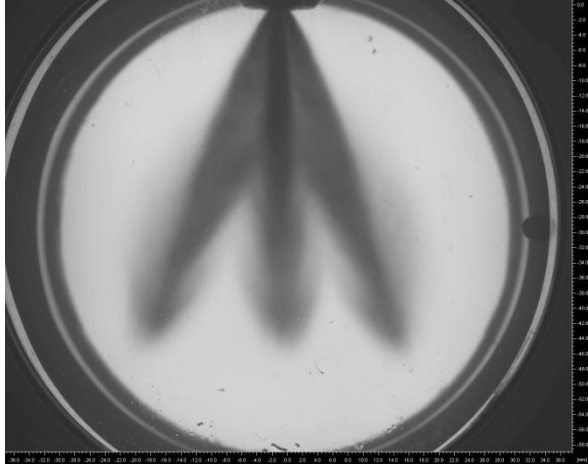
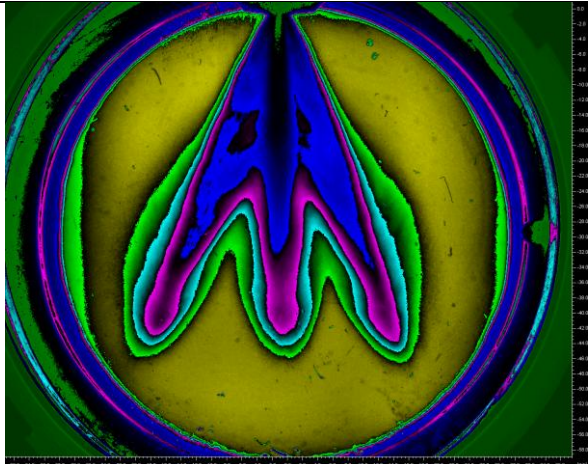
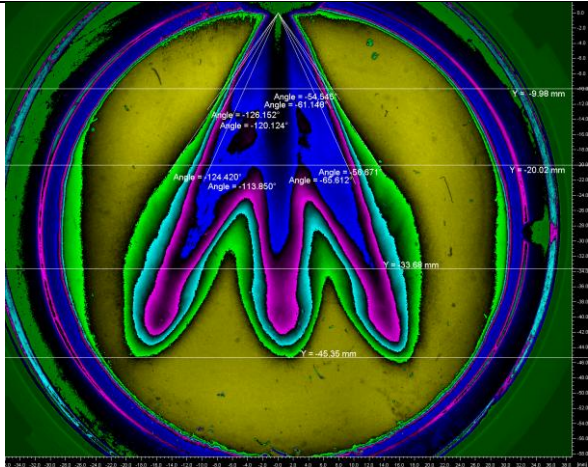
Occasionally it was necessary to take the top off the HPHT cell to allow cleaning of the inside of the window as fuel collects here and causes interference with the images. This was a particular problem at low ambient pressures and lower fuel temperatures as more fuel is impacting the viewing windows.

### Data Analysis

Once the raw images have been recorded by CamWare, they are processed using PCO PictureViewer. This software is specifically designed for processing spray images taken using CamWare and has several features which enable useful data to be extracted.

Raw image	The raw spray image recorded by CamWare is loaded.	 A circular spray image showing a dark, V-shaped spray pattern against a lighter background. A red double-headed vertical arrow is positioned in the center of the spray, with a red box below it containing the text "45mm".
Apply scale	An image is taken of a ruler in the same position as the injector. When this image is loaded it is used to apply a scale to all the images so that accurate spray penetration measurements can be made.	 A circular image showing a ruler placed vertically in the center. The ruler has markings in millimeters and centimeters, with numbers 21, 22, 23, 24, 25, 26, and 27 visible on the right side.

## Chapter 4 - Experimental Techniques and Facilities

<p>Average images</p>	<p>All 10 images at each test point are loaded in and the program automatically applies the scale. The mean of these images can then be calculated in order to enhance the main body of the spray and clarify the spray edges. A check should be made of each individual image before this is done.</p>	
<p>Colour manipulation</p>	<p>The grayscale mean image can then be modified using a variety of different colour scales to make the different intensity levels clearer and allow image analysis. Selection of the colour scale used depends on the parameter to be measured and the spray itself.</p>	
<p>Measurements</p>	<p>The angle between two points, vertical and horizontal distances can be measured and displayed on the image.</p>	

It is also possible to take an image of the injector with no spray which can be used as a background image and subtracted from each spray image so that only the spray remains against a uniform background. However, most of the time the spray was found to be clearly defined without subtracting the background so this was not always necessary.

Once all the necessary measurements have been collected they can be entered into a spreadsheet to allow comparisons to be made.

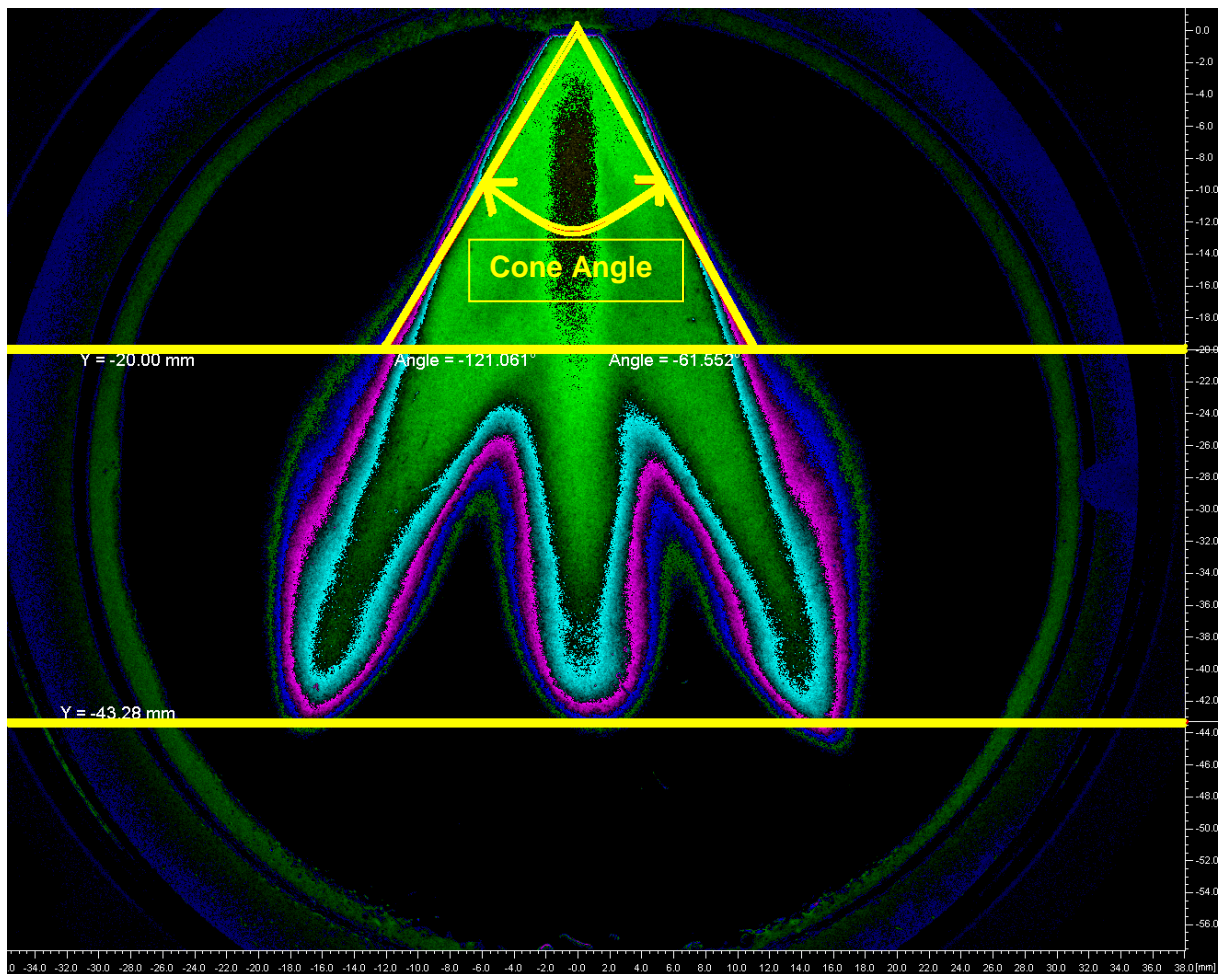


The same procedure is used for processing the images taken from underneath the spray, however, no geometric measurements were made as the scale and focus would vary through the depth of the spray. This is because the cone angle can already be measured from the side-view images and these images only show useful qualitative information.

### Macroscopic Characteristics

#### **Cone Angle**

Cone angle (CA) or spray angle is defined as the angle of the fully developed fuel spray. An example of cone angle for a multi-hole injector is shown in Figure 4.28. The raw greyscale image has been averaged and modified to show light intensity contours which represent spray density contours as these are much easier for the human eye to resolve than the raw image.



**Figure 4.28: Cone angle at 20mm downstream for a 60°CA multi-hole injector  
2ms ASOS**

There are many difficulties in measuring cone angle as even when the spray is fully developed, the angle is not constant for the whole spray. Some measurement techniques involve fitting a quadratic to the edge of the cone [111], whilst some rely on measuring the angle at a certain distance from the spray nozzle. Injector manufacturers all have their own in-house criteria for cone-angle measurement and, because of this, there is no standard measurement technique. Therefore, it is not possible to compare sprays from different manufacturers by simply using their quoted data. When comparing different sprays it is vital to decide on a definition of cone angle and use this for all measurements to allow meaningful comparisons to be made. For the experimental work in this project it has been decided that in order to accurately describe the complex shape of the spray, several measurements are needed. At 1.7ms after the start of injection, the angle is measured at 7.5mm and 15mm downstream of the injector tip, for the light intensity contour representing 50% spray density. At 2.0ms after start of injection the angle is measured at 10 and 20mm downstream of the injector tip, using the same light intensity contour. Cone angle is important as it defines the likelihood of the spray to impinge upon the cylinder walls, which is a major source of unburned HC emissions and also causes problems with dilution of engine oil.

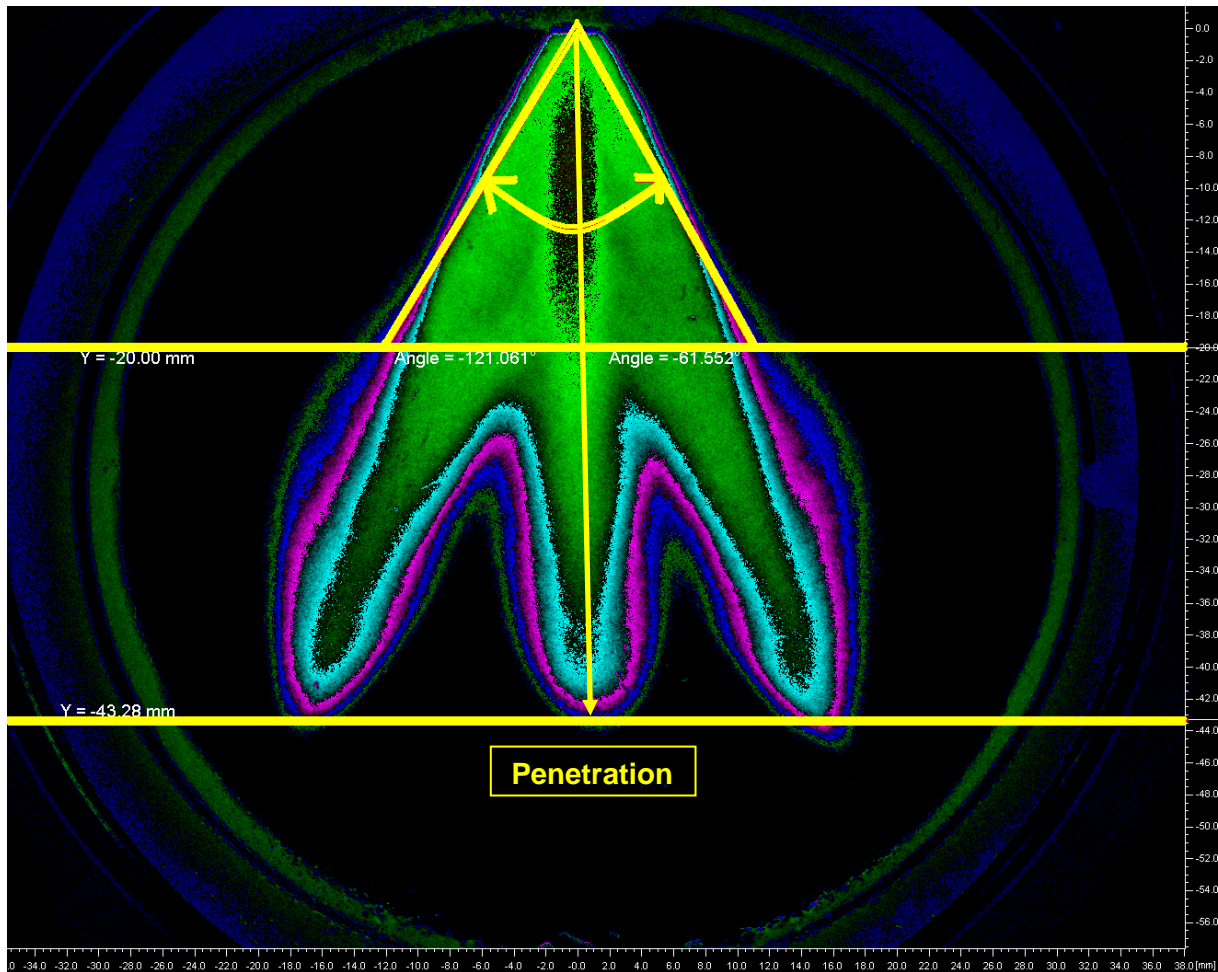
A balance must be struck between a cone angle which is wide enough to utilise as much air as possible, thus allowing maximum torque generation, whilst avoiding wall impingement.

### ***Tip Penetration***

Tip penetration is the distance which the leading edge of the spray has travelled at a given time. The tip penetration for the same multi-hole injector is shown in Figure 4.29.

Similar to cone angle, there is no standard for either the time after injection at which the penetration is measured or the intensity contour used to define the tip. Previous research [111] has used the intensity contour relating to 85% maximum density, however due to the different spray characteristics caused by flash boiling this was not suitable for the current study. Therefore the intensity contour representing 50% spray density was used.

Tip penetration is of great importance when designing injectors for stratified charge operation, as if the penetration is too great then spray will impinge on the piston crown, increasing HC emissions and diluting the engine oil. It also has an effect on cylinder wall wetting as a larger penetration gives more distance for the spray cone to spread out and impinge on the cylinder walls.



**Figure 4.29: Spray tip penetration for a 60°CA multi-hole injector – 2ms ASOS**

### **5. Preliminary Study: Spray Targeting Tool**

#### ***5.1 Introduction***

With the increasing use and the development of the second generation multi-stream GDI injectors, an important number of customers and engineers' demands concern the targeting of the spray inside the combustion chamber [115].

Few years ago, for the first generation pressure swirl GDI injectors, a simplified approach, as proposed later in this section, was not efficient. The fuel injection speed was moderate (around 50 m/s) and the strategy for targeting was complex with a strong interaction between the internal flow and the aerodynamics of the combustion chamber (air guided combustion) or the piston shape (wall guided combustion), so it was not possible to simulate the spray in the combustion chamber without performing 3D computational fluid dynamic (CFD), which was time-consuming, difficult and inaccurate concerning the validity of the results. An alternative to get a first idea of the spray targeting was to use a simple drawing software and to place conical shapes representing the sprays inside the combustion chamber. But this alternative was a rough approximation and could only be dedicated to the study of a single engine operating point.

For the second generation GDI injectors (multi-stream injector, piezo injector), the fuel injection speed is now higher (between 100m/s and 200m/s) and the spray is denser, so the influence of the combustion chamber aerodynamic is reduced. It is then possible to use a simplified approach for spray targeting based on negligible spray/air interactions and purely geometrical considerations of the sprays as a function of engine crank angle.

On the one hand, this simplified approach is faster than the CFD and on the other hand, the number of parameters that can vary simultaneously is more important, as for example:

- Injector position and holes orientation (multi-stream injector)
- Multiple injections
- Variable Valve Timing (VVT) more commonly used in modern engines
- Turbocharging more frequent, especially for downsizing.

## Chapter 5 - Preliminary Study: Spray Targeting Tool

---

The aim of this spray targeting tool is to determine the percentage of fuel quantity impacting:

- The Piston
- The Cylinder
- The Intake Valves
- The Spark Plug

for different injection parameters and engine speeds. Once these percentages of impact are obtained, the optimum injector geometry and engine injection strategy can be defined in order to obtain the best combustion and engine efficiency for a minimum pollution, to guarantee the mixture formation in both homogeneous and stratified mode, to reduce HC, CO and NO<sub>x</sub> emissions and to limit the impact of the spray on the cylinder walls (HC and Soot emissions), the piston, the intake valves and the spark plug

A large part of the soot emissions is due to the impact of the fuel on the cylinder walls [116], the aim is to minimise these impacts, and first of all, avoid any impact of the fuel on the intake valves, which generates a very negative effect on the combustion by affecting the air/fuel mixture inside the combustion chamber.

A simple Matlab program written (under Matlab Release 13) by Jean-Luc Fremaux [115] and Dr Jérôme Hélié from Continental AG in Toulouse is presented here. Basically this numerical tool simulates a spray shape inside the combustion chamber to evaluate the possible impacts using the geometrical data of the chamber, the intake valve lift profiles and the spray penetration and cone angle data obtained as detailed in chapter 4.

### ***5.2 Previous Spray Impact Tool***

A first try, using a simple Excel model, to simulate the targeting of the spray on the piston was previously performed. In this first model, the impact position was determined using a linear interpolation to obtain the spray position for the whole injection event, but the proportion of the spray impacting the piston was not calculated. This model did not simulate the impacts on the cylinder, valves and spark plug.

### **5.3 Hypothesis**

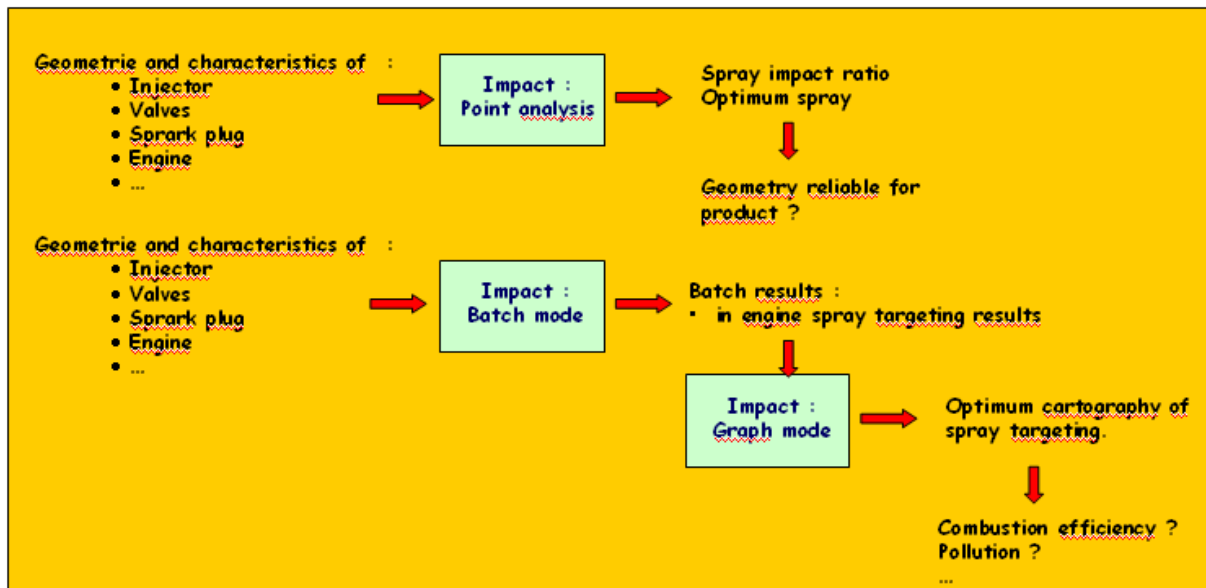
As mentioned previously, this simplified approach for spray targeting was based, at least for the first version of the program (some modifications have been added in the latest versions of the program), purely on geometrical considerations. It means that the physics of the spray is not taken into account, the temperature of the spray and the combustion chamber are assumed to be constant and the phenomenon of fuel evaporation is not considered.

### **5.4 IMPACT Tool**

The purpose of this program is to simulate the piston, valves and spray motion during an injection period, and determine the impacts with the spray. A graphic user interface allows a simpler use of the program. Only the first two versions of the code (IMPACT 1 and IMPACT 2) are presented in this section.

The first step of the program is to choose the operation mode from the three different functioning modes available:

- **Point analysis mode** concerns a single engine operating point illustrated graphically in time and space by the spray position inside the engine cylinder. An optimum spray position can be obtained from this mode (but the application of this configuration to actual engine operating conditions has to be validated experimentally with an optical engine).
- **Batch mode** (see appendix C) offers a multi-parameter variation allowing to explore a given engine mapping. An optimum spray targeting can be deduced which will help to minimise HC, CO and NOx emissions
- **Graph mode** (see appendix C) that allows the user to visualise the batch mode results. A graphic interface represents the spray impacts computed in the batch mode.



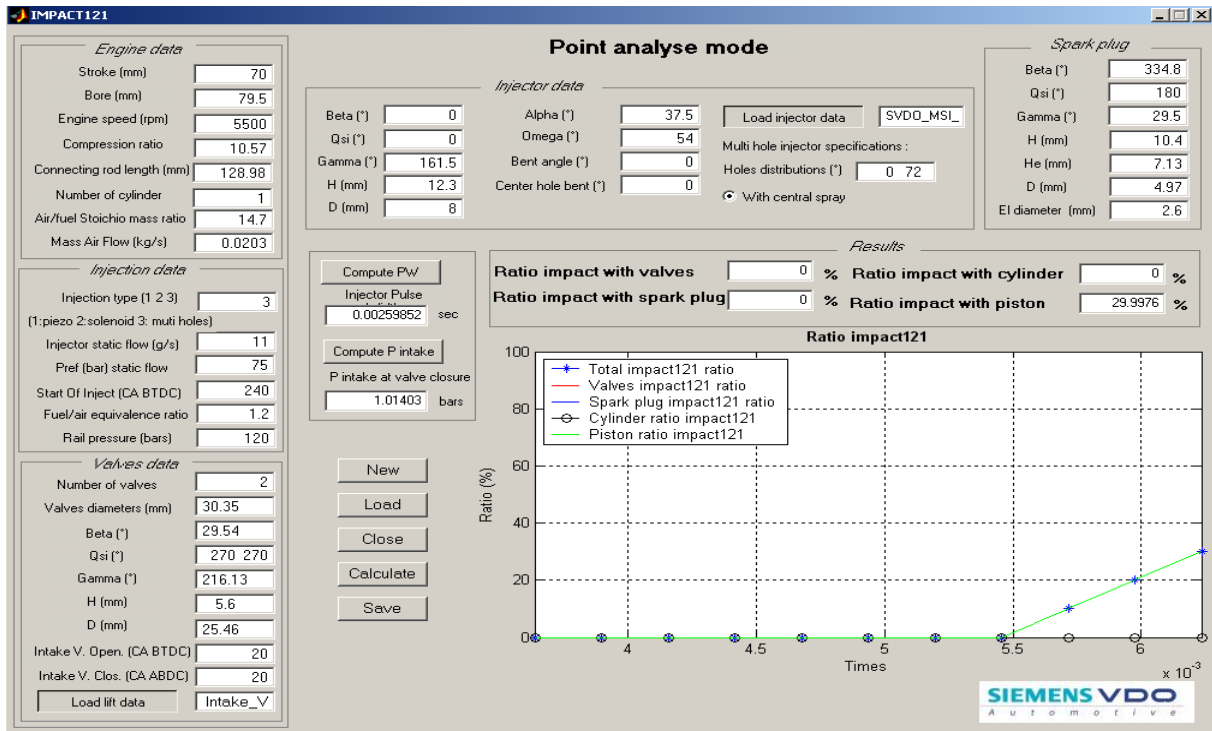
**Figure 5.1: IMPACT tool presentation**

### Point analysis mode:

The Point analysis concerns a single engine operating point illustrated graphically in time and space. All the engine geometry, valve timing and injection parameters can be modified to optimise the results. The following graphic user interface (see Figure 5.2) is prompted when the user chooses the point analysis mode. The user enters all data concerning the engine and injection data and then loads a text file containing the valve lift function of the crank angle degrees.

Two graphic windows are plotted at the end of the computation:

The first one, the result window (Figure 5.2), displays the impact ratios and a graph representing the impact ratio on the cylinder, valves, piston and spark plug versus the injection period.



**Figure 5.2: Point analysis mode graphic user interface**

In this graphic user interface, the user defines the geometrical data concerning:

- **Engine data:** Stroke, bore, (engine speed, compression ratio, connecting rod length, number of cylinders, AFR, mass air flow (MAF)
- **Injector data:** Geometrical positioning, injector type, hole distribution in case of a multi-stream injector, bent angle, static flow rate, injection pressure, fuel/air equivalence ratio...
- **Valves data:** Geometrical positioning, lift profiles

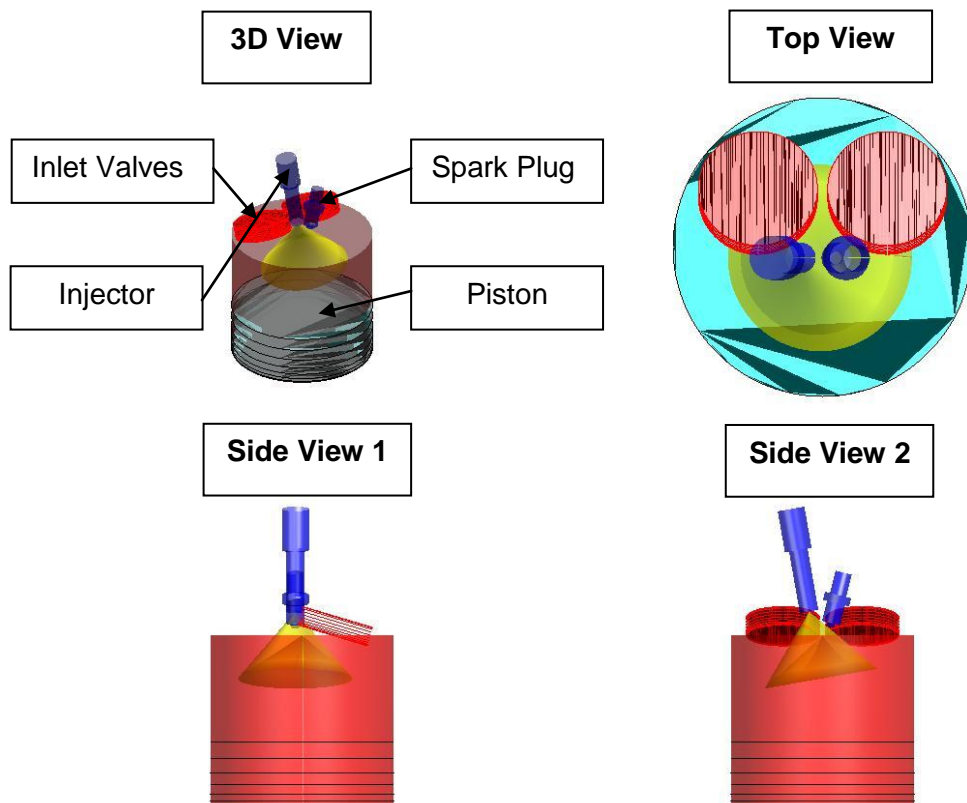
and obtains the impact ratios and a graph representing the impact ratio on the cylinder, valves, piston and spark plug versus the injection period. The results are given in terms of impact ratios, defined as the amount of fuel impacting on a given surface divided by the total mass of fuel injected.



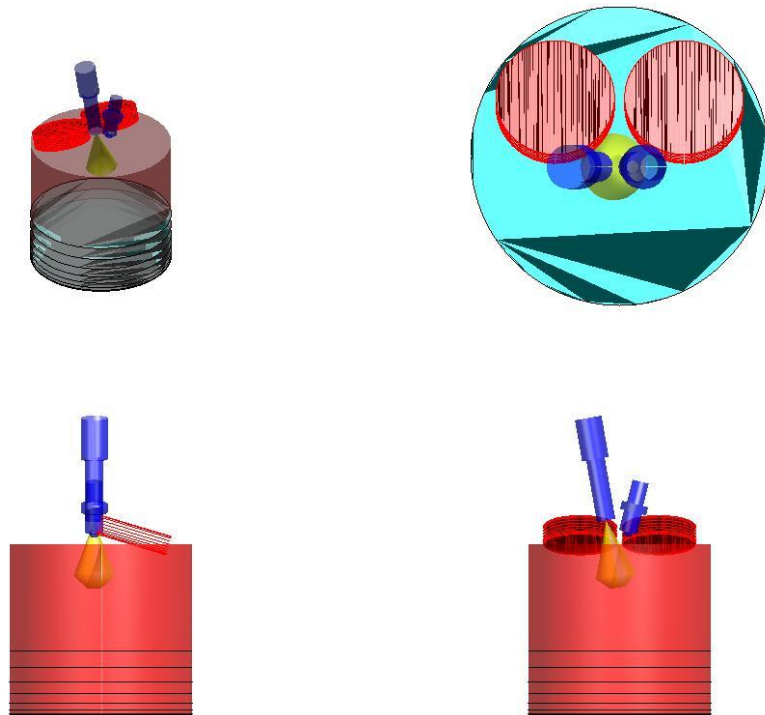
## Chapter 5 - Preliminary Study: Spray Targeting Tool

---

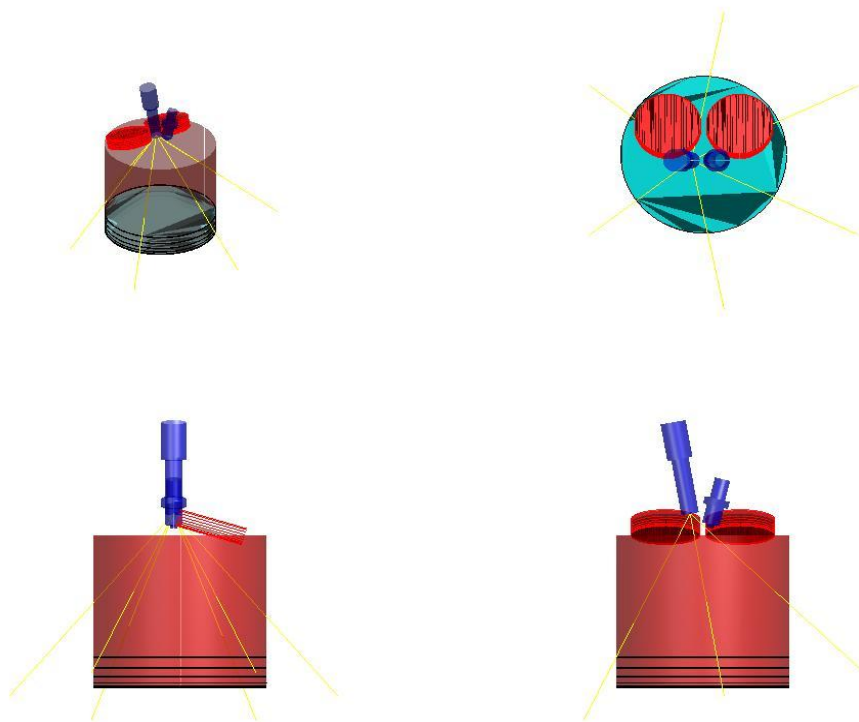
A second window (Figure 5.3, Figure 5.4 and Figure 5.5) is generated and represents a 3D visualisation that shows the cylinder geometry with the intake valves, piston, spark plug and successive spray positions during the injection period. This visualisation is important to understand and illustrate the reasons of a good or bad targeting. Instead of an animation, the pictures present the valves and piston at their different locations during the injection, and the spray at the end of injection.



**Figure 5.3: Point analysis mode graphic window for a piezo injector**



**Figure 5.4: Point analysis mode graphic window for a pressure swirl injector**



**Figure 5.5: Point analysis mode graphic window for a multi streams injector**

### The three versions first of IMPACT:

Originally, three versions of this IMPACT tool were available (IMPACT 1). All of them performed the same computation but did not offer the same application.

**The first version**, the one used and developed in this study, represents the most simple approach. The user enters all the engine geometrical and operational parameters, including the mass air flow rate, and the program returns the injector spray impact ratios on the cylinder, the piston, the intake valves and the spark plug as explained previously.

A correlation between spray impacts and soot emissions can then be performed in order to optimise the spray geometry.

**The second version** is the same as the first one but the mass air flow rate is computed by AMESim, a commercial engine simulation model, and not directly input by the user.

In **the third version**, the impact tool is integrated into AMESim and returns the impact ratios directly to AMESim, the target of AMESim being an optimal combustion efficiency.

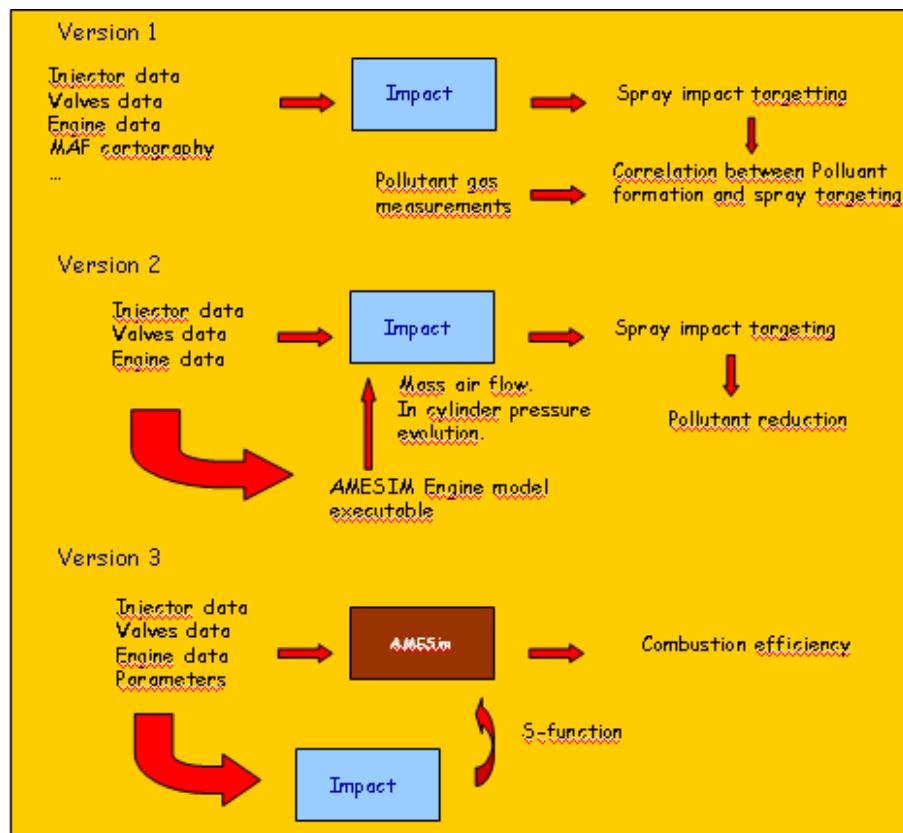


Figure 5.6: The three versions of IMPACT

### 5.5 Computation Algorithm Description

The IMPACT program is briefly described in this paragraph. An algorithm, available in appendix C, describes the computation with more details.

In a first step, the positions of the injector, the intake valves and the spark plug are defined by specifying their respective geometrical data. Then, from the following user parameters, the injection phasing (Start of Injection (SOI)), the injection duration (Pulse Width (PW)) and the injector type, a time vector for the computation is obtained. This time vector is important because it has an influence on the computation time and the result accuracy (see Appendix F).

The first value of the time vector is the value of the SOI converted in crank angle degrees and its last value corresponds to the SOI plus the PW, the time step is determined by the user.

$$time\_vector = SOI(s) : \frac{(SOI(s) + PW(s))}{time\_step} : PW(s) \quad (5.1)$$

It is then possible to deduce from the time vector the crankshaft angle displacement during the injection period:

$$\theta(t) = 60 * RPM * t \quad (5.2)$$

From the crankshaft angle displacement, it is possible to define the piston position during the injection period with the following geometrical relation function of the time (t):

$$piston\_motion = R \left( \cos(\theta(t)) + \sqrt{(\lambda^2 - \sin^2(\theta(t)))} \right) \quad (5.3)$$

The intake valve position is deduced from the intake valves lift (given by the user). The cylinder is modelled by a circle whose diameter is equal to the bore and the spark plug electrode is represented by a small cylinder.

## Chapter 5 - Preliminary Study: Spray Targeting Tool

---

The aim then is to position the spray in the combustion chamber and find a method which can be applied to all the injector types (piezo injector, multi-stream injector and pressure swirl injector). For a more realistic spray targeting, the spray envelop is defined with one line every degree (for example the spray cone for the piezo injector is defined with 360 lines). The cone angle of the spray is given by the user and assumed to be constant all along the injection.

Concerning the penetration of the spray, the user has to feed the program with a data file containing the penetration of the spray function of the injection time, the injection pressure and the back pressure inside the combustion chamber. The only way to obtain that kind of penetration data file is through the experiment, and as very few of them are available so far in the literature especially in hot conditions with varying over and sub-atmospheric back pressures. So here is the link with the experimental work performed in this study which will be developed in the next chapters.

### **Spray/intake valves impact:**

To obtain the impact position between the spray and the intake valves, the equation of the plane surface containing the valves is computed for each time step, and as each spray envelop line direction is defined, the coordinates of the impacts between the plane surface and the lines can be determined. Once the coordinates of the impacts are obtained, the program checks that their position is inside the circle describing the valves. If the impact position is not in the circle, it means there is no impact. Otherwise the program determines the impact time elevation for each valve. Then it repeats this process for each line of the spray envelop.

### **Spray/piston impact:**

To obtain the impacts between the spray and the piston, the spray projection in the cylinder axis is compared to the piston position. If the spray impacts the piston, which means:

$$Z_{\text{spray\_position}}(t) \geq \text{piston\_position}(t) \quad (5.4)$$

The program determines the piston/line impact time elevation for each line of the spray envelop.

### Spray/cylinder impact:

To obtain the impacts between the spray and the cylinder, the projection of the spray in the horizontal plane ((x,y) plane) is compared to the radius of the cylinder (half the bore). If the spray projection is equal or larger than the cylinder radius, which means:

$$X_{\text{spray\_position}}(t)^2 + Y_{\text{spray\_position}}(t)^2 \geq \left(\frac{\text{bore}}{2}\right)^2 \quad (5.5)$$

The program determines the spray/cylinder impact time elevation for each line of the spray envelop.

### **5.6 Spray morphology integration**

In the first version of the program (IMPACT 1), the piezo injector spray was modelled by a regular cone, the pressure swirl injector spray by an irregular cone (radius varying with the distance from the nozzle) and the multi-stream spray with one line per stream.

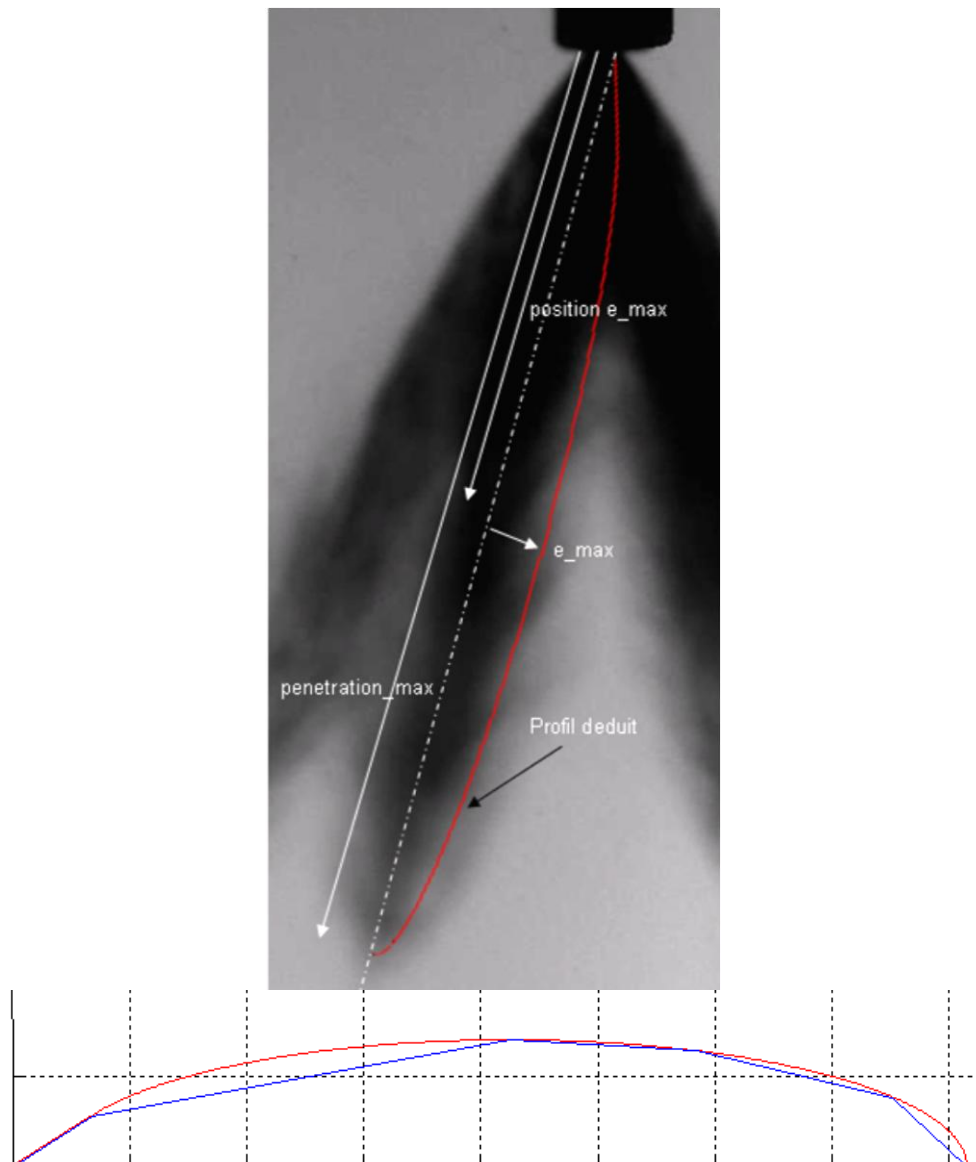
However, these spray envelops were not realistic enough to obtain accurate results, especially for the multi-stream injectors, since the spray characteristics (penetration, angle, width,...) depends on the back pressure, the rail pressure, the temperature and some other internal geometrical parameters. So, for a more realistic spray definition, a spray morphology was integrated into a second version of the program (IMPACT 2). Additional parameters, such as the rail pressure, an injection time function (depending on the air/fuel ratio, the mass flow rate and the injector static flow) and the in-cylinder pressure evolution during the injection period were integrated in the program.

The function for the Pulse Width computation is:

$$PW = (\Phi * (MAFF / n_{\text{cyl}}) * 120) / (rpm * pco) / Q_{\text{stat}} \quad (5.6)$$

where  $rpm$  is the engine speed,  $pco$  is the stoichiometric air/fuel mass ratio,  $\Phi$  is the air/fuel equivalence ratio,  $n_{\text{cyl}}$  the number of cylinders,  $MAFF$  is the intake mass air flow and  $Q_{\text{stat}}$  is the injector mass flow rate. The intake mass air flow ( $MAFF$ ) and the in cylinder pressure evolution can be extracted from the AMESim engine model computation, or, directly given by the user.

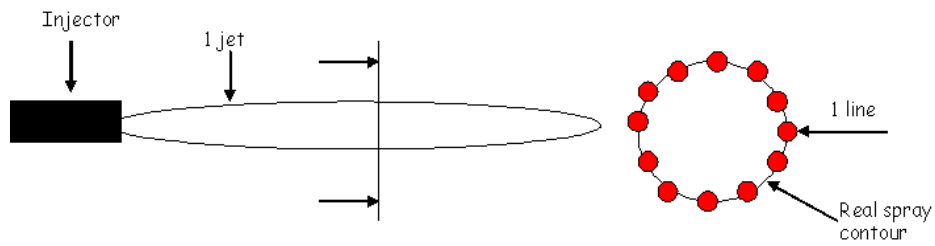
The multi-stream injector spray morphology is defined as follows:



**Figure 5.7: Spray morphology definition**

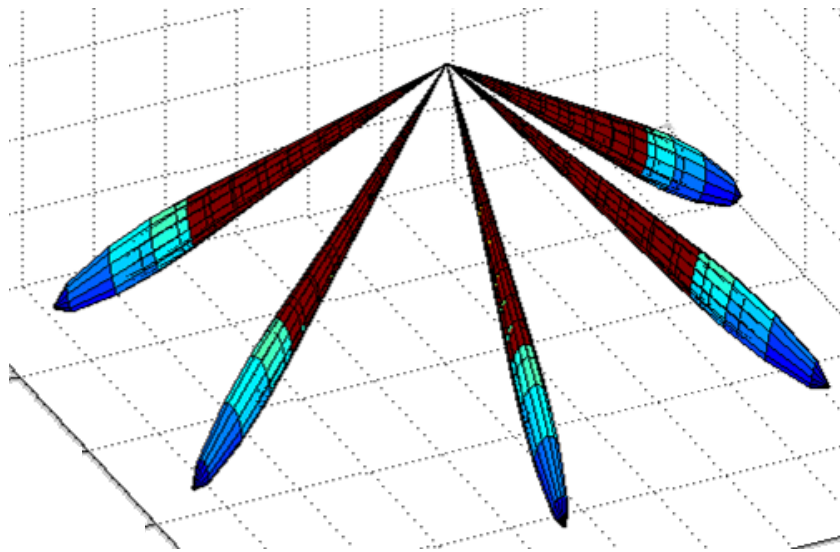
An image of the spray, where a single stream is isolated, is considered. The maximum penetration (*penetration\_max*) of the stream, its maximum thickness (*e\_max*) and the position, for which this maximum thickness (*position e\_max*) is obtained, are determined from the image. Then, from the blue line passing through 6 points defining the spray contour, the red line (half ellipse with major radius equal to  $\text{penetration\_max}/2$  and minor radius equal to *e\_max*) is extrapolated and used to define the stream.

Each stream is modeled by 13 red lines, one every 30 degrees as illustrated in Figure 5.8.



**Figure 5.8: Jet contour definition for morphology integration**

The same process is repeated for each stream to obtain the whole spray morphing used in IMPACT 2:

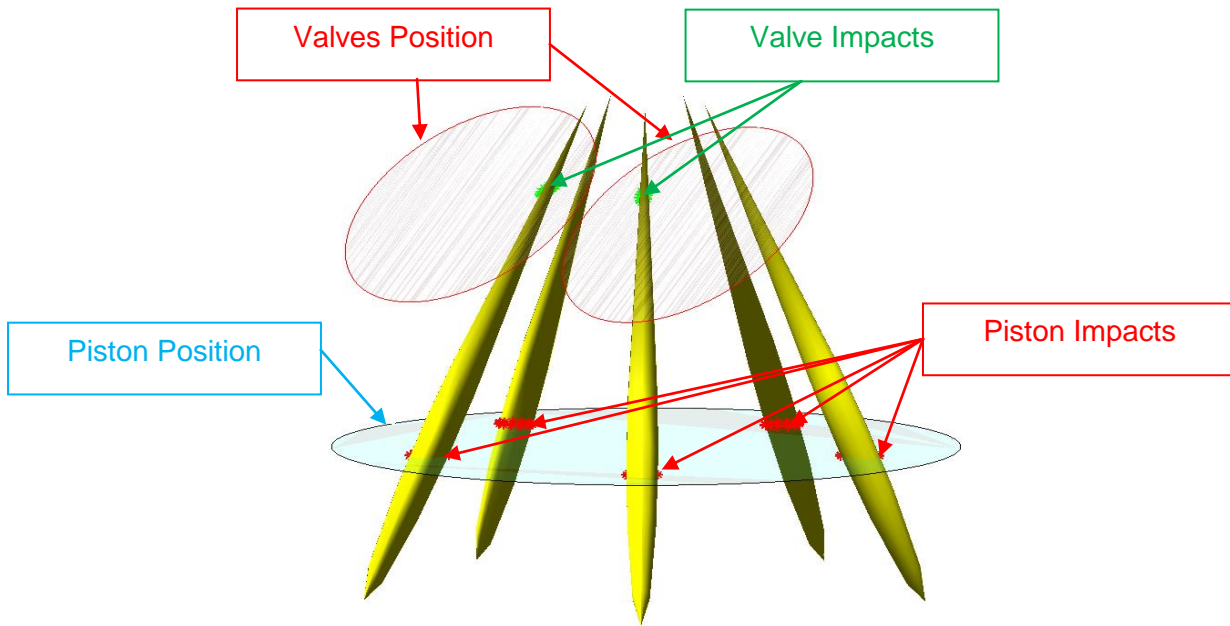


**Figure 5.9: Multi-stream injector morphology in IMPACT 2**

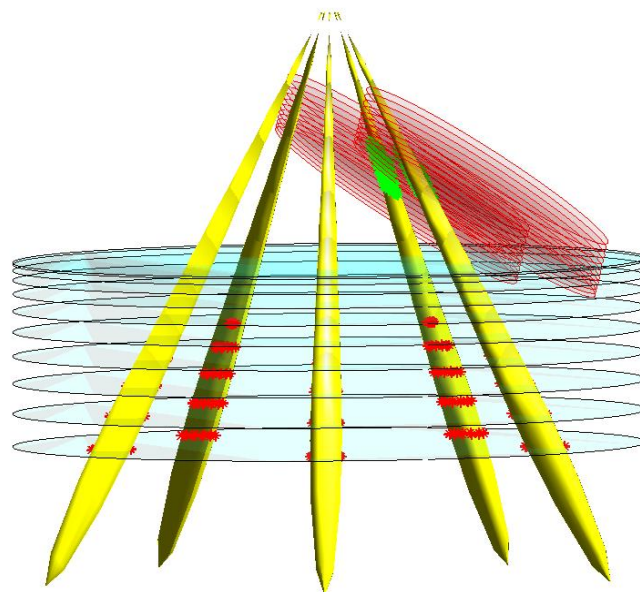
For the spray morphology integration, a new algorithm was used. The modifications affected the calculation of the spray/piston and spray/cylinder impacts. In fact, in order to find the impact positions between the spray and the piston, the equation of the plane surface containing the piston is computed for each time step. Moreover, knowing each spray envelop line direction the impact plane/line can be determined. To finish, the program checks if the plane/line impact position is inside the circle describing the piston.

The impact positions on the valves (green spots) and the piston (red spots) are illustrated in Figure 5.10. Positions are interpolated through the segment when a segment is found to belong partly to one side of the plane and partly to the other side. To calculate the spray impact ratios, the same procedure is repeated at each time step, as illustrated in Figure 5.11.





**Figure 5.10: Impact position calculation for one time step**

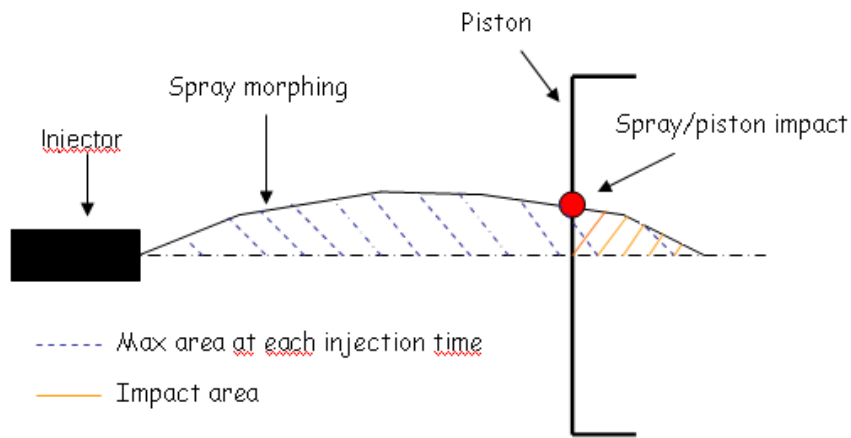


**Figure 5.11: Impact position calculation for the whole injection period**

## Chapter 5 - Preliminary Study: Spray Targeting Tool

---

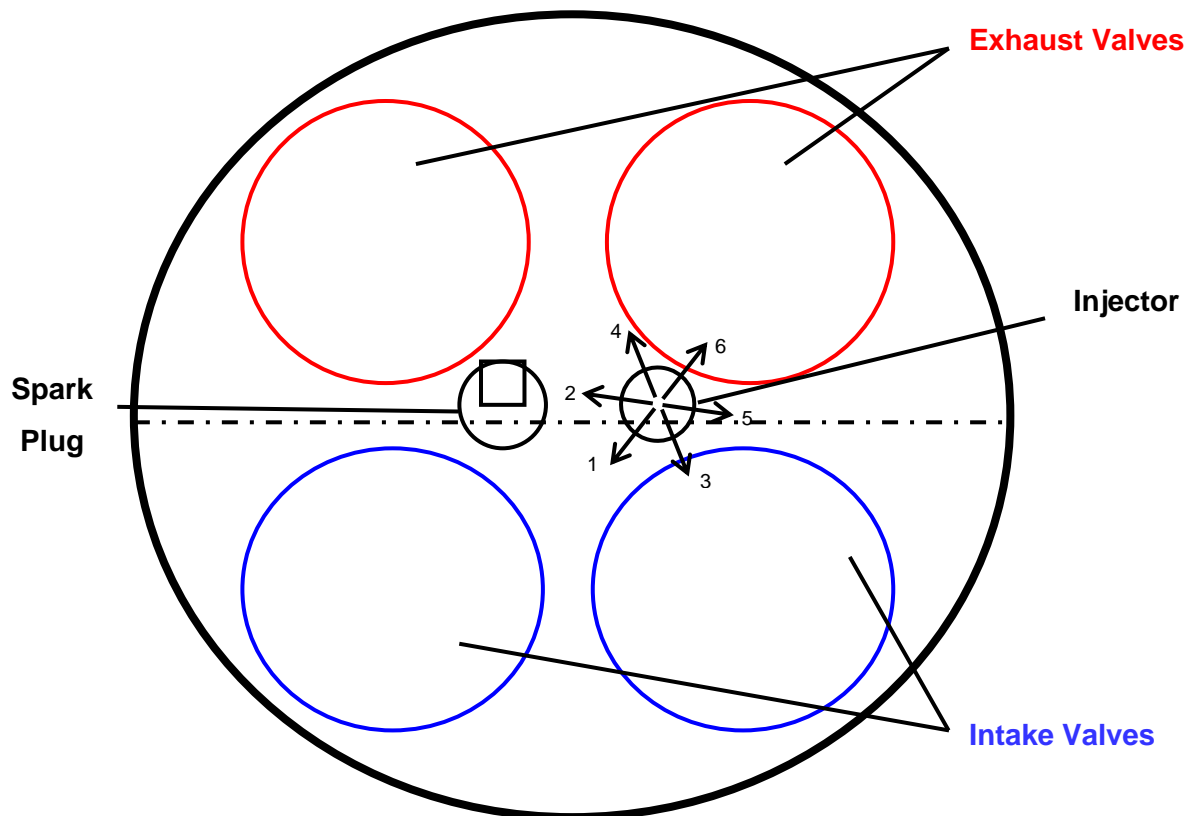
To compute the impact ratio the program calculates the ratio between the impact area and the whole area of the spray as illustrated below:



**Figure 5.12: Impact ratio calculation**

### 5.7 An Example of IMPACT Utilisation

In the following section, the use of the IMPACT tool is illustrated in the study of a Continental AG 6 holes multi-stream injector. The six holes are symmetrically positioned. A preliminary step prior to the use of IMPACT is an accurate definition the injector geometry and more particularly the orientation of the injector holes relative to the spark plug and the valves.



**Figure 5.13: Engine top-view with the orientation of the 6 holes multi-stream injector**

Figure 5.13 is a top-view schematic of an engine where the injector has been mounted. The positioning of the intake and exhaust valves, the spark plug and the injector with the orientation of the six holes are detailed in Figure 5.14 and Table 5.1.

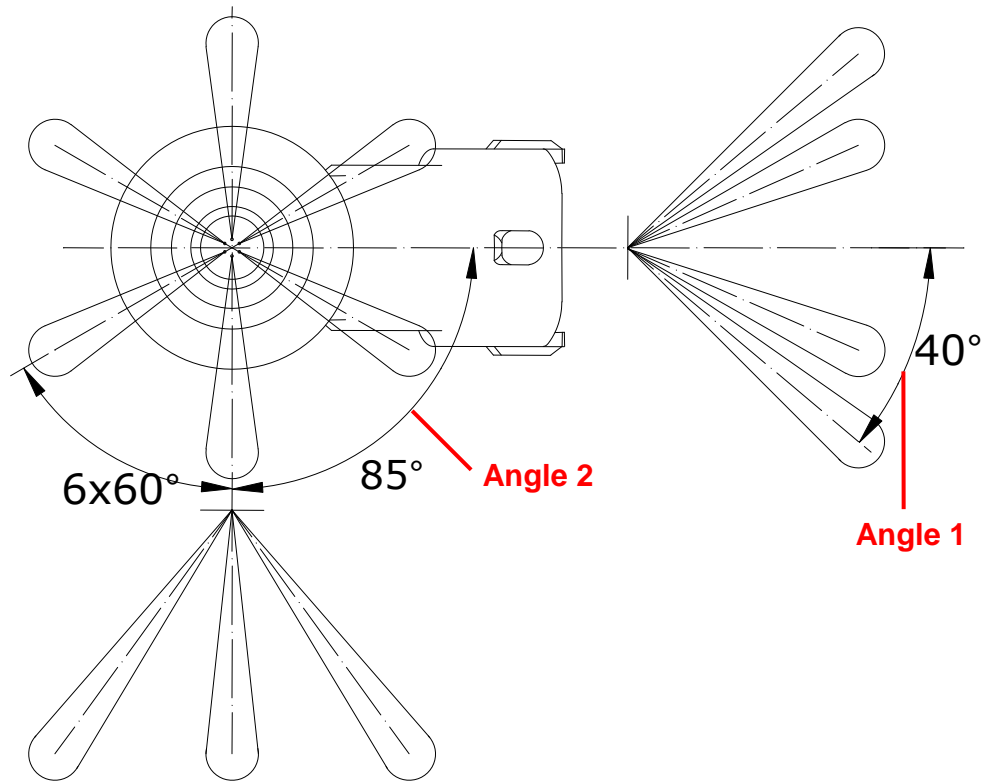


Figure 5.14: Orientation of the 6 holes multi-stream injector

Table 5.1: Injector stream angle definition

Jet	Angle "1" between jet axis and injector axis [°]	Angle "2" between spark plug direction and jet axis in vertical projection [°]
1	40	-35
2	40	25
3	40	-95
4	40	85
5	40	-155
6	40	145

## Chapter 5 - Preliminary Study: Spray Targeting Tool

Once the orientation of the 6 holes is defined, the user loads it in the IMPACT point analyse graphic user interface window and as previously explained the program returns two graphic windows at the end of the computation. The first one, the result window, Figure 5.15: IMPACT result window, shows the impact ratios and a graph representing the impact ratio on the cylinder, valves, piston and spark plug versus the injection period.

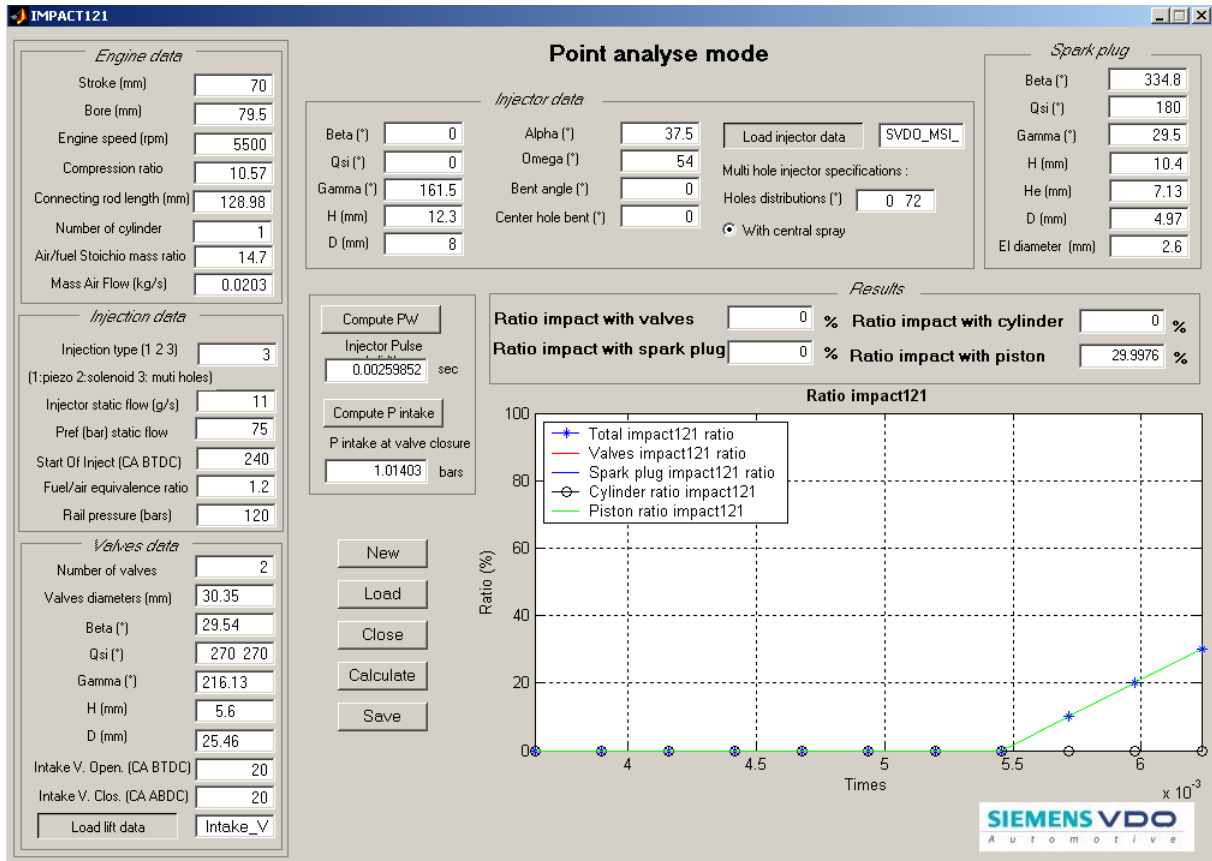
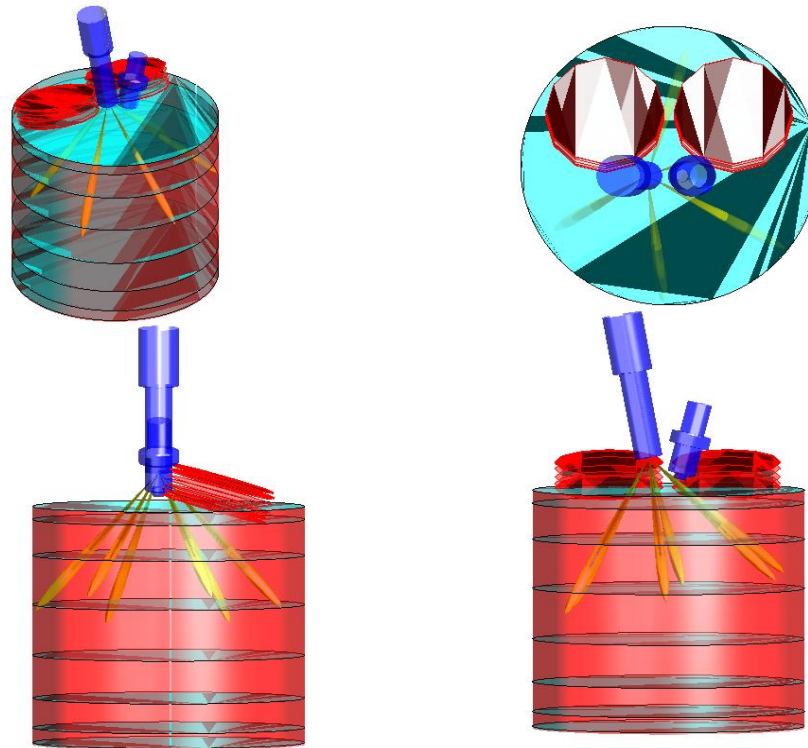


Figure 5.15: IMPACT result window

A second window is generated and represents a 3D visualisation, Figure 5.16: IMPACT graphic window (second version of the program including the spray morphology) below, which shows the cylinder geometry with the intake valves, piston, spark plug and spray position during the injection period. Here the calculation was performed with the second version of the program which includes the spray morphology.



***Figure 5.16: IMPACT graphic window (second version of the program including the spray morphology)***

The next chapter will discuss the experimental results of this investigation obtained on the atmospheric bench. First, a study of the influence of the pulse width and the fuel properties using a pressure swirl injector is presented. Then a radial and a circumferential PDA scan are performed to study the stream to stream interactions of multi-hole injectors.

### 6. Results: Atmospheric Bench

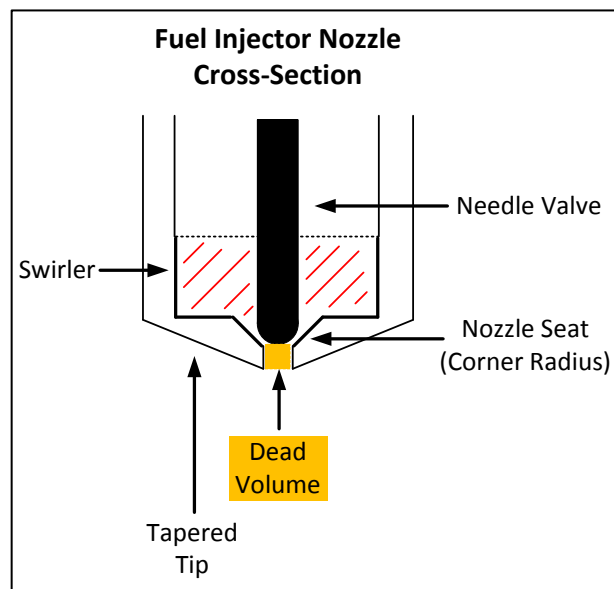
Before introducing the results, a brief summary of the details of the dynamics of GDI injectors is given along with their effects on spray morphology. An automotive fuel injector is a device which supplies a precise amount of fuel for mixing with air in an internal combustion engine. The fuel-air mixing can either occur outside (in-direct injection - IDI) or inside (direct injection - DI) the cylinder. In general, injectors which operate in conditions outside of the cylinder inject at low pressures (3-4bar), whereas DI injectors can inject at far greater pressures up to 200bar.

Several features (see Figure 6.1) define the geometric design of a particular injector for a given engine:

**Injection Pressure** - Higher injection pressure increases the velocity of the fuel exiting the nozzle, which provides greater tip penetration and atomisation.

**Nozzle Exit Hole** - A reduced nozzle exit-hole diameter has been seen to have the effect of significantly increasing the level of fuel atomisation [117].

**Dead Volume** - This refers to the volume in which the fuel can reside inside the injector following an injection. During the next injection, this fuel is forced into the cylinder without passing through the swirl chamber and thus does not have as much atomisation. This leads to locally fuel rich areas in the engine cylinder which are harder to vapourise and to combust and thus reduces engine power and increases emissions.



**Figure 6.1: Pressure swirl injector nozzle cross-section**

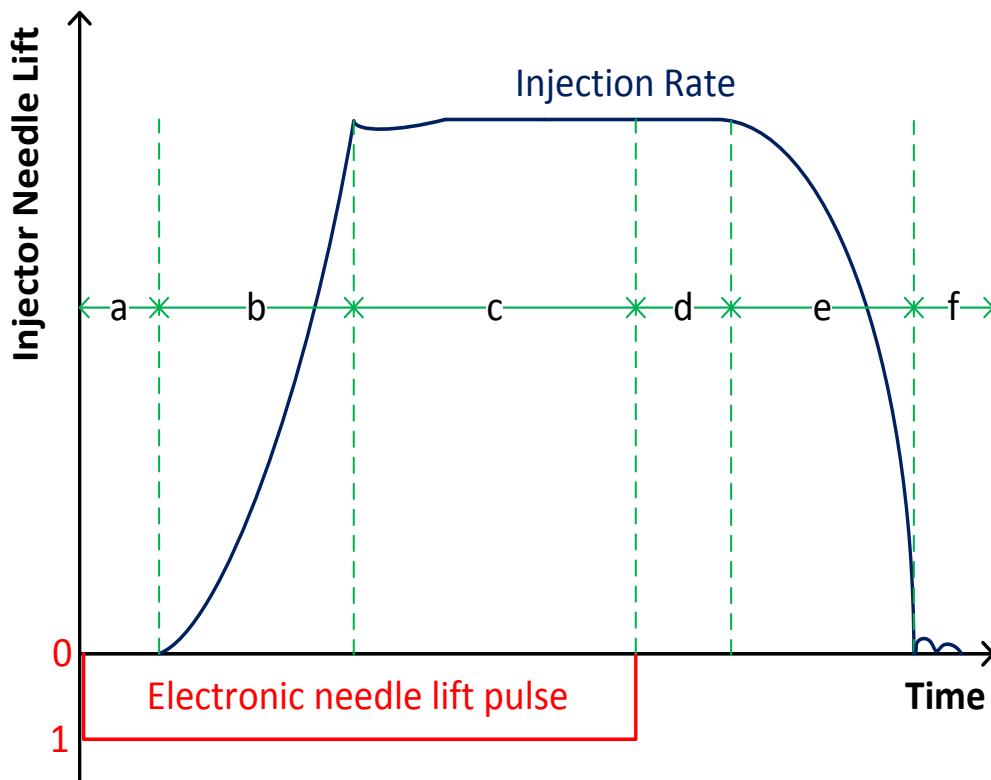
**Tapered Tip** - This is the exterior angle of the fuel injector nozzle and helps direct the fuel away from certain parts of the cylinder. Certain taper angles can create a cone angle which is different across its profile, which can allow progressive opening and closing of the fuel inlet passage [118].

**Corner Radius** - This represents the internal radius of the nozzle tip. Increasing the corner radius can lead to reduced cavitation film thickness [119].

Fuel Injection rate describes the profile of how gasoline is transferred from the injector nozzle to the cylinder over the period of one injection event. Injection rate is a crucial parameter in ensuring the combustion process meets current and future emission requirements for direct injection engines.

Computational Fluid Dynamic (CFD) models have often been created with the assumption that injection rate is constant, and hence the mass of fuel injected is directly proportional to the needle opening duration. However, experimental data shows a more complex link exists between the logical pulse, the injector's needle armature lift and fuel delivery rate.

The following series of events is a description of the standard operating conditions of a GDI fuel injector. Note that the time periods shown in Figure 6.2 are not exact, and are for indication purposes only.



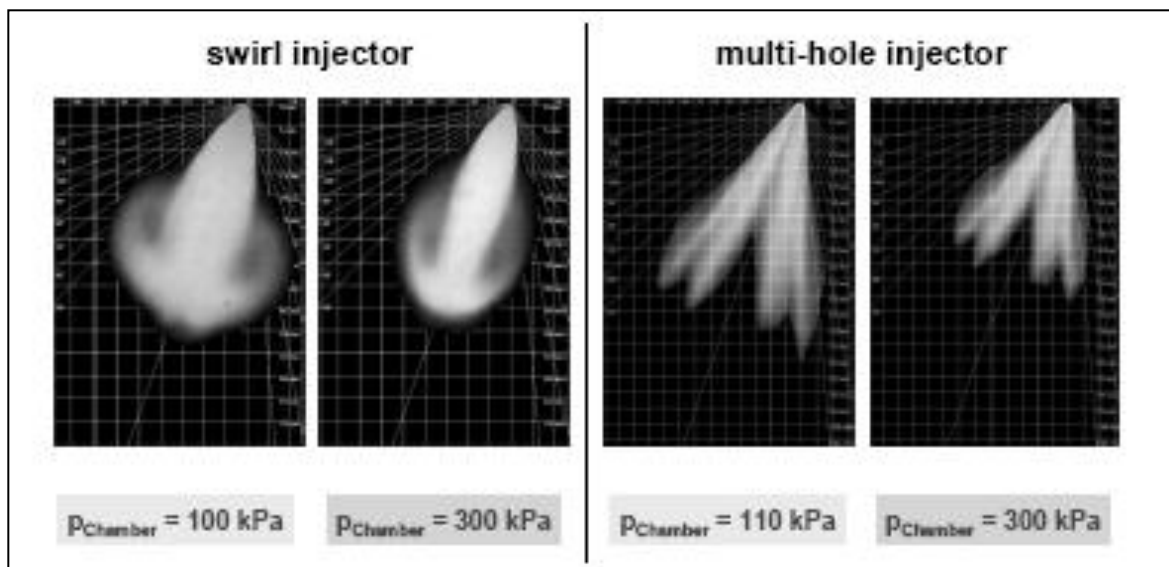
**Figure 6.2: Fuel Injector Dynamics**



- a.** The engine control unit (ECU) sends a 'square wave' open command to the fuel injector. There is a capacitance delay of approximately 300-1200 $\mu$ s, which is built into the injector to protect it from peak voltages.
- b.** Another short delay of around 300 $\mu$ s accounts for the mechanical delay as the fuel injector retracts the armature from being fully closed to fully open.
- c.** The small dip immediately after the fuel injector is fully open occurs as the armature builds sufficient velocity to cause it to bounce off the stopper. The bounce is not sufficient to drastically affect the rate of fuel being injected. Once fully open, the flow rate of the fuel injector is now at a maximum. The fully open time-based duration is dependent on the application of the fuel injector and engine load.
- d.** After the ECU commands the injector needle to close, fuel continues to exit for approximately 400 $\mu$ s. This represents the time taken to remove the magnetic field, which is holding the armature open.
- e.** The actual injector closing time accounts for the mechanical movement of the armature, from fully open to fully close. Nozzle closing can take up to 1ms, since the spring which closes the armature is weak compared to the magnetic force which opens the armature.
- f.** The velocity of the closing armature once again may cause a bounce, resulting in a couple of post-injections of small quantities of fuel.

In the present study, for most of the injectors tested, that were provided by Continental AG, for a given 3 ms pulse width signal, we consider 1ms for the solenoid pre-charge time, 0.2ms for the needle lift delay, 0.6ms of transient fuel delivery, 1.2ms of steady state fuel delivery. The needle starts closing at the end of the signal but we consider another 0.3ms for the needle to come back to its fully closed position. A needle bounce is observed approximately 4ms after the start of the signal causing a small quantity of fuel to be injected.

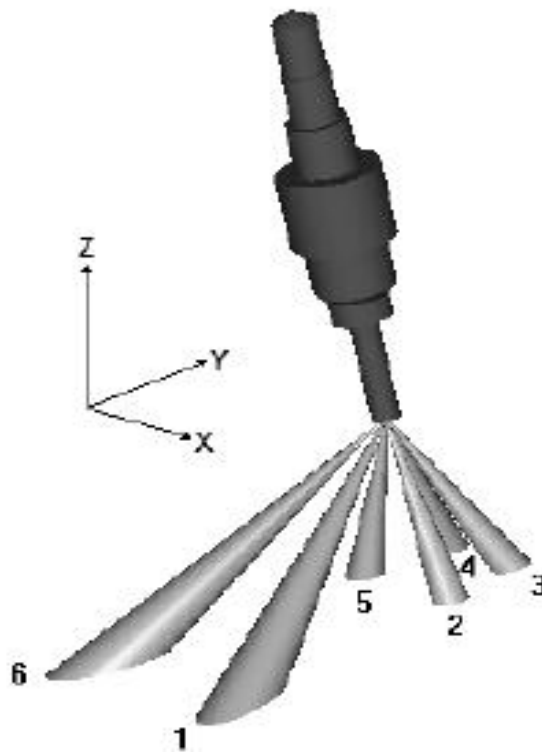
Pressure swirl and multi-hole injectors have been subject of extensive research for use within GDI engines. When in direct comparison, it has been found that a multi-hole injector has more desirable spray formation and control under increasing chamber backpressure. A pressure swirl injector spray at increasing ambient pressure decreases in width, creating poorer fuel/air interaction and weaker homogeneity. This is a possible cause of soot emissions due to localised rich AFR mixtures. It can be seen from Figure 6.3 that the multi-hole injector retains its spray angle at increasing chamber pressure. The smaller penetration of the multi-hole injector at greater pressures is advantageous due to the prevention of soot emissions from piston wetting. Directly comparing emissions from steady state engine operation at three load conditions for optimised swirl and multi-hole injectors was researched in [120]. It was concluded that at low loads conditions (0.5 and 2 bar BMEP) the multi-hole injector produced lower HC emissions, due to the multi-hole injector being able to build up a stable spray pattern quicker at short injection timings. At high load (4000 rpm and 10 bar BMEP) a lower fuel consumption was found while emissions remained roughly equal [60].



**Figure 6.3: Swirl and Multi-hole Injectors at different chamber pressures** [120]

The multi-hole injector design allows for a great variety of spray shapes, given by number, position and orientation of the holes. The ability of a multi-hole injector to produce well-atomised fuel spray is influenced by the number and diameter of the holes. There are different ways in which the nozzle holes can be configured. The nozzle can have more than six holes, be guided with an offset angle and use holes having different properties such as their  $l/d$  (length over diameter ratio, 0.7 to 2.5 for the injectors used in the current study). On the downside, multi-hole injectors are relatively sensitive against fouling when reducing hole diameters lower than 0.2mm.

Different injector configurations create different degrees of spray shear induced air motion. With the high fuel pressure in multi-hole injectors required to achieve sufficient atomisation, the fuel droplet velocity created is also high. The high velocity and therefore high droplet momentum forces air from within the spray vicinity to be entrained. Due to the pressure difference created the air will refill the original areas. This phenomenon is spray induced air motion. The high velocity and momentum creates a droplet mean direction that equals the direction of the nozzle holes, therefore changing the nozzle design has an effect on the amounts of air motion, which can be linked to the ease of vaporisation of fuel mixture.



**Figure 6.4: Potential variations within multi-hole injectors**<sup>[120]</sup>

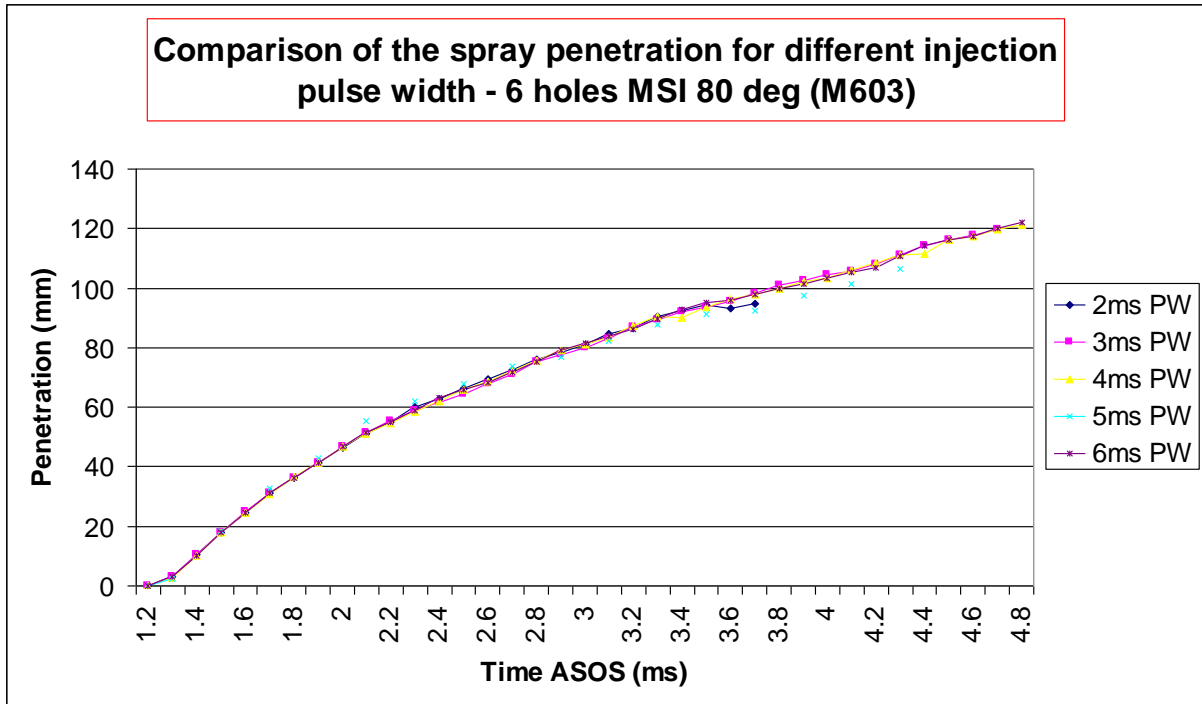
After a preliminary study, in section 6.1, where a pressure swirl injector was used to determine the influence of injection pulse width and fuel properties on the atomisation performance, this study will focus mainly on multi-hole type injectors used in GDI engine applications.

### **6.1 Pressure Swirl Injector**

#### 6.1.1 Influence of Injection Pulse Width

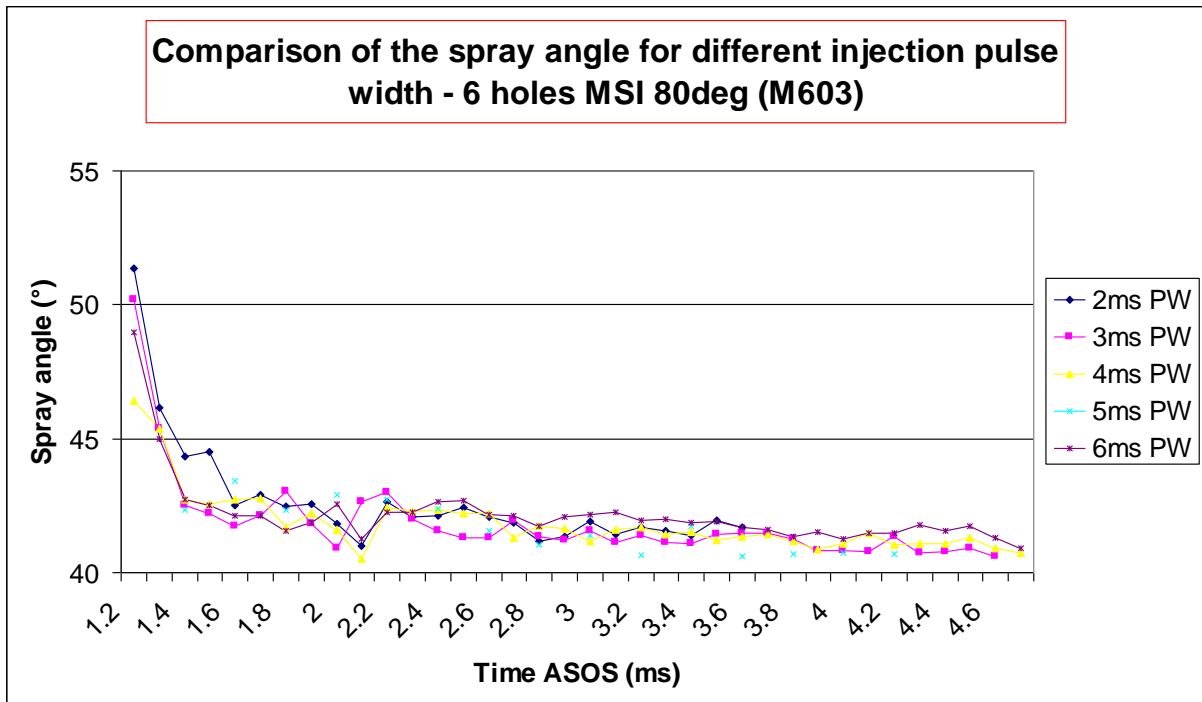
The atmospheric spray bench (described in section 4.2) was used to investigate the influence of the injection pulse width on the spray penetration and spray angle (defined as the angle between the injector axis and the plume axis) of a 6 hole symmetrical multi-stream injector (90° cone angle). However, the study was limited by the size and positioning of the backlit flash panel relative to the recording CCD camera. With the current set up, the maximum distance between the camera and the flash panel allowed a measurements of the spray penetration up to 4.8ms after the start of the signal (ASOS) for a fuel injection pressure of 120bar. However, as it can be observed in Figure 6.5, there is no noticeable influence of the injection pulse width (PW) on the spray penetration.

It can be noticed that, for 2ms injection pulse width, the spray penetrates only until approximately 3.8ms ASOS, after this period of time the spray edge is no longer clearly defined as the spray is evaporating. When using the  $D^2$  law of droplet evaporation (see appendix A) for the operating conditions, a droplet lifetime of around 2.5ms is obtained, which means that in the case of a 2ms pulse width injection (for which the actual fuel injection occurs between 1.2 and 2ms after the start of signal) the first droplets injected should have evaporated after around 3.7ms ASOS and the last droplets injected should be evaporated after 4.5 ms ASOS.



**Figure 6.5: Comparison of the spray penetration for different injector pulse width**

In a same way it can be observed in Figure 6.6 that there is no noticeable influence of the injection pulse width on the spray angle, the small differences only being due to the little variations in the spray edge used during the post-processing of the images.



**Figure 6.6: Comparison of the spray angle for different injector pulse width**

### 6.1.2 Influence of Fuel Properties

During the development and production of gasoline fuel injectors standard, less volatile fuels are used, rather than gasoline, to assess their performance. Furthermore, within the research community, idealised fuels are often used where the chemistry is simplified and well documented. This is particularly so with fuel spray studies in order to improve safety, [121], or to utilise Laser Induced Fluorescence, [122]. However, the use of single component fuels can have a pronounced effect on the spray, especially in engine like conditions, [123].

In this section, the effect of fuel type on the liquid break-up and atomisation is to be detailed for a modern pressure swirl gasoline direct injection system operating at 100 bar injection pressure and an injection duration of 1.0ms. Six different fuels were used, standard 95 RON gasoline, the test fuels Exxsol D40 and Stoddard, the single component fuels, N-heptane and iso-octane and E25, a blend of 75% gasoline with 25% ethanol.

**Table 6.1: Fuel Properties**

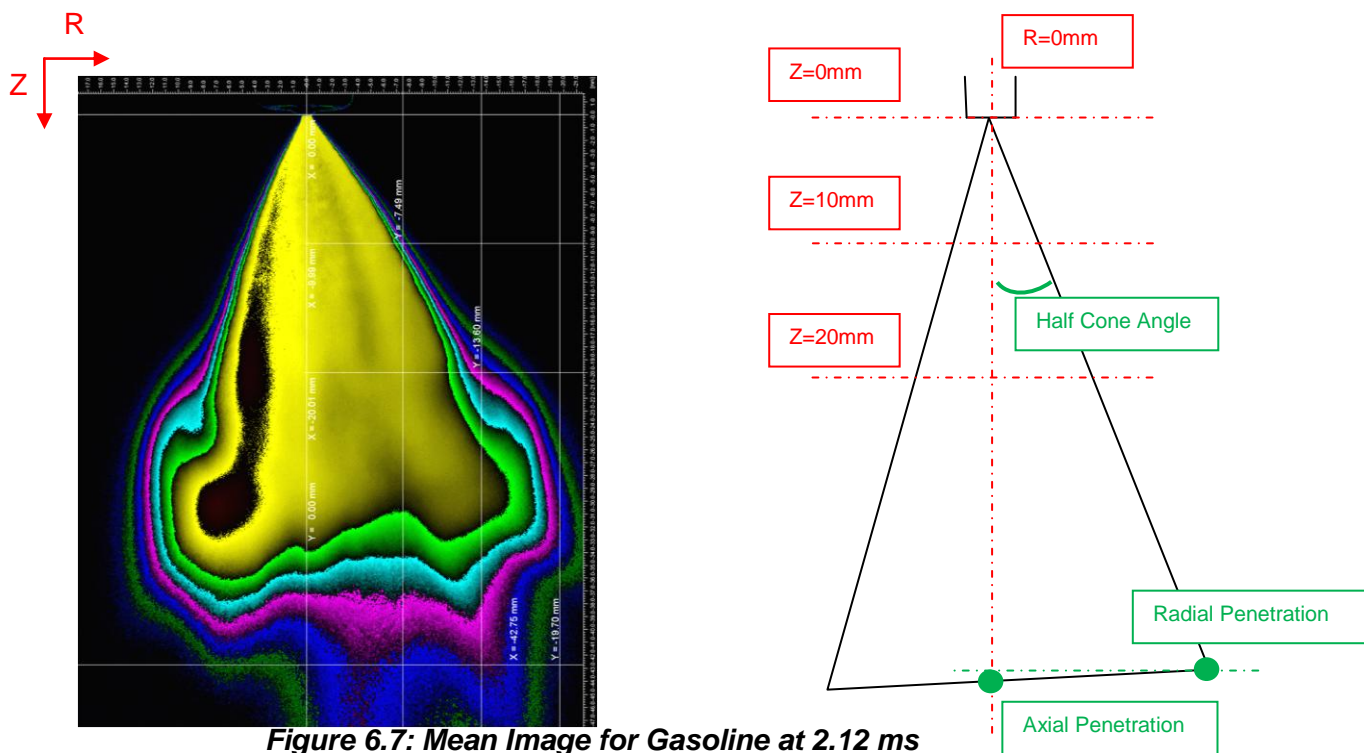
Fuel	Density Kg/m <sup>3</sup>	Kinematic Viscosity mm <sup>2</sup> /s	Surface tension mN/m
Gasoline	745	0.74	21.0
N-Heptane	682	0.60	20.14
Iso-Octane	690	0.72	18.77
E25	755	0.94	22.0
Exxsol	772	1.3	24.7
Stoddard	780	1.28	26

Mie imaging and the Phase Doppler technique were used to capture the spray morphology and map out the droplet flow field under atmospheric conditions for each fuel. Radial profiles of the axial and radial velocities and drop-size were measured at distances 10, 20, 40 and 80 mm below the nozzle tip. Each radial scan started from the geometric vertical axis through the nozzle tip and traversed out to the periphery of the spray. This horizontal traverse was computer controlled and programmed with a minimum radial step increment of 0.5, 1.0, 2.0 and 4.0 at Z = 10, 20, 40 and 80 mm respectively in order to resolve local high velocity gradients across the cone of the spray at each horizontal plane.

## Chapter 6 – Results: Atmospheric Bench

The spray cone angle and penetration were derived from the mean of 20 images obtained at the instant that the injector was programmed to close, i.e. 2.12 ms after the start of the injection timing trigger as this represented the full development of the cone. The spray boundary was quantified as the 50% image intensity threshold by using colour coded stepped intensity contours. The mean image obtained for gasoline is shown in Figure 6.7. The spray is asymmetric about the axis through the injector,  $R = 0$  mm, as the nozzle was configured to give a ‘bent angle’ of nominally  $7.5^\circ$  for targeting purposes.

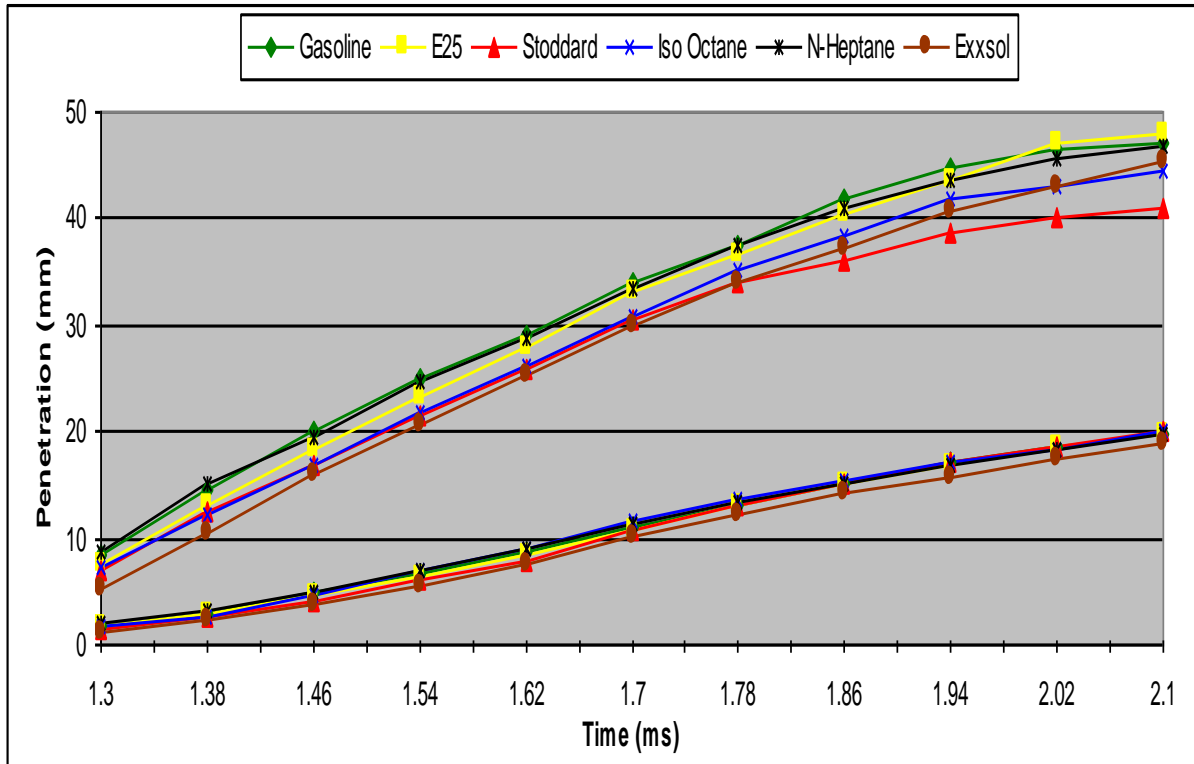
Two estimates of the half spray cone angle, relative to the injector axis, are given corresponding to  $Z = 10$  and  $20$  mm in Table 6.2, while the spray penetration is plotted, as a function of time, in Figure 6.8: Axial (upper) and Radial (lower) Penetration Profiles for the axial and radial penetration relative to the injector axis.



**Figure 6.7: Mean Image for Gasoline at 2.12 ms**

**Table 6.2: Fuel Spray Half Cone Angles**

Fuel	Half Cone Angle $Z = 10$ mm	Half Cone Angle $Z = 20$ mm
Gasoline	$36.83^\circ$	$34.22^\circ$
N-Heptane	$36.91^\circ$	$33.98^\circ$
Iso_Octane	$37.92^\circ$	$36.22^\circ$
E25	$37.23^\circ$	$35.85^\circ$
Exssol	$37.52^\circ$	$34.49^\circ$
Stoddard	$38.76^\circ$	$38.10^\circ$



**Figure 6.8: Axial (upper) and Radial (lower) Penetration Profiles**

For the near nozzle location of  $Z = 10$  mm gasoline exhibits the smallest cone angle of  $36.83^\circ$  and Stoddard, the largest at  $38.76^\circ$  so the variation in spray cone angle is less than  $2^\circ$ . The dominant physical process occurring in the spray is break-up of the liquid sheet downstream from the nozzle exit.

The spray cone angles are smaller for the 20 mm location and have a greater variation of  $4^\circ$ . There is a shear induced entrainment into the spray cone boundary which reduces the cone angle and, as the atomisation of the liquid fuel progresses differently for each fuel, large variations in the cone angle here can be expected.

There is a definite inverse correlation between the spray cone angle at  $Z = 10$  mm and the axial penetration of the spray cone boundary as seen in Figure 6.8. Gasoline and N-heptane have virtually equal low cone angles and high penetration rates while Stoddard has the largest cone angle and lowest axial penetration. It might be considered that the axial momentum accounts for this and the controlling fluid parameter would be the liquid density but this is not the case, especially since iso-octane,  $690 \text{ Kg/m}^3$  has a similar cone angle and axial penetration as Exxsol with a density of  $770 \text{ Kg/m}^3$ . Variations in fluid properties have no influence on the radial penetration as this is virtually identical for the fuels studied.



## Chapter 6 – Results: Atmospheric Bench

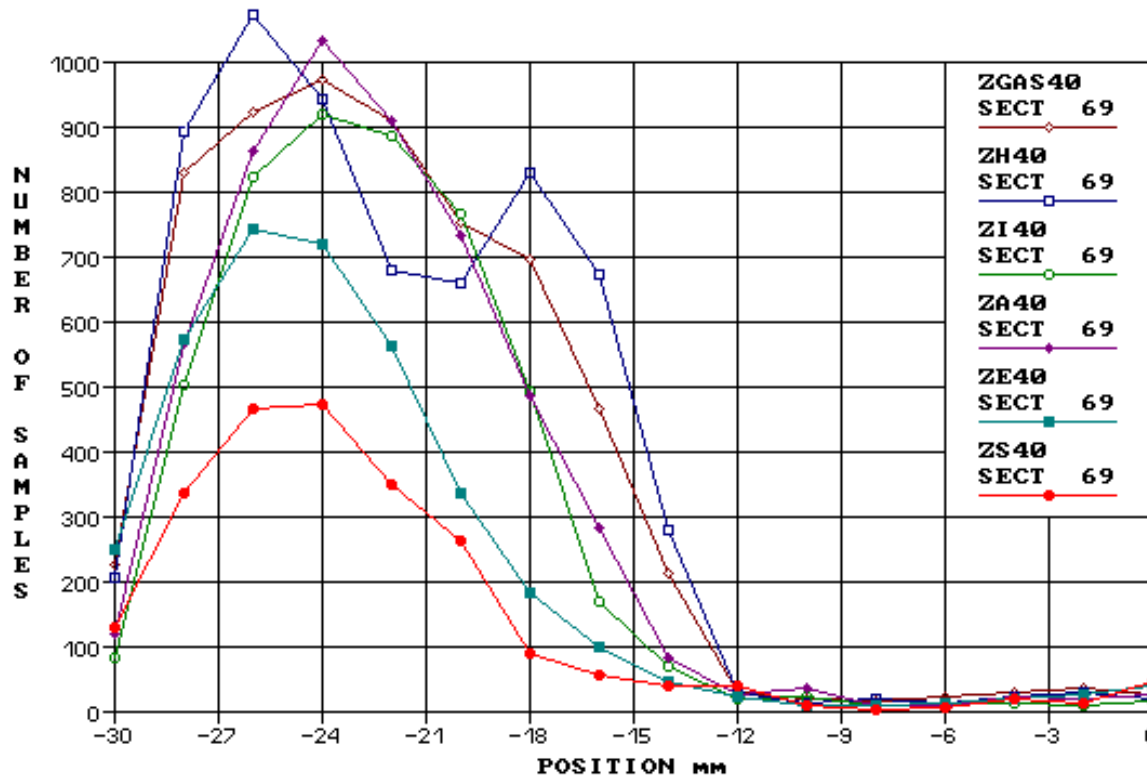
---

The determination of spray characteristics from spray images only yields information as regards the spray boundary, the spray morphology. With small differences to be expected in the sprays with the different fuels the emphasis was put on the spray dynamics as obtained by the PDA technique.

Rather than present all the PDA data it has been decided to concentrate on the data at  $Z = 40$  mm where the spray dynamics can be wholly attributed to the atomised fuel to droplet form. The raw PDA droplet data were time bin averaged into consecutive sectors of  $40 \mu\text{m}$  to provide time varying mean axial and radial droplet velocities and droplet size profiles.

Before presenting the data it is necessary to have some discussion on the accuracy and consistency of the PDA data. Since the intention is to quantify the differences between the fuels the emphasis is really on experimental consistency. The optical and electronic system parameters were adjusted for high gain, small droplet detection to minimise the effect of laser beam obscuration by the spray while ensuring rejection of opto-electronic noise. The system parameters were then fixed throughout the measurement programme. Before each measurement scan was made across a spray radius, the alignment of the optical system with the injector nozzle was confirmed.

The largest contributor to fluctuations in the estimates of droplet velocity and size is the number of samples collected in any one time bin. As the sprays are highly transient small time bins had to be chosen and the sample number in any time bin is related to the measurement location. As an indicator to the statistical significance of the data presented in this paragraph, a plot of the sample number in the time bin representing maximum axial droplet velocity for gasoline is shown in Figure 6.9. The sample number between the axis through the injector,  $R = 0$  mm and  $R = 12$  mm is low, the smallest count is between 10 and 20 samples at  $R = 8$  mm. However, as long as the velocity and drop-size variation are small inside the hollow cone then significant estimates can still be expected. Obscuration of the input laser beams is the primary cause for low data counts, particularly on the inside surface of the spray cone, i.e.  $R = 8$  to  $12$  mm. Nevertheless, the number counts here are high and the velocity and drop-size estimates should have a good statistical significance. Although these distributions cannot be used to quantify droplet density they serve as an indicator of the variation in atomisation quality, i.e. a high sample count, between the fuels. N-heptane, file ZH40, demonstrates a high level of atomisation especially on the inside of the spray cone. Gasoline, ZGAS40, Iso-octane, ZI40, and E25, ZA40, all show similar atomisation characteristics. As seen from the spray morphology results Exxsol, ZE40, and Stoddard, ZS40, are widely different.



**Figure 6.9: PDA sample number distributions in sector 69**

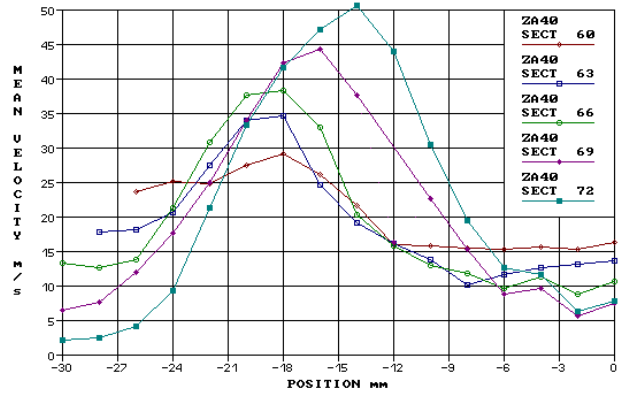
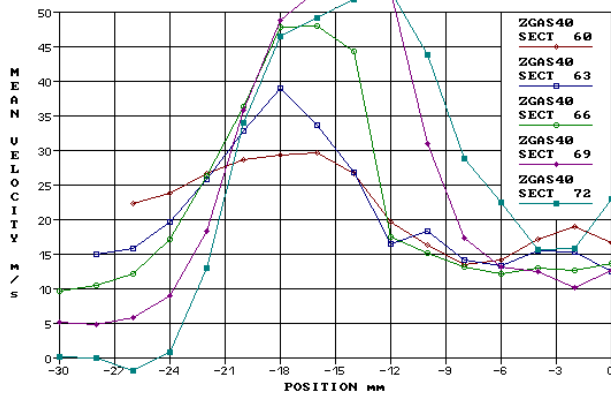
The mean droplet axial velocity profiles across the spray radius at Z = 40 mm are shown for each fuel in Figure 6.10. The cross-section for the measurement scan was the same as that used for estimates of the spray cone angle and penetration.

The time dependence is given by the sector number. With each sector being 40  $\mu$ s then sectors 60 to 72 represent the time total period 2.36 to 2.88ms. The time span corresponds to the establishment of the spray cone at 40 mm below the nozzle.

It must be remembered that these times refer to the time after the start of the electronic pulse of 2 ms which included a soak time of 1ms. This soak time improves the time response of the injector but there is a corresponding shift in time for the needle to open and for the actual fuel delivery to begin.

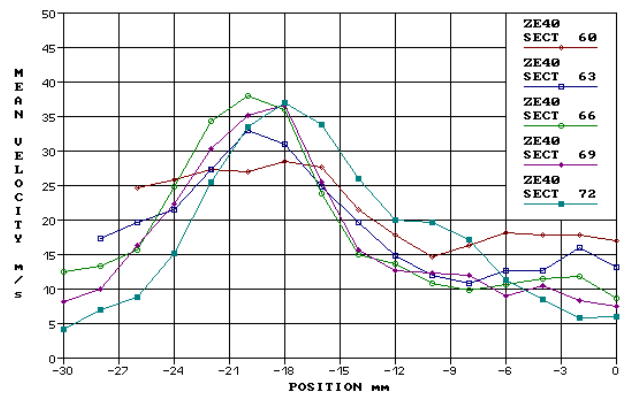
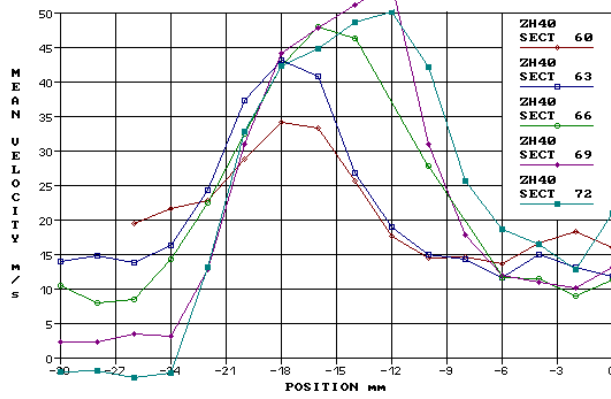
Apart from the industry test fuels, Exxsol and Stoddard, the general trend for the axial velocity profiles for the developing spray cones is for a peak, at approximately 30 m/s, to occur in the velocity profiles at a nominal radius of R = 18 mm at sector 60, i.e. 2.36 to 2.40ms. As time increases the peak velocity increases, up to 54 m/s, and its location moves towards R = 14 mm highlighting a transition of the spray towards the injector axis.

# Chapter 6 – Results: Atmospheric Bench



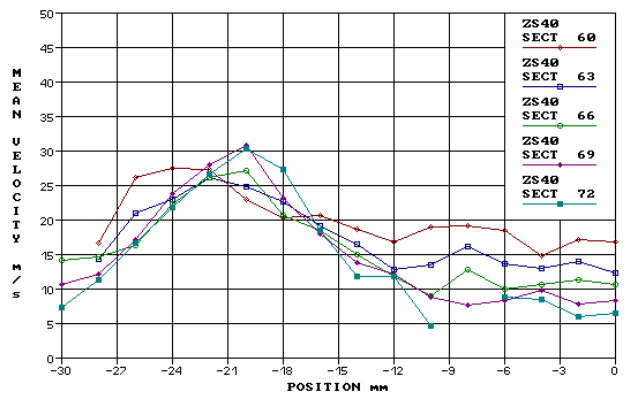
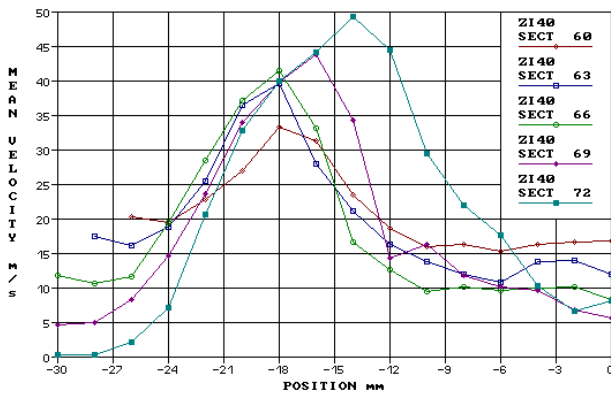
## Gasoline

## E25



## N-Heptane

## Exxsol



## Iso-Octane

## Stoddard

Figure 6.10: Axial Velocity Profiles 40 mm below the nozzle

## Chapter 6 – Results: Atmospheric Bench

---

As with the spray morphology data there are distinct similarities between the data for Gasoline and N-heptane and the data for Iso-octane and E25. The high axial penetration of Gasoline and N-heptane is confirmed with the highest recorded axial velocities of 54 m/s. However, between sectors 60 and 66 N-heptane demonstrates higher peak velocities and sample numbers, suggesting better atomisation.

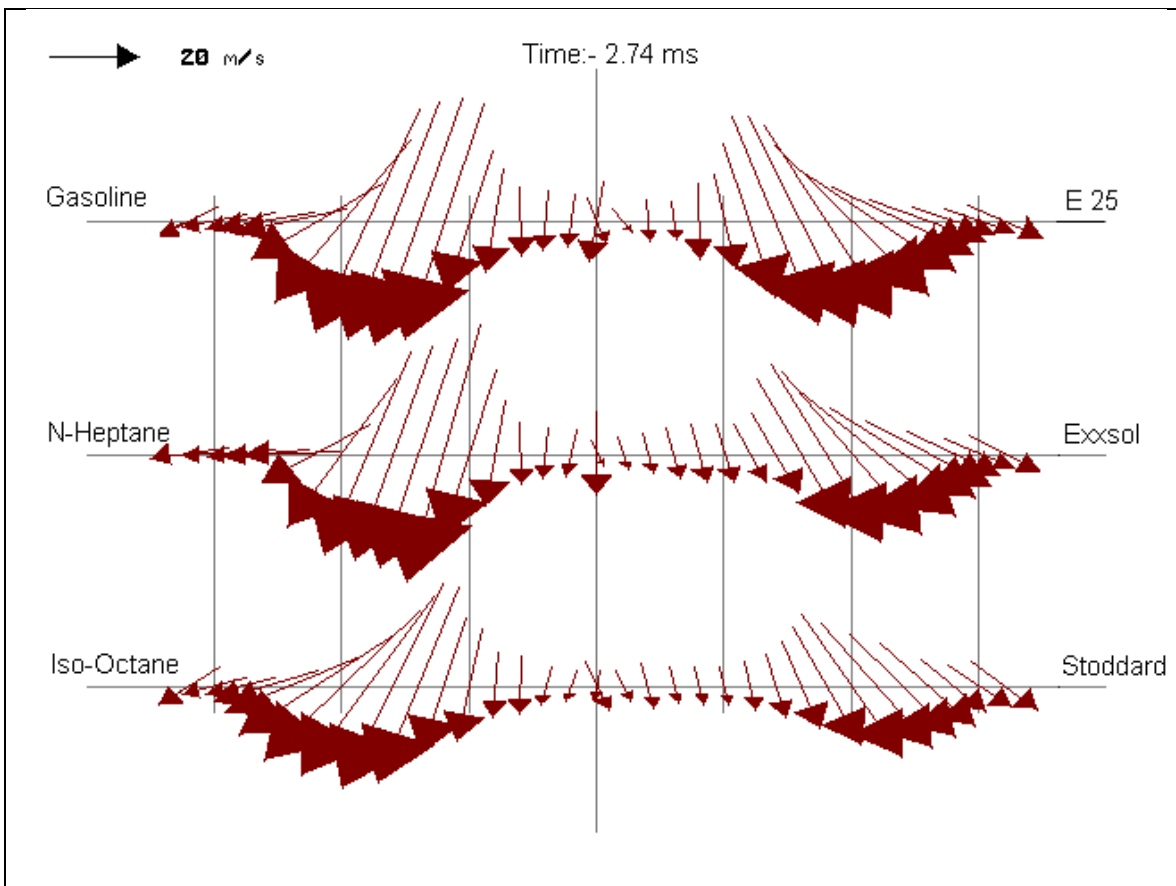
The PDA data also show that during the early cone development the Iso-octane spray cone develops faster than the E25 spray but between sectors 69 and 72 they are identical. However, this does not conform to the trend expected from the axial penetration data which shows E25 penetrating faster.

These four fuels demonstrate a very similar behaviour in the spray periphery,  $R > 24$  mm, with the axial velocities decaying from approximately 20 m/s at sector 60, down to near zero flow at sector 72. The axial velocity profiles are remarkably smooth inside the 'hollow cone' of the spray considering how few samples make up the velocity estimates but do show variation of up to 10 m/s as a function of time.

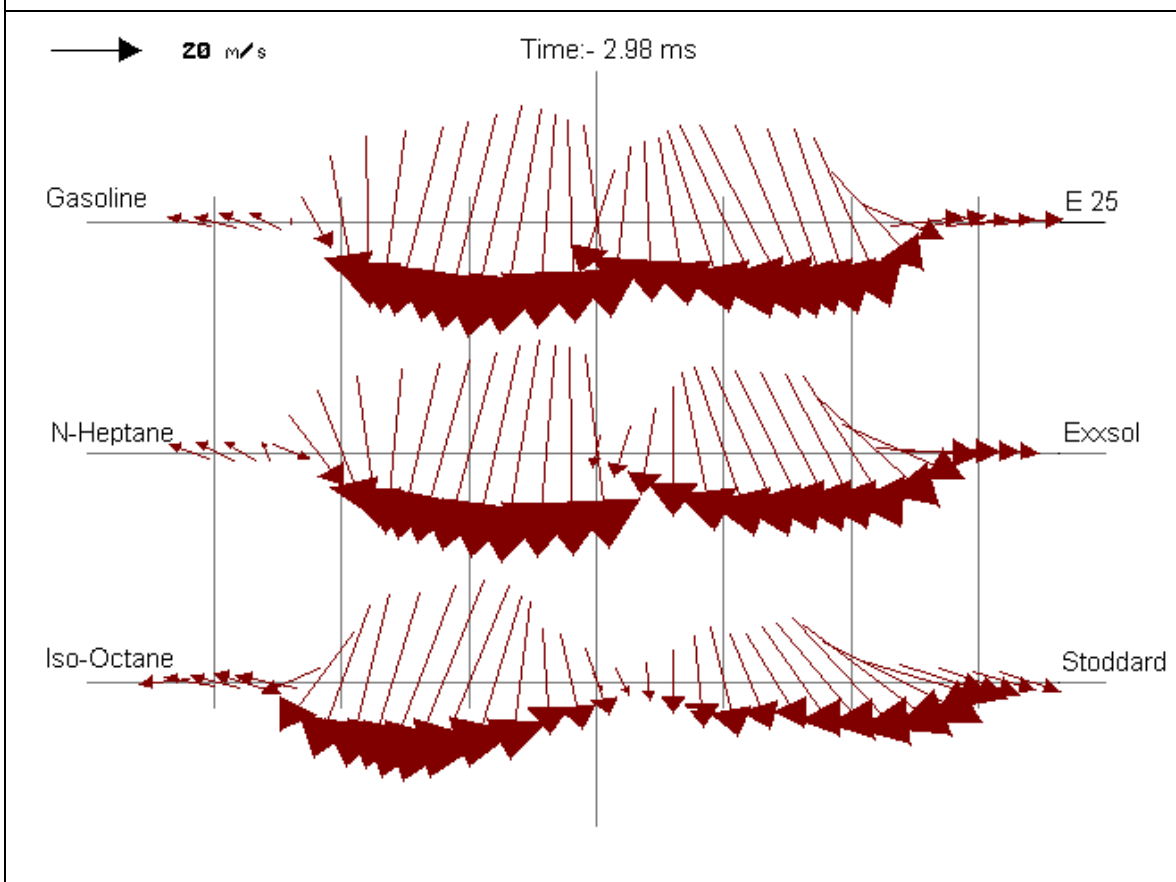
The poor axial penetration of the Exxsol and Stoddard sprays is due to the much lower droplet velocities, less than 40 m/s for Exxsol and only 30 m/s for Stoddard. Furthermore, the variation in axial velocity is small, less than 10 m/s, and the radial position of the peak velocity can be found between 18 and 20 mm for the whole duration of the spray cone development.

Whereas these velocity profiles are essential for quantifying small differences between the sprays they do not necessarily provide an intuitive picture of the spray dynamics. Rather than perform a similar analysis for the radial droplet velocity profiles the two velocity components have been combined to allow a presentation of the droplet vector flow field. Two time sectors have been chosen, that representing the maximum axial velocity, i.e. a time of 2.74ms, and the time at which the spray cone starts to collapse with the end of injection, a time of 2.98ms. These vector flow maps are shown in Figure 6.11 and Figure 6.12 respectively with the axis through the injector in the middle and with the vertical lines either side at  $R = 10, 20$  and 30 mm. The vectors have a constant 2mm spacing along the radius.

The flow angle and the velocity distribution across the spray cone are now readily visualised. The key to understanding the spray development lies with the magnitude of the vectors, the generation of the vortex, or recirculation zone, due to entrainment into the spray periphery and the transition of the spray towards the injector axis as the spray cone collapses.



**Figure 6.11: Flow field map at Z = 40 mm and Time 2.74 ms for all fuels**



**Figure 6.12: Flow field map at Z = 40 mm and Time 2.98 ms for all fuels**

## Chapter 6 – Results: Atmospheric Bench

---

The gasoline and N-heptane sprays have identical flow angles across the centre of the spray cone but the latter appears to be in advance of the gasoline spray as the flow vectors from 22 mm outwards are already turning into the vortex with a zero axial flow component.

The Iso-octane spray has much reduced flow vector magnitudes across the cone when compared to the above, but, since the radial flow components are similar to gasoline the effect is to produce a steeper flow angle although the vortex still has to form. These comments apply equally to the flow field for E25.

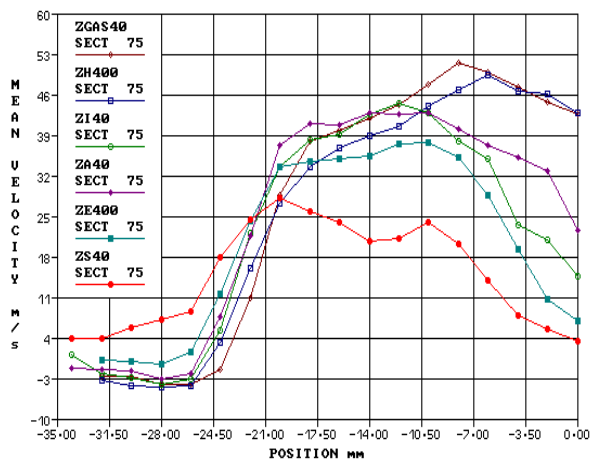
It is again obvious that Exxsol and Stoddard produce widely different flow fields to the other fuels. Since the axial flow component has reduced in comparison to the radial flow component the flow vectors are at steeper angles across the spray cone yet, with the reduced entrainment the vortex has yet to appear.

At the later time of 2.98 ms the vortex on the spray periphery is clearly seen in the case of N-heptane and gasoline while for iso-octane the vortex is only just formed. For E25 and Exxsol the axial flow component in the spray periphery has decayed to zero but, for Stoddard, the lag is appreciable as there is still no vortex appearing.

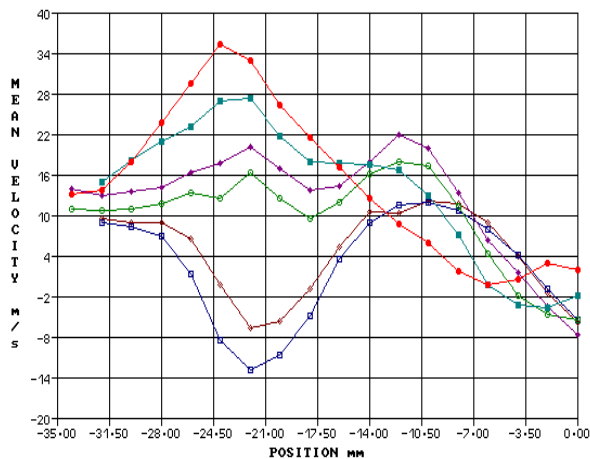
The largest difference between the fuels is seen in the manner that the sprays for gasoline and N-heptane tend to produce a full cone spray as the maximum vectors occur close to the injector axis. E25 is the only other fuel that is beginning to demonstrate this behaviour. The spray cone is still in evidence though for iso-octane, Exxsol and Stoddard.

To reinforce the differences between the fuels at this time the axial and radial droplet velocity and drop-size profiles are shown in Figure 6.13. The key to the profiles for each fuel is given in the top figure, where the file names, from top to bottom, refer to; gasoline, N-heptane, iso-octane, E25, Exxsol and Stoddard respectively.

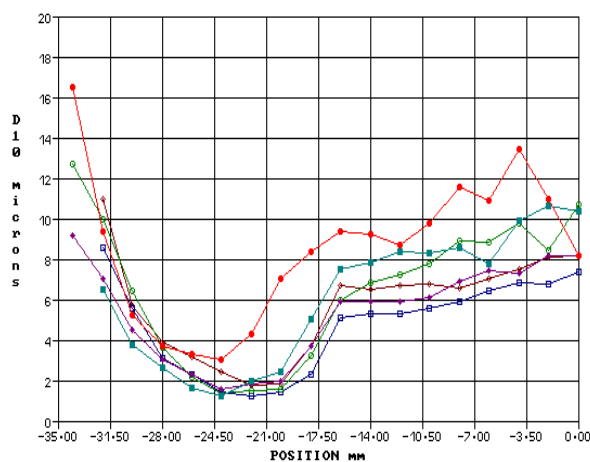
The peak in the axial velocity profile for gasoline and N-heptane occurs at  $R = 8$  and  $7$  mm respectively. As the full spray cone is bent, at an angle of nominally  $7.5^\circ$  to the injector axis, the expected offset for symmetry would be  $5$  mm. Furthermore, the sample distribution shows a dramatic increase in the sample count in the centre of the spray. To all intents and purposes these fuels produce a full cone spray after the collapse of the spray cone in the far field region downstream from the nozzle. The similarity between these two fuels is also seen in the radial velocity components where the negative flows occur during the high shear of the axial profiles at  $R = 22$  mm which correlates to the smallest drop-sizes recorded of less than  $2$  microns. The drop-size value plotted here is the arithmetic mean,  $D_{10}$  which is the most representative of the droplet evaporation rate.



**Axial Velocity**



**Radial Velocity**



**Drop-size**

**Figure 6.13: Velocity and drop-size profiles at Z = 40 mm and time 2.98 ms**

## Chapter 6 – Results: Atmospheric Bench

---

Inboard from the minima in the drop-size profiles there is a step change in the slope of the profile. This corresponds to the collapse of the inside surface of the spray cone. In this region N-heptane produces the smallest droplets, from 5 to 7  $\mu\text{m}$  followed by E25 and gasoline.

The droplets in the iso-octane and Exxsol sprays are some 2 to 3  $\mu\text{m}$  larger whereas for Stoddard the drop-size is double with up to 10  $\mu\text{m}$  diameter. However, the scatter is large due to a small sample number, but a minimum of 50, and a wide range in individual drop-sizes.

The drop-sizes in the spray periphery,  $R > 28$  mm increase dramatically from less than 4  $\mu\text{m}$  to approach 20  $\mu\text{m}$ . The axial velocity component for these droplets is virtually zero with a radial velocity component of between 10 and 15 m/s. Although Stoddard produces the largest drop-sizes it is also the slowest penetrating of the fuels.

The discussion above considered the drop-sizes for the fuels at the time of spray cone collapse. This part now considers the drop-size profiles during the development of the spray cone. Figure 6.14 complements Figure 6.10 which shows the axial velocity profiles 40 mm below the nozzle.

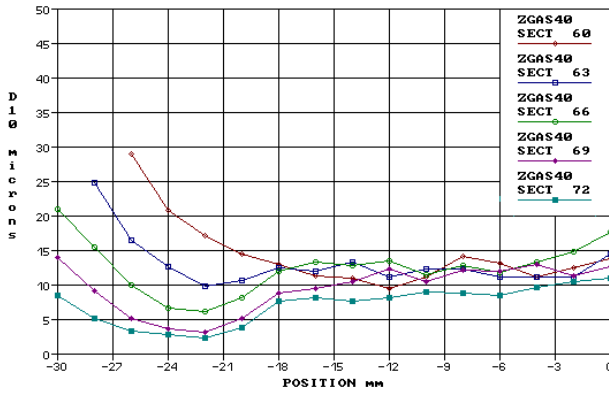
In comparing the temporal variation in drop-sizes with time for the fuels, it is convenient to sort the plots into three spatial domains,  $R = 0$  to 12 mm, 12 to 18 mm and 18 to 30 mm. The latter refers to the spray periphery and the high shear gradient of the axial velocity profiles. All fuels produce very similar droplet size profiles with a consistent decay in size with increasing time. Stoddard does produce drop-sizes that are some 10% higher than the other fuels.

In the region of the highest droplet velocities,  $R = 12$  to 18 mm there is a similar decrease in drop-size with time except for the early cone in sector 60. The high velocities also lead to a small variation in size particularly for the fuels that have low penetration rates, Stoddard, Exxsol and iso-octane.

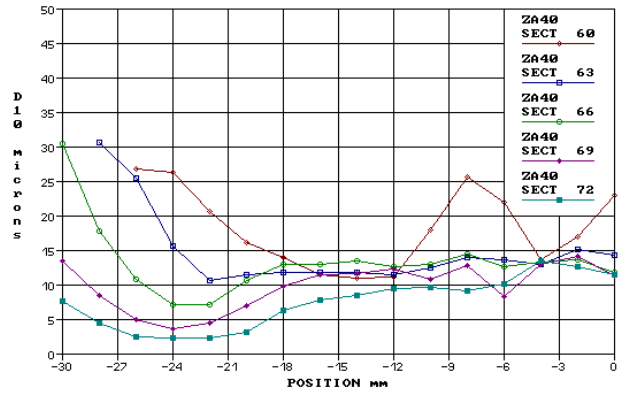
By far the largest variation in drop-sizes between the fuels can be found between the injector axis and the inside surface of the spray cone. Again, the drop-size profiles decay with time for each fuel, but, apart from gasoline each profile exhibits a definite peak centered about  $R = 8$  mm. The less penetrating the fuel spray the greater the peak drop-size. For these time sectors this region sees the transition from the pre-swirl component of the spray to the growth of the spray cone. Large mean drop-sizes here are a consequence of poor penetration and atomisation in the pre-swirl spray which results in a wide drop-size range with few small droplets.



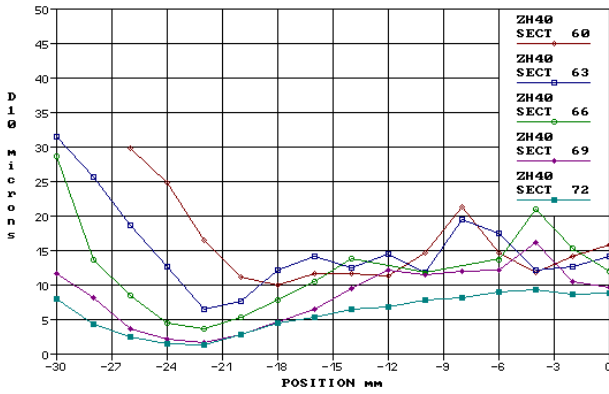
# Chapter 6 – Results: Atmospheric Bench



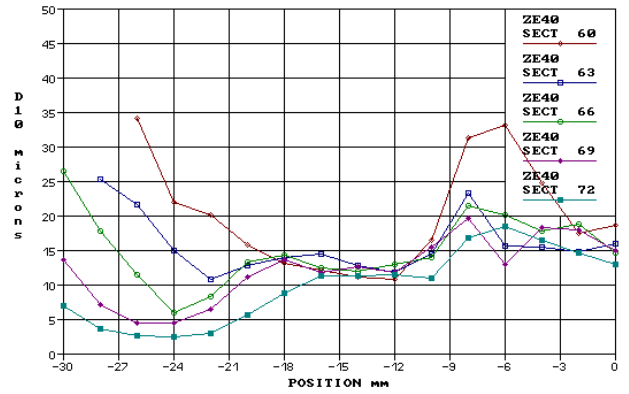
**Gasoline**



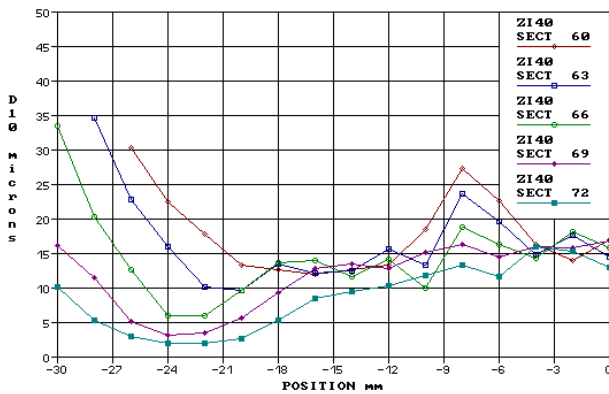
**E25**



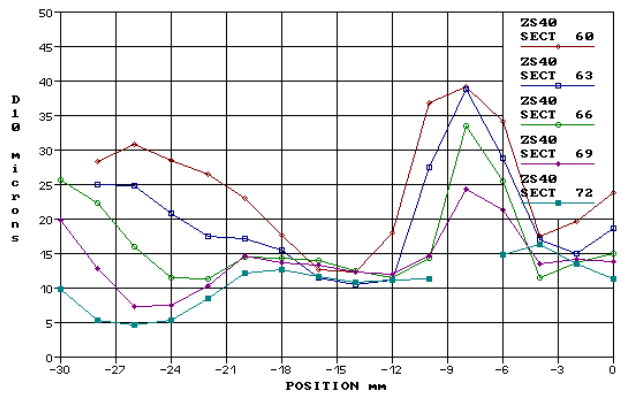
**N-Heptane**



**Exxsol**



**Iso-Octane**



**Stoddard**

**Figure 6.14: Drop-size Profiles 40 mm below the nozzle**

### 6.1.3 Summary

Mie imaging and the Phase Doppler technique have been used to determine the spray morphology and dynamics of the sprays produced by a pressure swirl GDI injector when operated with six different fuels. The need for using these fuels stems from scientific requirements to either model gasoline with a single component fuel or for safety reasons while in industry stable and well defined fuels are needed for injection calibration.

Basically N-heptane can be used to model gasoline as regards spray morphology and droplet dynamics. The same is true for iso-octane to model E25. However, for scientific purposes it would be difficult to relate data from Exxsol and Stoddard to describe a gasoline spray.

Compared with gasoline and n-heptane the other fuels produce lower axial penetration rates and higher spray cone angles. The radial penetration rates are not particularly sensitive to fuel type. The spray dynamics show that the spray cone development is essentially retarded. The axial velocities are reduced which leads to a decrease in the shear gradient, a reduction in entrainment and an increase drop-sizes. The consequences of this are the very late development of, firstly, the vortex just upstream from the leading edge of the spray cone and, secondly, production of a full cone spray after the spray cone collapses.

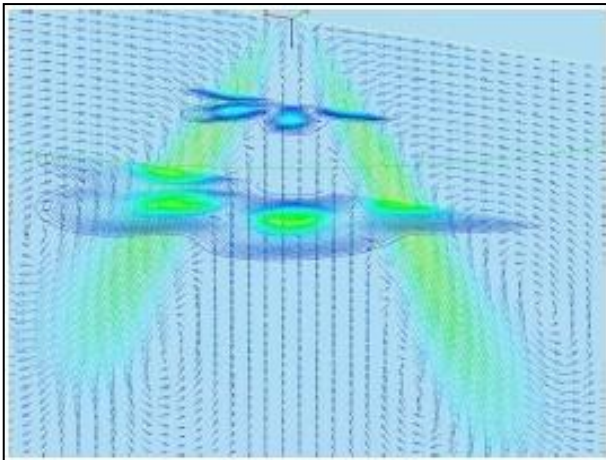
### 6.2 Multi-Hole Injector

In a horizontal plane through the spray cone of a pressure swirl injector there is a continuous ring like footprint of fuel. For the multi-hole injector the footprint has a ring of discrete islands of fuel. The interaction of each stream with the airflow is now more complex and if the stream spacing is small enough there will be stream to stream interactions.

#### 6.2.1 Plume Interactions

Dahlander et al. [124] analysed the way in which different configurations of symmetrical and asymmetrical multi-hole injectors influence the fuel distribution, air entrainment, cross flow velocity and turbulence. Their study was based on CFD only and the simulated sprays had been carefully tuned to experimental data with regards to spray formation, penetration and atomisation.

It was found, as illustrated in Figure 6.15, that for a six-hole injector, initially, air is entrained from the inside due to the vortex created by the spray front and upwards inside the spray

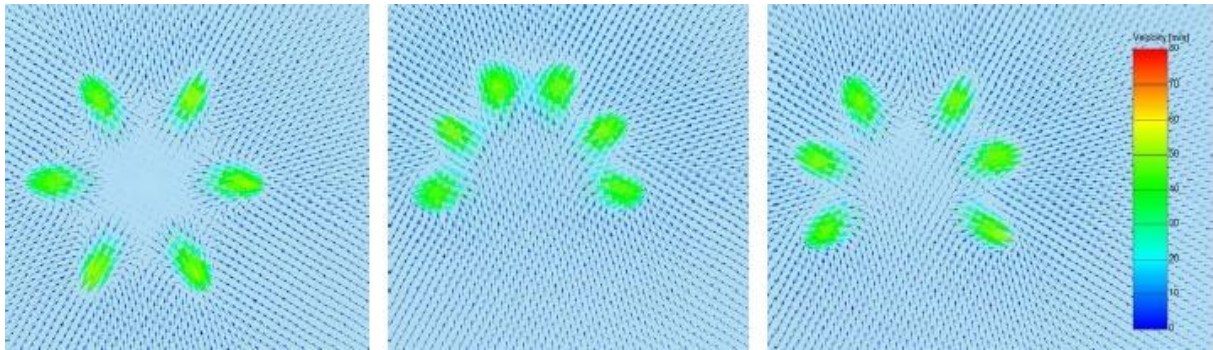


plume. As the spray develops there is a large inwardly pointing velocity field above the point of the vortex, this concludes that at this point there is no flow mechanism to transport the fuel in any other direction than towards the spray centre. This spray model's flow fields are mainly governed by single jet theory and do not link into the interaction between plumes unless located within close proximity.

**Figure 6.15: Air Entrainment due to spray front vortex**

The authors also investigated the interaction between the separate plumes of an injector. CFD was used to simulate the air motion caused by the interaction separately in the horizontal plane. In Figure 6.16, different types of asymmetrical six-hole injector were compared to a symmetrical injector with the same  $l/d$  ratio (10) and umbrella angle ( $85^\circ$ ).

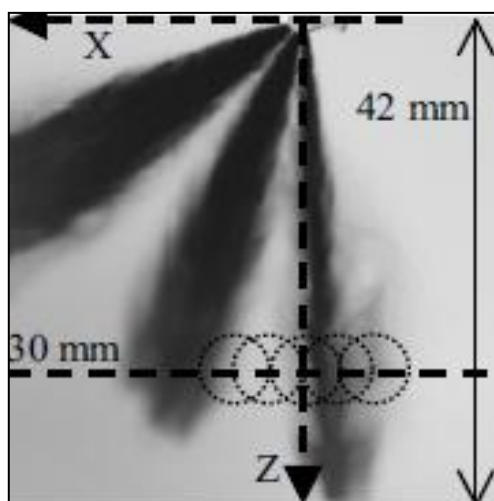
It was noticed that with the holes closer together in the asymmetric injectors the degree of plume interaction increased, as would be expected. There is a compromise to be made in the air entrainment between adjacent plumes and the air entrainment into the centre of the spray.



**Figure 6.16 – Plume interaction from multi-hole injector's spray**<sup>[124]</sup>

Blaisot, et al. [125] performed PDA, Laser Diffraction (LDG / Malvern) and Image Analysis (IMA) to characterise multi-hole injector gasoline sprays. Despite the significantly different measurement volumes, results obtained with the three techniques were shown in good agreement. The measurement volume of the PDA system was 60,000 times smaller than the LDG however both techniques showed similar trends. The laser in PDA has a Gaussian intensity distribution, which means that in the vicinity of the outer edge of the measurement volume large drops will be detected while smaller drops less so. This will mean that the amount of smaller drops will be underestimated.

The measurements were performed on a single plume of an asymmetrical multi-hole injector (see Figure 6.17) comparing results on the inner and outer edges; with and without interactions with other plumes. PDA was found to be producing higher results for drop-size on the outer edge of the plume than the other techniques. This was thought to have been due to the relatively low sample numbers passing through the measurement volume at this location. The greatest mean diameters were found at the leading edge of the spray on the outer side where conditions are favourable for fast evaporation of the smallest droplets



**Figure 6.17: Measurement location**<sup>[125]</sup>

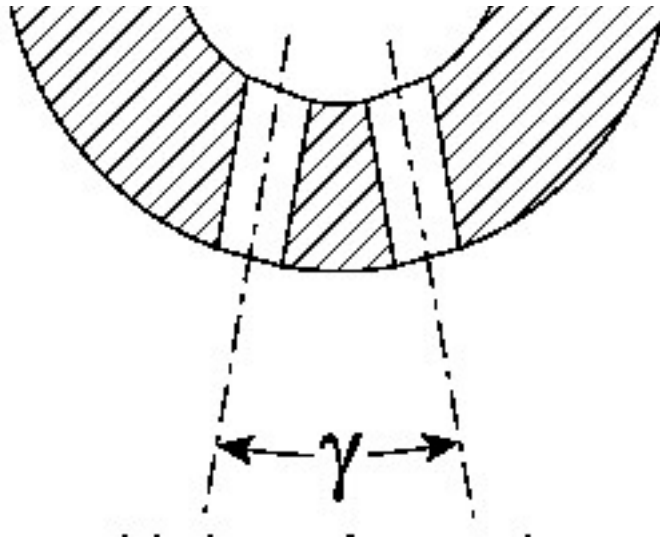
---

## Chapter 6 – Results: Atmospheric Bench

---

The axial velocity was found to decrease temporally throughout a single injection. The initial droplets are slowed by the drag in the ambient air; with the smallest droplets evaporating quickly so that only the larger drops with greater momentum are left. Later drops are protected by the initial drops creating a lower rate of evaporation of the smallest drops. This larger number of small drops has lower inertia and lower axial velocity. It was found that droplet velocities were greater on the side that is interacting with other plumes which is of particular interest to our study.

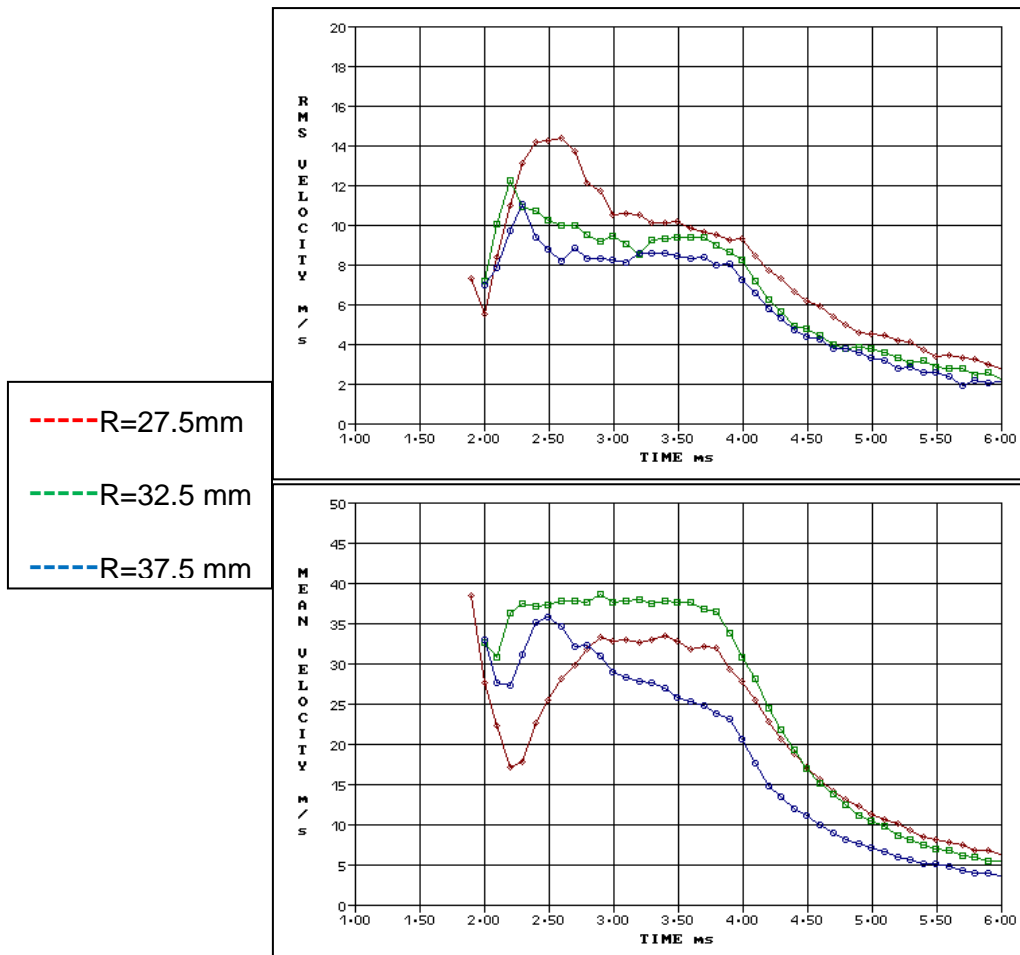
Experimental and computational studies were carried out by Sato et al. [126] to characterise the spray development and evaporation processes of multi-hole injector for direct injection spark ignition (DISI) engines. The main injector parameter to be investigated in this study was a diverging angle between neighboring two holes (see Figure 6.18). In the experimental study, the influence of the diverging angle on evaporation process of fuel spray from two-hole injector was investigated using Laser Absorption Scattering (LAS) measurement. A smaller diverging angle caused larger spray tip penetration since the momentum of the spray from one hole influences another, when two spray merge to one. Moreover, spray tip penetration decreased at certain diverging angle due to the negative pressure region between two sprays. Mechanisms behind the above spray behaviors were discussed using the detailed information on the spray and ambient gas flow fields obtained by the three dimensional computational fluid dynamics (CFD).



**Figure 6.18: Definition of Diverging Angle between Two Holes**

## Chapter 6 – Results: Atmospheric Bench

In a previous study by Wigley et al. [127] it has been found that the separate plumes within a multi-hole injector spray are not symmetrical. When assessing the spray using PDA it was found that, at a position of 5mm down the nozzle tip, the time varying axial mean velocity and RMS velocity either side of the stream central axis are different, as shown in Figure 6.19.



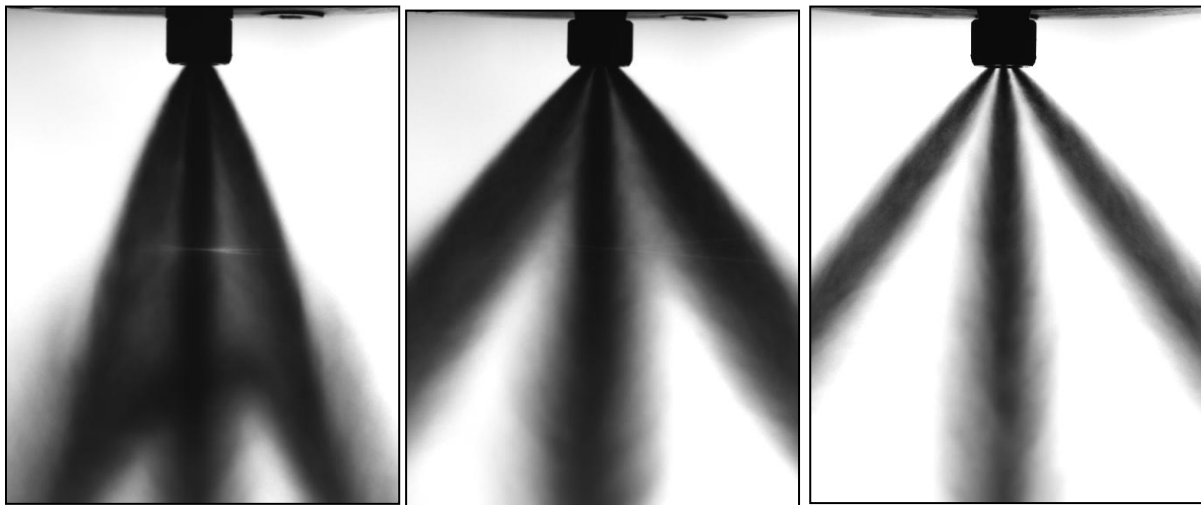
**Figure 6.19: Axial Mean and RMS Velocities of a Spray Jet<sup>[127]</sup>**

The figures of velocity profiles axially across the multi-hole spray plume show that the mean velocity is higher on the outer edge (R=37.5mm) at a time of 2.5ms after injection. The RMS velocity is shown to be lower on the outer edge of the stream than the inner at this time. The reasoning behind this must be an interaction between the inner surfaces of the plumes within a multi-hole injector generated by the exit orifice geometry.

## Chapter 6 – Results: Atmospheric Bench

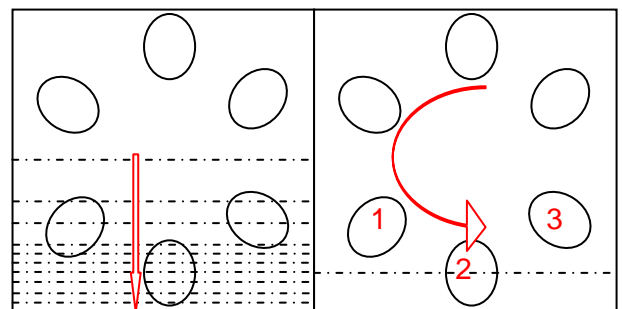
Three different injectors were used within this study of stream to stream interaction, two six-hole injectors and one three-hole injector. In order to characterise the effect of plume interaction it was not only important to investigate plumes on a single injector but to enable comparisons between the different injectors as the distance between plumes varies.

A six-hole injector with a 60 degree cone angle and one with a 90 degree cone angle were compared. The three-hole injector has a cone angle of 90 degrees; even though this specific injector has no practical engine use, it provided an example of minimal plume interaction and was used to compare with the 90°CA 6 hole injector.



**Figure 6.20: Six-hole 60 degree, six-hole 90 degree and 3 Hole 90 degree cone angle (from left to right)**

The aim of the work was to analyse the degree of interaction that occurs between separate plumes of multi-hole injectors. With PDA generating a small measurement volume and being a highly detailed measurement technique it is important that data collection is structured such that the required spray detail is achieved. Three locations below the injector nozzles were investigated; 20mm, 40mm and 60mm below the nozzle.

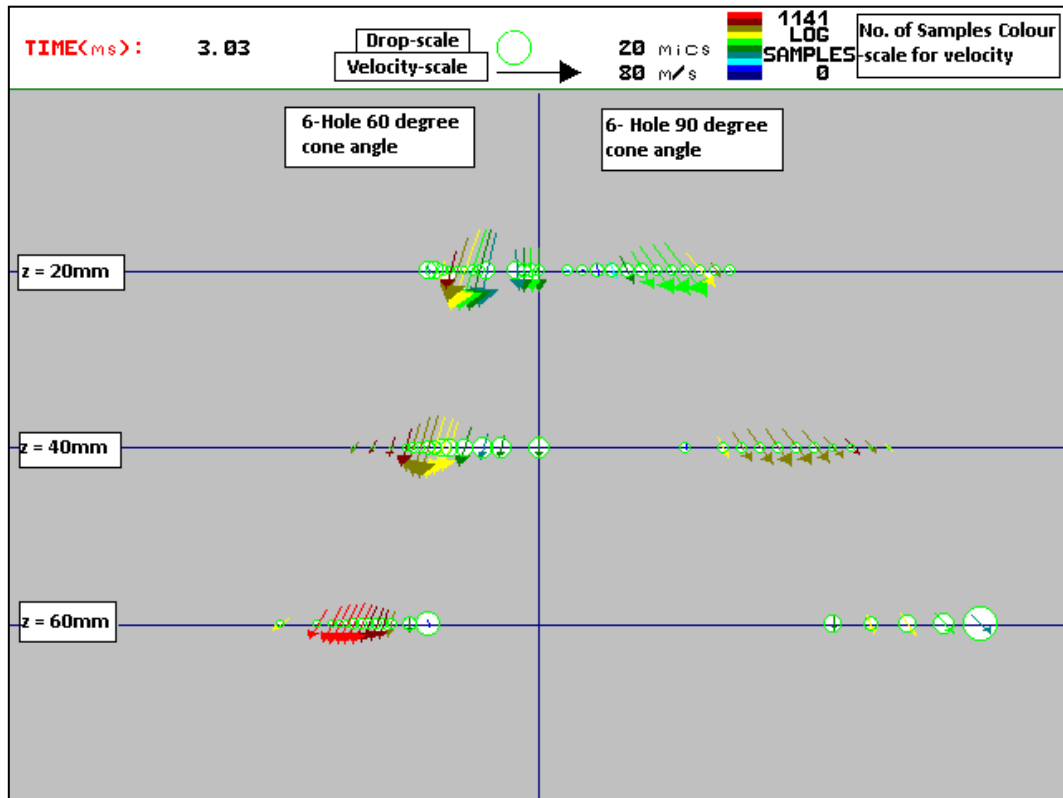


**Figure 6.21: PDA traverse scans. (Left radial scan, right circumferential scan)**

To investigate droplet size distribution and velocity across the plumes the automatic traverse was used to move the injector through the laser measurement volume. Measurements were taken over a wide range radially, extending from the centre of the spray to the outer edge of a single plume, with more measurements taken through the plume to provide greater detail.

## Chapter 6 – Results: Atmospheric Bench

Velocity vector and droplet diameter plots are used to show visually, areas of interest in both space and time from the radial traverse results. Velocity vectors show a combination of mean axial and mean radial velocities along with a scale of number of samples at each point. Droplet diameters are shown as the mean value  $D_{10}$  at each location and time sector, and scaled as circles.



**Figure 6.22** Vector plot produced from the radial scan. Arrows represent average droplet velocity, Circles represent average droplet diameters.

The detail from the centre of the spray outwards through a plume is not the only area of interest for this study; a circumferential scan at the three vertical distances is required. This is performed from the calculated middle point of a plume (defined as a combination of number of samples and shape distribution of mean axial velocities) and data are recorded at a set range of angles.

It is important that each of the injector spray temporal development is quantified in stages; initially, there is an increase in mean axial velocity as the spray is developing, this is followed by a period of steady injection and finally a gradual loss in axial velocity as the injection finishes. Data is processed from a total time period of 8ms per injection and processed into 160 data sectors comprising of 0.05ms of data. A full list of radial traverse measurement locations is shown in Table 6.3 to Table 6.5. The locations of plume centres used in circumferential scans for the three injectors at the three vertical locations are also shown.



**Table 6.3: Location of plume centre for radial scans at 20mm below injector nozzle**

Injector (z=20mm)	Initial Location	End Location	Measurement Points	Location of Plume Centre
60°CA 6-hole	0 (spray centre)	-15mm	16	-9mm
90 °CA 6-hole	0	-26mm	14	-18mm
90°CA 3-hole	0	-32mm	17	-20mm

**Table 6.4: Location of plume centre for radial scans at 40mm below injector nozzle**

Injector (z=40mm)	Initial Location	End Location	Measurement Points	Location of Plume Centre
60°CA 6-hole	0 (spray centre)	-25mm	14	-15mm
90°CA 6-hole	0	-47.5mm	15	-35mm
100°CA 3-hole	0	-47.5mm	15	-37.5mm

**Table 6.5: Location of plume centre for radial scans at 60mm below injector nozzle**

Injector (z=60mm)	Initial Location	End Location	Measurement Points	Location of Plume Centre
60°CA 6-hole	0 (spray centre)	-35mm	16	-25mm
90°CA 6-hole	0	-70mm	15	-50mm
100°CA 3-hole	0	-70mm	15	-55mm

The circumferential scans were used to provide a different aspect on plume to plume interaction compared to the radial traverse scans. The droplet size, axial and radial velocities of the drops in-between plumes are of particular interest along with drops affected by the location of nearby plumes.

Two different types of general circumferential scans were performed. For the six-hole injectors a 120 degree scan in steps of 5 degrees was the first scan. This started at the centre of one plume 1, through a middle plume 2 to the centre of a third plume 3 as shown in Figure 6.21. This gave a good range of data at a constant radius from the injector central axis. The second scan for the six-hole injectors was a 360 scan in steps of 30 degrees. This generated data at the centre of each of the six plumes and the centre point between the plumes. There was a slight change in data collection for the three-hole injector. Five measurements were taken at each plume in 5 degree steps from the plume centre (-10, -5, 0,

+5, +10°). Measurements at 30 degrees from each of the plumes were also performed to enable comparisons to be made with the six-hole 90 degree injector.

The data produced from the processing creates 8ms of data from the start of signal. There is an injection delay for electronic pre-charge of 1ms. The injector nozzle opening takes around 0.2-0.3ms with the first droplets reaching 20mm below the injector nozzle at around 1.6ms after start of signal (ASOS). The injection pulse width was 3ms with the axial velocity showing a drop from 3.6ms onwards. The steady state area of the spray is of interest within the results section of this section.

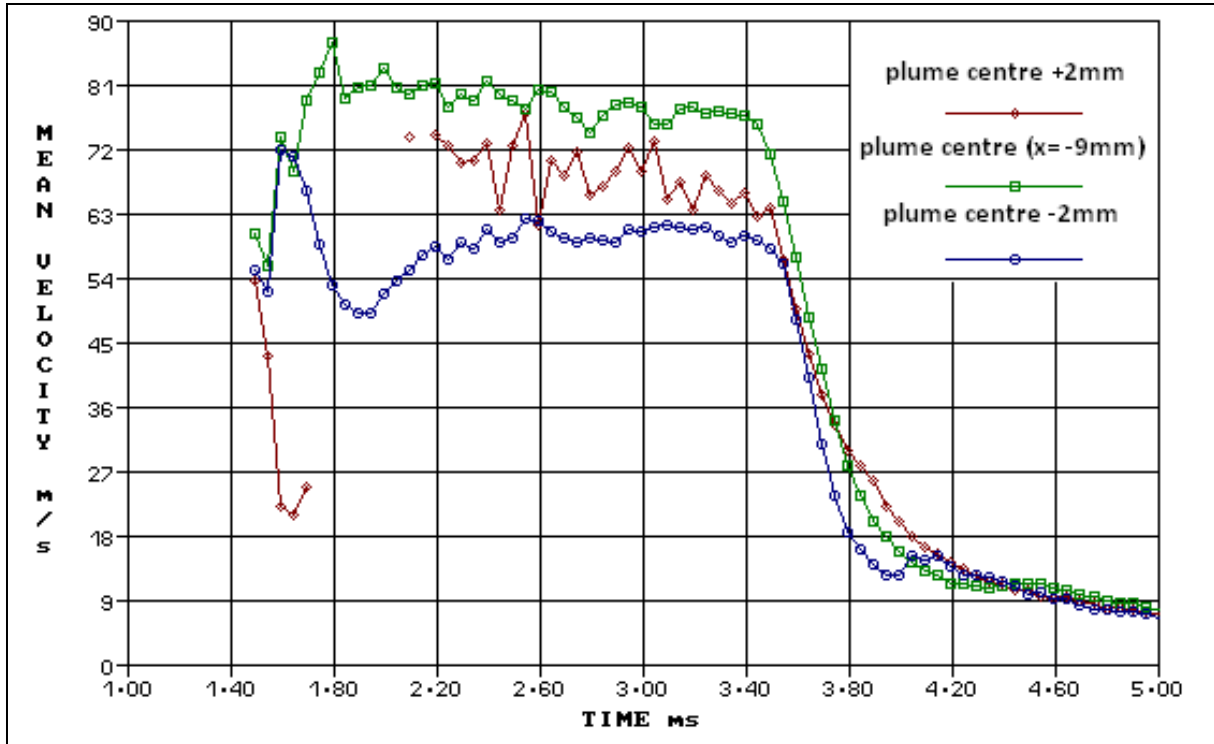
The results are broken down into the two separate sections of analysis; radial traverse scan and circumferential traverse scan. The radial traverse scan is used to discuss the effect of interactions of neighbour plumes on the inside edge of plumes compared to the outside edge. The three injectors have different distances between plumes so how great the interactions are, will be discussed. Much of the previous work on multi-hole injectors has been performed using the radial traverse scan; therefore a circumferential scan will provide a different form of analysis. The data should detail the droplets that are forced into the areas between the plumes.

### 6.2.2 Radial Traverse Scan

#### 6.2.2.1 *Droplet Velocities*

Initially it was important that the results produced by the PDA investigation of the three injectors agreed with finding in previous studies. It was mentioned in section 6.2.1 that higher mean velocities were found on the inside edge of a plume and the side of a plume towards another plume respectively. The following results show the mean axial velocities on the inside and outside edges of plumes.

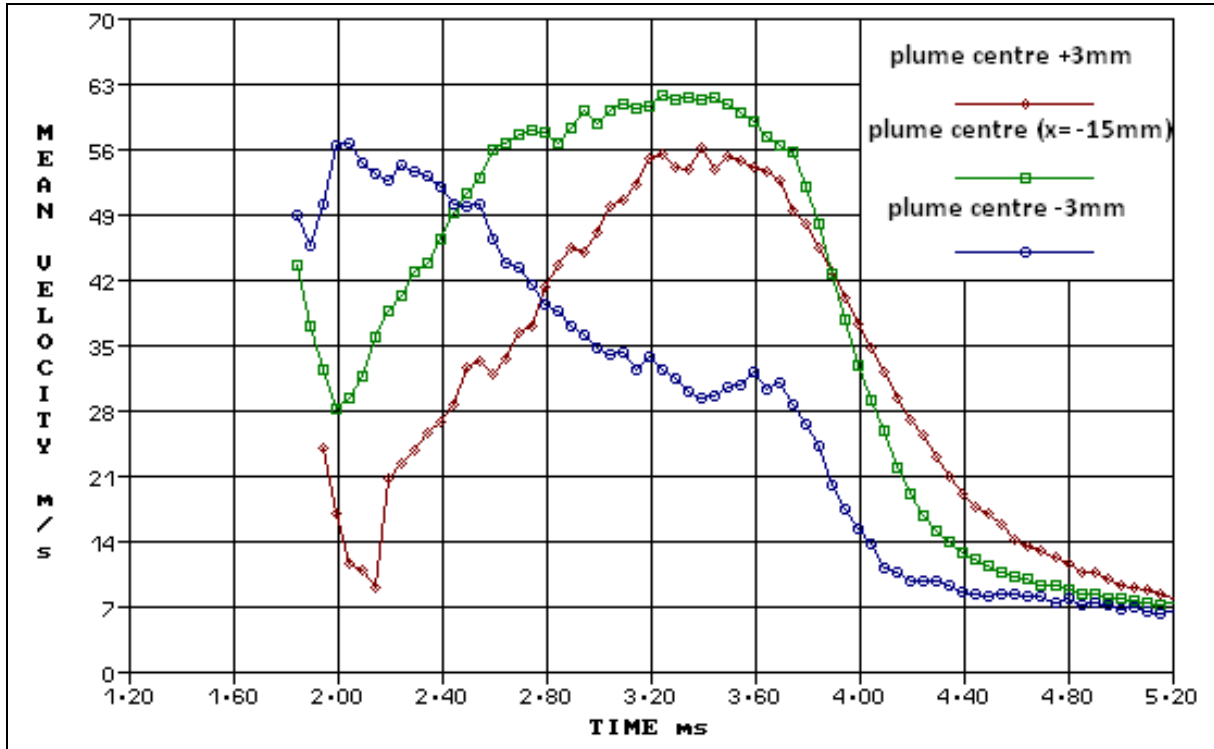
For the six-hole 60 degree CA injector, at a vertical distance of 20mm below the nozzle, the mean velocities at the plume centre and  $\pm 2$ mm (negative away from injector axis) on the inside and outside were compared. The time period on the graph was shortened to 1.0-5.0ms to highlight the steady state part of the spray in more detail.



**Figure 6.23: Mean Axial Velocity for centre, inside and outside of plume - 60°C*A* at  $z = 20\text{mm}$  - positive towards injector axis**

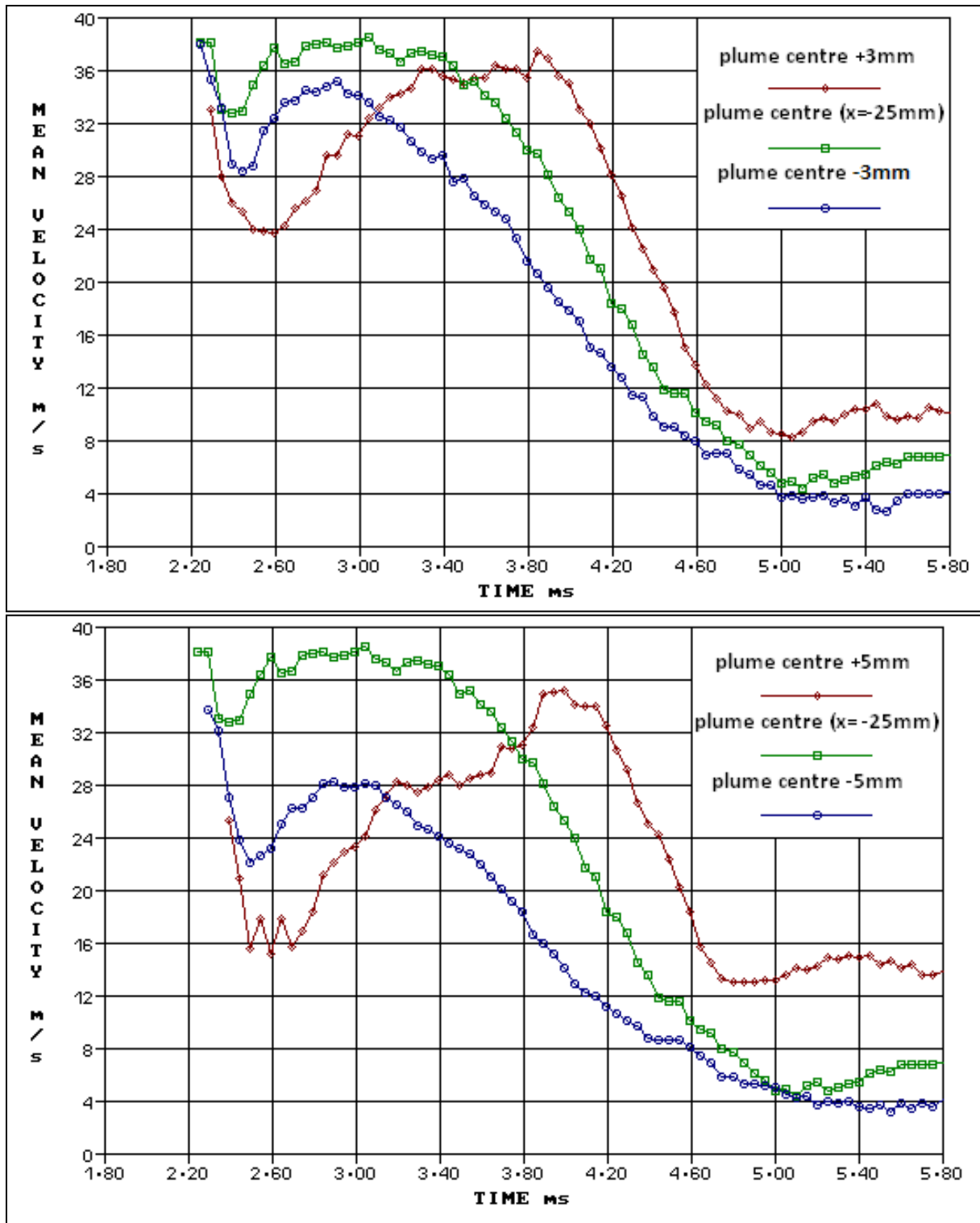
It is shown in Figure 6.23 that, at a vertical distance of 20mm from the injector nozzle, the axial velocity is higher at 2mm on the inside than on the outside of the plume. This is in agreement with results found by Blaisot, et al. [125]. (The lack of data, disruption of the red plot in Figure 6.23, is due to laser beam obscuration)

The mean axial velocity for the six-hole 60°C*A* injector at a distance of 40mm below the injector nozzle is shown in Figure 6.24. The axial velocity at the plume centre was compared to that at locations of  $\pm 3\text{mm}$  from the centre. These distances are on the outer edges of the plume with a significant number of samples to produce statistically significant data. Initially the mean axial velocity is higher on the outside of the plume but as the spray develops the velocity is higher on the inside. The initial part of the spray is affected by the ambient air while later in the spray plume, interaction should occur if present at all.



**Figure 6.24 Mean Axial Velocity for centre, inside and outside of plume – 60°C*A* at z = 40mm - positive towards injector axis**

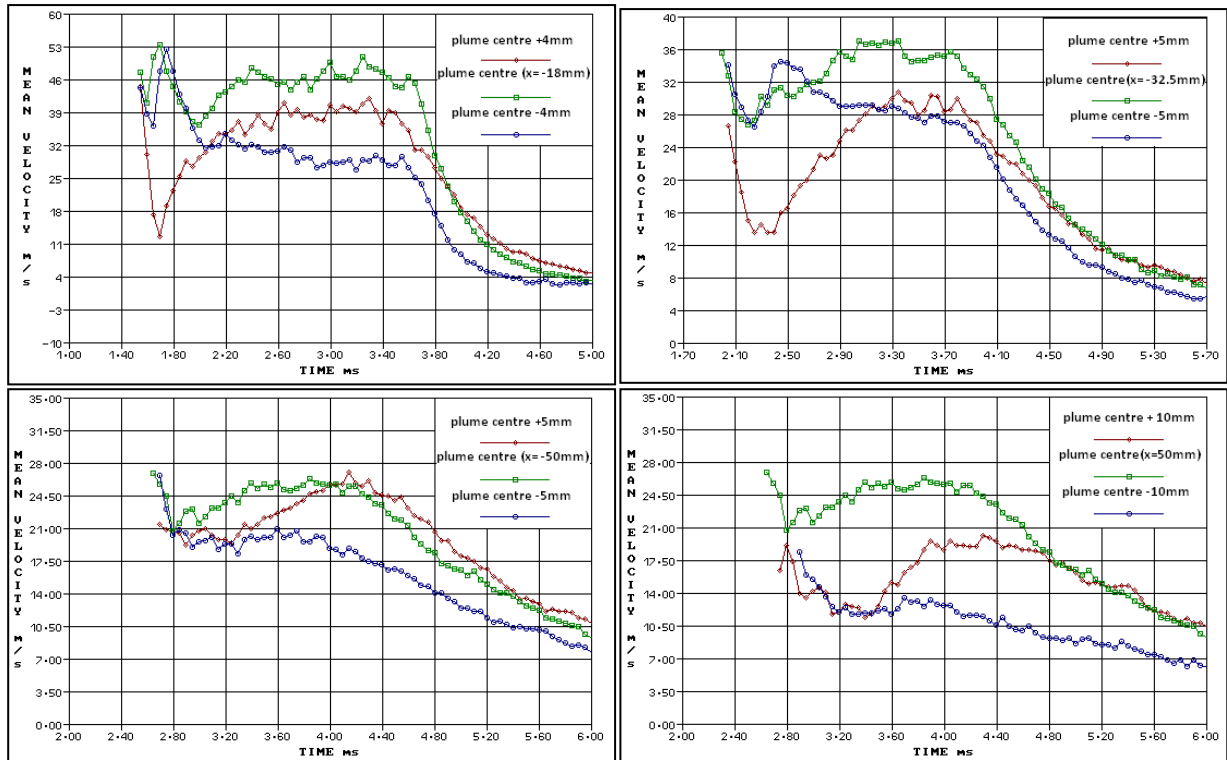
At 60mm below the injector nozzle the spray is more dispersed. It can be difficult to describe the exact point of the inside and outside of the plumes. For this case two locations are used to analyse the axial velocities,  $\pm 3\text{mm}$  and  $\pm 5\text{mm}$ . It can be seen in Figure 6.25 that the trend of axial velocities seen at  $z=40\text{mm}$  is similar at a distance of 60mm from the injector nozzle. The interesting feature within Figure 6.25 is how similar the two graphs are despite the different location within the spray. For this injector (six-hole 60°C*A*) it can be seen that initially the axially velocity is greater on the outer edge of the plume, but as the spray develops there is a significant increase of axial velocity on the inner edge of the plume. The end of injection is at approximately 3.6ms ASOS and this can be seen with the drop in axial velocities after this time at the three distances from the nozzle. Away from the nozzle a slower reduction in axial velocity can be observed as the droplets momentum are lower and the plume is greatly dispersed. An interesting phenomenon at  $z=60\text{mm}$  is that as the injection is ending the axial velocity on the inside of the plume is still increasing until around 0.5ms later. Also the velocity on the inside of the plume does not reach that of the plume centreline even at 5.8ms ASOS.



**Figure 6.25 Mean Axial Velocity for centre, inside and outside of plume – 60°C<sub>A</sub> at z = 60mm (±3mm top, ±5mm bottom) - positive towards injector axis**

## Chapter 6 – Results: Atmospheric Bench

The same figures are produced for the six-hole 90°CA and three-hole 90°CA injectors. It was important to establish whether the difference in axial velocities was linked to the injector nozzle design or whether nearby plumes affected droplet velocities. The results for the 90°CA six-hole injector are shown in Figure 6.26:

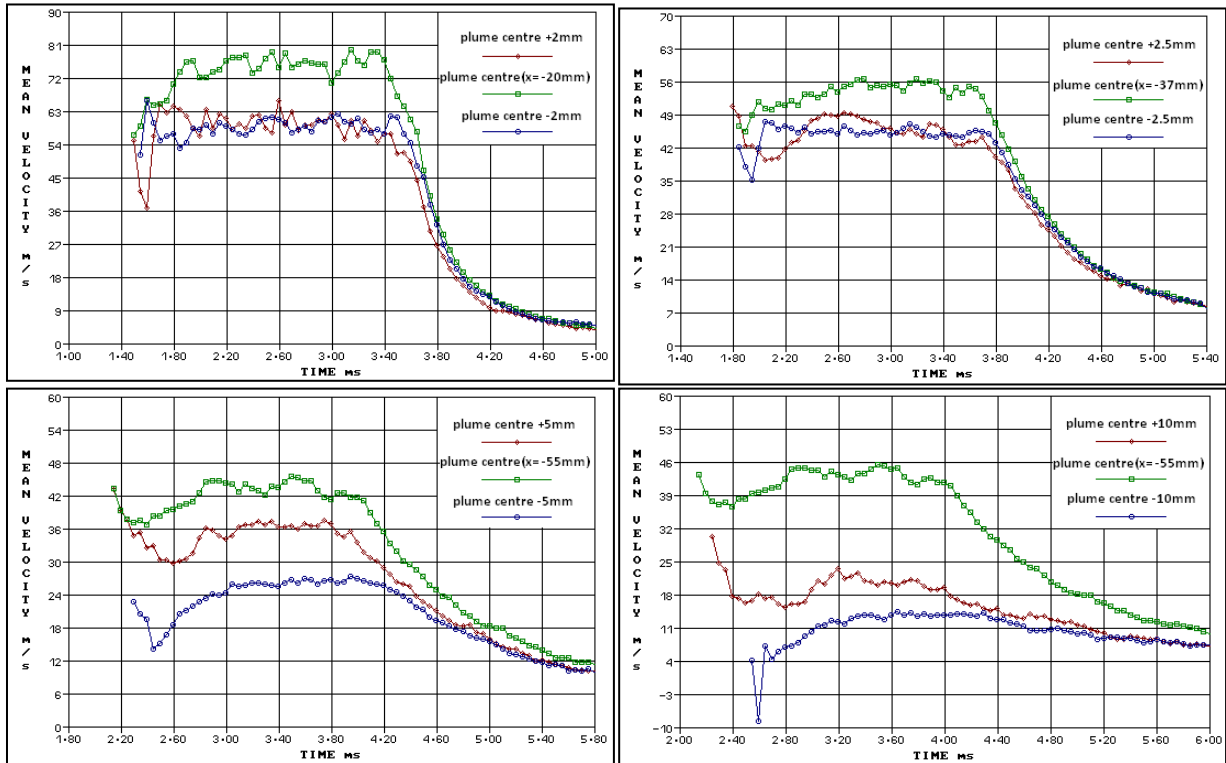


**Figure 6.26 Mean Axial Velocities for 6-hole 90°CA, top left z=20mm, ±4mm, top right z=40, ±5mm, bottom left z=60, ±5mm, bottom right z=60mm, ±10mm**

Similar results are obtained with the 90°CA injector with an initial higher velocity seen on the outer edge of the plume but as the spray develops into the steady part of injection there is once again a significant cross-over in velocities. It does appear, however, that the increase in velocity on the inner edge of the plumes on the 90°CA injector is not as great as the 60°CA at 40mm and 60mm below the nozzle. It is of interest that Figure 6.23 and Figure 6.26 (top left z=20mm) show similar profiles with velocity difference between the inside and outside staying relatively constant across the main part of the spray. There is no continued increase in axial velocity of the droplets on the inside of the spray beyond the end of injection. This shows a contrast in behaviour between the two six-hole injectors with different cone angles.

## Chapter 6 – Results: Atmospheric Bench

As the three-hole injector has a greater distance between plumes than the six-hole injectors the results will be useful to make comparisons. Graphs at the same vertical heights are shown in Figure 6.27:



**Figure 6.27 Mean Axial Velocities for 3-hole 90°CA, top left  $z=20\text{mm}$ ,  $\pm 2\text{mm}$ , top right  $z=40\text{mm}$ ,  $\pm 2.5\text{mm}$ , bottom left  $z=60\text{mm}$ ,  $\pm 5\text{mm}$ , bottom right  $z=60\text{mm}$ ,  $\pm 10\text{mm}$**

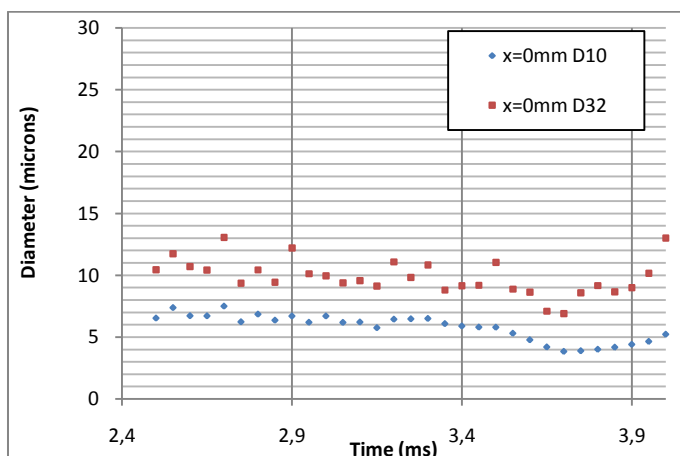
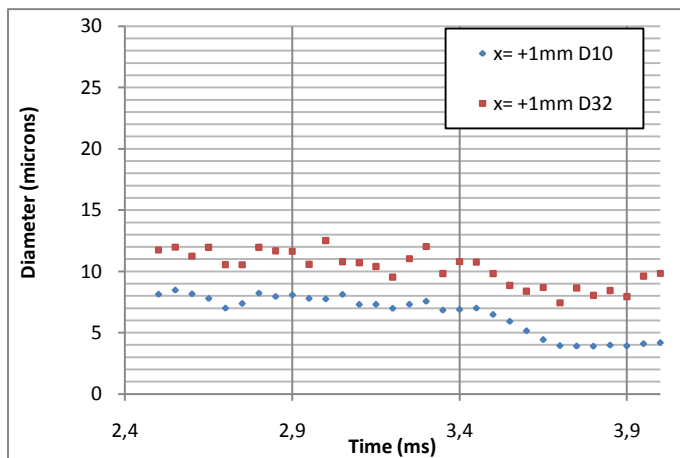
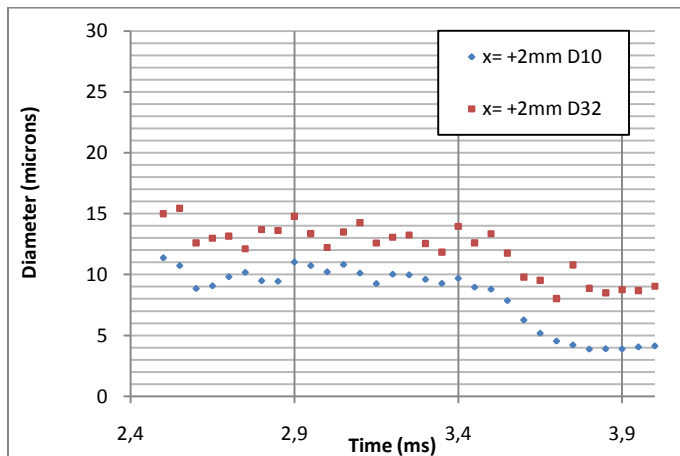
At 20mm and 40mm below the injector nozzle, the axial velocities on the inside and outside of the plume are comparable. This shows that the plumes from this injector are symmetrical around their axis and with a relatively large distance between plumes this agrees with the plume interaction theory. There is a difference between the velocities on the inside and outside of the plume at  $z=60\text{mm}$ . However, with the results seen at 20mm and 40mm, it would suggest that this is due to the centreline reading being taken at an incorrect location possibly 1 or 2mm slightly towards the outside of the plume (this would create higher results on inside than the outside as in Figure 6.26).

By comparing the mean axial velocity from data sectors of 0.05ms it has been shown that there is a significant difference in results for the velocity on the inside and outside of the plume. When the cone angle of a multi-hole injector is reduced the separate plumes are in closer proximity. The results from the three-hole injector show that this proximity increases the axial velocity found on the inside of plumes.

## Chapter 6 – Results: Atmospheric Bench

### 6.2.2.2 Drop-Size

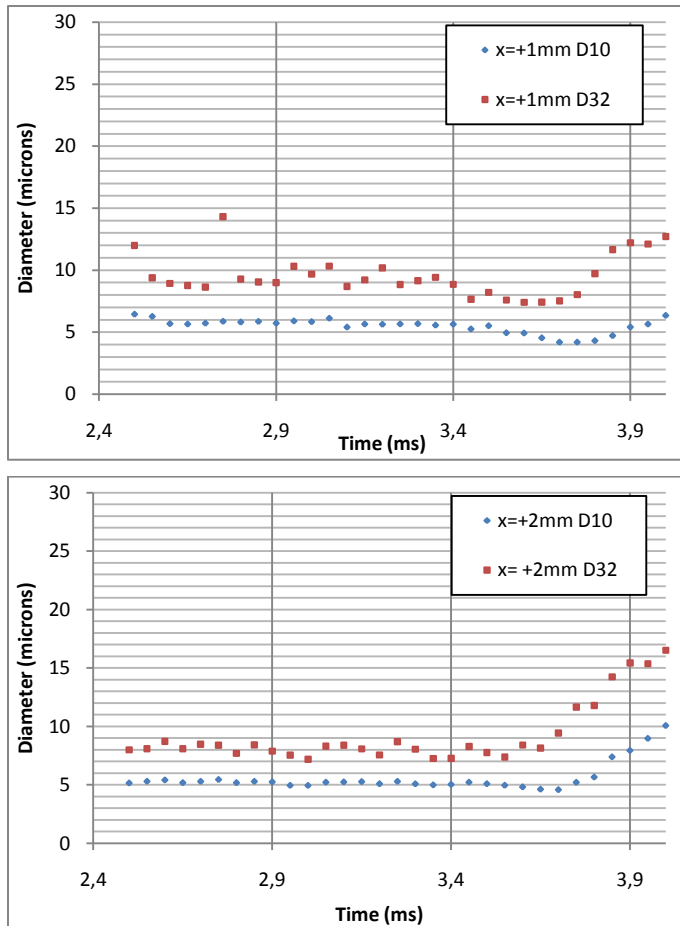
Within the PDA measurements two different drop-size results are produced, Sauter mean,  $D_{32}$ , and arithmetic mean,  $D_{10}$ . They are both used to measure the droplet diameter across the axial scan of the three injectors. As a difference in axial velocity is seen on either side of the plume this paragraph investigates whether the average drop-size follows a similar trend i.e. high drop-sizes correlate with higher velocities. The six-hole 60°CA injector results are shown below. If there is a trend between the velocity difference and the droplet size then it should be shown in greatest detail in the 60°CA injector results.



At the location closest to the nozzle ( $z=20\text{mm}$ ) five points were used for average drop-size measurements, the plume centreline and two 1mm steps either side. The time period of interest for the droplet diameter averages is the steady state part of the injection. The results are shown from 2.5ms to 4.0ms with 2.5ms-3.5ms being the timing before the injection ends. The inside of the plume is at a distance of  $x=+2\text{mm}$  from the plume centre. The droplet average diameters for the range 2.5-3.5ms are reasonably constant with the values for  $D_{10}$  and  $D_{32}$  being approximately  $10\mu\text{m}$  and  $14\mu\text{m}$  respectively. When at +1mm from the plume centre there is a slight reduction in droplet diameter average values from the position 1mm to the inside. This is shown in both  $D_{10}$  and  $D_{32}$  as across the range 2.5 to 3.5ms the diameter values are approximately  $8\mu\text{m}$  and  $11\mu\text{m}$ . There is a further decrease in the droplet diameter results at the central point of the plume ( $x=0$ ) from those on the inside edge. This is a significant trend as it shows that from the plume centre inwards the average drop diameter increases.

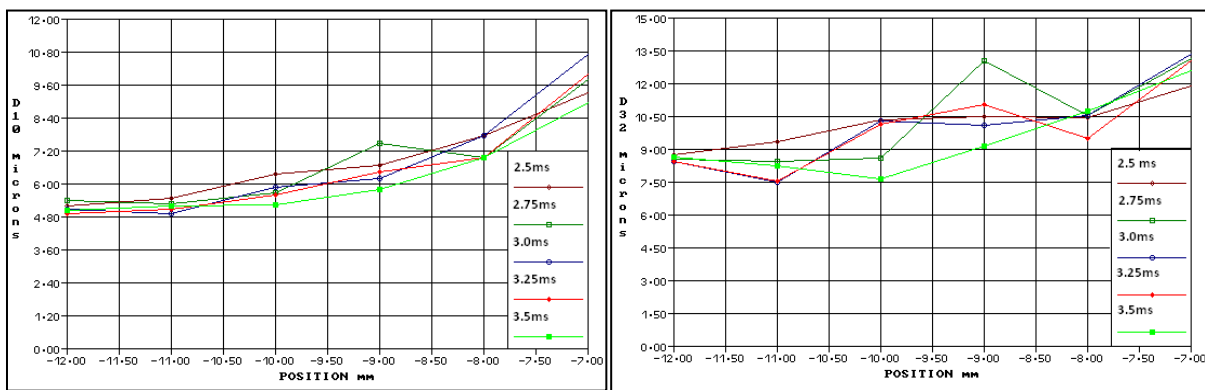


## Chapter 6 – Results: Atmospheric Bench



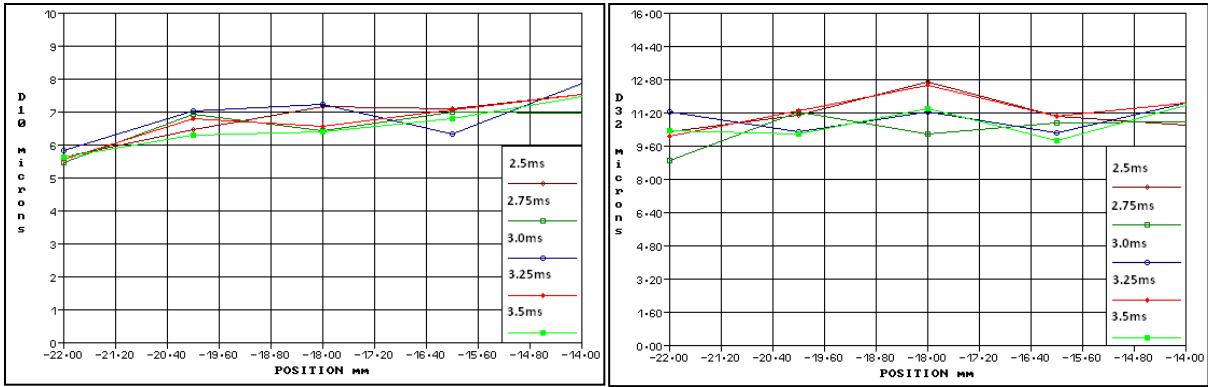
**Figure 6.28: D10 and D32 at +2, +1, 0, -1, -2mm from plume axis (negative away from spray centre line) - 6-hole 60°CA injector at z=20mm**

On the outside of the plume, at a distance of 1mm from the plume centre, the average droplet diameter  $D_{10}$  and  $D_{32}$  are approximately  $6\mu\text{m}$  and  $9\mu\text{m}$  respectively. This is lower than the droplet diameter measured at the plume centre. On the outside edge of the plume ( $x=+2\text{mm}$ ), where the spray is in contact with the ambient conditions the diameters across the 2.5-3.5ms range are constant. They are  $5\mu\text{m}$  for  $D_{10}$  and approximately  $8\mu\text{m}$  for  $D_{32}$ . This is again lower than at  $x=+1\text{mm}$  and means that the trend continues throughout the full cross section of the plume. The highest droplet diameters for the 60 degree cone angle injector at a vertical height of 20mm below the nozzle are found on the inside edge of the plume, decreasing across the plume.

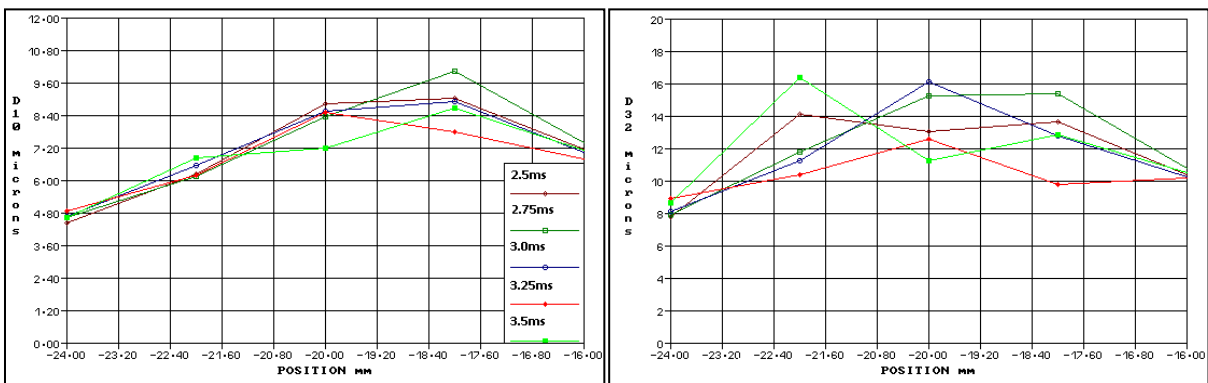


**Figure 6.29: Droplet size against axial position for 6-hole 60°CA injector at z=20mm 2.5 till 3.5ms ASOS - left  $D_{10}$  and right  $D_{32}$**

The drop-size trend for both  $D_{10}$  and  $D_{32}$  is shown against radial position in Figure 6.29. To establish whether this trend was linked to plume interaction due to the localised plumes, drop-size for the other injectors and at distances of 40mm and 60mm were required.



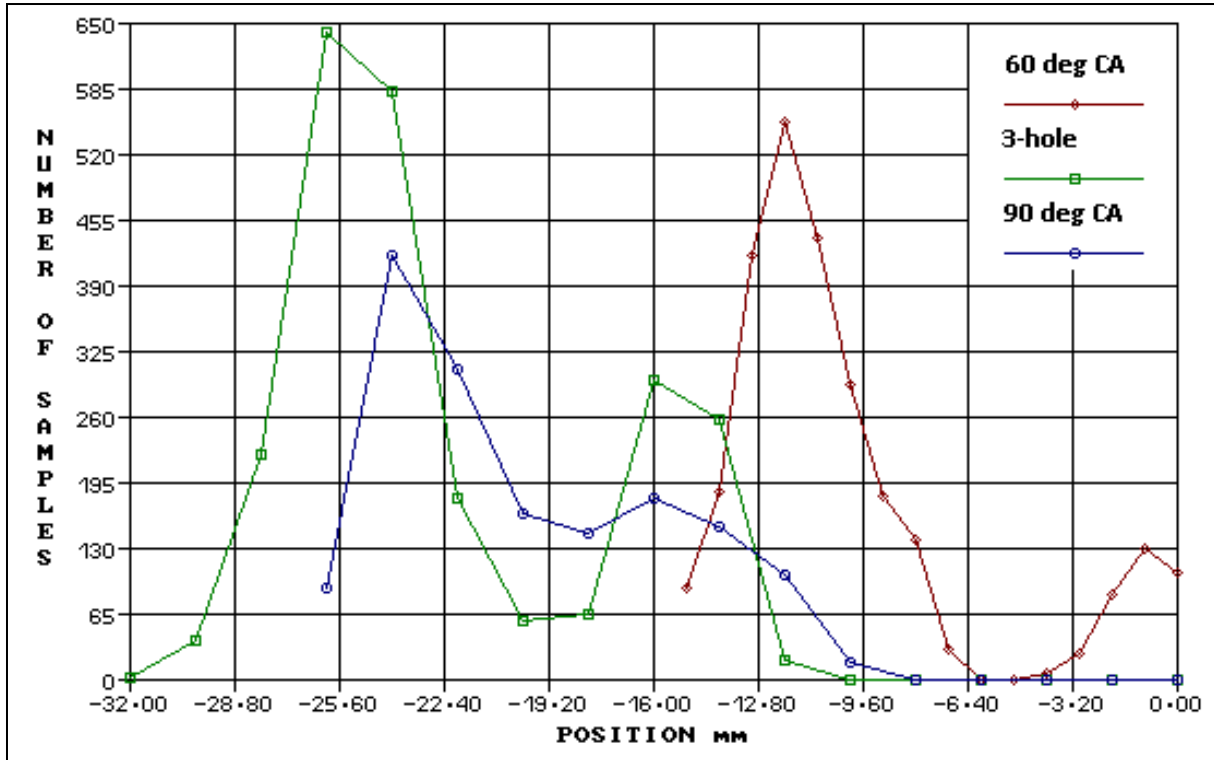
**Figure 6.30: Droplet size against axial position for 6-hole 90°CA injector at z=20mm  
2.5 till 3.5ms ASOS - left  $D_{10}$  and right  $D_{32}$**



**Figure 6.31: Droplet size against axial position for 3-hole 90°CA injector at z=20mm  
2.5 till 3.5ms ASOS - left  $D_{10}$  and right  $D_{32}$**

Using the results in Figure 6.30 the droplet size through the section of a plume, from the 90°CA injector at z=20mm and for the time interval 2.5 till 3.5ms ASOS, can be quantified. The increase in diameter for  $D_{10}$  and  $D_{32}$  from the outside of the plume to the inside shown for the 60°CA injector is not shown in Figure 6.30. The values of average  $D_{32}$  is relatively constant across the plume with a slight increase in average diameter from outside to inside for the arithmetic mean ( $D_{10}$ ).

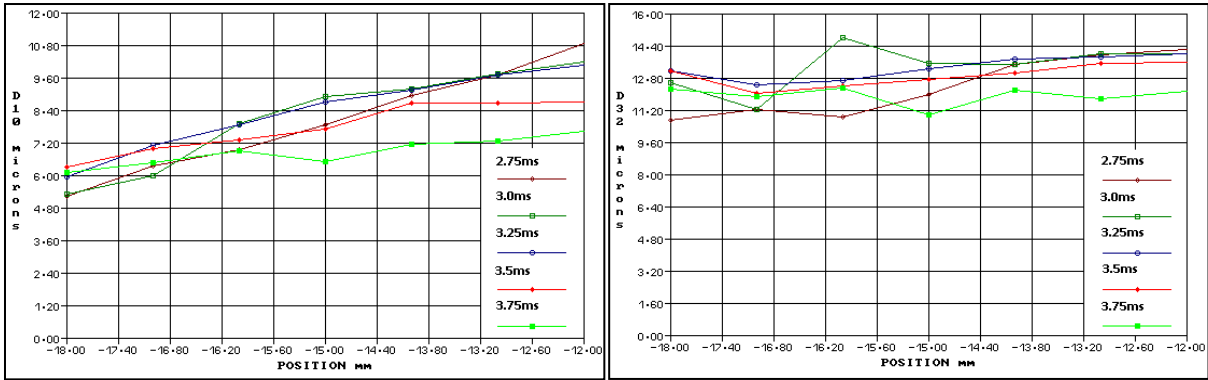
The three-hole 90°CA injector results at 20mm below the injector nozzle are shown in Figure 6.31. The results of diameter across the plume axially for the three-hole injector are different to the six-hole injectors. The peak average droplet diameter is at the plume centre with lower values found on the inside and outside. When checking the sample numbers (see Figure 6.32) against axial position for this injector there are much lower samples at this location. This suggests that the spray is very dense in the centre of the plumes for the three-hole injector causing less samples to be recorded due to attenuation. This may explain the higher droplet diameters with less of the smaller droplets being processed.



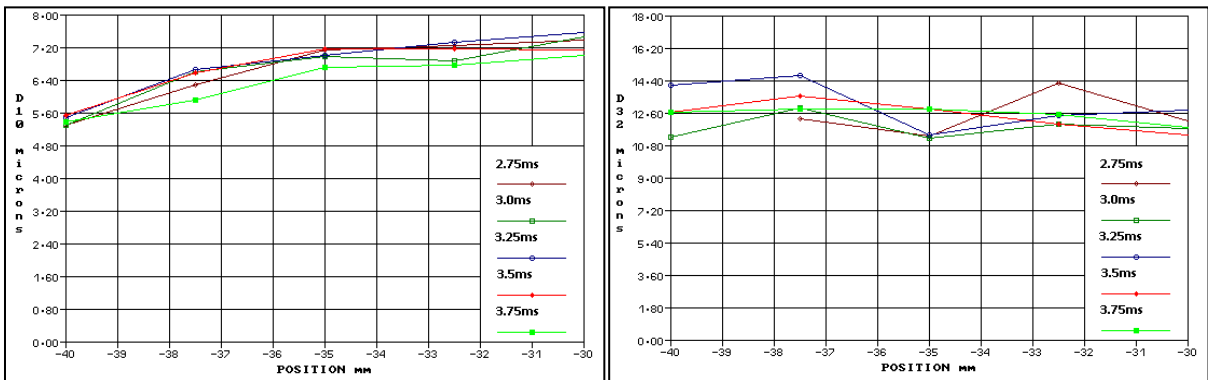
**Figure 6.32: Sample number at z=20mm for the three injectors**

To analyse the droplet diameter for each of the injectors at 40mm from the nozzle Figure 6.33 to Figure 6.35 are used. It is of interest that the results for droplet diameters across the plume cross-section are similar to those found at z=20mm. The 60°CA injector has a clear trend across the plume with average droplet sizes increasing from the outside towards the inside of the injector. The 6-hole 90°CA injector shows a fairly constant trend for D32 but an increasing D10 (from approx. 5.5 to 7.2µm) across the plume. However, the rate of diameter increase is not as high as for the 60°CA injector. As seen at 20mm the droplet size for the 3-hole 90°CA shows relative symmetry on either side of the plume, suggesting this injector plume is behaving as a single plume (i.e. no interaction).

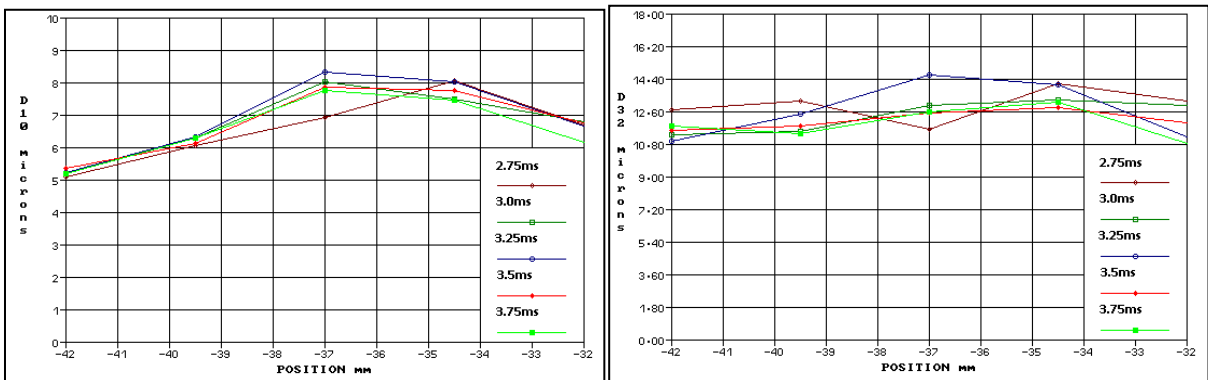
As seen on Figure 6.36 to Figure 6.38, at a distance of 60mm from the injector nozzle the separate plume are fairly well dispersed. Despite this it is interesting to find that the droplet diameter distributions across the plumes are similar to those found closer to the nozzle. The 60° CA injector still maintains the higher droplet diameters on the inside of the spray just as the injector maintained the higher axial velocities on the inside (see paragraph 6.5.1.1). The droplet diameters for the 6-hole 90°CA and the 3-hole 90°CA injector are consistent across the plume (for the 6-hole 90° CA angle larger droplets are observed at 3ms ASOS as it is early within the spray; the larger droplets have greater momentum and reach the measurement volume sooner).



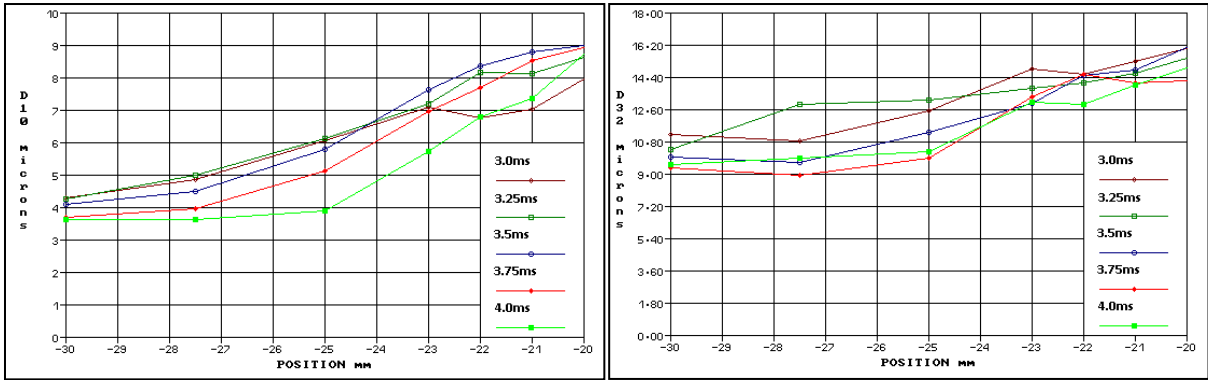
**Figure 6.33: Droplet size against axial position for 6-hole 60°CA injector at z=40mm  
2.75 till 3.75ms ASOS - left D<sub>10</sub> and right D<sub>32</sub>**



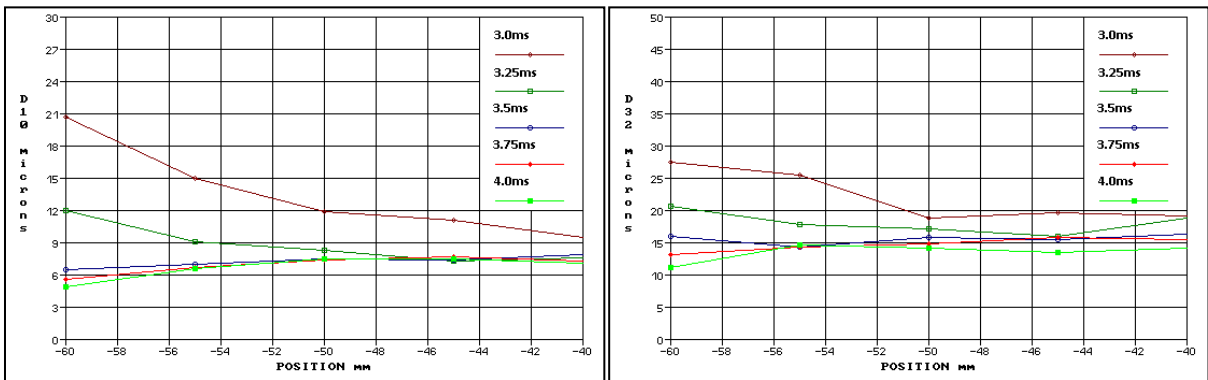
**Figure 6.34: Droplet size against axial position for 6-hole 90°CA injector at z=40mm  
2.75 till 3.75ms ASOS - left D<sub>10</sub> and right D<sub>32</sub>**



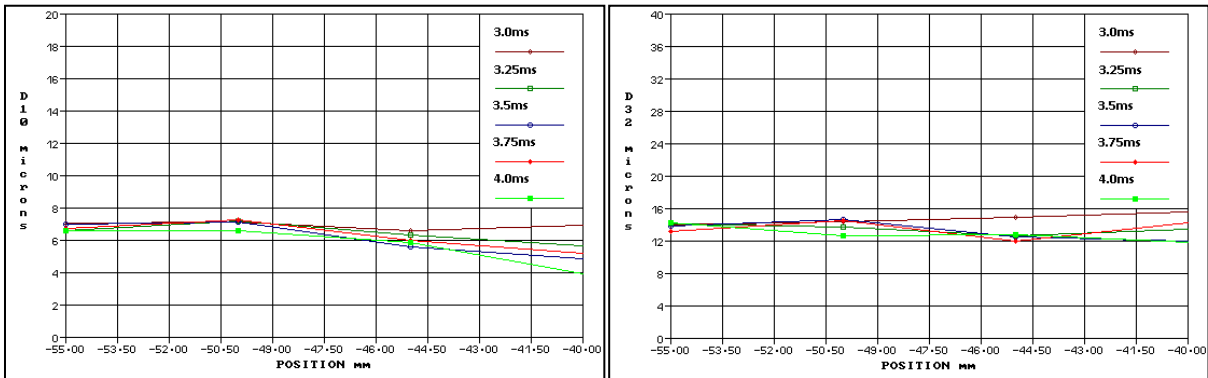
**Figure 6.35: Droplet size against axial position for 3-hole 90°CA injector at z=40mm  
2.75 till 3.75ms ASOS - left D<sub>10</sub> and right D<sub>32</sub>**



**Figure 6.36: Droplet size against axial position for 6-hole 60°CA injector at z=60mm  
3 till 4ms ASOS - left  $D_{10}$  and right  $D_{32}$**



**Figure 6.37: Droplet size against axial position for 6-hole 90°CA injector at z=60mm  
3 till 4ms ASOS - left  $D_{10}$  and right  $D_{32}$**



**Figure 6.38: Droplet size against axial position for 3-hole 90°CA injector at z=60mm  
3 till 4ms ASOS - left  $D_{10}$  and right  $D_{32}$**

### 6.2.2.3 Summary

The two previous sections have produced results that show consistency within the injector spray plumes. The axial velocity showed increases across the plume for both six-hole injectors with higher values found on the inside of the spray. The 60°CA injector showed a greater increase in velocities towards the inside than the 90°CA injector. This suggests that the cone angle affects the droplet axial velocities with a smaller cone angle creating a greater increase in velocities on the inside. The three-hole injector showed no difference in axial velocity on the inside and outside of the plume.

In terms of droplet diameters the 60°CA injector has on average larger droplets on the inside decreasing in size across the plume. Once again the 6-hole 90°CA injector shows the same trend at  $z=20\text{mm}$  with a smaller difference. This trend continues for the 60°CA injector at greater distances from the nozzle while the other injectors show a consistent droplet diameter across the plume.

The droplet diameter and axial velocity results suggest that the smaller the cone angle, and therefore closer the location of nearby plumes within multi-hole injectors, the higher the axial velocities and larger the droplets are found on the inside of plumes.

### 6.2.3 Circumferential Traverse Scan

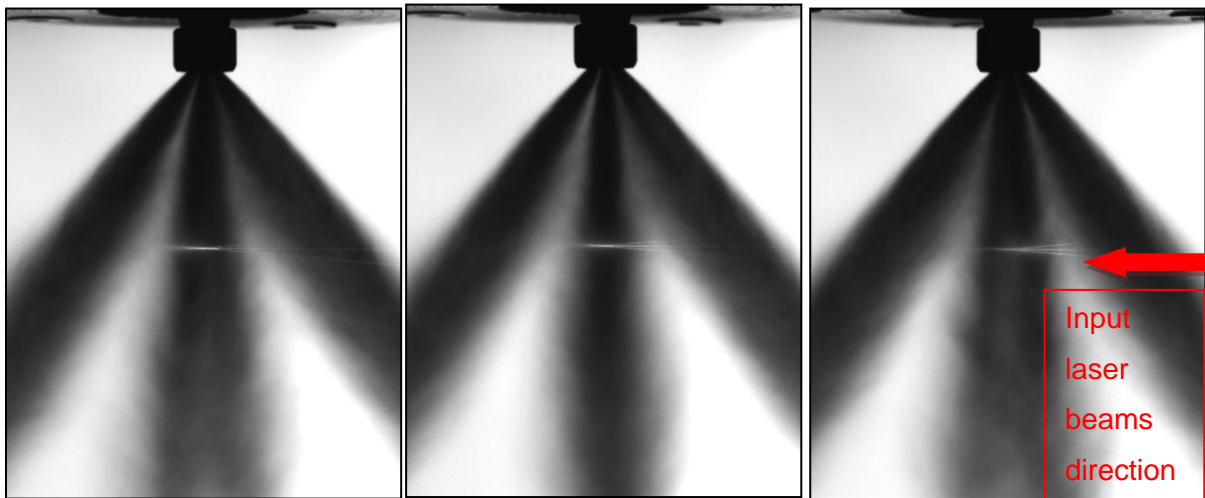
In addition to the radial traverse scans which are commonly encountered in the literature concerning PDA studies, the circumferential scans were used to provide a novel aspect on plume to plume interaction. The droplet size, axial and radial velocities of the drops in-between plumes are of particular interest along with drops affected by the location of nearby plumes.

As detailed in Table 6.3 to Table 6.5 the circumferential scans were performed from the point of plume centre at different locations around the injector. As the plume centres are at different distances from the central axis then the radial scans will have differing circumferences. It is important to establish the circumferential distance from the plume centre that a certain degree of turn creates. The total circumferential distances and the distance from a plume centre that a 5 degree or 30 degree turn creates are shown Table 6.6.

**Table 6.6: Distance moved during circumferential scan**

	Z(mm)	Plume centre (mm)	Circumferential distance (mm)	5° distance (mm)	30° distance (mm)
6- Hole 60 degree	20	-9	56.5	0.78	4.71
	40	-15	94.2	1.31	7.85
	60	-25	157.1	2.18	13.09
6- Hole 90 Degree	20	-18	113.1	1.57	9.43
	40	-35	220	3.06	18.33
	60	-50	314	4.36	26.2
3- Hole 100 Degree	20	-20	125.7	1.75	10.48
	40	-37.5	235.6	3.27	19.63
	60	-55	345.6	4.8	28.8

One factor that may affect the results processed within the circumferential scan is the variations dependant on which side of the plume the radial scan is performed. Suppose a 5 degree turn from the centre of the plume in either direction is compared. In one direction the laser beams reach the measurement volume with little disruption or attenuation from the injector spray as the plume beyond the measurement volume. With a turn of 5 degree from the plume centre in the opposite direction, the laser will pass through the injector plume before the measurement volume. This will reduce the amount of light so biasing detection towards larger droplets and reduce the number of samples processed.



**Figure 6.39: Three images from the circumferential scan - plume behind measurement volume (left) - plume in the centre of measurement volume (middle) - plume in front of measurement volume (right)**

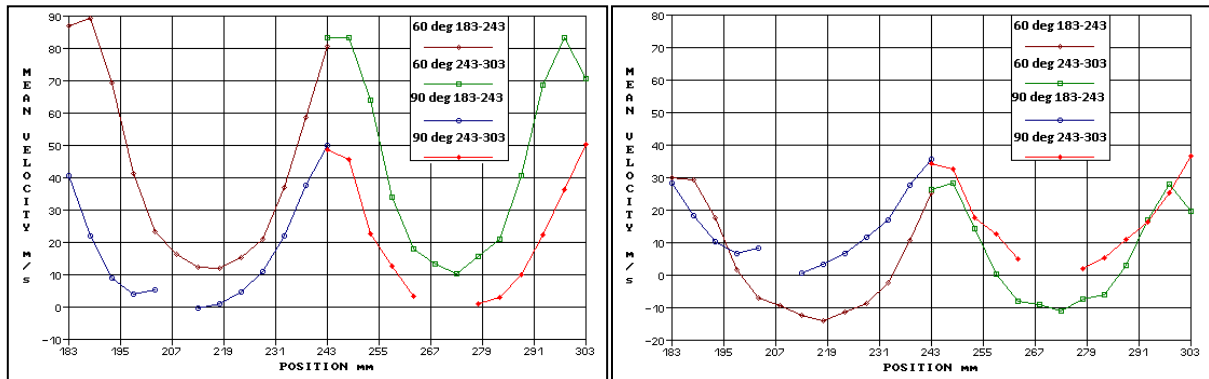
It can be seen in Figure 6.39 that there is a greater amount of visible light seen in the image on the left than the right. This shows that more droplets will be detected with the plume behind the measurement volume. For the result analysis it is important to note that a positive turn moves the plume in front of the measurement volume and vice-versa for a negative turn.

Droplet velocity and diameter around the injector at a constant radial distance from the injector were quantified using the circumferential scan data. Two different injector-to-injector comparisons were made. The two six-hole injectors were compared to provide information about how a change in cone-angle and therefore closer location of plumes affects drops within the spray. The second comparison made is between the 90°CA six-hole injector and the three-hole 90°CA injector. For the second comparison, as the cone angles are similar the circumferential distance is also similar meaning that 5 degree turns from the plume centre of each injector gives comparable results.



### 6.2.3.1 Six-hole 60°CA injector vs six-hole 90°CA injector

The scans from the centre of one plume through a central plume to the centre of a third plume in 5 degree steps were compared. In total this is a 120 degree scan to quantify droplet velocity and diameter. A second scan of 30 degree steps throughout the whole 360 degrees of the injector was made. Of particular interest is the axial velocity, radial velocity (component of velocity into or away from the plume centre) and droplet diameter  $D_{10}$ .



**Figure 6.40: Circumferential scan across three plumes - 60°CA and 90°CA injector - 20mm below injector nozzle – 2.5ms ASOS - axial velocity (left) - radial velocity (right)**

Note: On the plots in Figure 6.40, the x axis shows position in mm but it actually corresponds to an angular position in degree used for the circumferential scan.

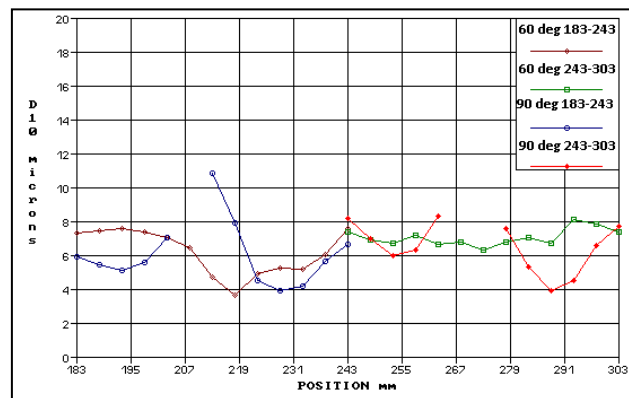
The axial and radial velocity profiles at 20mm below the injector nozzle and 2.5ms after the start of signal are presented in Figure 6.40. The 60°CA injector has a greater axial velocity but a lower radial velocity, with a positive radial velocity being away from the centre. This is expected as due to the cone angle of the injector and the direction of the plumes. The angle 243 on the graphs coincides with a plume centre; the results are fairly consistent on either side with slightly higher velocities shown on the positive side of the plumes (due to the plume being in front of the measurement volume). For the 60°CA injector, both the axial and radial velocity peaks corresponding to the 303° plume are slightly offset (around 298°); this is not shown at 243° or for the 90°CA injector, therefore there appears to be plume-to-plume variations within the injector.

The droplets between the plumes for the 90°CA injector show a significant reduction in velocities compared to the centre of the plume. This injector produces none or very few samples at the centre point between two plumes therefore droplets do not reach this point. However, analysing the shape of the graph suggests that the velocities tend to zero both in the axial and radial directions.

## Chapter 6 – Results: Atmospheric Bench

For the 60°CA injector at 20mm below the injector nozzle there are a greater amount of samples between the plumes than with the 90°CA injector. The droplet velocities are approximately 10m/s axially and -10m/s radially. This means that on average the drops are slowed from the main plume and are moving towards the centre of the injector. This suggests that for the injector with the smallest cone angle the air between the plumes is being entrained to the centre of the spray. This is likely to be due to the spray forcing the ambient air away at the start of injection generating a pressure reduction in the spray centre.

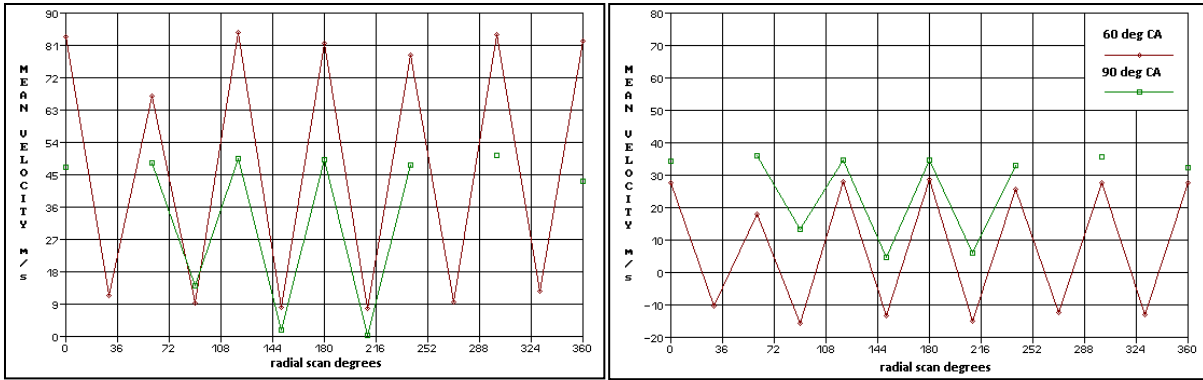
The droplet diameter is quantified using  $D_{10}$  and the same scan across the three plumes for the two injectors was used. Figure 6.41 shows the average droplet diameters for the sector at 2.5ms after injection at 20mm below the injector nozzle.



**Figure 6.41: Circumferential scan across three plumes - 60°CA and 90°CA injectors - 20mm below injector nozzle – 2.5ms ASOS -  $D_{10}$  droplet diameter**

For the 60°CA injector there are some inconsistencies found at the centre points between plumes. From 243 to 303 degrees the droplets show a relatively consistent diameter but from 183 to 243 there is a distinct reduction in average diameters between the plumes. The 90°CA injector shows consistent results over the three plumes. Droplet diameters in the centre of each plume (183, 243 and 303) are higher than those found on either side through 5-10 degrees. As the measurement volume is moved between the plumes the sample number is lower coinciding with an increase in values of  $D_{10}$ . With a lower sample number due to laser beam obscuration, it can often be found that PDA can over estimate droplet diameter.

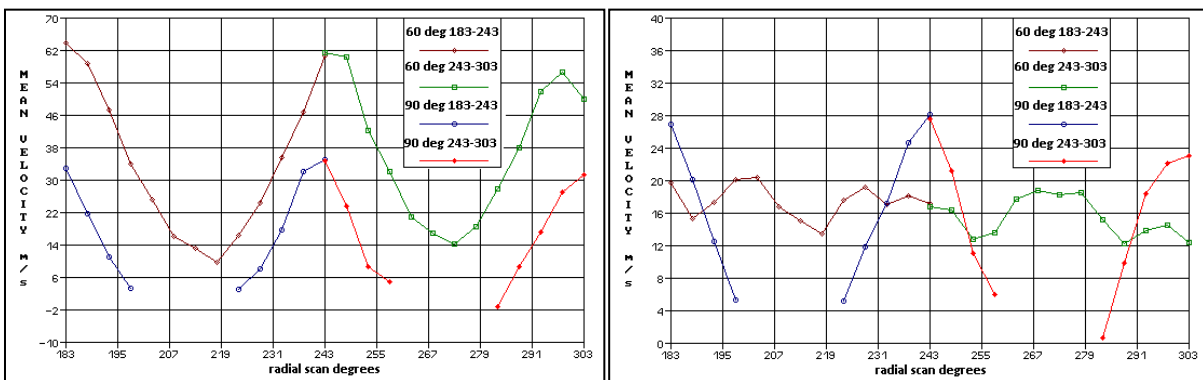
Note: The graph discontinuities observed in Figure 6.40 to Figure 6.44 are caused by laser attenuation leading to very few droplet samples being recorded.



**Figure 6.42: 360 degree circumferential scan - 60°CA and 90°CA injector - 20mm below injector nozzle – 2.5ms ASOS - axial velocity (left) - radial velocity (right) (zero on graph equivalent to plume 243 on Figure 6.40)**

The full circumferential scan shown in Figure 6.42 is a useful measure of consistency in velocities across all 6 plumes of the injectors. The values of axial and radial velocities at 30 degree intervals are similar to those found across the three plume scan. The peak at 60 degree on Figure 6.42 corresponds to the same plume located at 303° on Figure 6.40. Both radial and axial velocities are low at this peak which shows that there is an irregularity within this injector plume.

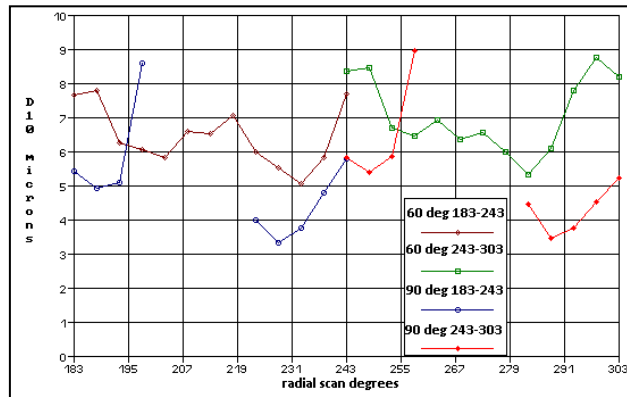
The two types of circumferential scans, described above, were performed at both 40mm and 60mm below the injector nozzle; the results at 40mm are as follows while the significance of the results at 60mm were low as very little droplets were detected outside the plumes within the 90°CA injector.



**Figure 6.43: Circumferential scan across three plumes - 60°CA and 90°CA injector - 40mm below injector nozzle – 2.5ms ASOS - axial velocity (left) - radial velocity (right)**

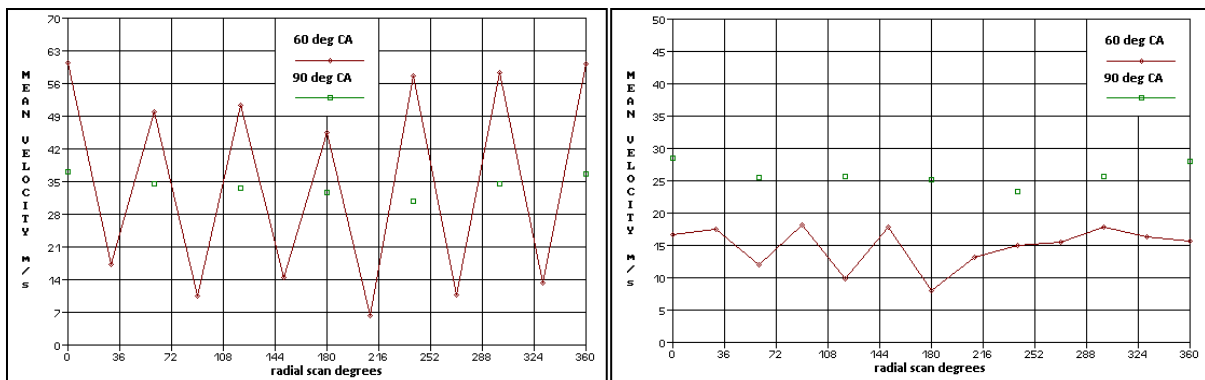
## Chapter 6 – Results: Atmospheric Bench

The axial velocity shown on the left of Figure 6.43 is consistent with the axial velocity obtained at 20mm below the injector nozzle. The lower peak at 303° is also shown at 40mm. There has been an interesting development in terms of radial velocities for the 60°CA injector. At 20mm the drops between the plumes had a negative velocity whereas, at 40mm, the velocity ranges between 12 and 20m/s across the three plumes. This suggests that the droplets located in-between the plumes are moving away from the spray towards the outside of the injector at an angle closer to the horizontal than the main spray.



**Figure 6.44: Circumferential scan across three plumes - 60°CA and 90°CA injectors - 40mm below injector nozzle – 2.5ms ASOS -  $D_{10}$  droplet diameter**

The data for droplet arithmetic diameter  $D_{10}$  at the same location show results that are similar either side of the central plume. At 40mm below the injector nozzle, the diameter for the 60°CA injector shows an increase toward plume centres. The droplets between the plumes in the circumferential scan are, on average, smaller than those found within the spray plumes. The droplet diameter for the 90°CA injector shows that there is a large amount of attenuation causing an over estimation on the positive side of the plume.



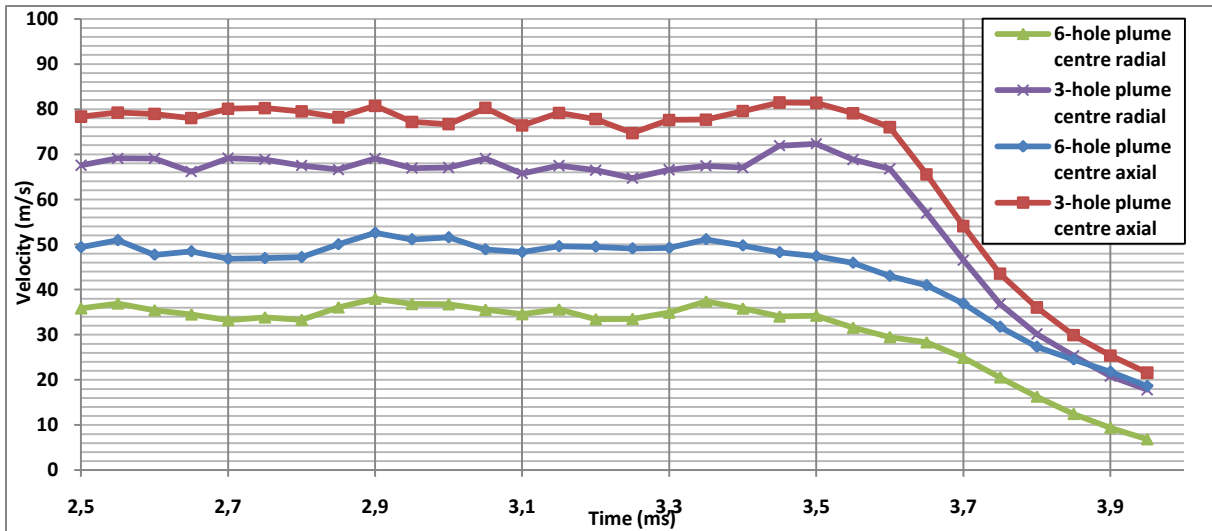
**Figure 6.45: 360 degree circumferential scan - 60°CA and 90°CA injector - 40mm below injector nozzle – 2.5ms ASOS - axial velocity (left) - radial velocity (right) - (zero on graph equivalent to plume 243 on Figure 6.43)**

The circumferential scans have shown differences in droplet velocities and droplet diameter found in the two six-hole injectors with different cone angle. Of particular interest are the droplets located between the plumes at 20mm from the injector nozzle. The results showed that, for the 60°CA injector, the droplets had a radial velocity towards the spray axis which suggests vortices caused by the plume front and pressure difference on the inside of the spray. It is only at 20mm below the injector nozzle that the inward velocity occurred as at 40mm the velocity is relatively constant across the three plumes. At this point the droplets are moving away from the spray relative to the plumes direction. The 90°CA injector does not show the same effects between the plumes. There are fewer droplets in between as the majority stay located within the plumes. The closer the plumes are, because of a small cone angle, the denser spray in the gaps between plumes is due to the interaction caused by the close proximities. Overall it appears as though there are interactions on the inside of plumes found in two of the three injectors testes. The six-hole 60 degree cone angle injector shows plume interaction at each of the three heights, with the six-hole 90 degree cone angle injector only showing an effect at 20mm below the injector nozzle. The three-hole injector shows symmetrical results on the inside and outside of the plume radially which suggest no plume to plume interaction.

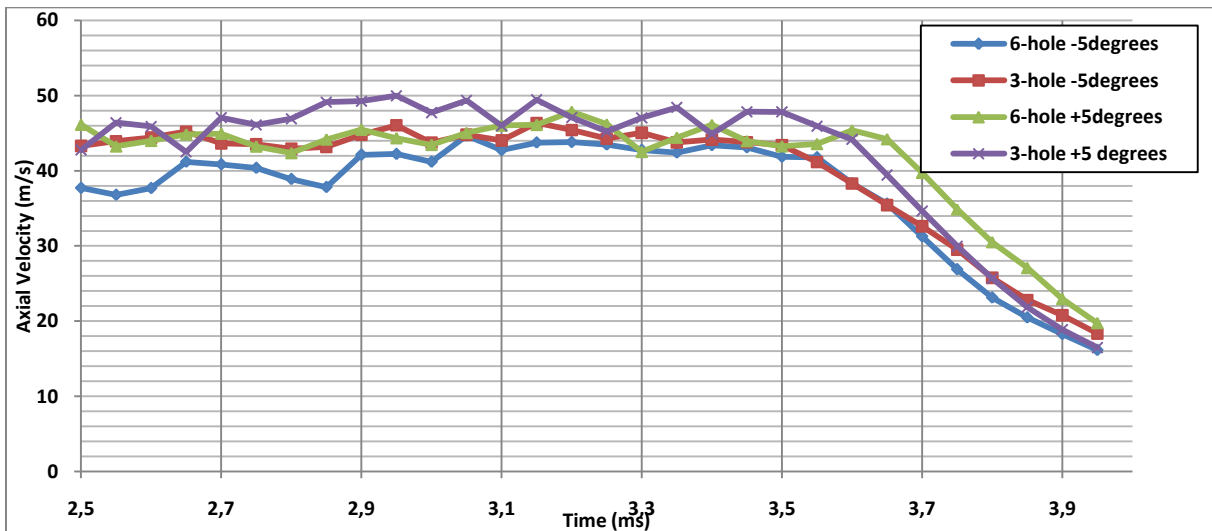
### *6.2.3.2 Six-hole 90°CA injector vs three-hole 90°CA injector*

For both the 6-hole 90°CA injector and the 3-hole 90°CA injector, the circumferential scan showed very few droplets between the plumes. This suggests that a similar scan to the one used to compare the two 6-hole injectors would not be effective. A different scan consisting of measurements at five locations was performed; the plume centre,  $\pm 5$  degrees and  $\pm 10$  degrees. Axial velocity, radial velocity and droplet diameter across the five points are shown in the following section of results.

Axial and radial velocities for the 6-hole 90°CA and the 3-hole injector are shown against time in Figure 6.46. The steady part of the injection is over the first 1ms shown in the graph from 2.5 till 3.5ms ASOS. The areas to the side of the plumes are of interest as droplet data in these areas is relatively unknown.

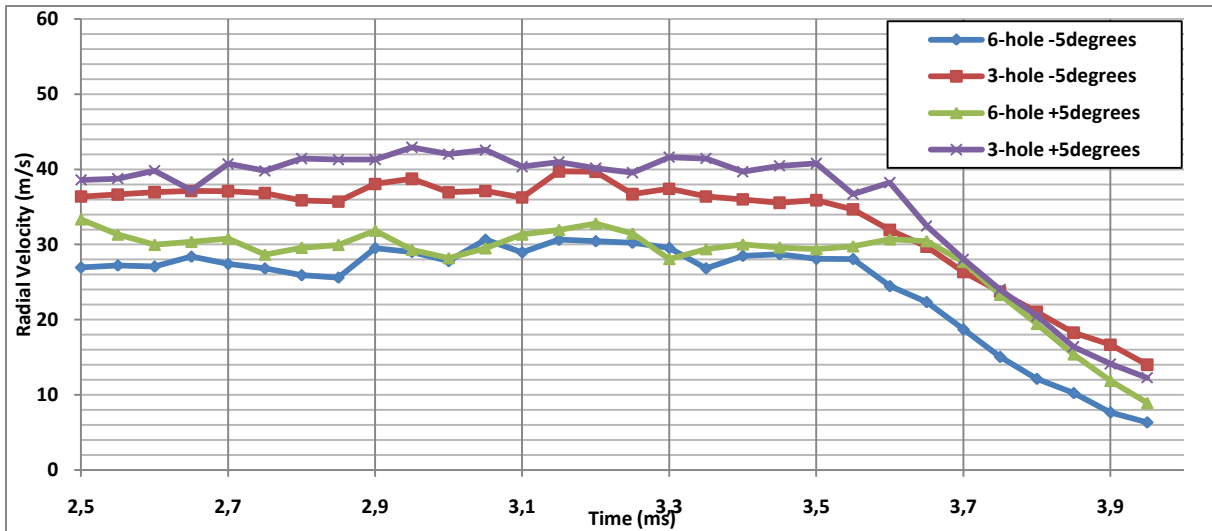


**Figure 6.46: Axial and Radial mean velocity against time at the centre point of the plume for the 6-hole 90°CA injector and 3-hole 90°CA injector at z=20mm**



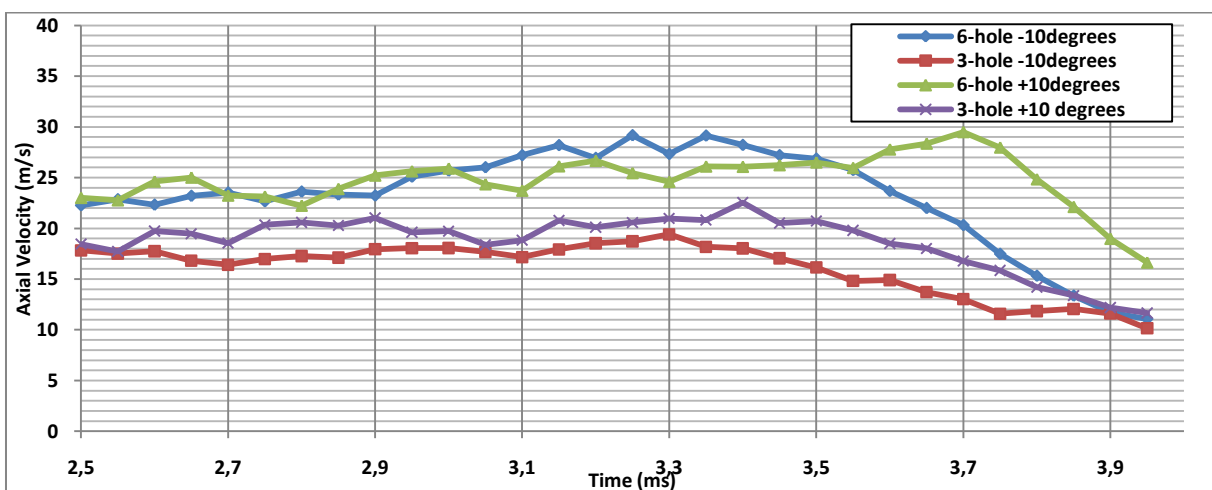
**Figure 6.47: Axial mean velocity against time for the 6-hole 90°CA injector and 3-hole 90°CA injector at z=20mm below the nozzle - ±5° rotation**

A 5 degree rotation around the injector axis in both directions for the two injectors is shown in Figure 6.47. There has been a significant decrease in mean axial velocity for the 3-hole injector while only a slight decrease for the 6-hole 90°CA injector. This implies that the 5 degree step for the 3-hole injector moves further to the outside of the plume than with the 6-hole 90°CA injector. Both injectors show a constant axial velocity across the time period 2.5ms to 3.5ms ASOS (steady part of the injection). For both injectors the axial velocity is higher on the positive turn side of the plume than on the negative. This shows that the attenuation caused by the plume being in front of the measurement volume gives a higher axial velocity.

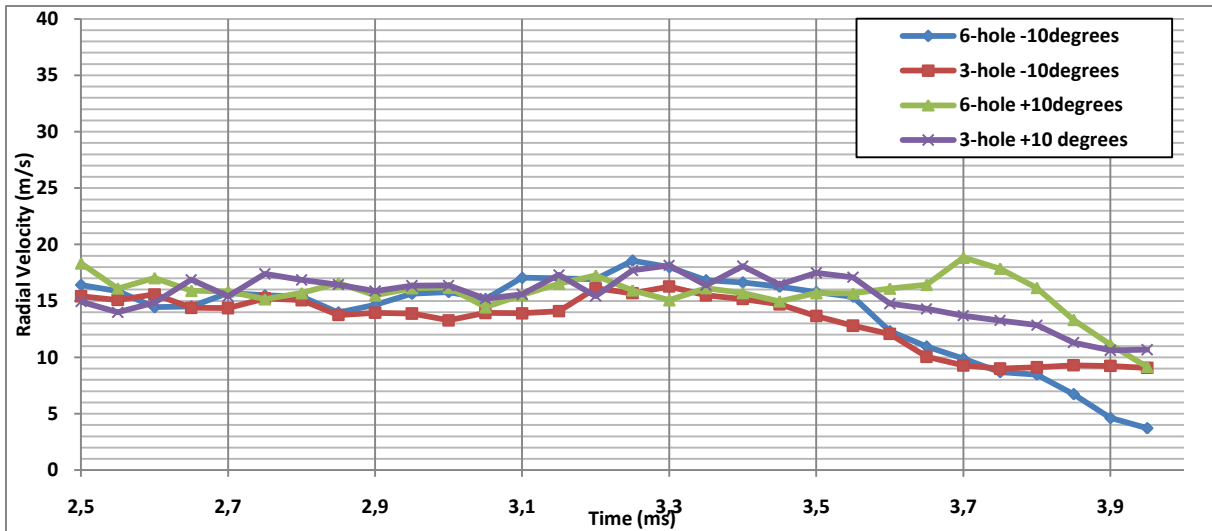


**Figure 6.48: Radial mean velocity against time for the 6-hole 90°CA injector and 3-hole 90°CA injector at z=20mm below the nozzle - ±5° rotation**

The radial velocity for the two injectors at 20mm below the injector nozzle are shown in Figure 6.48. The large decrease of average velocity compared to the velocity in the centre of the plume (from approx. 68m/s to 38m/s) is shown for the 3-hole injector, with the 6-hole injector showing a smaller decrease (from approx 35m/s to 30m/s). The difference between positive and negative turns is that higher radial velocity is found on the positive side. This is the same trend as seen for the axial velocity. This is unlikely to be realistic as the velocities should be relatively consistent either side of the plume. Beam attenuation through the plume is the cause of the variation in velocities for the circumferential scan. The same data for a 10 degree rotation is as follows.



**Figure 6.49: Axial mean velocity against time for the 6-hole 90°CA injector and 3-hole 100°CA injector at z=20mm below the nozzle - ±10° rotation**



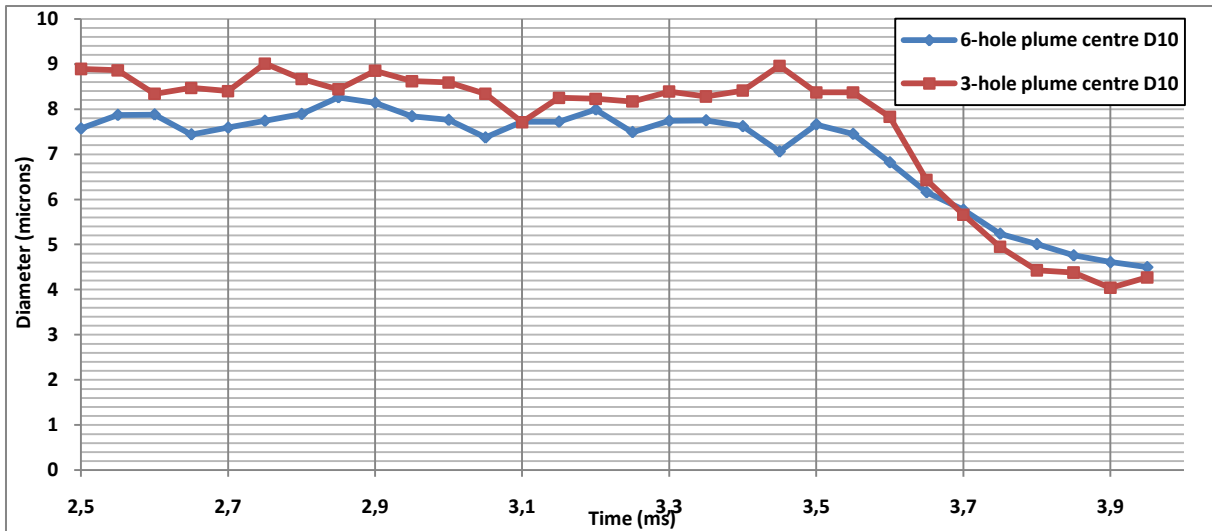
**Figure 6.50: Radial mean velocity against time for the 6-hole 90°CA injector and 3-hole 100°CA injector at z=20mm below the nozzle - ±10° rotation**

The figures for the 10 degree rotation around the injector axis initiated from the plume centre (Figure 6.49 and Figure 6.50) show more consistent results on both sides of the plumes. As the circumferential distance corresponding to the rotation is greater the denser part of the spray will have moved out of the laser beam plane, creating less disruption to the amount of light reaching the measurement volume.

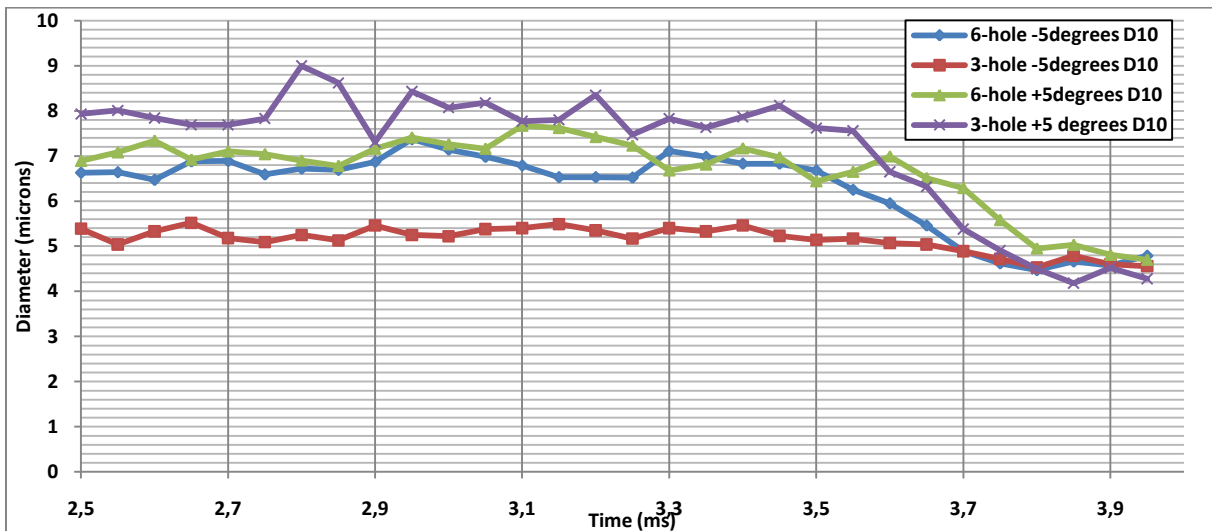
There is no noticeable difference between the two sides of the plume when comparing axial and radial velocities. At a distance of 20mm from the injector nozzle the radial scan (see section 6.2.2) showed there was a slight disruption within the 6-hole 90°CA injector due to the location of nearby plumes. At the same height for the three-hole injector there was no visible disruption on the inside of the plumes. Despite the differences to be expected between the two types of scan with regards to beam attenuation, the axial and radial velocities obtained with the circumferential scan are similar at 10° both side of the plume centre and hence do not show the trend observed with the radial scan for the 6-hole 90°CA injector.

Droplet arithmetic mean diameter calculations were analysed at the same locations for the circumferential scan. The Droplet data shown in Figure 6.51 at the centre of the plume is useful to describe the differences between the plumes of the two injectors. The mean diameter is approximately 1µm higher across the range of the 3-hole injector than the 6-hole 90°CA injector at the plume centre.



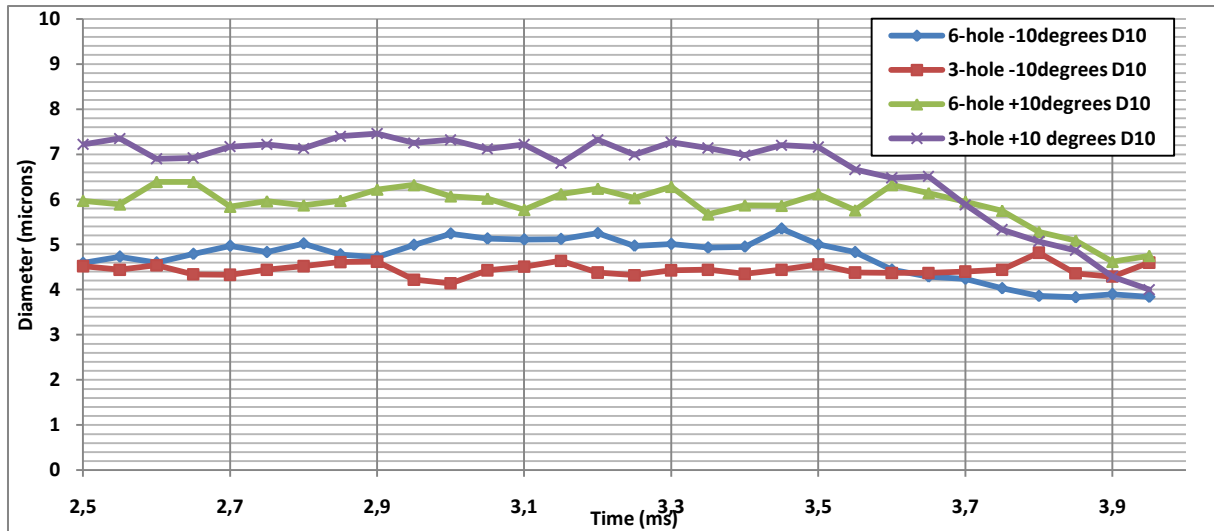


**Figure 6.51: Droplet diameter against time at the plume centre for the 6-hole 90°CA injector and 3-hole 90 degree injector at z=20mm below the nozzle**



**Figure 6.52: Droplet diameter against time for the 6-hole 90°CA injector and 3-hole 90°CA injector at z=20mm below the nozzle - ±5° rotation**

The droplet diameter obtained with a  $\pm 5^\circ$  rotation shows variations on either side of the plume. This was shown with the velocity variations for the  $\pm 5^\circ$  rotation and the higher droplet diameter on the positive turn coincide with the higher velocities. The attenuation on the positive side of the radial turn causes fewer droplets to be detected in the measurement volume. On average bigger drops are detected which in turn have higher velocities as they have more momentum than the small drops and hence are less affected by the aerodynamic forces. The  $\pm 10^\circ$  rotation results are shown in Figure 6.53



**Figure 6.53: Droplet diameter against time for the 6-hole 90°CA injector and 3-hole 90°CA injector at z=20mm below the nozzle - ±10° rotation**

The droplet diameters for the ±10° rotation are similar to those found at ±5°. The velocity data showed more consistency at ±10° on either side of the plume for both injectors. However, for the 3-hole injector, the contrast in droplet diameter between the positive and negative rotation is found at both ±5° and ±10mm. This is an odd result as it would be expected that, as the components of velocity showed consistency between the two sides of the plume, there would be consistency in the droplet sizes. In general, the average drop diameters are slightly smaller at the sides of the plume for both injectors by approximately 1micron, but it goes down to more than 3micron smaller in the case of the negative rotation for the 3-hole injector.

### 6.2.3.3 Summary

The circumferential scans have been used to quantify the droplet velocity and diameter at a radial distance corresponding to the plume centres for the three different injectors. In particular, a distance of 20mm below the injector nozzle was of interest as from the radial scan section results there appeared to be different degrees of interaction between injector plumes. The two 6-hole injectors were compared and the results showed that droplets in between the plumes on the 60°CA injector varied in terms of diameter and velocity vector. At 20mm downstream the injector nozzle, the drops were moving towards the spray centre while at 40mm the drops were moving away from the centre. This is caused by interactions with the ambient air and pressure differences caused by the fuel injection creating air induced spray motion. There were very little possibilities for comparing the 3-hole and 6-hole 90°CA injector in between the plumes as the amount of droplets detected by the PDA system was very reduced. For this comparison small degree changes around the plume were used. The results for this test had been difficult to quantify as attenuation was perceived when the injector plume was in front of the measurement volume. Also it appeared that both injectors produced plumes that would be symmetrical around their axis, it is difficult to compare the two injectors as the plumes they generate appeared different, created by different injector internal geometries. Therefore a  $\pm 5^\circ$  step for one injector measures a different section of the plume than the other.

The next section will discuss the results with regards to pressure chamber using various multi-stream injectors, first at over-atmospheric pressures and then at sub-atmospheric pressures to study the effects of flash boiling on the atomization performance of the injectors.

## 7. Results: Pressure Chamber

### 7.1 *Over-Atmospheric*

In this section, three injectors were analysed; they are shown below in Figure 7.1 to Figure 7.3. All three injectors are 6-hole symmetrical multi-stream GDI injectors provided by Continental AG (see Figure 7.4 and Appendix D for detailed geometrical characteristics) in order to study the influence of the nozzle geometry (cone angle, tip shape,...) on the atomisation performance.



**Figure 7.1: Injector 1: 6-hole 90° cone angle with a flat nozzle tip**




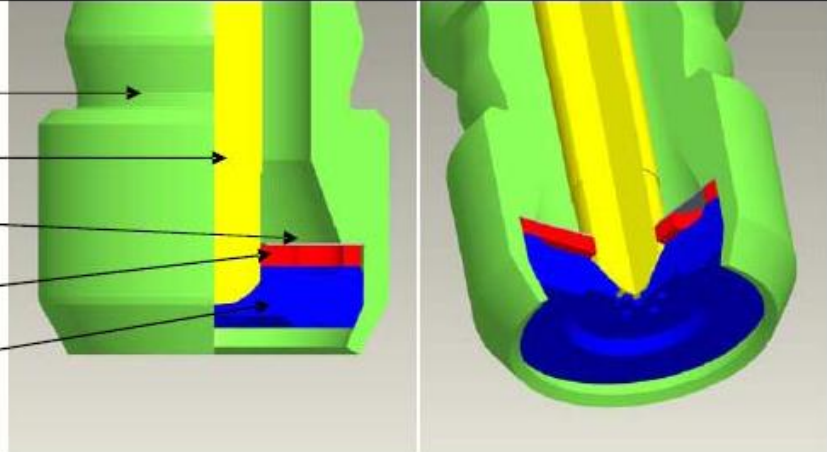


**Figure 7.2: Injector 2: 6-hole 90° cone angle with a concave nozzle tip**

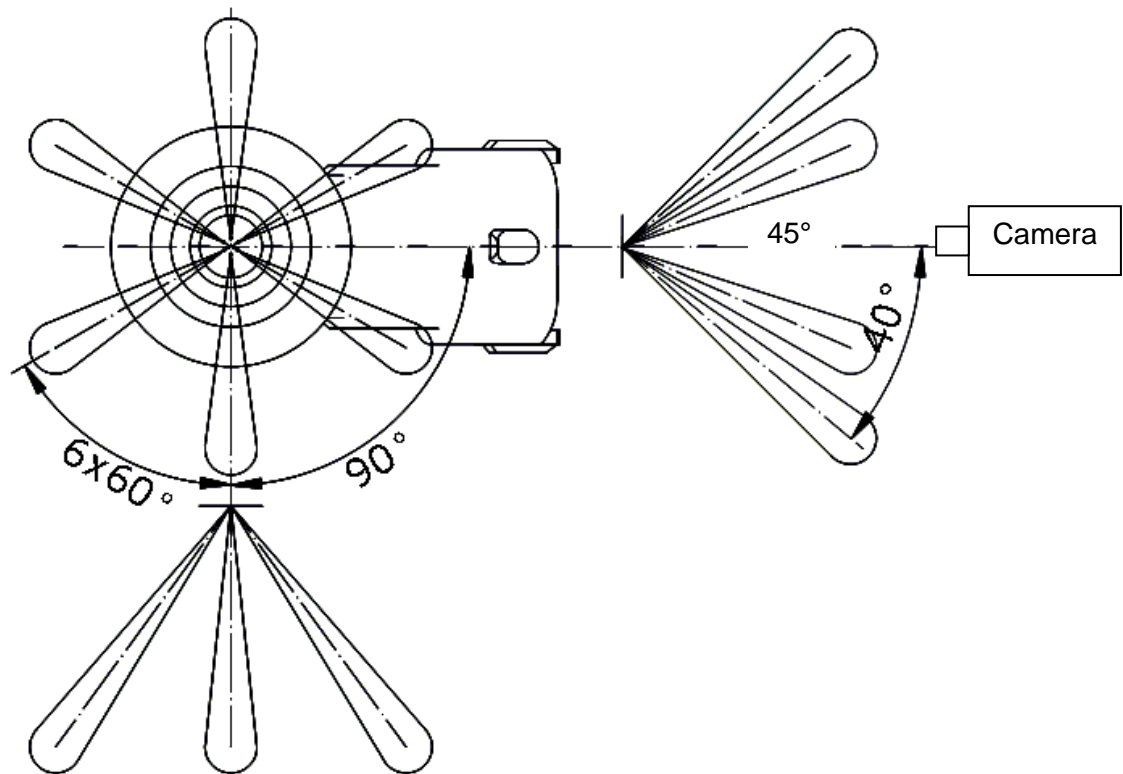


**Figure 7.3: Injector 3: 6-hole 60° cone angle with a concave nozzle tip**

Injector 3 was designed specifically with a 60° nozzle cone angle to prevent valve impact.

Geometrical Characteristics:	
Hole configurations:	5 to 8 holes ; possibility of center hole
	<div style="display: flex; justify-content: space-around; align-items: center;"> <div style="text-align: center;"> <p>Example:</p>  </div> <div style="text-align: center;"> <p>6+0</p>  </div> <div style="text-align: center;"> <p>5+1</p>  </div> <div style="text-align: center;"> <p>6+1</p> </div> </div>
Hole diameter: d	0.17 to 0.28mm
Hole Length: L (= seat plate thickness)	Low penetration injector: 0.20 mm High penetration injector: 0.46 mm
L / d	0.7 to 2.5
Sac-volume:	Without holes : 0.076 mm <sup>3</sup> With holes : maximum 0.450mm <sup>3</sup>
Maximum hole angle "B" (hole-injector axis)	45°
Assembly	

**Figure 7.4: Injector geometrical characteristics**



**Figure 7.5: Injector plume geometry<sup>[101]</sup> for injectors 1 and 2**

Injector 3 would have a  $30^\circ$  angle between plume and injector axis.

In addition to Figure 7.5, it should be noted that the nozzle holes are 0.6mm from the injector axis which must be accounted for when setting up the plume origin in the image viewer software.

Fuel pressures of 120bar and 190bar were tested. The injectors were positioned within the cell so that a single plume is clearly visible to the camera.

### 7.1.1 Intensity Contour Analysis

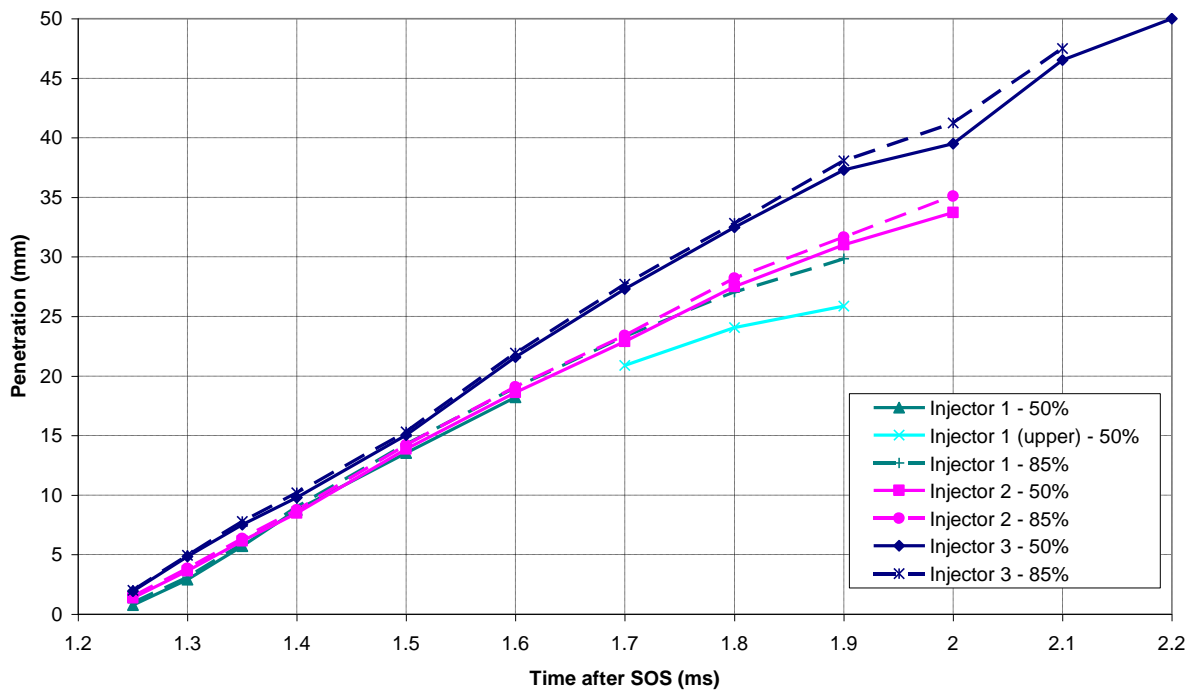
Following the review of a number of publications it was realised that there was a reasonable amount of variation in the intensity contour used to define the spray boundaries, and hence penetration of a spray. When an image is captured, the flash unit situated behind the spray, illuminates the spray and surrounding area providing a white background and the spray being highlighted by the shadow cast. A spray is not of uniform density and therefore has a variation in light that is transmitted to the camera. When post processing the images, it is possible to apply intensity contours to the image to allow easy identifications of areas of constant density. When a spray's penetration is defined, it is defined by the distance from the nozzle to a specific intensity contour and the difference in penetration at different intensity contours is of interest here.

Much of the importance of understanding a spray's penetration is to determine the percentage of the spray that will impact on the cylinder wall/piston/intake valve/spark plug. Therefore if a contour with a lower percentage of the maximum light intensity is used the penetration of a denser portion of the spray is used. No previous work could be found that quantifies the spray make-up at different intensity contours and therefore the exact intensity contour to use to best quantify a spray's penetration is unclear. Previous works ( [101], [51]) have used 50% and 85% of the maximum light intensity but due to the ambiguity of the choice of intensity contour to use, both 50% and 85% have been investigated and the differences in results evaluated.

One of the modifications made to the test equipment was the use of a new Fostec fibre optic flash panel. Due to the age of the old flash unit it had lost a large percentage of its maximum light output intensity. Thus when the change to the new panel was made, the difference in quality of image recorded was substantial. The change was made after the images for Injector 1 were taken and therefore the images recorded for Injector 2 and 3 were recorded using the new flash panel.

What became immediately clear when measuring the axial penetration for injector 1 was the increased difficulty in defining the penetration due to the reduced clarity of the intensity contours as a consequence of the reduced light intensity. This was especially apparent at 50% maximum intensity. At low injection timings (1.25ms -1.35ms ASOS) the definition of both contours was difficult and thus could introduce an element of uncertainty to the results at low injection timings for injector 1. It was clear that the 50% intensity contour on the lower spray plume was not defining the true penetration above 1.6ms ASOS for 50% intensity, and

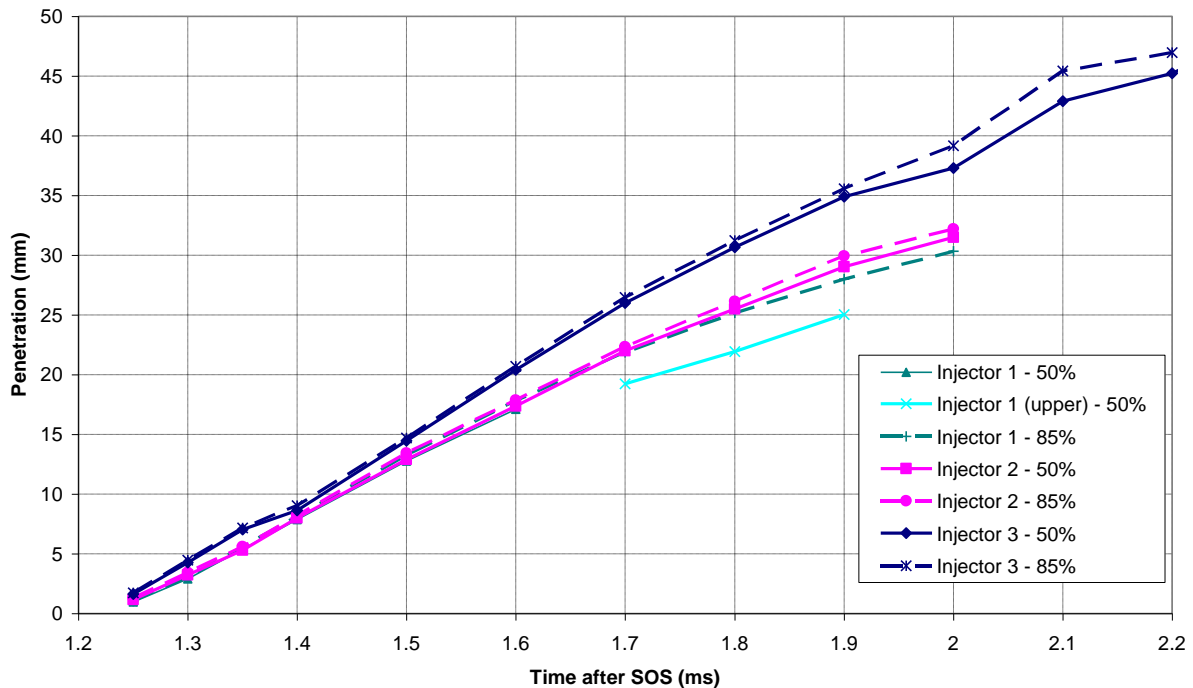
therefore the upper plume was used because it appeared to be a more true representation of the penetration. Although when the results were analysed, it was clear this was still not the case due to the large differences between the 50% and 85% intensity contours. This is shown in Figure 7.6 which compares axial penetration for 1bar backpressure, at 20°C at the two light intensity contours. The switch to the upper spray plume for Injector 1 at 50% light intensity is shown by the series 'Injector 1 - Upper'.



**Figure 7.6: An intensity contour comparison of axial penetration at 20°C 1bar backpressure with Injector 1**

What can also be observed from Figure 7.6 is the relatively small difference between 50% and 85% of the maximum light intensity. Since it is known that inside the spray plume the change in spray density can be very large over a very small distance, the small difference in axial penetration at 50% and 85% indicates that 50% and 85% are actually quite close to the extremities of the spray. This would also indicate that the percentage difference in droplet density would be small and thus either data recorded at 50% or 85% could be used for estimating penetration and the percentage of spray impact. This conclusion is acceptable assuming that the light intensity is sufficient. The trends mentioned here are also seen in the results taken at 2bar backpressure and for the radial penetration. The results for 2bar backpressure are shown in Figure 7.7.





**Figure 7.7: An intensity contour comparison of axial penetration at 20°C 2bar backpressure with Injector 1**

As has been proved previously, if the maximum light intensity is not sufficient, the definition of the intensity contour at 50% maximum light intensity will not be accurate and the 85% intensity contour should be used. To ensure continuity, for the remainder of the section 7.1 the intensity contour representing 85% of the maximum light intensity will be used to represent the spray penetration unless otherwise stated.

### 7.1.2 Injector Analysis

Images were recorded at 120bar injection pressure, 20°C charge temperature, 1 and 2bar charge backpressure for all three injectors tested. This has allowed a thorough evaluation of the variation in axial and radial penetration and cone angle with changing backpressure for each injector.

The results obtained with each injector for axial and radial penetration are shown in Figure 7.8 to Figure 7.11.

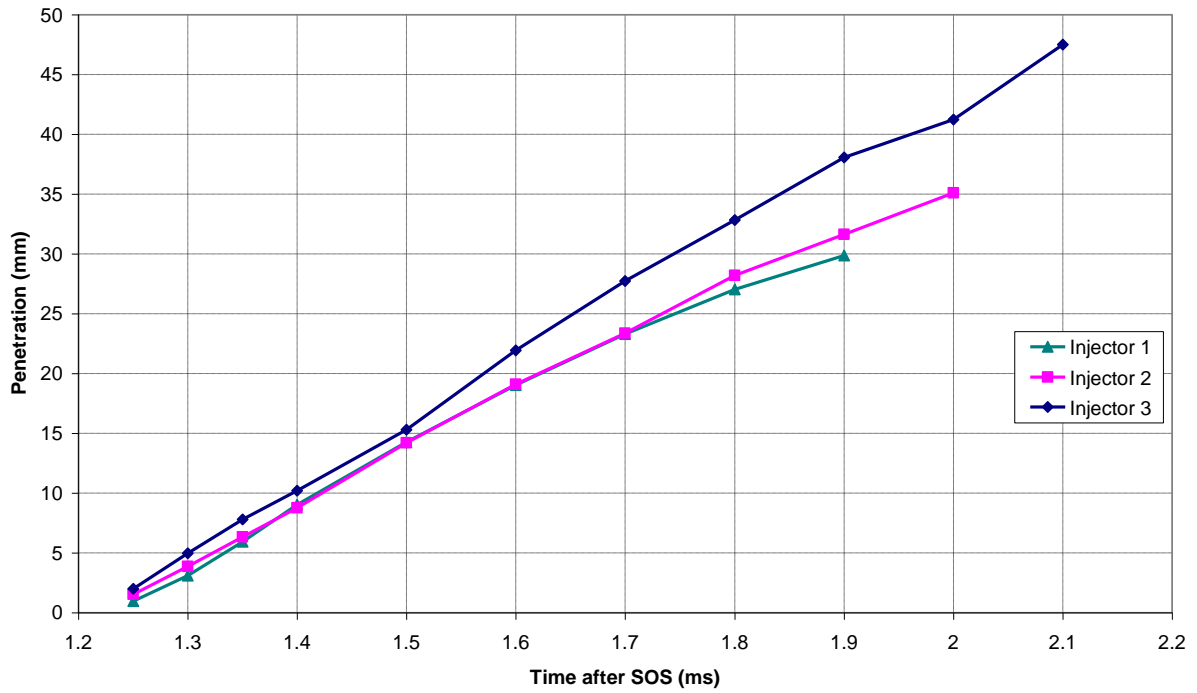


Figure 7.8: Axial penetration at 20°C 1bar backpressure

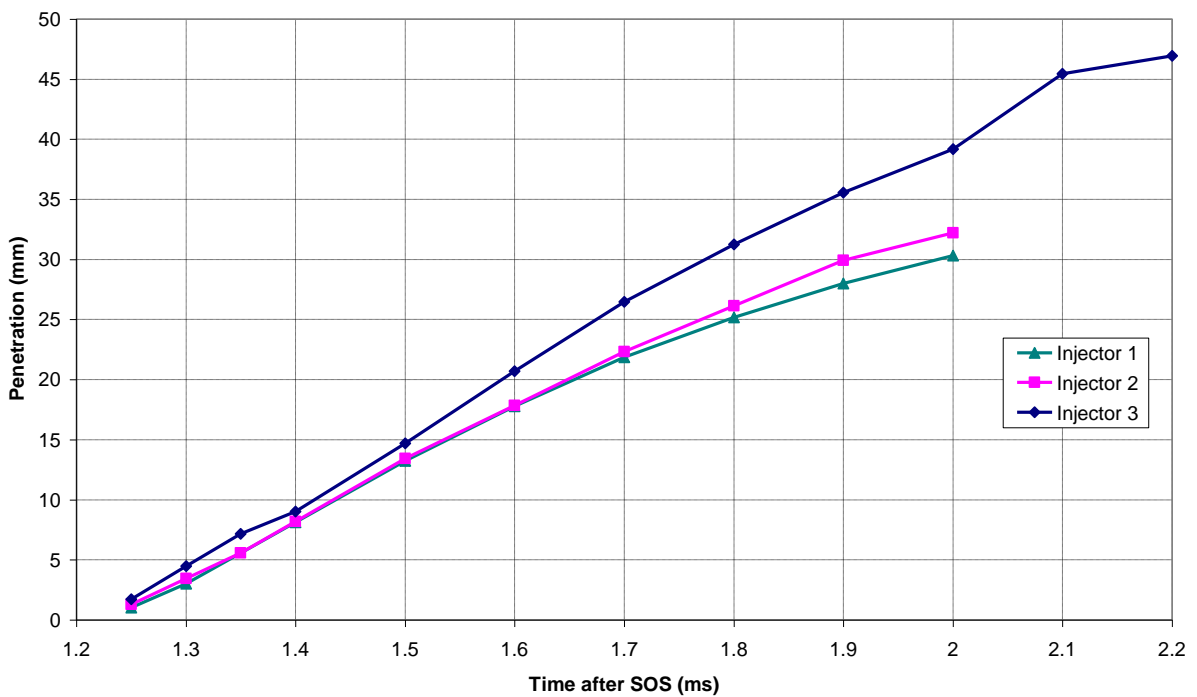
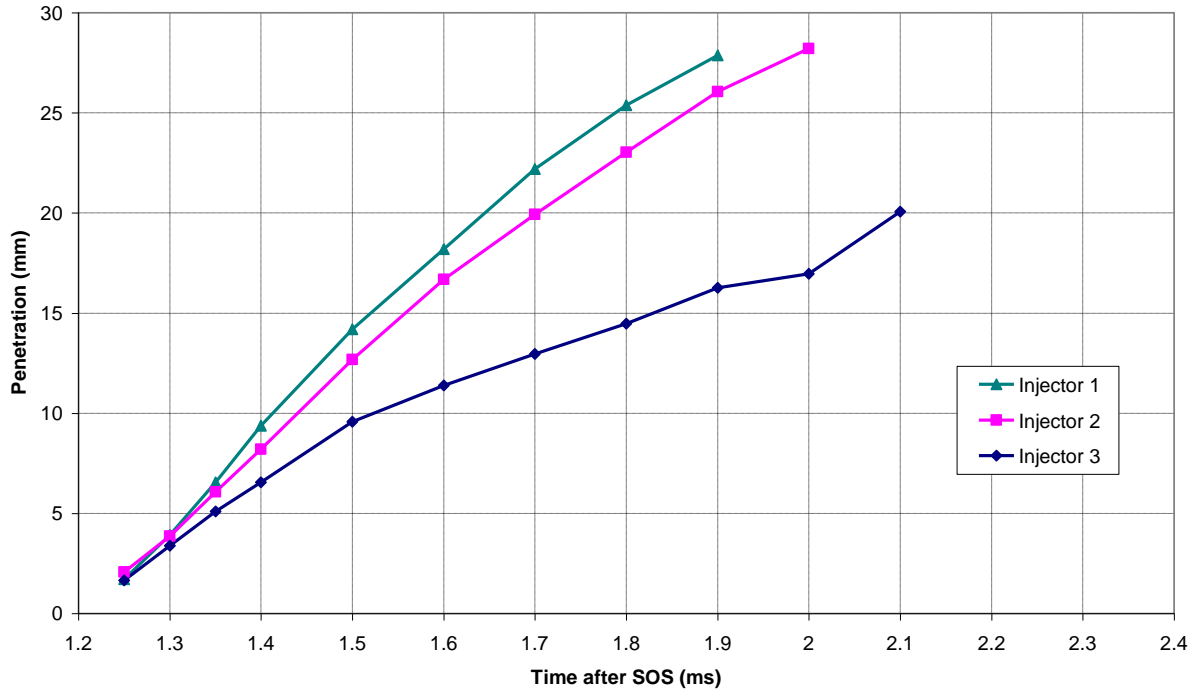
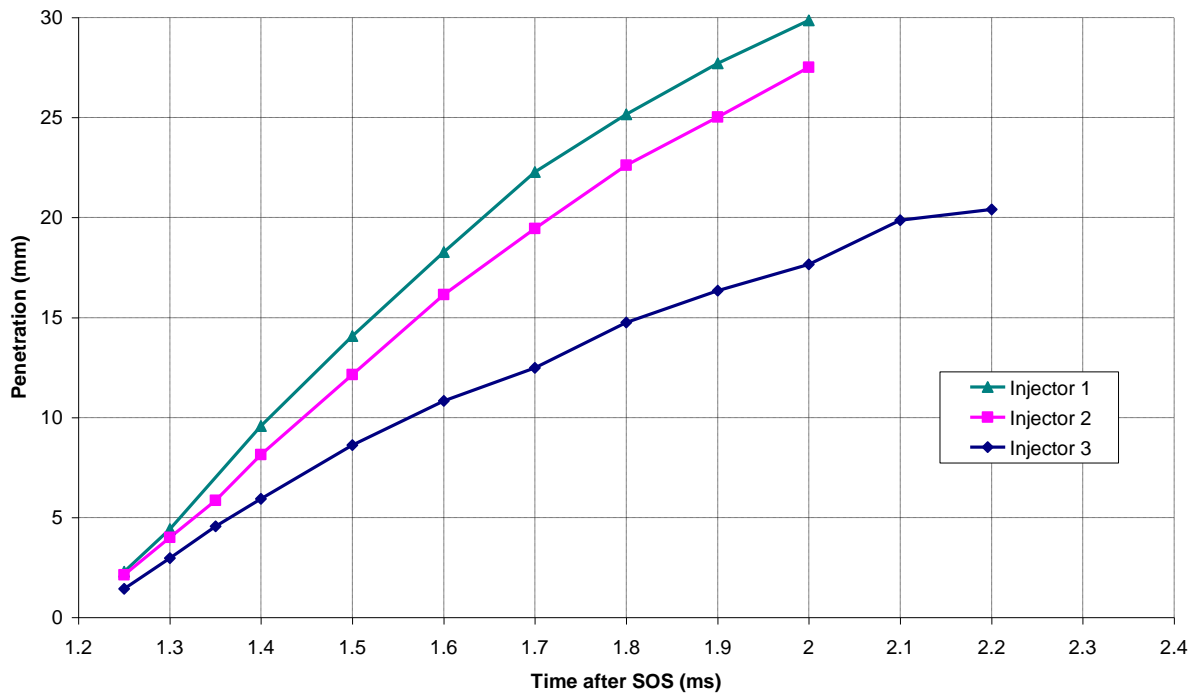


Figure 7.9: Axial penetration at 20°C 2bar backpressure




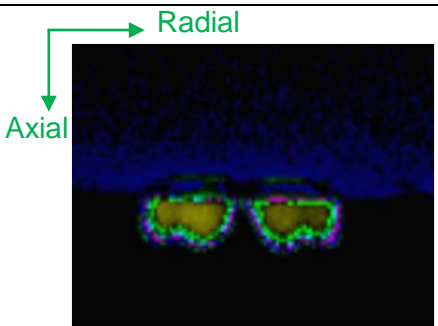
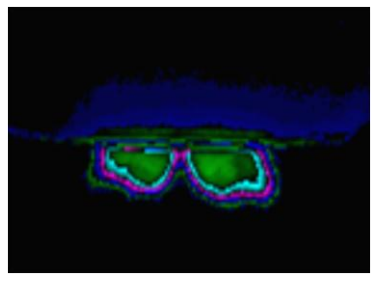

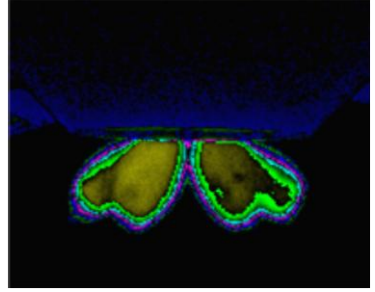
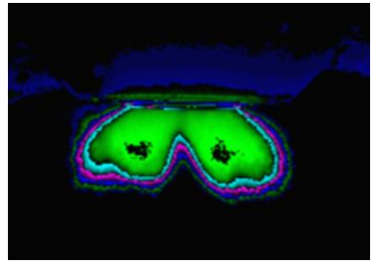
**Figure 7.10: Radial penetration at 20°C 1bar backpressure**

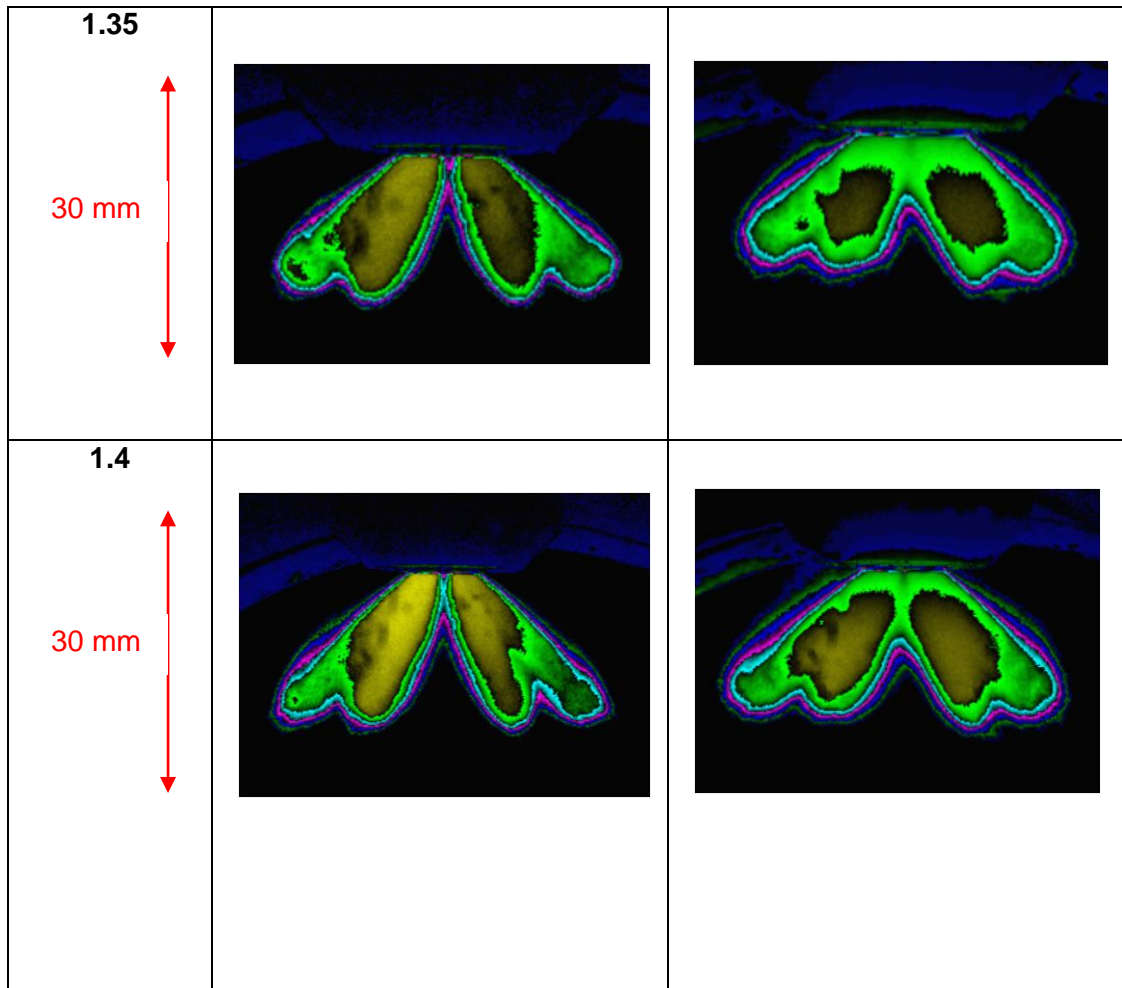


**Figure 7.11: Radial penetration at 20°C 2bar backpressure**

The axial penetration for injector 1 is shown to be lower than for injector 2 up to 1.4ms where their penetrations become almost equal for a period. This effect is shown at both 1 and 2bar backpressures. This is believed to be due to the affect of the nozzle tip geometry. Injector 1 has a smaller proportion of fuel around the centre of the nozzle tip and forces the fuel radially much more efficiently. Injector 2, although having very similar radial penetrations to injector 1 at these timings (radial penetration will be discussed later), maintains a larger portion of the fuel close to the injector nozzle centre. This is believed to be due to the concave tip on injector 2 constraining the initial spray formation and the flat tip found on injector 1 allowing the fuel to propagate outwards more efficiently. This is highlighted in Table 7.1: Spray density near the injector axis for injectors 1 and 2 with a series of images.

**Table 7.1: Spray density near the injector axis for injectors 1 and 2  
(1.25ms and 1.3ms below - 1.35ms and 1.4ms next page)**

Timing (ms ASOS)	Injector 1	Injector 2
<b>1.25</b>   <b>20 mm</b>		
<b>1.3</b>   <b>20 mm</b>		



The effect of the nozzle tip geometry is seen throughout the spray formation. Although seen to be unaffected during the initial injection period, the radial penetration with injector 1 is consistently larger than that seen with injector 2 at both 1 and 2bar backpressures after 1.3ms ASOS. This difference in radial penetration can be as large as 2.5mm at certain injection times and this affect is only due to the change in nozzle tip geometry.

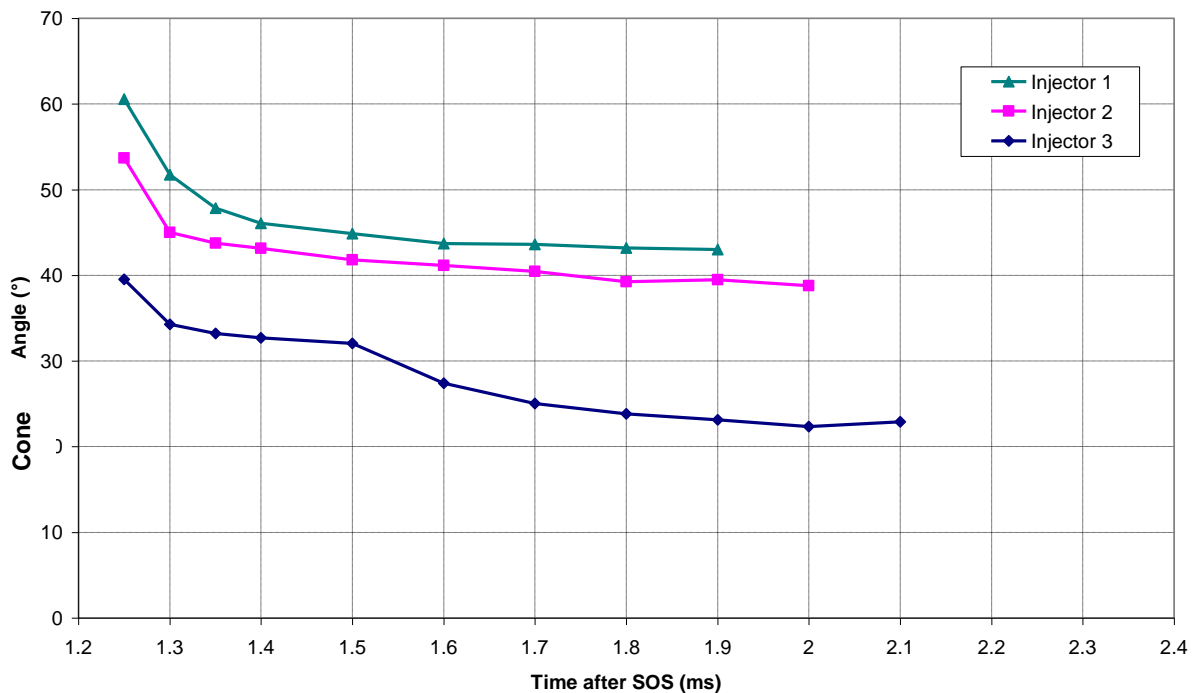
The axial penetration is also affected at larger timings. Although showing smaller radial penetrations, injector 2 exhibits larger axial penetrations and this affect is observed at both 1 and 2bar back pressures.

Unfortunately, due to time constraints, data were not available at different charge temperatures and therefore it is not possible to conclude that similar nozzle affects are seen with temperature, although since increasing the temperature of the cell, and thus the temperature of the nitrogen inside the cell, acts to reduce the density of the gas (increasing the backpressure increases the density of the nitrogen charge) similar trends with respect to changing the charge density are expected to be seen.

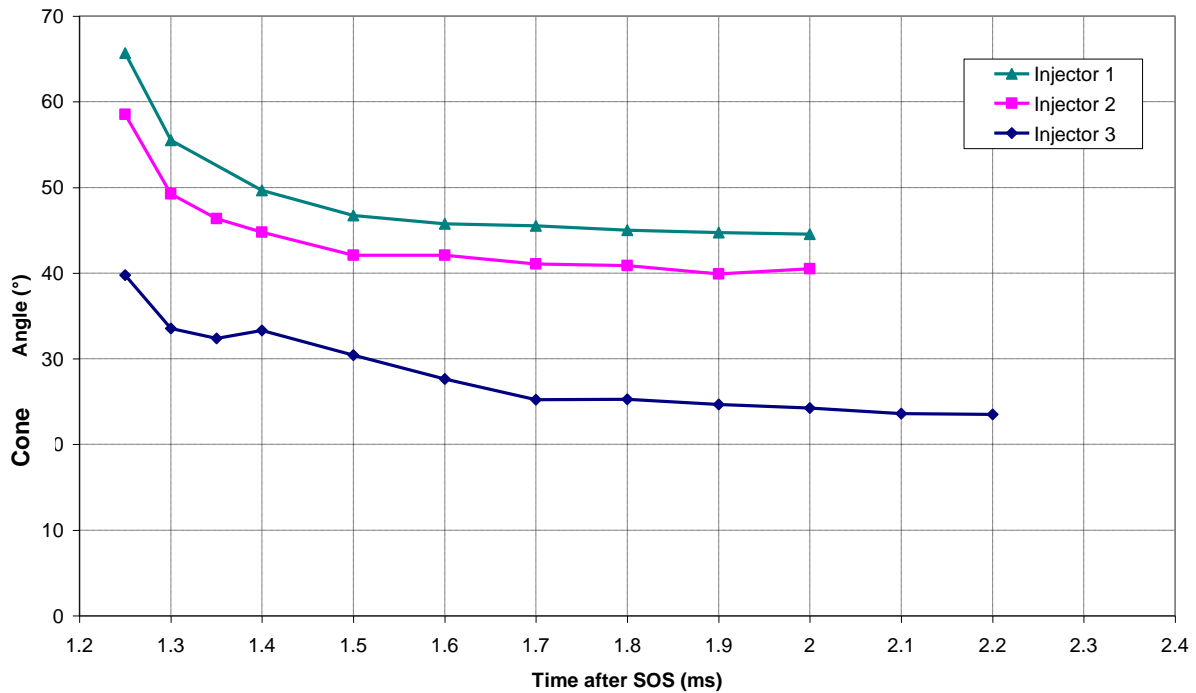
Thus it could be concluded that the difference between the nozzle tips of injectors 1 and 2 affects the initial and predominantly the later parts of axial penetration, but affects the radial penetration throughout the injection period. The flat nozzle tip on injector 1 shows reduced axial penetration during the initial and later stages of spray formation and increased radial penetration after 1.3ms ASOS when compared to the concave tip on injector 2.

Injector 3 has consistently higher axial penetrations and lower radial penetrations than both injector 1 and 2. This is due to the orientation of nozzle orifices, with it having a smaller nozzle cone angle of  $60^\circ$  opposed to  $90^\circ$  used with the other injectors. The radial penetration is seen to be affected to a larger degree than axial penetration, with a maximum difference in radial penetration of approximately 10mm at larger injection timings when compared to injectors 1 and 2.

The results for the spray cone angle are shown in Figure 7.12 and Figure 7.13.



**Figure 7.12: Cone angle at 20°C 1bar backpressure**


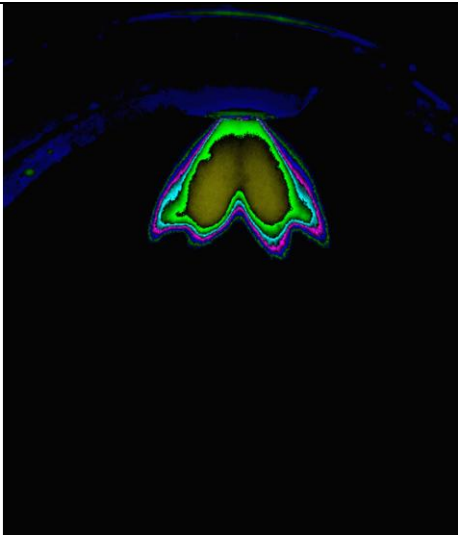

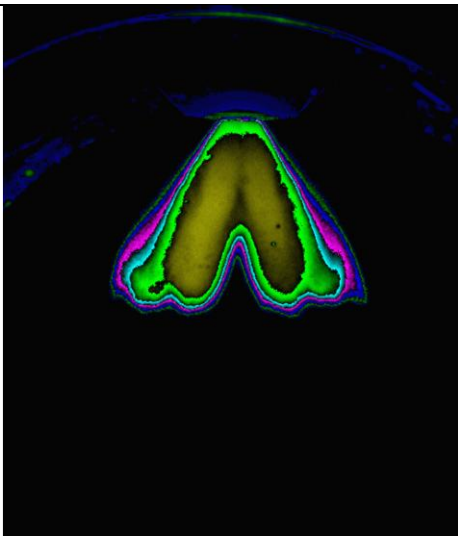

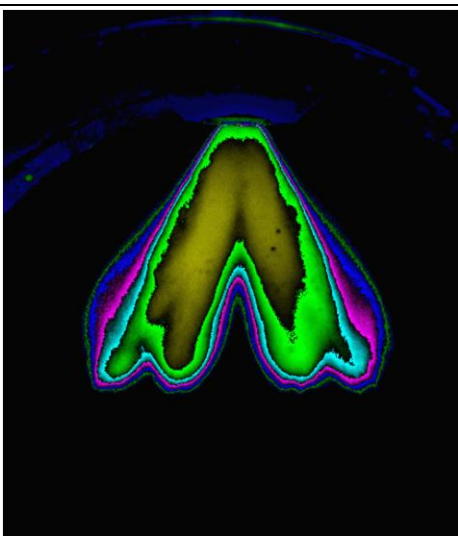


**Figure 7.13: Cone angle at 20°C 2bar backpressure**

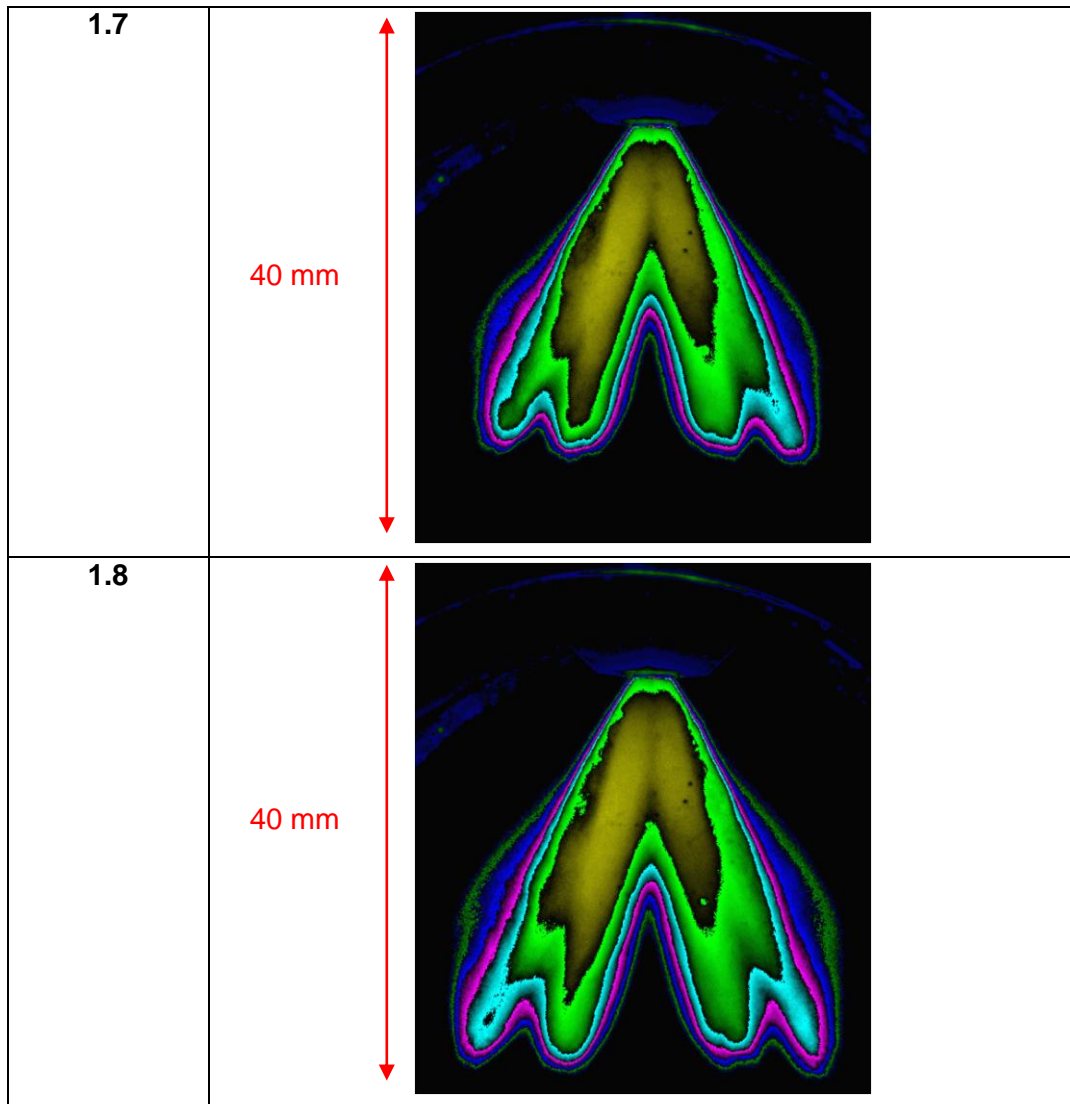
The cone angle for injector 1 is consistently higher than seen for injector 2. This is expected due to the higher radial penetrations seen with injector 1. The cone angle decreases but at a reducing rate converging on a constant angle with increasing injection timing. This trend is seen for both injector 1 and injector 2 but with injector 1 showing more uniformity.

The cone angle for injector 3 shows a similar reducing trend at timings up to 1.5ms ASOS at 1bar and 1.4ms at 2bar, always at a lower angle than injector 1 and 2 due to the nozzle hole orientation, but after these points the cone angle shows another reduction up to approximately 1.7ms where it begins to level again. This can be explained by examining the spray images themselves. Shown in Table 7.2 are a series of images showing the spray propagation for injector 3 at 20°C charge temperature and 1bar backpressure.

**Table 7.2: Spray propagation at 20°C and 1bar backpressure for injector 3  
(1.4ms to 1.6ms below - 1.7ms and 1.8ms next page)**

Timing (ms ASOS)	Injector 3 Image	
1.4		
1.5		
1.6		



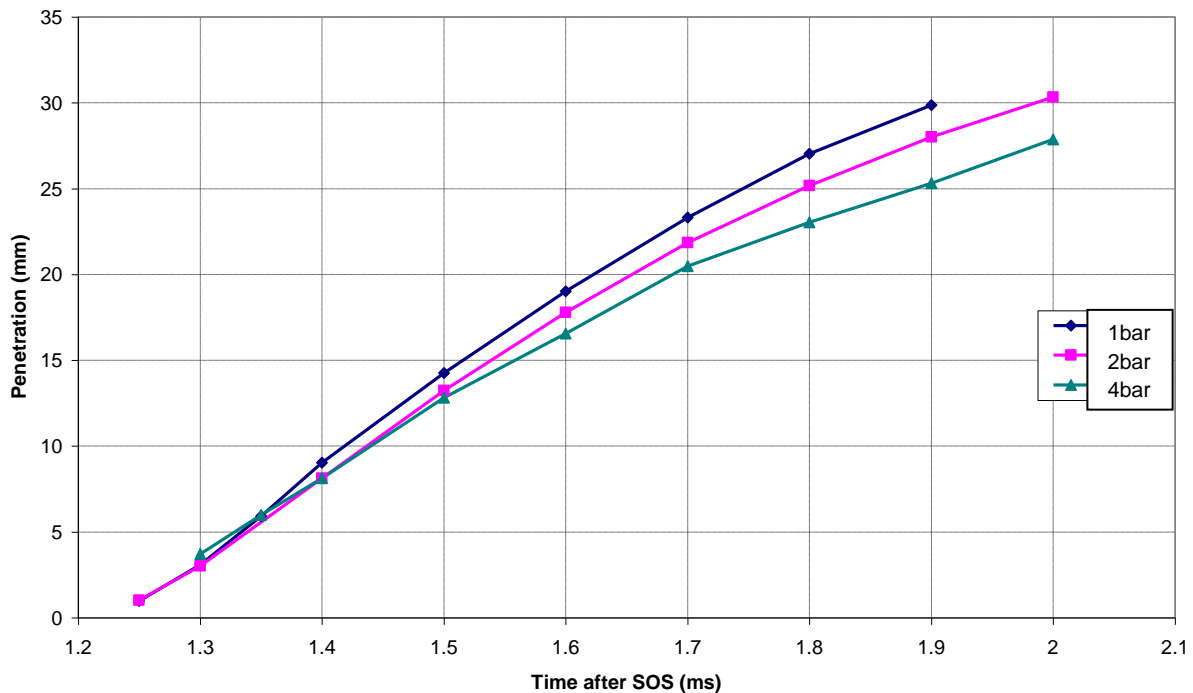


At 1.4ms ASOS the spray tip has become stretched and the intensity contours are wider at the tip showing large areas of low spray density. The spray is moving forward and pushing the charge in the cell outwards around the spray plumes. The charge movement around the plume causes the tip to be distorted and forces it around the outside of the plume, rejoining further down on the outside. This illustrates the affect of the spray forcing the charge around it as it progresses through the cell and that charge is entrained into the plume at the peripheries behind the tip of the plume. The sudden reduction in cone angle after 1.5ms is due to the head re-joining further down the plume, thus reducing the increase in radial penetration and reducing the cone angle. As this is occurring, the fuel behind it is forcing its way forwards re-creating the plume tip in a position slightly closer to the injector axis which then continues to propagate, stabilising the reduction in cone angle and levelling off in the same manner as seen with injector 1 and 2. Injectors 1 and 2 do not see the same phenomenon with each plume tip being separated sufficiently that it is not affected to the same degree by spray induced charge movement.

### 7.1.3 Backpressure Analysis

Images were taken with injector 1 at three different backpressures, 1, 2 and 4bar at a constant temperature 20°C and 120bar injection pressure.

The results observed for axial and radial penetration, and cone angle are shown in Figure 7.14 to Figure 7.16.



**Figure 7.14: Axial penetration at 20°C with Injector 1**

The axial penetration shows a clearly defined reduction with increasing backpressure but with very little affect being seen up to 1.35ms. This follows the hypothesis that as the backpressure increases at a constant temperature, the density of the charge increases. Increasing the density increases the aerodynamic drag the drops experience as they traverse the cell, reducing their kinetic energy and thus reducing their velocity and distance travelled.

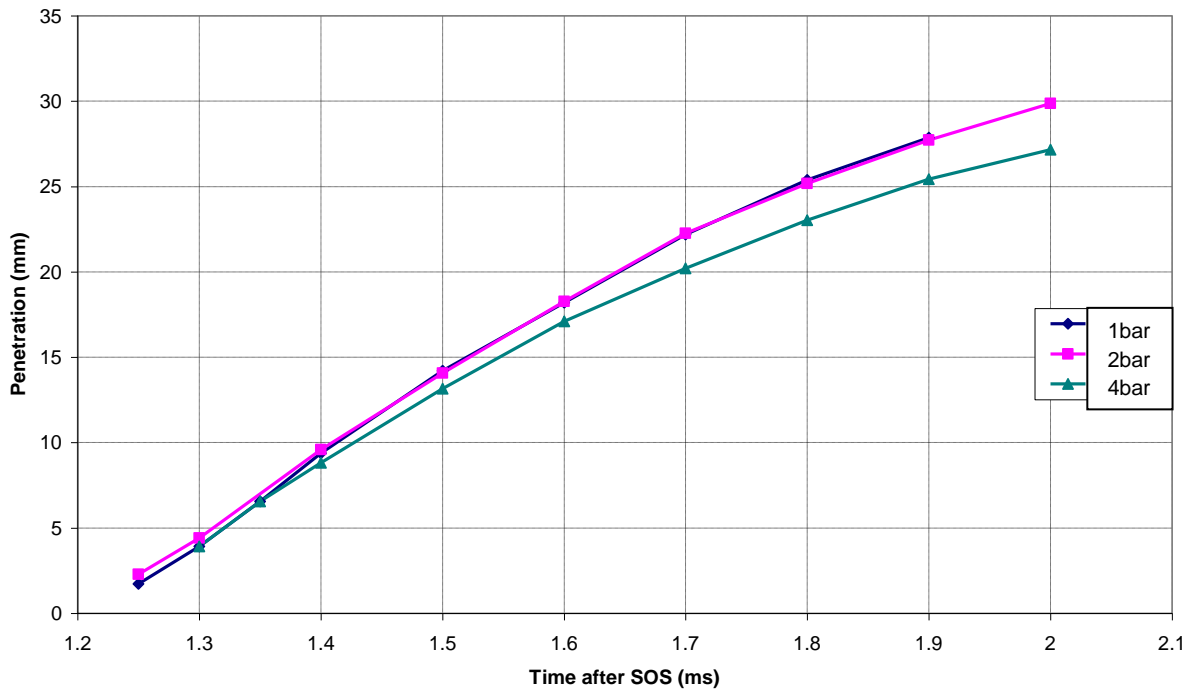


Figure 7.15: Radial penetration at 20°C with Injector 1

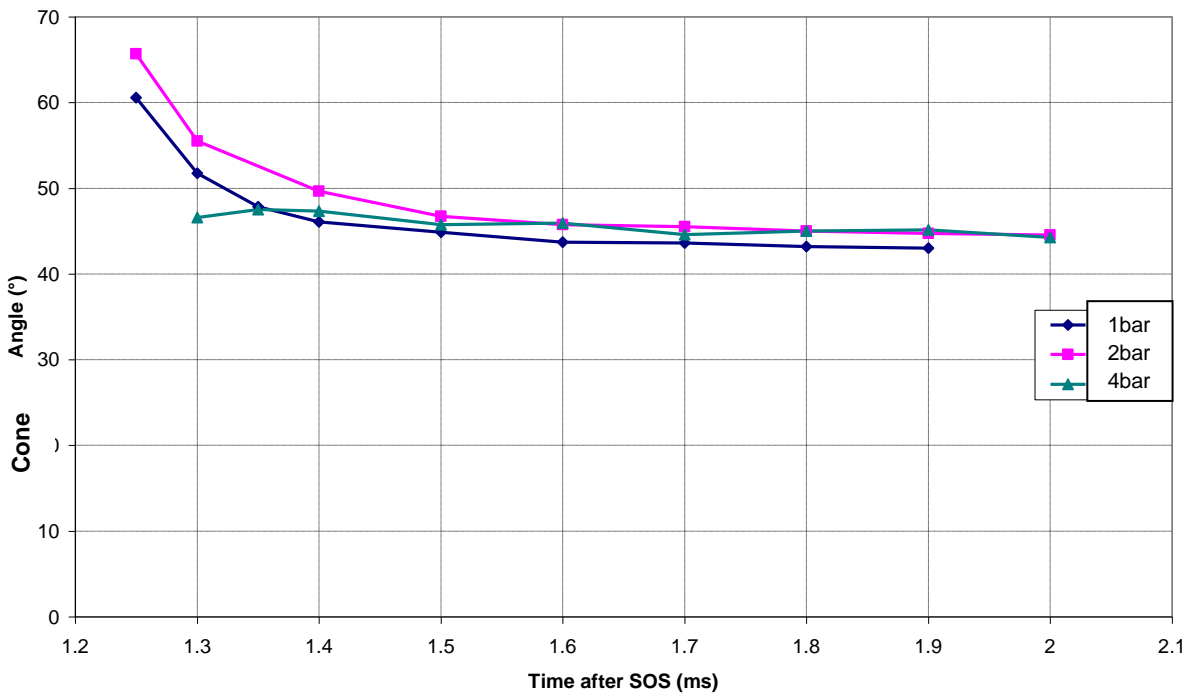


Figure 7.16: Cone angle at 20°C with Injector 1

## Chapter 7 – Results: Pressure Chamber


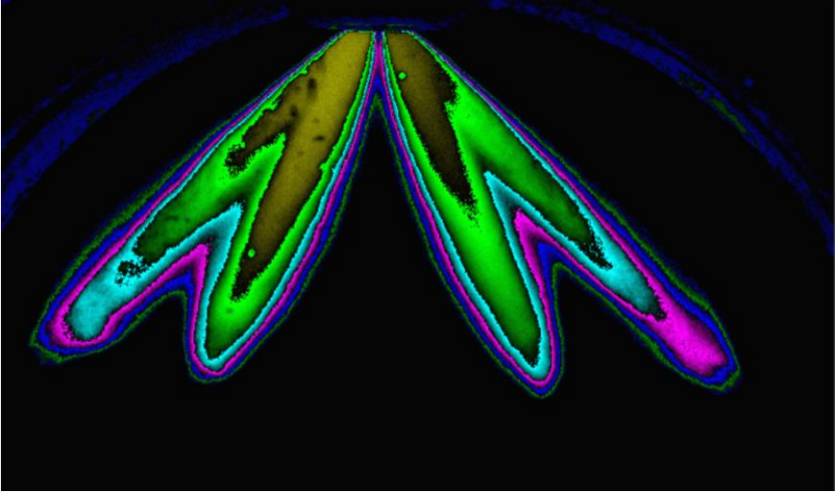

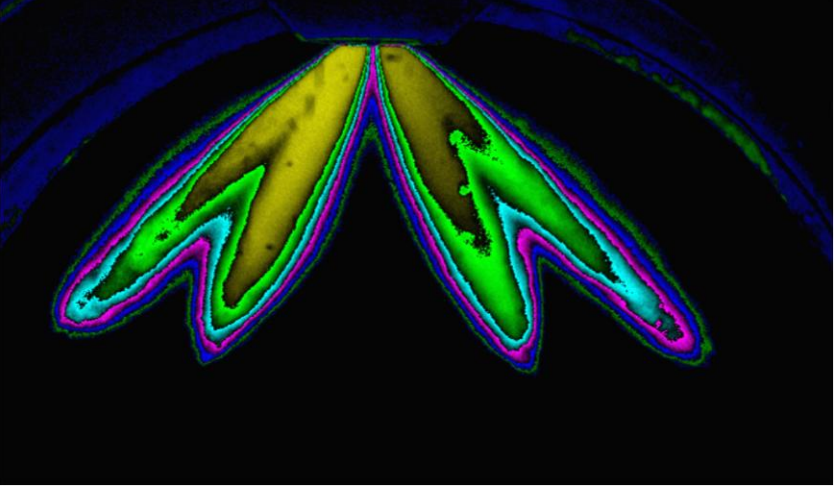
---

Another indication of the reduced axial penetration is that the intensity contours show increased fuel density closer to the plume tip at 4bar backpressure. This highlights the aerodynamics resistance felt by the plume tip and the spray core continuing unaffected, and this characteristic is amplified at higher backpressures.

Table 7.3 shows this effect with pseudo intensity plots at 1.7ms for injector 1 at 2 and 4bar. The kinetic energy of the spray exiting from each injector nozzle should be very similar since the fuel pressure is maintained constant. There is little difference in penetration during the initial stages of spray development because the fuel has had little interaction with the in-cell charge and thus their kinetic energies and hence penetrations are similar.

The radial penetration does not show a similar trend to the axial penetration. The radial penetration at 1 and 2bar backpressure is almost identical and only at 4bar backpressure is a drop in radial penetration seen. No easily identifiable reason for this is present in the images. The anomaly seen at 2bar backpressure could have been due to the cell pressure or temperature not being controlled properly and hence affecting the charge density. The in-cell pressure was not recorded for this part of the testing and the temperature data did not show anything that could have caused these errors thus no easily identifiable reason is present in the data reported in this section. Further testing should be completed to verify the measurement conditions and establish a reason for the anomaly of result.

**Table 7.3: Color scaled images - injector 1 at 1.7ms ASOS - 2 and 4bar backpressure**

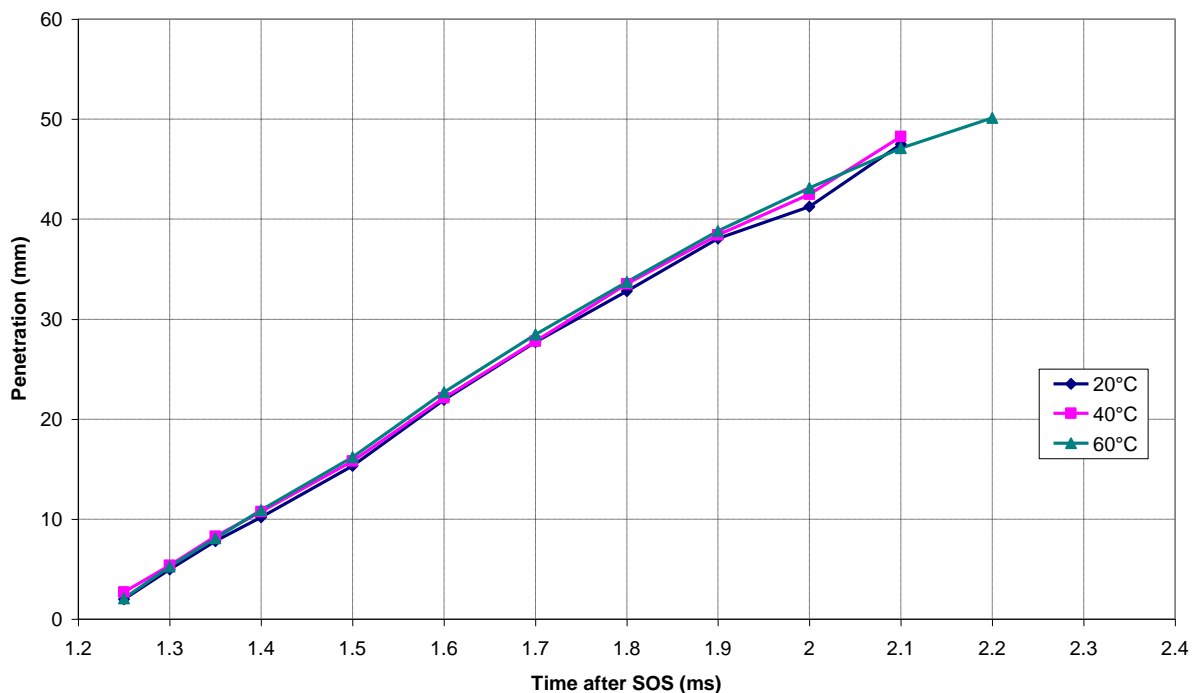
Backpressure (bar)	Injector 1 at 1.7ms
<p data-bbox="323 286 389 315"><b>2bar</b></p>  <p data-bbox="331 674 424 703">30 mm</p>	
<p data-bbox="323 1131 389 1160"><b>4bar</b></p>  <p data-bbox="331 1525 424 1554">30 mm</p>	

## Chapter 7 – Results: Pressure Chamber

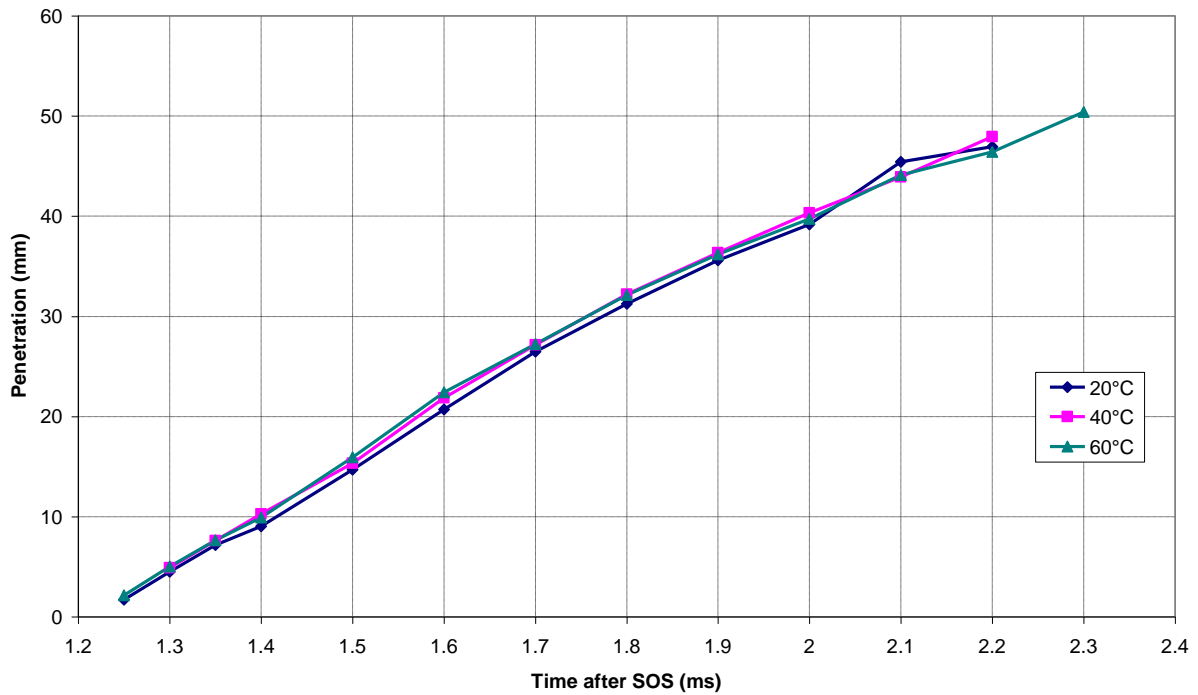
The cone angle results seen at 4bar backpressure, especially during the initial stages of spray development, do not follow a similar trend as seen previously. The initial cone angle is much lower but does not reduce much before levelling off at values very similar to those seen at 2bar backpressure. The initially low value is due to a higher axial penetration. The results observed from 1.3 till 1.5ms ASOS should be repeated to ensure measurement error is not at fault. The cone angle at 4bar levels off at similar values to those seen at 2bar due to the difference in axial and radial penetration between 2 and 4bar being fairly constant throughout the middle and later stages of spray development.

### 7.1.4 Temperature Analysis

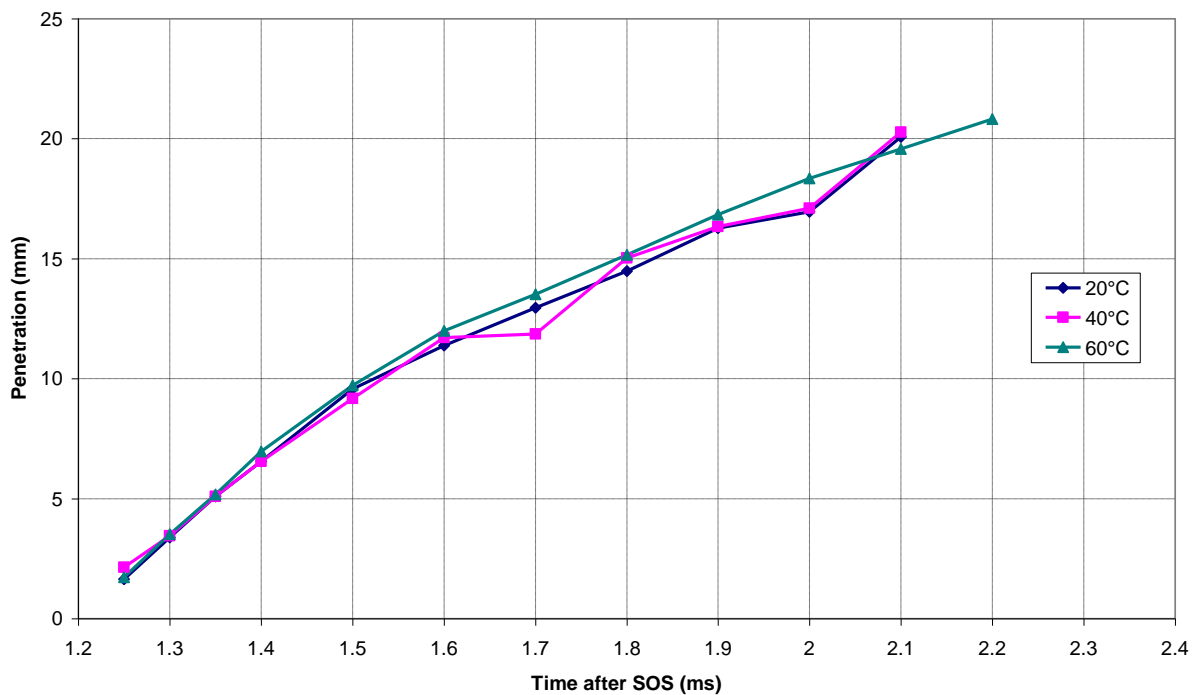
Injector 3 was tested at three different temperatures, 20°C 40°C 60°C, at 1 and 2bar backpressures and at constant 120bar injection pressure. The differences in axial and radial penetration and cone angle were examined. The results are shown in Figure 7.17 to Figure 7.22.



**Figure 7.17: Axial penetration at 1bar backpressure with Injector 3**



**Figure 7.18: Axial penetration at 2bar backpressure with Injector 3**



**Figure 7.19: Radial penetration at 1bar backpressure with Injector 3**

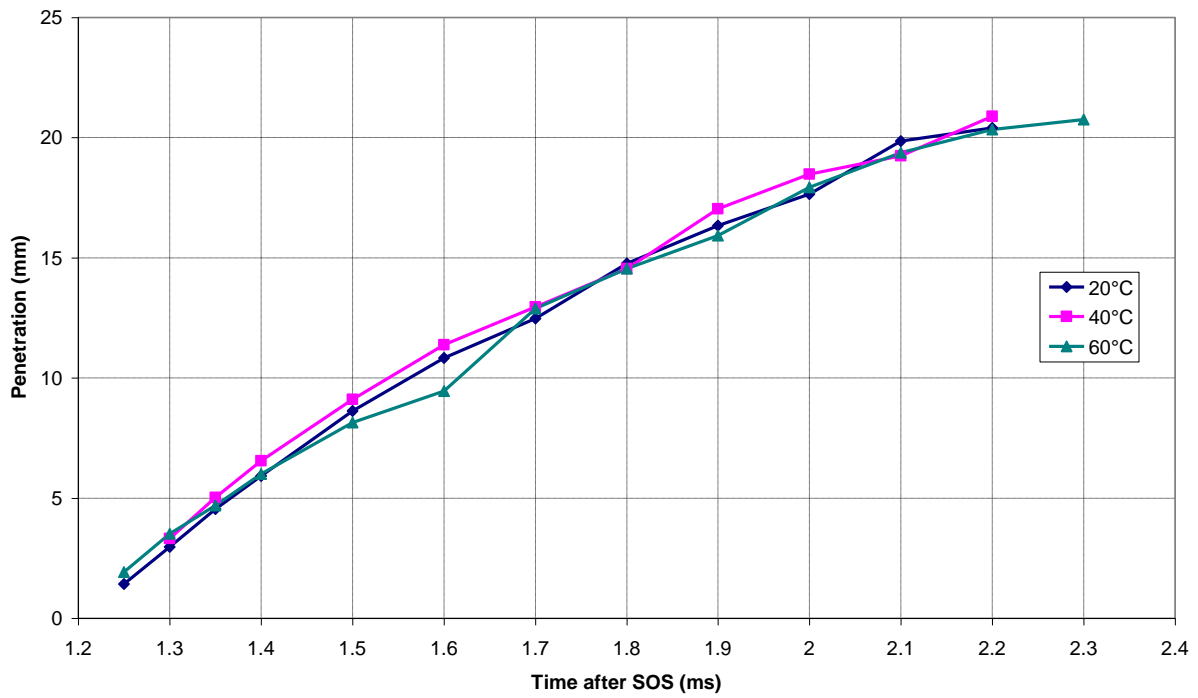


Figure 7.20: Radial penetration at 2bar backpressure with Injector 3

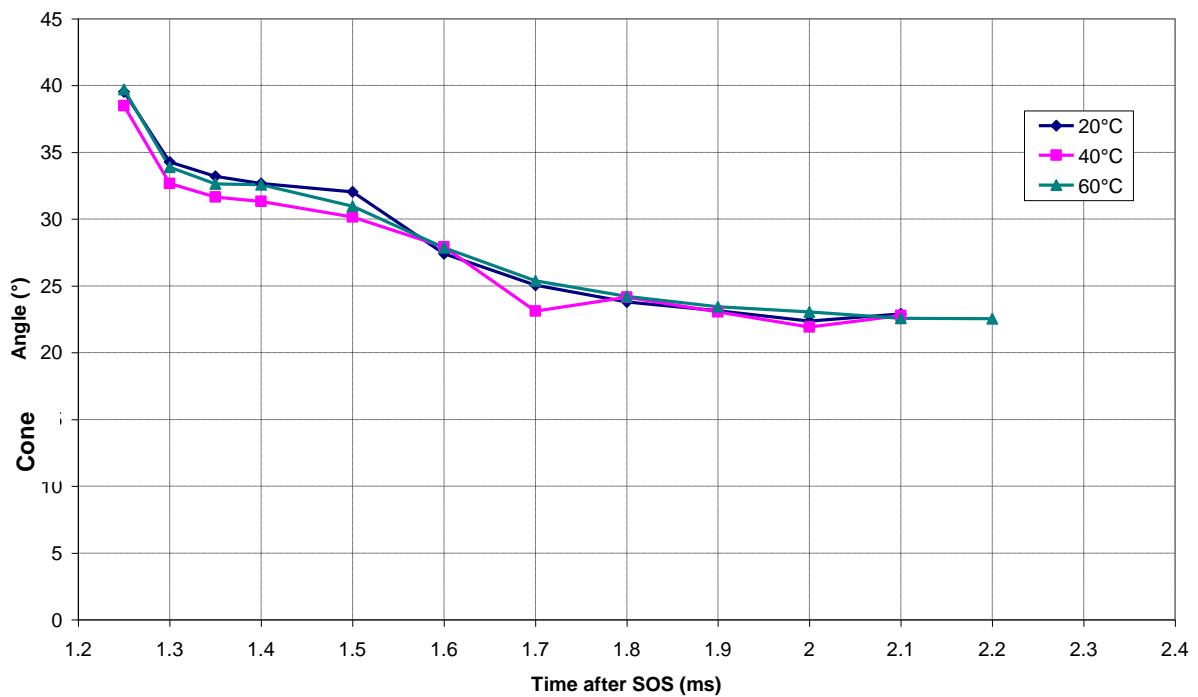
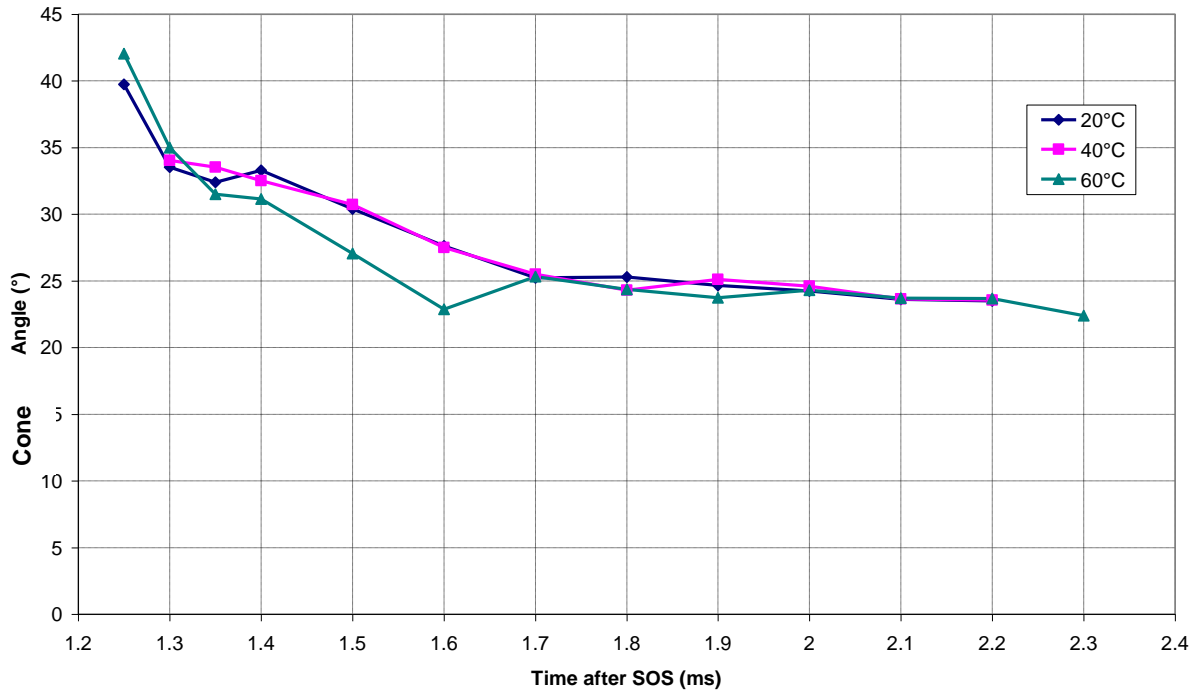


Figure 7.21: Cone angle at 1bar backpressure with Injector 3

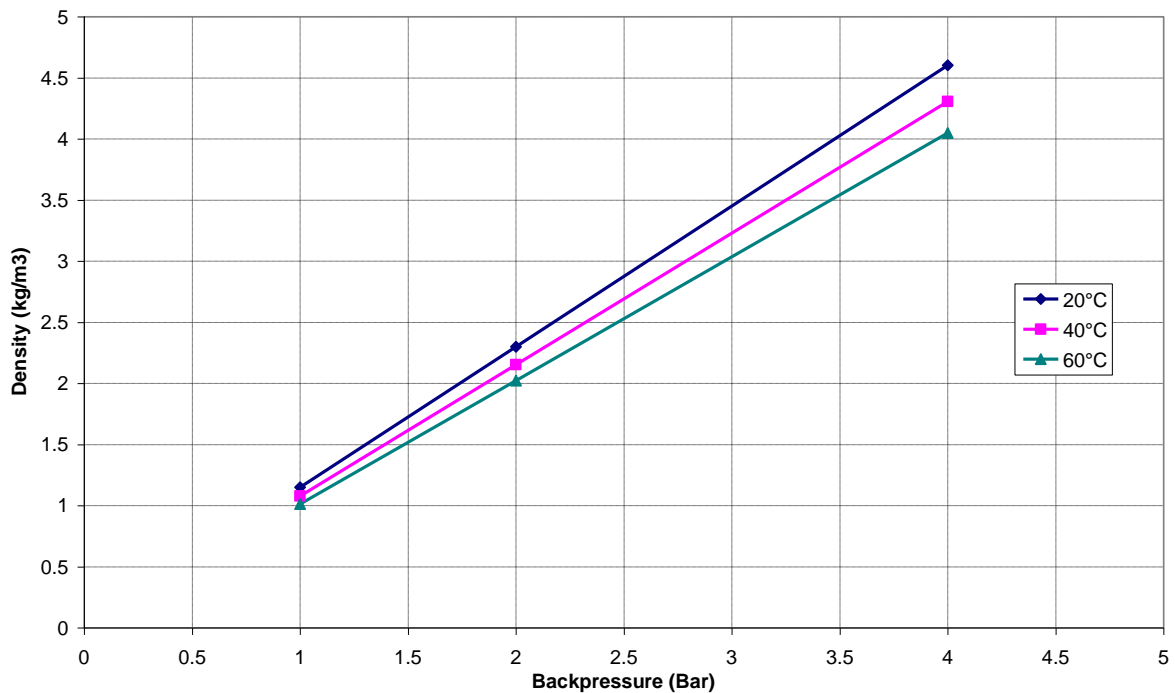




**Figure 7.22: Cone angle at 2bar backpressure with Injector 3**

What is immediately apparent is that for a constant backpressure there is not much difference in axial penetration at the three temperatures tested. This is due to the change in charge density being small at low backpressures of 1 and 2bar. This is proven by assuming the nitrogen charge acts as an ideal gas, then the density of the charge can be found using equation (7.1) and plotted as shown in Figure 7.23.

$$pV = mRT = m \frac{\tilde{R}}{M} T \quad \Rightarrow \quad D = \frac{m}{V} = \frac{Mp}{\tilde{R}T} \quad (7.1)$$



**Figure 7.23: A plot showing the change in charge density with varying cell backpressure and temperature**

What is noticeable is the drop in axial and radial penetration (seen at both 50% and 85% of maximum intensity contours) after 2ms ASOS at 60°C. This is believed to be due to localised flash boiling occurring within the spray. Flash boiling causes rapid boiling and atomisation of the lighter components of the fuel into smaller droplets. These droplets have smaller mass and therefore momentum, causing the aerodynamic affect to become larger and reduce their velocity and penetration. It is believed the spray is experiencing this affect at the later stages of spray development at 60°C. At 1bar backpressure, up to 2.0ms ASOS the axial penetration at 60°C is very similar to that seen at 40°C but at 2.1ms the penetration at 60°C is seen to be lower than at 20°C and 40°C. At 2bar backpressure the flash boiling point has moved to a later timing where it is not until 2.2ms ASOS that a lower axial penetration at 60°C is seen. This can be explained by the idea that as the pressure of a liquid is raised its boiling point also raised. The raised backpressure does not prevent flash boiling occurring but simply delays it.


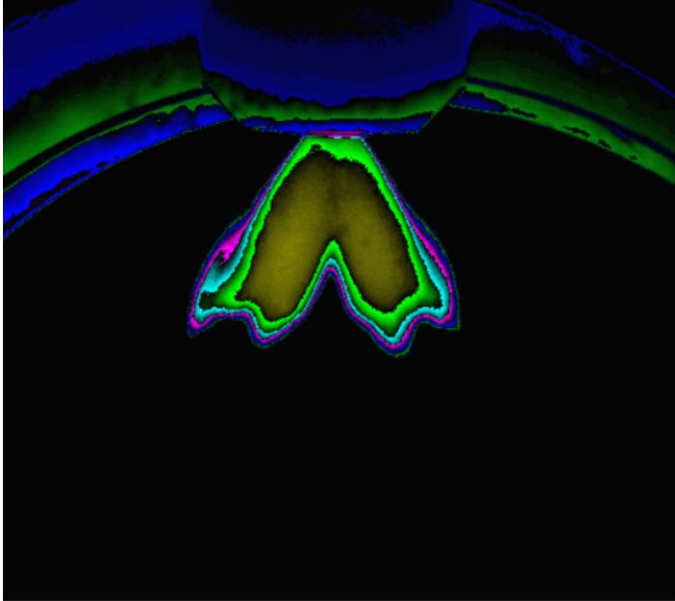

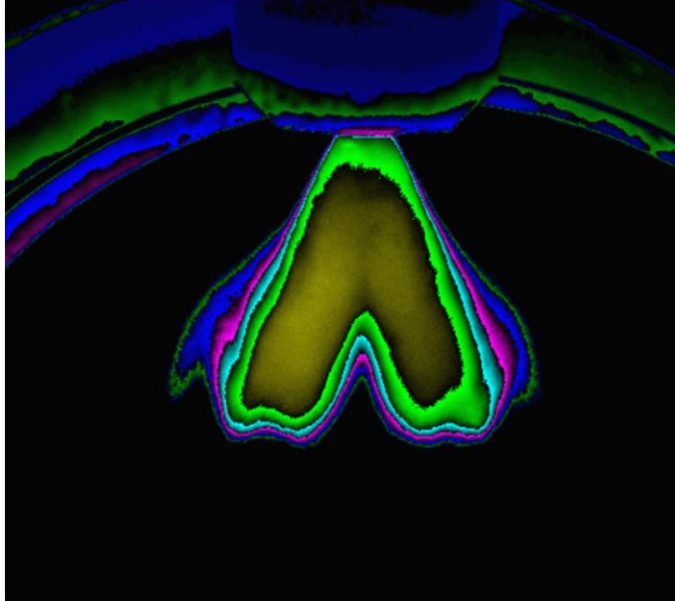
## Chapter 7 – Results: Pressure Chamber

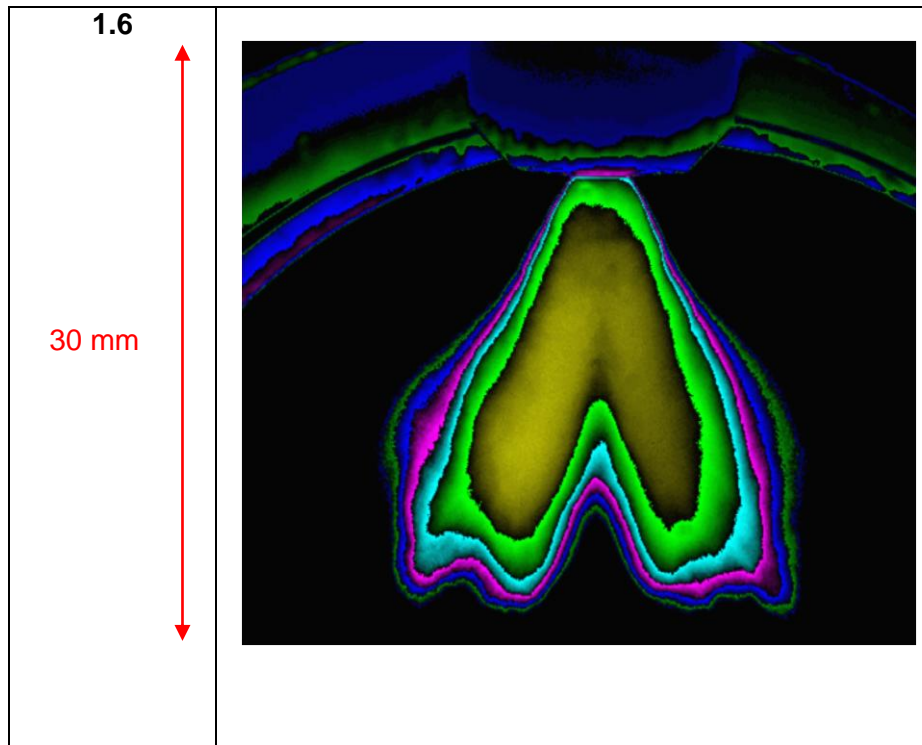
---

If it is assumed that the spray has its own internal pressure that will be equal to the injection pressure just prior to the injector nozzle, but will then vary depending on the position within the spray, as the spray propagates and spreads out its internal pressure will reduce. This reduction in pressure at these conditions could fall below the vapour pressure of certain constituents of the fuel and cause flash boiling. The higher initial backpressure (at 2bar) would cause the sprays' internal pressure to be higher, and would thus require increased expansion before the local spray pressure had reduced below the vapour pressure to cause flash boiling. Hence flash boiling occurring at a later injection timing at 2bar backpressure than at 1bar. This phenomenon is usually found in multi-component fuels where each components of differing vapour pressures and boiling points cause disruption within the drops. Flash boiling will be discussed in more detail later in section 7.2.

The results observed for radial penetration at 1 and 2bar and the three temperature variations show a similar correlation as seen with axial penetration. The cone angles at all three temperature conditions at 1bar back pressure are relatively similar throughout. At 2bar backpressure the results at 60°C show lower cone angles than both other temperature conditions. This is due to the lower radial penetration seen between 1.4 and 1.7ms ASOS as a consequence of the tip deformation. The tip deforms and is pushed around to the back of the plume lowering the radial penetration and thus cone angle until the tip is reformed with new drops from behind. This has been mentioned previously at 1bar, but, due to the increased backpressure, has a more significant affect and is thus why the radial penetration drops more at 2bar than at 1bar. Although tip deformation is visible at 20°C and 40°C, the degree of deformation is smaller. This is likely to be due to the higher charge density increasing the aerodynamic drag and thus increasing the deformation seen at the spray tip. Table 7.4 shows the tip deformation seen at 1.4 to 1.6ms ASOS, and the upper plume (not used for measurements) highlights this effect further

**Table 7.4: A series of images showing plume tip deformation with injector 3**

Timing (ms ASOS)	Injector 3 – 2bar backpressure, 60°C
<p data-bbox="411 338 459 371"><b>1.4</b></p>  <p data-bbox="371 645 467 678">30 mm</p>	
<p data-bbox="411 1077 459 1111"><b>1.5</b></p>  <p data-bbox="371 1384 467 1417">30 mm</p>	



### 7.1.5 Fuel Pressure Analysis

Injector 3 was also tested at two different fuel injection pressures, 120bar and 190bar. Tests at 20°C, 40°C and 60°C at two backpressures of 1 and 2bar were completed. The results are shown in Figure 7.24 to Figure 7.29.

An increase in injection pressure increases the pressure differential across the nozzle tip which acts to increase the exit velocity of the spray. This increases the aerodynamic resistance due to the increased shear force and the increased turbulence within the spray promotes disintegration. Lefebvre [17] states that an increase in jet turbulence increases the ratio of radial to axial component of velocity therefore increasing the cone angle, however this is not seen in the results observed with injector 3.

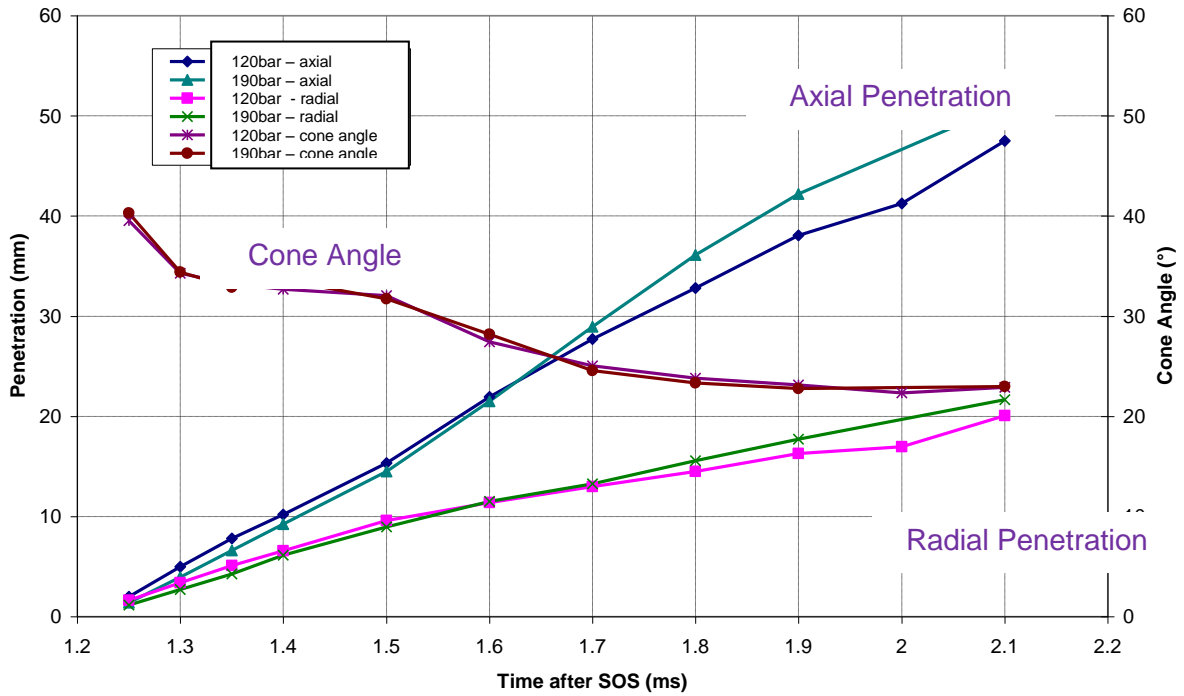


Figure 7.24: 120bar and 190bar at 20°C and 1bar backpressure with Injector 3

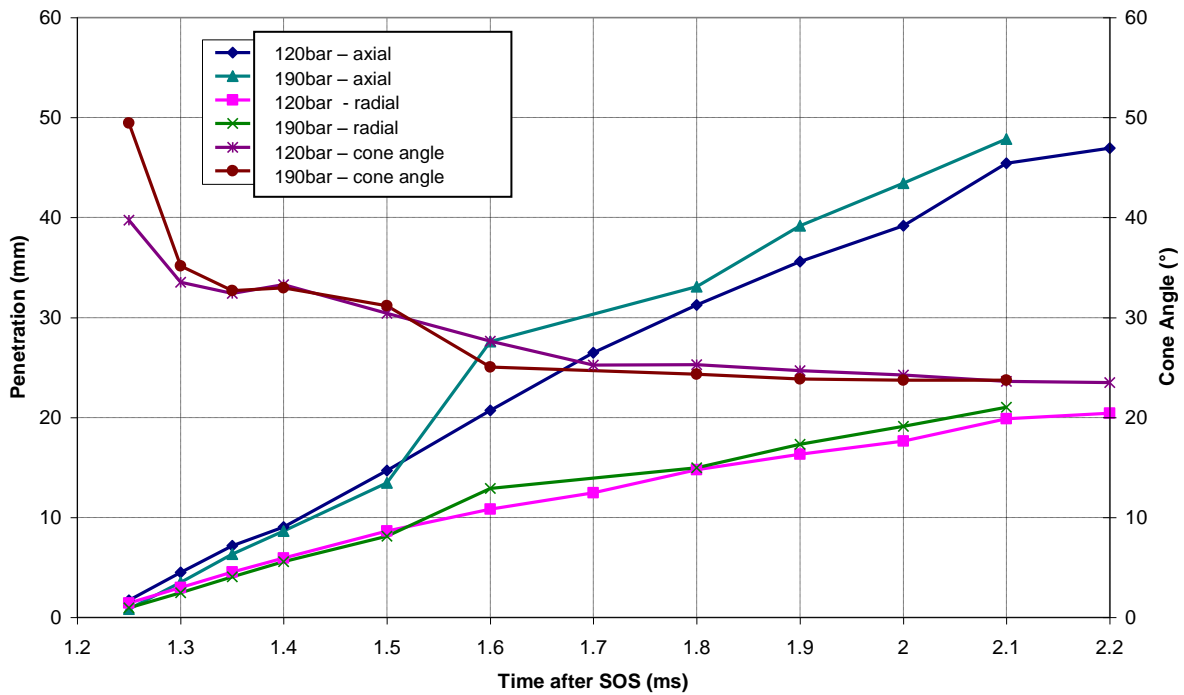


Figure 7.25: 120bar and 190bar at 20°C and 2bar backpressure with Injector 3

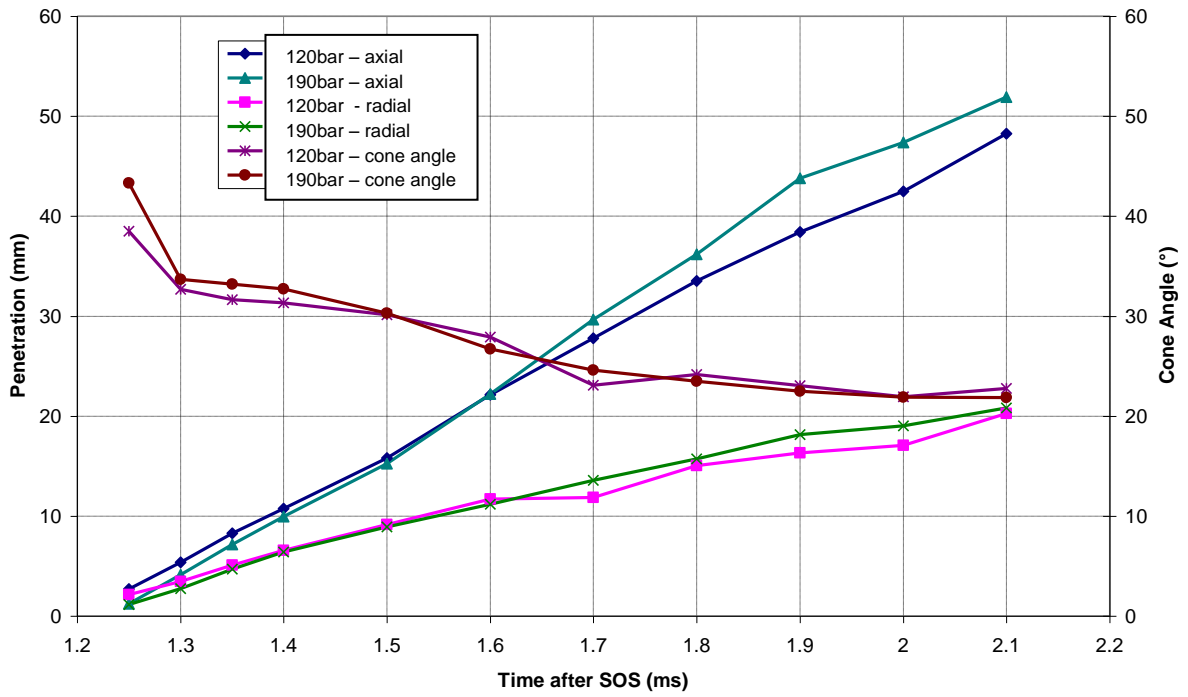


Figure 7.26: 40°C and 1bar backpressure with Injector 3

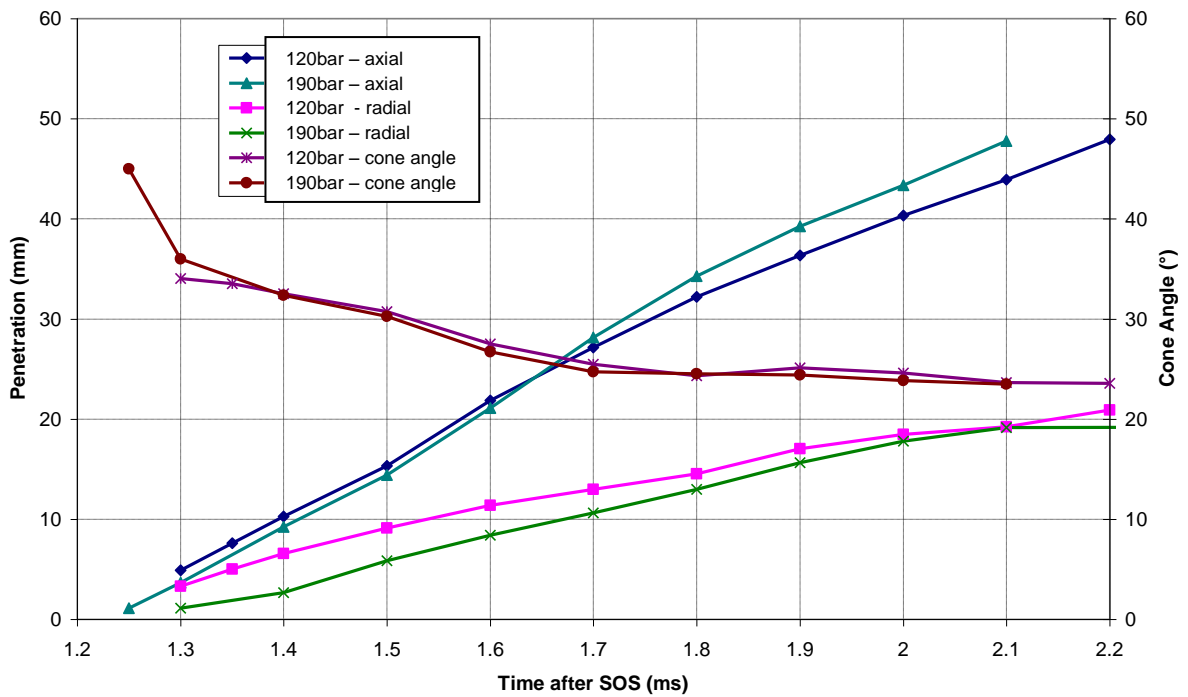
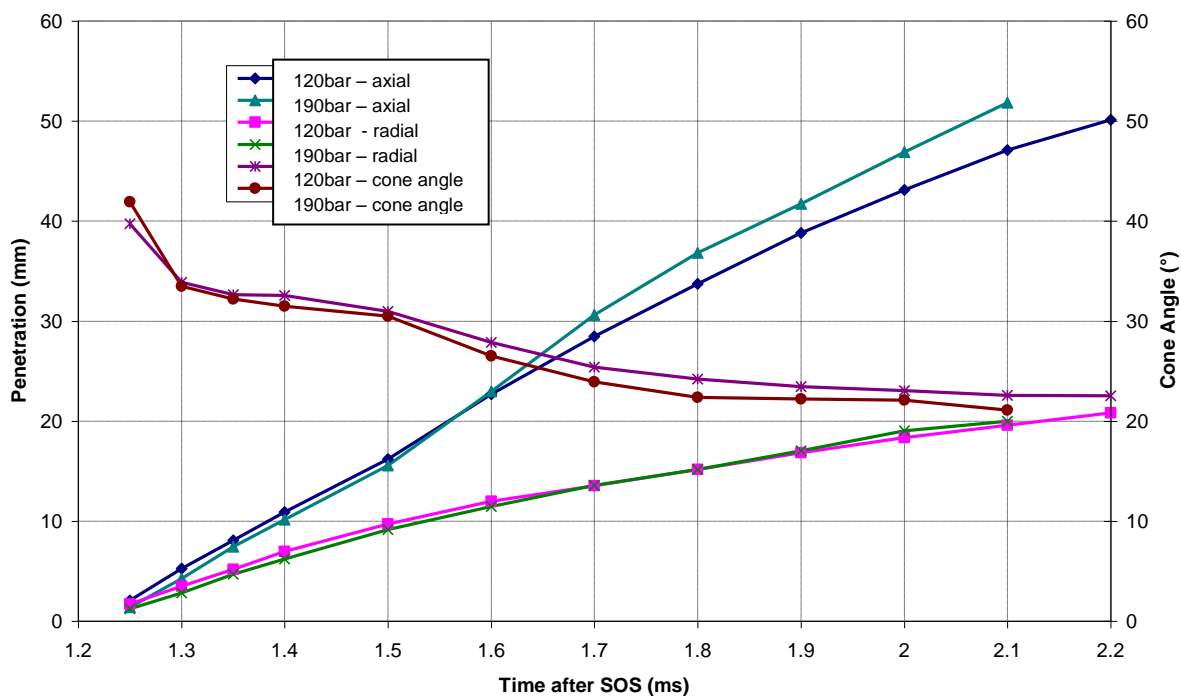
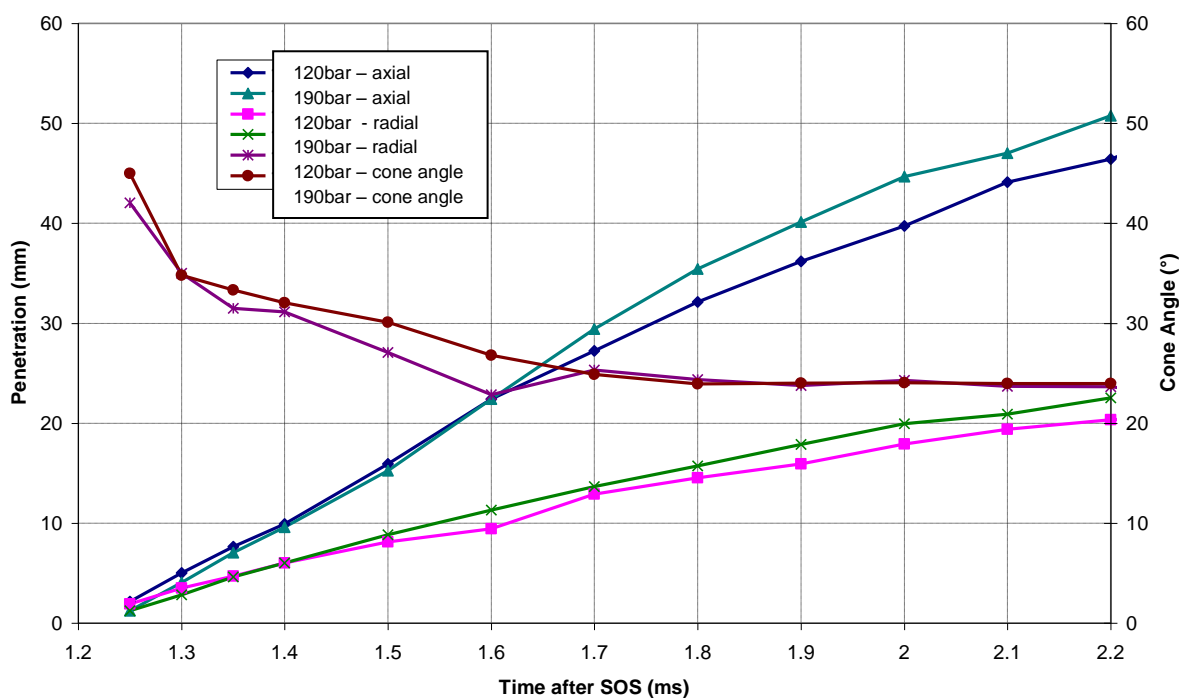


Figure 7.27: 40°C and 2bar backpressure with Injector 3



**Figure 7.28: 60°C and 1bar backpressure with Injector 3**

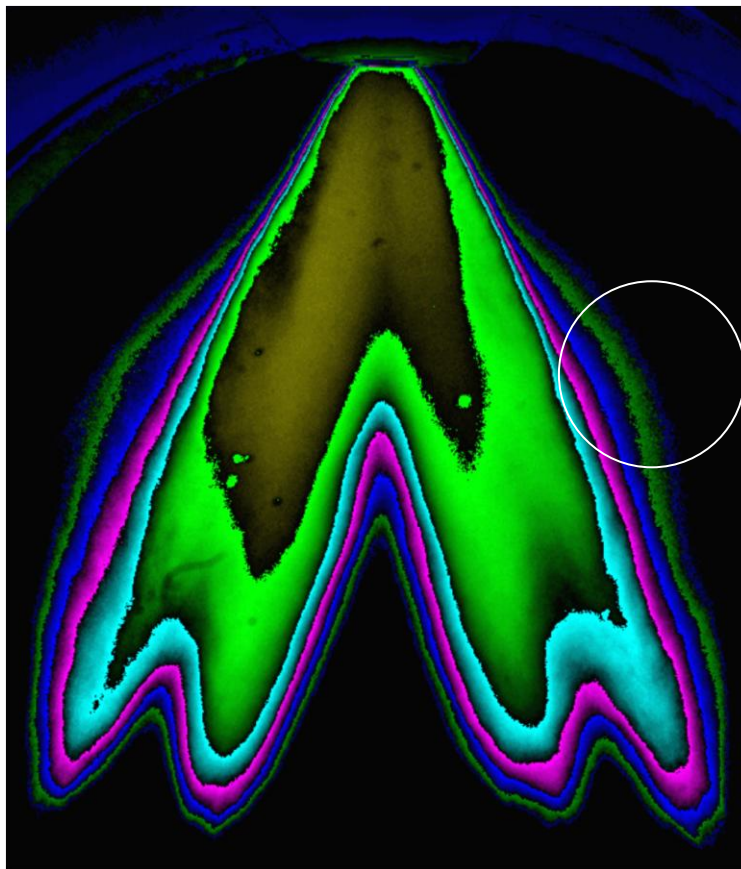


**Figure 7.29: 60°C and 2bar backpressure with Injector 3**



When raising the injection pressure, the initial axial penetration is smaller up to timings of 1.6ms ASOS. After this point, the penetration is larger with higher injection pressure. This trend also follows for radial penetration, although the point at which the penetration starts to become larger for higher injection pressures is not as well defined as with axial penetration. It is believed that this trend is due to the increased turbulence causing an increase in flow resistance inside the nozzle that restricts initial propagation and hence shows lower initial axial and radial penetration. What is interesting, and in fact contradictory to Lefebvre's statement, is the minimal difference in cone angle seen at the two injection pressures. At 20°C and 40°C very little difference is seen. There is a difference in results seen at 60°C at both 1bar and 2bar although, because the differences seen do not follow for each ambient charge pressure, it is unclear as to whether these are not just measurement uncertainties. During very early timings, 1.25ms and in some cases 1.3ms and 1.4ms ASOS, the spray does follow Lefebvre's theory but this difference quickly disappears thereafter.

The images also show an increase in waviness at the periphery of plume highlighting the effect of higher injection velocities. An example of this is shown in Figure 7.30 circled in white.



**Figure 7.30: Highlighting the increase in spray surface ripples due to increased fuel pressure**

### 7.1.6 Data Manipulation and Analysis

In this section, empirical relationships are going to be developed to produce estimates of the spray's axial and radial penetration for each injector at part load conditions that can be encountered during the operating cycle of a GDI engine. The data were manipulated using common mathematical techniques to interpolate and estimate its characteristics under specific conditions. The part load engine condition of interest was 1.65bar pressure, 45°C temperature and 190bar fuel pressure.

The axial and radial penetrations were of prime importance for estimation since these features determined the likelihood of a spray impact. Although the variation of a spray cone angle is relevant in terms of understanding spray characteristics, it is not relevant for the predictions under engine conditions and was therefore not analysed in this section.

The axial and radial penetration results for each injector at 20°C, 1 and 2bar were fitted with quadratic best fit lines calculated by the least squares method. The coefficients from each plot were then plotted against backpressure and linear best fit lines used to form equations for axial and radial penetration of each injector as a function of backpressure and time.

The results from this analysis are shown in Figure 7.31 to Figure 7.33. Equations 7.2 to 7.7 were extrapolated and provide a sensitivity check on the square, linear and constant terms of the results at 120bar injection pressure, and Figure 7.34 to Figure 7.38 give an example of how the estimated results using the formed equations matches the actual results.

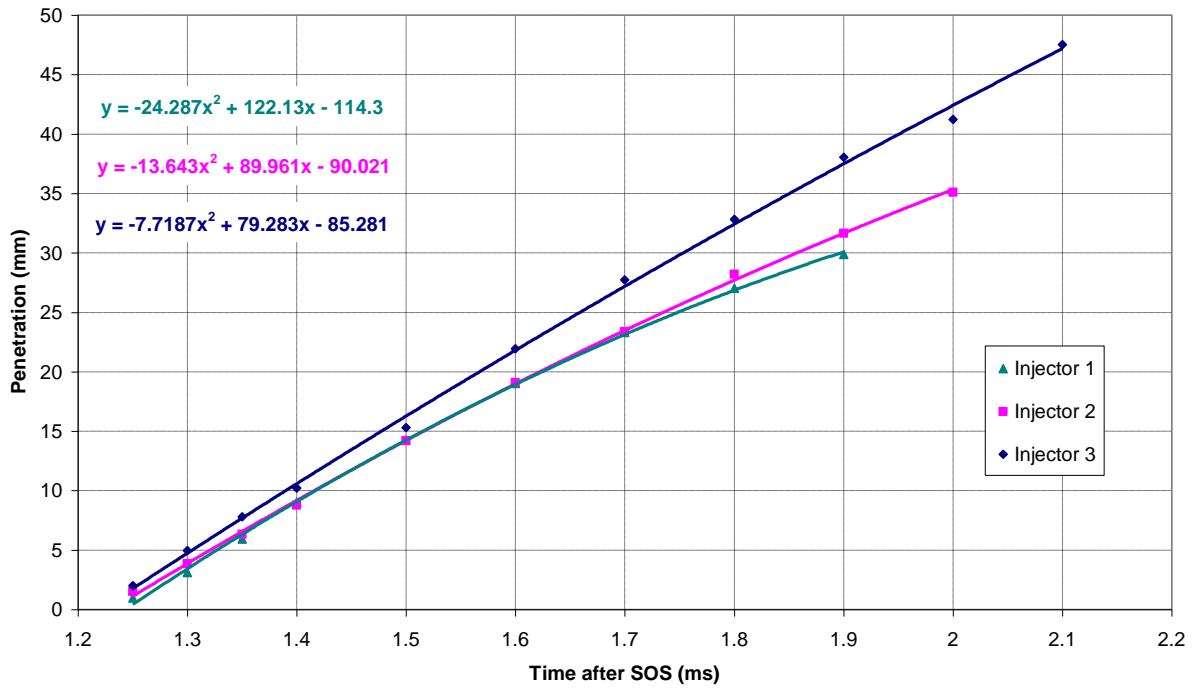


Figure 7.31: Axial penetration at 20°C and 1bar backpressure

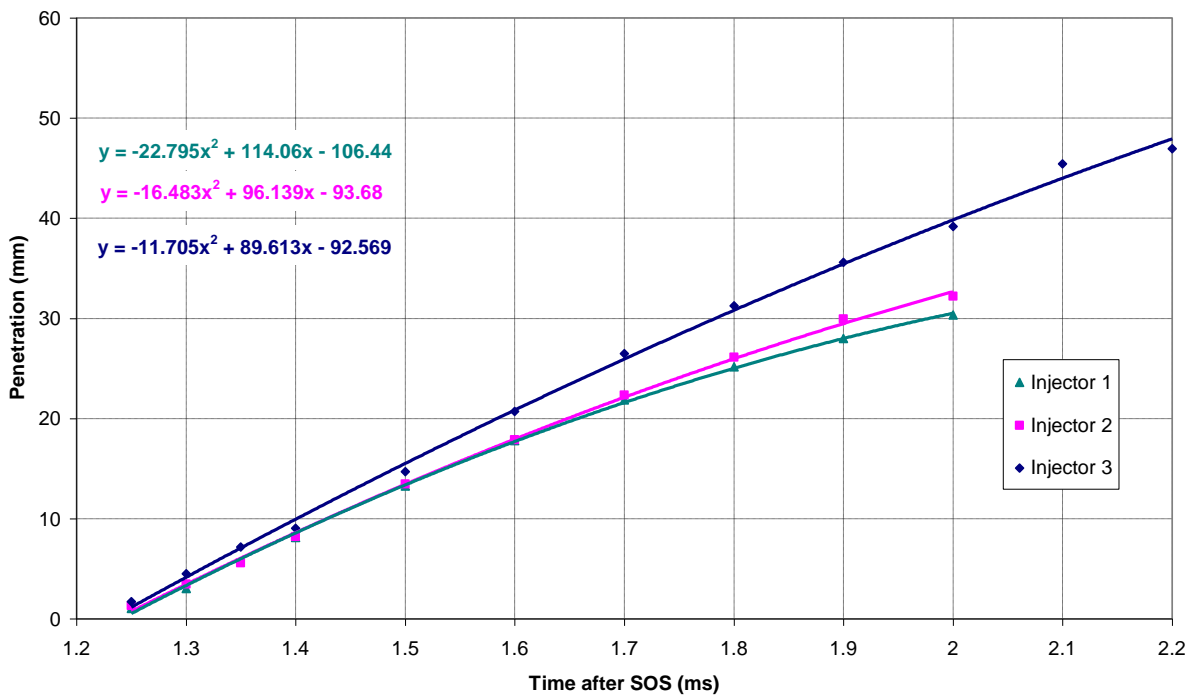
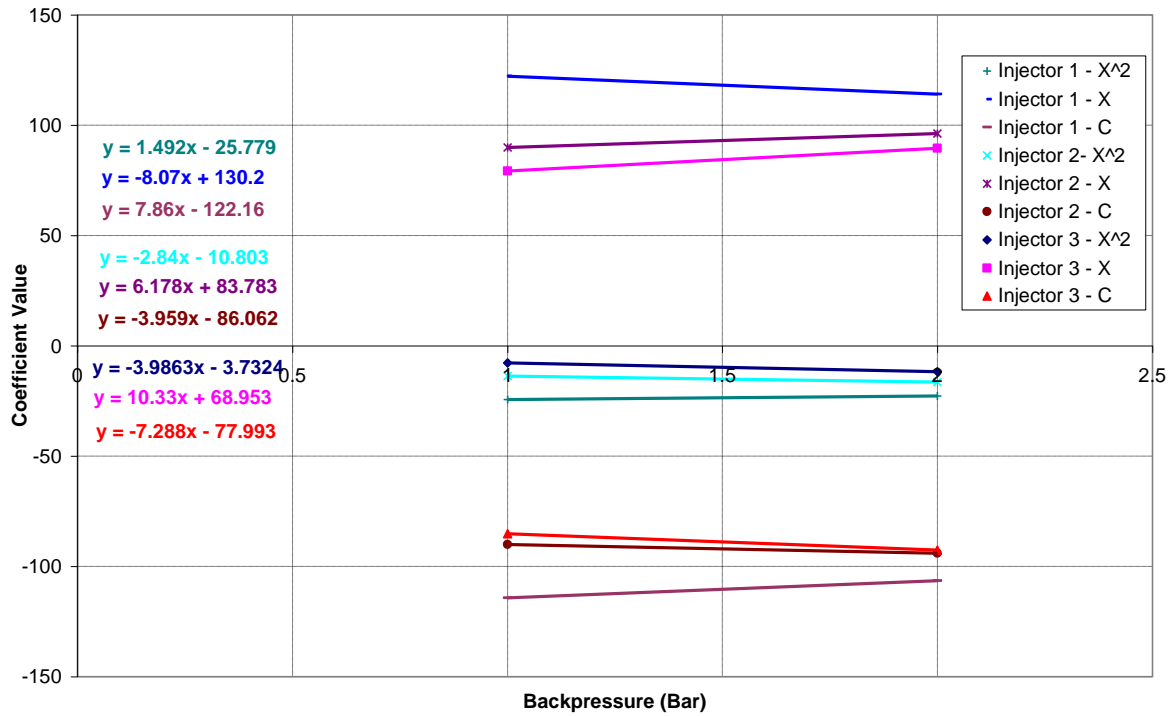


Figure 7.32: Axial penetration at 20°C and 2bar backpressure



**Figure 7.33: Best fit coefficients for axial penetration as a function of backpressure**

$$S_{Injector\ 1,\ axial} = (1.492p - 25.779)t^2 + (-8.07p + 130.2)t + (7.86p - 122.16) \quad (7.2)$$

$$S_{Injector\ 2,\ axial} = (-2.84p - 10.803)t^2 + (6.178p + 83.783)t + (-3.959p - 86.062) \quad (7.3)$$

$$S_{Injector\ 3,\ axial} = (-3.9863p - 3.7324)t^2 + (10.33p + 68.953)t + (-7.288p - 77.993) \quad (7.4)$$

where  $p$  is the in-cell charge pressure and  $t$  is the injection timing, and  $S$  is the axial penetration.

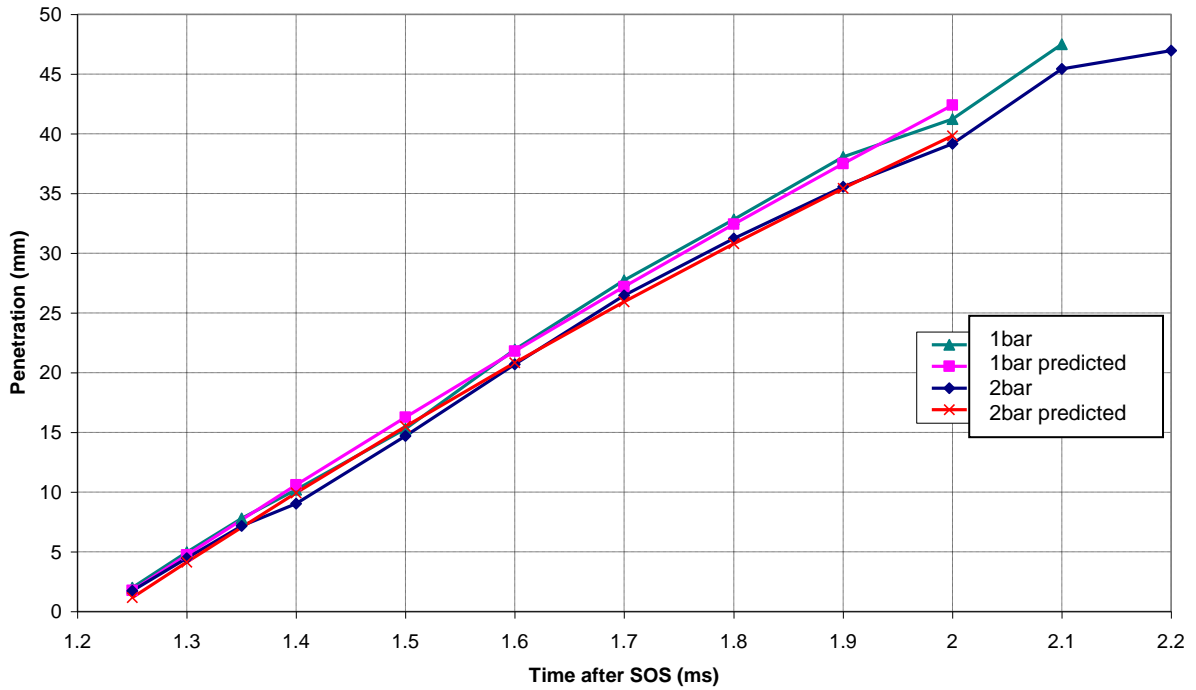


Figure 7.34: Predicted and actual results for axial penetration at 20°C as a function of backpressure for injector3

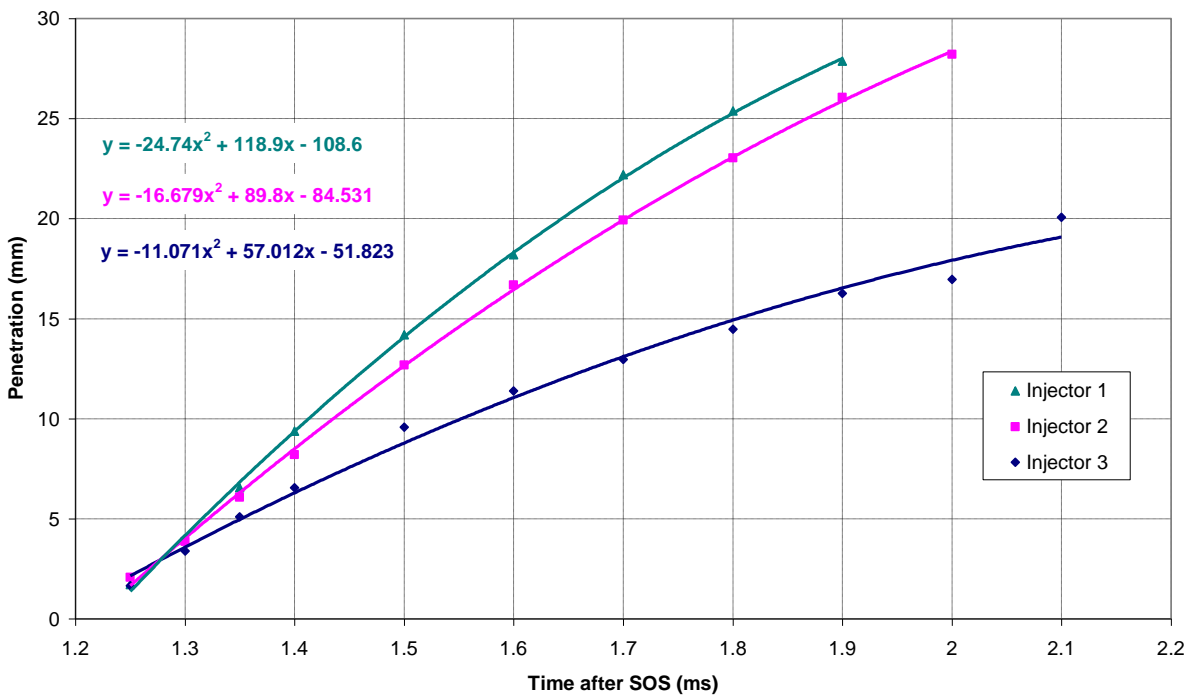


Figure 7.35: Radial penetration at 20°C and 1bar backpressure

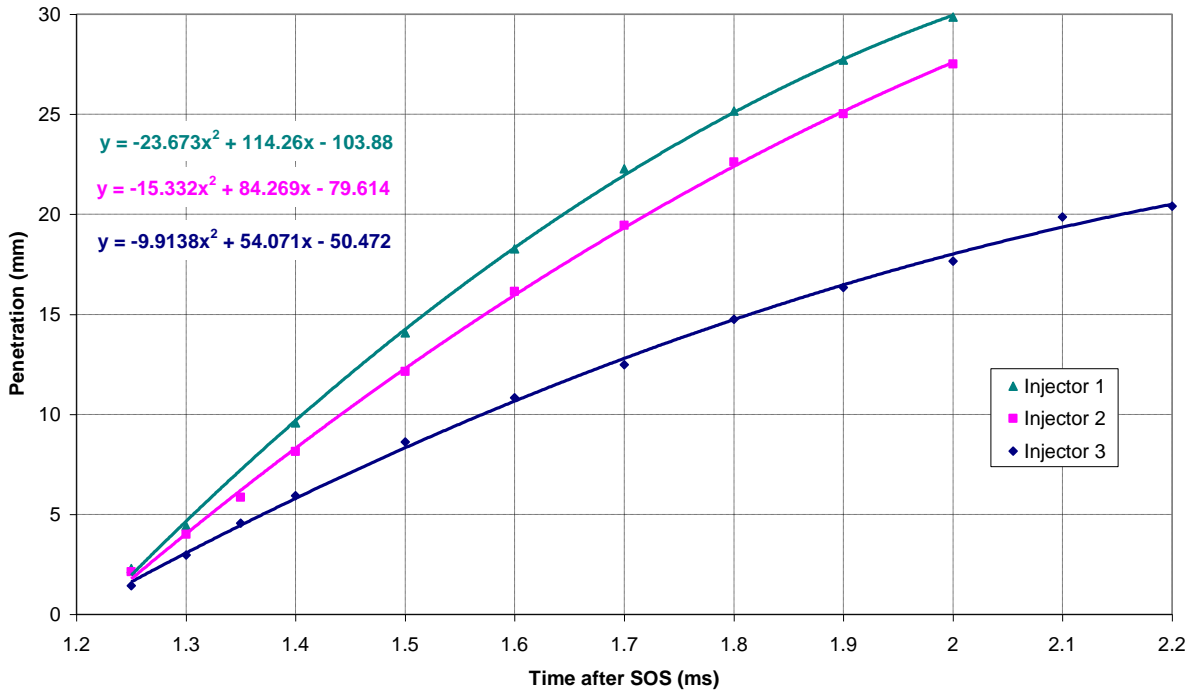


Figure 7.36: Radial penetration at 20°C and 2bar backpressure

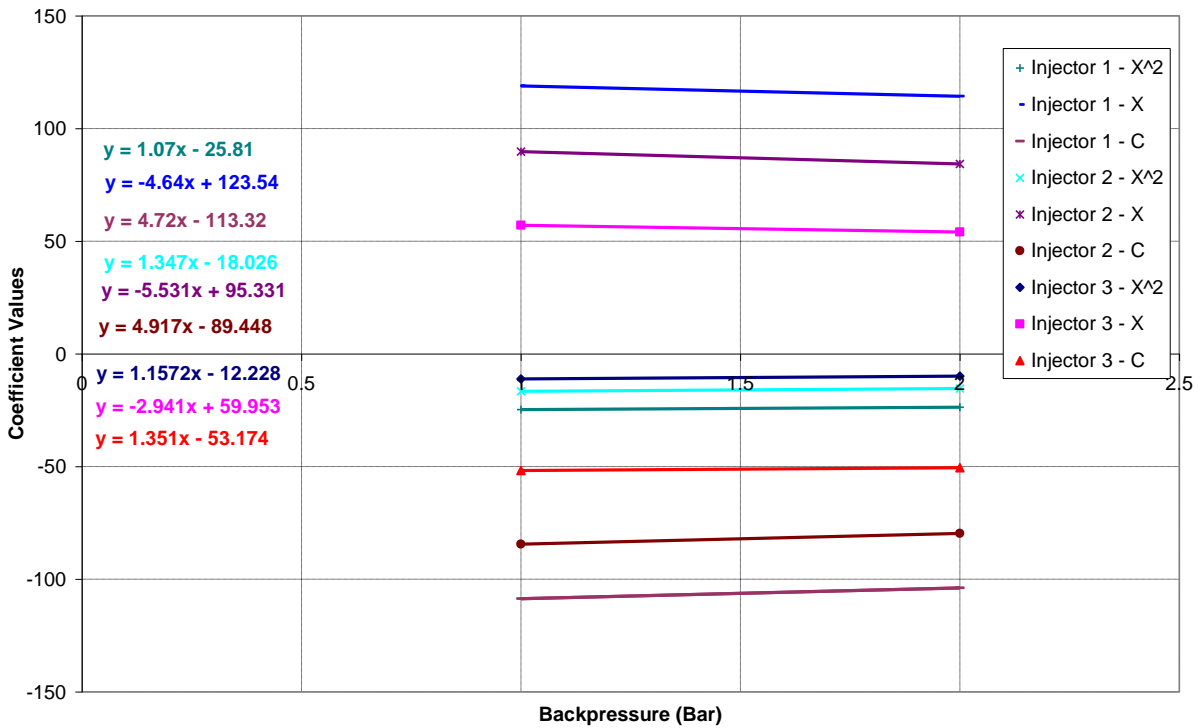
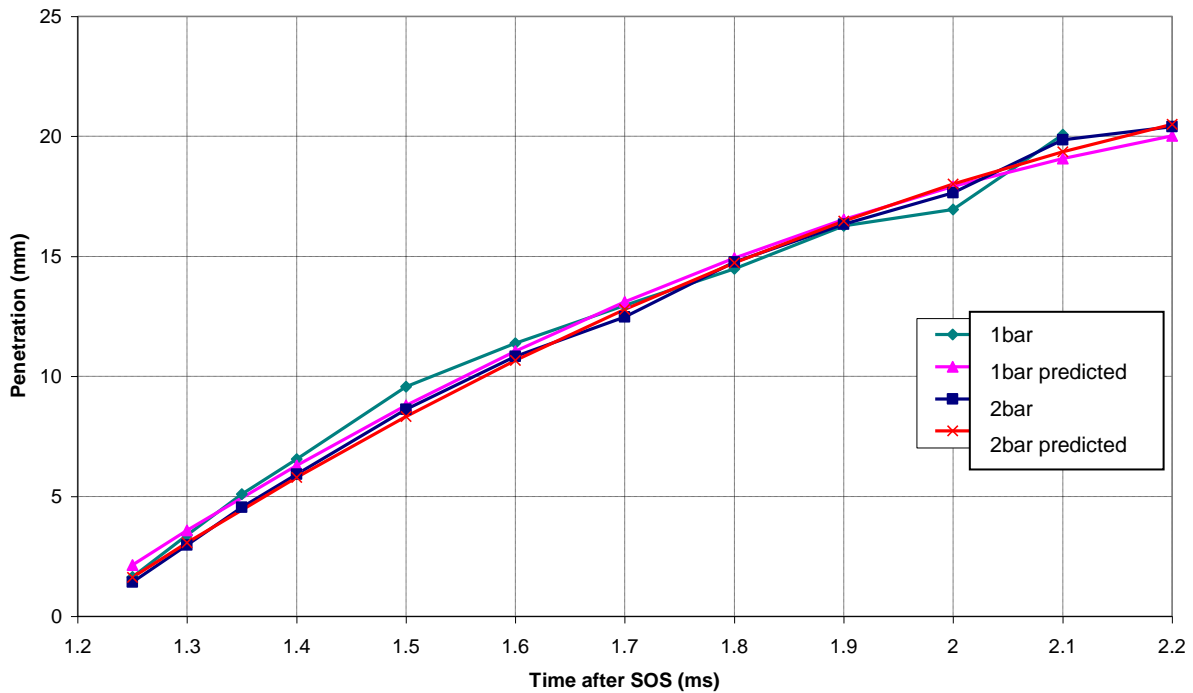


Figure 7.37: Best fit coefficients for radial penetration as a function of backpressure

$$S_{Injector\ 1,\ radial} = (1.07p - 25.81)t^2 + (-4.64p + 123.54)t + (4.72p - 113.32) \quad (7.5)$$

$$S_{Injector\ 2,\ radial} = (1.347p - 18.026)t^2 + (-5.531p + 95.331)t + (-4.917p + 89.448) \quad (7.6)$$

$$S_{Injector\ 3,\ radial} = (1.1572p - 12.228)t^2 + (-2.941p + 59.953)t + (1.351p - 53.174) \quad (7.7)$$



**Figure 7.38: Predicted and actual results for radial penetration at 20°C as a function of backpressure for injector3**

Considering Figure 7.34 to Figure 7.38 to provide an indication as to the accuracy of the predicted axial and radial penetration, it appears that a good approximation has been found, with the largest error being approximately 1mm for both predicted data sets.

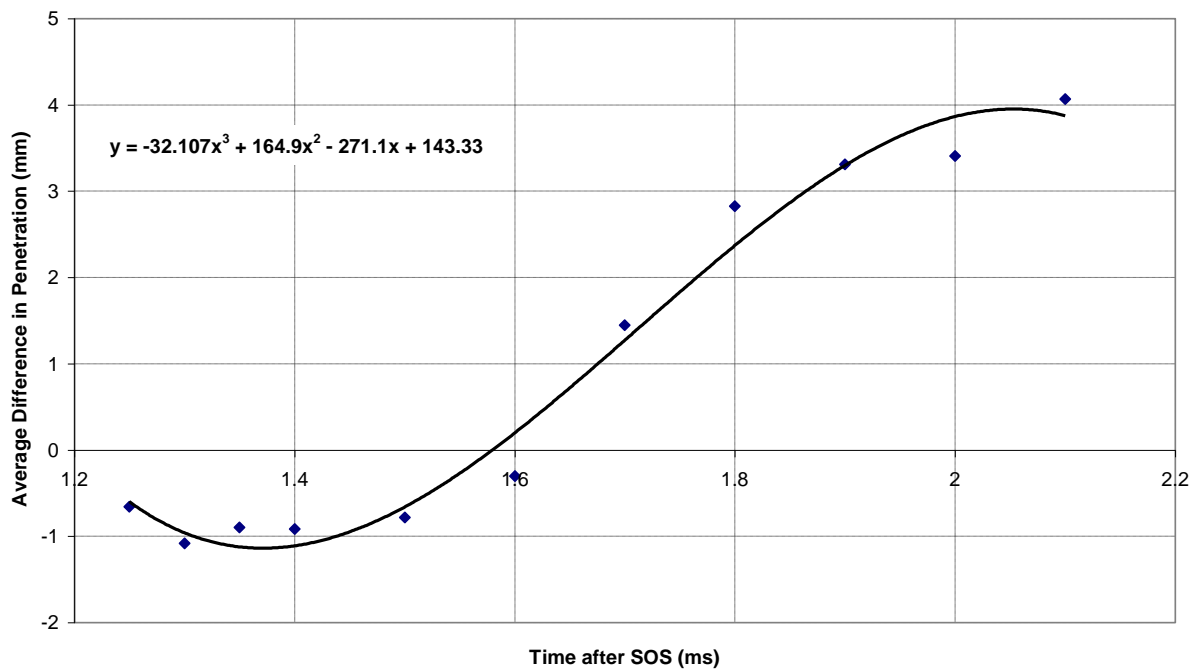
One issue with the data used is that only data for two pressure conditions are available and as such the linear best fit lines used to form the final equations, have been applied to only two data points and will not provide high levels of confidence. Therefore, to increase the statistical significance of the data, results should be gathered at additional pressure conditions.

The same technique developed above was also applied to the temperature data gathered with injector 3. This provided axial and radial penetration at 1 and 2bar for injector 3 as a function of temperature and time. The results from this analysis are shown in Appendix A. Once the equations for axial and radial penetration for injector 3, as a function of temperature and time were formed, a method of linking this and the equations formed previously as a function of backpressure was needed. There is no easy method of achieving this, and one method called neural networking was beyond the scope and time constraints of this study. Since the change in penetration with varying temperature was small, an approximation was made to assume that there was zero change in penetration with change in temperature. This would mean that predictions for penetration at the engine's part load conditions could be found, with only a small reduction in estimation accuracy. The estimation accuracy as a function of backpressure would only be compromised if predictions at higher charge temperatures were required due to a larger change in cell density.

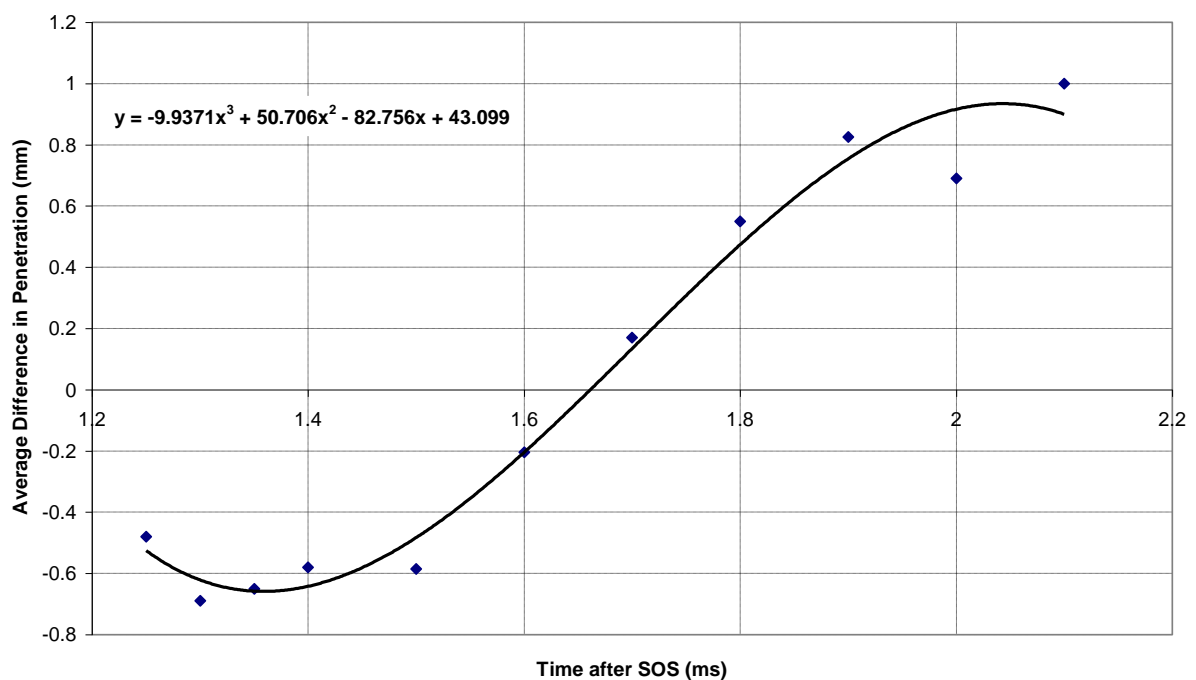
Due to the differences seen in axial and radial penetration with an increase in fuel injection pressure, a method of adjusting the penetration data at 120bar to predict the penetration at 190bar was created. Three different conditions were analysed for both axial and radial penetration from the results gathered with injector 3, and the difference in penetration between 120bar and 190bar was calculated. The three conditions chosen were based on results with the fewest anomalies. The differences over the injection timing range were averaged over the three conditions to find an average difference. The average difference was then plotted against injection timing and fitted with a third order polynomial calculated by the least squares method. The resultant formulae were applied to the results gathered with injector 1 and injector 2 at 120bar, and used to predict the additional axial or radial penetration as a consequence of the higher injection pressure. Figure 7.39 and Figure 7.40 show the results from this analysis and the formulae derived are shown in equations 7.8 and 7.9.

One of the limitations of this method is the best fit does not extrapolate correctly outside of the data range provided. If extrapolated, due to the polynomial the penetration will actually show a reducing trend after a peak penetration. This is obviously not the case and therefore the estimations can only be considered valid up to approximately 2.2ms ASOS. Another approximation made is that the effect of increasing injection pressure on injector 3 will be the same as seen with the other two other injectors. For improved accuracy, the tests should be repeated with injector 1 and 2, and a similar analysis performed for increased prediction accuracy.





**Figure 7.39: Derivation of the additional axial penetration moving from 120bar to 190bar injection pressure**



**Figure 7.40: Derivation of the additional radial penetration moving from 120bar to 190bar injection pressure**

$$S_{\text{Additional penetration, axial}} = -32.107t^3 + 164.9t^2 - 271.1t + 143.33 \quad (7.8)$$

$$S_{\text{Additional penetration, radial}} = -9.9371t^3 + 50.706t^2 - 82.756t + 43.099 \quad (7.9)$$

Therefore the final equations for injectors 1, 2 and 3 to predict axial and radial penetration at 190bar as a function of backpressure and injection time at low backpressures are:

### Injector 1

$$S_{\text{Injector 1, axial}} = [(1.492p - 25.779)t^2 + (-8.07p + 130.2)t + (7.86p - 122.16)] \\ + [-32.107t^3 + 164.9t^2 - 271.1t + 143.33] \quad (7.10)$$

$$S_{\text{Injector 1, radial}} = [(1.07p - 25.81)t^2 + (-4.64p + 123.54)t + (4.72p - 113.32)] \\ + [-9.9371t^3 + 50.706t^2 - 82.756t + 43.099] \quad (7.11)$$

### Injector 2

$$S_{\text{Injector 2, axial}} = (-2.84p - 10.803)t^2 + (6.178p + 83.783)t + (-3.959p - 86.062) \\ + [-32.107t^3 + 164.9t^2 - 271.1t + 143.33] \quad (7.12)$$

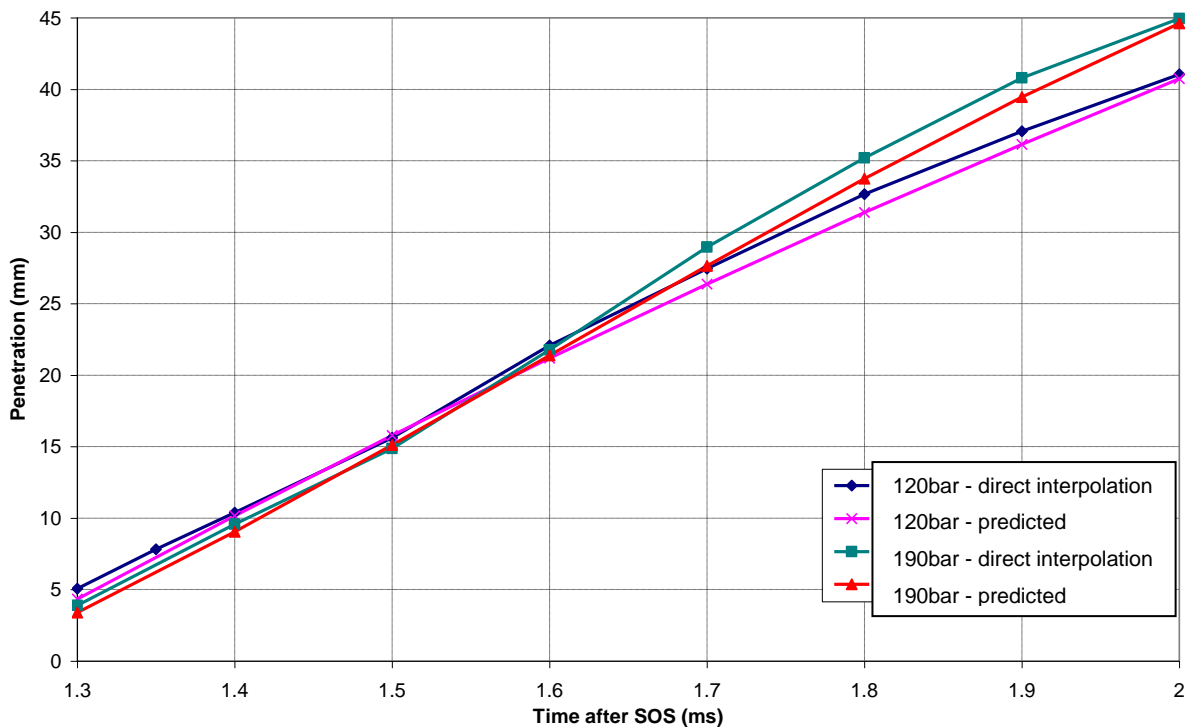
$$S_{\text{Injector 2, radial}} = (1.347p - 18.026)t^2 + (-5.531p + 95.331)t + (-4.917p + 89.448) \\ + [-9.9371t^3 + 50.706t^2 - 82.756t + 43.099] \quad (7.13)$$

### Injector 3

$$S_{\text{Injector 3, axial}} = (-3.9863p - 3.7324)t^2 + (10.33p + 68.953)t + (-7.288p - 77.993) \\ + [-32.107t^3 + 164.9t^2 - 271.1t + 143.33] \quad (7.14)$$

$$S_{\text{Injector 3, radial}} = (1.1572p - 12.228)t^2 + (-2.941p + 59.953)t + (1.351p - 53.174) \\ + [-9.9371t^3 + 50.706t^2 - 82.756t + 43.099] \quad (7.15)$$

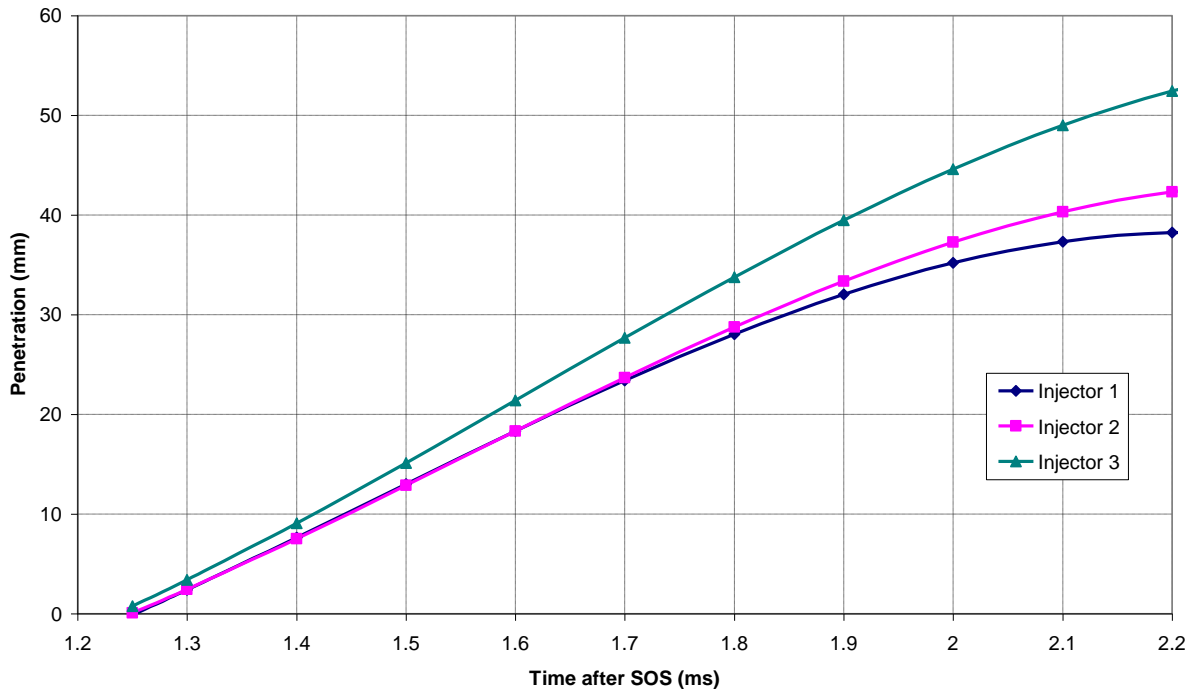
To prove the value of the derived equations, the predicted axial penetration for injector 3 was compared with results obtained by direct interpolation. Testing was performed at 1 and 2bar and 40°C and 60°C and therefore the engine part load condition could be directly interpolated for injector 3 only. The part load condition at 120bar was compared with equation 7.4 and the part load condition at 190bar was compared with equation 7.14. The results from this are shown in Figure 7.41.



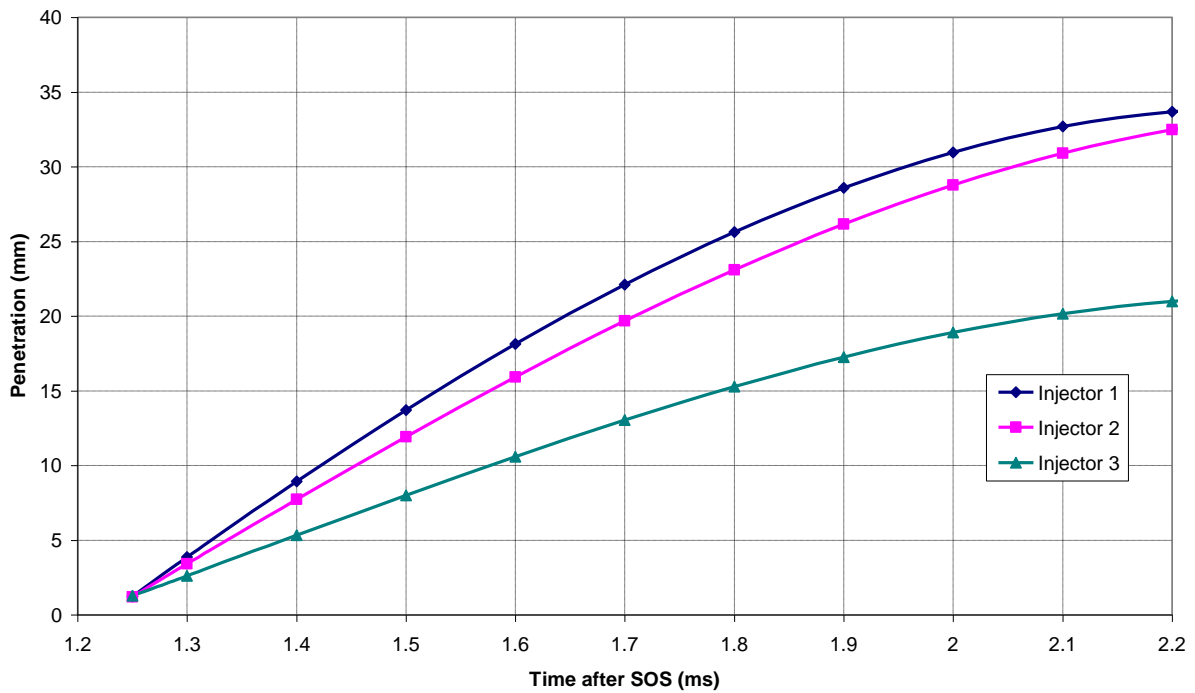
**Figure 7.41: Predicted axial penetration and the directly interpolated axial penetration at the part load engine condition**

The results show small differences of approximately 1.25mm and around the region of 1.8ms but apart from this show good agreement. The directly interpolated results are still an approximation and thus neither can be considered anything more than an estimation.

Satisfied with the accuracy of the derived equations, the predicted axial and radial penetration for all three injectors at the engine part load condition was extrapolated and the results are shown in Figure 7.42 and Figure 7.43.



**Figure 7.42: Predicted axial penetration for each injector at the engine part load condition**



**Figure 7.43: Predicted radial penetration for each injector at the engine part load condition**

### 7.1.7 Summary

The objective of the preceding sub-section was to investigate three different injectors and to form potential reasons for the differences in results seen in the engine environment. The results formed and analysed in the previous paragraph will act as a basis for the conclusions formed in reference to the emissions issues seen during engine testing.

The engine valve timing used during the engine testing is not known and thus several different scenarios are possible and will be commented on. It is known that two or more injection events are being used to prevent inlet valve impact when fresh charge is entering the cylinder. This would imply that because injection is not occurring during a valve opening event, significant spray distortion will not occur, although this is not always true since the air within an engine is never quiescent due to piston and valve movements, and in addition to this, the injection following the fresh charge entering the cylinder could be subjected to bulk air movements both radially and axially (swirl and tumble). Therefore two scenarios are considered when analysing the data, especially with respect to the radial component of penetration since the axial component can be considered a good approximation regardless of spray distortion:

1. The first injection occurs into almost quiescent charge and thus the radial penetration data gathered in the pressure chamber can be considered a good approximation,
2. The second injection is injected into a moving charge, thus the radial component of the data can only be taken as a severe approximation and could be vastly different.

The potential effect of the charge motion on the data and its influence on the emissions problem will also be considered.

From inspection of Figure 7.42, it can be seen that injector 3 has a significantly higher predicted axial penetration than both injector 1 and 2 at higher timings, 10mm larger than injector 2 and nearly 15mm larger than injector 1 at an injection timing of 2.2ms. The injection profile for injector 3 also does not appear to be levelling off like seen with injector 1 and 2. This would imply that if the predicted results could be extrapolated further its penetration would continue to rise before levelling off.

This testing is based upon is a 1.3 litre 3 cylinder engine. If an assumption is made that the engine is square (both bore and stroke are equal) or nearly square, then the bore and stroke dimensions can be calculated to be approximately 82mm. If the maximum distance between injector and piston crown at Bottom Dead Center (BDC) is 82mm, the spray could easily

impact the piston crown. Indeed, injector 3 shows axial penetrations greater than 50mm at 2.2ms and if the injection duration is continued until 4 or 5ms then piston crown impact is possible. Since the new generation of GDI engines are using spray guiding to guide the fuel to the spark plug, the piston crown is unlikely to be curve since it is not designed to guide the fuel to the spark plug. This would mean that fuel would impact the crown and not be deflected upwards, lowering atomisation efficiency and increasing hydrocarbon and soot emissions.

The predicted radial penetration at the engine operating conditions is shown in Figure 7.43 for all three injectors. Injector 1 and 2 show expected results of higher radial penetrations due to their increased nozzle plume angle. It appears a 30° increase in plume angle provides an increase in radial penetration of between 11-12mm at later injection timings. Injector 1 shows larger radial penetrations (and smaller axial penetrations at later injection timings) due to the difference in nozzle geometry. As mentioned previously, the flat nozzle allows the spray to spread out more easily and does not constrain the spray in the same manner as injector 2 that has concave nozzle geometry. As the initial spray is more centred around the injector axis with injector 2, the initial available surface area for charge entrainment is smaller but the increased penetration at later injection timings will mean improved charge utilisation and therefore improve the overall charge utilisation and entrainment.

If the bore of the cylinder is in the region of 82mm, with predicted radial penetration of almost 35mm for injectors 1 and 2 at 2.2ms, longer injection durations of 4 or 5ms could show radial penetration large enough for cylinder liner impact. With the instability issues due to charge motion seen with injector 3, injector 3 could also see radial penetrations approaching those seen with injectors 1 and 2 even though it has a 30° reduction in spray cone angle. The increased likelihood of spray distortion with injector 3 could also cause an unexpected inlet valve impact if the injection timing was being controlled to a fine degree to miss a valve opening event.

As mentioned previously, the plume tips formed with injector 3 are particularly sensitive to charge motion, and even in an almost quiescent charge in the pressure chamber, show tip deformation. This would indicate that any further increase in bulk air motion within the cell or as seen in the cylinder would cause more significant distortion of the tip and suggest that injector 3 is more likely to suffer increased spray distortion within the engine. This could affect the radial penetration sufficiently that either a cylinder liner or inlet valve impact could occur when otherwise not expected, even with the lower radial penetrations when compared to injector 1 and 2.

## Chapter 7 – Results: Pressure Chamber

---

The large variations in spray penetration and distribution seen during the engine testing could be explained by the large differences seen between the 60° and the 90° cone angle injectors (see Figure 7.8 to Figure 7.13), but more predominantly by the effect of charge motion and that a more significant effect could be seen with injector 3, when initial thoughts would suggest that injectors with larger cone angle would be more affected.

The reduction in emissions seen with a spray-valve impact is not easily understood and the actual cause is not possible to be identified with the data gathered during this testing and the little information provided of the problem. One idea is that, with a certain injection and valve timing, a valve impact is expected. However, with a significant spray distortion the impact is not actually occurring, thus not showing the increase in emissions expected.

The data and predictive equations created as a consequence of testing in the pressure chamber is also of great use to the development engineer. Using experimental equipment like the pressure chamber can provide predictions of how the spray will behave inside an engine. The predictions created here can not only be used to establish reasons for poor performance issues, it can also be used as a starting point when starting calibration development including injection timing, quantity and pressure strategies, and used when developing injector features, combustion chamber geometries and valve timing events.

Further to the additional uses of the data commented on above, the data is also of use to the research in fuel sprays in general. Our understanding of fuel sprays and the mechanics of the atomisation and spray propagation process is still not complete, numerical modelling of the whole injection event is not yet possible. Further testing in this field will lead us closer to a complete picture of the atomisation process and until this is fully understood the combustion process that follows will never be able to be predicted accurately. A thoroughly modelled combustion process will ultimately allow us to optimise the internal combustion engine.

The difference in penetration due to the intensity contour chosen was analysed initially. It was found that assuming there is sufficient light, the intensity contour representing 50% of the maximum light intensity provides very similar penetration profile to that seen at 85%. Even at later injection timings the maximum difference between intensity profiles is only approximately 2.5mm. This suggests that the difference in spray density between 85% and 50% is little and that either intensity contour could be used to form conclusions of penetration depth provided the original light intensity is large enough.

The nozzle tip geometry, injector 1 with a flat tip and injector 2 with a concave tip, was shown to affect the initial and later parts of the axial penetration profile. The concave tip increased the axial penetration in these regions. With respect to the radial penetration profile, the concave tip appeared to constrain the spray, reducing the radial penetration. The axial and radial penetration with a reduced nozzle cone angle produced predictable results, showing reduced radial penetration but increased axial penetration.

The change in spray axial penetration profile with increasing backpressure followed the theory. Little difference in penetration is seen at early injection timings due to the penetration being largely governed by kinetic energy created by the pressure differential across the nozzle tip. The axial penetration then increases but at a reducing rate with increasing charge backpressure due to the increased interaction with the charge and the increased aerodynamic drag. The radial penetration profile at 2bar did not follow the expected trend, the results showing a very similar profile to 1bar backpressure. No in-cell temperature or pressure data was available for this test condition and, therefore, it was not possible to measure the cell density. The cone angle data did not show the expected trend at early injection timings either. This is expected to be due to measurement uncertainties due to insufficient light intensity (older xenon flash panel used for this data set).

The temperature analysis proved that at low cell backpressures and with a small temperature scale, the change in charge density is small. Therefore the difference in both axial and radial penetration seen at the backpressure and temperature values evaluated was small. Points of localised flash boiling were found with reduced axial and radial penetration at later injection timings. The timing at which flash boiling occurred was found to be dependent on charge temperature and backpressure. Increasing the charge temperature increased the likelihood of flash boiling occurring, and increasing the charge pressure delayed the timing at which it occurred. Analysis of the spray images and cone angle data and showed the injector used for this part of the testing (injector 3) suffered from tip deformation due to aerodynamic effects, causing quite large variations in axial and radial penetrations when this occurred.

The effect of fuel pressure on the spray penetration showed similar results for both axial and radial penetration. Increasing the fuel pressure affect the internal flow, reducing the initial axial and radial penetration. Once the spray has exited the nozzle, the larger pressure differential causes higher exit velocities and thus increases both the axial and radial penetration of the spray.



## Chapter 7 – Results: Pressure Chamber

---

What is believed to be a flash boiling event was noticed during certain parts of the testing. Flash boiling appeared to occur with the lighter components being dragged towards the injector axis and the movement causing larger drops to follow their path. This caused all six plumes to collapse in on each other, and the spray remained in this state for approximately 10 injections before regaining its original spray/plume structure. Only individual injections could be monitored and therefore a single spray collapsing transiently could not be monitored, making it difficult to draw conclusions as to why this phenomenon occurred. This phenomenon only occurred at the higher charge temperatures of 40°C and 60°C and only for the first run after cleaning of the pressure chamber. Flash boiling is considered in detail in the next section.

### **7.2 Sub-Atmospheric**

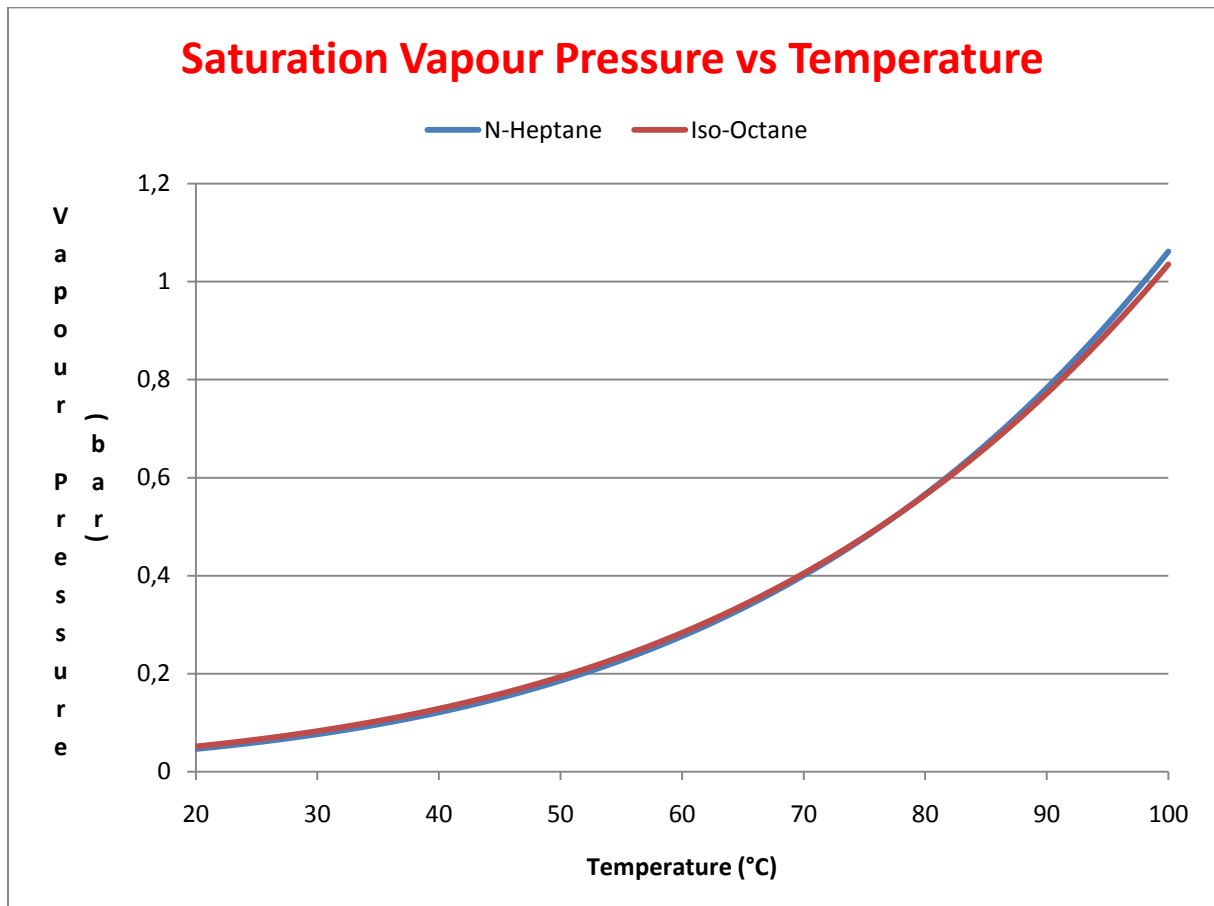
This final section deals with the topic of flash boiling of gasoline fuel sprays. As such, it is the major contribution to originality in this predominately industrially based work. A brief review of the subject of flash boiling in sprays will be given before detailing the experimental work.

Flash-boiling occurs when fuel is injected into a combustion chamber where the ambient pressure is lower than the saturation pressure of the fuel. It has been known that flashing is a favorable mechanism for atomizing liquid fuels. On the other hand, alternative fuels, such as gaseous fuels and oxygenated fuels, have been used to achieve low exhaust emissions in recent years. In general, most of these alternative fuels have high volatility and flash-boiling takes place easily in the fuel spray when injected into the hot combustion chamber of an internal combustion engine under high pressure. Multi-component mixtures of high- and low-volatility fuels have been considered in previous studies in order to control the spray and combustion processes in an internal combustion engine. It was found that the multi-component fuels produce flash-boiling with an increase in the initial fuel temperature. Therefore, it is important to investigate these flash-boiling processes in fuel sprays [98].

In the Kawano et al. [128] study, sub-models of a flash-boiling spray are constructed. These sub-models consider the bubble nucleation, growth, and disruption in the nozzle orifice and injected fuel droplets. The model was implemented in KIVA3V and the spray characteristics of multi-component fuel with and without flashing are numerically investigated. In addition, these numerical results were compared with experimental data obtained in a previous study using a constant volume vessel. The flashing spray characteristics from numerical simulation qualitatively showed good agreement with the experimental results. In particular, it was confirmed from both the numerical and experimental data that flash-boiling effectively accelerates the atomisation and vaporisation of fuel droplets. This means that a lean homogeneous mixture can be quickly formed using flash-boiling in a combustion chamber.

The flash boiling or flash vaporisation is a thermodynamic instability of a liquid jet that occurs under superheated conditions. As the pressure of an accelerated liquid goes below its saturation value, a metastable state is reached and then a rapid boiling of the liquid might occur. It must be underlined that cavitation is a particular form of evaporation which differs from fuel flash boiling. The difference is that flashing is thermodynamically driven while cavitation is mechanically driven. In flashing the fuel enters a nozzle (or an orifice) already in superheated conditions with respect to discharge pressure. Furthermore, the vapour bubble density is much higher in flashing than in cavitation because of the larger pressure at which evaporation occurs. The evaporation rate during flashing can be in turn affected by cavitation

since the latter makes available a liquid-vapour interface which greatly promotes the vapour bubble growth. This process can also occur during liquid fuel injection in internal combustion reciprocating engines. In both gasoline port fuel injection and direct injection engines, the liquid fuel might be injected into a gaseous ambient (port or cylinder) whose pressure is below the saturation pressure of one of the fuel blending components at the local temperature. This results in flash boiling of the fuel [107].



**Figure 7.44: N-Heptane and Iso-Octane saturation vapour pressure vs temperature**<sup>[129]</sup>

The saturation curves for single component fuels N-Heptane and Iso-Octane for the range of temperature of interest in spark ignition engines are presented in Figure 7.44: N-Heptane and Iso-Octane saturation vapour pressure vs temperature. It can be easily noted that a liquid fuel injected at a temperature of 50°C will likely undergo flashing if the ambient (port or cylinder) pressure is below its saturation vapour pressure, i.e., 0.2 bar. At 100°C flash boiling can occur at ambient pressure.

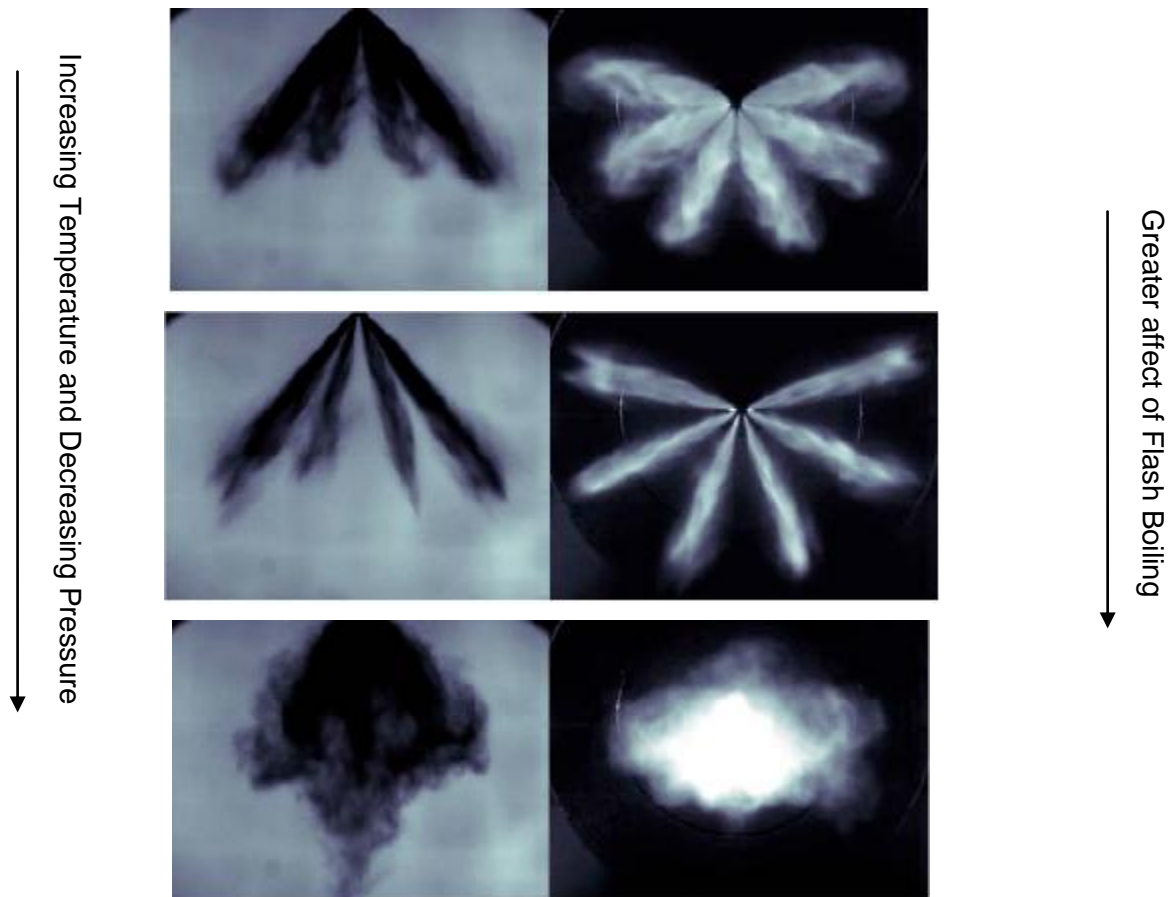
## Chapter 7 – Results: Pressure Chamber

The superheated condition of liquid fuel is the result of the combination of: the fuel temperature increase in high pressure pump GDI system, the heat exchange between injector and cylinder head, and a low discharge pressure.

It has been recognised that flash boiling may greatly affect the fuel-air mixing process because it modifies:

- A. The initial liquid droplets' diameter;
- B. The evaporation rate, mainly outside the nozzle;
- C. The liquid and vapour penetration;

Experimental images of the influence of superheating degree on the spray shape of a 6-hole multi-stream injector are shown in Figure 7.45 [87].



**Figure 7.45: Effect of backpressure and fuel temperature on flashing in GDI multi-hole spray<sup>[87]</sup>**

In both types of gasoline injection systems (i.e., GDI and PFI), the spray targeting is a fundamental step to achieve the best engine efficiency in terms of minimisation of fuel consumption, raw gas emission, and lubricant contamination with fuel. Thus, fuel flashing investigation and modelling are mandatory for achieving an optimised spray targeting. Bianchi et al. paper focuses on the modeling topic. In particular, the emphasis is on the development of a 1D code able to provide basic information on nozzle flow condition of a superheated fuel and to provide correct initial condition for 3D CFD spray simulations for the prediction of the mixture formation. The latter calculations need the accurate initialisation of liquid spray otherwise they provide misinterpreting results. It must be noted that a 1D model can also provide information on the effect of different parameters (fluid type, injection pressure, superheating degree) on liquid characteristics at nozzle exit [107].

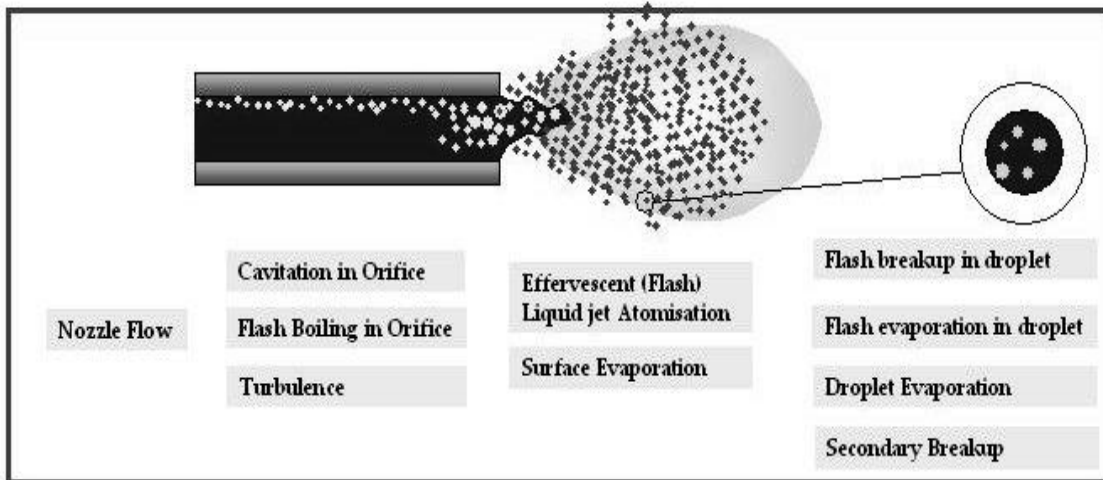
According to experimental results from Bianchi et al. [107], it can be concluded that depending on fuel composition, superheating degree, cavitation intensity, hydrodynamic condition and injector shape, a liquid jet undergoing a sudden expansion quickly evaporates if the local pressure goes below the saturation pressure. As a result the mass flow rate remains choked for any change in downstream pressure and an effervescent atomisation might also occur. Depending on the combination of the above mentioned parameters, two main regimes can be identified:

1. external flashing with surface evaporation at nozzle exit
2. internal flashing with effervescent atomisation at nozzle exit.

The first regime is likely occurring at low injection pressure (i.e. below 4 MPa) and/or in relatively very short nozzles or orifices. The second regime occurs at high injection pressure as those typical of GDI injection system.

Focusing the attention on GDI injection systems, the high turbulence levels in the nozzle flow perturbs strongly the vapour bubbles at their interface, thus contributing to an effervescent atomisation just outside the nozzle according to experimental evidence { [130], [131]}. It must be outlined that the effect of turbulence in atomising the liquid jet has been strongly enhanced by both the reach of a free surface condition at liquid jet surface { [132], [133]} and also by the presence of gaseous bubbles in the liquid core. The latter provide a free-surface interface which can be deformed by the turbulence energy at the corresponding scales. The newly atomised droplet will likely be in superheated conditions with respect to ambient pressure and contain vapour bubbles whose growth then causes the liquid droplet disintegration.

The main processes governing the dynamics of a superheated liquid fuel with a focus on a cylindrical nozzle typical of GDI multi-hole injectors are summarised in Figure 7.46.



**Figure 7.46: Schematic review of the physics involved in the flash boiling of a liquid issuing from nozzle<sup>[107]</sup>**

### 7.2.1 Experimental Configuration

In this section the effect of flash boiling on liquid break-up and atomisation is described in detail for two multi-stream gasoline direct injectors operating, with RON-95 gasoline and a fuel injection duration of 0.8 ms, into sub-atmospheric pressures between 1 and 0.1bar and temperatures between 20°C and 100°C. Both multi-stream injectors were supplied by Continental, one with a nominal external cone angle of 60° and a static flow rate of 18mm<sup>3</sup>/s at 120bar and the other, with a nominal external cone angle of 90°, had a static flow rate of 12mm<sup>3</sup>/s at 120bar. The 60° injector was tested at 120 and 200bar and the 90° injector at 120 and 180bar. The difference in upper limits was due to the maximum permissible fuel injection pressure for each injector. The high pressure fuel supply to the injector was achieved by two fuel pumps, the first, a low pressure pump mounted inside the fuel tank which supplied fuel at 3.5bar to the second, an external high pressure pump, which could operate at up to 200bar. The fuel output pressure to the injector was regulated by an adjustable pressure relief valve which returned the fuel spill to the fuel tank.

The injectors were fitted into the constant volume chamber with three windows for optical access. The pressure inside the chamber could be varied from 0.1bar to 10bar. A Buchi V700 vacuum pump was used to achieve the sub atmospheric pressure range while a nitrogen cylinder was used to pressurise the chamber up to 10bar. The chamber had two electro-actuated valves, an inlet valve linked to the pressure release valve of a nitrogen

cylinder and an outlet valve linked to a vacuum pump which was connected to an exhaust extractor. A pressure sensor was used to monitor the pressure inside the chamber.

The insulated chamber sits on top of a heating plate with a temperature control and an operating range between 20°C and 100°C. Considering the low injection repetition rate of 1Hz and the low fuel quantity injected during the 0.8ms injection duration, nominally 10 and 7 mg per shot for the 60° and 90° injectors respectively, it was assumed that conductive heat transfer through the injector was the main physical process affecting the temperature of the fuel injected into the chamber. Hence injector temperature was equal to the temperature of the chamber. A thermocouple measured the temperature of the gas in the chamber and displayed this information on a control interface and which was also used to determine the required power to the heating plate. The experimental setup is described with more details in chapter 4.

Mie imaging was performed with a 12 bit PCO CCD camera (1280 by 1024 pixels resolution) mounted in front of the optical access of the chamber and a xenon flash panel mounted in front of the opposite optical access. A pulse timing box was used to control the pulse width of the injection signal and the timing of the xenon flash panel and the camera relative to the start of the injection signal. This allowed images to be captured at different stages of the fuel spray development. The collected images are displayed on a PC running PCO CamWare software, which saved the images for post-processing.

Work carried out by Gebhard [97] investigated the effects of length to diameter ratio of a steel nozzle using water and found that for  $l/d < 3$ , there is no internal flash boiling inside the nozzle. Sato et al. [134] performed a similar study, also using water, and reported that the spray characteristic was not affected by bubble nucleation in nozzle orifice if the orifice length to orifice diameter ratio  $l/d$  was less than 7. The injectors used in this study have a ratio  $l/d < 2.5$ . However, due to the differences in the type of injector and fuel used we can not assume anything about the occurrence of flash boiling inside the nozzle of the injectors used in our study.

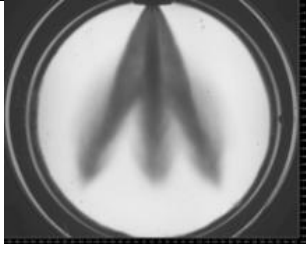

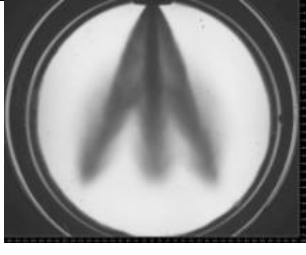

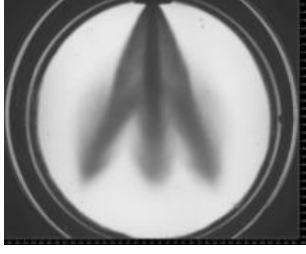

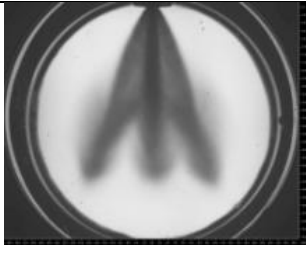
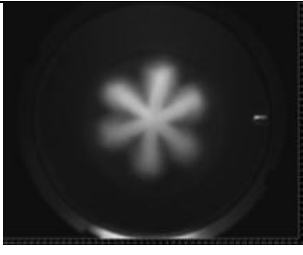
### 7.2.2 Qualitative Analysis

A qualitative analysis of the images was first undertaken to highlight the significant changes and phenomena visible in the spray images as the degree of superheat is increased. An overview of these changes for the side and plan view spray images are described in Table 7.5 for the 60° cone angle injector. These phenomena are also visible with the 90° cone angle injector but, with a greater separation of the streams, the effects of flash boiling on the spray are somewhat reduced.



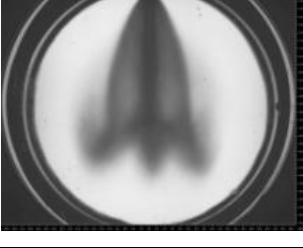


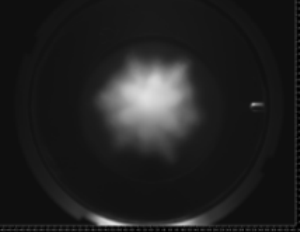
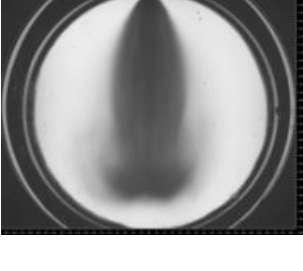
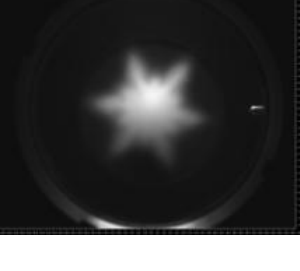
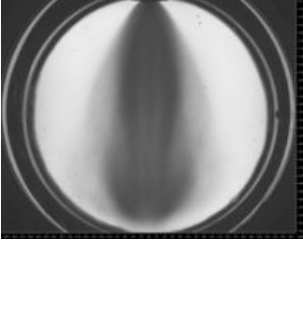
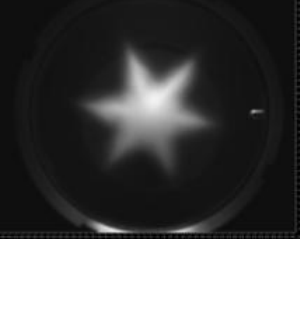
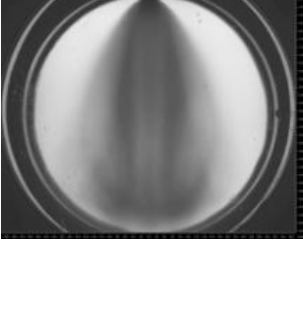
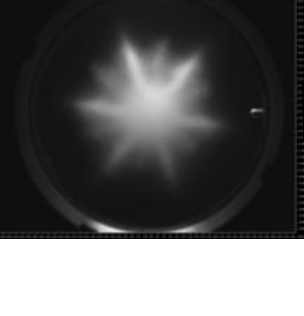
The main phenomena seen are:

- Collapse of streams towards centre of spray and the creation of a "tulip" envelope.
- Formation of recirculation zones.
- Reduction in spray density.
- Apparent re-orientation of spray streams.

**Table 7.5: Spray pattern evolution with reduction in cell pressure. 60° cone angle injector, 120bar Fuel @ 60°C, 2ms ASOS**

<p><b>0.969bar</b> Individual streams are clearly distinguishable</p>		
<p><b>0.9bar</b></p>		
<p><b>0.8bar</b></p>		
<p><b>0.7bar</b></p>		



<p><b>0.6bar</b></p> <p>Up to here only obvious changes are increases in stream penetration, width and interaction with a decrease in spray angle</p>		
<p><b>0.5bar</b></p> <p>Spray tip vortices forming on plume tips and spray is becoming more curved as it collapses inwards. Plan view image shows presence of spray in between streams</p>		
<p><b>0.4bar</b></p> <p>Spray takes on "tulip" shape and vortices become even clearer. Plan view image shows interstitial streams developing in between main streams</p>		
<p><b>0.3bar</b></p> <p>"Tulip" shape is narrower and penetration is increased. Original streams barely visible as interstitial streams dominate. Appears as if spray has rotated</p>		
<p><b>0.2bar</b></p> <p>Spray collapses with central core surrounded by a fine cloud of spray. Spray width increases at the tip. Original streams have disappeared and interstitial streams continue to grow</p>		
<p><b>0.1bar</b></p> <p>Spray width increases but density reduces. New streams visible between interstitial streams. Are mainstreams reappearing or is there interaction between interstitial streams?</p>		

## Chapter 7 – Results: Pressure Chamber

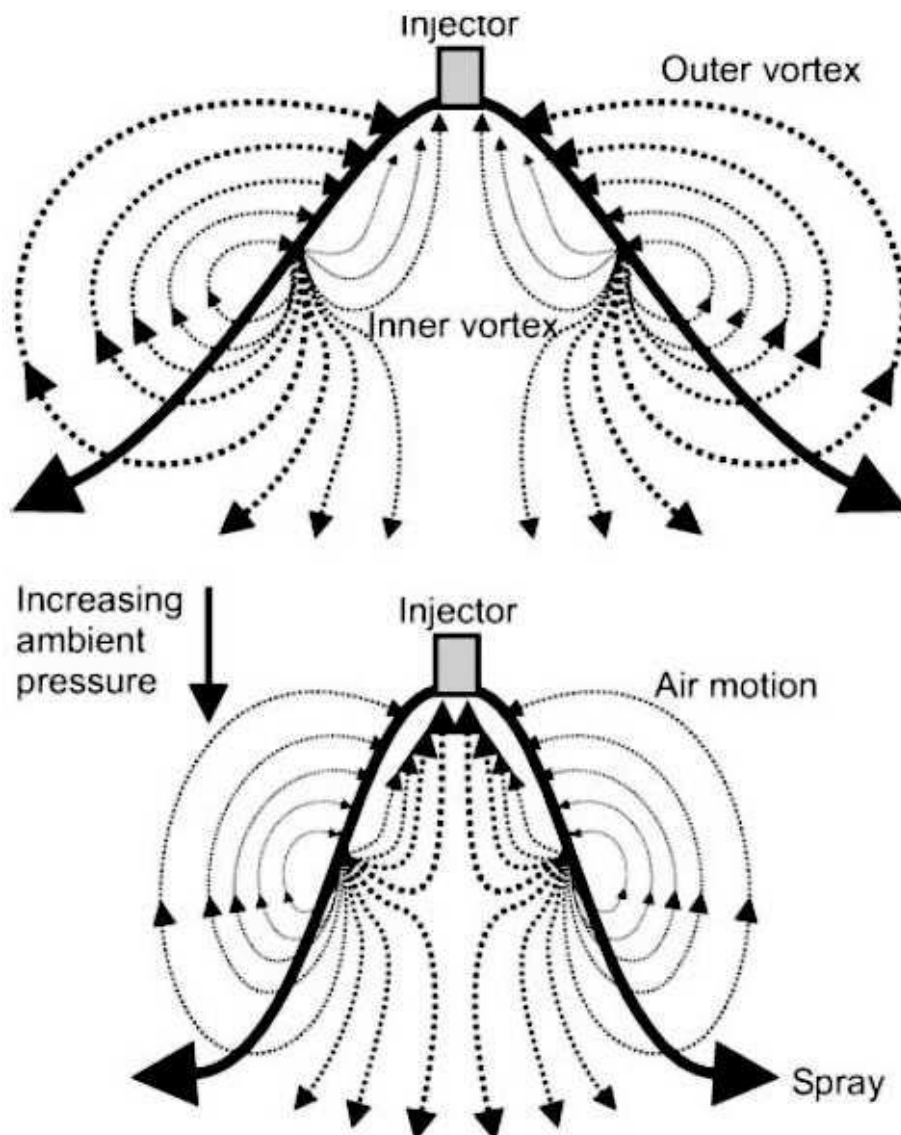
---

The spray developments for chamber pressures from 0.969 to 0.3bar at a fixed temperature of 60°C are shown in Table 7.5. As the pressure is reduced the individual spray streams collapse inwards towards the spray axis. At 0.4bar the side image shows the individual spray streams are indistinguishable and the spray has formed a tulip shape, with recirculation zones around the stream tips. This is very similar to the spray shapes seen by Zhao et al. [2] and Reitz [103] with a pressure-swirl injector when the ambient pressure is increased. As the cell pressure is further reduced, to 0.2bar, the spray width increases and a cloud of fine spray can be seen surrounding the main spray body. The spray width is further increased as ambient pressure is reduced to 0.1bar. At the same time a reduction in spray density is observed, suggesting that an increased proportion of the spray from the injector has vapourised due to flash boiling.

Research on spray formation from pressure-swirl injectors has attempted to explain the reasons behind spray collapse. Work carried out by Delay et al [135] using fluorescent particle image velocimetry showed that interaction between the spray and the surrounding air caused the formation of vortices on both the inside and the outside of the spray cone. The inner vortex was seen to pull in air from the outside of the cone and this dragged relatively small droplets with it, causing the edge of the spray to curve and eventually collapse. Similar work, using the phase Doppler technique was carried out by Allocca et al. [136] and the same phenomenon was observed. A recirculation zone is clearly visible around the spray tip for the 0.5 and 0.4bar images in Table 7.5. It is likely that the same aerodynamic effects are responsible for the recirculation in each case, and the collapsed stream recirculation is the result of the individual recirculation zones interacting as the streams collapse inwards. The recirculation zones themselves are due to aerodynamic interaction between the fuel spray and the surrounding air. This is the same mechanism responsible for spray collapse, but in this case the outer vortex causes the observed effect [2].

The plan view images for 0.5 to 0.3bar in Table 7.5 show an apparent rotation of the spray streams about the injector axis. Inspection of the 0.5bar image shows that there is no physical rotation of the spray, rather, additional interstitial streams develop between the main streams and the main streams themselves disperse, as observed by Dahlander [87]. Once the pressure has reached 0.2bar, the original streams are almost invisible and the interstitial streams dominate the spray. As the pressure is further reduced these streams extend in the radial direction and increase in width. It is also noticed at 0.1bar that more streams grow in between the interstitial streams. The presence of spray between the main streams is due to the interaction between individual streams as the spray collapses inwards. This interaction, which can be classified by the distance at which the individual streams are joined, increases

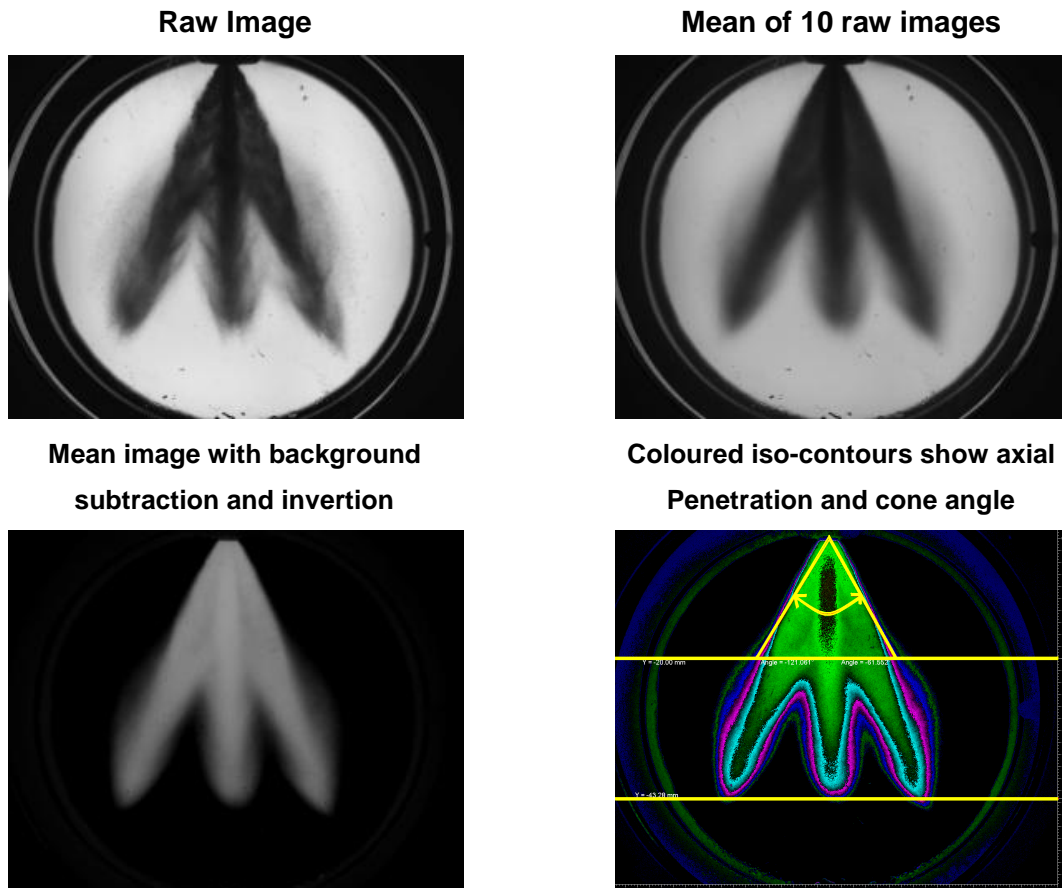
with increasing superheat, as seen in the side images in Table 7.5. A further contributory factor to the interaction between streams is, again, the formation of vortices due to aerodynamic interaction between the fuel spray and the surrounding air. Whereas in a pressure-swirl injector toroidal vortices form on the inside and outside of the cone (see Figure 7.47: Pressure-swirl atomiser: mechanisms of spray/air interactions when increasing the ambient pressure), in a multi-hole injector the vortices form around each spray stream. This leads to interaction between neighbouring streams as the vortices transport droplets from one stream to another. This transfer increases as the level of flash boiling increases. Therefore, the increased visible stream interaction with increased degree of superheat is likely to be due to a combination of the individual streams being bent inwards and the individual streams interacting with one another due to the interaction of the vortices.



**Figure 7.47: Pressure-swirl atomiser: mechanisms of spray/air interactions when increasing the ambient pressure<sup>[137]</sup>**

### 7.2.3 Quantitative Analysis

The image processing technique detailed in Figure 7.48 allows simple quantification of the spray cone angle and axial penetration. The 50% intensity contours have been used to identify the spray boundaries with cone angle measured at 20mm downstream from the nozzle. All the quantitative data presented in this section can be used to further develop the IMPACT tool presented in Chapter 5.



**Figure 7.48: Image processing technique**

#### 7.2.3.1 Spray Characteristics - Chamber Pressure

Varying the ambient pressure in the chamber alters the fuel's boiling point and, as a result, changes the degree of superheat. This affects the spray penetration, cone angle, and the shape of the spray. It can be seen in Figure 7.49 that as pressure is reduced and the degree of superheat of the fuel increases it has the effect of increasing the spray angle. These increases are greatest below approximately 0.3bar ambient pressure. Spray width decreases further downstream as the spray collapses inwards on itself, creating a curved spray profile (see Table 7.5).

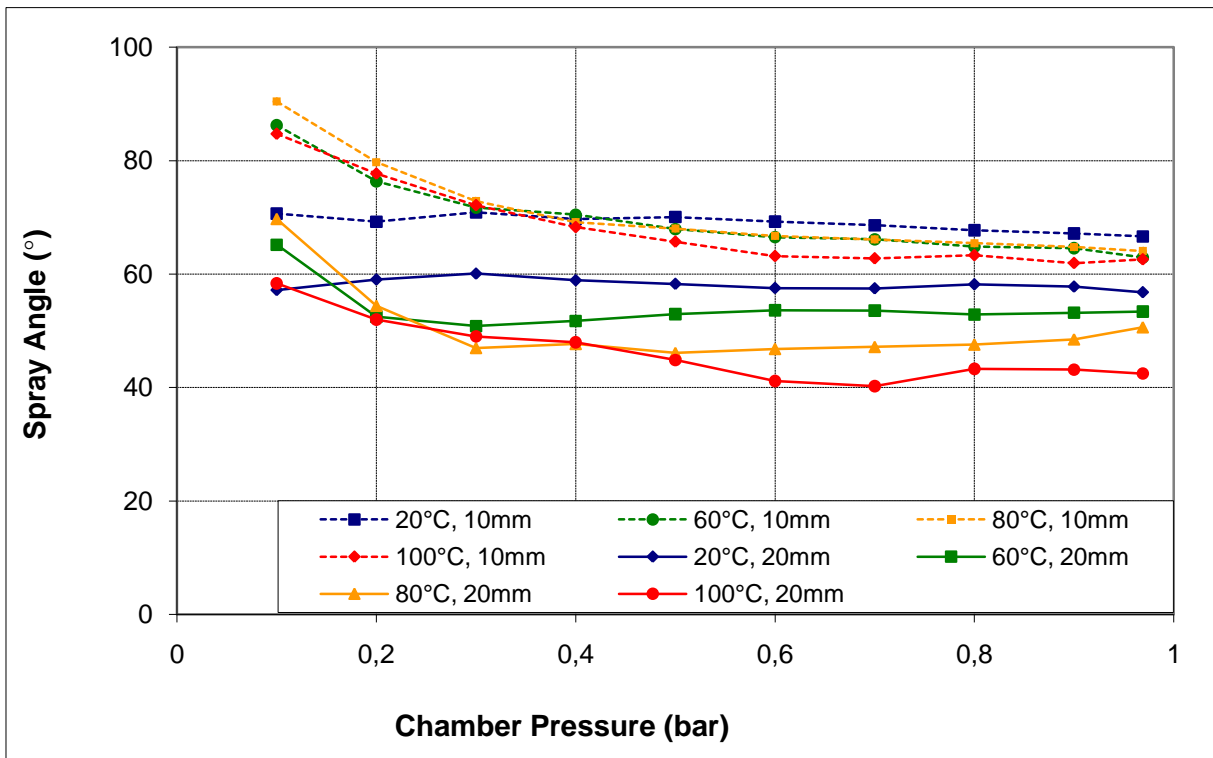


Figure 7.49: Spray angle comparison for ambient pressure variation. 60° cone angle injector, 120bar Fuel, 2ms ASOS

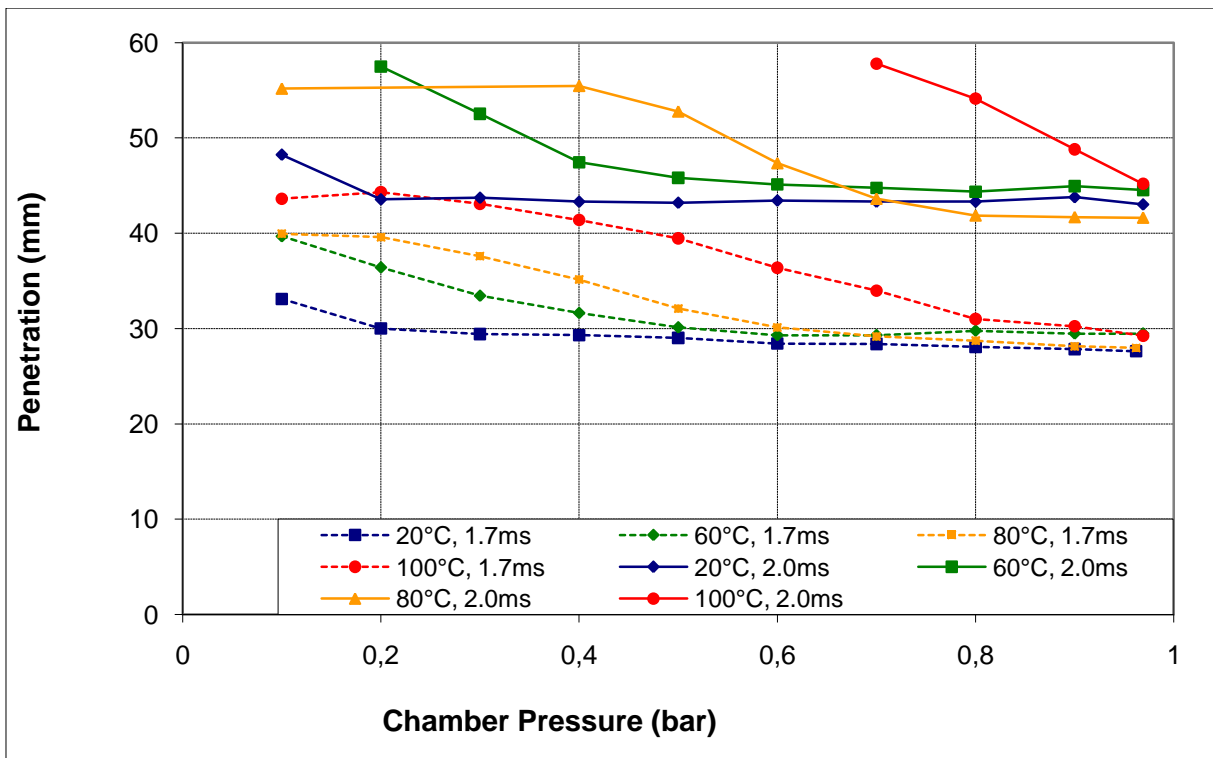


Figure 7.50: Penetration comparison for ambient pressure variation. 60° cone angle injector, 120bar Fuel, 2ms ASOS

The spread of spray angles over the temperature range is greatest further from the injector tip, particularly at ambient pressures close to 1.0bar. The spray angle for 20°C fuel temperature is relatively stable compared to the other fuel temperatures as pressure is decreased, and in fact decreases only slightly from 0.3 to 0.1bar at 20mm downstream, which appears to be the opposite behaviour to the general trend. Spray angles are lower for higher fuel temperatures.

The penetration data displayed in Figure 7.50 show an increase in penetration as ambient pressure is decreased mainly due to the reduced air density causing less aerodynamic resistance to the spray. The higher the temperature of the spray then the greater the penetration as pressure is reduced. This is particularly noticeable at 2.0ms ASOS, where it can be seen that the 100°C spray begins to increase in penetration immediately as pressure is reduced, whilst the 20°C spray remains relatively unchanged until the chamber pressure is reduced to 0.2bar. The penetration for 60°C and 100°C fuel temperatures extended beyond the viewing window of the chamber as pressure was reduced.

### *7.2.3.2 Spray Characteristics - Chamber Temperature*

Increasing the temperature of the fuel is another way of increasing the degree of superheat of the fuel as it is injected into the chamber. The trends for changes in spray angle and penetration due to temperature are shown in Figure 7.51 and Figure 7.52. Data for spray angle, Figure 7.51, are not shown between 0.9 and 0.6bar as there is very little change. The trends, as temperature is increased, vary for different ambient pressures. The spray angle increases with temperature for low ambient pressures but decreases with temperature for higher ambient pressures. In all cases, the spread of spray angles over the pressure range increased at higher temperatures, suggesting that spray was affected to a greater extent at the extremes of pressure. Also, the spray width reduced further from the injector tip, showing that the spray boundary was curved as it collapsed inwards. Spray angle was greater for lower pressures at all conditions but with two exceptions. At 0.96bar ambient pressure and 20mm downstream, the decrease in angle with increase in fuel temperature was lower than that for 0.5bar between 60 and 80°C, resulting in the higher pressure condition having a greater spray angle. This trend changed at 100°C and the 0.96bar conditions followed the general trend of reduced spray angle at higher ambient pressure.

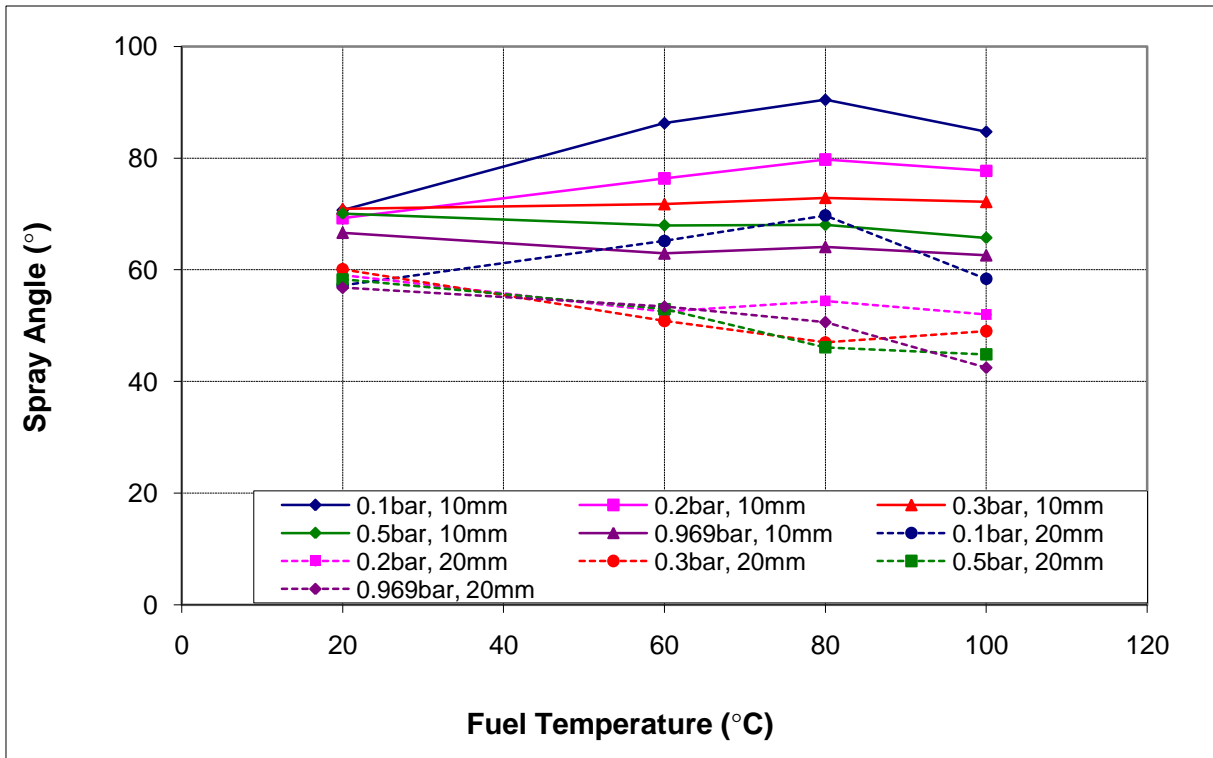


Figure 7.51: Spray angle comparison for fuel temperature variation. 60° cone angle injector, 120bar Fuel, 2ms ASOS

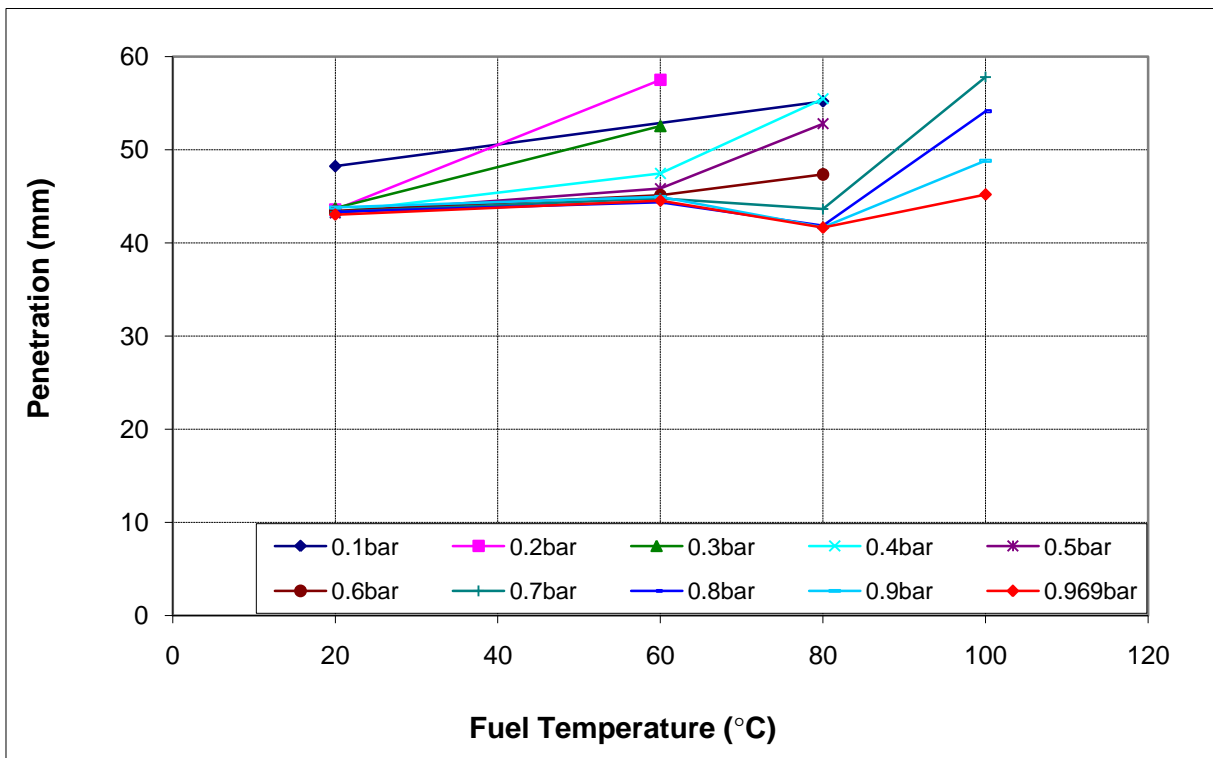


Figure 7.52: Penetration comparison for fuel temperature variation. 60° cone angle injector, 120bar Fuel, 2ms ASOS

Spray penetration data are shown in Figure 7.52. The general trend is for increased penetration as fuel temperature is increased and the spread of penetration values also increases with temperature. There are, however, several exceptions to this general rule. There was a decrease in penetration between 60°C and 80°C before an increase between 80°C and 100°C for pressure conditions from 0.7 to 0.96bar.

Due to the limited diameter of the viewing window the spray tip was out of range for the lowest chamber pressure conditions. This was due to the original choice of a 2ms ASOS image time and a much reduced aerodynamic drag on the spray causing maximum penetration. An interesting point is that the penetration for 0.1bar went off the scale at 60°C, returned at 80°C and then left again at 100°C whereas for the other pressure conditions there was no return once the spray tip was out of range.

The increase in penetration with increased temperature is most likely a result of the change in shape of the spray. As temperature is increased, the intensity of flash boiling increases and causes the fuel spray to collapse. This collapsed spray has liquid fuel more concentrated on the spray axis and, as such, has a reduced aerodynamic drag relative to spray with six individual streams.

### *7.2.3.3 Spray Characteristics - Fuel Pressure*

Higher fuel pressures increase the spray velocity as it exits the injector nozzle which affects droplet break-up and atomisation by altering the Weber number.

Spray angle data, Figure 7.53, show that in general, higher fuel pressures give increased spray angles. This is likely to be due to the increased pressure differential between the fuel and the atmosphere causing increased break-up and atomisation generating smaller droplets which are more susceptible to the aerodynamic conditions in the chamber. The trends for both fuel pressures are similar but this similarity is reduced at lower ambient pressures, for example, the 20°C-120bar data show a reduction in spray angle between 0.3 and 0.1bar whereas the general trend is for an increase.



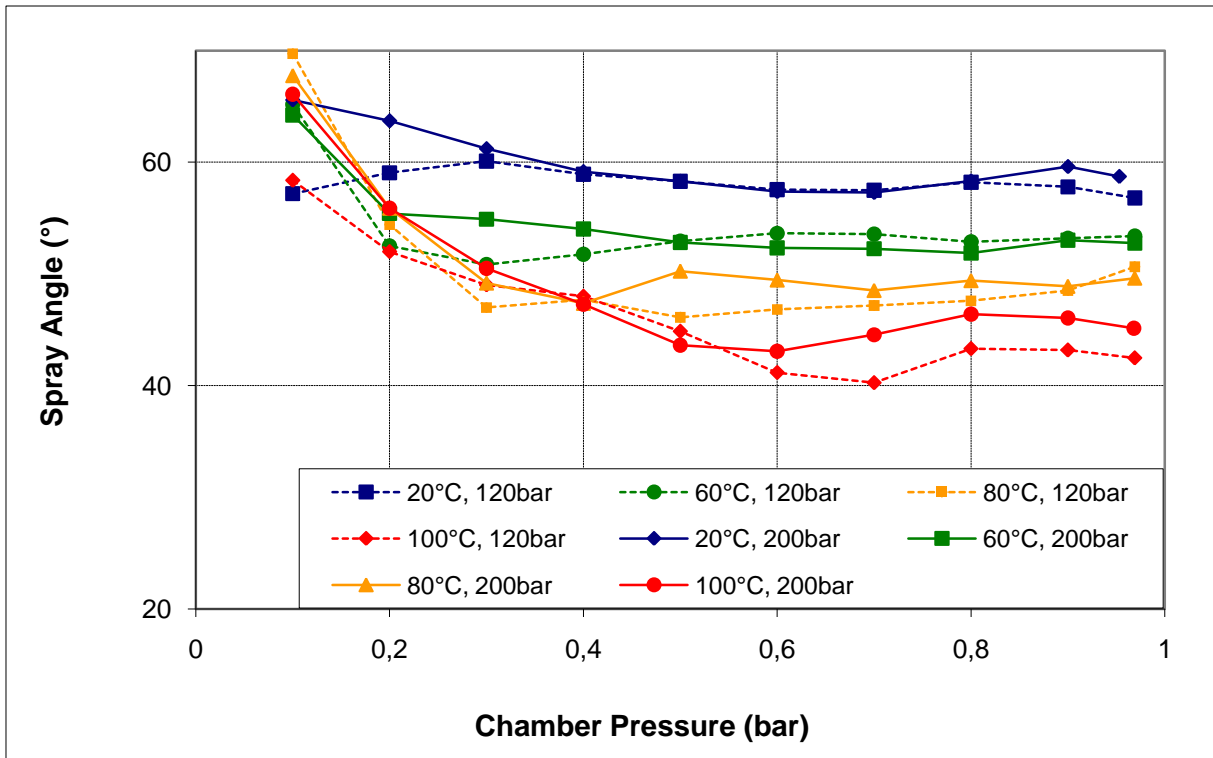


Figure 7.53: Spray angle comparison for fuel pressure variation. 60° cone angle injector, 2ms ASOS, 20mm downstream

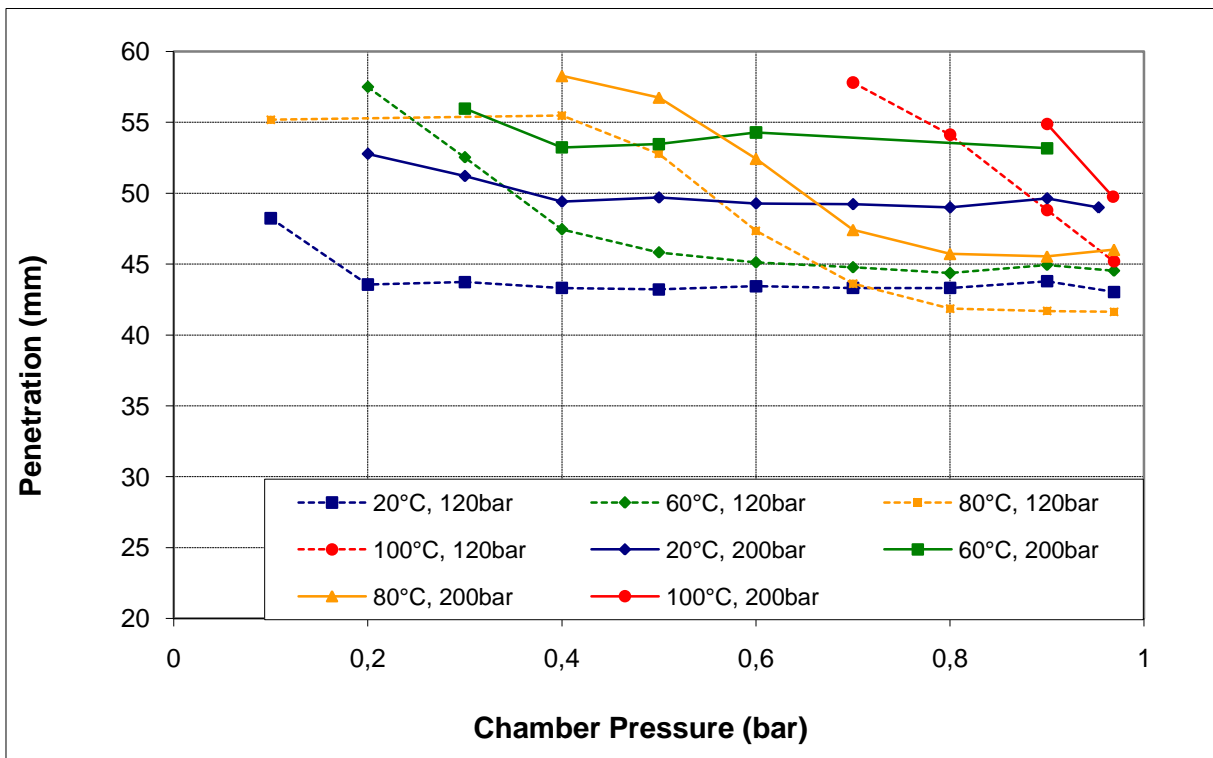


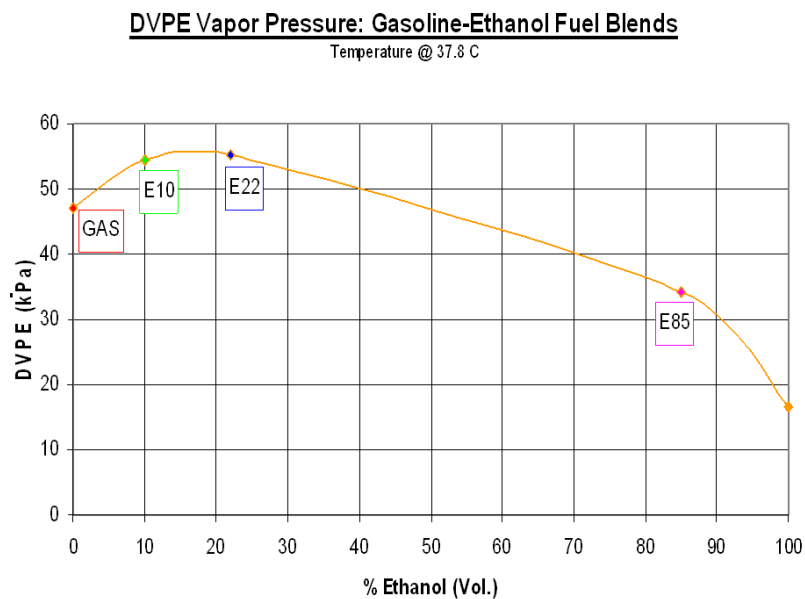
Figure 7.54: Penetration comparison for fuel pressure variation. 60° cone angle injector, 2ms ASOS

## Chapter 7 – Results: Pressure Chamber

Fuel penetration data are shown in Figure 7.54. Higher fuel supply pressures give increased penetration due to the increase in velocity of the fuel droplets as they leave the injector. Once again the trends are very similar regardless of fuel pressure.

### 7.2.3.4 Fuel Comparison

Gasoline and E22 fuels were tested to investigate how fuel properties affect flash boiling. Spray angle data are shown in Figure 7.56. E22 and gasoline present very similar trends at 20 and 40°C. Spray angle obtained with E22 becomes larger than the one obtained with gasoline at 60°C with the greatest variation seen at 100°C fuel temperature. Penetration data are shown in Figure 7.57. It is clear that E22 has lower spray penetration than gasoline over the entire ambient pressure range, with the exception of 100°C fuel temperature, 0.96bar ambient pressure at 2.0ms ASOS. E22 shows the same general trends as gasoline of increased penetration with a decrease in ambient pressure and an increase in fuel temperature.



**Figure 7.55: In Reid vapour pressure profile for gasoline-ethanol fuel blends**<sup>[138]</sup>

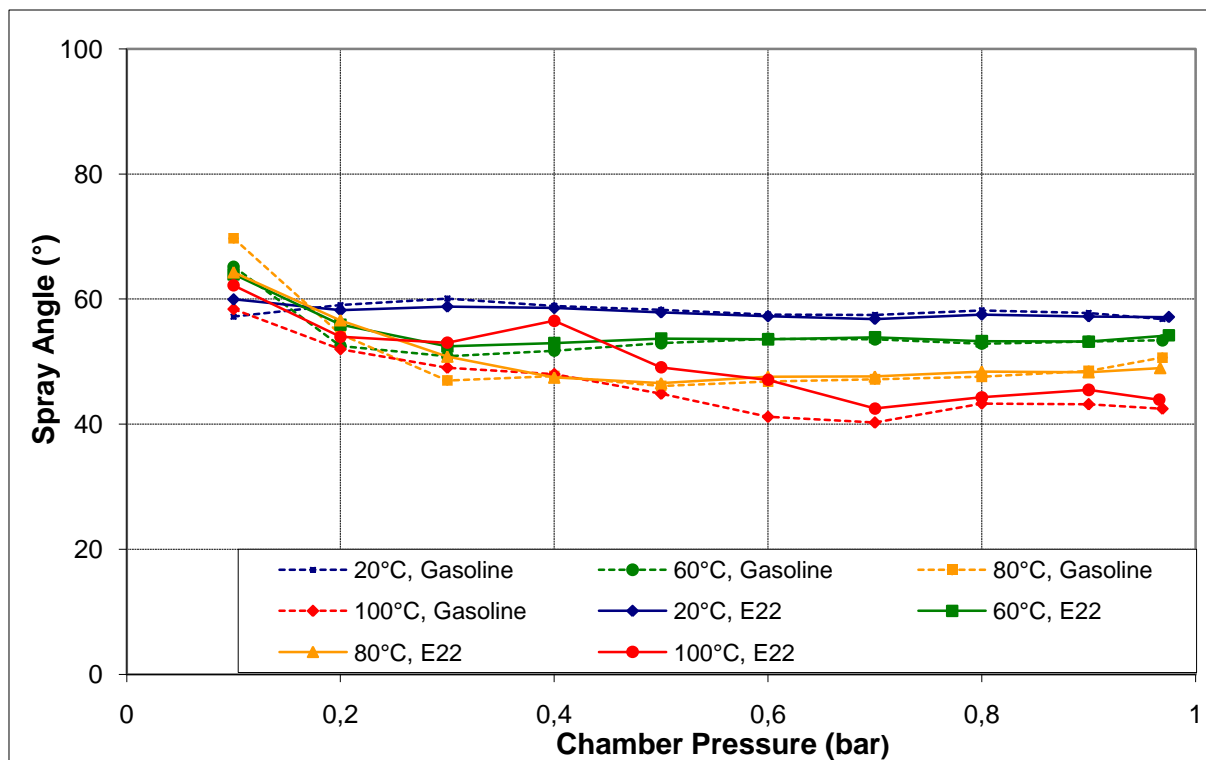


Figure 7.56: Spray angle comparison for fuel type variation. 60° cone angle injector, 120bar injection pressure, 2.0ms ASOS, 20mm downstream

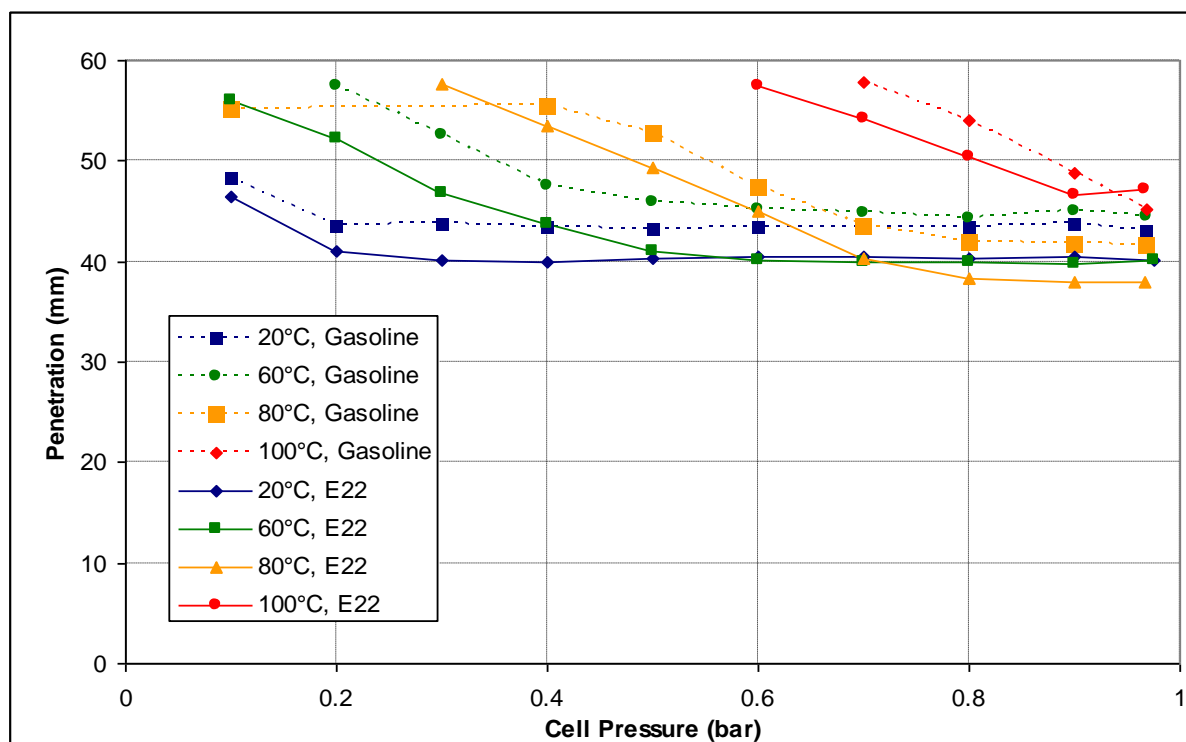
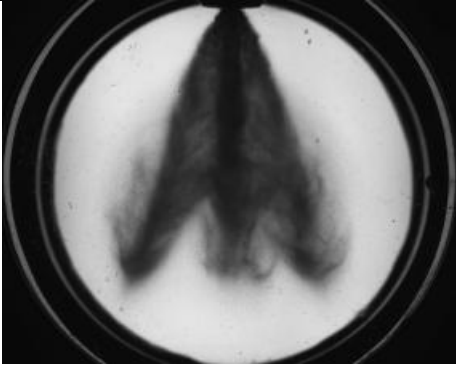
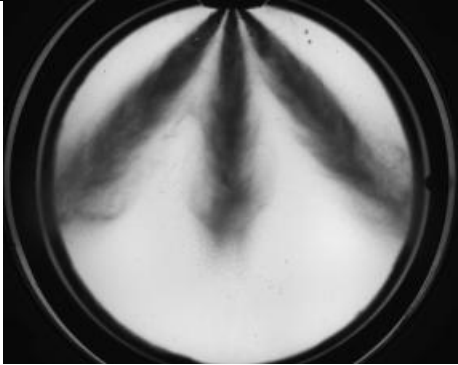
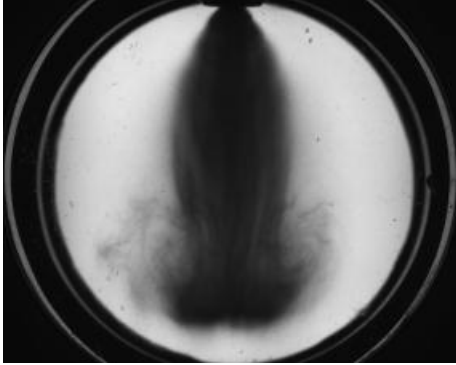
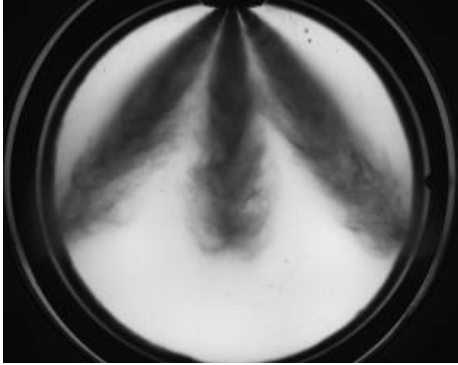


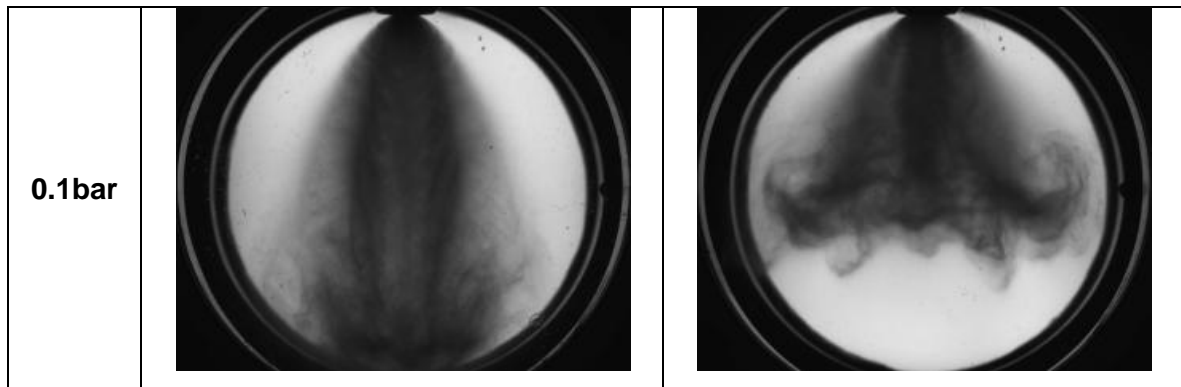
Figure 7.57: Penetration comparison for fuel type variation. 60° cone angle injector, 120bar injection pressure, 2.0ms ASOS

### 7.2.3.5 Injector Comparison

To investigate whether a change in nozzle geometry and spray pattern would lead to a variation in spray characteristics two injectors were tested, one with a nominal cone angle of 60° and the other with a nominal cone angle of 90°. As expected, it can be observed in Table 7.6 that the 90° injector, with its increased cone angle, has a reduced axial penetration relative to the 60° injector. For the images shown at 0.3bar, the 60° injector spray is fully collapsed whereas for the 90° injector spray streams are just beginning to turn inwards. This demonstrates that the spray from the 60° injector is collapsing earlier than the 90° injector as the chamber pressure is decreased. This is due to the fact that as the spray streams for the 60° injector are closer together they interact more with each other and start collapsing with a lower degree of superheat

**Table 7.6: Spray pattern evolution. Injector comparison-120bar FP-60°C-2ms ASOS**

	60° cone angle injector	90° cone angle injector
<b>0.6bar</b>		
<b>0.3bar</b>		



In Table 7.6, it can also be noticed that, as the chamber pressure is reduced further, the variation in penetration for the 90° injector spray is smaller than for the 60° injector. As a consequence the tulip shape is wider for the 90° injector. These observations have also been made as the fuel temperature is increased. This suggests that for injectors with large spray stream angles the fuel spray penetration is more robust to increases in the degree of superheat.

Note: More detailed image tables for the 60° and 90° cone angle injectors obtained with E22 are available in Appendix J.

### 7.2.4 Summary

The flash boiling effects on spray evolution has been described for two multi-stream gasoline direct injectors operating with RON-95 gasoline at 120 bar and 200 bar pressure with fuel injection into sub- atmospheric pressures between 1 and 0.1bar and temperatures between 20°C and 100°C.

The general trend is that as the degree of superheat is increased, through either fuel temperature increase or ambient pressure decrease, the individual spray streams collapse inwards towards the injector axis, thereby reducing the diameter of the spray footprint. Once fully collapsed, the individual streams are no longer visible, but, as the degree of superheat is further increased interstitial streams become visible between the main stream locations. These then grow away from the injector axis in the radial direction, resulting in the diameter of the spray footprint increasing. These trends were also visible over the range of temperatures studied at a fixed pressure. This suggests that the mechanisms behind the spray changes relies on a combination of both temperature and pressure as regards boiling point of the fuel.

The dependence of the flash boiling on both temperature and pressure for a multi-component fuel is highly complex. However, this level of complexity is likely to increase as gasoline-alcohol blends become more common place in fuel spray studies. In the mean time an analysis of sprays with single component fuels with a range of boiling points representative of the range found for gasoline, like iso-octane or n-heptane, should help reducing the complexity of the flash-boiling study.

The results found are difficult to describe concisely due to the complex nature of the superheat effects. The following summary is therefore based on general trends.

**Table 7.7: Results summary**

<b>Variable</b>	<b>Spray Angle</b>	<b>Penetration</b>
Ambient pressure decrease	Increased	Increased
Fuel temperature increase	Increased	Increased
Fuel pressure increase	Increased	Increased
Fuel type	Greatest with E22	Greatest with gasoline
Injector type	Greatest with Hotfire 90°	Greatest with Lotus 60°

## Chapter 7 – Results: Pressure Chamber

---

The results suggest that the degree of superheat is determined by a combination of ambient pressure, fuel temperature, fuel pressure and fuel chemical properties. The injector type, defined by the spacing of the individual spray plumes, determines the necessary degree of superheat to cause flash boiling. This makes predicting the onset of flash boiling difficult as it depends on many variables.

## 8. Conclusions and Recommendations for Future Work

### 8.1 Summary

*Table 8.1: Summary of available data*

<u>Injector Type</u>	<i>Pressure Swirl</i>	<i>Multi-Stream</i>
<b><u>Present Investigation</u></b>		
<b><i>Ambient Pressure</i></b>	Atmospheric	0.1bar to 10bar
<b><i>Fuel Pressure</i></b>	120bar	120bar and 190bar
<b><i>Fuel Temperature</i></b>	Atmospheric	20°C to 100°C
<b><i>Fuel Type</i></b>	Gasoline E25 Iso-Octane N-Heptane Exxsol Stoddard	Gasoline E22 Iso-Octane N-Heptane
<b><i>Cone Angle</i></b>	90°	60° and 90°
<b><i>Injection Duration (Pulse Width)</i></b>	2ms to 5ms	2ms
<b><i>Injector Type</i></b>	Single Central Hole	3-Hole 6-Hole (Symmetrical)
<b><i>Penetration</i></b>	Available for all operating conditions	Available for all operating conditions
<b><i>Mean Velocity</i></b>	Axial and Radial	Axial and Radial (atmospheric conditions only)
<b><i>Mean Drop Size</i></b>	D <sub>10</sub> and D <sub>32</sub>	D <sub>10</sub> and D <sub>32</sub> (atmospheric conditions only)
<b><i>Flash Boiling</i></b>	No	Yes



### 8.1.1 IMPACT Tool

One source of engine emissions in GDI engines is due to the unintended spray impact on either piston, cylinder liner, intake valve or spark plug. An impact causes a cooling of the spray, reducing vaporisation and causing the air-fuel mixture to be burnt rich, increasing particulate and hydrocarbon emissions. The direction and penetration velocity of a spray can be determined to produce an empirical model for the spray morphology, which, in conjunction with the time varying engine geometry can be used to determine the probability of the spray impacting on the engine valves, liner or piston. Contact with the intake valve can occur if the valve movement intercepts the spray, although this is very time dependent and various valve timing and fuel injection strategies are employed to prevent any impact. Contact with any of the three geometries can occur if the spray is distorted due to in-cylinder airflow. The inlet valve timing and lift profile can therefore be very influential on the spray structure itself.

Stansfield et al. [82] investigated the difference in results gathered with three different spray measurement mediums; an atmospheric bench, a pressure chamber and an optical engine, with a view of quantifying the validity of using less representative measurement methods (the atmospheric spray bench and the pressure chamber) to investigate spray characteristics. One key aspect of their work was that even with significant spray distortion due to intake charge entering the cylinder, the spray axial penetration was similar to that seen when the intake valve timing prevented charge entering the cylinder during injection. It was also reported that a good approximation of the axial penetration was achieved when the same conditions were generated in the pressure chamber, thus proving that the pressure chamber could be used to predict in-cylinder spray penetration characteristics.

Therefore the penetration and cone angle data obtained in the pressure chamber can be used in the IMPACT tool to provide, for specific multi-hole injectors and under a range of engine relevant thermodynamic conditions for which plume to plume interaction and flash boiling can be neglected, a very useful approximation of the spray impact inside the combustion chamber.

---

## Chapter 8 – Conclusions and Recommendations for Future Work

---

### 8.1.2 Plume to Plume Interactions

The second part of the experimental work was set to investigate the possibility of interactions found due to the close location of plumes within multi-hole injectors. Comparison of different injector designs has shown that droplets within plumes of multi-hole injectors can be affected by the proximity of other plumes. Droplets on the inside edge of a plume have a greater axial velocity (velocity along the injector axis) than those found on the outside for the injectors that have closely located plumes. Drop diameters are also different on the side of plumes interacting with other plumes and this becomes less prominent with a greater cone angle of the injector. Plumes that are closer together create a distortion such that the spray is no longer symmetrical around its axis, whereas, as the plumes become more distant each plume tends to be more symmetrical as if the plumes were separate, i.e. approaching single jets.

Phase Doppler Anemometry was used to measure the droplet diameters and two directions of droplet velocity at locations around the injectors. Three different multi-hole injectors were used for the investigation each having plumes at different distances apart. A six-hole injector with a cone angle of  $60^\circ$  had the smallest distance between plumes, while a second six-hole injector had a  $90^\circ$  cone angle. A third injector with three holes  $120$  degrees apart with a cone angle of  $90^\circ$  was also used. Phase Doppler Anemometry is a highly detailed measurement technique that has a very small measurement volume. The areas of the injector sprays that were of greatest importance were used for the analysis and these were composed through two different types of scans; a radial and a circumferential scan. The radial scan was performed at locations from the spray centre line outwards through the axis of a plume to the outer edge of the plume and the circumferential scan was performed at points around the injector at constant distance equal to that of the plume centre. Both of the scans were performed at three different distances from the injector nozzle; 20mm, 40mm and 60mm.

At 20mm below the injector nozzle, when comparing the axial velocities of the six-hole  $60^\circ$  cone angle injector at equal distances on the inside and outside of plume, they were found to be higher on the inside. Further away from the nozzle the results showed further contrast with axial velocity on the outside of the plume initially being higher, but as the spray develops the velocity on the inside sharply increases. The same measurements on the six-hole  $90^\circ$  cone angle injector also showed an increase in velocities on the inside of the plume but not as sharp as for the injector with the smaller cone angle. The velocities for the third injector; the three-hole  $90^\circ$  cone angle injector showed symmetry around the plume centre. As the

## Chapter 8 – Conclusions and Recommendations for Future Work

---

axial velocity on the inside of the plume increased as the distance between plumes decreased it is clear that this was an effect of the plume interaction.

When using the radial scan to measure droplet diameters a similar trend to the axial velocity was found. The average droplet arithmetic mean diameter  $D_{10}$  for the six-hole 60° cone angle injector was 5µm at 2mm from the plume centre on the outside and increased through to 10µm at 2mm on the inside. An increase in diameter from the outside to the inside is seen at 20, 40 and 60mm below the injector nozzle but the difference is less prominent the further away. This increase in diameter is also seen at 20mm for the six-hole 90° cone angle injector but this was also less prominent than the smaller cone angle injector. The three-hole 90° cone angle injector does not show this trend as its droplet diameters are relatively symmetrical at either side of the plume centre.

The radial scan shows that multi-hole injectors with plumes that are close together create interactions changing the distribution of the fuel in the plumes in terms of axial velocity and droplet diameter. The six-hole 60° cone angle injector shows interaction on the plume inside edge at the three vertical heights, the six-hole 90° cone angle injector shows interaction at 20mm only while the three-hole 90° cone angle injector appears symmetrical at all vertical locations.

The circumferential scans were used to provide further information about plume interaction within the three injectors. When comparing the two six-hole injectors, the velocities between the plumes on the circumferential scan were found to be different. At all vertical heights the 90° cone angle injector's velocities showed no fuel between the plumes. However, the 60° cone angle injector showed varied results. At 20mm below the injector nozzle the droplets between the plumes on average had a negative radial velocity, showing air entrainment into the centre of the spray. At 40mm the radial and axial velocity components show that the drops are moving away from the plume towards the outside of the spray. This is due to the spray front causing a vortex at the sides of the spray along with pressure differences created as the spray from injectors with small cone angle force the ambient air away. There are likely to be different directions of velocities found in between the plumes for the 60° cone angle injector if measurements were taken at further vertical heights. The circumferential scans for the six-hole 90° cone angle injector and three-hole 90° cone angle injector showed symmetrical results once the degree movement went beyond the plume attenuation but no sign of plume interaction through air entrainment was found even at 20mm below the injector nozzle.

## Chapter 8 – Conclusions and Recommendations for Future Work

---

Overall it was found that the distance between plumes affects the amount of interaction. The injector with the smallest cone angle showed plume interaction effects on droplet size and velocities at all three vertical heights, the six-hole injector with the wider cone angle showed slight interaction at 20mm but little further away from the nozzle. The three-hole injector showed no signs of plume interaction behaving symmetrically as though it was three separate plumes.

The performance of GDI engines is highly dependent on fuel spray development. The main requirements are:

- Small droplet size ( $D_{32}$  less than  $20\mu\text{m}$ ) to ensure all fuel is vaporised prior to ignition.
- High air utilisation to enable maximum power output.
- No spray impingement for reduced HC emissions and improved fuel economy.

Thus, the characteristics of the injector must be matched to the combustion chamber during engine development to ensure maximum benefits are attained from the GDI system. The spray characterisation work has led to empirical relationships that when incorporated into the targeting tool IMPACT will play a major role in helping the development engineers to tailor injection systems to specific combustion systems.

### 8.1.3 Flash Boiling

When a hot engine is running at idle, fuel which has been warmed via conduction of heat from the cylinder head can be injected into a low pressure environment. If the ambient pressure in the cylinder is lower than the saturation pressure of the fuel at that temperature then flash boiling can occur. Flash boiling has been found to significantly alter the shape of the fuel spray, therefore consideration must be given to the behaviour of flash boiling sprays if an engine is likely to create these conditions.

Flash boiling reduces droplet size and increases vaporisation and therefore has potential to reduce engine-out HC emissions and improve fuel economy as an increased percentage of fuel injected will undergo combustion. At the same time, penetration and spray angle are increased, leading to the possibility of spray impingement on the cylinder walls which has potential to increase engine-out HC emissions as fuel is captured by the cylinder wall oil film and released during the exhaust stroke. The increase in penetration is very unlikely to cause a problem with impingement on the piston crown as flash boiling conditions are created during the intake stroke, when the piston is moving away from the injector. To ensure flash boiling does not cause increased emissions it is necessary to carefully control the injector positioning and tip design to limit the possibility of fuel spray impingement.

There are several factors which have been investigated and found to affect flash boiling:

- Ambient pressure
- Fuel temperature
- Fuel chemical composition
- Fuel pressure
- Injector tip configuration

The first three factors in the list affect the degree of superheat of the fuel as it is injected into the cylinder. A fuel's boiling point is reduced with a reduction in ambient pressure. As the fuel temperature is increased inside the injector, this boiling point can be far surpassed, particularly if the ambient pressure in the pressure chamber is very low. The short duration of the injection process is such that no heat energy is lost via conduction to the surrounding gas. The combination of the temperature and injection duration effects raises the degree of superheat when fuel is injected from the high pressure condition inside the injector to the low pressure condition inside the pressure chamber. The fuel boiling point is also dependent on the chemical composition of the fuel. By definition, a fuel with a relatively low boiling point will

## Chapter 8 – Conclusions and Recommendations for Future Work

---

have a higher degree of superheat than a fuel with a relatively high boiling point under the same atmospheric conditions. The effects are complicated in the case of multi-component fuels where some components reach their boiling point at lower temperatures than others.

Increased fuel pressure increases the exit velocity of fuel from the injector. This increases the aerodynamic shear forces on the fuel droplets and encourages droplet break-up. This directly affects spray development, but is not related to flash boiling. It is possible that this droplet break-up affects the intensity of flash boiling but the results are inconclusive and more work needs to be done to fully understand the effects of fuel pressure on flash boiling. One way in which fuel pressure could affect the degree of superheat is that if fuel with a very low boiling point was used, higher fuel pressures would allow higher fuel temperatures to be reached without causing problems with vapour lock in the fuel lines. However, modern GDI fuel pressures of 120bar are high enough to keep standard fuel in their liquid state at temperatures likely to be seen under regular operating conditions.

Injector tip configuration (number of holes and their positioning,  $l/d$  ratio, cone angle and tip shape i.e. flat or concave) defines the spacing of the individual spray plumes of a multi-hole injector and controls the required degree of superheat for the fuel spray to collapse inwards. This is because if the plumes are close together to start with, as in the six-hole  $60^\circ$  cone angle injector case, less superheat is required to increase the level of plume interaction to the point at which spray collapse occurs. In other words, injector configuration does not affect flash boiling itself, but affects the intensity of the phenomena caused by flash boiling.

Images of the spray recorded have shown that flash boiling causes some phenomena which are impossible to fully explain without knowledge on the behaviour and temperature of individual droplets in the spray. These include the apparent rotation of the injector spray with increased degree of superheat,

Addition of ethanol to standard gasoline fuel has the potential to offset  $\text{CO}_2$  output, as the  $\text{CO}_2$  generated during combustion is absorbed by the plants grown to produce the fuel. It is important to realise that addition of ethanol does not reduce  $\text{CO}_2$  tailpipe emissions, as the amount of fuel combusted for a given power output has to be increased to make up for the decrease in calorific value of the fuel. This means that the targets set out by the automobile manufacturer associations worldwide are even less likely to be met with increased use of ethanol unless the  $\text{CO}_2$  offset effect is taken into account.

## Chapter 8 – Conclusions and Recommendations for Future Work

---

The results have shown that E22 fuel behaves significantly differently to gasoline when undergoing flash boiling and hence care must be taken by manufacturers when converting vehicles to use ethanol-based fuels, particularly if the proportion of ethanol is increased in future years. This difference is due to the change in the two-phase region of the fuel mixture. It is very difficult to determine the precise saturation point of any multi-component fuel as each compound boils at a different temperature. Also the presence of low boiling point components induces vaporisation of higher boiling point components. This makes it difficult to predict exactly when flash boiling is likely to occur in a multi-component fuel. The results show that the fuel spray does not transition from non-flashing to flashing at one easily recognisable point, rather, part of the fuel spray begins to flash boil and as the degree of superheat is further increased, more and more of the fuel flash boils. This adds further complexities to any modelling as the observed phenomena occur at different degrees of superheat and these vary for different operating conditions, fuels and injectors.

Recent advances in computing power mean that CFD modelling of fuel sprays is a viable tool for assisting in engine development. It is necessary that a flash-boiling mechanism be included in any model so that the spray shape changes under flash-boiling conditions can be accounted for. This part of the model is likely to be very complicated to produce as the effects have shown to be highly complex. If a complete spray development, air movement and combustion model can be developed which takes account of flash boiling then it will enable rapid optimisation of combustion chamber and injector design, allowing further reduction in harmful emissions at a reduced development cost. The results obtained in this study aids in the understanding, development and validation of such models.

### **8.2 Recommendations for future work**

#### 8.2.1 Rigs

The in-cell temperature and pressure measurement instrumentation proved adequate in determining the actual in-cell conditions. However, it was found that neither pressure nor temperature was being controlled to sufficient accuracy. The control logic did not allow long enough for the charge temperature to lower to that of the cell after pressurisation. A large variation in temperature was also seen, especially at the higher control temperatures of 80°C and 100°C. A reduction in charge temperature of around 1-2°C was observed following injection. This is due to conductive heat transfer from the charge to the spray during injection and atomisation. Like the in-cell temperature, a relatively large variation in in-cell pressure was also noted and seen to be as large as 10% in places. This is due to either poor control of the inlet and purge valves or due to valve actuation being too slow. Therefore longer settling times are needed alongside with larger and faster inlet and purge valves, the latter being essential for PDA measurements with realistic time scales.

Both the light sheet and PDA setups are relatively easy to apply to spray on an atmospheric spray bench but the limited optical access available in the pressure chamber make it more difficult in these cases. A chamber with larger windows allowing simultaneous recording of side and underneath images of the spray while performing PDA measurements would provide very useful information and allow a more accurate analysis of the spray dynamics. In the current study, the temperature of the injected fuel is assumed to be the same as the chamber temperature, however, a more accurate control of the injector temperature would be beneficial.

#### 8.2.2 Imaging

It would be useful to use a light-sheet to illuminate a cross section of the spray. Currently the images captured show the entire spray and this makes it difficult to know the exact shape in 3D. Capturing cross sectional images would generate knowledge on the composition of the centre of the spray, for example, whether the spray cone is hollow or filled with droplets. Laser sheet imaging could be used as well to provide patterning of the spray.



### 8.2.3 PDA

The shadowgraph imaging technique, used for the flash boiling study described in section 7.2, is very useful for investigating the behaviour of the bulk spray, however it is not suited to investigate the mechanisms behind this behaviour. To do this, information on the size and velocity of individual droplets is required and for this a laser-based technique such as PDA should be employed. There are several phenomena which PDA could be used to further investigate.

**Droplet Distribution:** Using PDA to measure droplet distribution would help to confirm the presence of additional spray plumes. Currently these plumes are visible on the underneath images but not the side images and using a completely different method of detecting droplets in this region would help to confirm exactly what is happening.

**Droplet Size:** The change in droplet size with increased degree of superheat could be measured. This would help to confirm whether severity of spray collapse is related to droplet size. It would also be possible to measure the size of the droplets in the interstitial plumes, observed under 0.5bar backpressure with the six-hole 60° cone angle injector, to see if they are smaller than the droplets in the main plumes.

**Droplet Velocity:** Measurement of droplet velocity throughout the spray would help confirm whether the collapse is due to movement of particles inwards towards the spray axis due to air movement caused by formation of vortices, similar to the collapse of pressure-swirl injector spray.

All the three multi-hole injectors, used in the plume interaction study described in section 6.2, have established sprays at a height of 20mm below the injector nozzle. For the two six-hole injectors plume interaction is occurring while there is no interaction for the three-hole injector. Therefore it would be interesting to perform macro imaging and 1D PDA to establish whether the six-hole injectors show distinct plumes or if the three-hole injector shows plume interaction closer to the nozzle.

## Chapter 8 – Conclusions and Recommendations for Future Work

---

PDA measurements in the near nozzle regions of transient hollow cone high pressure swirl GDI fuel sprays have been attempted successfully by Pitcher et al. [139]. Imaging of the spray with the input laser beams identifies the bulk spray morphology, the spray density, the propagation of the input laser beams and the location of the PDA measurement volume. It was revealed that the major problem to obtaining successful PDA data in the near nozzle region of the hollow cone spray was the obscuration of the input beams when the measurement volume was aligned with the inside surface of the spray cone when the input laser beams would be obscured before the crossover. When the measurement volume is positioned on the spray cone centre line multiple scatter from droplets and remnants of the liquid sheet in, or near, the measurement volume results in a significantly reduced signal validation rate, the effects of which could be reduced by increased data acquisition times [139]. The probability of successful PDA measurements can be increased by minimising the dimensions of the measurement volume, maximising the probability of laser beam crossover and droplet detection and performing preliminary measurements to establish the trade off between increasing the 'system gain' and optical noise break through on the data. Reducing a PDA system configuration from two component to one component velocity provides another option for maximising the probability of the formation of the laser beam crossover albeit at the cost of reducing the full measurement potential [140].

Mojtabi et al. [140] detailed analysis of velocity and drop-size measurements made with 1D and 2D PDA system configurations in the primary break-up region of the dense spray produced by a GDI multi-stream injector has attempted to quantify the effects caused by laser beam and measurement volume obscuration. The 3-hole injector allowed one particular spray stream to be studied without any interference from the other streams while maintaining stream similarity with a conventional 6 hole injector. The probability of only two laser beams crossing in the spray and generating a valid signal is significantly greater for the 1D system. This is readily seen in the sample number plots where, in some cases sample numbers can be a factor of two larger and this gives the velocity and drop-size data greater statistical significance. The 1D configuration also provides better estimates of the smaller size classes but it was found that reduced beam quality does not lead to a simple exclusion of the lowest sizes. Effectively all sizes below 10 microns would be discriminated against. Whereas this affects the arithmetic mean values the Sauter mean values are less affected. Where the droplet velocities are concerned there are only small differences in the profiles across the spray stream, at the 2% level, between the 1D and 2D systems. The overall conclusion is that for dense sprays a 1D PDA system configuration provides the best estimates of sample number, droplet velocity and size with a 2D configuration providing adequate estimates of the droplet trajectory [140].

### 8.2.4 Injectors

Injector geometry, with not only the hole layout but also the internal geometry, plays an important part in the plume interactions and flash boiling phenomena observed. Therefore it would be useful to perform measurements with only one varying characteristic between each injector tested. For example if symmetrically designed six-hole injectors that had the same  $l/d$  ratio but with a range of cone angles were used then a quantified rate of interactions may be able to be established. Another example would be six-hole injectors with common  $l/d$  and cone angle that were asymmetrically designed such that the plumes were closer in terms of radial distance. Furthermore, information concerning detailed internal geometry of the injector prototype used in our study is very difficult to obtain from the manufacturers supplying the injectors, so the influence of the cavitation effects occurring inside the injector (initiated in the needle seat and observed around the sharp edges at the entrance of the needle holes) is difficult to quantify. Both phenomena, cavitation and flash-boiling, are a transition from liquid to vapor due to a drop in pressure. In contrast to nucleate boiling, the enthalpy for vaporisation is not provided at walls during the phase change process, but is instead provided by inter-phase heat transfer. A gross distinction between cavitating and flash-boiling nozzle flow is simply that the enthalpy of the cavitating flow is below the saturated liquid enthalpy at the downstream pressure, while the enthalpy of the flash-boiling flow exceeds the saturated liquid enthalpy at the downstream pressure.

### 8.2.5 Fuels

Although it is valuable to perform experiments with real fuels such as gasoline and E22, it is difficult to quantify fuel properties which are important to flash boiling as the fuels contain many different compounds. Therefore it would be useful to test with specific blends of fuels for which properties such as volatility are known, as the effect of specific fuel properties could then be determined.

**Bibliography**

- [1] L. Bayvel and Z. Orzechowski, *Liquid Atomization.*: Taylor and Francis, 1993.
- [2] F. Zhao, D.L. Harrington, and M.C. Lai, *Automotive Gasoline Direct Injection Engines.*, SAE Textbook, 2002.
- [3] [www.dieselnet.com/standards/eu/ld.php](http://www.dieselnet.com/standards/eu/ld.php).
- [4] [www.greencarcongress.com](http://www.greencarcongress.com).
- [5] [www.wikipedia.com](http://www.wikipedia.com).
- [6] K. Hoag, "Engine Performance and Design," University of Wisconsin, Lecture Notes 2005.
- [7] [www.eia.doe.gov](http://www.eia.doe.gov).
- [8] [www.ams.usda.gov](http://www.ams.usda.gov).
- [9] H.L. MacLean, L.B. Lave, R. Lankey, and S. Joshi, "A Life-Cycle Comparison of Alternative Automobile Fuels," *J. Air and Waste Manage. Assoc.*, vol. 50, pp. 1769-1779, 2000.
- [10] S. Peterson, A. Hieronymus, M. Meyer, and C. Dawes, "The New Silverado: An Ethanol (E85) Conversion," University of Nebraska-Lincoln, Technical Report 2000.
- [11] "Biofuel Raises Global Dilemmas". BBC News Article, January 17th 2006.
- [12] Orbital Engine Company, "A Testing Based Assessment to Determine Impacts of a 10% and 20% Ethanol Gasoline Fuel Blend on Non-Automotive Engines," 2003.

- [13] J.B. Heywood, *Internal Combustion Engine Fundamentals*, McGraw Hill ed., 1988.
- [14] H. Heisler, *Advanced Engine Technology*, Butterworth Heinemann ed., 1995.
- [15] M. Goodwin, *Transient Liquid sheets and their relationship to GDI sprays*. Ph.D. Thesis, 2004.
- [16] G. Wigley, M.S. Goodwin, and G. Pitcher, "Fuel Break-up and Atomisation in the Near Nozzle Region of a GDI Injector," in *IMEchE, Fuel Injection Systems*, 2002.
- [17] Arthur H Lefebvre, *Atomization and Sprays*. New York and Washington D.C.: CRC Press, 1989.
- [18] N. Dombrowski and W.R. Johns, "The Aerodynamic Instability and Disintegration of Viscous Liquid Sheets," *Chemical Engineering Science* , vol. 18, pp. 203-214, 1963.
- [19] S.P. Lin and R. D. Reitz, "Drop and Spray Formation from a Liquid Jet," *Annu. Rev. Fluid Mech.*, vol. 30, pp. 85-105, 1998.
- [20] S.P. Lin, *Breakup of Liquid Sheets and Jets*. Clarkson University Postdam, New-York/USA: Cambridge University Press, 2003.
- [21] R.D Reitz, *Atomization and Other Breakup Regimes of a Liquid Jet*. Ph.D. Thesis, Princeton University, 1978.
- [22] C. Webber, "Disintegration of Liquid Jets," *Z. Angew. Math. Mech.*, vol. 11, no. 2, pp. 136-159, 1931.
- [23] Z. Farago and N. Chigier, "Morphological classification of disintegration of round liquid jets in a coaxial air stream ," *Atomization and Sprays*, vol. 2, p. 137–153, 1992.
- [24] N. Czerwonatis and R. Eggers, "SprayStrahlzerfall und Tropfenwiderstand in Verdichteten Gasen. Tagungsband Spray," in *5th Workshop uber Techniken der*

- Fluidzerstaubung und Untersuchungen von Spruhvorgängen*, Bremen, 1999, pp. 99, 3:1–8.
- [25] W.O.H. Mayer and R. Branam, "Atomization characteristics on the surface of a round liquid jet," *Experiments in Fluids*, vol. 36, no. 10.1007/s00348-003-0675-0, p. 528–539, 2004.
- [26] J. Cousin, G. Vich, and S. Nally, "Formation and Primary Breakup of Conical Liquid Sheets Discharged by Pressure Swirl Injectors. Experimental and Theoretical Investigation," in *ICLASS*, Pasadena, CA, 2000.
- [27] K. Kurachi, T. Serizawa, K. Wada, S. Kato, and H. Ito, "Investigation on Measurement of Diesel Spray Breakup Length by Using Doppler Signals," *SAE Technical Paper Series*, no. 2001-01-0533, 2001.
- [28] Yu Pan and Kazuhiko Sugaa, "A Numerical Study on the Breakup Process of Laminar Liquid Jets into a Gas," *Physics of Fluids*, vol. 18, no. 052101, 2006.
- [29] M. Y. Ghannam, "Mathematical Formulation for Hydrodynamic Stability of Fluidic Jets," *SAE Technical Paper Series*, no. 2002-01-0216, 2002.
- [30] Ariane Vallet and Roland Borghi, "Modélisation eulerienne de l'atomisation d'un jet liquide," *C. R. Acad. Sci. Paris*, no. 327, pp. 1015-1020, 1999.
- [31] Brad A. VanDerWege and Simone Hochgreb, "Effects of Fuel Volatility and Operating Conditions on Fuel Sprays in DISI Engines: (1) Imaging Investigation," *SAE Technical Paper Series*, no. 2000-01-0535, 2000.
- [32] S. Strauss and Y. Zeng, "The Effect of Fuel Spray Momentum on Performance and Emissions of Direct-Injected Two-Stroke Engines," *SAE Technical Paper Series*, no. 2004-32-0013, 2004.
- [33] T. Benson, "Combustion," NASA Glenn Research Center, Technical Report, 2004.

- [34] Robert Bosch GmbH, Ed., *Automotive Handbook*.: 6th Edition, pg 485, 2004.
- [35] Xiaohua Fang et al., "Factors Controlling the Drop Evaporation Constant," *J. Phys. Chem. B*, vol. 109, no. 20554-20557, 2005.
- [36] G. M. Faeth, "Evaporation and combustion of sprays," *Prog. Energy Comb. Sci.*, vol. 9, pp. 1-76, 1983.
- [37] N. Ashgriz and P. Givi, "Binary Collision Dynamics of Fuel Droplets," *International journal of heat and fluid flow*, vol. 8, no. 3, pp. 205-210, 1987.
- [38] Gwon Hyun Ko, Hong Sun Ryou, Nahm Keon Hur, Seung Woo Ko, and Myoung O Youn, "Numerical Study on Bouncing and Separation Collision Between Two Droplets Considering the Collision-Induced Breakup," *Journal of Mechanical Science and Technology*, vol. 21, pp. 585-592, 2007.
- [39] Soo-Young No, "Definition and Correlation for Spray Angle in Plain-orifice Atomizers," in *ILASS Japan*, Yokohama, December 2006, pp. 141-146.
- [40] Soo-Young No, "Correlations for Prediction of Diesel Fuel Spray Penetration," in *ILASS-Europe*, Mugla, Turkia, 2007.
- [41] J.M. Desantes, R. Payri, F.J. Salvador, and J. Gimeno, "Prediction of Spray Penetration by Means of Spray Momentum Flux," *SAE Technical Paper Series*, no. 2006-01-1387, 2006.
- [42] [www.worldenergy.org](http://www.worldenergy.org).
- [43] C.T. Change and P.V. Farrell, "A Study on the Effects of Fuel Viscosity and Nozzle Geometry on High Injection Pressure Diesel Spray Characteristics," *SAE Technical Paper Series*, no. 970353, 1997.
- [44] W.A. Sirignano, *Fluid Dynamics and Transport of Droplets and Sprays*, Cambridge

- University Press ed. ISBN 0 521 63036 3 hardback, 1999.
- [45] Brad A. VanDerWege and Simone Hochgreb, "Effects of Fuel Volatility and Operating Conditions on Fuel Sprays in DISI Engines: (2) PDPA Investigation," *SAE Technical Paper Series*, no. 2000-01-0536, 2000.
- [46] Kun Tong, Bryan D. Quay, James V. Zello, and Domenic A. Santavicca, "Fuel Volatility Effects on Mixture Preparation and Performance in a GDI Engine During Cold Start," *SAE Technical Paper Series*, no. 2001-01-3650, 2001.
- [47] S.K. Chen and A.H. Lefebvre, "Spray Cone Angles of Effervescent Atomizers," *Atomisation and Sprays*, vol. 4, pp. 291-301, 1994.
- [48] Rudolf J Schick, "An Engineers Practical Guide to Drop Size," Spraying Systems Company,.
- [49] R.E. Canaan, J.E. Dec, and R.M. Green, "The Influence of Fuel Volatility on the Liquid-Phase Fuel Penetration in a Heavy-Duty D.I. Diesel Engine," *SAE Technical Paper Series*, no. 980510, 1998.
- [50] Brad A. VanDerWege, Todd H. Lounsberry, and Simone Hochgreb, "Numerical Modeling of Fuel Sprays in DISI Engines Under Early-Injection Operating Conditions," *SAE Technical Paper Series*, no. 2000-01-0273, 2000.
- [51] G. Wigley, M. Mojtabi, M. Williams, and G. Pitcher, "The Effect of Fuel Properties on Liquid Breakup and Atomisation in GDI Sprays," in *ICLASS06-075*, 2006.
- [52] Cornel Stan, Ed., *Direct Injection Systems for Spark-Ignition and Compression-Ignition Engines*, SAE International ed. ISBN: 978-0-7680-0610-0, 2000.
- [53] H. Ando, Y. Iwamoto, O. Nakayama, K. Noma, and T. Yamauchi, "Development of Gasoline Direct Injection Engine," *SAE Technical Paper Series*, no. 970541, 1997.
- [54] H.-E. Albrecht, M. Borys, N. Damaschke, and C. Tropea, *Laser Doppler and Phase*



*Doppler Measurement Techniques*, Springer ed., 2003.

[55] [www.mitsubishi-motors.com](http://www.mitsubishi-motors.com).

[56] A.C. Alkidas, A.M. Lippert, D.L. Reuss, J. Liedtke, and K.-J. Wu, "Fuel Economy and Emissions from a Two-Valve Direct-Injection S.I. Engine Operating in the Stratified-Combustion Regime," University of Wisconsin Engine Research Center, Technical Paper 2003.

[57] J. Raimann, S. Arndt, R. Grzeszik, I. Ruthenber, and P. Wörner, "Optical Investigations in Stratified Gasoline Combustion Systems with Central Injector Position Leading to Optimized Spark Locations for Different Injector Designs," *SAE Technical Paper Series*, no. 2003-01-3152, 2003.

[58] G. Wigley et al., "Air-Fuel Mixing in a Homogeneous Direct Injection Spark Ignition Engine with a Fully Variable Valve Train System," in *Haus der Technik, 7th. International Congress – Engine Combustion Processes*, Munich, 2005.

[59] G. Pitcher, M.S. Goodwin, and G. Wigley, "Relationship between In-cylinder Flow and Pressure and GDI Spray Propagation," in *International Symposium on Applications of Laser Techniques to Fluid Mechanics*, Lisbon, 2004.

[60] C. Döring, S. Fehler, S. Kampmann, and C. Preussner, "GDI: International Between Mixture Preparation, Combustion System and Injector Performance," *SAE Technical Paper Series*, no. 980498, 1998.

[61] J. Serras-Pereira, P.G. Aleiferis, D. Richardson, and S. Wallace, "Spray Development, Flow Interactions and Wall Impingement in a Direct-Injection Spark-Ignition Engine," *SAE Technical Paper Series*, no. 2007-01-2712, 2007.

[62] K. Kawajiri, T. Yonezawa, H. Ohuchi, M. Sumida, and H. Katashiba, "Study of Interaction Between Spray and Air Motion, and Spray Wall Impingement," *SAE Technical Paper Series*, no. 2002-01-0836, 2002.

[63] B. Lecointe and G. Monnier, "Downsizing a Gasoline Engine Using Turbocharging with

- Direct Injection," *SAE Technical Paper Series*, no. 2003-01-0542, 2003.
- [64] R. Szengel et al., "The TSI with 88 kW – the expansion of the Volkswagen family of fuel-efficient gasoline engines," in *28. Internationales Wiener Motorensymposium*, 2007.
- [65] N. Brouzos, B. Leach, Y. Li, and H. Zhao, "Managing controlled auto-ignition combustion by injection on a direct-injection gasoline engine," in *IMEchE*, 2007.
- [66] Peter Dahlander and Ronny Lindgren, "Multi-hole Injectors for DISI Engines: Nozzle Hole Configuration Influence on Spray Formation," *SAE Technical Paper Series*, no. 2008-01-0136, 2008.
- [67] Anand H. Gandhi et al., "Spray Characterization in a DISI Engine During Cold Start: (1) Imaging Investigation," *SAE Technical Paper Series*, no. 2006-01-1004, 2006.
- [68] Anand H. Gandhi et al., "Spray Characterization in a DISI Engine During Cold Start: (2) PDPA Investigation," *SAE Technical Paper Series*, no. 2006-01-1003, 2006.
- [69] P.E Kapus and H Fuchs, *Optical Investigations during Cold Start.:* International Symposium on Comustion Diagnostics, 2008.
- [70] J. Lee, K. Nishida, and M. Yamakawa, "An Analysis of Ambient Air Entrainment into Split Injection D.I. Gasoline Spray by LIF-PIV Technique," *SAE Technical Paper Series*, no. 2002-01-2662, 2002.
- [71] X. Liu et al., "Quantitative Characterization of Near-Field Fuel Sprays by Multi-Orifice Direct Injection Using Ultrafast X-Tomography Technique," *SAE Technical Paper Series*, no. 2006-01-1041, 2006.
- [72] H. Hiroyasu, M. Shimizu, and M. Arai, "The Breakup of High Speed Jet in a High Pressure Gaseous Atmosphere," in *Proceedings of the 2nd International Conference on Liquid Atomisation and Spray Systems*, Madison, Wisconsin, 1982, pp. 69-74.
- [73] H. Hiroyasu and M. Arai, "Fuel Spray Penetration and Spray Angle in Diesel Engine,"

*Trans JSAE*, vol. 21, pp. 5-11, 1980.

- [74] G.N. Abramovich, *Theory of Turbulent Jet*, MIT Press ed. Cambridge, 1963.
- [75] R.D. Reitz and F.V. Bracco, "Reitz, R. D. On the Dependence of Spray Angle and Other Spray Parameters on Nozzle Design and Operating Conditions", *SAE Technical Paper Series*, no. 790494, 1979.
- [76] F.V. Bracco, B. Chehroudi, S.H. Chen, and Y. Onuma, "On the Intact Core of Full Core Sprays," *SAE Trans.*, vol. 94, no. 850126, 1985.
- [77] M. Arai, M. Tabata, H. Hiroyasu, and M. Shimizu, "Disintegrating Process and Spray Characterization of Fuel Jet Injected by a Diesel Nozzle," *SAE Technical Paper Series*, no. 840215, 1984.
- [78] D. L.S. Hung, D. M. Chmiel, and L. E. Markle, "Application of an Imaging-based Diagnostic Technique to Quantify the Fuel Spray Variations in a Direct-Injection Spark-Ignition Engine," *SAE Technical Paper Series*, no. 2003-01-0062, 2003.
- [79] Loïc De Francqueville et al., "Experimental Investigation of the Air Entrainment Characteristics Within the Periphery of a Gasoline Direct Injection (GDI) Spray by PIV," in *ILASS Americas*, Irvine, CA, 2005.
- [80] A. Chatterjee, "An introduction to the proper orthogonal decomposition," *Current Science*, vol. 78, no. 7, pp. 808-817, April 2000.
- [81] Rudolf J. Schick, *An Engineer's Practical Guide to Drop Size*, Spraying Systems Co.® ed. Wheaton, Illinois/USA, 1997.
- [82] P. Stansfield, G. Wigley, M. Mojtabi, and G. Pitcher, "Variations in GDI Spray Propagation Under a Variety of Ambient and Engine Conditions," in *8th International Congress - Engine Combustion Processes - LTT - Haus der Technik*, Munich, 2007.
- [83] P. Stansfield, G. Wigley, G. Pitcher, H. Nuglisch, and J. Jedelsky, "Investigation into spray cone oscillations in a gasoline direct injection fuel spray," in *ILASS Europe*,

Orleans, France, 2005.

- [84] Robert M. Siewert, "A Phenomenological Engine Model for Direct Injection of Liquid Fuels, Spray Penetration, Vaporization, Ignition Delay, and Combustion," *SAE Technical Paper Series*, no. 2007-01-0673, 2007.
- [85] S. Tonini, M. Gavaises, C. Arcoumanis, A. Theodorakakos, and S. Kometani, "Multi-Component Fuel Vaporization Modelling and its Effect on Spray Development in Gasoline Direct Injection Engines," *Proc. IMechE*, vol. 221 Part D: J. Automobile Engineering, no. 10.1243/09544070JAUTO545, pp. 1321-1341, 2007.
- [86] G.G. Nasr, A.J. Yule, and L. Bendig, *Industrial Sprays and Atomization: Design, Analysis and Applications*, Springer-Verlag London Limited ed. Great Britain, 2002.
- [87] P. Dahlander, "High-Speed Photography and Phase Doppler Anemometry Measurements of Flash-Boiling Multi-Hole Injector Sprays for Spray-Guided Gasoline Direct Injection," in *SIAMUF*, 2006.
- [88] B. A. VanDerWege, *The Effects of Fuel Volatility and Operating Conditions on Sprays from Pressure-Swirl Fuel Injectors*, Ph.D. Thesis, Ed. Massachusetts Institute of Technology, USA, 1999.
- [89] K-E. Rossmeißl and M. Wirth, "Influence of the Nozzle Geometry on the Atomization of Superheated Liquids," in *19th Annual Meeting of the Institute for Liquid Atomization and Spray Systems (Europe)*, Nottingham , 6-8 September 2004.
- [90] E. Sher, T. Bar-Kohany, and A. Rashkovan, "Flash-Boiling Atomization," *Science Direct*, 2007.
- [91] M. S. Plesset and A. Prosperetti, "Bubble Dynamics and Cavitation," *Annual Revue of Fluid Mechanics*, pp. 9: 145-85, 1977.
- [92] S. Escobar-Vargas et al., "Bubble growth characterization during fast boiling in an enclosed geometry," *International Journal of Heat and Mass Transfer*, vol. 52, pp. 5102-5112, 2009.

- [93] Dar-Lon Chang and Chia-Fon F. Lee, "Development of a simplified bubble growth model for flash boiling sprays in direct injection spark ignition engines," *Proceedings of the Combustion Institute*, vol. 30, pp. 2737-2744, 2005.
- [94] Paolo Oresta, Roberto Verzicco, Detlef Lohse, and Andrea Prosperetti, "Heat Transfer Mechanisms in Bubbly Rayleigh-Bénard Convection," *Phys. Rev. E*, vol. 80, no. 2, 2009.
- [95] A.J. Robinson and R.L. Judd, "The Dynamics of Spherical Bubble Growth," *International Journal of Heat and Mass Transfer*, vol. 47, pp. 5101-5113, 2004.
- [96] Kunito Okuyama, Shoji Mori, Kimihiro Sawa, and Yoshihiro Iida, "Dynamics of boiling succeeding spontaneous nucleation on a rapidly heated small surface," *International Journal of Heat and Mass Transfer*, vol. 49, p. 2771-2780, 2006.
- [97] P. Gebhard, *Zerfall und Verdampfung von Einspritzstrahlen aus lamellenbildenden Düsen*. Ph.D Thesis, Technische Universität München, pg. 23-25, 1996.
- [98] D. Kawano, Y. Goto, M. Odaka, and J. Senda, "Modeling Atomization and Vaporization Processes of Flash-Boiling Spray," *SAE Technical Paper Series*, no. 2004-01-0534, 2004.
- [99] S.V. Stralen and R. Cole, *Boiling phenomena.*: Hemisphere Pub., 1979.
- [100] S. Suma and M. Koizumi, "Internal boiling atomization by rapid pressure reduction of liquids," *Trans JSME (B)*, vol. 43, pp. 4608-4617, 1977.
- [101] P. Stansfield, M. Mojtabi, G. Wigley, and G. Pitcher, "GDI Spray Propagation under a Variety of Ambient and Engine Conditions," in *LTT*, Munich, 2007.
- [102] J. Senda, Y. Wada, D. Kawano, and H. Fujimoto, "Improvement of Combustion and Emissions in Diesel Engines by Means of Enhanced Mixture Formation Based on Flash Boiling of Mixed Fuel," *International Journal of Engine Research*, vol. 9, no. 1, pp. 15-27, 2008.

- [103] R. D. Reitz, "A Photographic Study of Flash-Boiling Atomization," *Aerosol Science and Technology*, pp. 12:3, 561 - 569, 1990.
- [104] J. Bouilly, "Flash Boiling Occurrence - Understanding of the Phenomenon," Continental AG, Toulouse, Internal Report 2008.
- [105] Geanette Polanco, Arn Erik Holdø, and George Munday, "General Review of Flashing Jet Studies," *Journal of Hazardous Materials*, vol. 173 , pp. 2-18, 2010.
- [106] B.S. Park and S.Y. Lee, "An experimental investigation of the flash atomization mechanism," *Atomization and Sprays*, vol. 4, pp. 159-179, 1994.
- [107] G. M. Bianchi, C. Forte, S. Negro, and P. Pelloni, "A 1d Model for the Prediction of Flash Atomization in Gdi Multi-Hole Injectors: Preliminary Results," *SAE Technical Paper Series*, no. 2008-01-2516, 2008.
- [108] S. Gopalakrishnan and D. P. Schmidt, "A Computational Study of Flashing Flow in Fuel Injector Nozzles," *SAE Technical Paper Series*, no. 2008-01-0141, 2008.
- [109] Y. Ra and R. D. Reitz, "A Vaporization Model for Discrete Multi-Component Fuel Sprays," *International Journal of Multiphase Flow*, vol. 35, pp. 101-117, 2009.
- [110] S. Eisenberg, "Diesel Spray Investigation with Ultra-High-Speed Camera UltraSpeedStar," LaVision GmbH, Germany,.
- [111] G. Wigley, G. Pitcher, D. Law, B. Schneider, and S. Rogers, "Effect of Compression Pressure on the Spray Morphology of GDI Pressure-Swirl Injectors," in *COMODIA*, 2001.
- [112] Graham Wigley, Graham K. Hargrave, and John Heath, "A High Power, High Resolution LDA/PDA System Applied to Gasoline Direct Injection Sprays," *Part. Part. Syst. Charact.*, vol. 16, pp. 11-19, 1999.
- [113] Graham Pitcher and Graham Wigley, "Simultaneous Two-Component Velocity and Dropsizes Measurements in a Combusting Diesel Spray," in *Seventh International*

*Symposium on Applications of Laser Techniques to Fluid Mechanics*, Lisbon, Portugal, 1994.

- [114] R. Wilkie, "The Effects of Temperature and Pressure on a GDI Fuel Spray," Loughborough University Aeronautical and Automotive Engineering Department, BEng. Final Year Project Report 2005.
- [115] Jean-Luc Fremaux, "Engine modelisation with AMEsim software and tool development for spray targeting in direct injection engine with Matlab," Continental AG., Toulouse, MSc. final year project, June 2005.
- [116] Hakan Sandquist, Ronny Lindgren, and Ingemar Denbratt, "Sources of Hydrocarbon Emissions from a Direct Injection Stratified Charge Spark Ignition Engine," *SAE Technical Paper Series*, no. 2000-01-1906, 2000.
- [117] M. Blessing, G. Konig, C. Kruger, U. Michels, and V. Schwarz, "Analysis of flow and cavitation phenomena in Diesel injection nozzles and its effects on spray and mixture formation," DaimlerCrysler AG, Stuttgart, Germany, 2003.
- [118] Malcolm James Nunney, *Light and Heavy Vehicle Technology*, ISBN 0750680377 Fourth Edition, Ed.: Butterworth-Heinemann, 2007.
- [119] D. P. Schmidt, C. J. Rutland, M. L. Corradini, P. Roosen, and O. Genge, "Cavitation in Two-Dimensional Asymmetric Nozzles," *SAE Technical Paper Series*, no. 1999-01-0518, 1999.
- [120] J Gerhardt, A Kufferath, and T Landefeld, "Gasoline Direct Injection - SULEV Emissions Concept," SAE 2004-01-0041, 2004.
- [121] K.H. Lee, C.H. Lee, and C.S. Lee, "Analysis of size-classified spray structure and atomization mechanism for a gasoline direct injector," *Atomization and Sprays*, vol. 14, pp. 545-562, 2004.
- [122] C. Shulz and V. Sick, "Tracer-LIF Diagnostics: Quantitative Measurement of fuel concentration, temperature and fuel/air ratio in practical combustion systems," *Prog.*

*Energy Combustion Science*, vol. 31, pp. 75-121, 2005.

- [123] M.C. Drake, T.D. Fansler, A.S. Solomon, and G.A. Szekely, "Piston fuel films as a source of smoke and hydrocarbon emissions from a wall controlled spark ignited direction-injection engine," *SAE Technical Paper Series*, no. 2003-01-0547, 2003.
- [124] Petter Dahlander and Ronny Lindgren, "Multi-hole Injectors for DISI Engines: Nozzle Hole Configuration Influence on Spray Formation," SAE 2008-01-0136, 2008.
- [125] Jean-Bernard Blaisot, David Dechaume, Nicholas Fdida, and Alain Floch, "Drop Size Measurement Techniques applied to Gasoline Sprays," Como Lake, Italy, ILASS08-7-7, 2008.
- [126] K. Sato et al., "Spray and Evaporation Characteristics of Multi-Hole Injector for DISI Engines - Effect of Diverging Angle Between Neighboring Holes," *SAE Technical Paper Series*, no. 2009-01-1500, 2009.
- [127] G. Wigley, G. Pitcher, H. Nuglisch, J. Helie, and N. Ladomatos, "Fuel Spray Formation and Gasoline Direct Injection," in *8th AVL International Symposium*, 2008.
- [128] D. Kawano et al., "Numerical Study on Flash-Boiling Spray of Multicomponent Fuel," *Wiley Periodicals, Inc.*, pp. Heat Transfer—Asian Research, 35 (5), 2006.
- [129] Iranian Chemical Engineers Website. Antoine Coefficients for Vapor Pressure. [www.IrChe.com](http://www.IrChe.com).
- [130] A.E. Catania, A. Ferrari, M. Manno, and E. Spessa, "Comprehensive Thermodynamic Approach to Acoustic Cavitation Simulation in High-Pressure Injection Systems by a Conservative Homogeneous Two-Phase Barotropic Flow Model," *ASME Journal of Engineering for Gas Turbines and Power*, vol. 128, no. 2, pp. 434-445, April 2006.
- [131] C. von Kuensberg Sarre, S.C. Kong, and R.D. Reitz, "Modeling the Effects of Injector Nozzle Geometry on Diesel Sprays," *SAE Technical Paper Series*, no. 1999-01-0912, 1999.



- [132] G.M. Bianchi, F. Minelli, S. Zaleski, and R. Scardovelli, "3D Large Scale Simulation of the High Speed Liquid Jet Atomization," *SAE TRANSACTIONS - Journal of Passenger Cars-Mechanical Systems*, vol. 116-2007, no. ISBN978-0-7680-1987-2, April 2008.
- [133] E.D. Villiers, D.A. Gosman, and H.G. Weller, "Large Eddy Simulation of Primary Diesel Spray Atomization," *SAE Technical Paper Series*, no. 2004-01-0100, 2004.
- [134] K. Sato, C. Lee, and N. Nagai, "A study on atomization process of superheated liquid," *Trans JSME (B)*, vol. 50, pp. 1743-1752, 1984.
- [135] G. Delay, R. Bazile, G. Charnay, and H. J. Nuglish, "Temporal Dependency of Air Entrainment to Liquid Flow Rate Variations," in *12 th International symposium on application of laser techniques to fluid mechanics*, Lisbon, 2004.
- [136] L. Allocca and G. Valentino, "Droplet Size and Velocity Distributions of a Transient Hollow-Cone Spray for GDI Engines," *Particle and particle systems characterization*, vol. 18, p. 262–270, 2001.
- [137] G. Rottenkolber et al., "Spray Analysis of a Gasoline Direct Injector by Means of Two-Phase PIV," *Experiments in Fluids*, vol. 32, pp. 710-721, 2002.
- [138] R Dewhurst, *PDA of GDI sprays with Gasoline Ethanol Mixtures.*: Loughborough University, 2008.
- [139] G. Pitcher, G. Wigley, and P.A. Stansfield, "Interpretation of Phase Doppler Measurements in a Dense Transient Fuel Spray," in *13th International Symposium on Applications of Laser Techniques to Fluid Mechanics*, Lisbon, 2006.
- [140] M. Mojtabi, G. Wigley, J. Jedelsky, and J. Helie, "A Comparison between One and Two Component Velocity and Size Measurements in a Dense Spray," in *ILASS – Europe 2010, 23rd Annual Conference on Liquid Atomization and Spray Systems*, Brno, Czech Republic, September 2010.
- [141] J.S. Chin and A.H. Lefebvre, "Effective Values of Evaporation Constant for Hydrocarbon Fuel Drops," in *Proceeding of the 20th Automotive Technology Development Contractor*

*Coordination Meeting*, 1982, pp. 325-331.

- [142] E. Giffen and A. Muraszew, *The atomisation of liquid fuels*, Chapman and Hall ed., 1953.
- [143] H. Hiroyasu, "Diesel Engine Combustion and Its Modelling," *COMODIA Proceedings* , pp. 53-75, 1985.
- [144] Nick Chadwick, "Imaging Analsis of GDI Fuel Sprays under Flash Boiling Conditions," 2008.
- [145] Dr. Graham Wigley, "Introduction to light scattering and optical diagnostics for the analysis of air flows and fuel sprays," 2007.
- [146] G Baranescu, "Some Characteristics of Spark Assisted Direct Injection Engines," 1983.
- [147] P Aleiferis, D Richardson, J Serrar-Pereira, and S Wallace, "Spray Development in a Direct-Injection Spark Ignition Engine ," SAE 2007-01-2712, 2007.
- [148] Z van Romunde, P Aleiferis, R Cracknell, and H Walmsley, *Effect of Fuel Properties on Spray Development from a Multi-Hole DISI Engine Injector.*: SAE International, 2007.
- [149] Lu Zhang and Janusz Kulon, "Real-Time Velocity Estimation of a Charged Particle using Phase Locked Loop and Quadrature Demodulation Techniques," 2007.
- [150] Dr. G Wigley, G Pitcher, Dr. H Nuglisch, Dr. J Helie, and Prof. N Ladommatos, "Fuel Spray Formation and Gasoline Direct Injection," 2008.
- [151] B. Zuo, A. M. Gomes, and C. J. Rutland, "Modeling Superheated Fuel Sprays and Vaporization," *International Journal of Engine Research*, vol. 1, no. 4, pp. 321-336, 2000.
- [152] J. Zhang et al., "Experimental Study on Flashing Atomization of Methane/Liquid Fuel

- Binary Mixtures," *Energy & Fuels*, vol. 19, pp. 2050-2055, 2005.
- [153] H. Zhang, *Evaporation of a Spherical Moving Fuel Droplet over a Wide Range of Ambient Pressures within a Nitrogen Environment*, Ph.D. Thesis, Ed. University of Nebraska, USA, 2000.
- [154] Pisit Yongyingsakthavorn, Jean Cousin, Christophe Dumouchel, and Jerome Helie, "Piezo Spray Drop-Size Measurements by Laser Diffraction Technique in Presence of Multiple Scattering Effects," in *ILASS*, Como Lake, Italy, 2008.
- [155] Pisit Yongyingsakthavorn, Pумыos Vallikul, Bundit Fungtammasan, and Christophe Dumouchel, "Application of the maximum entropy technique in tomographic reconstruction from laser diffraction data to determine local spray drop size distribution," *Experiments in Fluids*, vol. 42, no. 10.1007/s00348-007-0257-7, pp. 471-481, 2007.
- [156] H. W. M. Witlox and P. J. Bowen, "Flashing Liquid Jets and Two-Phase Dispersion," Det Norske Veritas Ltd, Contract Research Report 403/2002, 2002.
- [157] S. Wissel et al., "Droplet Velocity Measurements in Direct-Injection Diesel Sprays Under High-Pressure and High-Temperature Conditions by Laser Flow Tagging," *SAE Technical Paper Series*, no. 2008-01-0944, 2008.
- [158] A. Wildgen and J. Straub, "The Boiling Mechanism in Superheated Free Jets," *International Journal of Multiphase Flow*, vol. 15, no. 2, pp. 193-207, 1989.
- [159] G. Wigley, M. Goodwin, G. Pitcher, and D. Blondel, "Experimental Study Of Density Effect On Air Entrainment In Quasi-Steady Gasoline Dense Sprays By F-PIV," in *11th Int Symp on Applications of Laser Techniques to Fluid Mechanics*, Lisbon, Portugal, 2002.
- [160] G Wigley, R Dewhurst, M Gold, and R Spragg, *Imaging and Phase Doppler Analysis of GDI Fuel Sprays with Gasoline-Ethanol Mixtures.*: ILASS, 2008.
- [161] X. Wang and W. Su, "Influence of Injection Pressure Fluctuations on Cavitation inside a Nozzle Hole at Diesel Engine Conditions," *SAE Technical Paper Series*, no. 2008-01-

0935, 2008.

- [162] M. M. Vieira and J. R. Simões-Moreira, "Low-Pressure Flashing Mechanisms in Iso-Octane Liquid Jets," *Journal of Fluid Mechanics*, vol. 572, pp. 121-144, 2007.
- [163] J.W.G. Turner et al., "The HOTFIRE Homogeneous GDI and Fully Variable Valve Train Project - An Initial Report," *SAE Technical Paper Series*, no. 2006-01-1260, 2006.
- [164] K. Triballier, C. Dumouchel, and J. Cousin, "A Technical Study on the Spraytec Performances: Influence of Multiple Light Scattering and Multi-Modal Drop-Size Distribution Measurements," *Experiments in Fluids*, vol. 35, no. 10.1007/s00348-003-0674-1, pp. 347-356, 2003.
- [165] F. Theunissen, "Percent Ethanol Estimation on Sensorless Multi-Fuel Systems; Advantages and Limitations," *SAE Technical Paper Series*, no. 2003-01-3562, 2003.
- [166] B. Sturtevant and J. E. Shepherd, "Evaporative Instability at the Superheat Limit," *Applied Scientific Research*, vol. 38, pp. 85-97, 1982.
- [167] Peter Spiekermann, Sven Jerzembeck, and Norbert Peters, "The Influence of Fuel Boiling Temperature on Common Rail Spray Penetration and Mixture Formation for Ethanol and Propylene-Glycol," *SAE Technical Paper Series*, no. 2008-01-0934, 2008.
- [168] C. Soteriou, R. Andrews, and M. Smith, "Further Studies of Cavitation and Atomization in Diesel Injection," *SAE Technical Paper Series*, no. 1999-01-1486, 1999.
- [169] M. Skogsberg, P. Dahlander, R. Lindgren, and I. Denbratt, "Effects of Injector Parameters on Mixture Formation for Multi-Hole Nozzles in A Spray-Guided Gasoline DI Engine," *SAE Technical Paper Series*, no. 2005-01-0097, 2005.
- [170] J. R. Simões-Moreira and J. E. Shepherd, "Evaporation Waves In Superheated Dodecane," *Journal of Fluid Mechanics*, vol. 382, pp. 63-86, 1999.
- [171] J. R. Simões-Moreira, "Oblique Evaporation Waves," *Shock Waves*, vol. 10, pp. 229-234,

2000.

- [172] Junmei Shi, Harald Baecker, Milos Tichy, and Wolfgang Bauer, "Numerical and Experimental Investigation of Fuel Injection and Droplet Evaporation in a Pressure Chamber for the Development of Gasoline Direct Injection," in *ILASS*, Como Lake, Italy, 2008.
- [173] Michael H. Shelby, Brad A. VanDerWege, and Simone Hochgreb, "Early Spray Development in Gasoline Direct-Injected Spark Ignition Engines," *SAE Technical Paper Series*, no. 980160, 1998.
- [174] J. Serras-Pereira, P.G. Aleiferis, D. Richardson, and S. Wallace, "Mixture Preparation and Combustion Variability in a Spray-Guided DISI Engine," *SAE Technical Paper Series*, no. 2007-01-4033, 2007.
- [175] J. Serras-Pereira, P.G. Aleiferis, D. Richardson, and S. Wallace, "Characteristics of Ethanol, Butanol, Iso-Octane and Gasoline Sprays and Combustion from a Multi-Hole Injector in a DISI Engine," *SAE Technical Paper Series*, no. 2008-01-1591, 2008.
- [176] Jiro Senda, Yoshiyuki Hojyo, and Hajime Fujimoto, "Modelling of Atomization Process in Flash Boiling Spray," *SAE Technical Paper Series*, no. 941925, 1994.
- [177] J. Senda and H. Fujimoto, "Multicomponent Fuel Consideration for Spray Evaporation Field and Spray-Wall Interaction," *SAE Technical Paper Series*, no. 2001-01-1071, 2001.
- [178] J. Senda, Y. Hojyo, and H. Fujimoto, "Modeling on Atomization and Vaporization Process in Flash Boiling Spray," *Society of Automotive Engineers of Japan, Inc.*, vol. 15, pp. 291-296, 1994.
- [179] I. Schmitz, W. Ipp, and A. Leipertz, "Flash Boiling Effects on the Development of Gasoline Direct-Injection Engine Sprays," *SAE Technical Paper Series*, no. 2002-01-2661, 2002.
- [180] I. Schmitz and A. Leipertz, "Comparison of the Flash-Boiling Influence on the Spray Structure of a High Pressure Swirl Injector and of a Mulithole Injector for GDI Engines,"

in *ICLASS-2006*, Kyoto, Japan, 2006.

- [181] H. Roth, M. Gavaises, and C. Arcoumanis, "Cavitation Initiation, Its Development and Link with Flow Turbulence in Diesel Injector Nozzles," *SAE Technical Paper Series*, no. 2002-01-0214, 2002.
- [182] E. Robert, J. Lettry, M. Farhat, P. A. Monkewitz, and F. Avellan, "Cavitation Bubble Behavior Inside a Liquid Jet," *Physics of Fluids*, vol. 19, no. 6, 2007.
- [183] D.-R. Rhim and P. V. Farrell, "Effect of Gas Density and the Number of Injector Holes on the Air Flow Surrounding Non-Evaporating Transient Diesel Sprays," *SAE Technical Paper Series*, no. 2001-01-0532, 2001.
- [184] D.-R. Rhim and P. V. Farrell, "Air Flow Surrounding Burning Transient Diesel Sprays," *SAE Technical Paper Series*, no. 2002-01-2668, 2002.
- [185] C. Resagk, R. du Puits, and A. Thess, "Error estimation of laser-Doppler anemometry measurements in fluids with spatial inhomogeneities of the refractive index," *Experiments in Fluids*, vol. 35, no. 10.1007/s00348-003-0679-9, pp. 357-363, 2003.
- [186] C. Resagk, R. du Puits, and A. Thess, "Error estimation of laser-Doppler anemometry measurements in fluids with spatial inhomogeneities of the refractive index," *Experiments in Fluids*, vol. 35, no. 10.1007/s00348-003-0679-9, pp. 357-363, 2003.
- [187] P. Reinke and G. Yadigaroglu, "Explosive Vaporization of Superheated Liquids by Boiling Fronts," *International Journal of Multiphase Flow*, vol. 27, pp. 1487-1516, 2001.
- [188] M. M. Rahman, H. Suzuki, H. Ishii, Y. Goto, and M. Odaka, "Effect of Boiling Point Differences of Two-Component Normal Paraffin Fuels on Combustion and Emission in CI Engines," *SAE Technical Paper Series*, no. 2003-01-0757, 2003.
- [189] Y. Ra and R. D. Reitz, "The Application of a Multicomponent Droplet Vaporization Model to Gasoline Direct Injection Engines," *International Journal of Engine Research*, vol. 4, no. 3, pp. 193-218, 2003.

- [190] Y. Ra and R. D. Reitz, "A Model for Droplet Vaporization for Use in Gasoline and HCCI Engine Applications," *Transactions of the ASME*, vol. 126, pp. 422-428, April 2004.
- [191] Brice Prosperi, Jerome Helie, and Rudy Bazile, "Experimental Study Of Density Effect On Air Entrainment In Quasi-Steady Gasoline Dense Sprays By F-PIV," in *13th Int Symp on Applications of Laser Techniques to Fluid Mechanics*, Lisbon, Portugal, 2006.
- [192] S.W. Park, S.H. Bang, K.H. Lee, C.S. Lee, and J.H. Lee, "Atomization Characteristics of Common-rail Diesel Injector with Multi-hole," *SAE Technical Paper Series*, no. 2003-01-1833, 2003.
- [193] D. Papoulias, E. Giannadakis, N. Mitroglou, M. Gavaises, and A. Theodorakakos, "Cavitation in Fuel Injection Systems for Spray-Guided Direct Injection Gasoline Engines," *SAE Technical Paper Series*, no. 2007-01-1418, 2007.
- [194] R. D. Oza and J. F. Sinnamon, "An Experimental and Analytical Study of Flash-Boiling Fuel Injection," *SAE Technical Paper Series*, no. 830590, 1983.
- [195] J. M. Nouri, N. Mitroglou, Y. Yan, and C. Arcoumanis, "Internal Flow and Cavitation in a Multi-Hole Injector for Gasoline Direct-Injection Engines," *SAE Technical Paper Series*, no. 2007-01-1405, 2007.
- [196] Soo-Young No, "Definition and Correlation for Spray Angle in Non-Reacting Diesel Fuel Sprays," *Journal of ILASS-Korea*, vol. 11, no. 4, 2006.
- [197] Koichi Nakata et al., "The Effect of Ethanol Fuel on a Spark Ignition Engine," *SAE Technical Paper Series*, no. 2006-01-3380, 2006.
- [198] A. Miyajima et al., "Experimental Characterization of Flat-Spray Injector in Gasoline Direct Injection Engines," *SAE Technical Paper Series*, no. 2003-01-0061, 2003.
- [199] N. Mitroglou, J.M. Nouri, Y. Yan, M. Gavaises, and C. Arcoumanis, "Spray Structure Generated by Multi-Hole Injectors for Gasoline Direct-Injection Engines," *SAE Technical Paper Series*, no. 2007-01-1417, 2007.

- [200] Shelley Minteer, *Alcoholic Fuels*, Taylor & Francis Group ed. Saint Louis University, Missouri/USA, 2006.
- [201] K. H. Liew, E. Urip, S. L. Yang, and C. J. Marek, "An Interactive Microsoft® Excel Program for Tracking a Single Evaporating Droplet in Crossflow," NASA, NASA/TM—2004-212910, 2004.
- [202] M. J. Lee, Y. W. Kim, J. Y. Ha, and S. S. Chung, "Effects of Watery Vapor Concentration on Droplet Evaporation in Hot Environment," *International Journal of Automotive Technology*, vol. 2, no. 3, pp. 109-115, 2001.
- [203] P. C. Le Clercq and J. Bellan, "Direct Numerical Simulation of a Transitional Temporal Mixing Layer Laden with Multicomponent-Fuel Evaporating Drops Using Continuous Thermodynamics," *Physics of Fluids*, vol. 16, no. 6, pp. 1884-1907, June 2004.
- [204] D. Kawano, "Numerical Study on Flash-Boiling Spray of Multicomponent Fuel," in *FISITA World Automotive Congress*, Barcelona, 2004.
- [205] Kenneth Kar, Tristan Last, Clare Haywood, and Robert Raine, "Measurement of Vapor Pressures and Enthalpies of Vaporization of Gasoline and Ethanol Blends and Their Effects on Mixture Preparation in an SI Engine," *SAE Technical Paper Series*, no. 2008-01-0317, 2008.
- [206] P.E. Kapus, A. Fuerhapter, H. Fuchs, and G.K. Fraidl, "Ethanol Direct Injection on Turbocharged SI Engines - Potential and Challenges," *SAE Technical Paper Series*, no. 2007-01-1408, 2007.
- [207] J. E. Jiménez, C. Méndez, F. Castro, F. V. Tinaut, and B. Giménez, "Experimental Comparison Between Conventional and Bio-Derived Fuel Sprays," *SAE Technical Paper Series*, no. 2001-01-1072, 2001.
- [208] David L.S. Hung et al., "Gasoline Fuel Injector Spray Measurement and Characterization – A New SAE J2715 Recommended Practice," *SAE Technical Paper Series*, no. 2008-01-1068, 2008.



- [209] A.J. Heather, G. Wigley, and H.K. Versteeg, "Prediction of the near-field spray issued via a pressure-swirl atomiser," in *ILASS Europe*, Orleans, France, 2005.
- [210] A. J. Heather and G. Wigley, "CCD Imaging and PDA Analysis of a Bosch Multi-Hole Injector," Loughborough University, 2005.
- [211] R. Hasegawa et al., "Two-Dimensional Gas-Phase Temperature Measurements Using Phosphor Thermometry," *Applied Physics B*, vol. 88, pp. 291-296, 2007.
- [212] David L Harrington, Fuquan Zhao, and Ming-Chia Lai, "Automotive Gasoline Direct-Injection Engines," 2002.
- [213] C. N. Grimaldi, L. Postrioti, C. Stan, and R. Tröger, "Analysis Method for the Spray Characteristics of a GDI System with High Pressure Modulation," *SAE Technical Paper Series*, no. 2000-01-1043, 2000.
- [214] Denis W. Gill, "Injection Rate Gauge for Loughborough Univeristy - Pass Off Information and User Instructions," Fuel & Engine Managements System, 2002.
- [215] T. Gemci, K. Yakut, N. Chigier, and T. C. Ho, "Experimental study of flash atomization of binary hydrocarbon liquids," *International Journal of Multiphase Flow*, no. 30, p. 395–417, 2004.
- [216] J. Galpin, J. Cousin, G. Corbinelli, and S. Sivieri, "A One Dimensional Model for Designing Pressure Swirl Atomizers," *SAE Technical Paper Series*, no. 2005-01-2101, 2005.
- [217] D. L. Frost, "Dynamics of Explosive Boiling of a Droplet," *Physics of Fluids*, vol. 31, no. 9, pp. 2554-2561, 1988.
- [218] Nicolas Fdida, Jean-Bernard Blaisot, Alain Floch, and David Dechaume, "Drop Size Measurement Techniques Applied to Gasoline Sprays," in *ILASS*, Como Lake, Italy, 2008.

- [219] I. Düwel, M. C. Drake, and T. D. Fansler, "High-Speed, High-Resolution Laser Imaging of Multihole Fuel Sprays in a Firing Spray-Guided Direct-Injection Gasoline Engine," in *ILASS-Europe 19th Annual Conference*, Nottingham, England, 2004.
- [220] C. Dumouchel, P. Yongyingsakthavorn, and J. Cousin, "Light Multiple Scattering Correction of Laser-Diffraction Spray Drop-Size Distribution Measurements," *International Journal of Multiphase Flow*, vol. 35, pp. 277-287, 2009.
- [221] H. Du, J. Liu, and J. Tang, "A CFD Investigation on the Nozzle of Orifices Distributing in Different Space Layers," *SAE Technical Paper Series*, no. 2008-01-0948, 2008.
- [222] M.C. Drake and D.C. Haworth, "Advanced gasoline engine development using optical diagnostics and numerical modeling," *Proceedings of the Combustion Institute*, vol. 31, pp. 99-124, 2007.
- [223] Lee G. Dodge, Deborah J. Rhodes, and Rolf D. Reitz, "Drop-size measurement techniques for sprays: comparison of Malvern laser-diffraction and Aerometrics phase/Doppler," *Journal of Applied Optics*, vol. 26, no. 11, pp. 2144-2154, June 1987.
- [224] G. Delay, M. Marchal, and H. J. Nuglisch, "Behaviour of a Piezo Injector Spray in Presence of a Steady Cross Flow," IMFT-Siemens VDO Automotive, Toulouse, 2004.
- [225] J. Cousin and H.J. Nuglisch, "Modeling of Internal Flow in High Pressure Swirl Injectors," *SAE Technical Paper Series*, no. 01P-161, 2001.
- [226] M. A. Comer, P. J. Bowen, S. M. Sapsford, and C. J. Bates, "Critical Appraisal of Current Laser Diagnostic Techniques for G-DI Spray Kinematic Quantification," *Optical Diagnostics in Engineering*, vol. 5, no. 1, pp. 39-50, 2001.
- [227] D.-L. Chang and C.-F. F. Lee, "Preliminary Computational Studies of Flash Boiling for Fuel Injectors in Gasoline Direct Injection Automotive Engines," in *37th Intersociety Energy Conversion Engineering Conference (IECEC)*, 2002.
- [228] P.A. Caton, L.J. Hamilton, and J.S. Cowart, "An Experimental and Modeling Investigation into the Comparative Knock and Performance Characteristics of E85,"

- Gasohol [E10] and Regular Unleaded Gasoline [87(R+M)/2]," *SAE Technical Paper Series*, no. 2007-01-0473, 2007.
- [229] Edouard Berrocal, Elias Kristensson, Mattias Richter, Mark Linne, and Marcus Alden, "Multiple Scattering Suppression in Planar Imaging of Dense Sprays by Means of Structured Illumination," in *ILASS*, Como Lake, Italy, 2008.
- [230] H. Bensler, L. Kapitza, J. Raposo, and U. Reisch, "A New Experimental Method for Determining Port Generated Swirl Flow," *SAE Technical Paper Series*, no. 2002-01-2846, 2002.
- [231] B. Argueyrolles et al., "Influence of Injector Nozzle Design and Cavitation on Coking Phenomenon," *SAE Technical Paper Series*, no. 2007-01-1896, 2007.
- [232] C. Arcoumanis, H. Flora, M. Gavaises, N. Kampanis, and R. Horrocks, "Investigation of Cavitation in a Vertical Multi-Hole Injector," *SAE Technical Paper Series*, no. 1999-01-0524, 1999.
- [233] L. Araneo, G. Brunello, A. Coghe, and R. Dondé, "Effects of Fuel Temperature and Ambient Pressure on a GDI Swirled Injector Spray," *SAE Technical Paper Series*, no. 2000-01-1901, 2000.
- [234] M. Adachi et al., "Measurement of Fuel Vapor Concentration in Flash Boiling Spray by Infrared Extinction/Scattering Technique," *Society of Automotive Engineers of Japan, Inc*, vol. 17, pp. 231-237, 1996.
- [235] Commission of the European Communities, "Reducing CO<sub>2</sub> emissions from light-duty vehicles," 2007.
- [236] American Council for an Energy Efficient Economy, "2007 Energy Bill Fuel Economy Update," 2007 (December 5th).
- [237] K. Tong, B.D. Quay, J.V. Zello, and D.A. Santavicca, "Fuel Volatility Effects on Mixture Preparation and Performance in a GDI Engine during Cold Start," *SAE Technical Paper Series*, no. 2001-01-3650, 2001.

- [238] (Edited by) Cornel Stan, *Direct Injection Systems for Spark-Ignition and Compression-Ignition Engines.*, 2000.
- [239] Rolf D. Reitz and Youngchul Ra, "A Vaporization Model for Discrete Multi-Component Fuel Sprays," *International Journal of Multiphase Flow*, vol. 35, pp. 101-117, 2009.
- [240] P.E Kapus and H Fuchs, *Optical Investigations during Cold Start*. Baden Baden, Germany: International Symposium on Combustion Diagnostics, 2008.

## Appendices

### **Appendix A D2 law of droplet evaporation**

(Atomization and sprays, Arthur H. Lefebvre [17])

During the steady state period of an evaporating drop, its diameter at any instant may be related to its initial diameter by the expression:

$$D_0^2 - D^2 = \lambda_{st} t \quad (1)$$

where  $\lambda_{st}$  is the steady state evaporation constant.

The drop lifetime during this period is  $t_{st} = \frac{D_0^2}{\lambda_{st}}$  (2)

When the heat-period is too long to be neglected, the time required to fully evaporate the drop is obtained as the sum of the unsteady state period and the steady state period, i.e.:

$$t_e = \Delta t_{hu} + \Delta t_{st} = \frac{D_0^2 - D_1^2}{\lambda_{hu}} + \frac{D_1^2}{\lambda_{st}} \quad (3)$$

where  $D_1$  is the diameter of the drop at the end of the heat-up period and  $\lambda_{hu}$  is the evaporation constant during the heat-up period.

The total drop lifetime when we consider the heat up period and the convective effects (relative motion between the drops and the surrounding air or gas) is:

$$t_e = \Delta t_{hu} + \frac{\left[ D_0^2 - \lambda_{hu} \Delta t_{hu} \left( 1 + 0.3 \text{Re}_{hu}^{0.5} \text{Pr}_g^{0.33} \right) \right]}{\lambda_{st} \left( 1 + 0.3 \text{Re}_{st}^{0.5} \text{Pr}_g^{0.33} \right)} \quad (4)$$

in which  $\text{Re}_{hu}$  and  $\text{Re}_{st}$  are based respectively on the diameter of the drop during the heat-up period and the steady state period and  $\text{Pr}$  is the Prandtl number.

Then we can define an “effective” value of evaporation constant to be assigned to any given fuel at any stipulated conditions of ambient pressure, temperature, velocity and drop size as:

$$\lambda_{eff} = \frac{D_0^2}{t_e} \quad (5)$$

This concept of an effective value of evaporation constant considerably simplifies calculations of the drop lifetime as:

$$t_e = \frac{D_0^2}{\lambda_{eff}} \tag{6}$$

**Numerical application:**

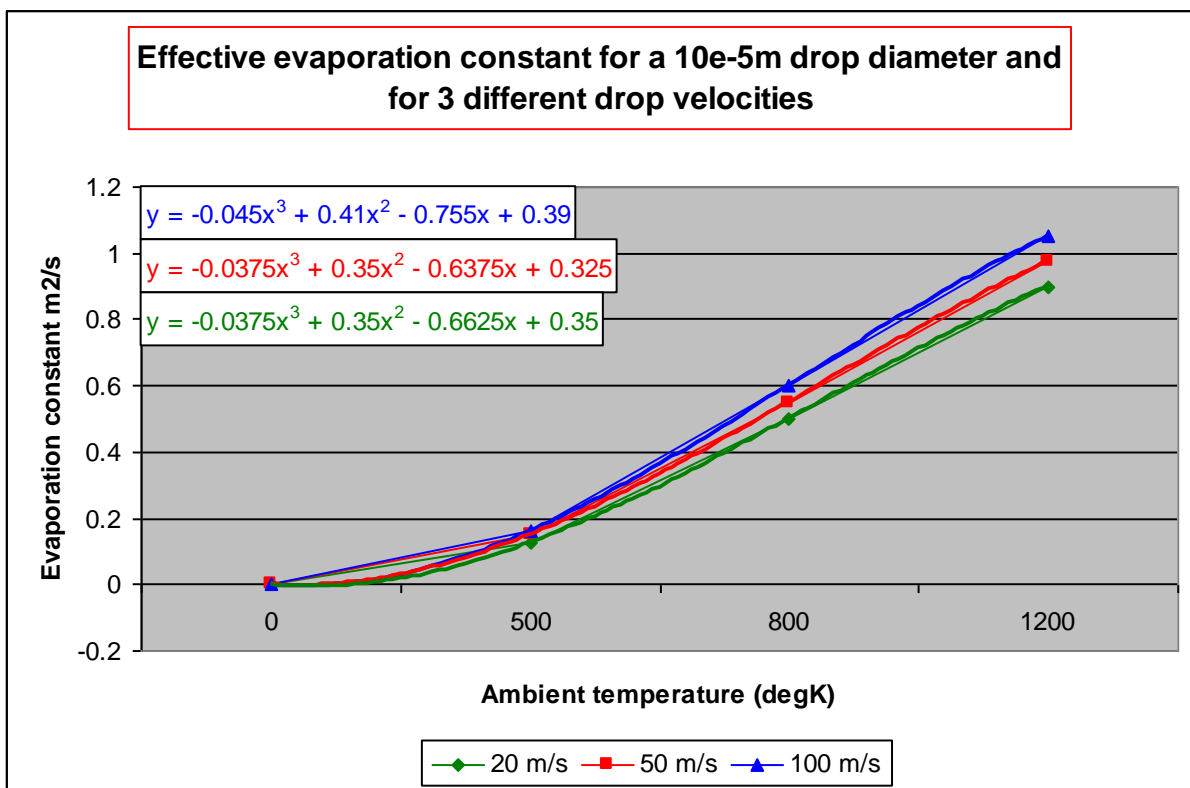
We want to calculate the lifetime of a  $D_0 = 10 \cdot 10^{-6}$  m initial diameter droplet of gasoline in an injector spray where the ambient pressure and temperature are 1 bar and 293 K, and the average relative velocity  $U$  between the air and the drop is around 50 m/s. The normal boiling temperature of gasoline is 420 deg K.

We obtain by interpolation of Chin and Lefebvre [141] results that for  $P = 100$  kPa and  $UD_0 = 500$  (m/s)( $10^{-6}$ m) (see Figure A.1):

$$\lambda_{eff} \approx 0.04 \cdot 10^{-6} \text{ m}^2/\text{s}$$

which gives a drop lifetime of:

$$t_e = \frac{D_0^2}{\lambda_{eff}} = \frac{(10 \cdot 10^{-6})^2}{0.04 \cdot 10^{-6}} = 2.5 \text{ ms}$$



**Figure A.1: Effective evaporation constant for a  $10^{-5}$ m drop diameter and 3 different relative velocities between the drop and the air**

**Appendix B Penetration of a single droplet in air**

(The atomisation of liquid fuels, Giffen, E and Muraszew, A [142])

For the movement of a single spherical droplet discharged into still air with initial velocity  $v_0$ , neglecting the effect of gravity, the equation of motion is:

$$m \frac{dv}{dt} + R = 0$$

where  $m$  is the mass of the droplet and  $R$  is the air resistance given by:

for laminar flow ( $Re < 2$ ),  $R = 3\pi\eta_{air}vd$

for semi-turbulent flow ( $2 < Re < 500$ ),  $R = \pi(0.05\rho_{air}v^2d^2 + 5\eta_{air}vd)$

for turbulent flow ( $Re > 500$ ),  $R = 0.055\pi\rho_{air}v^2d^2$

where  $\rho_{air}$  is the density of the air,  $\eta_{air}$  is the viscosity of the air and  $d$  the diameter of the droplet.

With these expressions and using  $m = \frac{\pi}{6}d^3\rho_{fuel}$ , we obtain:

for laminar flow,  $\frac{dv}{dt} = -\frac{18\eta_{air}}{d^2\rho_{fuel}}v$

(1)

for semi-turbulent flow,  $\frac{dv}{dt} = \frac{0.3\rho_{air}}{d\rho_{fuel}}v^2 - \frac{30\eta_{air}}{d^2\rho_{fuel}}v$  (2)

for turbulent flow,  $\frac{dv}{dt} = -\frac{0.33\rho_{air}}{d\rho_{fuel}}v^2$  (3)

When we integrate these equations we obtain:

for laminar flow,  $v = v_0 e^{-\frac{18\eta_{air}}{d^2\rho_{fuel}}t}$  (4)

and for the penetration of the droplet,  $v = \frac{ds}{dt}$  gives  $s = \frac{d^2\rho_{fuel}}{18\eta_{air}}v_0 \left( 1 - e^{-\frac{18\eta_{air}}{d^2\rho_{fuel}}t} \right)$  (5)

$$\text{for semi-turbulent flow, } v = \frac{1}{\left(\frac{0.01d\rho_{air}}{\eta_{air}} + \frac{1}{v_0}\right) e^{\frac{30\eta_{air}t}{d^2\rho_{fuel}}} - \frac{0.01d\rho_{air}}{\eta_{air}}} \quad (6)$$

$$\text{and for the penetration, } s = \frac{d\rho_{fuel}}{0.3\rho_{air}} \ln \left[ 1 + \frac{0.01d\rho_{air}}{\eta_{air}} v_0 \left( 1 - e^{-\frac{30\eta_{air}t}{d^2\rho_{fuel}}} \right) \right] \quad (7)$$

$$\text{for turbulent flow, } v = \frac{v_0}{1 + \frac{0.33\rho_{air}}{d\rho_{fuel}} v_0 t} \quad (8)$$

$$\text{and for the penetration, } s = \frac{d\rho_{fuel}}{0.33\rho_{air}} \ln \left( 1 + \frac{0.33\rho_{air}}{d\rho_{fuel}} v_0 t \right) \quad (9)$$

**Numerical application:**

We consider a  $10 \cdot 10^{-6}$  m diameter droplet of gasoline discharged by an injection of 120 bar into air at atmospheric pressure and ambient temperature 20 deg C.

So we have:

Droplet diameter,  $d = 10 \cdot 10^{-6}$  m (approximation from PDA measurements performed with our 6 holes multi-streams injector)

Air density at 20 deg C,  $\rho_{air} = 1.205 \text{ kg/m}^3$

Air viscosity at 20 deg C,  $\eta_{air} = 15.11 \cdot 10^{-6} \text{ m}^2/\text{s}$

Gasoline density at 20 deg C,  $\rho_{gas} = 725 \text{ kg/m}^3$

The discharge coefficient can be determined experimentally by measuring the volume of liquid discharged from an atomiser of known orifice size, during a given time interval and with a given pressure drop across the atomiser. If  $V$  is the volume of liquid,  $v$  its velocity,  $a$  the area of the orifice,  $p$  the pressure difference across the orifice and  $t$  the time, then

$$V = avt = atC_d \sqrt{\frac{2gp}{\rho}} \text{ from which } C_d = \frac{V}{at \sqrt{\frac{2gp}{\rho}}}$$



Let's consider one single hole from our 6 holes multi-streams injector whose theoretical static flow rate is  $Q_s = 7.64 \text{ g/s}$  at 70bar with n-heptane (density at 20 deg C,  $\rho_{hept} = 682 \text{ kg/m}^3$ ).

The discharge coefficient for one hole is:

$$C_d = \frac{7.64 * 10^{-3}}{6 * 682} = \frac{0.001273}{4092} = 0.516$$

The initial velocity is  $v_0 = C_d \sqrt{\frac{2gp}{\rho_{gas}}} = 93.89 \text{ m/s}$

The corresponding value of Reynolds number for flow around the droplet is

$$Re_0 = \frac{\rho_{air} v_0 d}{\eta_{air}} = 74.57$$

showing that the flow is initially in the semi-turbulent range.

The flow will become laminar when  $Re = 2$  and then its velocity will be  $v = \frac{v_0 * 2}{Re_0} = 2.52 \text{ m/s}$

The time for the velocity to fall to this value is found from the equation (7) i.e.:

$$2.52 = \frac{1}{\left( \frac{0.01 * 10^{-6} * 1.2}{15.11 * 10^{-6}} + \frac{1}{93.89} \right) e^{\frac{30 * 15.11 * 10^{-6}}{10^{-10} * 725} t} - \frac{0.01 * 10^{-6} * 1.2}{15.11 * 10^{-6}}}$$

giving  $t = 4.999 * 10^{-4} \text{ s}$  i.e. approximately 0.5 ms

The velocity and penetration at any time less than this value are found by inserting the chosen value of  $t$  in the equations (6) and (7):

$$v = \frac{1}{\left( \frac{0.01 * 10^{-5} * 1.2}{15.11 * 10^{-6}} + \frac{1}{v_0} \right) e^{\frac{30 * 15.11 * 10^{-6}}{10^{-10} * 725} t} - \frac{0.01 * 10^{-5} * 1.2}{15.11 * 10^{-6}}} = \frac{1}{\left( 7.94 * 10^{-3} + \frac{1}{93.89} \right) e^{625241t} - 7.94 * 10^{-3}}$$

$$s = 20.14 \ln \left[ 1 + 0.7457 * \left( 1 - e^{-62524t} \right) \right] \text{ m}$$

For  $t > 0.5$  ms, the flow is laminar with an initial velocity  $v_0 = 2.52$  m/s

The velocity and penetration at any time from the beginning of this stage are given by the equations (4) and (5), which become:

$$v = v_0 e^{-\frac{18 * 15.1 * 10^{-6}}{10^{-10} * 725} t} = 2.52 e^{-375145t} \text{ m/s}$$

$$s = 0.67 (1 - e^{-375145t}) \text{ m}$$

So the maximum penetration in laminar flow (when  $t$  is infinite in equation (6)) is 0.67 m.

**Appendix C Hiroyasu model**

(Diesel Engine Combustion and Its Modelling, H. Hiroyasu [143])

We consider the Hiroyasu and Arai (1980) quasi-steady model for spray penetration without swirl whose equations are:

$$\text{For } 0 < t < t_b \quad S = S_1 = 0.39 \left( \frac{2\Delta P}{\rho_{fuel}} \right)^{0.5} t \quad (1)$$

$$\text{For } t_b < t \quad S = S_2 = 2.95 \left( \frac{\Delta P}{\rho_{air}} \right)^{0.25} (d_0 t)^{0.5} \quad (2)$$

$$\text{With} \quad t_b = 28.65 \frac{\rho_{fuel} d_0}{\sqrt{\rho_{air} \Delta P}} \quad (3)$$

Where  $\Delta P = P_i - P_a$  is the difference between the injection pressure and the ambient pressure (Pa) and  $d_0$  is the nozzle hole diameter.

**Numerical application:**

In our case we consider one single hole, from our 6 holes multi-streams injector, whose diameter is  $d_0 = 0.18 \cdot 10^{-3}$  m.

Air density at 20 deg C,  $\rho_{air} = 1.205$  kg/m<sup>3</sup>

Gasoline density at 20 deg C,  $\rho_{gas} = 725$  kg/m<sup>3</sup>




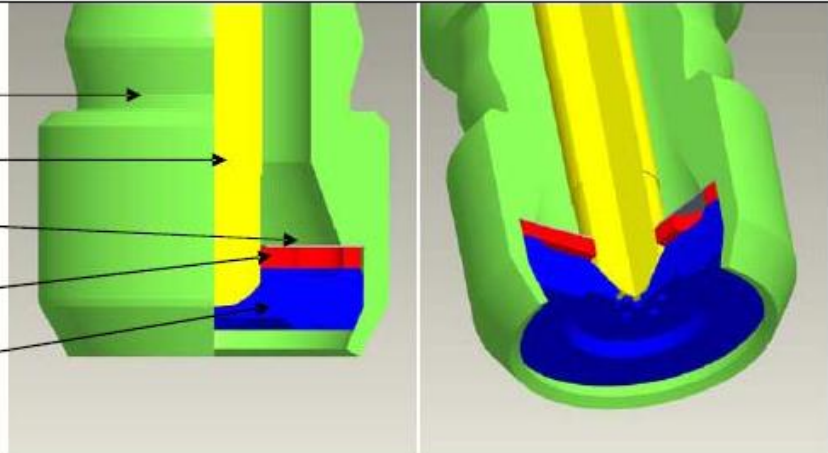
For 1bar backpressure we have  $\Delta P = 120-1 = 119$  bar =  $119 \cdot 10^5$  Pa

With these values, we obtain  $t_b = 1.0058$  ms

For 2, 4, 6, 8 and 10 bar backpressure,  $\Delta P$  is smaller so  $t_b > 1.0058$  ms and for our experimental measurements the time range goes from 0 to 0.8 ms after start of injection so we will be using the equation (1) of the Hiroyasu and Arai model i.e. for 1 bar backpressure at 20 deg C:

$$S = S_1 = 0.39 \left( \frac{2 \cdot 119 \cdot 10^5}{725} \right)^{0.5} t = 70.66 t$$

**Appendix D Geometrical characteristics and functioning of Continental Automotive second generation multi-stream injectors**

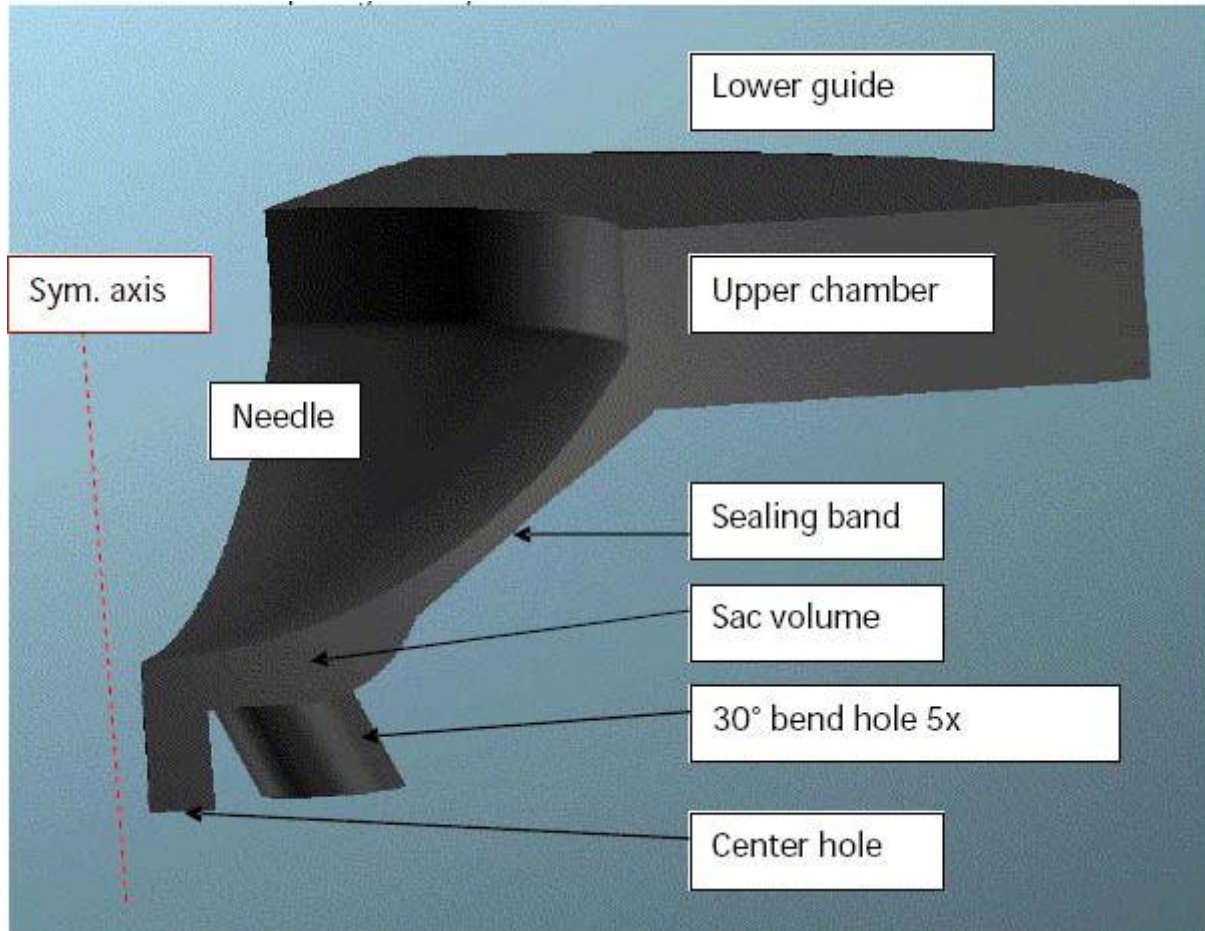
Geometrical Characteristics:				
Hole configurations:	5 to 8 holes ; possibility of center hole			
	<u>Example:</u>	6+0 	5+1 	6+1 
Hole diameter: d	0.17 to 0.28mm			
Hole Length: L (= seat plate thickness)	Low penetration injector: 0.20 mm High penetration injector: 0.46 mm			
L / d	0.7 to 2.5			
Sac-volume:	Without holes : 0.076 mm <sup>3</sup> With holes : maximum 0.450mm <sup>3</sup>			
Maximum hole angle "B" (hole-injector axis)	45°			
Assembly				

**Figure C.1: Geometrical characteristics**

The functioning of the MSI injector is based on the operating mode of a standard solenoid injector:

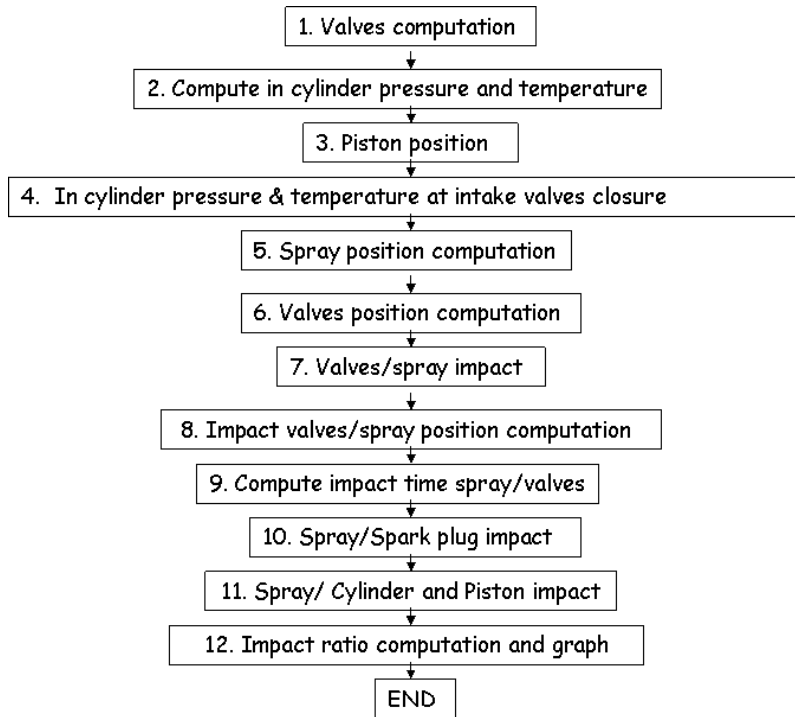
- The injector is pressurised with fuel up to 200bar.
- A current signal applied to a coil creates a magnetic field that creates a magnetic force.
- Applied on the needle, this magnetic opening force is greater than the closing forces (created by the fuel pressure (hydraulic force) and the spring return).
- When the magnetic field is applied, the needle lifts up to a precise cote (55 µm).
- Fuel flows through the sealing gap to the hole inlets.

- Holes are generating spray jets.
- When the current signal stops, the closing forces (hydraulic + spring) move the needle down to its closed position.

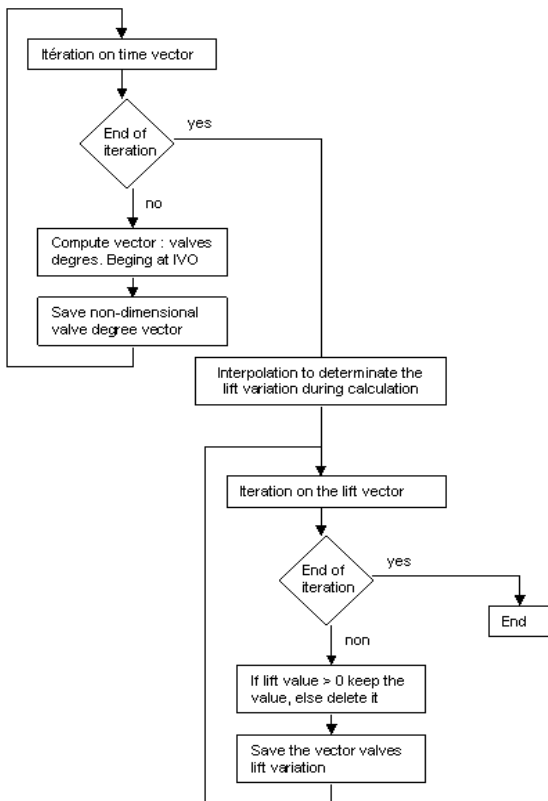


**Figure C.2: Schematic of 1/5 of the injector seat for a 5+1 hole configuration**

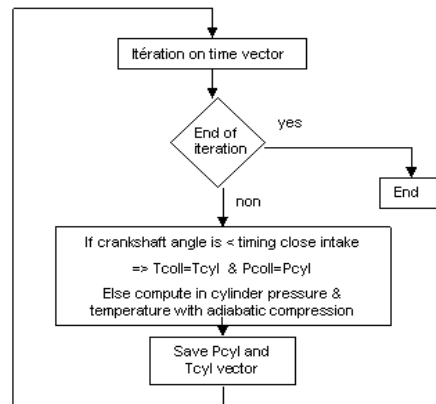
**Appendix E IMPACT tool algorithm**



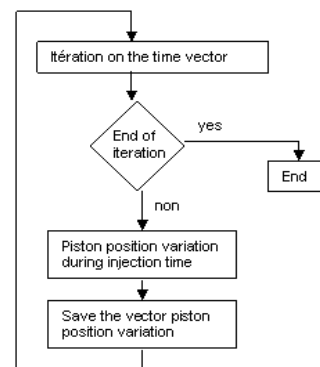
**1. Valves calculation**



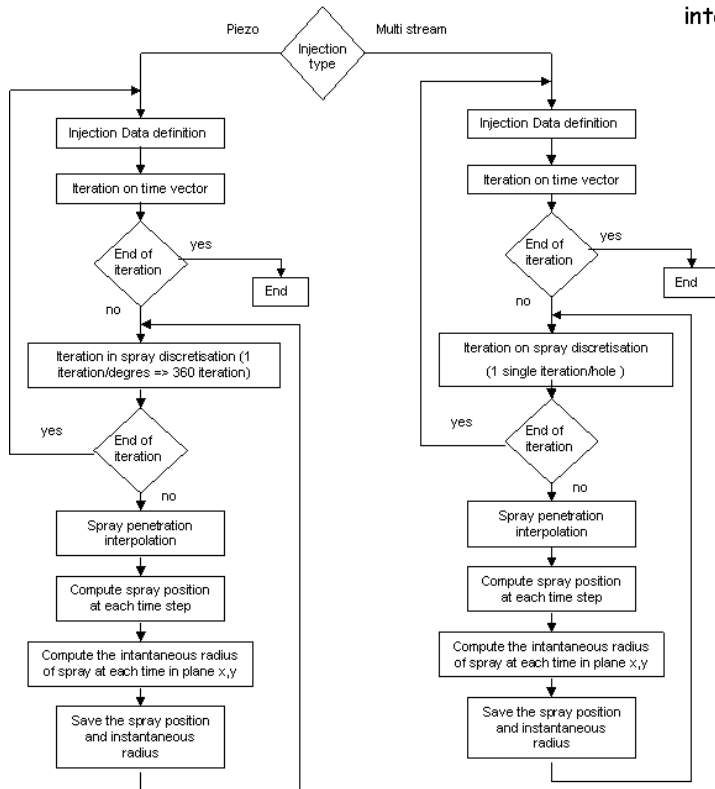
**2. To Compute in-cylinder pressure and temperature**



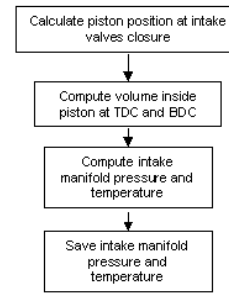
**3. Piston position**



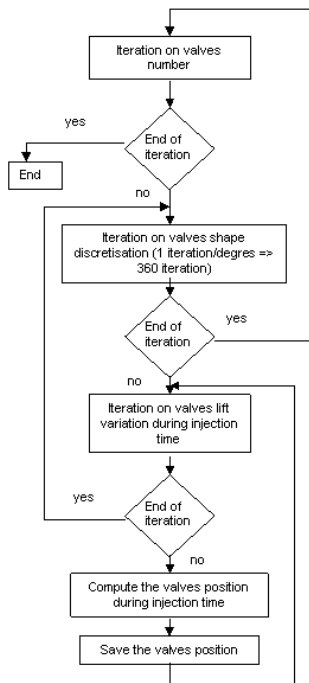
5. Spray position computation



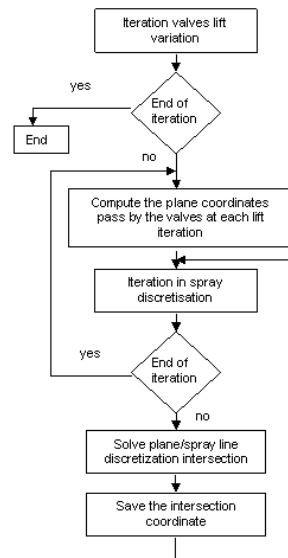
4. In cylinder pressure & temperature at intake valves closure



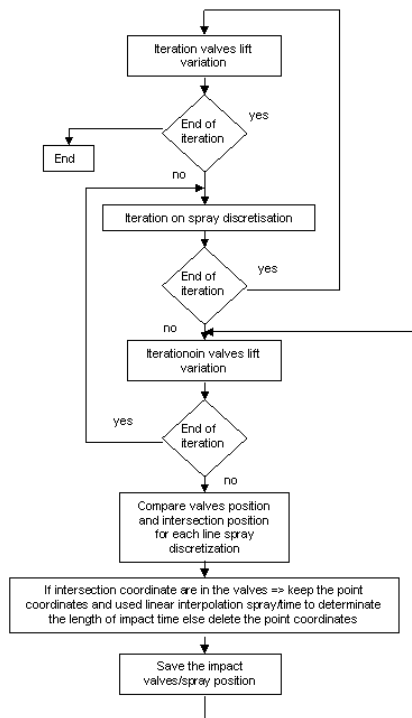
6. Valves position computation



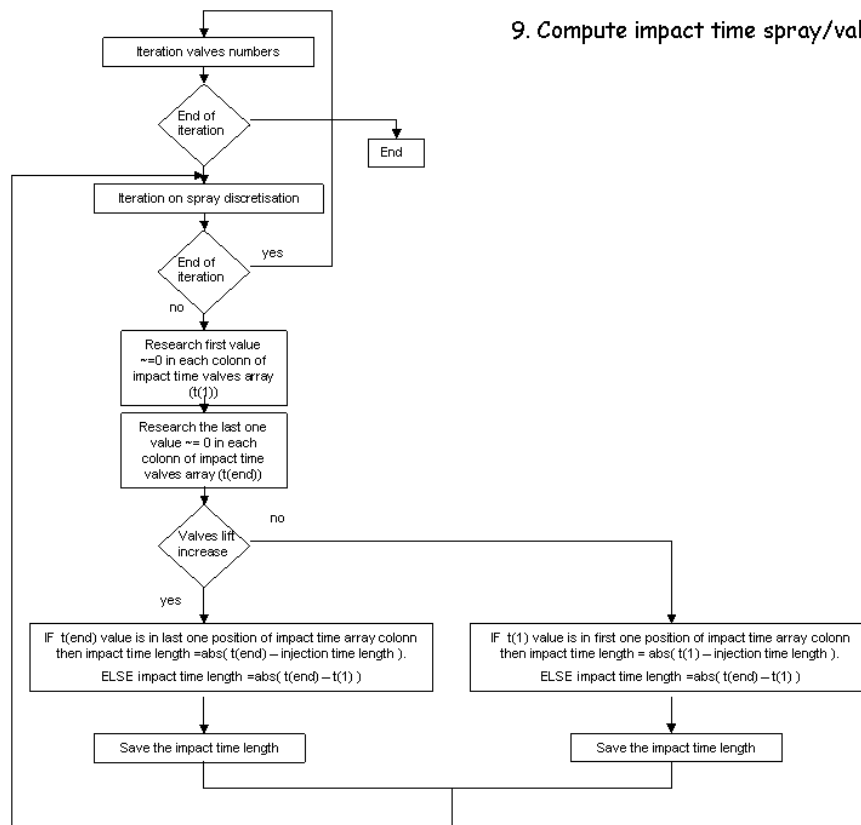
7. Valves/spray impact



8. Impact valves/spray position computation

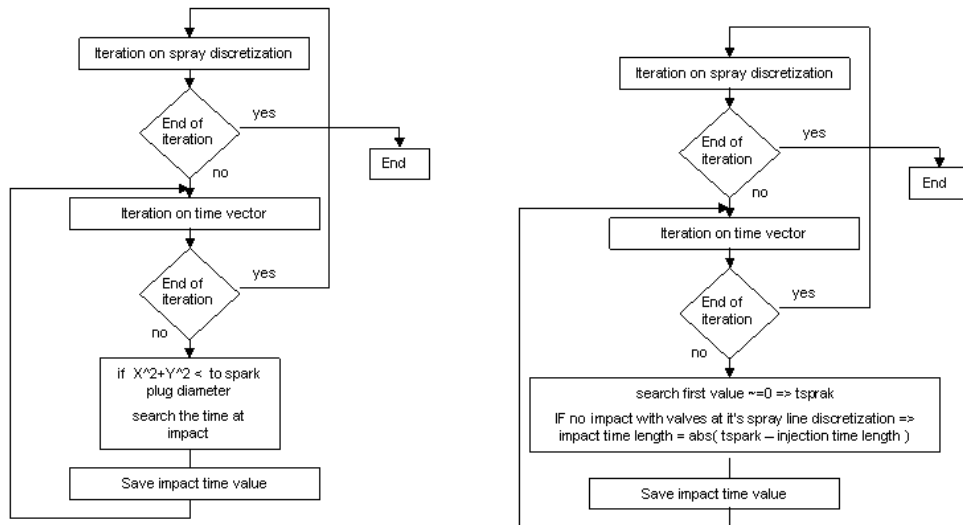


9. Compute impact time spray/valves



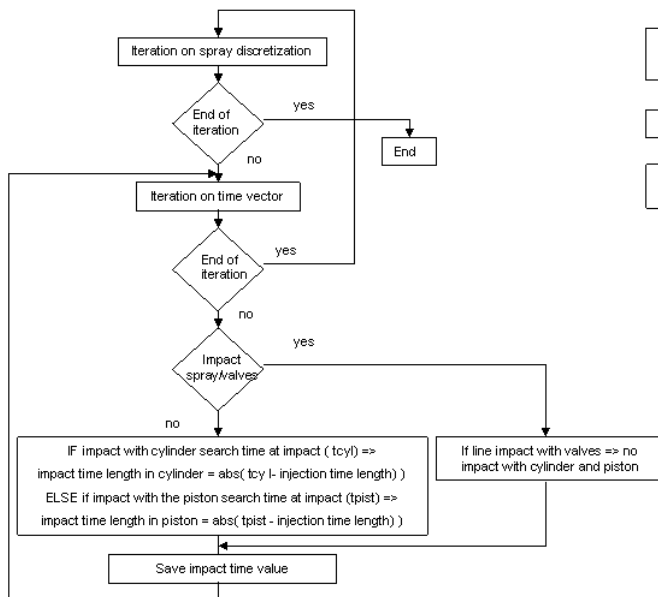


10. Spray/Spark plug impact

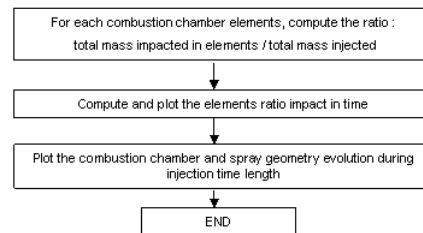


X & Y = spray projection in (X,Y) plan of sprak plug

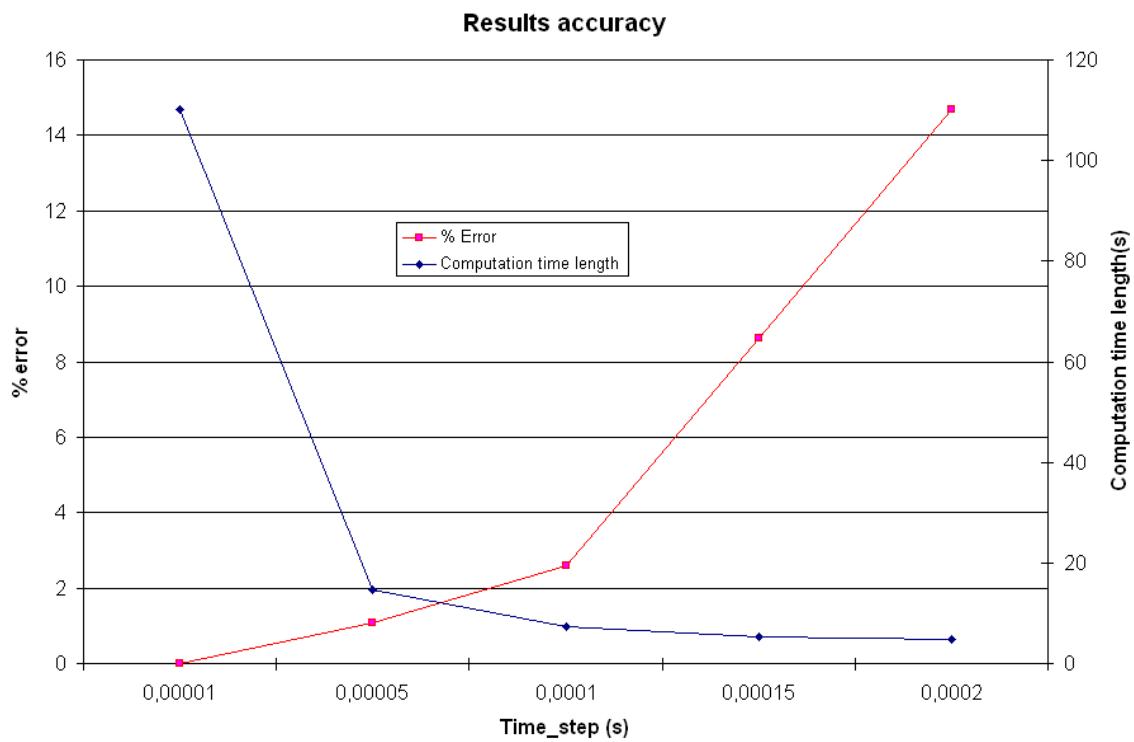
11. Cylinder and Piston spray impact



12. Impact ratio computation and graph

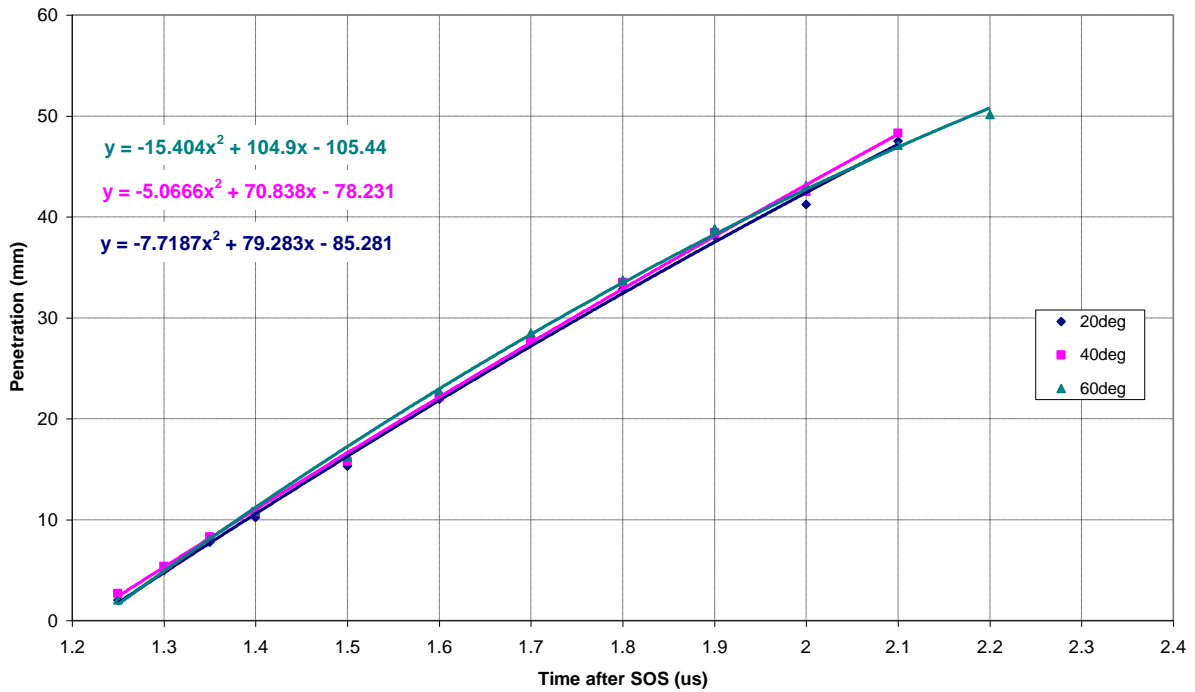


**Appendix F IMPACT results accuracy**

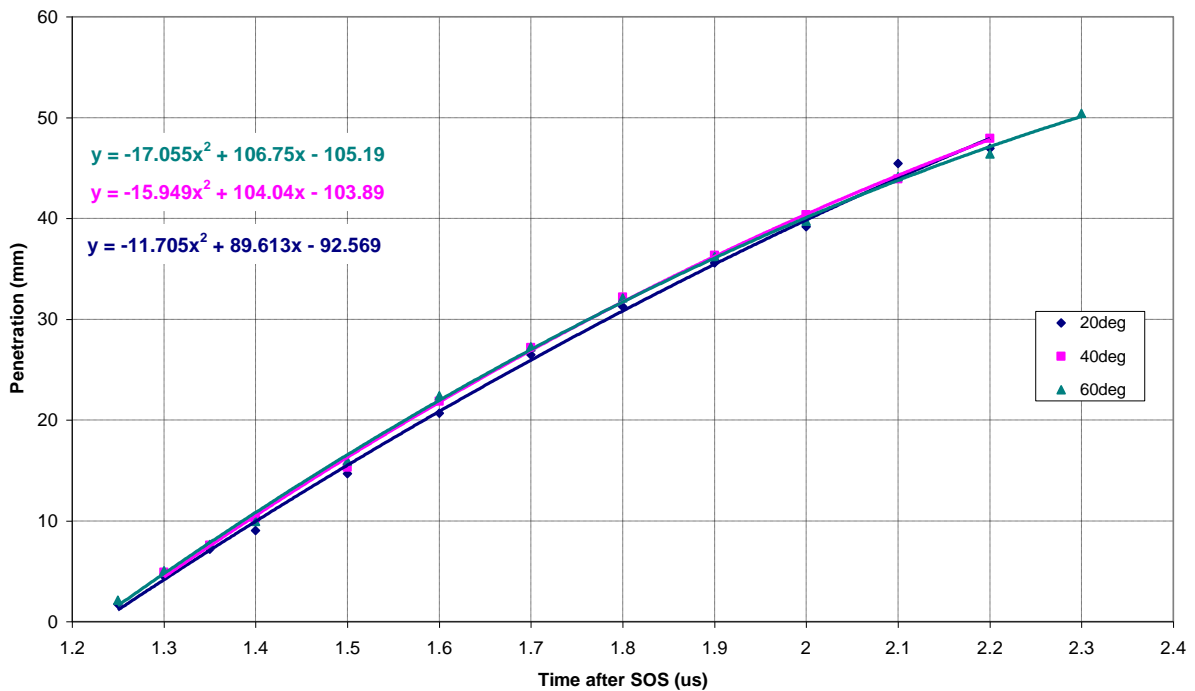


This graph shows the competition between the computation time and the percentage of error as function of the time step. A big time step increases the percentage of error and improves the computation time length. On the contrary, a small time step increases considerably the computation time and improves the results accuracy. In IMPACT we use 0.0001 sec for the time step.

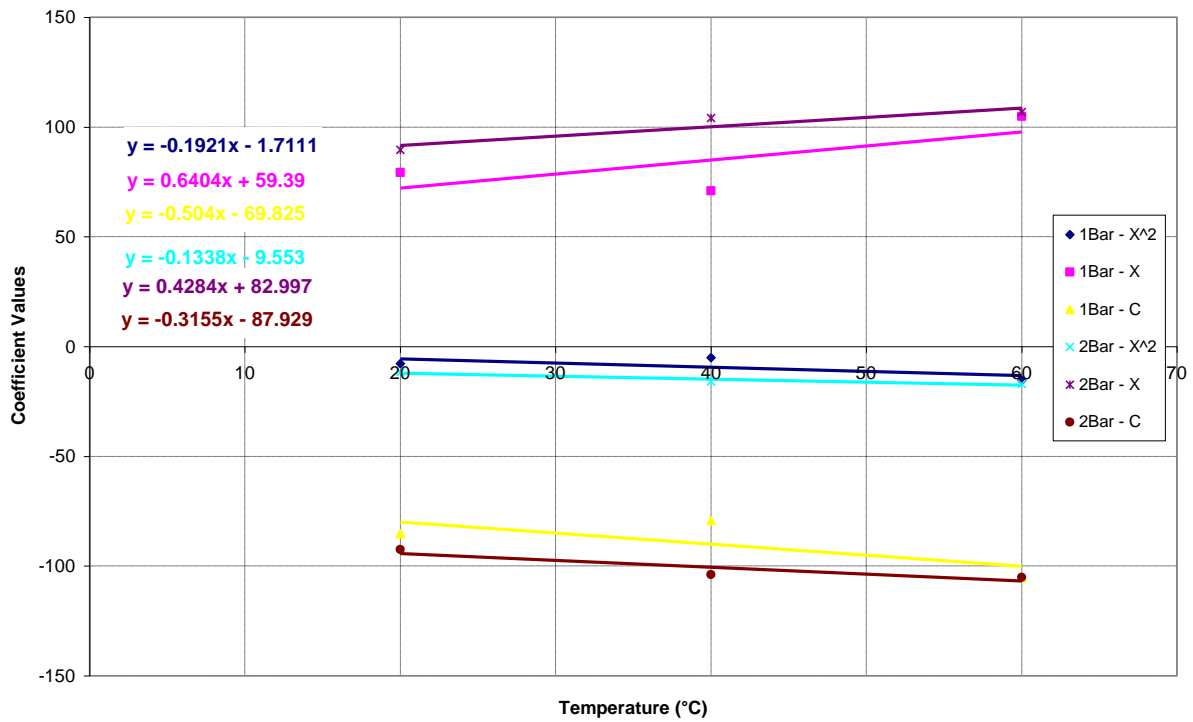
**Appendix G Spray Predictions as a Function of Temperature**



**Figure G 1 – Predictions for axial penetration at 20°C and 1Bar backpressure as a function of temperature**



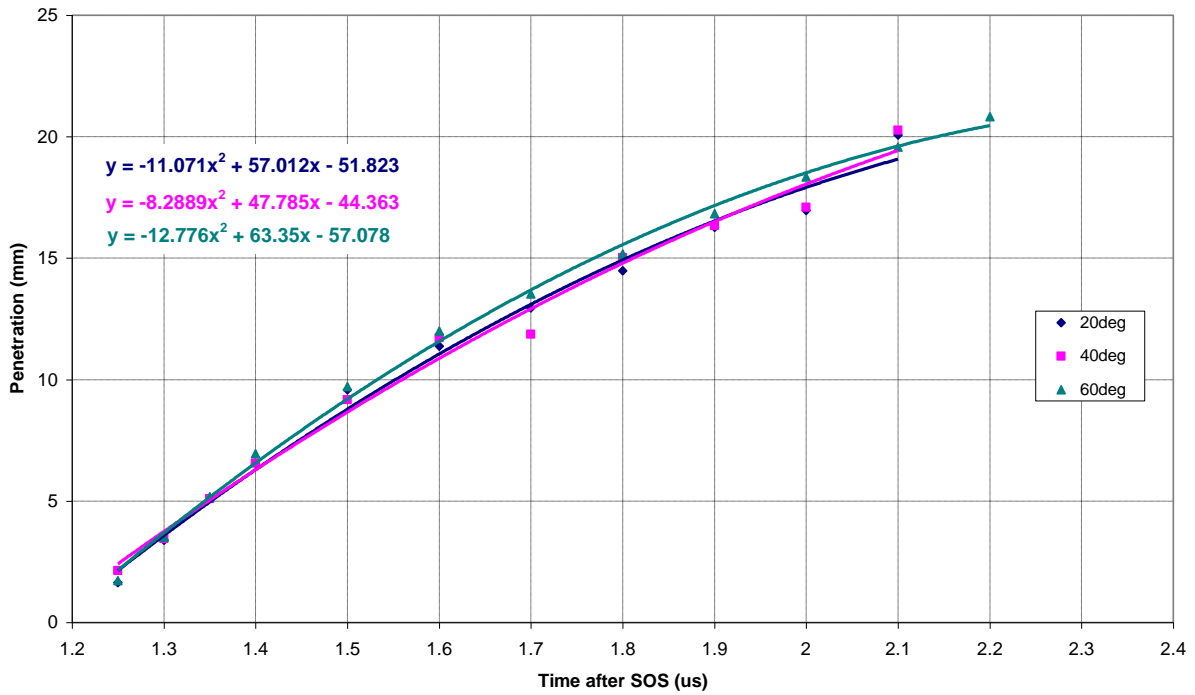
**Figure G 2 – Predictions for axial penetration at 20°C and 2Bar backpressure as a function of temperature**



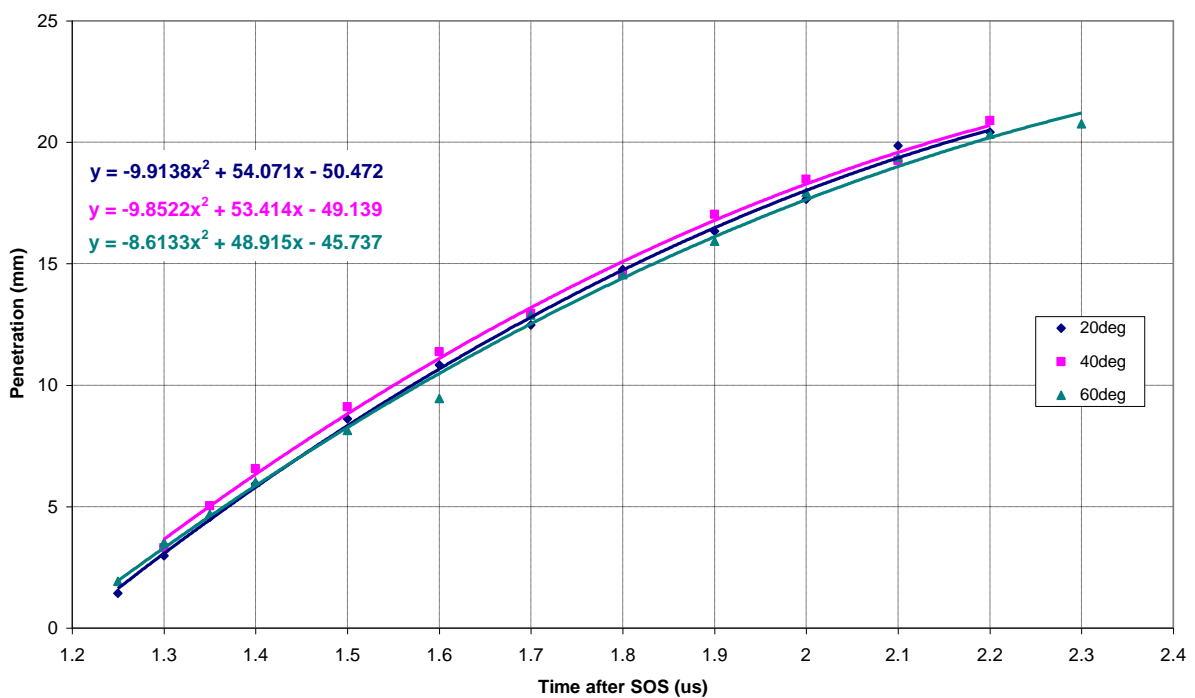
**Figure G 3 - Best fit coefficients for axial penetration as a function of temperature**

$$S_{1\text{Bar}, \text{axial}} = (-0.1921T - 1.7111)t^2 + (0.6404T + 59.39)t + (-0.504T - 69.825)$$

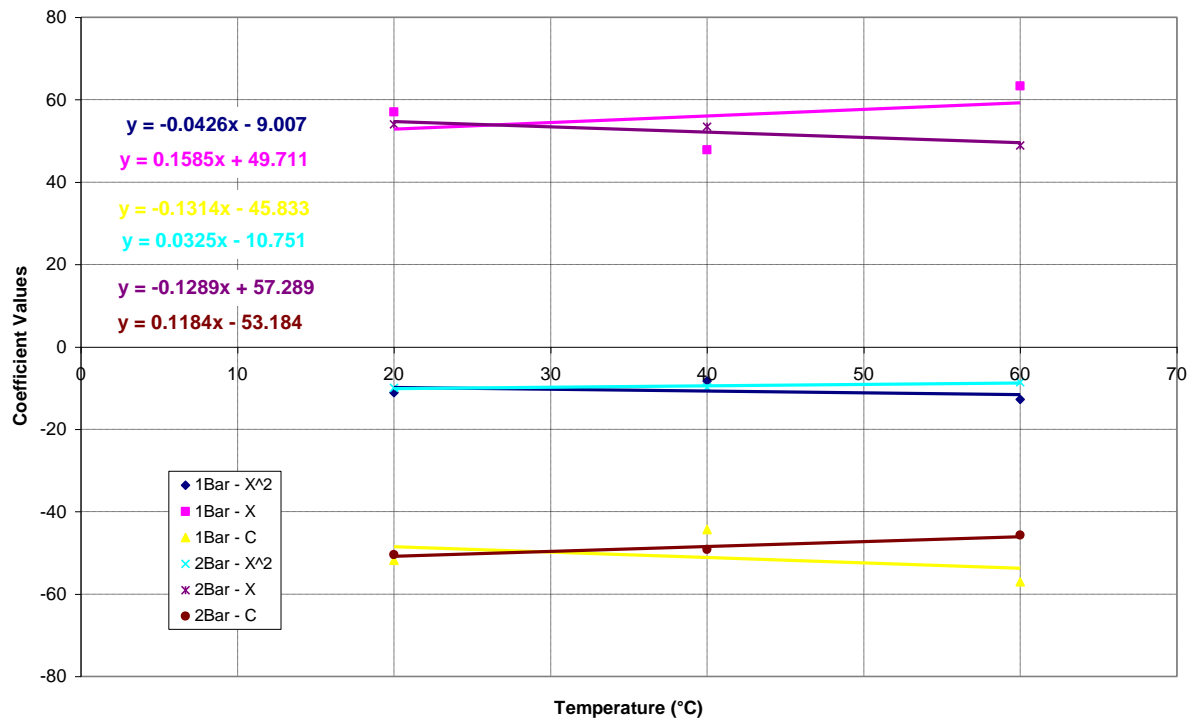
$$S_{2\text{Bar}, \text{axial}} = (-0.1338T - 9.553)t^2 + (0.4284T + 82.997)t + (-0.3155T - 87.929)$$



**Figure G 4 – Predictions for radial penetration at 20°C and 1Bar backpressure as a function of temperature**



**Figure G 5 – Predictions for radial penetration at 20°C and 2Bar backpressure as a function of temperature**

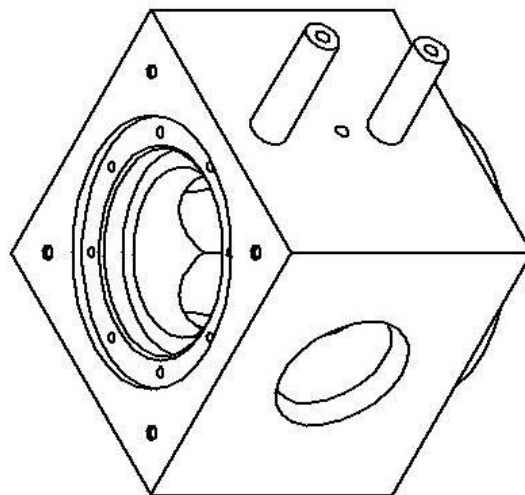
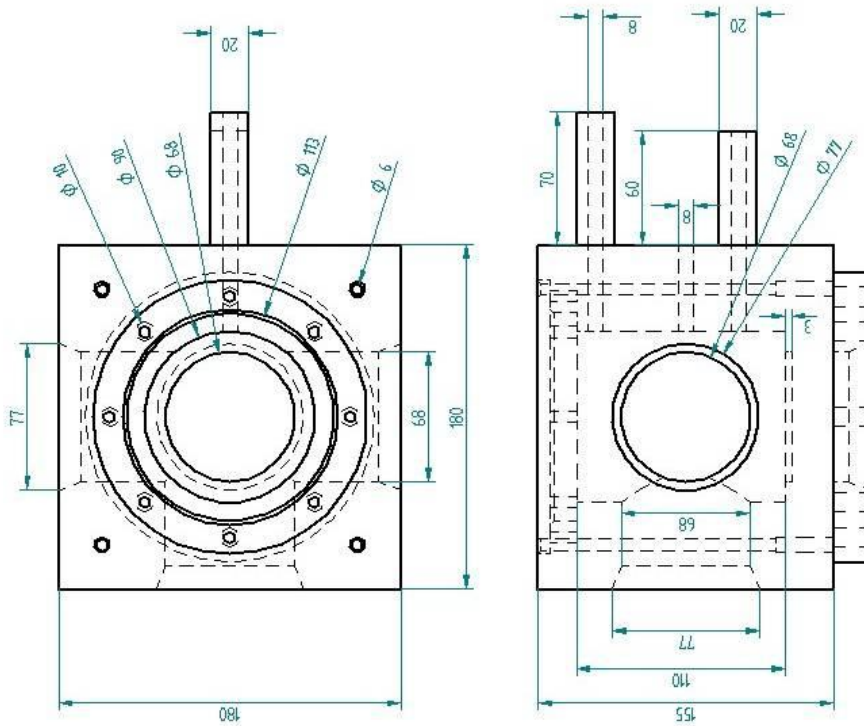


**Figure G 6 - Best fit coefficients for radial penetration as a function of temperature**

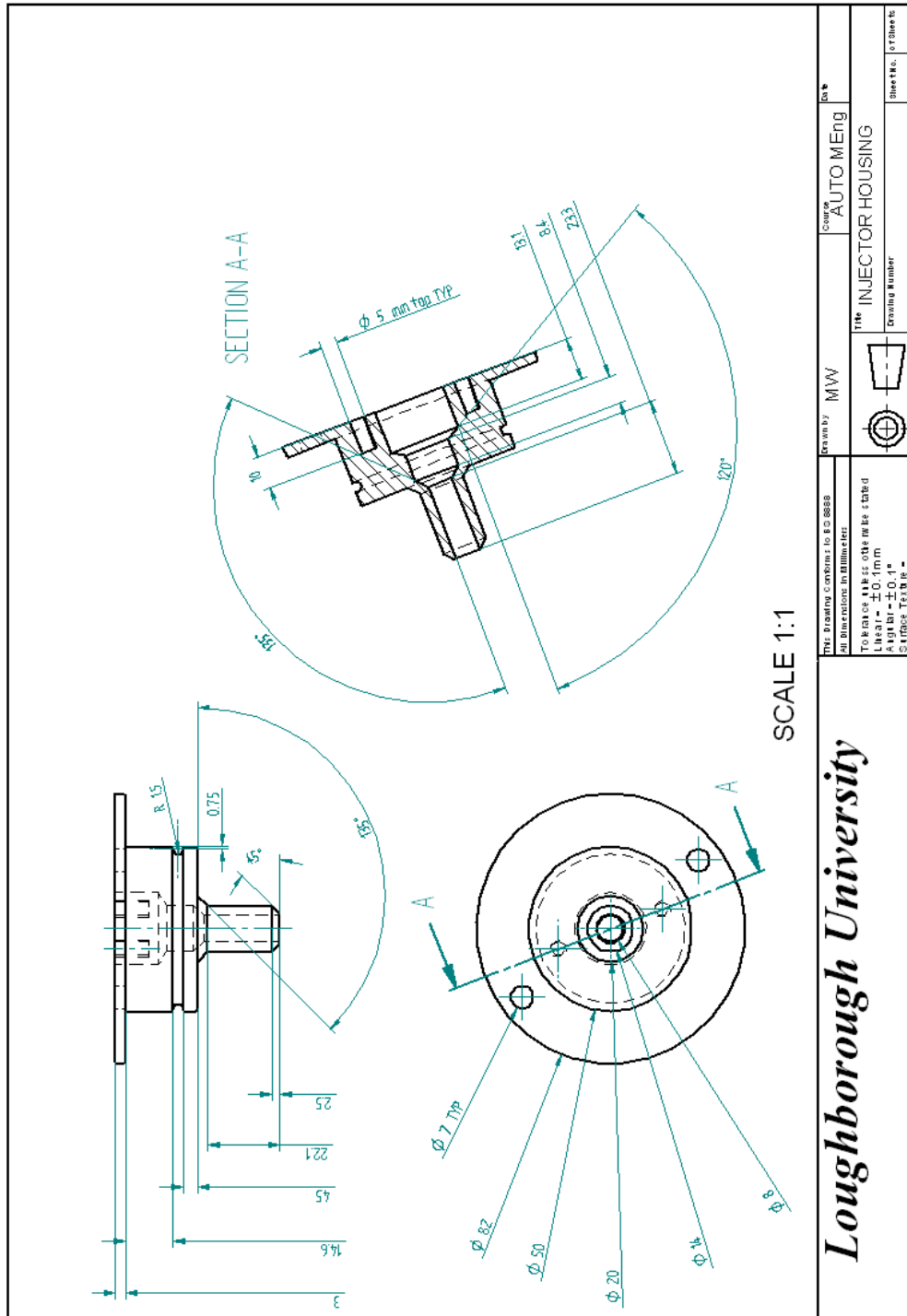
$$S_{1\text{Bar}, \text{radial}} = (-0.0426T - 9.007)t^2 + (0.1585T + 49.711)t + (-0.1314T - 45.833)$$

$$S_{2\text{Bar}, \text{radial}} = (0.0325T - 10.751)t^2 + (-0.1289T + 57.289)t + (0.1184T - 53.184)$$

**Appendix H Technical drawing of the HPHT cell**



Appendix I Technical drawings of the injector housing



**Loughborough University**